Study on Avalanche Breakdown in GaN

March 2020

Takuya MAEDA

Electronic Science and Engineering
Kyoto University

Abstract

Nowadays, reduction of energy losses in power conversion systems is strongly required toward sustainable society. Silicon power devices have been playing the main role in power electronics as a commodity. However, owing to research and development for a long time, Silicon power devices have faced the material limit determined by its physical properties, and it is difficult to improve the device performance drastically.

Gallium Nitride (GaN), which is a direct bandgap semiconductor with a bandgap of 3.42 eV, is one of the most promising candidates as a material for the next-generation power devices. Owing to its high critical electric field ($\sim$3 MV/cm) and high electron mobility, on-resistance of GaN devices can be reduced to 1/1000 compared to Si devices. So far, due to the lack of GaN freestanding substrates, GaN has been grown on foreign substrates such as sapphire, Silicon, and Silicon Carbide. Heteroepitaxial GaN includes a lot of crystal defects and its devices are dominated by effects of the defects. Thus, GaN devices have *lateral* structure to avoid effects of defects such as AlGaN/GaN high electron mobility transistors. On the other hand, recently, GaN freestanding substrates become available and GaN *vertical* devices fabricated on GaN native substrates have attracted much attention. Using this homoepitaxial GaN, it is expected that we can pull out and investigate the material property of GaN unleashed from the effects of the defects. Although there have been some reports on GaN-on-GaN devices which showed excellent performances, fundamental studies on material properties and device physics using GaN-on-GaN are still limited.

An impact ionization coefficient is one of the most important physical properties in a semiconductor material. Since impact ionization coefficients determine breakdown voltage and safe-operating area of a power device, its value is essential to be determined toward precise designing and characterization of a power device. However, for GaN, there are no precise data of the impact ionization coefficients due to the difficulty of the measurement.

For the determination of the impact ionization coefficients, a test device with high avalanche capability and low reverse leakage current is needed. Edge termination to perfectly eliminate electric field crowding at the device edge is necessary. In addition, the measurements of both an electron-injected photocurrent by illumination for a p-type side and a hole-injected photocurrent by illumination for an n-type side are required. However, it is impossible to inject holes from the n^+-side in GaN, since the light penetration depth and the carrier diffusion length are much shorter than the thickness of the substrate.

In this dissertation, the author studies on avalanche breakdown characteristics in GaN power devices. In Chapter 1, the author describes the background of this study and the main unresolved issues of GaN power devices. After that, the purpose of this study is shown.

In Chapter 2, the author proposes the beveled-mesa termination as an edge termination for GaN devices. Using TCAD simulation, the author quantitatively shows the design strategy of the beveled-mesa termination that a shallow beveled-mesa and a lightly doped p-layer are effective to alleviate electric field crowding. In addition, GaN p-n junction diodes with negative beveled-mesa termination are demonstrated, which clearly showed the alleviation of electric field crowding.

In Chapter 3, the breakdown characteristics of the GaN p-n junction diodes with double-side-depleted sallow bevel termination, in which electric field crowding does not occur, were investigated. The fabricated devices showed low reverse leakage current, high avalanche capability, increase in the breakdown voltage with elevating temperature and uniform luminescence at breakdown. These are strong evidences that uniform (nearly ideal) avalanche breakdown occurs in the devices. The devices exhibited the breakdown field of 2.8–3.5 MV/cm, which are the best among all the GaN devices reported previously.

In addition, the GaN p^+/n^- and p^-/n^+ junction diodes were fabricated and their breakdown characteristics were investigated. The breakdown characteristics in GaN did not depend on the conduction types of the drift layers. This result indicates that the difference between the impact ionization coefficient of electrons and that of holes is not so large. This is consistent with the results in Chapter 5.

In Chapter 4, the optical absorption induced by the Franz-Keldysh effect in GaN devices under high electric field was investigated. Under sub-bandgap illumination, a photocurrent in GaN p-n junction diodes significantly increased with increasing reverse-bias voltage. The increase was prominent as the wavelength approached to the fundamental absorption edge of GaN. The author calculated the photocurrent with consideration of the absorption coefficients in depletion layer as a function of electric field, and the voltage and wavelength dependences of the photocurrent were successfully reproduced well.

In Chapter 5, the author proposes a novel method to measure the impact ionization coefficients of electrons and holes. Utilizing the above- and sub-bandgap illuminations for GaN p^-/n^+ junction photodiodes, the electron-injected and hole-injected (Franz-Keldysh-induced) photocurrents were obtained, respectively. Based on the elaborate calculation of the unmultiplicated photocurrents, the multiplication factors were extracted with a wide range precisely. By analyzing the obtained multiplication factors, the impact ionization coefficients of electrons and holes in GaN were extracted separately. The simulated avalanche breakdown characteristics using the obtained data well reproduced the experimental data, indicating that the obtained impact ionization coefficients are precise and reliable.

In Chapter 6, the author summarizes this study and shows the future prospects.

Acknowledgements

This dissertation was written based on the work done at Kyoto University, Japan, where I did my Ph.D. studies. During this time, many people supported and encouraged me in so many ways, and I would like to express my deep gratitude to all of them.

First of all, I would like to express my most sincere gratitude to Professor Tsunenobu Kimoto for his continuous and attentive supervision, invaluable advices and suggestions, and ceaseless encouragement through fruitful discussions. I have been deeply inspired by not only his research philosophy but also his generous and graceful personality. I would like to thank Professor Hirofumi Yamada and Associate Professor Mitsuru Funato for their valuable advice and critical comments as well as suggestions through refereeing this dissertation.

I am especially obliged to Professor Jun Suda in Nagoya University, who had been Associated Professor in Kyoto University until March 2017. He always provided me with many constructive, wonderful advises and stimulating comments as well as continuous encouragement and support on this work. I strongly feel that his affectionate and sometimes strict guidance and education extremely grew me in my Ph.D. life. I would like to express my deep gratitude to Associate Professor Masahiro Horita, who had been Assistant Professor in Kyoto University until September 2018. He always kindly gave me constructive comments and instructed me how to use experimental facilities. Owing to his help, I could conduct my experiments smoothly in Rohm Plaza of Kyoto University and C-TECs of Nagoya University. I also express my sincere gratitude to Prof. Yuji Ando for valuable discussions.

I would like to greatly appreciate Assistant Professor Yusuke Nishi for his valuable comments, support in my daily work and whole maintenance management of experimental systems. I would like to also thank to Assistant Professor Mitsuaki Kaneko for his insightful comments and warm encouragements. I would like to express my gratitude to Assistant Professor Hajime Tanaka for his providing me with a lot of constructive comments and suggestions through fruitful and deep discussions. I also thanks to Assistant Professor Takafumi Okuda for his a lot of fruitful discussions.

I express my deep gratitude to Professor Shizuo Fujita and Lecture Kentaro Kaneko for their constructive comments and suggestions not only about research at various conferences and Rohm Plaza. I also express my deep gratitude to Professor Yoichi Kawakami and Assistant Professor Ryota Ishii for their stimulating comments and invaluable suggestions especially in conferences on nitride semiconductors.

I would like to special acknowledge Professor Tetsu Kachi in Nagoya University for providing me with an opportunity of collaborative works about avalanche breakdown in GaN with Toyota Central R&D Labs., Inc. and Nagoya University. He gave me a great deal of his invaluable comments and warm encouragement. I would like to express my deep gratitude to Dr. Tetsuo Narita in Toyota Central R&D Labs., Inc. Through our collaborated work, he always gave me fruitful discussions, stimulating comments and constructive suggestions. Owing to his growth technique of a homoepitaxial GaN, I could obtain the devices as I designed. I would also like to express my deep gratitude to Dr. Masakazu Kanechika, Dr. Hiroyuki Ueda and Dr. Tsutomu Uesugi in Toyota Central R&D Labs., Inc. for their constructive comments and suggestions. Owing to their help, the shallow beveled-mesa structure for GaN p-n junction diodes was successfully formed. In addition, I would like to express my gratitude to Mr. Shinji Yamada in Nagoya University for his constructive comments and suggestions. Owing to his help, the vertical deep mesa structure for GaN p-n junction diodes was obtained by ICP-RIE system. I also thanks to Mr. Hideki Sakurai in Nagoya University for his gracious support in my stay in Nagoya University, and I enjoyed fruitful discussions about Mg-ion implantation into GaN. I also thanks to Mr. Takashi Ishida for his comments and fruitful discussions.

I would like to express my gratitude to Dr. Masaya Okada, Dr. Masaki Ueno and Dr. Yoshiyuki Yamamoto for constructive comments and suggestions, and their help for my study on a GaN Schottky barrier diode.

I would like to deep express my deep gratitude to Professor Debdeep Jena, Professor Huili Grace Xing, Dr. Zongyang Hu, Mr. Wenshen Li in Cornell University for the discussion of the analysis method of recombination current in a p-n junction diode. In addition, I am much indebted to Professor Debdeep Jena, Prodessor Huili Grace Xing and Dr. Kazuki Nomoto for their gracious host in Cornell University and giving me the opportunities of my seminar talks prior to IEDM2018 and IEDM2019. I am very looking forward to joining their group as a postdoc after getting my Ph.D.

I would like to express my sincere gratitude to Professor Shigefusa F. Chichibu in Tohoku University for the discussion of the minority carrier lifetime, capture cross sections and origins of the non-radiative recombination centers in GaN. In addition, I would like to thank Professor Shigefusa F. Chichibu, Associated Professor Kazunobu Kojima and Assistant Professor Kohei Shima in Tohoku University for their kind host in Tohoku University and giving me the opportunity of my seminar talk prior to IWN2018.

I would like to show my deepest gratitude to Dr. Shigeyoshi Usami in Mitsubishi Electric Co., who was in a student in Nagoya University (Amano Laboratory), for the fruitful and invaluable discussions of reverse-bias characteristics of GaN p-n junction diodes many times. He provided me with a lot of insightful and constructive comments, cheerful encouragements and interesting conversations. In addition, Dr. Shigeyoshi Usami and I engaged as leaders of the IWN2018 student event, and I would like to express my deep gratitude to all the stuff members.

I would like to express my gratitude to Professor Tetsuo Hatakeyama in Toyama Prefecture University for fruitful and deep discussions about current-transport mechanism in Schottky barrier diodes and impact ionization coefficients in SiC. I also express my gratitude to Associate Professor Yuichiro Matsushita in Tokyo Institute of Technology for the discussion of the first principle calculation. I also thank to Dr. Kazuhiro Mochizuki in National Institute of Advanced Industrial Science and Technology for his insightful comments about the thermionic emission-diffusion transport in a GaN Schottky barrier diode. I would like to express my deep gratitude to Dr. Fumimasa Horikiri in SCIOCS for his fruitful comments and information about photoelectrochemical etching for GaN. In addition, he gave me a lot of constructive and stimulating comments in many conferences. I would like to show my gratitude to Assistant Professor Momoko Deura and Assistant Professor Takuya Hoshii for their organizing ISYSE, which provides young researchers with great opportunities of communication and interaction.

I express my deep gratitude to Dr. Hiroki Niwa in Mitsubishi Electric Co., who was my senior colleague, for his insightful and constructive comments. Owing to his doctoral thesis on the impact ionization coefficients in SiC, I could well understand avalanche breakdown in SiC and also deepen my study on GaN. I also thank Dr. Takuma Kobayashi in Friedrich-Alexander-Universität (FAU) Erlangen-Nürnberg, who was also my senior colleague, for his insightful comments, suggestions and encouragements (often with a couple of bottles of wine). I would like to deep gratitude to Mr. Naoki Sawada and Mr. Kazutaka Kanegae in "GaN group" in Kyoto University for the fruitful discussions on Hall-effect measurements and DLTS studies in GaN. Especially, I spent wonderful time with Mr. Kanegae for 4 years and attended a lot of conferences together. I am also very indebted to his kind instruction and maintenance of electrode deposition systems. I would like to thank Mr. Xilun Chi for the discussion of reverse-bias characteristics of 4H-SiC p-n junction devices. Owing to the devices fabricated by him, I could investigate the Franz-Keldysh effect in 4H-SiC and its anisotropy. I express my gratitude to Dr. Stefanakis Dionysios in Kyoto University for the discussion of the impact ionization coefficients in SiC, and he also helped my simulation study. I also thank Mr. Masahiro Hara in Kyoto University and Mr. Ryosuke Murase in Nagoya University for the invaluable discussions of Schottky interface characteristics in SiC and GaN.

I would like to express my gratitude to Mr. Akifumi Iijima, Mr. Taro Enokizono, Ms. Kana Hiramatsu, Mr. Ying Xin Zhao, who were my colleague in Kimoto Lab., for sharing pleasant time in our laboratory. I would also thank to Mr. Keito Aoshima in Nagoya University for his kind help and support in my stay in Nagoya University.

I would express my deep gratitude to Mr. Yoshinobu Matsuda for his kind mentoring in my internship in Kawakami Lab. and fruitful discussions in many conferences. I also express my gratitude to Ms. Riena Jinno in Fujita Lab. for her stimulating comments and suggestions. I also thank Mr. Katsuhiro Kishimoto in Kyoto University, Mr. Takumi Yamada in Osaka University, Mr. Shota Kaneki in Hokkaido University, Mr. Yuto Ando,

Mr. Kazuki Ohnishi, Mr. Hayata Fukushima, Mr. Seiya Kawasaki in Nagoya University for the fruitful discussions and cheerful conversations in various conferences.

I would like to thank Mr. Masahiro Nakadai, Mr. Sou Hasegawa, Mr. Tomoharu Karashima, Mr. Ryuki Toyomoto and Mr. Takaaki Ikebata in Kyoto University for sharing pleasant time and giving me heartful encouragements. I also thank Mr. Shinichi Kan and Mr. Shuma Fujita. I am very proud of my precious memories spending with them in Rohm Plaza of Kyoto University.

I would like to thank Mr. Takahiro Murotani in Kyoto University. I have been very encouraged and motivated by him through fruitful and interesting discussions every time as a good friend.

My special thanks also go to all members in Kyoto University (Kimoto Laboratory), Dr. Hirokazu Fujiwara, Dr. Hironobu Akita, Dr. Yuichiro Tokuda, Dr. Satoshi Nakazawa, Dr. Satoshi Asada, Mr. Hiroki Sasakura, Mr. Hiroaki Fujihara, Mr. Kyosuke Yamada, Mr. Yutaka Kuriyama, Mr. Eiji Saito, Mr. Kazuto Hirai, Mr. Keita Tachiki, Mr. Takahisa Ono, Mr Shunsuke Kamata, Mr. Ryosuke Matsui, Mr. Koji Ito, Mr. Naoki Kanegami, Mr. Masashi Nakajima, Mr. Toshiki Miyatani, Mr. Shoma Yamashita, Mr. Masaya Arahata, Mr. Chansoon Koo, Mr. Toshiya Kobayashi, Mr. Yuto Tsuchiya, Mr. Kazutaka Yamada, Mr. Takuya Ohku, Mr. Ryoya Ishikawa, Mr. Makoto Imuro, Mr. Mizuki Sato, Mr. Qimin Jin, Mr. Eui Hyeon Do, and I also thanks to all members in Nagoya University (Suda Laboratory), Mr. Keisuke Sakao, Mr. Koki Tsurimoto, Mr. Meguru Endo, Mr. Satomu Furuta, Mr. Shohei Rokuno, Mr. Num Kyumgpil, Mr. Tomohiro Ueda, Mr. Junya Sawada, Mr. Yuichi Shibata, Mr. Daiki Tanaka, Mr. Kazufumi Hirukawa.

For very kind support in my daily work, I also wish to thank Ms. Yoriko Ohnaka in Kimoto Laboratory and Ms. Yuki Ishida in Suda Laboratory.

This work was supported in part by the Japan Society for the Promotion of Science (JSPS) through the Grant-in-Aid for Research Fellow (18J20080). This work was also supported by the Council for Science, Technology and Innovation (CSTI), the Cross-ministerial Strategic Innovation Promotion Program (SIP), Next-generation power electronics (funding agency: NEDO), and MEXT "Program for research and development of next-generation semiconductor to realize energy-saving society". The author also thanks to Murata Science Foundation, Kyoto University Foundation and Marubun Research Promotion Foundation for their travel and participant grants for oversea international conferences.

Finally, I sincerely wish to thank my parents for their understanding, support, and heartfelt encouragement.

Takuya MAEDA

Kyoto, March 2020

Contents

Chapter 1

Introduction

1.1 Background

The invention of semiconductor-based solid-state devices is one of the greatest innovations in the human history. Large scale integrated circuits (LSI) based on complementary metal-oxide-semiconductor (CMOS) technology enabled a variety of electrical products such as computers and smart phones, and they keep evolving. The spread of the Internet to the people has been changing our society significantly and drastically.

The role of semiconductor devices is not limited to the logic and memory operations. Semiconductor devices play a role of "transformation of energy". Electrical energy can be transformed to optical, thermal and mechanical energy, and their inverses can be also transformed by, for example, light emitting diodes, solar cells, Seebeck thermocouple devices, Peltier devices, piezoelectric sensors and actuator devices, etc. Of course, the transformation from electrical energy to electrical energy is possible and very important.

The electrical power conversion through semiconductor devices, "power electronics", which converts electric power itself (voltage, frequency, etc.) into the suitable form so that electrical power can be transmitted and supplied with minimum energy loss, is a key building block in our society. However, the efficiency of power conversion is typically 85–95% using currently available technology, which is not high enough, because approximately 10% of the electric power is lost as heat at every power conversion. In general, the efficiency of power electronics is mainly limited by the performance of semiconductor power devices. Reduction of energy losses in power devices is one of the most crucial issues of this century.

Power devices have only two roles as a rectifier or a switch working as "ON" or "OFF". A diode and a transistor, which consist of p-n junction, Schottky and Ohmic (metal/semiconductor) junction, and/or MOS structure, are used as a rectifier and a switch, respectively. Power devices are desired to work as 0 Ω conductors at the ON-state and ∞ Ω resistors at the OFF-state without breakdown. However, an actual device has on-resistance (R_{on}), turn-on voltage (V_{on}), breakdown voltage (V_{B}) and reverse leakage current. Hence, energy losses intrinsically occur in power electronics.

Major applications of power devices include power supplies, motor control, heating, robotics, electric/hybrid vehicles, traction, lighting ballasts, and electric power transmission, as shown in Fig. 1.1 [1]. The development of high-voltage and low-loss power devices is also essential for the construction of future smart grids.

Nowadays, Silicon (Si) is commonly used to fabricate a power device owing to the availability of high-quality and large-area wafers. Furthermore, the demand to the logic application has boosted the enormous amount of fundamental studies in both material physics and process technologies in Si. Owing to long-standing of research and development more than 50 years, Si power devices such as metal-oxide-semiconductor field effect transistors (MOSFETs) and insulated gate bipolar junction transistors (IGBTs) are used in low power systems such as consumer electronics, and high power systems such as motor control in railway or electric vehicles. However, Si power devices have been matured and faced to the material limit. Although there have been attempts to overcome the classical-physical limit by introducing novel device structures, it is getting extremely difficult to improve the performance of the Si power devices significantly. Toward the sustainable society in the future, drastic reduction of energy losses in power conversion systems, which Si cannot realize, is needed.

For unipolar devices with non-punch-through structure, both R_{on} and V_{B} are determined by a thickness and a doping concentration of a voltage-blocking layer and written as

$$R_{\mathrm{on}} = \frac{1}{en\mu} \cdot \frac{d}{A}, \quad V_{\mathrm{B}} = \frac{W_{\mathrm{b}} E_{\mathrm{cr}}}{2}. \tag{1.1}$$

Then, there is the trade-off relationship between R_{on} and V_{B}, which can be written as [2]

$$R_{\mathrm{on}} A = \frac{4V_{\mathrm{B}}^2}{\varepsilon_{\mathrm{s}} \mu E_{\mathrm{cr}}^3}. \tag{1.2}$$

e, n, μ are the elementary charge, a carrier concentration and a carrier mobility, respectively. d and A are a thickness of a voltage-blocking layer and a device area, respectively. W_{b} is a depletion layer width at breakdown. E_{cr} is the critical electric field, which is defined as the maximum electric field in a semiconductor device at the ideal breakdown. ε_{s} is the dielectric constant of a semiconductor. This relationship strongly depends on E_{cr} because R_{on} is proportional to E_{cr}^{-3}. It should be noted that this unipolar limit of R_{on} versus V_{b} is for the resistance of the voltage-blocking layer. The resistance of an actual power device includes other parasitic components which are not negligible.

For power devices, the breakdown mechanism is basically "avalanche breakdown". Under high reverse bias, carriers are accelerated, and when they obtain energy sufficiently higher than the bandgap, they cause impact ionizations and generate electron-hole pairs. The generated carriers also cause impact ionization continuously, resulting in carrier multiplication. When the bandgap is wide, a carrier needs high energy to cause an impact ionization, resulting in high critical electric field (small impact ionization coefficients). Recently, new semiconductor materials with a *wide-bandgap* have attracted much attention as promising candidates for the next-generation power devices.

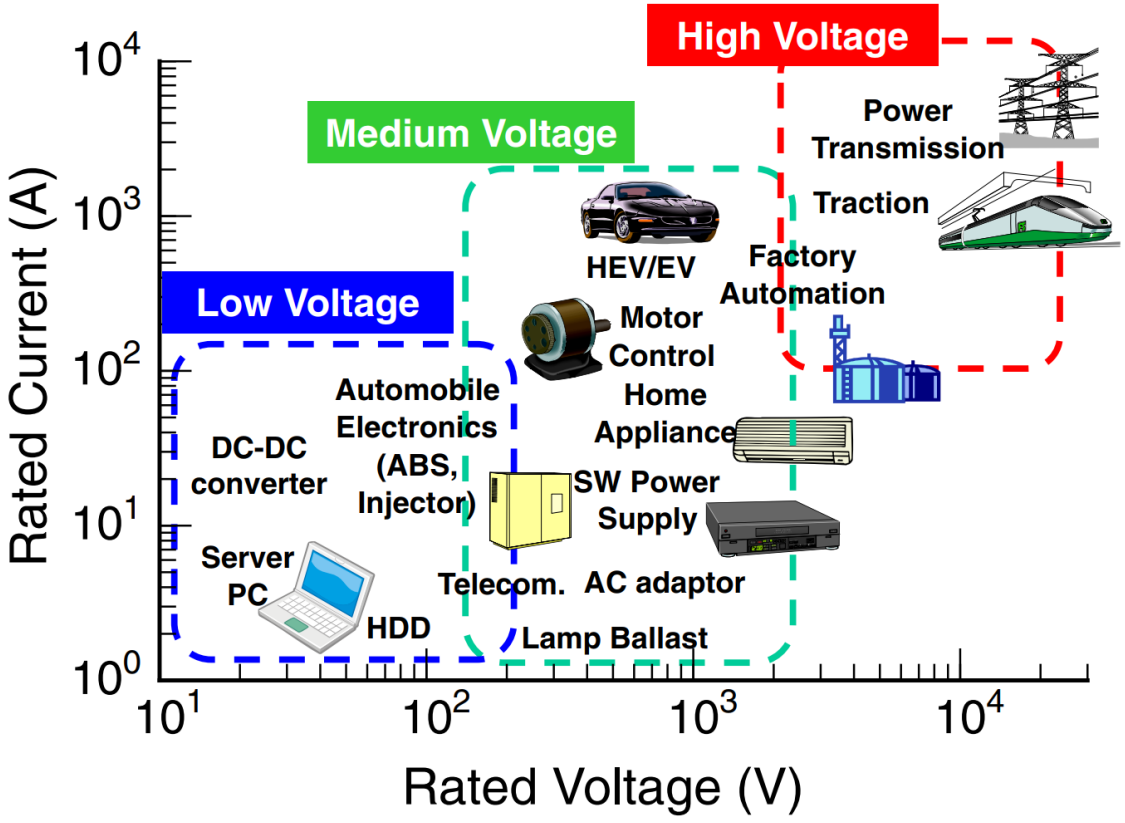

Figure 1.1: Major territories of individual unipolar and bipolar power devices for Si and SiC in terms of the rated blocking voltage.

1.2 Wide-Bandgap Semiconductors: "Beyond Si"

Silicon Carbide (SiC), Gallium Nitride (GaN), Gallium Oxide (Ga_2O_3), Diamond, etc. are known as wide-bandgap semiconductors, which are promising candidates as a "Beyond Si" material for the high V_B and low R_{on} power devices owing to their high E_{cr}. Table 1.1 shows the physical properties of Si, GaAs, 4H-SiC and GaN. Both SiC and GaN have approximately E_{cr} ~3 MV/cm, which is 10 times higher than that of Si. The SiC and GaN devices can endure the same breakdown voltage using 1/10 of the thickness and ×100 of the doping concentration compared with Si devices. Thus, the on-resistance can be reduced to about 1/1000 of Si devices at a given breakdown voltage as shown in Fig. 1.2.

Silicon Carbide

SiC is a IV-IV compound material with unique physical and chemical properties. Among the numerous SiC "polytypes", 4H-SiC has been the choice for power devices owing to the availability of high-quality epitaxial wafers and superior physical properties [3].

As a material for power devices, 4H-SiC has many exceptional superiorities as below:

- Availability of high-quality bulk and epitaxial wafers
  Owing to extensive studies in the last two decades [4], high-quality and large (4"–6") 4H-SiC epitaxial wafers are commercially available nowadays. The dislocation density is relatively low (3000–6000 cm^{-2}). The stacking fault density is very low (<1 cm^{-2}). Both n- and p-type control across a wide doping range (10^{14}–10^{19} cm^{-3}) is available.

- Mature process technology
  Formation of selective n- and p-type regions by ion implantation is possible. The ability of SiC to form silicon dioxide (SiO_2) as a native oxide is also another important advantage for device fabrication. In addition, deep-trench etching and filling epitaxial regrowth [5] has been studied toward 4H-SiC superjunction MOSFETs [6].

- Long carrier lifetime
  Owing to the indirect bandgap and low defect density, a (minority) carrier lifetime in 4H-SiC is relatively high. A major lifetime killer was identified as the $Z_{1/2}$ center (carbon vacancy, V_C) [7, 8], and lifetime control in μs order is achieved. This enables the conductivity modulation in bipolar devices, resulting in the drastic reduction of on-resistance (the switching loss increases).

- High thermal conductivity
  While a device operation, cooling is the very important issue. High thermal conductivity enables simplification of cooling system, resulting in miniaturization of the total size of the power module. It should be noted that the low intrinsic carrier concentration is also great merit for high temperature operation, resulting in simplification of cooling system.

Table 1.1: Physical properties of Si, GaAs, 4H-SiC and GaN (data given at room temperature).

Property	Si	GaAs	4H-SiC	GaN
Crystal Structure	Diamond	Zincbrende	4H	Wurtzite
Lattice Constant (Å)	5.43	5.65	$a = 3.09$ $c = 10.08$	$a = 3.19$ $c = 5.19$
Band Structure	Indirect	Direct	Indirect	Direct
Bandgap (eV)	1.12	1.42	3.26	3.42
Electron Mobility (cm^2/Vs)	1350	8500	1000 ($\perp$ c) 1200 ($\parallel$ c)	1300 (bulk) 2000 (2DEG)
Hole Mobility (cm^2/Vs)	450	400	120	30
Electron Saturation Velocity (cm/s)	1×10^7	1×10^7	2.2×10^7	2.7×10^7
Critical Electric Field (MV/cm)	0.3	0.3	2.6–2.8	$\sim$3
Thermal Conductivity (W/cmK)	1.5	0.46	4.9	2.0
Relative Permittivity	11.9	12.8	9.7 ($\perp$ c) 10.3 ($\parallel$ c)	9.5 ($\perp$ c) 10.4 ($\parallel$ c)

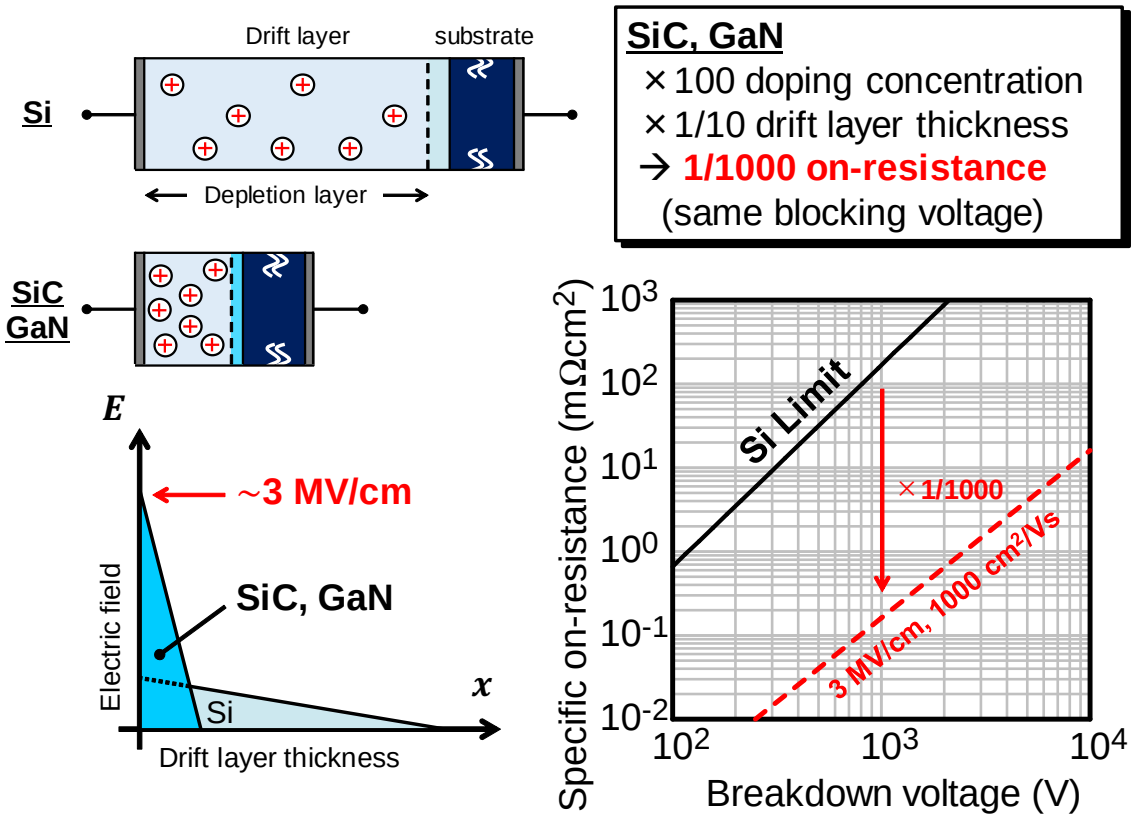

Figure 1.2: Electric field distribution in a one sided abrupt junction for Si and a wide-bandgap material (SiC, GaN) at the same breakdown voltage. Owing to about 10 times higher critical electric field ($\sim$ 3 MV/cm) of SiC and GaN than that in Si, the thickness of the voltage-blocking layers for SiC and GaN power devices can be reduced tenfold and the doping concentration can be increased by two orders of magnitude compared with the Si counterpart with the same blocking voltage. The trade-off relationship between on-resistance and breakdown voltage for a wide bandgap material roughly calculated by using $E_{\mathrm{cr}} = 3$ MV/cm and $\mu = 1000$ cm^2/Vs is shown compared with "Si Limit" [24].

In recent years, the 1 kV-class Schottky barrier diodes and the MOSFETs are commercially available by several vendors. Recently, SiC power devices are used in the inverters of the TESLA cars. The intensive studies of SiC bipolar devices toward ultra high voltage (>10 kV) are also on going and PiN diodes [9–11] and switching devices [11–14] have been demonstrated. The remaining issues, such as bipolar degradations caused by recombination-enhanced dislocation glide phenomena [15], very low MOS channel mobility [16, 17] and reliability, have been faced and intensively studied [18–23]. In addition, the reduction of wafer&process costs are also the significant issue toward more expansion of the market.

Gallium Nitride

GaN is a III-V compound material with unique physical and chemical properties. GaN has a direct bandgap of 3.42 eV which is wider than that of Si (1.12 eV) and 4H-SiC (3.26 eV). The availability of the alloys and heterostructures of nitride families, GaN, InN and AlN, is a notable superiority for electronic and optical device applications. So far, the study on GaN-based materials has been mainly performed for an application to optical devices, blue light emitting diodes (LEDs) and laser diodes (LDs). As you know, Prof. Akasaki, Prof. Amano and Prof. Nakamura were awarded the 2014 Nobel Prize in Physics "for the invention of efficient blue light-emitting diodes which has enabled bright and energy-saving white light sources." [25–27]. Nowadays, GaN-based blue, white and green LEDs and violet laser diodes are commercially available, which are brightly illuminating our living world.

At an AlGaN/GaN heterostructure, a two-dimensional electron gas (2DEG) is induced by the combination of the internal spontaneous and piezoelectric polarization fields and band offsets [28–30]. The high electron mobility and saturation velocity of electrons in the 2DEG with the high breakdown voltage allows high frequency RF amplifiers, and fast high-voltage switching. GaN-based high electron mobility transistors (HEMTs) are making an impact in the arenas of microwave electronics for communications, and power electronics.

These GaN-based devices have been fabricated on foreign substrates such as sapphire, Si and SiC. Owing to the differences of the lattice mismatch and thermal expansion between GaN and substrates, a lot of crystal defects are unintentionally introduced. The devices basically take lateral structure to avoid the effect of the many crystal defects. The device characteristics suffered from the effect of the crystal defects. Thus, fundamental properties are not still investigated due to the difficulty to characterize the intrinsic GaN.

Recently, it has become possible to fabricate high-quality GaN freestanding substrates by several methods [31–34]. Homoepitaxial GaN grown on a GaN bulk substrate (GaN-on-GaN) becomes available. Since the critical electric field is considered to be related to the bandgap, the critical electric field in GaN is expected to be higher than that in 4H-SiC. The electron mobility is also higher. Owing to these superior and unique properties, GaN has a great potential to realize more energy-efficient power devices compared to Si and 4H-SiC. In the next section, the author briefly describes the history and the current status of GaN.

1.3 Gallium Nitride (GaN)

1.3.1 History of GaN as a Material for Optical Devices

Since GaN has a direct bandgap of 3.42 eV and the alloys with InN (0.6 eV) and AlN (6.2 eV) can cover a remarkably wide spectral range from deep-ultraviolet to infrared regions (200–1800 nm) according to the bandgaps as shown in Fig. 1.3, these nitride materials have attracted much attention as a material for a blue LED. However, crystal growth of GaN was almost impossible due to the lack of a lattice-match substrate. The melt growth of GaN is also almost impossible due to the high vapor pressure of nitrogen.

In 1969, Maruska and Tientjen at first time synthesized single-crystal GaN on sapphire substrate, which is stable at high temperature (>1000°C) ammonia ambient, by hydride vapor phase epitaxy (HVPE) [35]. The obtained GaN surface had very rough like a ground glass. The undoped crystals have a very high inherent electron concentration ($\sim 10^{19}$ cm^{-3}), which is probably related to a high density of nitrogen vacancies. They tried to realize p-type conducting GaN using Ge as the dopant, but the results were difficult to reproduce.

In 1986, Amano *et al.* reported on high quality GaN grown on sapphire substrates by metal organic vapor phase epitaxy (MOVPE) using low-temperature AlN buffer layers [36]. The obtained GaN thin films had optically flat surfaces free from cracks. In 1989, Amano *et al.* realized distinct p-type conduction in Mg-doped GaN by the low-energy electron-beam irradiation (LEEBI) treatment [37]. The hole concentration of $\sim 2 \times 10^{16}$ cm^{-3} and the hole mobility of ~ 8 cm^2/Vs were obtained by the Hall-effect measurement at room temperature. The GaN p-n junction LED with strong near-band-edge emission was demonstrated for the first time. These two breakthroughs unleashed the potential of GaN and made the beginning of the intensive researches and developments.

In 1994, Nakamura *et al.* in Nichia Chemical Industries, Ltd. demonstrated high brightness InGaN/AGaN double-heterostructure blue LEDs [38]. Owing to quantum well structure, high brightness and high quantum efficiency were achieved. The InGaN blue, green and yellow LEDs were also demonstrated in 1995 [39]. In 1996, InGaN-based multi-quantum-well-structure blue LDs were also demonstrated [40].

Although high quality GaN thin films were achieved by a low-temperature AlN buffer layer [36], the crystal still included high dislocation density of 10^8–10^{10} cm^{-2} [41–43]. It was well known that a dislocation in a semiconductor act as a lifetime killer, and an efficiency of a LED is decreased by defects [44, 45]. Nonetheless, InGaN-based LEDs exhibited high efficiencies [38]. Narukawa *et al.* reported that the self-formed In-rich regions act as quantum dots and excitons are localized [46, 47]. Chichibu *et al.* concluded that this anomalous high efficiency is attributed to nano-scale potential fluctuations originating from the intrinsic compositional modulation of InGaN with an extremely short carrier diffusion length [48].

Owing to the breakthroughs followed by the intensive studies for several decades, nitride semiconductors have made miracle progress and been developed.

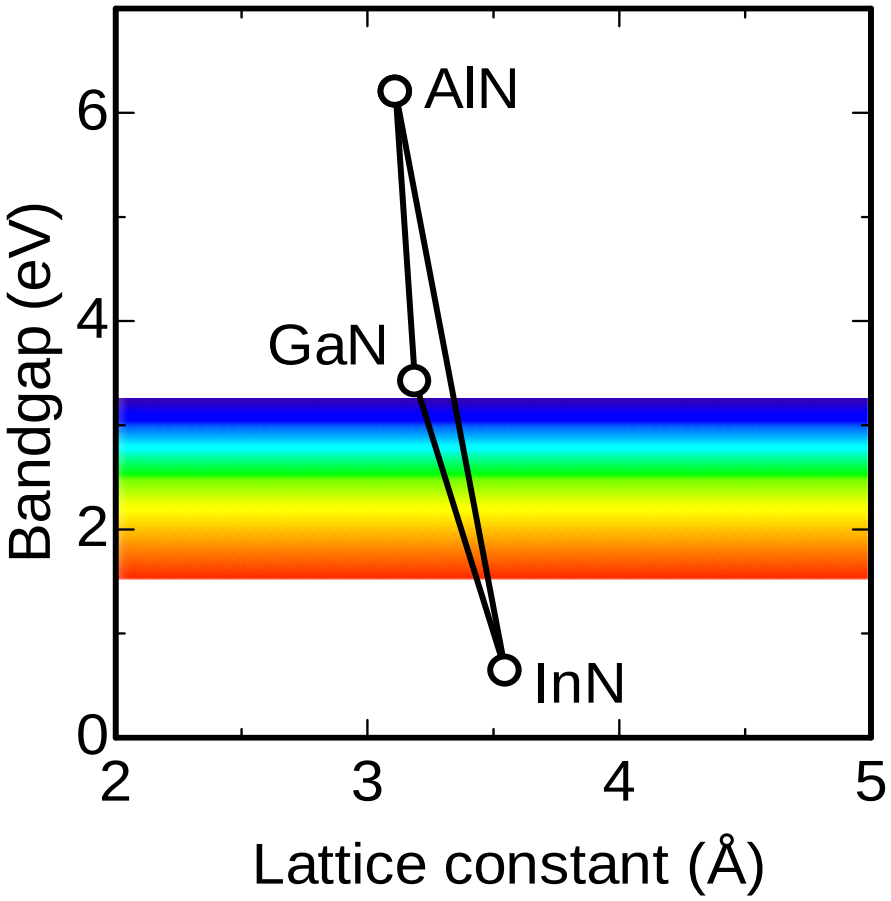

Figure 1.3: Bandgap energy and a-axis lattice constant of III-nitride semiconductors.

A GaN-based LED fabricated on a sapphire substrate which including high threading dislocation density became a commodity. On the other hand, high dislocation density was a serious problem for GaN-based LDs, which need high current density ($\sim$kA/cm^2) operation. It was revealed that dislocations deteriorate the lifetime of a GaN-based LD [49]. Due to the demand for a GaN-based LD with long lifetime, the studies on GaN bulk substrates with low dislocation density became active around 2000.

HVPE method

The hydride vapor phase epitaxy (HVPE) method for growth of a GaN bulk crystal has been studied for long years [31, 32, 50–52]. Owing to its high growth rate (several hundreds μm/h–1 mm/h), a HVPE method is considered to be suitable for the growth of a thick GaN layer. The main issues are suppression of crack generation and reduction of threading dislocation density (TDD). In 1997, Usui *et al*. succeeded to grow a crack-free GaN thick layer over 20 μm with a TDD of $\sim 10^7$ cm^{-2} on a GaN/sapphire template by facet initiated epitaxial lateral overgrowth (FIELO) using a SiO_2 stripe mask [50]. Oshima *et al*. developed a void-assisted separation (VAS) method for fabricating large-diameter freestanding GaN wafers [52]. GaN/sapphire templates with a TiN nano-net were used as starting substrates for HVPE growth of thick GaN layers. Nano-voids formed under TiN reduce the stress between GaN and sapphire, which enabled very thick GaN layers. The mirror-like surface without cracks were obtained. The TDD was 5×10^6 cm^{-2}. In 2018, Fujikura *et al*. in SCIOCS successfully realized macrodefect-free, large (2–6 in.) and thick +*c*-oriented GaN bulk crystals by the VAS method as shown in Fig. 1.4 [32]. By using hardness control with HVPE condition adjustment, the nanoindentation hardness of the GaN crystal was found to be increased drastically from its original value below 20 GPa up to 22 GPa. As a result, crack-free GaN bulk crystals with a diameter of 55 mm after cylindrical gliding and thickness over 6 mm were obtained. The TDD was $\sim 10^5$ cm^{-2}.

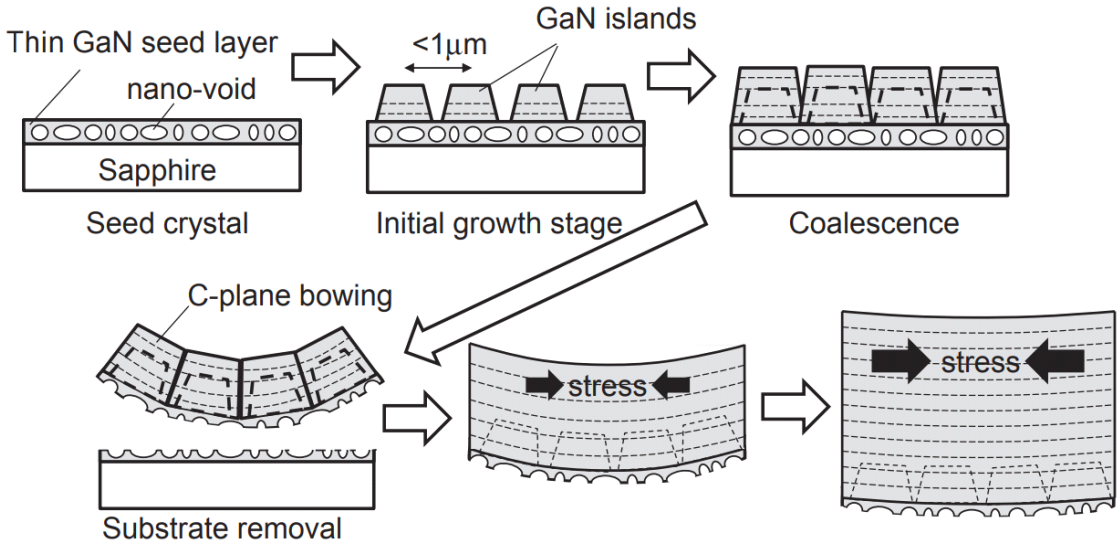

Figure 1.4: Sequence of the void-assisted separation (VAS) method used for reduction of the stress between sapphire and GaN grown by HVPE reported in Fujikura *et al.* [32].

Ammonothermal method

In the ammonothermal method, GaN is synthesized in NH_3 solvent with various ammonobasic mineralizers at around 600°C under 800–5000 atmospheric pressure using the noble-metal coated autoclave [33, 53–55] as shown in Fig. 1.5. It is possible to grow large-diameter seeds with excellent structural properties. Owing to the supercritical condition close to the equilibrium, repeatable and highly controlled re-crystallization process are achieved. The growth temperature is relatively low. Moreover, as the long-duration processes are possible, one can grow large crystals and slice them in arbitrary directions. Mikawa *et al.* reported on the GaN ingot with extremely low TDD ($<10^4$ cm^{-2}) grown by supercritical acidic ammonia technology (SCAAT^{TM}) [54], in which the noble metals were less than detection limits. The remaining issue is reduction of oxygen impurities ($\sim 10^{19}$ cm^{-3}) incorporated into the GaN crystal. In addition, a large autoclave which can endure high pressure (>800 atmospheric pressure) is required toward the growth of large-diameter GaN wafers.

Na flux method

In the Na flux method, GaN can be synthesized in relatively low pressure ($\sim$ 30 atmospheric pressure) at 600–800°C in a Na-Ga mixed melt, in which the solubility of nitrogen is enhanced compared to a Ga melt [56–62]. In 1997, Yamane *et al.* synthesized GaN single crystals for the first time [56]. In 2008, Kawamura *et al.* found that a carbon additive could suppress the unfavorable generation of polycrystals in a crucible without reduction in the yield of GaN in the Na flux method [58]. The growth rate was also enhanced up to $\sim$20 μm/h owing to the formation of C-N bonds. In 2014, Imade *et al.* reported that low-curvature (a radius of curvature >100 m) and large-diameter (2 in.) GaN wafers with a TDD of 10^2 cm^{-2} by the multi point seed (MPS) method [59]. However, the lattice constants of the GaN wafer grown by this technique expanded due to oxygen incorporation in pyramidal facets. Very recently, Imanishi *et al.* succeeded in suppressing pyramidal facet growth by promoting lateral growth at the initial growth as shown in Fig. 1.6, and the oxygen concentration was drastically reduced to 1.5×10^{17} cm^{-3} [61].

Owing to these intensive studies, GaN freestanding substrates are commercially available from several vendors. However, the cost is still very expensive, and GaN electronic devices are also still mainly fabricated on cost-effective foreign substrates such as Si and SiC.

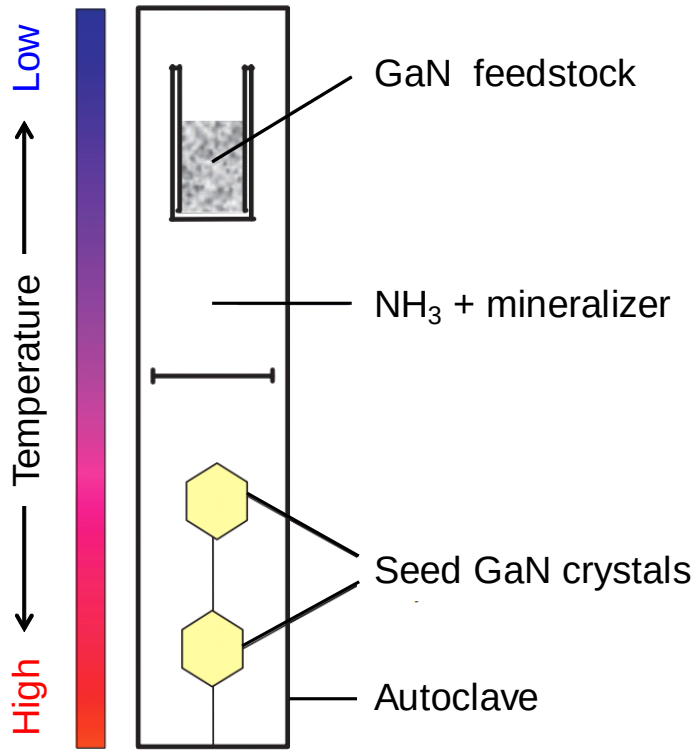

Figure 1.5: Schematic of the GaN bulk crystal growth by an ammonothermal method. The figure was made based on [33].

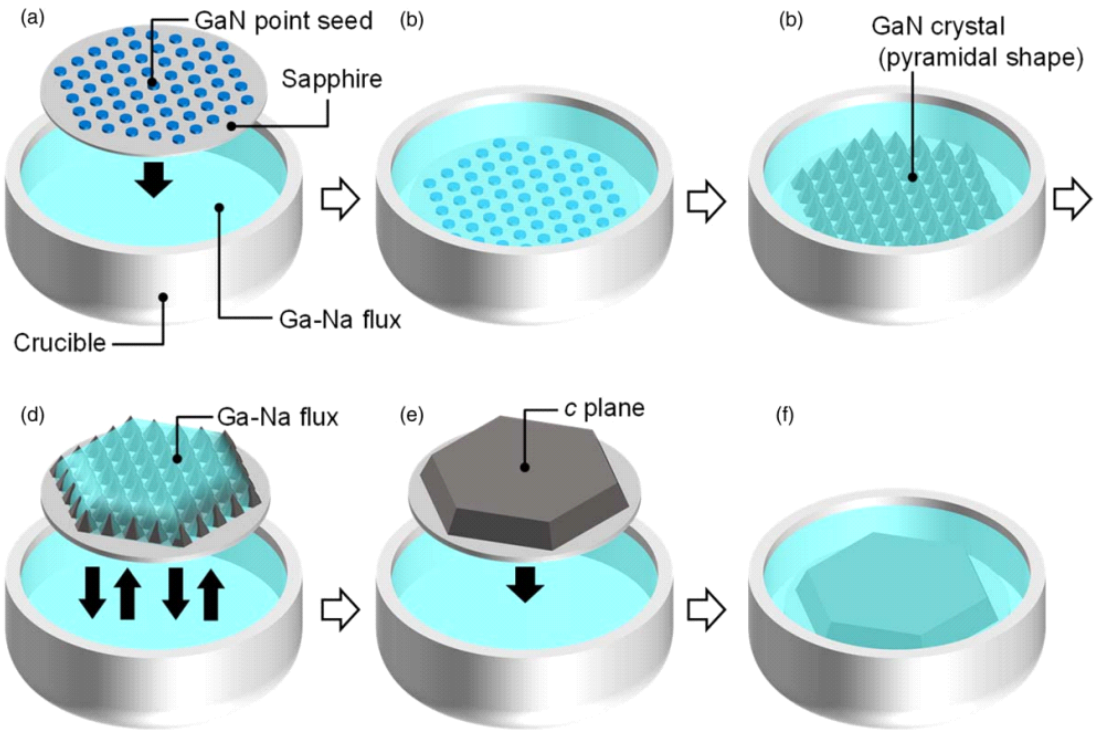

Figure 1.6: Schematic drawings of surface flattening process by promoting lateral growth of Na-flux method reported by Imanishi *et al.* [61, 62].

1.3.2 GaN-on-Si Power Devices

Since only nitride semiconductors can realize high bright blue LEDs and there are no competitors, GaN on sapphire substrates has been able to make a good business. However, in terms of the power device application, Si power MOSFETs and Si IGBTs have been already widespread and they exhibit excellent cost performance. GaN power devices need to win the cost-performance competition, not only the performance. Reduction of the fabrication cost should be a critical issue for the GaN power devices to make them commercially available.

Table 1.2 shows the available substrates for GaN devices and their sizes and costs. Although the lattice mismatch between Si and GaN is slightly larger than that between sapphire and GaN, Si substrates are very large and very cheap. Therefore, GaN power devices fabricated on Si substrates (GaN-on-Si) have been intensively studied in a few decades.

Use of Si substrates drastically reduces the fabrication costs; however, cracks and large bowing of epitaxial films caused by the mismatches of thermal expansion and lattice constant between III–V nitride and Si is technical obstacles. In 1999, Ishikawa *et al.* reported that a single crystal GaN thin film was successfully grown on a Si(111) substrate by MOVPE [63]. The AlGaN/AlN intermediate buffer layers could relaxes the stress caused by large lattice mismatch between the epitaxial layers and the Si substrate, which improved the quality of GaN [64–67]. Although the high quality GaN epitaxial layers on Si substrates became available, the threading dislocation density is still very high ($>10^8$ cm^{-2}). To avoid the effect of dislocations, GaN-on-Si devices usually have lateral structure.

There have been a lot of reports on AlGaN/GaN HEMTs utilizing 2DEG with high electron density and high electron mobility [67–77]. The typical device structures are shown in Fig. 1.7. In principle, the characteristics of HEMTs are the normally-on, since 2DEG exists without gate bias. However, the normally-off operations for high-power switching applications are strongly needed from the viewpoint of the safe operation. Toward normally-off operation, the recessed gate, p-GaN gate and MOS gate structures have been proposed. Kaneko *et al.* reported that normally-off gate injection transistor (GIT) using recessed p-GaN gate structure [71, 78]. In this device, the current collapse was also suppressed by hole injections from drain-connected p-region as shown in Fig. 1.8. However, in p-GaN gate structure, gate leakage current becomes large over 3 V. Recently, Nakazawa *et al.* demonstrated 20 A/730 V AlGaN/GaN MIS-HFET using AlON gate insulator, serving normally-off operations [79]. Nowadays, 600 V-class GaN-on-Si power transistors are commercially available by several vendors (Panasonic, Transphorm, GaN Systems, etc.).

For power device application, vertical structure is better due to sustaining high breakdown voltage without enlarging chip size [80], suitability to have peak electric field away from the surface (easier to manage electric field), and superior thermal performance [81]. Therefore, GaN-on-Si vertical power devices also have attracted attention, and several groups have reported on GaN-on-Si vertical power devices [82–89]. In these devices, the reduction of reverse leakage current originating from high dislocation density is the crucial issue.

Table 1.2: Available substrates for GaN devices and their sizes and costs. The lattice mismatch between GaN and substrates, and the thermal conductivity are also shown.

Substrate	Available Size	Cost/cm^2	Lattice Mismatch	Thermal Conductivity
Si	300 mm (12 in.)	∼\$0.08	−17%	1.5 W/cm·K
Sapphire	100 mm (4 in.)	∼\$2.2	+15%	0.42 W/cm·K
SiC	150 mm (6 in.)	∼\$6	+3.4%	4.9 W/cm·K
GaN	50 mm (2 in.)	∼\$100	0%	2.0 W/cm·K

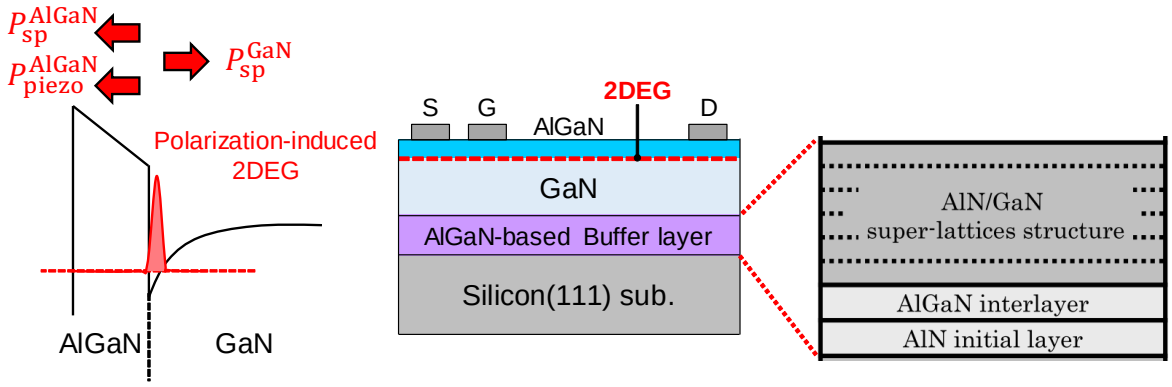

Figure 1.7: The typical device structure of an AlGaN/GaN HEMT on a Si substrate. Owing to internal spontaneous and piezoelectric polarization fields and band offsets, 2DEG with the high electron mobility and high saturation velocity is induced in the heterostructure. The diagram of the AlGaN-based buffer layer is also shown, which reduces the stress between GaN and Si.

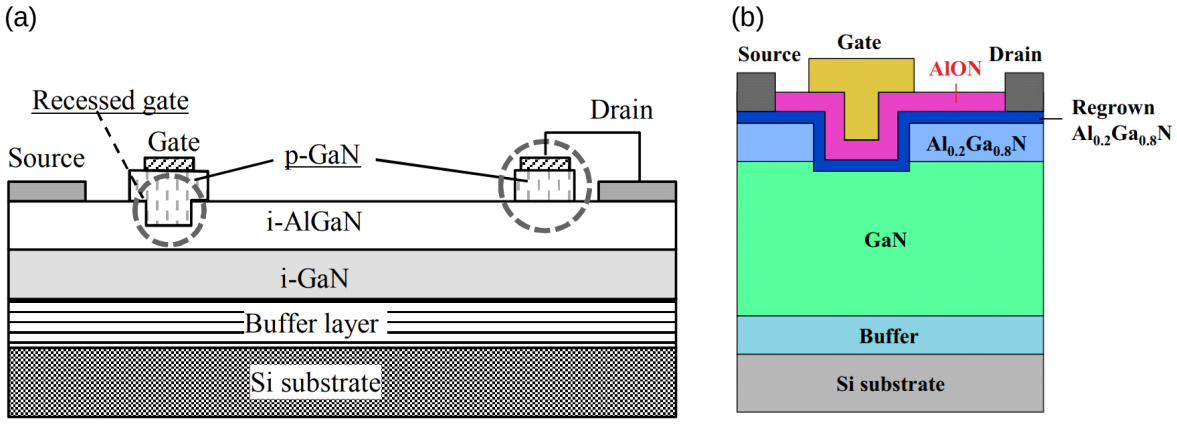

Figure 1.8: Device structures of (a) the hybrid-drain-embedded GaN GIT [78] fabricaed on a Si substrate and (b) the AlGaN/GaN MIS-HFET using AlON gate insulator fabricated on a Si substrate [79]

1.3.3 GaN-on-GaN Power Devices

Recently, it has become possible to obtain high quality GaN freestanding substrates due to the demand as the substrates for blue/violet laser diodes with long lifetimes. The cost of a GaN substrate is still very expensive (about three orders of magnitude higher than the cost of a Si substrate per unit area). However, the growth of GaN bulk crystals have kept being developed, and large-size (4–6 in.) and high-quality (TDD$\sim 10^4$ cm^{-2}) GaN bulk substrates become available by HVPE [32]. The studies on the liquid phase growth of GaN bulk crystals (Ammonothermal method [55], Na flux method [61]), which are suitable for mass production of large crystals, have also been performed. It is expected that large-diameter and high-quality GaN substrates will be available with lower cost in the future.

The use of GaN substrates enables homoepitaxial growth of GaN layers. The lattice mismatch between the substrate and the epilayer is 0%; therefore, high quality GaN epilayers can be obtained without buffer layers which are crucial in GaN-on-Si devices. It is expected that the full potential of GaN can be unleashed in homoepitaxial GaN [90, 91], which is contrast to GaN-on-Si devices including a lot of crystal defects. In addition, the vertical structure can be employed to GaN-on-GaN due to a conductive GaN substrates [80]. GaN power devices fabricated on GaN freestanding substrates (GaN-on-GaN) also have attracted great attention as the next generation power devices.

In recent decades, here have been a number of reports on GaN-on-GaN power devices. In 2002, Johnson *et al*. fabricated GaN vertical Schottky barrier diodes (SBDs) using 200 μm thick GaN freestanding substrates [92]. The breakdown voltage of 160 V and 1.7 mΩcm^2 as initial results. In 2007, Kanechika *et al*. demonstrated a vertical insulated gate AlGaN/GaN heterojunction FET fabricated on a GaN freestanding substrate [93]. A clear transistor operation with a specific on-resistance of 2.6 mΩcm^2 and a threshold voltage of -16 V was obtained. In 2008, Kodama *et al*. demonstrated GaN-based trench gate MOSFET. Owing to the dry etching followed by the anisotropic wet etching using tetramethylammonium hydride (TMAH), smooth U-shape trench structures were successfully obtained [94]. The normally-off operation with a threshold voltage of 10 V and breakdown voltage of 180 V which occurred at the gate insulator film was obtained. In 2010, Saitoh *et al*. demonstrated extremely low on-resistance of 0.71 mΩcm^2 and high breakdown voltage (1.1 kV) GaN-on-GaN SBDs [95]. In 2013, Chowdhury *et al*. demonstrated a GaN current aperture vertical electron transistor (CAVET) fabricated on a GaN bulk substrate using Mg-ion-implanted current blocking layers, which exhibited the breakdown voltage of 250 V and the on-resistance of 2.2 mΩcm^2 [96]. In 2014, Nie *et al*. demonstrated 1.5 kV/2.2 mΩcm^2 vertical GaN-on-GaN transistors [97]. In 2015, Nomoto *et al*. demonstrated GaN-on-GaN p-n diodes (PNDs) with 3.48 kV and 0.95 mΩcm^2 using beveled-long field plate edge termination [98]. Kizillyali *et al*. fabricated 4 kV and 2.8 mΩcm^2 vertical GaN PNDs with low leakage currents using Ar-implantation-based junction termination extension, which showed high avalanche capability [99]. Ohta *et al*. also fabricated vertical

GaN PNDs with high breakdown voltage over 4 kV using field plate edge termination [100]. Oka *et al.* demonstrated 1.8 mΩcm^2 GaN-based trench MOSFETs for 1.2 kV-class operation [101]. In 2016, Nomoto *et al.* fabricated 1.7 kV/0.55 mΩcm^2 GaN-on-GaN PNDs with high avalanche capability and positive temperature coefficient of breakdown voltage [102]. Shibata *et al.* reported 1.7 kV/1.0 mΩcm^2 normally-off vertical GaN-on-GaN transistor with regrown p-GaN/AlGaN/GaN semi-polar gate structure [103]. In 2017, Li *et al.* designed and fabricated GaN-on-GaN trench junction barrier Schottky (JBS) rectifiers using epitaxial p-n junctions and etched Schottky junctions [104]. Zhang *et al.* also demonstrated vertical GaN JBS rectifiers by selective ion implantation [105]. Sun *et al.* fabricated GaN-on-GaN FinFETs with breakdown voltage of 800 V and on-resistance of 0.36 mΩcm^2 [106]. In 2018, Wang *et al.* fabricated GaN PNDs with partially compensated edge termination, which exhibited the breakdown voltage of 1.68 kV and the on-resistance of 0.15 mΩcm^2 [107]. Ji *et al.* fabricated large-area in-situ oxide GaN interlayer-based vertical trench MOSFETs (OG-FETs) [108]. The breakdown voltage of 350 V and the on-resistance of 7.6 mΩcm^2 were obtained, although a single unit cell device exhibited the breakdown voltage of 700 V and the on-resistance of 0.98 mΩcm^2. In 2019, Oka *et al.* successfully demonstrated the 100 A operation of large-area (3 mm$\times$3 mm) GaN-on-GaN trench MOSFETs with a current distribution layer [109]. The breakdown voltage of 730 V and the on-resistance of 1.8 mΩcm^2 were achieved in the large-area GaN device. Tanaka *et al.* demonstrated 1.2 kV/1.4 mΩcm^2 GaN-on-GaN planar MOSFET fabricated by an all ion implantation process [110].

Figure 1.9 shows the benchmark plot of breakdown voltage versus on-resistance for state-of-the-art GaN-on-GaN power devices: SBDs [95, 111], PNDs [99, 102, 112, 113], MOSFETs [101, 109], FinFETs [106, 114] and heterojunction FETs [97, 103, 115]. The Si unipolar limit and the GaN unipolar limit roughly calculated using $E_{\mathrm{cr}} = 3$ MV/cm, $\mu_{\mathrm{e}} = 1000$ cm^2/Vs and $\varepsilon_{\mathrm{s}} = 10.4\varepsilon_0$ are shown as the black solid line and the red broken line, respectively. Since the conductivity modulation is not clearly observed in GaN PNDs due to very short carrier lifetime [91], the data of the reported GaN bipolar PNDs are also plotted. These devices exhibited excellent performances[1], which are close to the roughly calculated GaN unipolar limit. However, there are many unsolved issues to develop GaN power devices.

[1]It should be noted that the on-resistance of a power device depends on the device size: the effect of current spreading in an epilayer and a substrate significantly decreases the on-resistance for a small-size device.

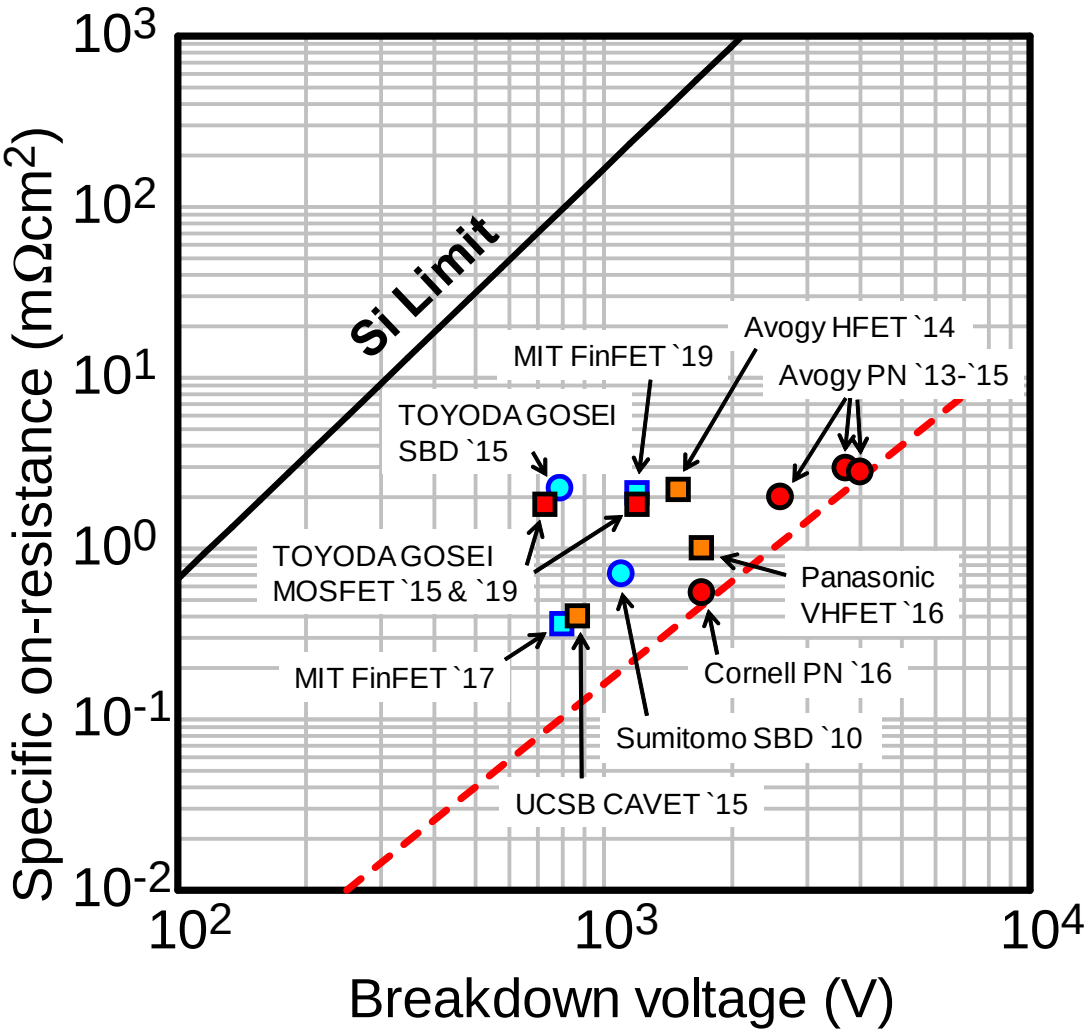

Figure 1.9: The trade-off relationship between breakdown voltage versus specific on-resistance for state-of-the-art GaN power devices: SBDs [95, 111], PNDs [99, 102, 112, 113], MOSFETs [101, 109], FinFETs [106, 114] and heterojunction FETs [97, 103, 115]. The Si unipolar limit and the curve calculated from Eq. (1.2) using $E_{\rm cr} = 3$ MV/cm, $\mu_{\rm e} = 1000$ cm^2/Vs and $\varepsilon_{\rm s} = 10.4\varepsilon_0$ as the estimated GaN unipolar limit are also shown as the black solid line and the red broken line, respectively.

1.4 Key Issues for GaN Power Devices

Although a number of GaN-on-GaN power devices have been reported, almost all papers mainly have discussed the device performance (breakdown voltage, on-resistance, threshold voltage, etc.). Since a homoepitaxial GaN layer is less affected by defects, intrinsic characteristics of GaN is expected to be obtained. For example, Suda *et al.* reported the nearly ideal current-voltage (I–V) characteristics in GaN-on-GaN SBDs [90]. The forward and reverse I–V characteristics can be explained by thermionic emission and thermionic field emission as shown in Fig. 1.10, respectively. Hu *et al.* reported that textbook-like I–V characteristics with diffusion current and Shockley-Read-Hall recombination current were observed in GaN-on-GaN PNDs [91]. Sawada *et al.* reported on the Hall-effect measurement for homoepitaxial n-GaN [116]. A remarkably high electron mobility of 1300 cm^2/Vs at 300 K for carrier concentration of 2×10^{15} cm^{-3} was achieved, which is limited by the polar optical phonon scattering, not the scattering by dislocations. Toward developing GaN power devices more, fundamental studies on material science, device physics and process technology in GaN are essential. The main issues are described below.

Bulk crystal growth

Large-diameter, high-quality and low-cost GaN freestanding substrates are essential to make a business of GaN-on-GaN power devices.

Epitaxial growth

Wide-range doping controllability, high growth rate, and elimination of unintentionally doped impurities and intrinsic defects are required. The MOVPE system is usually used for epitaxial growth of GaN. However, carbon atoms originating from the precursors (trimethylgallium) are unintentionally incorporated into GaN ($\sim 10^{16}$ cm^{-3}). Recently, HVPE is also proposed for epitaxial growth of GaN. Fujikura *et al.* reported a high-purity semi-insulating GaN layer with a carrier concentration of 2×10^{14} cm^{-3} grown by quartz-free HVPE [117]. In addition, regrowth is key technology to expand the freedom of the device fabrication.

Selective p-type doping by Mg ion implantation

Selective p-type doping is key technology to expands the freedom of the device fabrication. For example, formation of low-resistivity region for ohmic contacts, p-body layer for double-implanted MOSFETs, p-islands for junction barrier Schottky (JBS) [104, 105] and merged PiN-Schottky (MPS) rectifiers [118], and edge termination structure such as junction termination extension [10, 24]. Owing to recent intensive studies [119–121], clear p-type conduction by Mg-ion implantation has been achieved very recently.

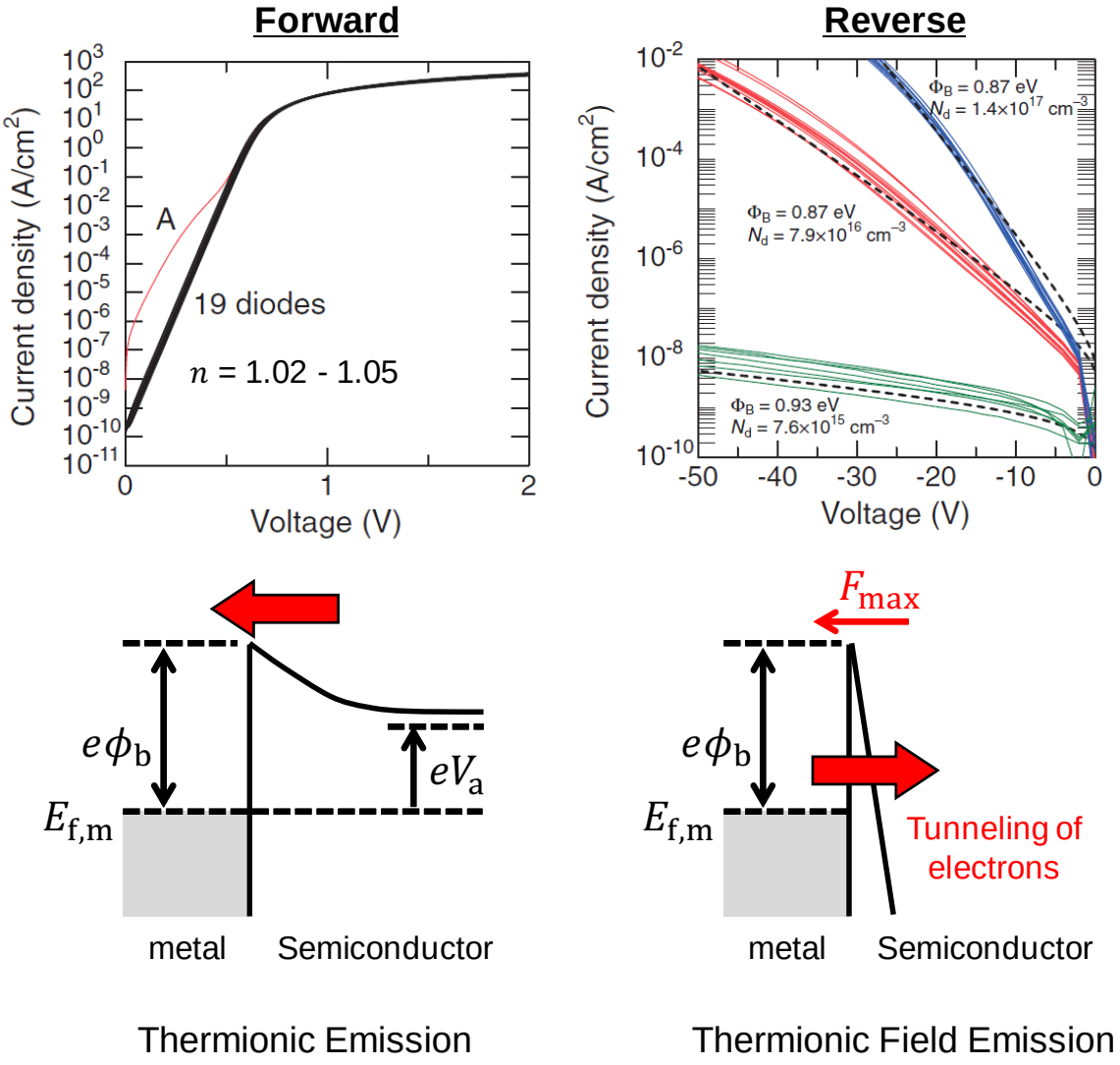

Figure 1.10: The nearly ideal I-V characteristics observed in GaN-on-GaN SBDs reported by Suda *et al.* [90]. The thermionic emission with the ideality factor close to unity and the thermionic field emission were observed in forward and reverse characteristics, respectively.

Etching

Etching is a key technology for fabrication of GaN power devices and has been used in many processes, such as the recess-gate for normally-off operation [122], mesa isolation for each device on a wafer [123], edge termination for p-n diodes [124, 125], and trench-gate fabrication for vertical MOSFETs [101]. Dry etching is usually used. However, dry etching induces the damage near the etched surface [126–128]. The reduction of etching damage is needed, and TMAH wet etching after dry etching has been performed in many reports [94, 129, 130]. Photoelectrochemical etching is also proposed as a damageless wet etching technique [131–134]

Control of MOS interface

Since normally-off transistors require a positive gate voltage to be turned on, a MOS gate is absolutely necessary to suppress the forward gate current flow. For GaN, SiO_2 [135, 136], Al_2O_3 [137], AlSiO [138] and AlON [139] have been mainly investigated as a gate oxide. Recently, Hashizume *et al.* reported on the effect of post metallization annealing (PMA) on interface properties of Al_2O_3/GaN structures [137]. The C–V curves were well improved and the interface state density was significantly reduced by PMA at most 4×10^{10} $cm^{-2}eV^{-1}$. There have been several reports on a channel mobility in GaN over 100 cm^2/Vs [135, 136, 140], which is much higher than that in 4H-SiC. The characterization and improvement of MOS channel characteristics and the reliability of gate oxide films are needed.

Understanding of fundamental properties

The study on fundamental physical properties such as doping characteristics, carrier mobility, saturation drift velocity, crystal defects (point defects, dislocations, etc.), impact ionization coefficients, etc. are very important scientifically and practically.

Sawada *et al.* reported that the Hall-effect measurement in homoepitaxial n-GaN layers for many samples with various donor concentrations systematically in detail [116, 141]. Figure 1.11 shows the temperature dependence of hole concentration and hole mobility in homoepitaxial p-GaN. The electron mobility is mainly limited by polar optical phonon scattering and ionized impurity scattering for >200°C and <200°C, respectively. The carrier compensation for samples with donor concentrations below 5×10^{16} cm^{-3} can be explained by residual carbon and the electron trap E3 ($E_C - 0.6$ eV). For samples with higher donor concentrations, it was found that a proportional relationship between donor concentration and compensating acceptor concentration, indicating the self-compensation effect by a third compensation source as shown in Fig. 1.12.

Horita *et al.* reported that the Hall-effect measurement in homoepitaxial p-GaN layers for samples with various Mg concentrations [142]. Figure 1.13 shows the temperature dependence of hole concentration and hole mobility in homoepitaxial p-GaN. Due to the deep activation energy of Mg ($\sim$ 220 meV), the acceptors were not fully ionized in these temper-

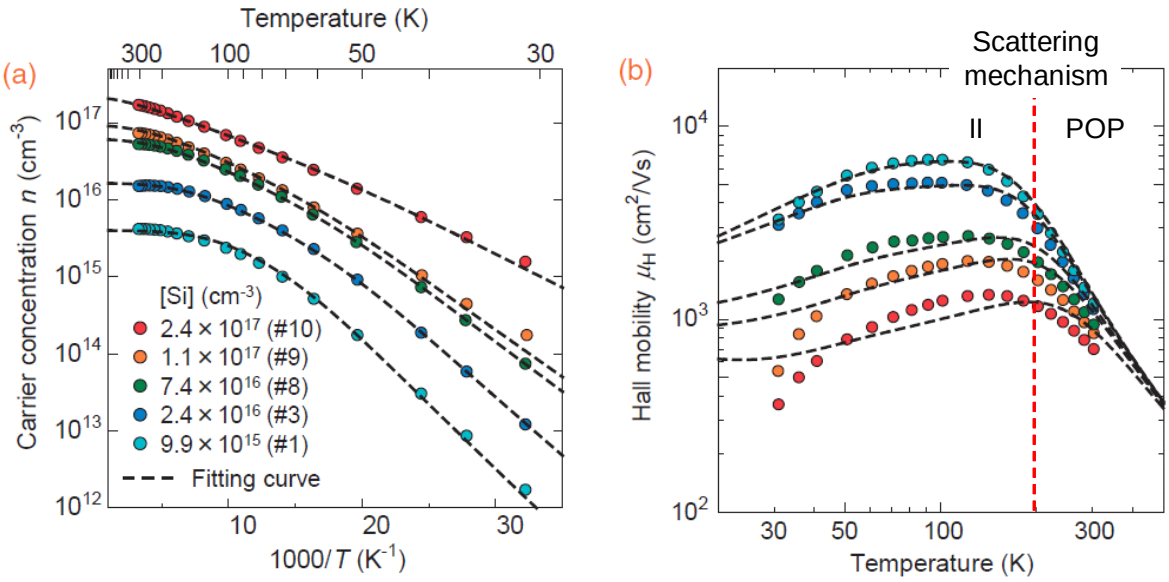

Figure 1.11: (a) Carrier concentration and (b) Hall mobility versus temperature in the range of 30–300 K for samples with various Si concentrations reported by Sawada *et al.* [116]. The mobility is limited by polar optical phonon scattering and ionized imprity scattering for $T \geq 200$ K and $T \leq 200$ K, respectively.

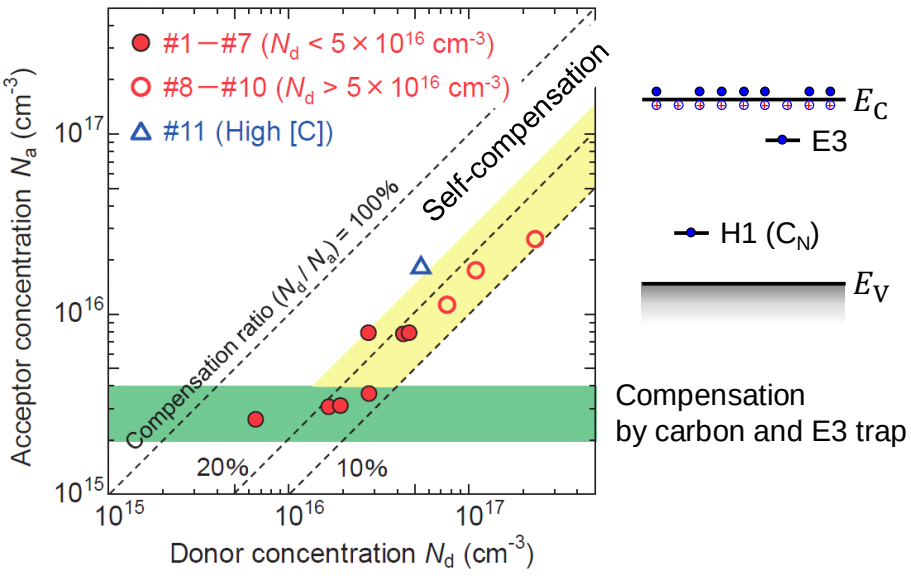

Figure 1.12: Compensating acceptor concentration versus donor concentration estimated through temperature-dependent Hall-effect measurements [116]. The [C] of the sample (blue triangle) is much higher than those of other samples.

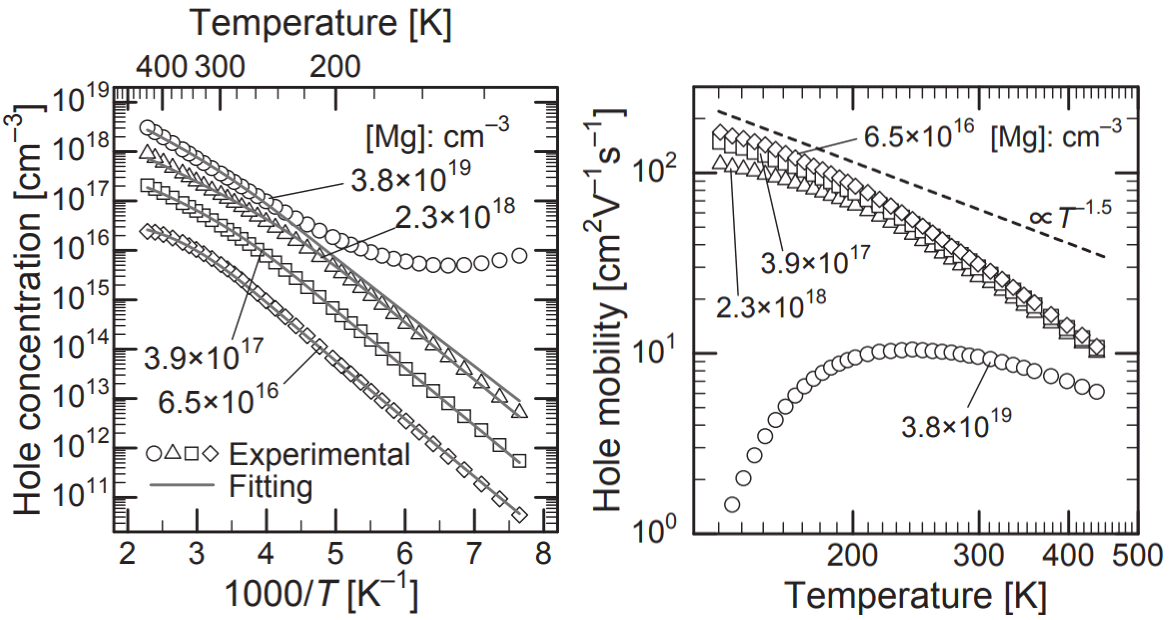

Figure 1.13: (a) Carrier concentration and (b) Hall mobility versus temperature for samples with various Mg concentrations reported by Horita *et al*. [142].

ature range. The sample with [Mg] of 3.8×10^{19} cm^{-3} shows the anomalous characteristics, the mechanism of which may be hopping conduction [143], at low temperature (<250°C). The hole mobility of the lightly Mg-doped GaN samples with [Mg] less than 4×10^{17}cm^{-3} saturated $\sim$ 30 cm^2/Vs with decreasing [Mg], which may be limited by phonon-scattering.

Narita *et al.* investigated the effect of carbon on the hole mobility and hole concentration in homoepitaxial p-GaN [144] by the Hall-effect measurement. Figure 1.14 shows the hole concentration and Hall-effect mobility versus temperature for samples with varying [C]. With increasing [C], the increase in the compensation donor concentration and the decrease in the mobility at low temperature were observed, which indicated that carbon atoms in p-GaN act as ionization donors and cause carrier compensation. Based on the deep-level transient spectroscopy (DLTS) measurements, it was revealed that carbon on the nitrogen site (C_N) having two different charged states ($0/-1$ and $+1/0$) can compensate an electron and a hole in n-type and p-type GaN layers, respectively.

The point defects in GaN have been investigated by DLTS-based studies [145–147]. Tokuda *et al.* performed the deep-level-transient-spectroscopy (DLTS) study on GaN, and major electron and hole traps, E3 ($E_C-0.58$ eV), H1 ($E_V+0.88$ eV), etc. were reported [145]. Kanegae *et al.* proposed the method to measure the hole trap in n-GaN in precise utilizing sub-bandgap photoexcitation [147, 148].

The effect of the dislocations on the device characteristics was well investigated [149–153]. Usami *et al.* investigated the correlation between dislocations and leakage current in reverse-biased homoepitaxial p-n junction. Based on the combination studies of emission microscope observation, cathodoluminescence observations, observation of etch pits using KOH etching and transmission electron microscopy, closed-core pure screw dislocations having the Burgers vector = $1\boldsymbol{c}$ cause leakage current [149]. In the subsequent study, it was found that a large leakage current is generated by nanopipes formed from screw dislocations, and the device yield can be improved by suppressing the transformation of screw dislocations to nanopipes by increasing the growth pressure as shown in Fig. 1.15 [151]. In addition, it is also observed that the dislocations cause reverse leakage current in GaN p-n junction but do not effect on avalanche breakdown voltage [153].

As mentioned above, there are a number of crucial issues for GaN power devices, and many researchers have been tackling these issues. Some of crucial issues still remain. Especially, the impact ionization coefficients are very important, since they determine the breakdown voltage and safe operating area of a power device. For GaN, although there have been a few reports [154–156], there are no precise values of the impact ionization coefficients due to the difficulty to measure. The accurate device simulation of avalanche breakdown is still lacking, and the critical electric field in GaN, which determines the unipolar limit (R_{on} vs. V_B) of GaN, is still not clear.

In this dissertation, the author focuses on the study on avalanche breakdown in GaN. In the following section, the author describes the main issues and the current status of the study on avalanche breakdown in GaN.

	Growth conditions		Hall-effect			SIMS	
Sample	T (K)	P (kPa)	$N_a \times 10^{16}$ (cm^{-3})	$N_d \times 10^{16}$ (cm^{-3})	ΔE_a (eV)	[Mg] $\times 10^{16}$ (cm^{-3})	[C] $\times 10^{16}$ (cm^{-3})
#1	1303	80	20	1.6	0.212	9.6	0.2
#2	1253	40	18	3.0	0.221	12	2.1
#3	1203	40	16	5.9	0.227	8.5	4.8

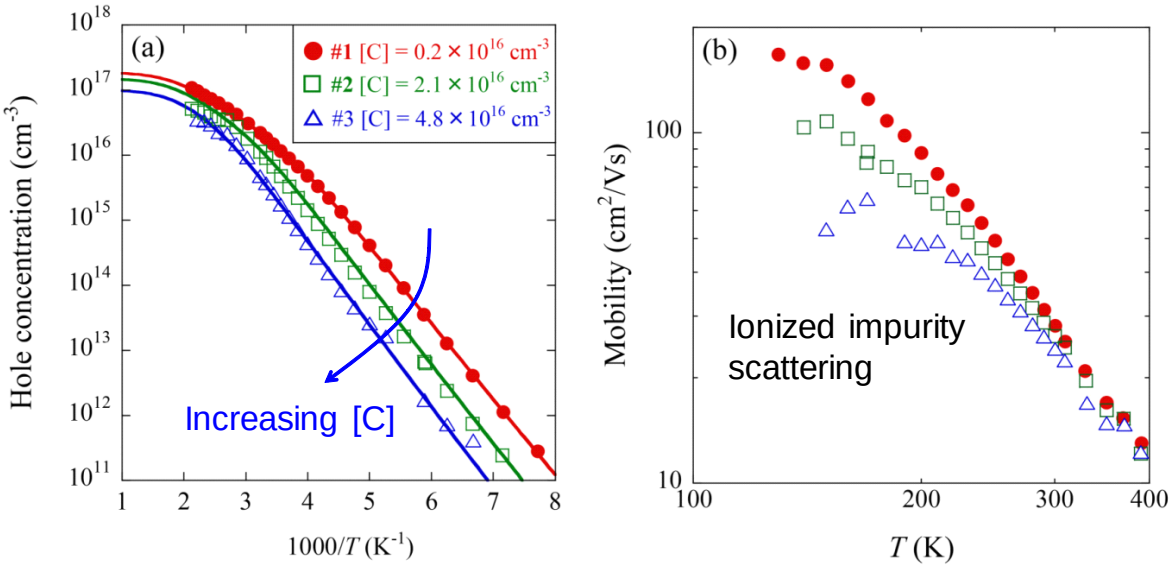

Figure 1.14: (a) Carrier concentration and (b) Hall mobility versus temperature for samples with various C concentrations reported by Narita *et al.* [144]. The table of growth conditions, Hall-effect results, and impurity concentrations for representative samples are also shown.

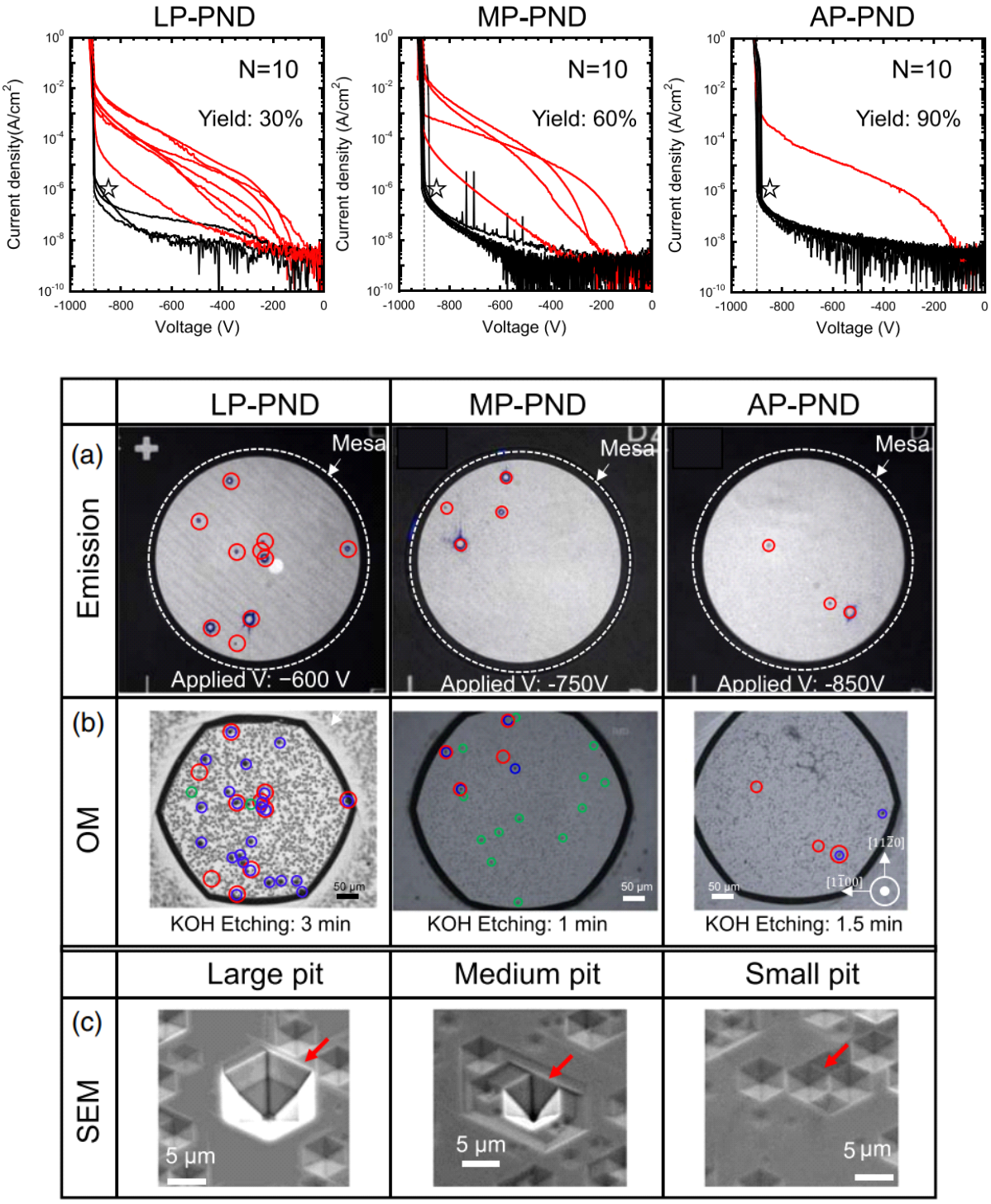

Figure 1.15: Reverse I–V characteristics of GaN PNDs, the epilayers of which were grown in low pressure (LP, 500 hPa), middle pressure (MP, 750 hPa) and high pressure (HP, 1000 hPa) conditions, reported by Usami *et al.* [151]. "N" denotes the number of measured devices. (a) Emission images and (b) corresponding optical microscope (OM) images of LP-PND, MP-PND, and AP-PND after forming etch pits. Red circles indicate leakage spots and blue, green circles show the positions of large pits and medium pits, respectively. The hexagonal mesa shape was formed during KOH etching. (c) Bird's-eye SEM images of etch pits.

1.5 Study on Avalanche Breakdown in GaN

The mechanism of breakdown in a semiconductor power device is usually dominated by impact ionization of carriers and its avalanche phenomenon. Figure 1.16 shows the band diagram of a semiconductor to which high electric field is applied. When a reverse bias voltage applied to a power device is increased, the electric field in the depletion region increases, resulting in acceleration of the mobile carriers to higher velocities. With further increase in the electric field, the mobile carriers gain sufficient kinetic energy from the electric field, so that their interaction with the lattice atoms produces the excitation of electrons from the valence band to the conduction band. This is referred to as the "impact ionization". Since the electron-hole pairs created by impact ionization also undergo acceleration by the electric field in the depletion region, they participate in creation of further pairs of electrons and holes. Consequently, impact ionization is a multiplicative phenomenon, which produces a cascade of mobile carriers being transported through the depletion region leading to a significant current flow through it. The device is unable to sustain the application of higher voltage due to the rapid increase of current, which originates from the avalanche multiplication diverging to the infinity. This is referred to as the "avalanche breakdown".

Ideally, the avalanche breakdown voltage in a power device is determined by the electric field distribution in the depletion layer and the impact ionization coefficients. The electric field distribution is determined by the doping (space charge) concentration, the thickness of the voltage-blocking later and the dielectric constant. For GaN, the dielectric constant (ε_s) was investigated by various methods [157–162]. The most cited values for the limiting low-frequency ε_s are 10.4±0.3 for $\varepsilon^{||}$ and 9.5±0.3 for $\varepsilon^{\perp}$, determined by the analysis of the angular dependences of the infrared reflectivity and absorption [157]. Kane *et al* determined ε_s of 10.6±0.3 for $\varepsilon^{||}$ in the kHz frequency range by the capacitance-voltage measurement [158]. Thus, the value of $\varepsilon_{s,||} = 10.4\varepsilon_0$ seems to be reliable. However, the value of the impact ionization coefficients in GaN are still missing.

The impact ionization coefficients, defined as "the number of electron-hole pairs generated by a carrier progressing under electric field per unit distance," are one of the most important physical properties in a semiconductor material. For accurate device simulation of avalanche breakdown in GaN power devices, the values of the impact ionization coefficients are essential. The experimental determination of the impact ionization coefficients is very challenging. Since it is impossible to measure impact ionization coefficients directly, the impact ionization coefficients are obtained by the photomultiplication measurements [163–165]: the avalanche multiplications of optical beam-induced currents for electron-injection and hole-injection conditions are measured and analyzed in a reverse-biased device. Although the studies for other mature semiconductor materials have been performed, the method cannot be diverted for GaN. The author describes the main issues of the experimental determination of impact ionization coefficients for GaN.

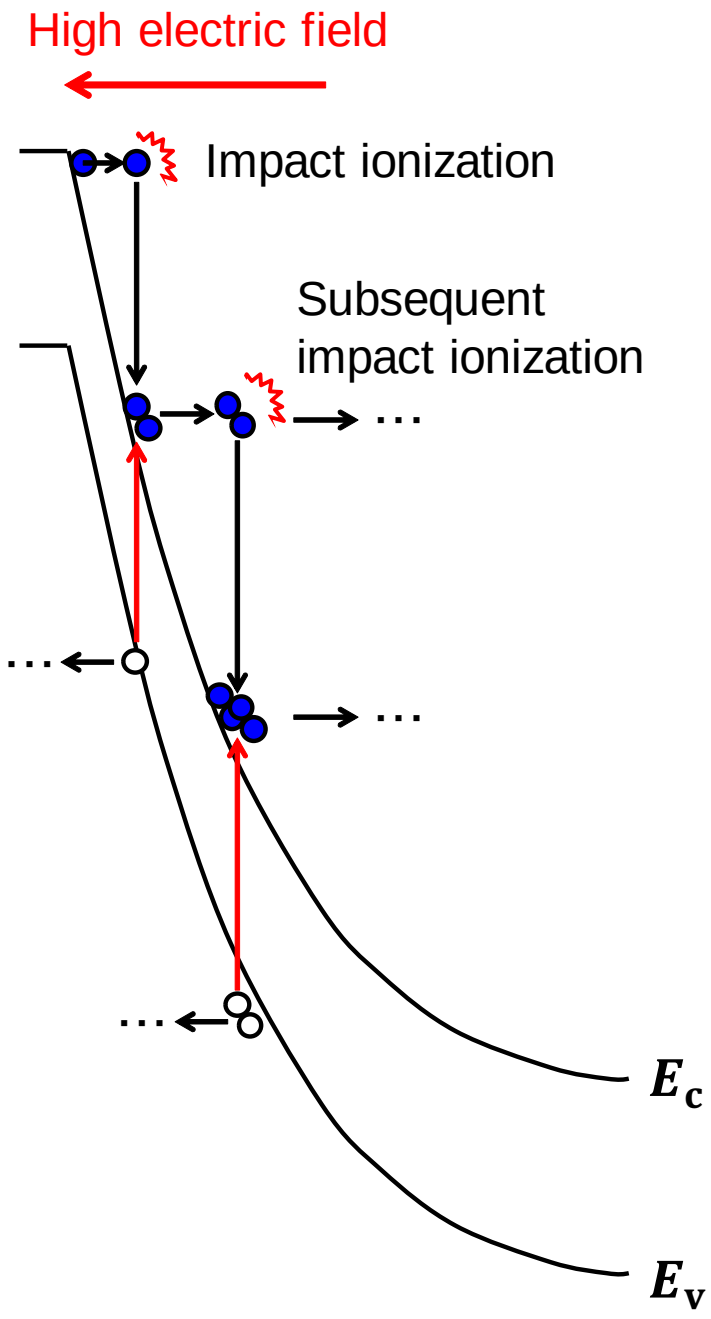

Figure 1.16: Schematic band diagram of an avalanche multiplication in a semiconductor p-n junction under reverse bias.

Reduction of leakage current

In GaN-on-Si power devices, the reverse leakage current is very large and increases with reverse bias voltage [82, 83]. The very large current flows before ideal avalanche breakdown voltage, which limits the breakdown voltage of the device. To measure avalanche multiplication clearly, a device with low reverse leakage current is need. GaN-on-GaN devices with low threading dislocation density can overcome this issue.

Edge termination to alleviate electric field crowding

In an actual device with a finite size, electric field crowding occurs at the junction edge, which causes the local and premature breakdown at the position where electric field crowding occurs [24, 166]. When a premature breakdown occurs in a device, high current density flows at the local point and significant Joule heating causes the destruction of the devices (catastrophic breakdown). To apply high electric field and to measure the avalanche multiplication, a device with good edge termination which can alleviate electric field crowding sufficiently is needed. It should be noted that a device with good edge termination can endure the Joule heating at breakdown and the same breakdown characteristics can be reproduced, which allows the reliable measurement of the avalanche multiplication.

Fundamental study on avalanche breakdown

Although some reports estimated the breakdown electric field under the assumption of electric field crowding [99, 102], the experimental value of breakdown electric field (peak electric field in the depletion layer at the breakdown) in GaN power devices is still missing. Based on the study on edge termination, the fabrication and characterization of GaN power devices without electric field are needed. The fundamental data of avalanche breakdown in GaN power devices are very important, which allows to compare the data with the theoretical critical electric fields simulated by using the impact ionization coefficients.

Measurement method of electron- and hole-injected photocurrents

To obtain impact ionization coefficients of electrons and holes, the measurements of electron-injected and hole-injected photocurrents are needed. Since GaN is a direct bandgap semiconductor, both the penetration depths for above-bandgap light and carrier diffusion length are extremely short ($<$1 μm). A thickness of a GaN substrate is several hundreds μm; therefore, it is impossible to obtain hole injection from the back side illumination.

The measurement method itself needs to be considered and established. In this dissertation, the author investigates the unique sub-bandgap absorption induced by high electric field, which is known as the Franz-Keldysh effect [167, 168]. The novel measurement method of avalanche multiplication utilizing the Franz-Keldysh effect is proposed.

1.6 Purpose and Outline of This Study

The purpose of this dissertation is understanding the avalanche breakdown characteristics in GaN to determine the impact ionization coefficients and the critical electric field. Toward accomplishing the purpose, the author studies the edge termination to alleviate electric field crowding, the breakdown electric field in GaN p-n junctions, the photocurrent induced by the sub-bandgap optical absorption induced by the Franz-Keldysh effect, and the impact ionization coefficients in GaN.

In Chapter 2, the author simulates electric field distribution in the beveled-mesa structure with various acceptor concentrations and mesa angle using TCAD, and the design space of the beveled-mesa edge termination is presented accordingly and fabricated using currently available GaN device processing technologies. Based on the simulation result, the negative bevel GaN p-n junction diodes were fabricated with shallow bevel angles and various Mg acceptor concentrations. Breakdown voltages and breakdown electric fields were investigated with respect to the Mg concentrations.

In Chapter 3, the author investigates breakdown characteristics in GaN p-n junction diodes with various epitaxial structures. At first, the author proposes the double-side-depleted shallow bevel termination, where the doping concentrations of p- and n-layers are comparable and the depletion layer extends to the both p- and n-sides. Based on the results in Capter 2, electric field crowding does not occur in this structure. The GaN p-n junction diodes with various doping concentrations are fabricated and the reverse current-voltage characteristics were investigated in detail. The author also fabricates GaN p-n junction diodes with one-side abrupt p^+/n^- and p^-/n^+ junctions. For these devices, vertical deep-etch termination is formed to avoid electric field crowding. The conduction-type dependence of a breakdown characteristics for n- and p-type drift layers is investigated.

In Chapter 4, the reverse-voltage dependence of photocurrents in a Ni/n-GaN Schottky barrier diode and a GaN p-n junction diode under sub-bandgap illumination are investigated. Although the wavelength of the irradiated light is longer than the GaN absorption edge, significant increases in the photocurrents were observed and the increases were more prominent as the wavelength was closer to the absorption edge. The author calculated the photocurrent considering the optical absorption induced by the Franz-Keldysh effect in the depletion layer based on the theory of the electroabsorption and compared with the experimental data. The voltage, wavelength and temperature dependences of the photocurrent induced by the Franz-Keldysh effect in GaN devices are discussed.

In Chapter 5, the author proposes the novel method to measure an avalanche multiplication utilizing the Franz-Keldysh effect. The Franz-Keldysh effect has a unique signature: sub-bandgap optical absorption induced by the Franz-Keldysh effect selectively occurs at high electric field region. In addition, the photocurrent induced by the FK effect is very predictable as discussed in Chapter 4. These signatures may be useful to solve the issues to measure the impact ionization coefficients in GaN. At first, the voltage dependence of the

Franz-Keldysh-induced photocurrents in the GaN p-n junction diodes with the double-side-depleted shallow bevel termination fabricated in Chapter 3 is investigated. The devices are free from electric field crowding and exhibited low reverse leakage current and high avalanche capability, which allow to measure the photocurrents up to near the breakdown voltages. The method to extract an avalanche multiplication factor in the Franz-Keldysh-induced photocurrent is presented and discussed. After that, the photomultiplication measurements were conducted for a GaN p^-/n^+ junction diode under above- and sub-bandgap illuminations. For the above-bandgap illumination, the light is absorbed at near surface, and the generated electrons diffuse and reach the depletion layer edge, resulting in electron injection. For sub-bandgap light, selective absorption near the p-n junction interface (high electric field region) due to the Franz-Keldysh effect, resulting in hole injection. The electron- and hole-injected photocurrents are analyzed in detail based on the physics, and multiplication factors are extracted. By analyzing the multiplication factors, the impact ionization coefficients are obtained. The obtained data and the simulated breakdown characteristics in GaN are discussed. The critical electric field and the trade-off relationship between on-resistance and breakdown voltage are presented.

Finally, in Chapter 6, the author summarizes this dissertation and suggests the future outlooks.

References

[1] T. Kimoto, *Jpn. J. Appl. Phys.* **54**, 040103 (2015).

[2] B. J. Baliga, *IEEE Electron Device Lett.* **10(10)**, pp.455–457 (1989).

[3] T. Kimoto and J. A. Cooper, *Fundamentals of Silicon Carbide Technology*, (Wiley, 2014), pp.1–37.

[4] D. Nakamura, I. Gunjishima, S. Yamaguchi, T. Ito, A. Okamoto, H. Kondo, S. Onda, and K. Takatori, *Nature* **430**, 1009 (2004).

[5] K. Mochizuki, S. Ji, R. Kosugi, Y. Yonezawa, and H. Okumura, *IEDM Tech. Digest* (2017) p. 35.4.

[6] R. Kosugi, S. Ji, K. Mochizuki, K. Adachi, S. Segawa, Y. Kawada, Y. Yonezawa, and H. Okumura, *Proc. of Int. Symp. on Power Semiconductor Device and ICs* (2019) p. pp. 39-42.

[7] N. T. Son, X. T. Trinh, L. S. Lovlie, B. G. Svensson, K. Kawahara, J. Suda, T. Kimoto, T. Umeda, J. Isoya, T. Makino, T. Ohshima, and E. Janzén, *Phys. Rev. Lett.* **109**, 187603 (2012).

[8] K. Kawahara, X. T. Trinh, N. T. Son, E. Janzén, J. Suda, and T. Kimoto, *J. Appl. Phys.* **115**, 143705 (2014).

[9] A. Agarwal, M. Das, S. Krishnaswami, J. Palmour, J. Richmond, and S.-H. Ryu, in *Mater. Res. Soc. Symp. Proc.* **815**, pp.243–254 (2004).

[10] H. Niwa, J. Suda, and T. Kimoto, *Appl. Phys. Express* **5**, 064001 (2012).

[11] N. Kaji, H. Niwa, J. Suda, and T. Kimoto, *IEEE Trans. Electron Devices* **62(2)**, pp.374–381 (2015).

[12] H. Miyake, T. Okuda, H. Niwa, T. Kimoto, and J. Suda, *IEEE Electron Device Lett.* **33(11)**, pp.1598–1600 (2012).

[13] E. V. Brunt *et al.*, *Proc. of Int. Symp. on Power Semiconductor Device and ICs* (2014) p. 358.

[14] S. Matsunaga, T. Mizushima, K. Takenaka, Y. Kikuchi, A. Koyama, Y. Yonezawa, and H. Okumura, *IEDM Tech. Digest* (2019) p. 20.2.

[15] J. P. Bergman, H. Lendenmann, P. A. Nilsson, U. Lindefelt, and P. Skytt, *Mater. Sci. Forum* **353–356**, 299–302 (2001).

[16] N. S. Saks, S. S. Mani, and A. K. Agarwal, *Appl. Phys. Lett.* **76**, 2250 (2000).

[17] H. Li, S. Dimitrijev, H. B. Harrison, and D. Sweatman, *Appl. Phys. Lett.* **70**, 2028 (1997).

[18] T. Tawara *et al.*, *J. Appl. Phys.* **120**, 115101 (2016).

[19] A. Iijima and T. Kimoto, *J. Appl. Phys.* **126**, 105703 (2019).

[20] D. Okamoto, H. Yano, K. Hirata, T. Hatayama, and T. Fuyuki, *IEEE Electron Device Lett.* **31(7)**, pp.710–712 (2010).

[21] S. Nakazawa, T. Okuda, J. Suda, T. Nakamura, and T. Kimoto, *IEEE Trans. Electron Devices* **62(2)**, 309 (2015).

[22] T. Kobayashi, S. Nakazawa, T. Okuda, J. Suda, and T. Kimoto, *Appl. Phys. Lett.* **108**, 152108 (2016).

[23] M. Noguchi, T. Iwamatsu, H. Amishiro, H. Watanabe, K. Kita, and S. Yamakawa, *IEDM Tech. Digest* (2017) p. 9.3.

[24] B. J. Baliga, *Fundamentals of Power Semiconductor Devices*, (Springer, 2008), pp. 91–166.

[25] I. Akasaki, *Rev. Mod. Phys.* **87**, 1119 (2015).

[26] H. Amano, *Rev. Mod. Phys.* **87**, 1133 (2015).

[27] S. Nakamura, *Rev. Mod. Phys.* **87**, 1139 (2015).

[28] M. A. Khan, J. N. Kuznia, J. M. Van Hove, N. Pan, and J. Carter, *Appl. Phys. Lett.* **60**, 3027 (1992).

[29] A. Bykhovski, B. Gelmont, and M. Shur, *J. Appl. Phys.* **74**, 6734 (1993).

[30] F. Bernardini, V. Fiorentini, and D. Vanderbilt, *Phys. Rev. B* **56**, R10024 (1997).

[31] K. Fujito, S. Kubo, H. Nagaoka, T. Mochizuki, H. Namita, and S. Nagao, *J. Cryst. Growth* **311**, 10 (2009).

[32] H. Fujikura, T. Konno, T. Suzuki, T. Kitamura, T. Fujimoto, and T. Yoshida, *Jpn. J. Appl. Phys.* **57**, 065502 (2018).

[33] R. Dwiliński, R. Doradziwiliński, J. Garczyński, L. P. Sierzputowski, A. Puchalski, Y. Kanbara, K. Yagi, H. Minakuchi, and H. Hayashi, *J. Cryst. Growth* **311**, 10 (2009).

[34] M. Imanishi, Y. Todoroki, K. Murakami, D. Matsuo, H. Imabayashi, H. Takazawa, M. Maruyama, M. Imade, M. Yoshimura, and Y. Mori, *J. Cryst. Growth* **427**, 87 (2015).

[35] H. P. Maruska and J. J. Tietjen, *Appl. Phys. Lett.* **15**, 10 (1969).

[36] H. Amano, N. Sawaki, I. Akasaki, and Y. Toyoda, *Appl. Phys. Lett.* **48**, 3 (1986).

[37] H. Amano, M. Kito, K. Hiramatsu, and I. Akasaki, *Jpn. J. Appl. Phys.* **28**, 12 (1989).

[38] S. Nakamura, T. Mukai, and M. Senoh, *Appl. Phys. Lett.* **64**, 1687 (1994).

[39] S. Nakamura, M. Senoh, N. Iwasa, and S. Nagahama, *Jpn. J. Appl. Phys.* **34**, L797 (1995).

[40] S. Nakamura, M. Senoh, S. Nagahama, N. Iwasa, T. Yamada, T. Matsushita, H. Kiyoku, and Y. Sugimoto, *Jpn. J. Appl. Phys.* **35**, L74 (1996).

[41] R. C. Powell, N. -E. Lee, Y. -W. Kim, and J. E. Greene, *J. Appl. Phys.* **73**, 189 (1993).

[42] W. Qian, M. Skowronski, M. De.Graef, K. Doverspike, L. B. Rowland, and D. K. Gaskill, *Appl. Phys. Lett.* **66**, 1252 (1995).

[43] D. Kapolenk, X. H. Wu, B. Heying, S. Keller, B. P. Keller, U. K. Mishra, S. P. DenBaars, and J. S. Speck, *Appl. Phys. Lett.* **67**, 1541 (1995).

[44] A. H. Herzog, D. L. Keune, and M. G. Craford, *J. Appl. Phys.* **43**, 600 (1972).

[45] W. A. Brantley, O. G. Lorimor, P. D. Dapkus, S. E. Haszko, and R. H. Saul, *J. Appl. Phys.* **46**, 2629 (1975).

[46] Y. Narukawa, Y. Kawakami, M. Funato, Sz. Fujita, S. Fujita, and S. Nakamura, *Appl. Phys. Lett.* **70**, 981 (1997).

[47] Y. Narukawa, Y. Kawakami, M. Funato, Sz. Fujita, S. Fujita, and S. Nakamura, *Phys. Rev. B* **55**, 4 (1997).

[48] S. F. Chichibu, A. Uedono, T. Onima, B. A. Haskell, A. Chkraborty, T. Koyama, P. T. Fini, S. Keller, S. P. DenBaars, J. S. Speck, U. K. Mishra, S. Nakamura, S. Yamaguchi, S. Kamiyama, H. Amano, I. Akasaki, J. Han, and T. Sota, *Nature Materials* **5**, 810 (2006).

[49] S. Nagahama, N. Iwasa, M. Senoh, T. Matsushita, Y. Sugimoto, H. Kiyoku, T. Kozaki, M. Sano, H. Matsumura, H. Umemoto, K. Chocho, and T. Mukai, *Jpn. J. Appl. Phys.* **39**, L647 (2000).

[50] A. Usui, H. Sunakawa, A. Sakai, and A. A. Yamaguchi, *Jpn. J. Appl. Phys.* **36**, L899 (1997).

[51] K. Motoki, T. Okahisa, R. Hirota, S. Nakahata, K. Uematsu, and N. Matsumoto, *J. Cryst. Growth* **305**, 377 (2007).

[52] Y. Oshima, T. Eri, M. Shibata, H. Sunakawa, K. Kobayashi, T. Ichihashi, and A. Usui, *Jpn. J. Appl. Phys.* **42**, L1 (2003).

[53] Q. Bao, M. Saito, K. Hazu, K. Furusawa, Y. Kagamitani, R. Kayano, D. Tomida, K. Qiao, T. Ishiguro, C. Yokoyama, and S. F. Chichibu, *Cryst. Growth Des.* **13**, 4158 (2013).

[54] Y. Mikawa, T. Ishinabe, S. Kawabata, T. Mochizuki, A. Kojima, Y. Kagamitani, and H. Fujisawa, *Proc. of SPIE* **9363**, 936302-1 (2015).

[55] D. Tomida, Q. Bao, M. Saito, K. Kurimoto, F. Sato, T. Ishiguro, and S. F. Chichibu, *Appl. Phys. Express* **11**, 091002 (2018).

[56] H. Yamane, M. Shimada, S. J. Clarke, and F. J. DiSalvo, *Chem. Mater.* **9**, 413 (1997).

[57] M. Kawahara, F. Kawamura, M. Yoshimura, Y. Mori, T. Sasaki, S. Yanagisawa, and Y. Morikawa, *J. Appl. Phys.* **101**, 66106 (2007).

[58] M. Kawamura, M. Morishita, M. Tanpo, M. Imade, M. Yoshimura, Y. Kitaoka, Y. Mori, and T. Sasaki, *J. Cryst. Growth* **310**, 3946 (2008).

[59] M. Imade, M. Imanishi, Y. Todoroki, H. Imabayashi, D. Matsuo, K. Murakami, H. Takazawa, A. Kitamoto, M. Maruyama, M. Yoshimura, and Y. Mori, *Appl. Phys. Express* **7**, 035503 (2014).

[60] T. Yamada, M. Imanishi, K. Nakamura, K. Murakami, H. Imabayashi, D. Matsuo, M. Honjo, M. Maruyama, M. Imade, M. Yoshimura, and Y. Mori, *Appl. Phys. Express* **9**, 071002 (2016).

[61] M. Imanishi, K. Murakami, T. Yamada, K. Kakinouchi, K. Nakamura, T. Kitamura, K. Okummura, M. Yoshimura, and Y. Mori, *Appl. Phys. Express* **12**, 045508 (2019).

[62] Y. Mori, M. Imanishi, K. Murakami, and M. Yoshimura, *Jpn. J. Appl. Phys.* **58**, SC0803 (2019).

[63] H. Ishikawa, G.-Y. Zhao, N. Nakada, T. Egawa, T. Jimbo, and M. Umeno, *Jpn. J. Appl. Phys.* **38(5)**, L492 (1999).

[64] M. Yanagihara, Y. Uemoto, T. Ueda, T. Tanaka, and D. Ueda, *Phys. Status Solidi A* **206(6)**, pp.1221–1227 (2009).

[65] Y. Fukushima and T. Ueda, *Jpn. J. Appl. Phys.* **49**, 032101 (2010).

[66] R. Liu, F. A. Ponce, A. Dadgar, and A. Krost, *Appl. Phys. Lett.* **83(5)**, 860 (2003).

[67] M. Ishida, T. Ueda, T. Tanaka, and D. Ueda, *IEEE Trans. Electron Devices* **60(10)**, pp.3053–3059 (2013).

[68] N.-Q. Zhang, B. Moran, S. P. DenBaars, U. K. Mishra, X. W. Wang, and T. P. Ma, *Phys. Status Solidi A* **188**, 213 (2001).

[69] W. Saito, T. Tanaka, M. Kuraguchi, K. Tsuda, I. Omura, T. Ogura, and H. Ohashi, *IEEE Trans. Electron Devices* **50**, 2528 (2003).

[70] Y. Dora, A. Chakraborty, L. McCarthy, S. Keller, S. P. DenBaars, and U. K. Mishra, *IEEE Electron Device Lett.* **27**, 713 (2006).

[71] Y. Uemoto, M. Hikita, H. Ueno, H. Matsuo, M. Ishida, M. Yanagihara, T. Ueda, T. Tanaka, and D. Ueda, *IEEE Trans. Electron Devices* **54(12)**, pp.3393–3399 (2007).

[72] Y. Uemoto, D. Shibata, M. Yanagihara, H. Ishida, H. Matsuo, S. Nagai, N. Batta, M. Li, T. Ueda, T. Tanaka, and D. Ueda, *IEDM Tech. Digest* (2007) p. pp.861–864.

[73] Y. Wang, M. Wang, B. Xie, C. P. Wen, J. Wang, Y. Hao, W. Wu, K. J. Chen, and B. Shen, *IEEE Electron Device Lett.* **34(11)**, pp.1370–1372 (2013).

[74] O. Hilt, A. Knauer, F. Brunner, E. Bahat-Treidel, and J. Würfl , *Proc. of Int. Symp. on Power Semiconductor Device and ICs* (2010) p. pp.347–350.

[75] U. K. Mishra, P. Parikh, and Y.-F. Wu, *Proc. of IEEE* **90(6)**, pp.1022–1031 (2002).

[76] M. Kuzuhara, J. T. Asubar, and H. Tokuda, *Jpn. J. Appl. Phys.* **55**, 070101 (2016).

[77] K. J. Chen, O. Häberlen, A. Lidow, S. I. Tsai, T. Ueda, Y. Uemoto, and Y. Wu, *IEEE Trans. Electron Devices* **64(3)**, pp.779–795 (2017).

[78] S. Kaneko, M. Kuroda, M. Yanagihara, A. Ikoshi, H. Okita, T. Morita, K. Tanaka, M. Hikita, Y. Uemoto, S. Takahashi, and T. Ueda, *Proc. of Int. Symp. on Power Semiconductor Device and ICs* (2015) p. pp.41–44.

[79] S. Nakazawa, H.-A. Shih, N. Tsurumi, Y. Anda, T. Hatsuda, T. Ueda, M. Nozaki, T. Yamada, T. Hosoi, T. Shimura, H. Watanabe, and T. Hashizume, *IEDM Tech. Digest* (2017) p. 25.1.

[80] T. Uesugi and T. Kachi, *in CS Mantech. Tech. Dig.* (2011) p. pp.1–4.

[81] Y. Zhang, M. Sun, Z. Liu, D. Piedra, H. -S. Lee, F. Gao, T. Fujishima, and T. Palacios, *IEEE Trans. Electron Devices* **60(7)**, pp.2224–2230 (2013).

[82] Y. Zhang, M. Sun, D. Piedra, M. Azize, X. Zhang, T. Fujishima, and T. Palacios, *IEEE Electron Device Lett.* **35(6)**, pp.618–620 (2014).

[83] Y. Zhang, H.-Y. Wong, M. Sun, S. Joglekar, L. Yu, N. A. Braga, R. V. Mickevicius, and T. Palacios, *IEDM Tech. Digest* (2015) p. 35.1.

[84] S. Mase, Y. Urayama, T. Hamada, J. J. Freedsman, and T. Egawa, *Appl. Phys. Express* **9**, 111005 (2016).

[85] C. Liu, R.-A. Khadar, and E. Matioli, *IEEE Electron Device Lett.* **39(1)**, pp.71–74 (2017).

[86] R. A. Khadar, C. Liu, L. Zhang, P. Xiang, K. Cheng, and E. Matioli, *IEEE Electron Device Lett.* **39(3)**, pp.401–404 (2018).

[87] Y. Zhang, M. Yuam, N. Chowdhury, K. Cheng, and T. Palacios, *IEEE Electron Device Lett.* **39(5)**, pp.715–718 (2018).

[88] R. A. Khadar, C. Liu, R. Soleimanzadeh, and E. Matioli, *IEEE Electron Device Lett.* **40(3)**, pp.443–446 (2019).

[89] Y. Zhang, A. Dadgar, and T. Palacios, *J. Phys. D : Appl. Phys.* **51**, 273001 (2018).

[90] J. Suda, K. Yamaji, Y. Hayashi, T. Kimoto, K. Shimoyama, H. Namita, and S. Nagao, *Appl. Phys. Express* **3**, 101003 (2010).

[91] Z. Hu, K. Nomoto, B. Song, M. Zhu, M. Qi, M. Pan, X. Gao, V. Protasenko, D. Jena, and H. G. Xing, *Appl. Phys. Lett.* **107**, 243501 (2015).

[92] J. W. Johnson, A. P. Zhang, W.-B. Luo, F. Ren, S. J. Pearton, S. S. Park, Y. J. Park, and J.-I. Chyi, *IEEE Trans. Electron Devices* **49(1)**, pp.32–36 (2002).

[93] M. Kanechika, M. Sugimoto, N. Soejima, H. Ueda, O. Ishiguro, M. Kodama, E. Hayashhi, K. Itoh, T. Uesugi, and T. Kachi, *Jpn. J. Appl. Phys.* **46**, 21 (2007).

[94] M. Kodama, M. Sugimoto, E. Hayashi, N. Soejima, O. Ishiguro, M. Kanechika, K. Itoh, H. Ueda, T. Uesugi, and T. Kachi, *Appl. Phys. Express* **1**, 021104 (2008).

[95] Y. Saitoh, K. Sumiyoshi, M. Okada, T. Horii, T. Miyazaki, H. Shiomi, M. Ueno, K. Katayama, M. Kiyama, and T. Nakamura, *Appl. Phys. Express* **3**, 081001 (2010).

[96] S. Chowdhury, M. H. Wong, B. L. Swenson, and U. K. Mishra, *IEEE Electron Device Lett.* **33(1)**, pp.41–43 (2012).

[97] H. Nie, Q. Diduck, B. Alvarez, A. P. Edwards, B. M. Kayes, M. Zhang, G. Ye, T. Prunty, and D. Bour, *IEEE Electron Device Lett.* **35(9)**, pp.939–941 (2014).

[98] K. Nomoto, Z. Hu, B. Song, M. Zhu, M. Qi, R. Yan, V. Protasenko, E. Imhoff, J. Kuo, N. Kaneda, T. Mishima, T. Nakamura, D. Jena, and H. G. Xing, *IEDM Tech. Digest* (2015) p. 9.7.

[99] I. C. Kizilyalli, T. Prunty, and O. Aktas, *IEEE Electron Device Lett.* **36(10)**, pp.1073–1075 (2015).

[100] H. Ohta, N. Kaneda, F. Horikiri, Y. Narita, T. Yoshida, T. Mishima, and T. Nakamura, *IEEE Electron Device Lett.* **36(11)**, pp.1180–1182 (2015).

[101] T. Oka, T. Ina, Y. Ueno, and J. Nishii, *Appl. Phys. Express* **8**, 054101 (2015).

[102] K. Nomoto, B. Song, Z. Hu, M. Zhu, M. Qi, N. Kaneda, T. Mishima, T. Nakamura, D. Jena, H. G. Xing, and , *IEEE Electron Device Lett.* **37(2)**, pp.161–164 (2017).

[103] D. Shibata, R. Kajitani, M. Ogawa, K. Tanaka, S. Tamura, T. Hatsuda, M. Ishida, and T. Ueda, *IEDM Tech. Digest* (2016) p. 10.1.

[104] W. Li, K. Nomoto, M. Pilla, M. Pan, X. Gao, D. Jena, and H. G. Xing, *IEEE Trans. Electron Devices* **64(4)**, pp.869–872 (2017).

[105] Y. Zhang, Z. Liu, M. J. Tadjer, M. Sun, D. Piedra, C. Hatem, T. J. Anderson, L. E. Luna, A. Nath, A. D. Koehler, H. Okumura, J. Hu, X. Zhang, X. Gao, B. N. Feigelson, K. D. Hobart, and T. Palacios, *IEEE Electron Device Lett.* **38(8)**, pp.1097–1100 (2017).

[106] M. Sun, Y. Zhang, X. Gao, and T. Palacios, *IEEE Electron Device Lett.* **38(4)**, pp.509–512 (2017).

[107] J. Wang, L. Cao, J. Xie, E. Beam, R. McCarthy, C. Youtsey, and P. Fay, *Appl. Phys. Lett.* **113**, 023502 (2018).

[108] D. Ji, C. Gupta, A. Agarwal, S. H. Chan, C. Lund, W. Li, S. Keller, U. K. Mishra, and S. Chowdhury, *IEEE Electron Device Lett.* **39(5)**, pp.711–714 (2018).

[109] T. Oka, T. Ina, Y. Ueno, and J. Nishii, *Proc. of Int. Symp. on Power Semiconductor Device and ICs* (2019) p. 303.

[110] R. Tanaka, S. Takashima, K. Ueno, H. Matsuyama, Y. Fukushima, M. Edo, and K. Nakagawa, *Ext. Abst. of Int. Conf. on Solid State Devices and Materials* (2019) p. 443.

[111] N. Tanaka, K. Hasegawa, K. Yasunishi, N. Murakami, and T. Oka, *Appl. Phys. Express* **8**, 7 (2015).

[112] I. C. Kizilyalli, A. P. Edwards, H. Nie, D. Disney, and D. Bour, *IEEE Trans. Electron Devices* **60**, 10 (2013).

[113] I. C. Kizilyalli, A. P. Edwards, H. Nie, D. Bour, T. Prunty, and D. Disney, *IEEE Electron Device Lett.* **35(2)**, pp.247–249 (2014).

[114] Y. Zhang, M. Sun, J. Perozek, Z. Liu, A. Zubair, D. Piedra, N. Chowdhury, X. Gao, K. Shepard, and T. Palacios, *IEEE Electron Device Lett.* **40(1)**, pp.75–78 (2019).

[115] R. Yeluri, J. Lu, C. A. Hurni, D. A. Browne, S. Chowdhury, S. Keller, J. S.Speck, and U. K. Mishra, *Appl. Phys. Lett.* **106**, 183502 (2015).

[116] N. Sawada, T. Narita, M. Kaechika, T. Uesugi, T. Kachi, M. Horita, T. Kimoto, and J. Suda, *Appl. Phys. Express* **11**, 041001 (2018).

[117] H. Fujikura, T. Konno, T. Yoshida, and F. Horikiri, *Jpn. J. Appl. Phys.* **56**, 085503 (2017).

[118] H. Niwa, J. Suda, and T. Kimoto, *IEEE Trans. Electron Devices* **64(3)**, pp.874–881 (2016).

[119] T. Niwa, T. Fujii, and T. Oka, *Appl. Phys. Express* **10**, 091002 (2017).

[120] T. Narita, T. Kachi, K. Kataoka, and T. Uesugi, *Appl. Phys. Express* **10**, 016501 (2017).

[121] H. Sakurai, M. Omori, S. Yamada, Y. Furukawa, H. Suzuki, T. Narita, K. Kataoka, M. Horita, M. Bockowski, J. Suda, and T. Kachi, *Appl. Phys. Lett.* **115**, 142104 (2019).

[122] A. Wakejima, A. Ando, A. Watanabe, K. Inoue, T. Kubo, Y. Osada, R. Kamimura, and T. Egawa, *Appl. Phys. Express* **8**, 026502 (2015).

[123] T. Maeda, T. Narita, H. Ueda, M. Kanechika, T. Uesugi, T. Kachi, T. Kimoto, M. Horita, and J. Suda, *Jpn. J. Appl. Phys.* **58**, SCCB14 (2019).

[124] T. Maeda, T. Narita, H. Ueda, M. Kanechika, T. Uesugi, T. Kachi, T. Kimoto, M. Horita, and J. Suda, *IEEE Electron Device Lett.* **40(6)**, pp.941–944 (2019).

[125] H. Fukushima, S. Usami, M. Ogura, Y. Ando, A. Tanaka, M. Deki, M. Kushimoto, S. Nitta, Y. Honda, and H. Amano, *Jpn. J. Appl. Phys.* **58**, SCCD25 (2019).

[126] S. Yamada, M. Omori, H. Sakurai, Y. Osada, R. Kamimura, T. Hashizume, J. Suda, and T. Kachi, *Appl. Phys. Express* **13**, 016505 (2020).

[127] K. J. Choi, H. W. Jang, and J. Lee, *Appl. Phys. Lett.* **82**, 1233 (2003).

[128] Z. Liu, J. Pan, A. Asano, K. Ishikawa, K. Takeda, H. Kondo, O. Oda, M. Sekine, and M. Hori, *Jpn. J. Appl. Phys.* **56**, 026502 (2017).

[129] M. Itoh, T. Kinoshita, C. Koike, M. Takeuchi, K. Kawasaki, and Y. Aoyagi, *Jpn. J. Appl. Phys.* **45(5A)**, pp.3988–3991 (2006).

[130] Y. Zhang, M. Sun, Z. Liu, D. Piedra, J. Hu, X. Gao, and T. Palacious, *Appl. Phys. Lett.* **110**, 193506 (2017).

[131] F. Horikiri, Y. Narita, and T. Yoshida, *Jpn. J. Appl. Phys.* **57**, 086502 (2018).

[132] F. Horikiri, H. Ohta, N. Asai, Y. Narita, T. Yoshida, and T. Mishima, *Appl. Phys. Express* **11**, 091001 (2018).

[133] Y. Kumazaki, K. Uemura, T. Sato, and T. Hashizume, *J. Appl. Phys.* **12**, 184501 (2017).

[134] M. Toguchi, K. Miwa, F. Horikiri, N. Fukuhara, Y. Narita, T. Yoshida, and T. Sato, *Appl. Phys. Express* **12**, 066504 (2019).

[135] H. Otake, K. Chikamatsu, A. Yamaguchi, T. Fujishima, and H. Ohta, *Appl. Phys. Express* **1**, 011105 (2008).

[136] S. Takashima, K. Ueno, H. Matsuyama, T. Inamoto, M. Edo, T. Takahashi, M. Shimizu, and K. Nakagawa, *Appl. Phys. Express* **10**, 121004 (2017).

[137] T. Hashizume, S. Kaneki, T. Oyobiki, Y. Ando, S. Sasaki, and K. Nishiguchi, *Appl. Phys. Express* **11**, 124102 (2018).

[138] D. Kikuta, K. Ito, T. Narita, and T. Kachi, *Appl. Phys. Express* **13**, 026504 (2020).

[139] T. Hosoi, K. Watanabe, M. Nozaki, T. Yamada, T. Shimura, and H. Watanabe, *Jpn. J. Appl. Phys.* **58**, SCCD16 (2019).

[140] D. Ji, W. Li, and S. Chowdhury, *IEEE Trans. Electron Devices* **65(10)**, pp.4271–4275 (2018).

[141] N. Sawada, *Master Thesis* , Kyoto University [in Japanese] (2017).

[142] M. Horita, S. Takashima, R. Tanaka, H. Matsuyama, K. Ueno, M. Edo, T. Takahashi, M. Shimizu, and J. Suda, *Jpn. J. Appl. Phys.* **56**, 031001 (2017).

[143] P. Kozodoy, H. Xing, S. P. DenBaars, U. K. Mishra, A. Saxler, R. Perrin, S. Elhamri, and W. C. Mitchel, *J. Appl. Phys.* **87**, 1832 (2000).

[144] T. Narita, K. Tomita, Y. Tokuda, T. Kogiso, M. Horita, and T. Kachi, *J. Appl. Phys.* **124**, 215701 (2018).

[145] Y. Tokuda, *ECS Transactions* **75(4)**, pp.39–49 (2016).

[146] K. Kanegae, H. Fujikura, Y. Otoki, T. Konno, T. Yoshida, M. Horita, T. Kimoto, and J. Suda, *Appl. Phys. Lett.* **115**, 012103 (2019).

[147] K. Kanegae, T. Narita, K. Tomita, T. Kachi, M. Horita, T. Kimoto, and J. Suda, *Jpn. J. Appl. Phys.* **59**, SGGD05 (2020).

[148] K. Kanegae, M. Horita, T. Kimoto, and J. Suda, *Appl. Phys. Express* **11**, 071002 (2018).

[149] S. Usami, Y. Ando, A. Tanaka, K. Nagamatsu, M. Deki, M. Kushimoto, S. Nitta, Y. Honda, H. Amano, Y. Sugawara, Y.-Z. Yao, and Y. Ishikawa, *Appl. Phys. Lett.* **112**, 182106 (2018).

[150] S. Usami, N. Mayama, K. Toda, A. Tanaka, M. Deki, S. Nitta, Y. Honda, and H. Amano, *Appl. Phys. Lett.* **114**, 232105 (2019).

[151] S. Usami, A. Tanaka H. Fukushima, Y. Ando, M. Deki, S. Nitta, Y. Honda, and H. Amano, *Jpn. J. Appl. Phys.* **58**, SCCB24 (2019).

[152] T. Hamachi, S. Takeuchi, T. Tohei, M. Imanishi, M. Imade, Y. Mori, and A. Sakai, *Jpn. J. Appl. Phys.* **58**, 161417 (2019).

[153] S. Usami, *Ph.D. Dissertation*, (2018), Nagoya University [in Japanese].

[154] R. McClintock, J. L. Pau, K. Minder, C. Bayram, P. Kung, M. Razeghi, and , *Appl. Phys. Lett.* **90**, 141112 (2007).

[155] A. M. Özbek, Ph.D. Dissertation, (2012), North Carolina University.

[156] L. Cao, J. Wang, G. Harden, H. Ye, R. Stillwell, A. J. Hoffman, and P. Fay, *Appl. Phys. Lett.* **112**, 262103 (2018).

[157] A. S. Barker and Jr. and M. Ilegems, *Phys. Rev. B* **7(2)**, pp.743–750 (1973).

[158] M. J. Kane, M. J. Uren, D. J. Wallis, P. J. Wright, D. E. J. Soley, A. J. Simon, and T. Martin, *Semicon. Sci. Technol.* **26**, 085006 (2011).

[159] W. Soluch, E. Brzowski, M. Lysakowska, and J. Sadura, *IEEE Trans. Ultrasonic, Ferroelectrics, and Frequency Control* **58**, 11 (2011).

[160] M. T. Hibberd, V. Frey, B. F. Spencer, P. W. Mitchell, P. Dawson, M. J. Kappers, R. A. Oliver, C. J. Humphreys, and D. M. Graham, *Solid State Com.* **247**, 68 (2016).

[161] F. Bernardini, V. Fiorentini, and D. Vanderbilt, *Phys. Rev. Lett.* **79**, 20 (1997).

[162] K. Karch, J.-M. Wagner, and F. Bachstedt, *Phys. Rev. B* **57**, 12 (1998).

[163] R. Van Overstraeten and H. De Man, *Solid State Electron.* **13**, pp.583–608 (1970).

[164] G. E. Bulman, V. M. Robbins, and G. E. Stillman, *IEEE Trans. Electron Devices* **32(11)**, pp.2454–2466 (1985).

[165] H. Niwa, J. Suda, and T. Kimoto, *IEEE Trans. Electron Devices* **62(10)**, pp.3326–3333 (2015).

[166] T. Hiyoshi, T. Hori, J. Suda, and T. Kimoto, *IEEE Trans. Electron Devices* **55(8)**, pp.1841–1846 (2008).

[167] V. W. Franz, *Z. Naturf.* **13a**, 484 (1958).

[168] L. V. Keldysh, *Soviet Physics JETP* **7**, 788 (1958).

Chapter 2

GaN p-n Junction Diodes with Beveled-Mesa Termination

2.1 Introduction

The high critical electric field and high electron mobility of GaN make it a promising candidate for next-generation power devices. Recently, it has become possible to obtain high-quality GaN bulk substrates by several methods [1–4], and vertical GaN devices fabricated on GaN substrates have attracted much attention. Therefore, there have been many reports on vertical GaN devices with high breakdown voltage and low on-resistance [5–28].

All semiconductor devices have a finite size and have a surface and a junction edge. Then, electric field crowding spontaneously occurs by a presence of a curled equivalent potential at the edge. Under high reverse bias voltage, high electric field at the edge causes local premature breakdown before parallel-plane junction reaches the one-dimensional uniform breakdown. To enhance the breakdown voltage closer to the uniform breakdown, edge termination to alleviate electric field crowding at the device edge is essential.

Although the reported GaN devices exhibited high breakdown voltage [10, 13, 25], electric field still remained at the device edge and the premature breakdown occured. To improve breakdown voltage, avalanche capability and reliability of GaN power devices, the fundamental study on edge termination is essential with consideration of currently available process technology for GaN power devices. In addition, a good edge termination which can sufficiantly alleviate electric field crowding allows to measure an avalanche breakdown up to the ideal paralell-plane junction breakdown. This enables the fundamental study on avalanche breakdown in GaN without the effect of electric field crowding. In this section, the author introduces typical edge terminations, and the discusses applicability to GaN power devices. There are a lot of configurations of edge terminations [29] as shown in Fig. 2.1:

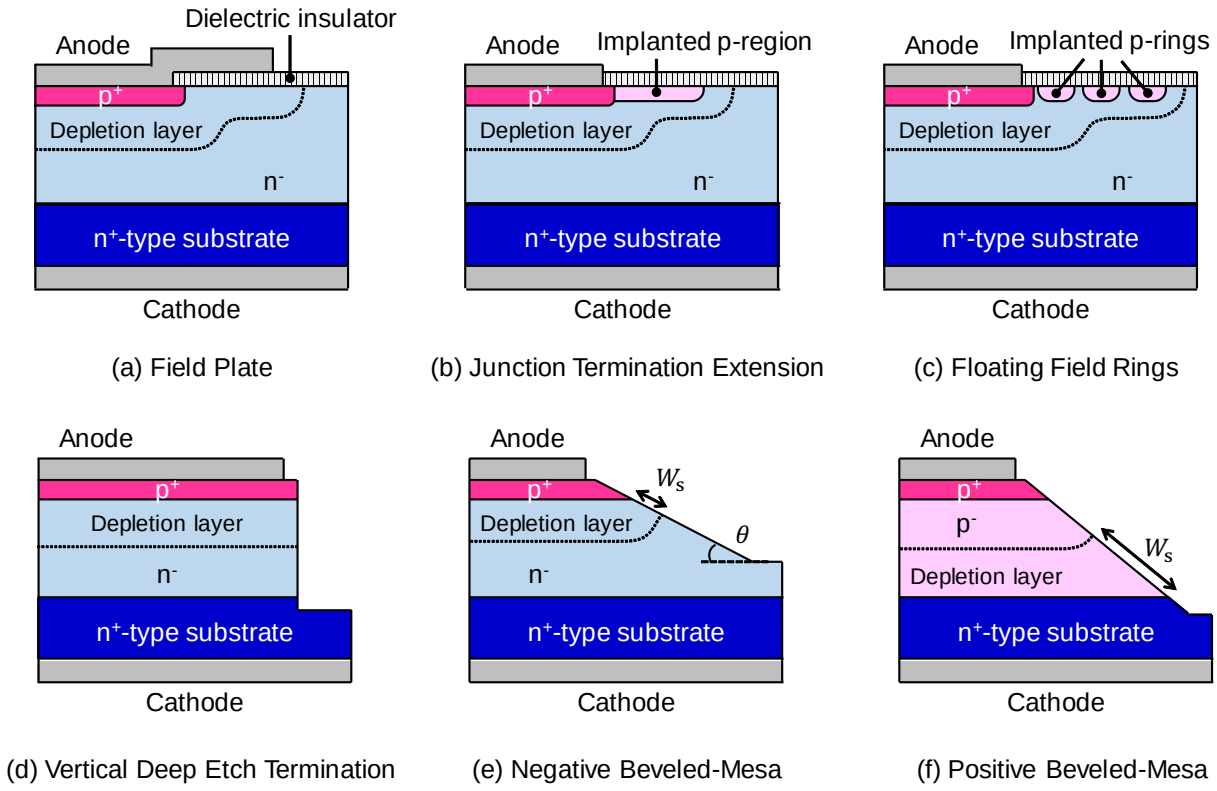

Figure 2.1: Examples of fundamental edge termination structures: (a) field plate, (b) junction termination extension, (c) floating field ring, (d) vertical deep etch termination, (e) negative beveled-mesa, (f) positive beveled-mesa. Reducing curvature of depletion layer edge gives alleviation of electric field crowding at the edge.

Field Plate

The field plate (FP) structure consists of matal-insulator-semiconductor (MIS) around the junction edge as shown in Fig. 2.1(a). The electric field at the edge can be modulated by the application of a bias voltage to the metal. Practically, the FP is formed by extending the connect metal for the p^+-region over the field insulator at the edge of the junction. The application of a negative bias to the p^+-region to reverse bias the p-n junction also provides a negative bias to the FP, resulting in an expansion of the depletion region along the surface. The reduction of electric field crowding at the cylindrical junction will increase the breakdown voltage. However, it should be noted that a high electric field can be produced at the edge of the FP, which results in premature breakdown of the device at the FP edge.

Junction Termination Extension

The junction termination extension (JTE) is formed by selective doping of p-region with a relatively low acceptor concentration around the junction edge as shown in Fig. 2.1(b). If the charge within the p-region is too low, it has little impact on the electric field distribution and the electric field crowding will occur at the edge of the p^+-region. If the charge is too high, it will merely serve as an extension of the p^+-region and electric field crowding will occur at the JTE edge. The precise control of the JTE dose is essential to maximize the breakdown voltage. If the depleted JTE length is much longer than the depletion layer width of the main junction, the surface electric field can be reduced to below that for a parallel-plane junction. Consequently, the breakdown voltage of this termination can approach to the ideal parallel-plane junction breakdown.

Floating Field Rings (Multiple-Zone JTE)

The multiple floating field rings termination is an elegant approach to improve the performance of the edge termination. For example, in the case of Si, the decrease in the JTE dose along the way from the main junction to the exterior can be obtained by a single implantation process using a mask with a variable window size which forms the smaller effective doping concentration for a narrow window, combined with a suitable annealing step to diffuse the dopant sideways between the windows. In principle, the use of multiple floating field rings allows increasing the breakdown voltage of planar junctions arbitrarily close to the parallel-plane breakdown voltage by the addition of a very large number of rings. However, in practice, the addition of floating rings occupies more space, resulting in a large die size and cost.

Vertical Deep Etch Termination

Mesa isolation with vertically deep mesa can also alleviate electric field crowding at the junction edge to form one-dimensional electric field profile. When the etching depth is shallower than the depth of the depletion layer edge in the deeper side (in n-type region),

electric field crowding occurs at the mesa bottom. On the other hand, when the etching depth is deeper than the depth of the depletion layer edge, electric field crowding does not occur in the device. Therefore, a etching technology to form a moat isolation deeper than the depletion layer edge at the breakdown is needed.

Beveled-Mesa Termination

There are two configurations of beveled-mesa structure; the positive bevel and the negative bevel, as shown in Fig. 2.1(e) and (f). For the p-n junction with tapered-mesa structure, the negative bevel is defined as that where the space charge concentration in the upper-side layer is higher than that in the lower-side layer. Due to the lack of a p-type GaN bulk substrate, for GaN, the conduction type of a drift layer determines the position of the p-n junction interface and extension direction of the depletion layer. In the negative bevel device, the depletion layer at the surface (W_s) is not wider than that at the bulk. Therefore, it is counterintuitive to make use of a negative bevel termination in power devices. However, it is known that a reduction of the surface electric field can be obtained through the use of a shallow bevel angle combined with a low space charge concentration in the upper layer.

For mature semiconductors such as Si and SiC, JTE-based structures are often employed [30–34], since the charge within the p-region can be precisely adjusted with the ion implant dose, providing better control and uniformity over the charge at the edges of the junction. Niwa *et al.* reported a 4H-SiC PiN diode with space-modulated two-zone JTE as shown in Fig. 2.2 [31, 35, 36]. The lateraly tapered profile of the sophisticated JTE was realized by space-modulation of floating field rings, which enlarged the tolerance to the deviation of effective JTE dose compared with a conventional JTE. Owing to the JTE, electric field at the surface was well suppressed, resulting in the record breakdown voltage of 21.7 kV (81% of the ideal breakdown voltage). Saitoh *et al.* developed V-groove trench gate SiC MOSFETs with a double reduced surface field (RESURF) JTE formed by sequential ion implantations combined with regrowth as shown in Fig. 2.3 [34]. The RESURF effect is well obtained with the reduction of the JFET resistance owing to a high n-type doping density in a surface drift layer. The breakdown voltage of 1.6 kV (94% of the ideal breakdown voltage) was achieved with the low on-resistance of 2.4 $m\Omega cm^2$. In Si vertical superjunction devices such as CoolMOS, lateral/surface superjunction types can also be employed as shown in Fig. 2.4 [33, 37, 38], which minimize the area taken by the termination and increase their immunity to parasitic charges.

So far, selective doping of p-region by Mg ion implantation for GaN had been considered to be challenging (or impossible). Nevertheless, recently, Mg ion implantation into GaN and its thermal treatment have been tenaciously studied and developed [39–42]. Sakurai *et al.* has reported that a high activation (>70%) of Mg ions implanted into a homoepitaxial GaN achieved by 1673 K annealing in ultra-high-pressure (1 GPa) nitrogen ambient without a protection cap layer [42]. Clear p-type conduction with hole concentration of 3.6×10^{16} cm^{-3}

and hole mobility of 24 cm^2/Vs at 300 K were confirmed by Hall-effect measurements. This is the strong evidence that selective p-doping by Mg ion implantation into GaN is possible. In addition, very recently, Tanaka *et al* reported that GaN-on-GaN double implanted (DI)-MOSFET fabricated by all ion implantation process [28]. However, it is still a fundamental research stage and there are no report on GaN devices with JTE structure using Mg ion implantation.

The reported GaN devices have other edge terminations without selective p-type doping, such as FP-based termination [7, 12, 13, 24, 25], ion-implantation isolation [9–11, 16, 43], ion implanted bilayer edge terminations [14, 15, 44], hydrogen plasma edge termination [16, 45], etc. Zhang *et al*. reported 1200 V/1 mΩcm^2 GaN vertical Fin power FETs with FP termination [25]. Figure 2.5 shows the device structure. The electric field distribution in the device under the reverse bias of 1200 V was simulated. It was observed that the extremely high electric field over 8 MV/cm was applied to the edge of the oxide film, which caused the premature breakdown. The peak electric field at the parallel-plane junction was estimated to 2.3 MV/cm. Kizilyalli *et al*. reported high voltage vertical GaN p-n junction diodes with ion-implantation isolation. Figure 2.6 shows (a) the device structure, (b) schematic drawing of the edge termination [46, 47], (c) top view image of the device and (d) corresponding simulated electrostatic potential elucidating the effect of the JTE implants [10]. An edge termination structure spreads the potential applied to the anode over a distance which is greater than the drift region thickness by a factor of about 4.5. The process uses two separate implant steps, which can form the modulated p-type rings. Owing to the edge termination, the device exhibited high breakdown voltage of 4 kV with high avalanche capability. However, it was noted that the net donor concetration in the drift layer was difficult to be determined, and the estimated breakdown electric field had a large error (2.0–2.7 MV/cm). Dickerson *et al*. reported GaN vertical p-n junction diodes with a bilayer edge termination, which consists of nitrogen-implanted compensated i-region and remained p-region as shown in Fig. 2.7(a) [44]. The implant plofile can be controlled by changing the implantation energy. Figure 2.7(b) shows the simulated breakdown voltage versus the thickness of the remained p-region (t_p). When t_p is too thin, electric field crowding occurs at the edge of the main junction as shown in Fig. 2.7(c). When $t_p = 26$ μm, electric field is well spread between main junction and the termination edge, resulting in highest breakdown voltage. When t_p is too thick, electric field crowding occurs at the termination edge. The optimized device exhibited the high breakdown voltage of 2.6 kV. However, the variation of the breakdown voltage in the same wafer is large due to the variations in p^+-epilayer thickness, which could vary up to $\sim 20\%$ [44].

These edge terminations suppressed electric field crowding at the device edges, so that high breakdown voltages and high figure-of-merits were realized. However, electric field crowding still remained and premature breakdown occurred in these devices. To improve a breakdown voltage approaching to the ideal parallel-plane breakdown voltage, the study on edge termination which can eliminate electric field crowding is required.

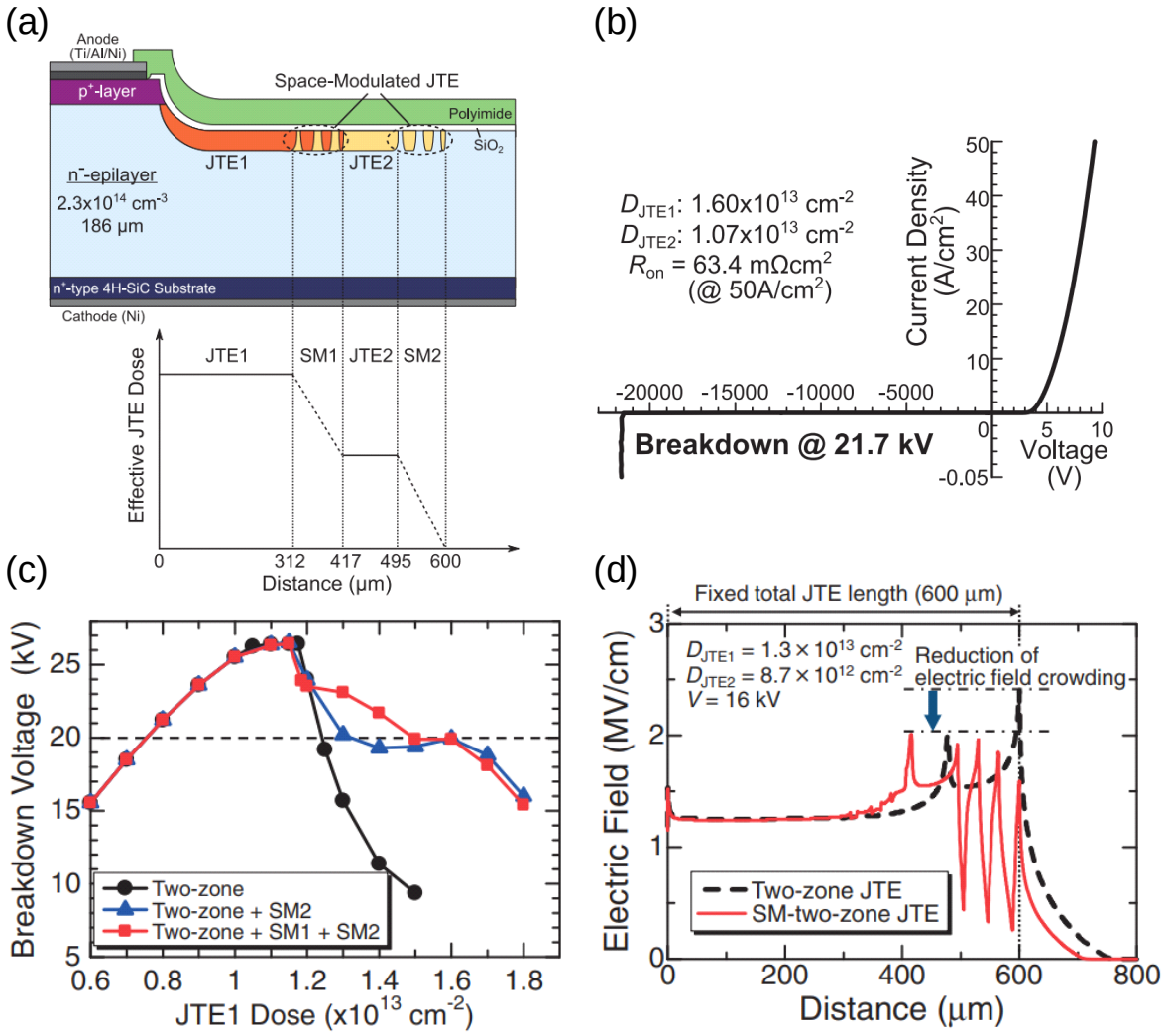

Figure 2.2: (a) Schematic cross section of a 4H-SiC PiN diode with SM-JTE [31]. Effective JTE dose can be modulated by designing the width and interval of floating rings. (b) I–V characteristics of the diode, (c) Simulated breakdown voltage vs. JTE1 dose. Optimal dose ranges can be widened by SM-JTE. (c) Electric field profiles inside the JTE region.

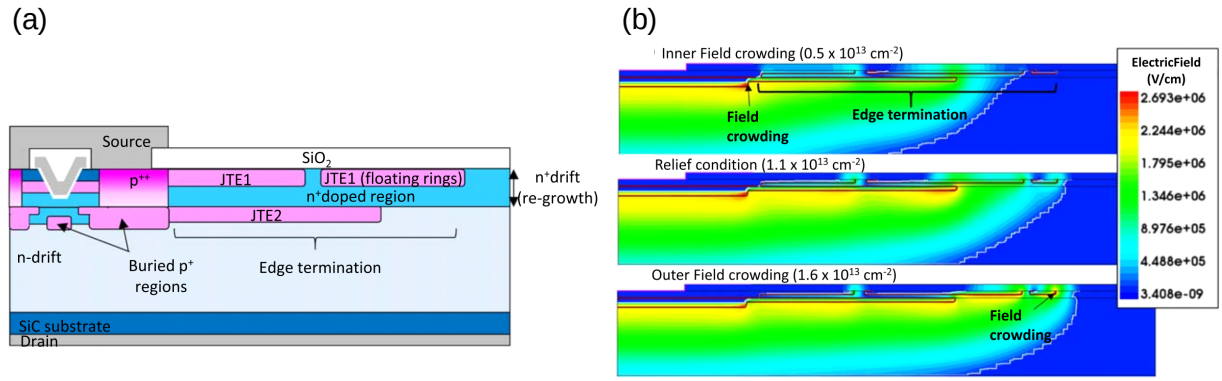

Figure 2.3: (a) Double RESURF JTE realized by regrowth of n^+-type drift layer and multiple ion implantations, which was employed in 4H-SiC V-groove MOSFET [34]. (b) Simulated electric field distribution in the double RESURF JTE. electric field crowding is well reduced by this structure.

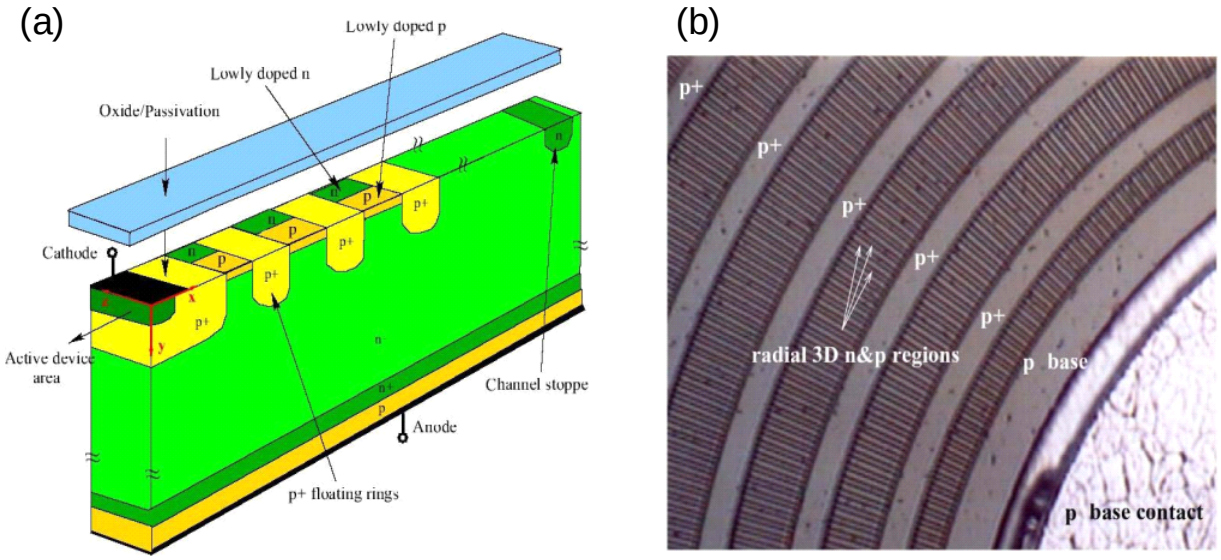

Figure 2.4: (a) Schematic and (b) SEM image of p^+ floating rings featuring n/p super-junction stripes between rings in the termination area. High voltage Si IGBT employs this structure [33, 37].

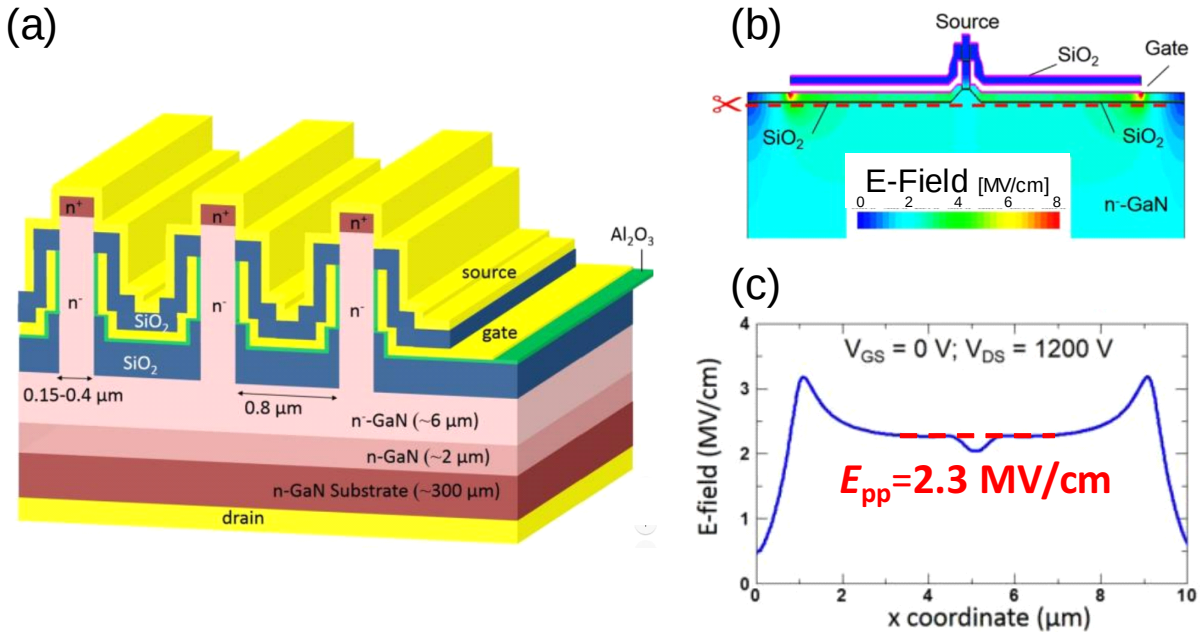

Figure 2.5: (a) Device structure of a GaN vertical Fin power FETs with field plate structure reported by Zhang *et al*. [25], (b) the simulated electric field distribution in the FinFET under reverse bias of 1200 V, and (c) the simulated electric field profile along the cutline shown in (b).

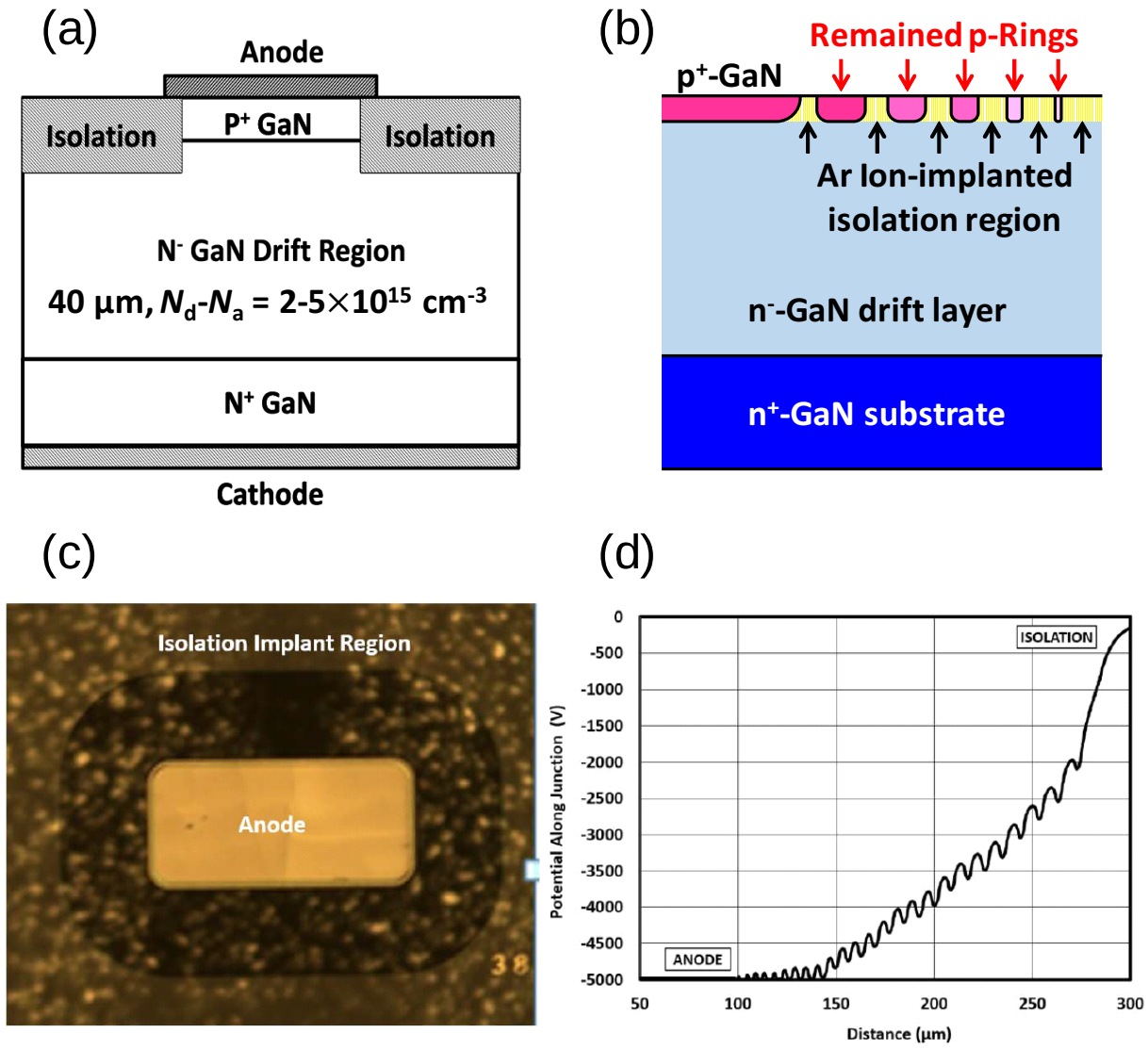

Figure 2.6: (a) Device structure of a GaN p-n junction diode with ion-implanted isolation termination reported by Kizilyalli *et al.* [10], (b) the schematic drawing of the edge termination formed by the two step ion implantation, (c) device top view image, and (d) corresponding simulated electrostatic potential elucidating the effect of the JTE implants.

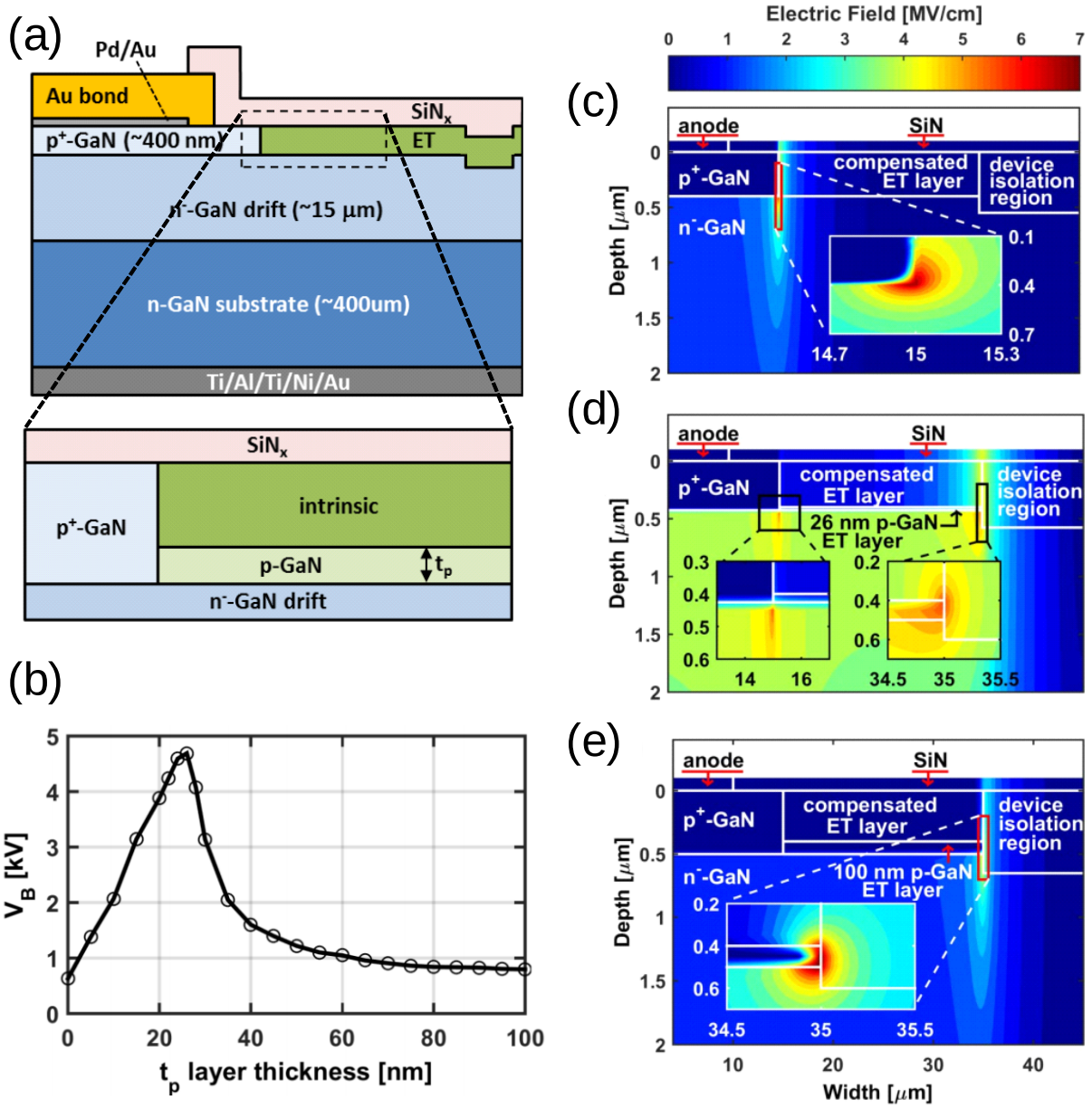

Figure 2.7: (a) Device structure of a GaN p-n junction diode with a bilayer termination reported by Dickerson *et al.* [44], (b) the simulated breakdown voltage versus the thickness of the p-layer (t_p), and Electric field distributions for (c) $t_p = 0$ nm, (d) $t_p = 26$ nm and (e) $t_p = 100$ nm.

Mesa structure, which is formed by etching process, can be also used as edge termination. Basically, an epitaxial layer needs to be etched down to a substrate to avoid an depletion layer reaching the mesa bottom (in other words, the mesa height needs to be longer than the depletion layer width at the breakdown). Thus, breakdown voltage of a device with mesa termination is limited by the etching process technology. A GaN device with an even thin drift layer exhibits high breakdown voltage owing to its high critical electric field (for example, parallel-plane breakdown voltage of 600 V can be realized by drift layer thickness of $\sim$5 μm and doping concentration of $\sim 3\times10^{16}$ cm^{-3}). Thus, mesa termination is potentially useful for GaN power devices with relatively low breakdown voltage.

In this study, the author proposes the beveled-mesa termination for GaN power devices. The two-dimensional electric field distributions in the beveled-mesa structure with various acceptor concentrations and mesa angle were investigated by using TCAD simulation, and devices were designed accordingly and fabricated using currently available GaN device processing technologies. The negative bevel GaN PNDs were fabricated with shallow bevel angles and various Mg acceptor concentrations. Breakdown voltages and breakdown electric fields are experimentally investigated with respect to the Mg concentrations in upper-side p-layers.

2.2 Device Design by TCAD Simulation

The two-dimensional electric field distribution in the bevel mesa is investigated using Sentaurus TCAD. Figure 2.8 shows a schematic cross section of a vertical GaN p-n junction diode with beveled-mesa termination. In the simulation, the non-punch through condition is considered (the thicknesses of epitaxial layers (d_p, d_n) are sufficiently thick). A target breakdown voltage of 500 V was set. The parallel-plane breakdown field can be written as

$$E_\mathrm{pp} = \sqrt{\frac{2e\,(V_\mathrm{d} - V_\mathrm{b})}{\varepsilon_\mathrm{s}} \cdot \frac{N_\mathrm{a} N_\mathrm{d}}{N_\mathrm{a} + N_\mathrm{d}}}. \tag{2.1}$$

e, V_d, V_B, N_a, N_d are elementary charge, built-in potential, breakdown voltage, an acceptor concentration in a p-layer and a donor concentration in an n-layer, respectively. For GaN, the dielectric constant (ε_s) was investigated by various methods [48–53]. The most cited values for the limiting low-frequency ε_s are 10.4±0.3 for $\varepsilon^{||}$ and 9.5±0.3 for $\varepsilon^{\perp}$, determined by the analysis of the angular dependences of the infrared reflectivity and absorption [48]. Kane *et al* determined ε_s of 10.6±0.3 for $\varepsilon^{||}$ in the kHz frequency range by the capacitance-voltage measurement [49]. In this study, the author uses the value of $\varepsilon_\mathrm{s} = 10.4\varepsilon_0$. In the simulations, $N_\mathrm{d}N_\mathrm{a}/(N_\mathrm{d} + N_\mathrm{a})$ of 5.15×10^{16} cm^{-3} is maintained to keep the parallel-plane breakdown voltage at 500 V (E_pp = 3.0 MV/cm). The ratio of an acceptor concentration to a donor concentration ($N_\mathrm{a}/N_\mathrm{d}$) and a mesa angle θ are varied.

Figure 2.9 shows the simulated electric field distributions for N_a of (a) 1×10^{18} cm^{-3}, 6×10^{17} cm^{-3} and 2×10^{17} cm^{-3} with θ of 30°. The electric field profiles along the p-n junction interfaces are also shown. With decreasing N_a, an expansion of the depletion layer to the p-side comes to be wider. Then, an electric field crowding becomes significantly reduced and the position where the maximum electric field occurs moves to the inside. Figure 2.10 shows the simulated electric field distributions for θ of (a) 30°, (b) 10°, and (c) 1° with N_a of 2×10^{17} cm^{-3}. With decreasing θ, the depletion layer at the surface becomes wider and mainly expands to the p-side. Then, surface electric field is remarkably reduced.

Figure 2.11 shows $E_\mathrm{pp}/E_\mathrm{max}$ as a function of $N_\mathrm{a}/N_\mathrm{d}$ for θ = 1–30°. For the negative bevel ($N_\mathrm{a}/N_\mathrm{d} > 1$), a suppression of electric field crowding can be obtained by a combination of small $N_\mathrm{a}/N_\mathrm{d}$ and small θ. For example, for $\theta = 10°$, $E_\mathrm{pp}/E_\mathrm{max} > 95\%$ can be obtained when $N_\mathrm{a}/N_\mathrm{d} < 4$. For the positive bevel ($N_\mathrm{a}/N_\mathrm{d} < 1$), electric field crowding does not occur. Here, the author mentions an applicability of the beveled-mesa termination for GaN power devices. The relationship shown in Fig. 2.11 does not depend on $N_\mathrm{d}N_\mathrm{a}/(N_\mathrm{d} + N_\mathrm{a})$ and an applied voltage as far as non-punch-through condition and sufficient deep etching are satisfied, confirmed by the TCAD simulations. A breakdown voltage of a device with the same θ can be increased with maintaining $N_\mathrm{a}/N_\mathrm{d}$ by changing doping concentrations, epitaxial thicknesses, and an etching depth. Recently, it is now possible to control a Mg doping level of ca. 1×10^{17} cm^{-3} [54–56]; thus, for $\theta = 10°$, the beveled-mesa termination is practically suitable for devices with relatively low breakdown voltages (up to 1.2 kV-class).

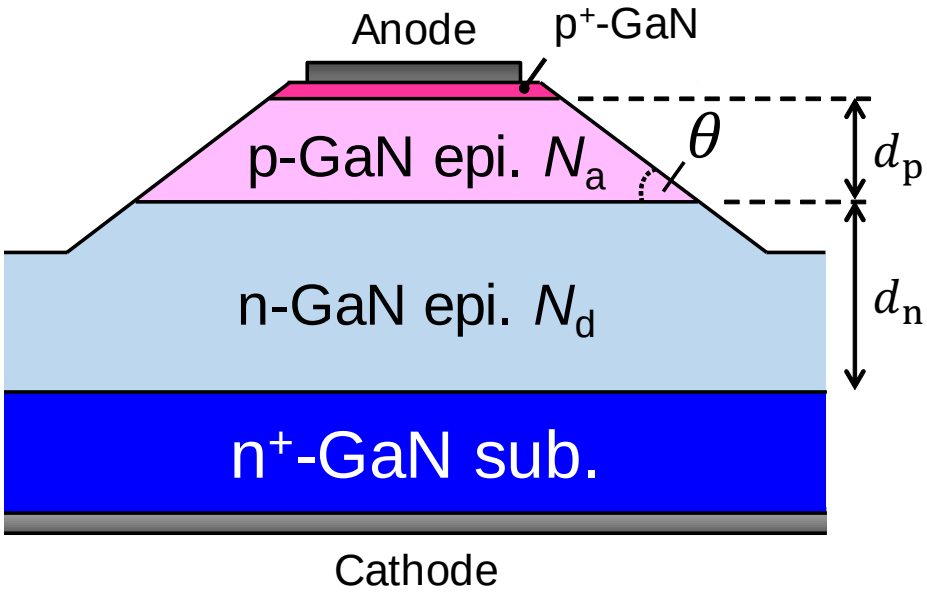

Figure 2.8: Schematic cross section of a GaN p-n junction diode with beveled-mesa termination ($0° < \theta < 90°$).

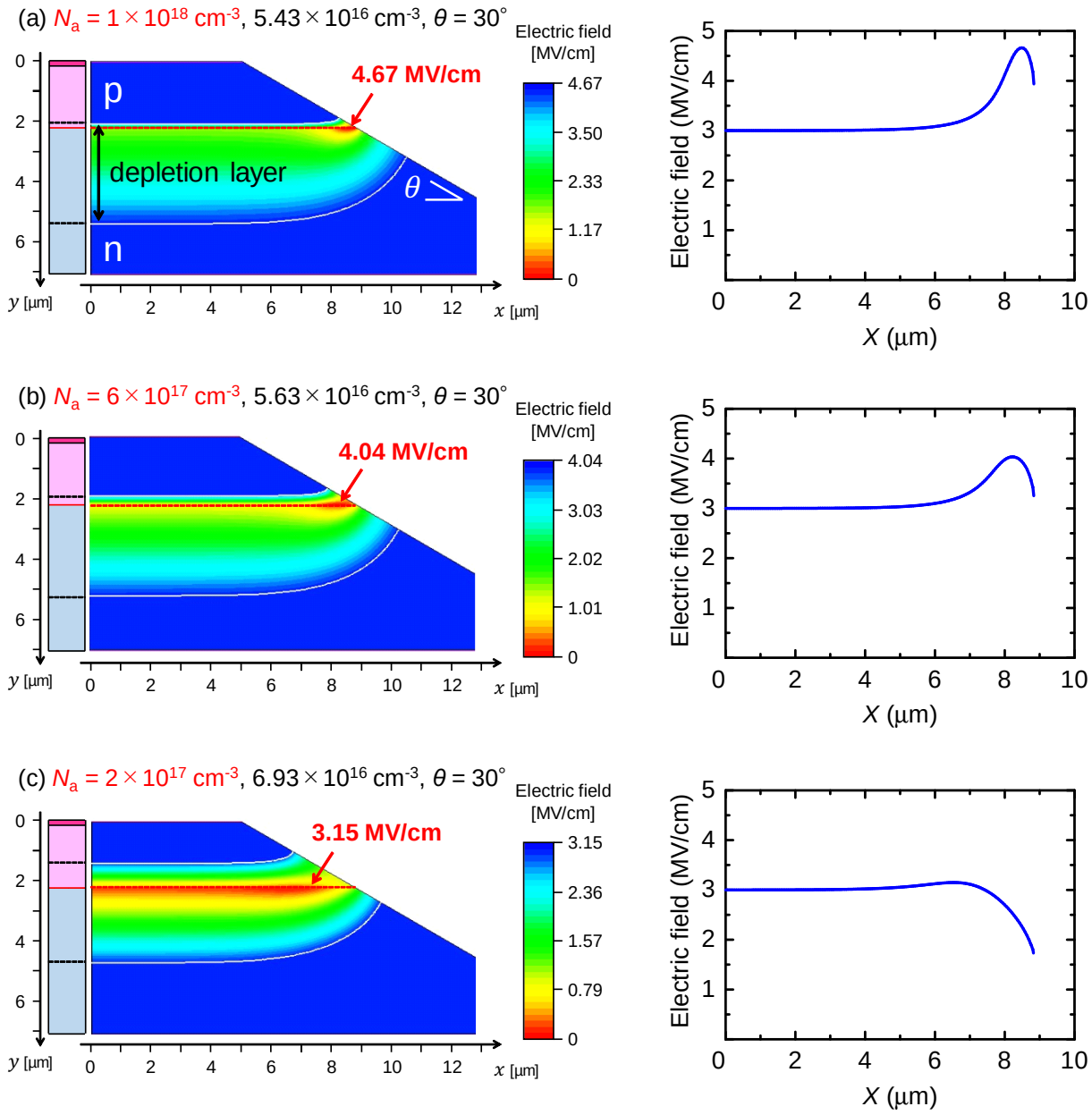

Figure 2.9: Simulated 2-D electric field distributions of the beveled-mesa structures for acceptor concentrations of (a) 1×10^{18} cm^{-3}, (b) 6×10^{17} cm^{-3} and (a) 2×10^{17} cm^{-3} with mesa angle of 30°. The electric field profiles along the p-n junction interfaces are also shown.

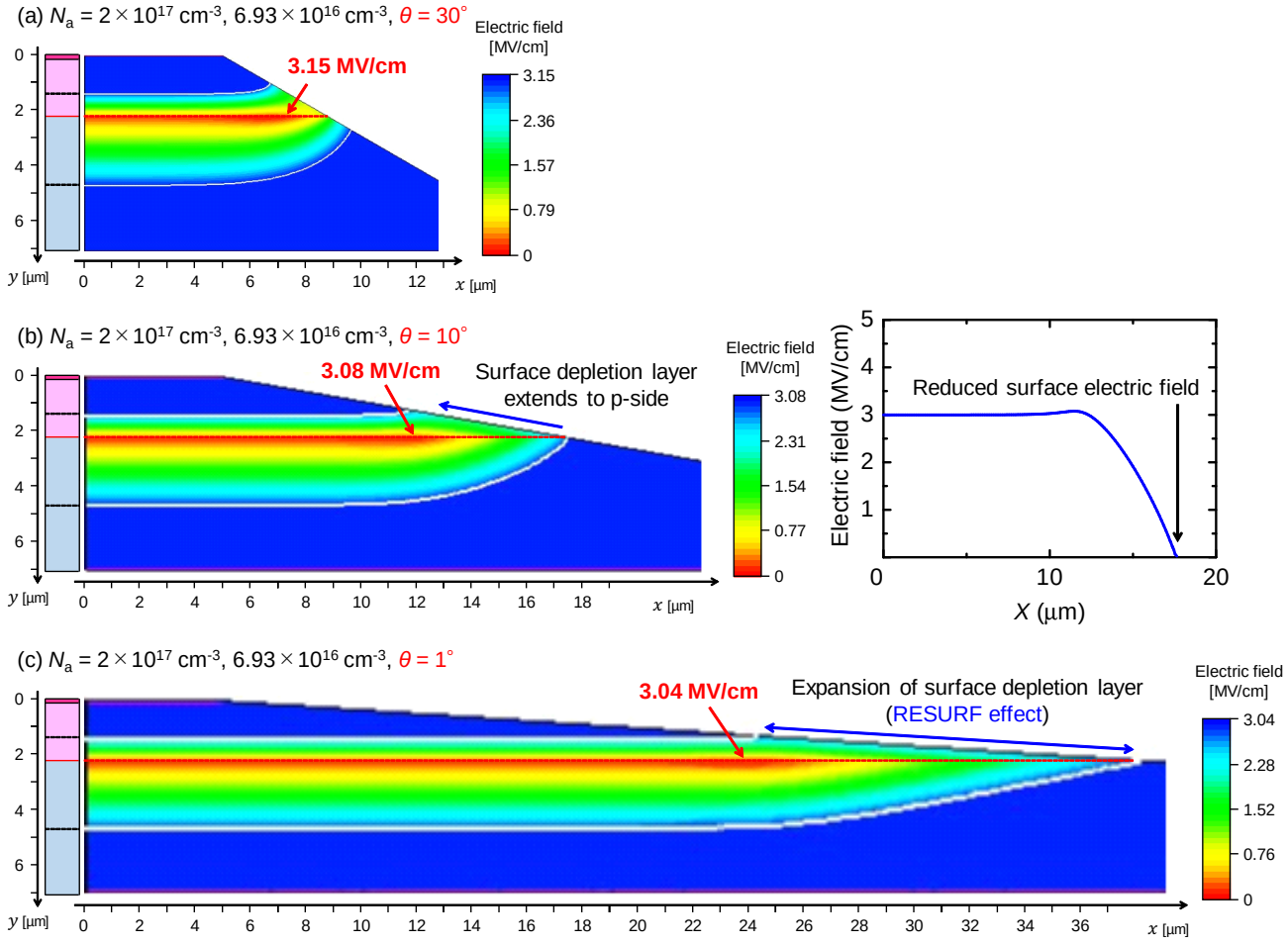

Figure 2.10: Simulated 2-D electric field distributions of the beveled-mesa structures for acceptor concentrations of 2×10^{17} cm^{-3} with mesa angles of (a) 30°, (b) 10° and (c) 1°.

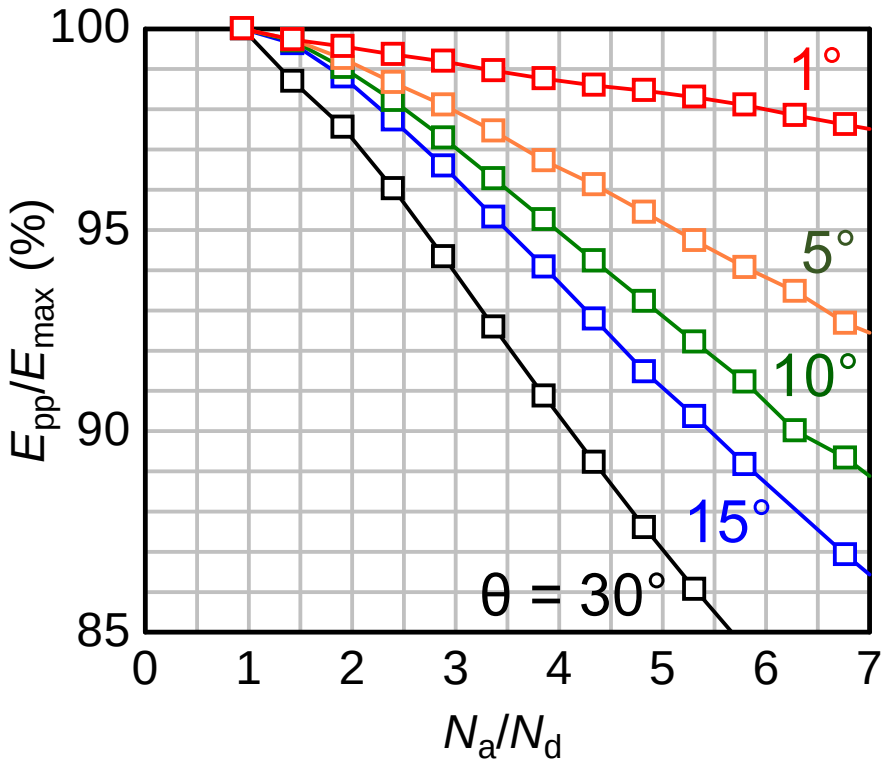

Figure 2.11: Simulated relationship between electric field crowding ($E_{\mathrm{pp}}/E_{\mathrm{max}}$) vs. $N_{\mathrm{a}}/N_{\mathrm{d}}$. With decreasing $N_{\mathrm{a}}/N_{\mathrm{d}}$ and θ, electric field crowding comes to be alleviated. When $N_{\mathrm{a}}/N_{\mathrm{d}} < 1$, electric field crowding does not occur.

2.3 Fabrication of GaN p-n Junction Diodes with Shallow Beveled-Mesa Structure

To confirm the effect of the beveled-mesa termination on suppression of electric field crowding and demonstrate a nearly ideal avalanche breakdown, three negative bevel GaN p-n junction diodes were fabricated with a shallow bevel angle (ca. 10°) and various Mg concentrations (PN1-3). The device structure is shown in Fig. 2.8. The fabrication process flow is shown in Fig. 2.12. The 5 μm thick n-layers, 2 μm thick p-layers, and 0.2 μm thick p^+-layers with Mg concentration of 8×10^{19} cm^{-3} were grown by metalorganic vapor phase epitaxy (MOVPE) on GaN bulk substrates grown by hydride vapor phase epitaxy (HVPE). Photolithography with thick photoresist (AZP4620, MicroChemicals) was performed first, followed by high-temperature post bake (200°C, 3 min) using a hot plate. This post bake causes thermal reflow of the patterned photoresist, which produces a lens-like structure with an edge angle of approximately 10° [57, 58]. Here, a Cl_2-based inductively coupled plasma-reactive ion etching (ICP-RIE) was performed. Under a conventional etching condition, the selectivity of the GaN/photoresist was almost unity. The edge part of the lens-like photoresist mask was translated to GaN, and a beveled-mesa angle of approximately 10° was successfully formed. The mesa height was 3.5 μm. The formation of a smooth mesa surface without structural defects was confirmed by scanning electron microscopy (SEM) observations as shown in Fig. 2.13. The anode and cathode electrodes were formed by the deposition of Ni/Au on the epitaxial layer and Ti/Al/Ni on the backside of the substrate, respectively. Finally, sintering process was performed for 10 min in 550 °C, O_2 ambient to obtain p-ohmic contacts. The contact resistance of $\sim$1 mΩcm^2 was obtained by transfer length method (TLM), and the devices showed good rectifying characteristics.

By secondary ion mass spectrometry (SIMS), the uniform distributions of Si in the n-layers and Mg in the p-layers were confirmed along the depth as shown in Fig. 2.14. The capacitance-voltage (C–V) characteristics of PN1-3 were measured at the frequency of 500 kHz, and clear linearity was observed in all the devices in the C^{-2}–V plots from 0 V to near breakdown voltage as shown in Fig. 2.15, which indicates that the donors in the n-layers and the acceptors in the p-layers are uniformly distributed along the depth as expected from the SIMS results. From the analyses of the slopes in the C^{-2}–V plots using the below relationship

$$\frac{N_\mathrm{a}N_\mathrm{d}}{N_\mathrm{a}+N_\mathrm{d}} = -\frac{2}{\varepsilon_\mathrm{s}eA^2\left(dC^{-2}/dV\right)}, \tag{2.2}$$

$N_\mathrm{a}N_\mathrm{d}/(N_\mathrm{a}+N_\mathrm{d})$ of 5.5×10^{16}, 5.7×10^{16}, and 6.1×10^{16} cm^{-3} were obtained. It should be noted that a junction area (A) was elaborately determined from a mesa bottom diameter, a mesa angle, an etching depth and a p-layer thickness. The obtained $N_\mathrm{a}N_\mathrm{d}/(N_\mathrm{a}+N_\mathrm{d})$ were almost the same as [Mg][Si]/([Mg]+[Si]) for each device. These results suggest that the compensations by carbon atoms or other sources are negligible. The doping concentrations in PN1–3 obtained by SIMS and C–V measurements are summarized in Table 2.1.

Table 2.1: Doping concentrations in the fabricated GaN PNDs (PN1-3) obtained from SIMS and C–V measurements. [Mg][Si]/([Mg]+[Si]) and $N_\mathrm{a}N_\mathrm{d}/(N_\mathrm{a}+N_\mathrm{d})$ are almost same for all the devices, indicating the compensation effect by carbon atoms or other sources are very low and negligible.

	[Mg] (cm^{-3})	[Si] (cm^{-3})	[Mg][Si]/([Mg]+[Si]) (cm^{-3})	$N_\mathrm{a}N_\mathrm{d}/(N_\mathrm{a}+N_\mathrm{d})$ (cm^{-3})
PN1	2.6×10^{17}	7.0×10^{16}	5.5×10^{16}	5.5×10^{16}
PN2	3.4×10^{17}	6.9×10^{16}	5.7×10^{16}	5.7×10^{16}
PN3	4.8×10^{17}	6.9×10^{16}	6.0×10^{16}	6.1×10^{16}

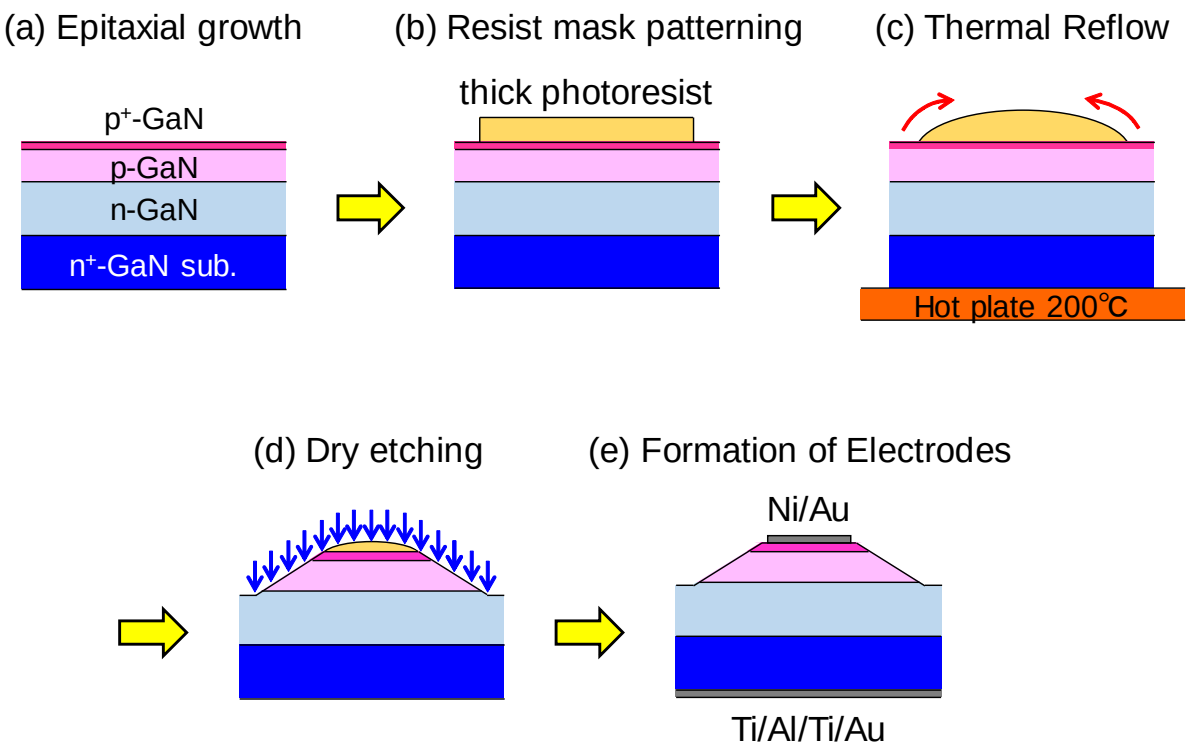

Figure 2.12: Fabrication process flow of a GaN p-n junction diode with beveled-mesa termination.

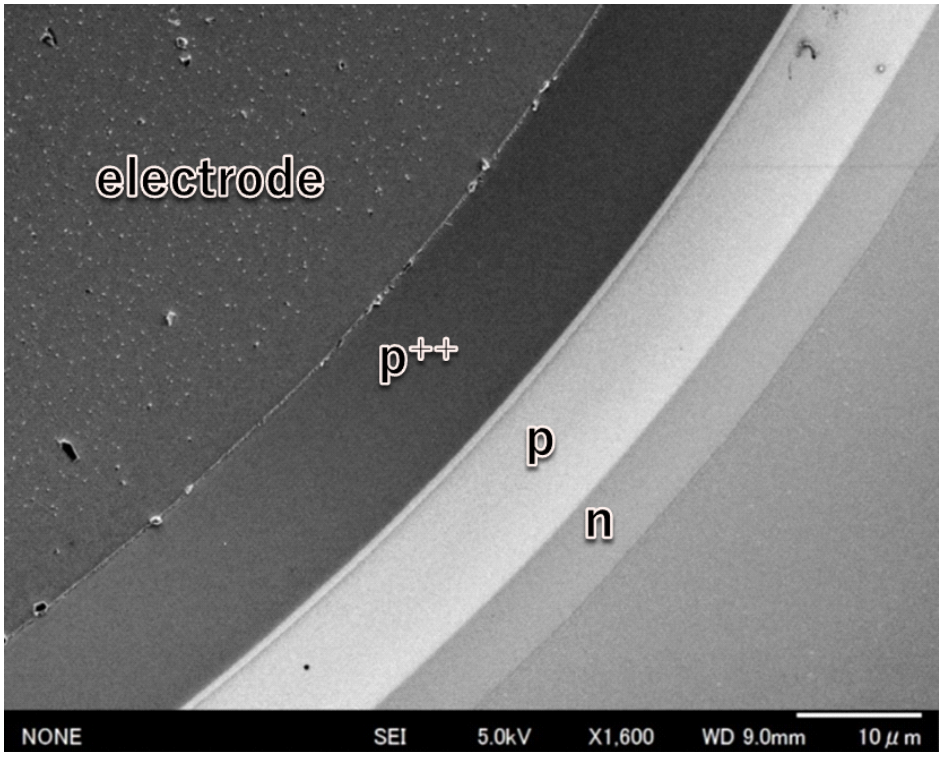

Figure 2.13: Scanning electronic microscope (SEM) image of the beveled-mesa surface.

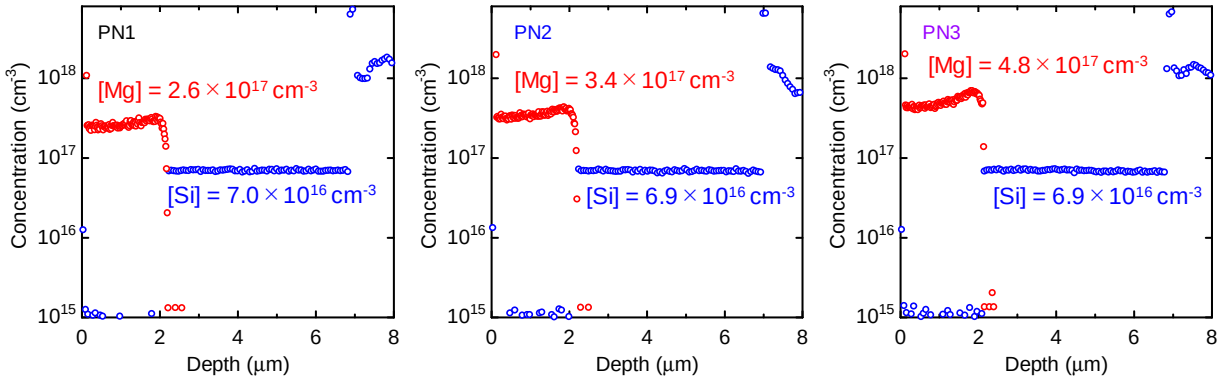

Figure 2.14: Si and Mg profiles along the depth direction for PN1, PN2 and PN3 obtained by SIMS.

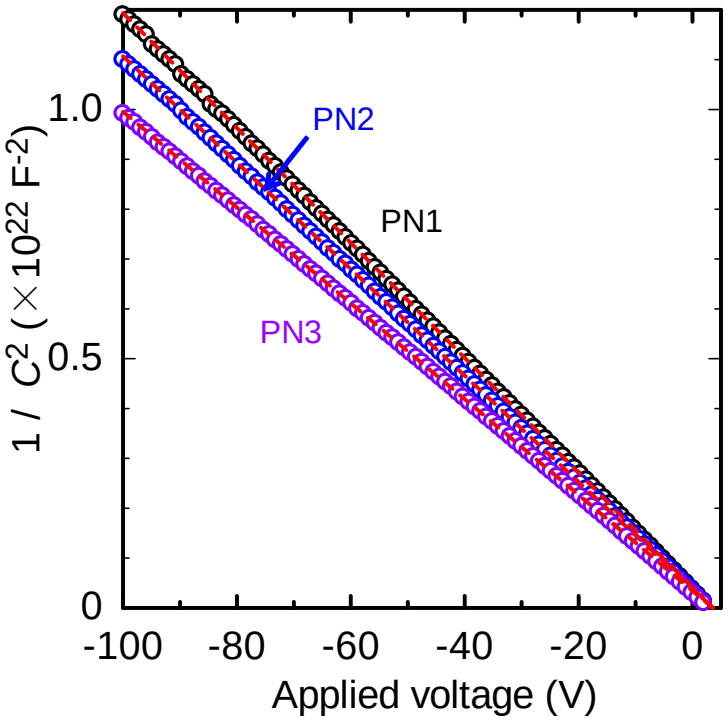

Figure 2.15: Capacitance–voltage characteristics of PN1–PN3.

2.4 Breakdown Characteristics in GaN p-n Junction Diodes

2.4.1 Reverse Current-Voltage Characteristics

The breakdown characteristics of the fabricated GaN p-n junction diodes with negative-beveled mesa termination were measured. To avoid air sparking, the devices were dipped into liquid fluorinert. Figure 2.16 shows the reverse current-voltage (I–V) characteristics for GaN p-n junction diodes with junction diameters of 450 μm. The reverse leakage currents were very small in all the devices. Breakdown voltages of 425, 385, and 345 V were obtained for the PN1, PN2, and PN3 devices, respectively. Variations of the breakdown voltages among the devices in the same wafer were very small. All the devices exhibited high avalanche capabilities: the same breakdown characteristics can be reproduced many times without catastrophic breakdown. Figure 2.17 shows the breakdown voltages and parallel-plane breakdown fields for the PN1, PN2, and PN3 devices as a function of the Mg concentration. The breakdown voltage and breakdown field increased with a decrease in the Mg concentration, which indicates that suppression of electric field crowding was successfully achieved using a lightly doped p-GaN layer. This tendency corresponds well to the relationship between $E_{\rm pp}/E_{\rm max}$ and $N_{\rm a}/N_{\rm d}$ obtained by the simulations (Fig. 2.11). The breakdown field of 2.86 MV/cm was obtained for PN1. Based on the simulation, $E_{\rm pp}/E_{\rm max}$ was approximately 96% ($N_{\rm a}/N_{\rm d} = 3.7$, $\theta = 10^{\circ}$).

2.4.2 Temperature Dependence of Breakdown Voltage

The temperature dependences of the breakdown voltages in the devices were also investigated. Figure 2.18 shows (a) the reverse I–V characteristics of PN1 at 223, 298, and 373 K and (b) the temperature dependence of the breakdown voltage in PN1. The breakdown voltage increased with elevating temperature, which is the signature of an avalanche breakdown: carriers come to be difficult to obtain high energy owing to the increasing phonon scattering rate with elevating temperature. The breakdown field also increased with elevating temperatures from 2.86 MV/cm at 298 K to 2.90 MV/cm at 373 K.

2.4.3 Electroluminescence at Breakdown

At an avalanche breakdown process, many electron-hole pairs are generated and their recombinations occur, which results in electroluminescence [59]. Figure 2.19 shows images of

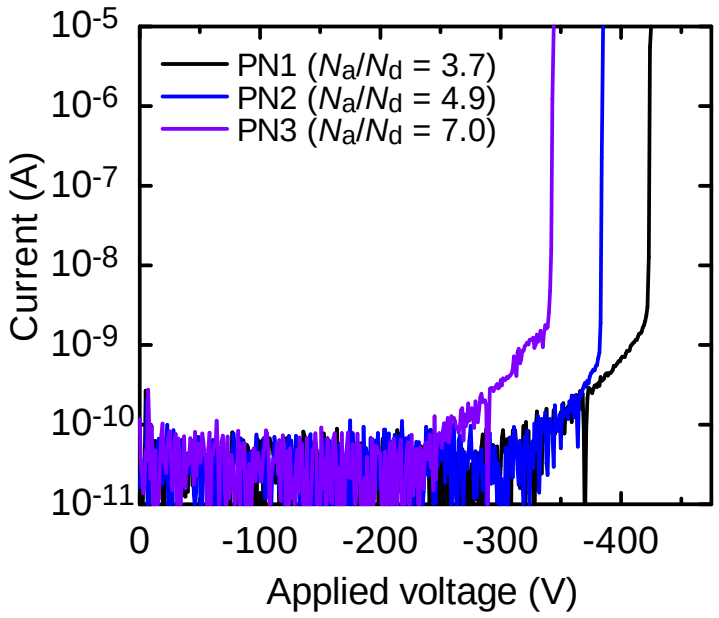

Figure 2.16: Reverse current–voltage characteristics of PN1–PN3.

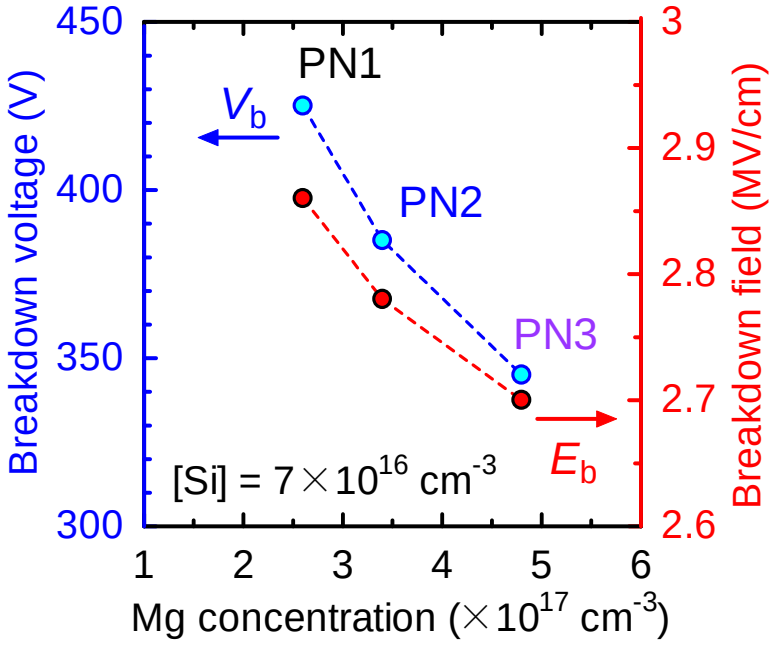

Figure 2.17: Breakdown voltage and breakdown field vs. Mg concentration for PN1–PN3.

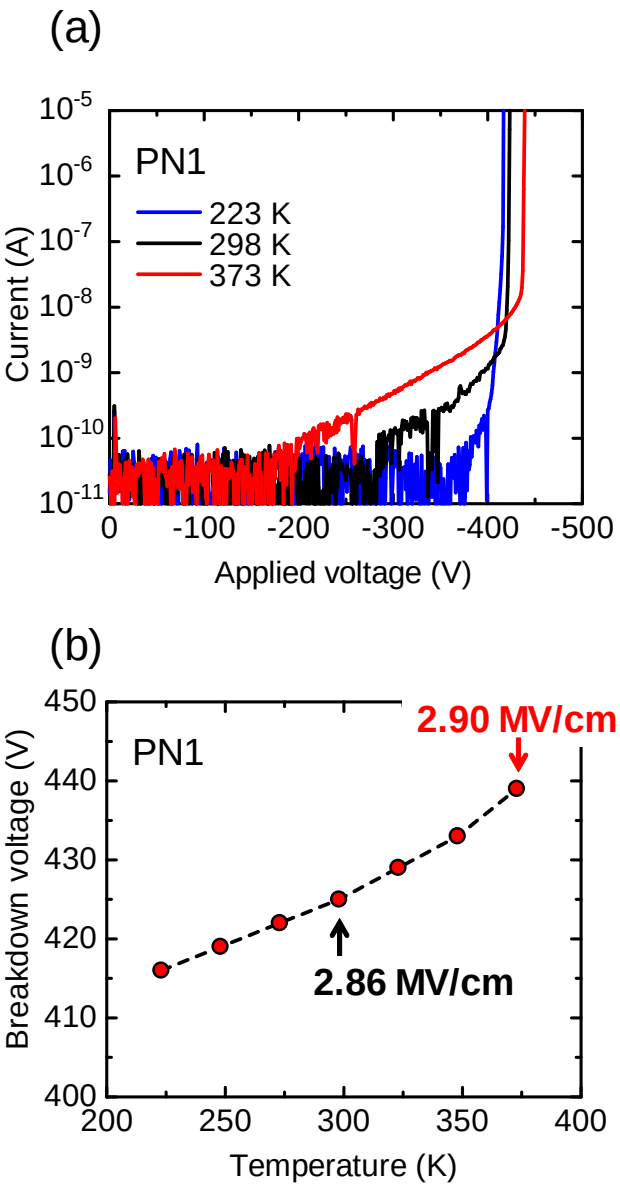

Figure 2.18: (a) Reverse current–voltage characteristics of PN1–PN3 at 223, 298 and 373 K, (b) temperature dependence of the breakdown voltage for PN1.

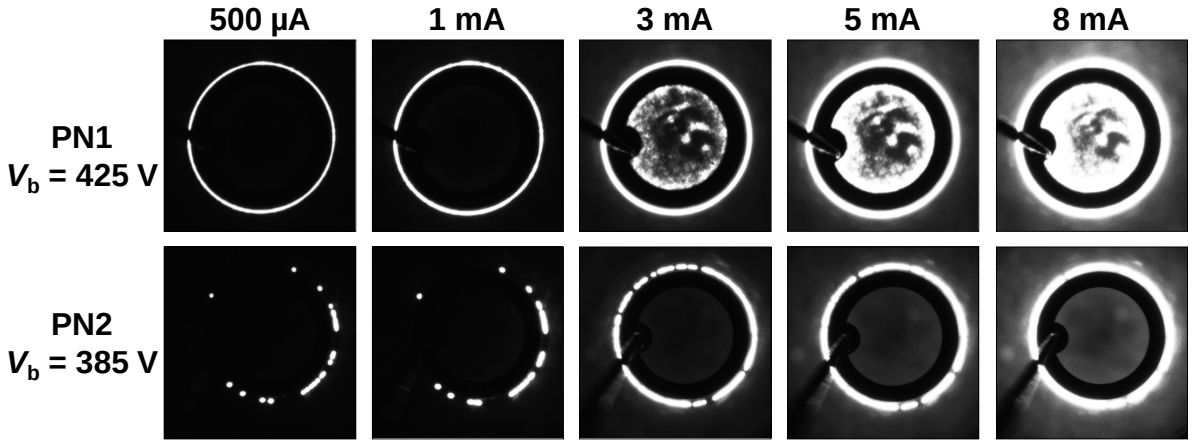

Figure 2.19: Luminescence at the breakdown for PN1 and PN2 at various current level obtained by cooled-CMOS camera (exposure time: 1 s). Ring electrodes were used for luminescence observations.

breakdown luminescence in PN1 and PN2 at various current levels obtained by a cooled-CMOS camera. Ring electrodes were used for observation of the luminescence. For PN1, uniform luminescence at the entire *periphery* was observed at low current level (<1 mA), while the area emitting light increased with the current level and luminescence at the inside of the ring electrode was observed. This indicates that the breakdown in PN1 may be close to the uniform avalanche breakdown [60, 61] which will be discussed in Chapter 3, although electric field crowding still remains at the edge. In contrast, for PN2 (and PN3), luminescence started to be observed at the several parts of the devices periphery. Although the area emitting light also increased with the current level, luminescence at the inside of the ring electrode was not observed. This reflects the localized avalanche breakdown and current crowding due to stronger electric field crowding. The inhomogeneous breakdown could be due to the slope shape which may not be perfectly smooth.

2.5 Discussion

Effect of Dry Etching Damage

The dry etching may induce the point defects near the surface. Kawahara *et al* reported that the significant compensation or deactivation of acceptors occurs in p-type 4H-SiC after dry etching, which may be caused by introducing a large amount of hydrogen and oxygen atoms. This can be recovered by high temperature annealing. However, various kind of defects are generated by RIE into 4H-SiC and the average of total defect concentration of 5×10^{14} cm^{-3} in the region ranging from 0.3 μm to 1.0 μm remains even after annealing [62].

To investigate the effect of the dry etching on GaN, the cross sectional carrier distributions in the fabricated beveled-mesa structure was investigated by non-linear dielectric microscopy (SNDM) [63]. Figure 2.20 shows the obtained cross-sectional carrier distributions from the SNDM measurement. A presence of holes is clearly confirmed in the p-layer and the disappear of holes by dry etching is not observed. At the surface, carriers are not detected. This may be the surface depletion or the measurement problem. If a surface depletion exists, the electric field crowding does not occur, confirmed by TCAD simulation. Thus, dry etching damage near the surface is considered not to effect on the space charge distribution and breakdown characteristics.

Termination Area of Beveled-Mesa Structure

Area efficiency of an edge termination is important because edge termination increase a device size, device cost and $R_{\mathrm{on}}A$. The termination length of the beveled-mesa structure (l_{BM}) can be written as $l_{\mathrm{BM}} = d_{\mathrm{etch}}/\tan(\theta)$. Thick p-layer (deep d_{etch}) and small θ increase l_{BM}. In this study, l_{BM} was about 20 μm (d_{etch} = 3.5 μ and $\theta = 10^{\circ}$). Considering this relationship, the area efficiency can be discussed and compared with other edge terminations.

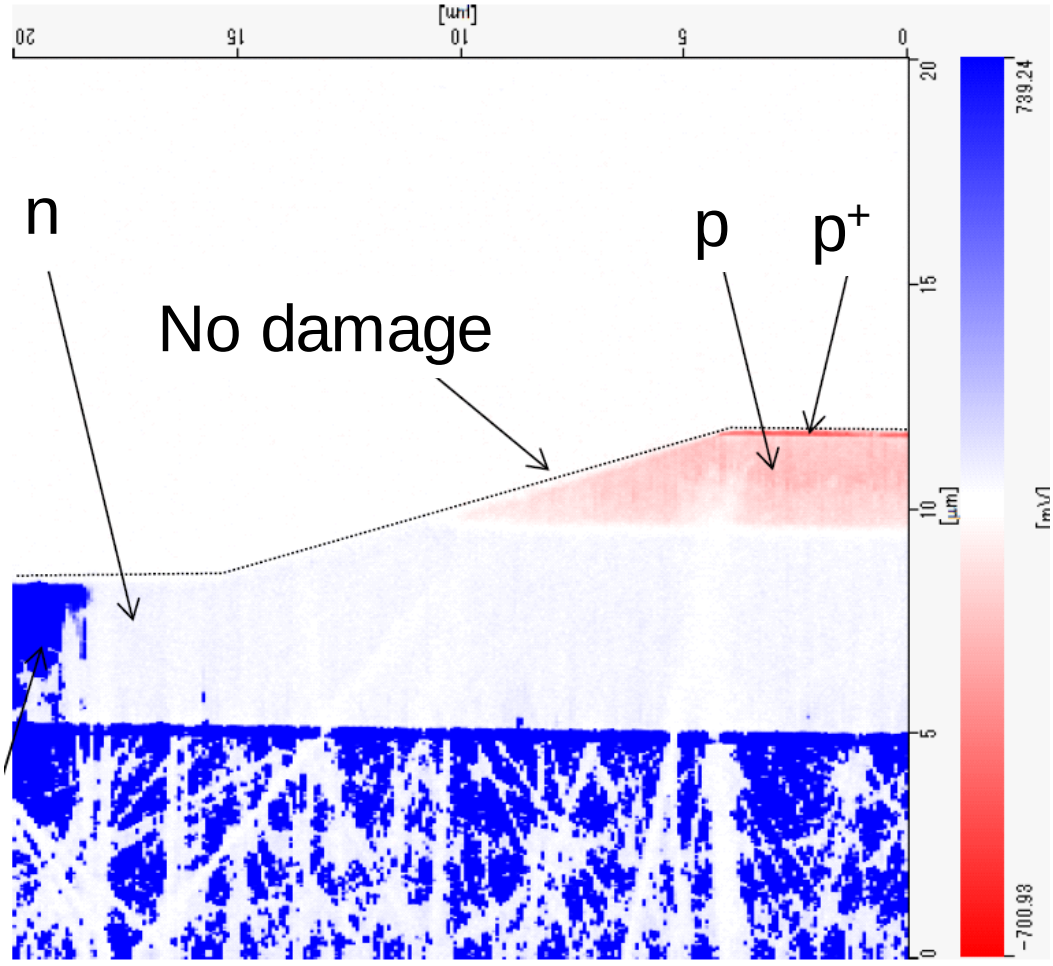

Figure 2.20: Cross-sectional carrier profiles of the edge of the fabricated GaN p-n junction diode obtained by SNDM measurement.

Reduction and Control of Mesa Angle

Small N_a/N_d and small mesa angle are effective to reduce electric field crowding in the beveled-mesa structure. In particular, the beveled-mesa termination is useful for trench MOSFETs, since a p-body layer can be used for the p-layer for the termination. However, the N_a in the p-body layer is required to be optimized for MOS interface characteristics such as threshold voltage. In addition, a thick and low Mg-doped p-layer has high resistance because of low hole mobility. Therefore, especially for a practical application, N_a/N_d is usually larger than unity. To alleviate electric field crowding more, extremely small angle ($\sim 1^\circ$) is needed. To reduce and control the mesa angle, there are two strategies: (1) reducing an angle of the mask at the edge part, (2) reducing the selectivity of GaN/mask. For (1), an optimization of post bake condition, multiple etching to form effective small angle mesa [64, 65] or gray scale lithography (modulation of illumination dose at the edge) are possible ways to reduce an angle of the mask. For (2), changing a material of the mask or etching condition are possible ways. The author tried to reduce the selectivity by reducing the gas ratio of Cl_2/BCl_3. Then, small angle of 7° was achieved. However, the etched surface came to be very rough and depositions of many reaction products and their micro-masking via dry etching were observed simultaneously. Optimization of the etching condition without deteriorating the etched surface is needed.

Vertical Deep-Mesa termination

Very recently, Fukushima *et al*. reported on a vertical GaN p-n junction diode with deeply etched mesa termination, which exhibited high avalanche capability [61]. Figure 2.21 shows the simulated electric field distributions in the p-n junction diode with reverse bias of 800 V for various mesa depths. When the etching depth is shallower than the depth of the depletion layer edge in the deeper side (in n-type region), electric field crowding occurs at the mesa bottom. On the other hand, when the etching depth is deeper than the depth of the depletion layer edge, electric field crowding does not occur in the device. Therefore, an etching technology to form a moat isolation deeper than the depletion layer edge in the deeper side at the breakdown is needed. Fukushima *et al*. performed ICP-RIE with pure Cl_2 gas using an Ni/Ti/Ni/Ti/Ni (50 nm/25 nm/100 nm/25 nm/100 nm) stacked metal mask, which realized the very high etching selectivity of GaN/mask [61]. The device with the etch depth of 10.8 μm exhibited the breakdown voltage of approximately 900 V and the breakdown electric field of 2.4 MV/cm.

In the Chapter 3, the author also fabricates GaN p-n junction diodes with vertical deep-etch termination using Cl_2-based ICP-RIE using a SiO_2 mask. Although the high electric field exists at the p-n junction interface of the mesa surface, GaN p-n junction diodes with avalanche capability are achieved using a polyimide passivation layer.

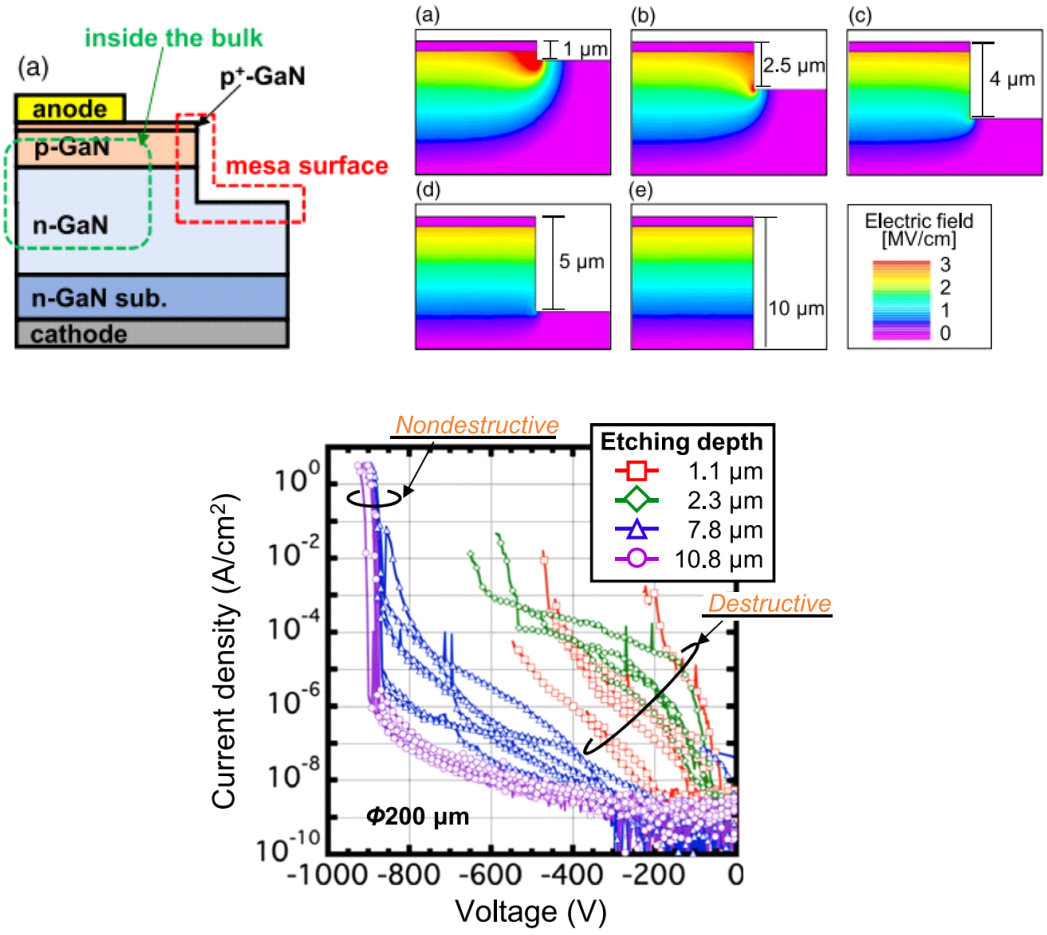

Figure 2.21: The simulated electric field distributions of the p-n junction diodes when a reverse bias of 800 V was applied for the etching depths of (a) 1.0, (b) 2.5, (c) 4.0, (d) 5.0 and (e) 10 μm, reported by Fukushima *et al.* [61]. The reverse I–V characteristics of vertical GaN p-n junction diodes with different etching depths are also shown.

2.6 Summary

In this work, GaN p-n junction diodes with negative beveled-mesa termination were designed and fabricated. The author quantitatively found that small N_a/N_d and small θ are effective to alleviate electric field crowding confirmed by TCAD simulation. The breakdown voltage of the fabricated devices increased as the Mg concentration was decreased. The devices exhibited high avalanche capability and the positive temperature dependence of the breakdown voltage. For the devices with the highest breakdown voltage of 425 V, a parallel-plane breakdown field of 2.86 MV/cm was achieved. This edge termination is useful for GaN power devices with relatively low breakdown voltage, as well as devices employed for fundamental studies on the breakdown characteristics.

References

[1] K. Fujito, S. Kubo, H. Nagaoka, T. Mochizuki, H. Namita, and S. Nagao, *J. Cryst. Growth* **311**, 10 (2009).

[2] H. Fujikura, T. Konno, T. Suzuki, T. Kitamura, T. Fujimoto, and T. Yoshida, *Jpn. J. Appl. Phys.* **57**, 065502 (2018).

[3] R. Dwiliński, R. Doradziwiliński, J. Garczyński, L. P. Sierzputowski, A. Puchalski, Y. Kanbara, K. Yagi, H. Minakuchi, and H. Hayashi, *J. Cryst. Growth* **311**, 10 (2009).

[4] M. Imanishi, K. Murakami, T. Yamada, K. Kakinouchi, K. Nakamura, T. Kitamura, K. Okummura, M. Yoshimura, and Y. Mori, *Appl. Phys. Express* **12**, 045508 (2019).

[5] M. Kanechika, M. Sugimoto, N. Soejima, H. Ueda, O. Ishiguro, M. Kodama, E. Hayashhi, K. Itoh, T. Uesugi, and T. Kachi, *Jpn. J. Appl. Phys.* **46**, 21 (2007).

[6] M. Kodama, M. Sugimoto, E. Hayashi, N. Soejima, O. Ishiguro, M. Kanechika, K. Itoh, H. Ueda, T. Uesugi, and T. Kachi, *Appl. Phys. Express* **1**, 021104 (2008).

[7] Y. Saitoh, K. Sumiyoshi, M. Okada, T. Horii, T. Miyazaki, H. Shiomi, M. Ueno, K. Katayama, M. Kiyama, and T. Nakamura, *Appl. Phys. Express* **3**, 081001 (2010).

[8] S. Chowdhury, B. L. Swenson, and U. K. Mishra, *IEEE Electron Device Lett.* **29(6)**, pp.543–545 (2008).

[9] I. C. Kizilyalli, A. P. Edwards, H. Nie, D. Bour, T. Prunty, and D. Disney, *IEEE Electron Device Lett.* **35(2)**, pp.247–249 (2014).

[10] I. C. Kizilyalli, T. Prunty, and O. Aktas, *IEEE Electron Device Lett.* **36(10)**, pp.1073–1075 (2015).

[11] H. Nie, Q. Diduck, B. Alvarez, A. P. Edwards, B. M. Kayes, M. Zhang, G. Ye, T. Prunty, and D. Bour, *IEEE Electron Device Lett.* **35(9)**, pp.939–941 (2014).

[12] K. Nomoto, Z. Hu, B. Song, M. Zhu, M. Qi, R. Yan, V. Protasenko, E. Imhoff, J. Kuo, N. Kaneda, T. Mishima, T. Nakamura, D. Jena, and H. G. Xing, *IEDM Tech. Digest* (2015) p. 9.7.

[13] K. Nomoto, B. Song, Z. Hu, M. Zhu, M. Qi, N. Kaneda, T. Mishima, T. Nakamura, D. Jena, H. G. Xing, and , *IEEE Electron Device Lett.* **37(2)**, pp.161–164 (2017).

[14] J. Wang, L. Cao, J. Xie, E. Beam, R. McCarthy, C. Youtsey, and P. Fay, *IEDM Tech. Digest* (2017) p. 9.6.

[15] J. Wang, L. Cao, J. Xie, E. Beam, R. McCarthy, C. Youtsey, and P. Fay, *Appl. Phys. Lett.* **113**, 023502 (2018).

[16] H. Fu, K. Fu, X. Huang, I. Baranowski, T-H. Yang, and Y. Zhao, *IEEE Electron Device Lett.* **39(7)**, pp.1018–1021 (2018).

[17] R. Kajitani, H. Handa, S. Ujita, D. Shibata, K. Tanaka, M. Ogawa, H. Ishida, S. Tamura, M. Ishida, and T. Ueda, *Ext. Abst. of Int. Conf. on Solid State Devices and Materials* (2015) p. 1056.

[18] W. Li, K. Nomoto, M. Pilla, M. Pan, X. Gao, D. Jena, and H. G. Xing, *IEEE Trans. Electron Devices* **64(4)**, pp.869–872 (2017).

[19] Y. Zhang, Z. Liu, M. J. Tadjer, M. Sun, D. Piedra, C. Hatem, T. J. Anderson, L. E. Luna, A. Nath, A. D. Koehler, H. Okumura, J. Hu, X. Zhang, X. Gao, B. N. Feigelson, K. D. Hobart, and T. Palacios, *IEEE Electron Device Lett.* **38(8)**, pp.1097–1100 (2017).

[20] T. Oka, Y. Ueno, T. Ina, and K. Hasegawa, *Appl. Phys. Express* **7**, 021002 (2014).

[21] T. Oka, T. Ina, Y. Ueno, and J. Nishii, *Appl. Phys. Express* **8**, 054101 (2015).

[22] T. Oka, T. Ina, Y. Ueno, and J. Nishii, *Proc. of Int. Symp. on Power Semiconductor Device and ICs* (2019) p. 303.

[23] D. Shibata, R. Kajitani, M. Ogawa, K. Tanaka, S. Tamura, T. Hatsuda, M. Ishida, and T. Ueda, *IEDM Tech. Digest* (2016) p. 10.1.

[24] M. Sun, Y. Zhang, X. Gao, and T. Palacios, *IEEE Electron Device Lett.* **38(4)**, pp.509–512 (2017).

[25] Y. Zhang, M. Sun, D. Piedra, J. Hu, Z. Liu, Y. Lin, X. Gao, K. Shepard, and T. Palacios, *IEDM Tech. Digest* (2017) p. 9.2.

[26] C. Gupta, C. Lund, S. H. Chan, A. Agarwal, J. Liu, Y. Enatsu, S. Keller, and U. K. Mishra, *IEEE Electron Device Lett.* **38(3)**, pp.353–355 (2017).

[27] D. Ji, C. Gupta, S. H. Chan, A. Agarwal, W. Li, S. Keller, U. K. Mishra, and S. Chowdhury, *IEDM Tech. Digest* (2017) p. 9.4.

[28] R. Tanaka, S. Takashima, K. Ueno, H. Matsuyama, Y. Fukushima, M. Edo, and K. Nakagawa, *Ext. Abst. of Int. Conf. on Solid State Devices and Materials* (2019) p. 443.

[29] B. J. Baliga, *Fundamentals of Power Semiconductor Devices*, (Springer, 2008), pp. 91–166.

[30] G. Feng, J. Suda, and T. Kimoto, *IEEE Trans. Electron Devices* **59(2)**, pp.414–418 (2011).

[31] H. Niwa, J. Suda, and T. Kimoto, *Appl. Phys. Express* **5**, 064001 (2012).

[32] H. Miyake, T. Okuda, H. Niwa, T. Kimoto, and J. Suda, *IEEE Electron Device Lett.* **33(11)**, pp.1598–1600 (2012).

[33] F. Udrea, G. Deboy, and T. Fujihira, *IEEE Trans. Electron Devices* **64(3)**, pp.713–727 (2017).

[34] Y. Saitoh, T. Masuda, H. Michikoshi, H. Shiomi, S. Harada, and Y. Mikamura, *Jpn. J. Appl. Phys.* **58**, SBBD11 (2019).

[35] H. Niwa, G. Feng, J. Suda, and T. Kimoto, *Proc. of Int. Symp. on Power Semiconductor Device and ICs* (2012) p. pp.381–384.

[36] H. Niwa, G. Feng, J. Suda, and T. Kimoto, *IEEE Trans. Electron Devices* **59(10)**, pp.2748–2752 (2012).

[37] F. Udrea, T. Trajkovic, J. Thomsonb, L. Coulbeckb, P.R. Waindb, G.A.J. Amaratunga, and P. Taylorb, *Proc. of Int. Symp. on Power Semiconductor Device and ICs* (2001) p. pp.129–132.

[38] Q. Qian, W. Sun, J. Zhu, and S. Liu, *IEEE Electron Device Lett.* **31**, 12 (2010).

[39] T. Niwa, T. Fujii, and T. Oka, *Appl. Phys. Express* **10**, 091002 (2017).

[40] T. Narita, T. Kachi, K. Kataoka, and T. Uesugi, *Appl. Phys. Express* **10**, 016501 (2017).

[41] M. Takahashi, A. Tanaka, Y. Ando, H. Watanabe, M. Deki, M. Kushimoto, S. Nitta, Y. Honda, K. Shima, K. Kojima, S. F. Chichibu, K. J. Chen, and H. Amano, *Phys. Status Solidi B* **1900554**, 1–7 (2019).

[42] H. Sakurai, M. Omori, S. Yamada, Y. Furukawa, H. Suzuki, T. Narita, K. Kataoka, M. Horita, M. Bockowski, J. Suda, and T. Kachi, *Appl. Phys. Lett.* **115**, 142104 (2019).

[43] A. M. Ozbek and B. J. Baliga, *IEEE Electron Device Lett.* **32(3)**, pp.300–302 (2011).

[44] J. R. Dickerson, A. A. Allerman, B. N. Bryant, A. J. Fischer, M. P. King, M. W. Moseley, A. M. Armstrong, R. J. Kaplar, I. C. Kizilyalli, O. Aktas, J. J. Wierer, and Jr., *IEEE Trans. Electron Devices* **63(1)**, pp.419–425 (2016).

[45] H. Fu, K. Fu, S. R. Alugubelli, C. Y. Cheng, X. Huang, H. Chen, T.-H. Yang, C. Yang, J. Zhou, J. Montes, X. Deng, X. Qi, S. M. Goodnick, F. A. Ponce, and Y. Zhao, *IEEE Electron Device Lett.* **41(1)**, pp.127–130 (2020).

[46] H. Nie, A. P. Edwards, D. R. Disney, R. J. Brown, and I. C. Kizilyalli, *U.S. Patent* (2016) p. 8716716.

[47] J.R. Laroche, F. Ren, K. W. Baik, S. J. Pearton, B. S. Shelton, and B. Peres, *J. Electron. Mater.* **34**, 4 (2005).

[48] A. S. Barker and Jr. and M. Ilegems, *Phys. Rev. B* **7(2)**, pp.743–750 (1973).

[49] M. J. Kane, M. J. Uren, D. J. Wallis, P. J. Wright, D. E. J. Soley, A. J. Simon, and T. Martin, *Semicon. Sci. Technol.* **26**, 085006 (2011).

[50] W. Soluch, E. Brzowski, M. Lysakowska, and J. Sadura, *IEEE Trans. Ultrasonic, Ferroelectrics, and Frequency Control* **58**, 11 (2011).

[51] M. T. Hibberd, V. Frey, B. F. Spencer, P. W. Mitchell, P. Dawson, M. J. Kappers, R. A. Oliver, C. J. Humphreys, and D. M. Graham, *Solid State Com.* **247**, 68 (2016).

[52] F. Bernardini, V. Fiorentini, and D. Vanderbilt, *Phys. Rev. Lett.* **79**, 20 (1997).

[53] K. Karch, J.-M. Wagner, and F. Bachstedt, *Phys. Rev. B* **57**, 12 (1998).

[54] T. Narita, Y. Tokuda, T. Kogiso, K. Tomita, and T. Kachi, *J. Appl. Phys.* **123**, 161405 (2018).

[55] T. Kogiso, T. Narita, H. Yoshida, Y. Tokuda, K. Tomita, and T. Kachi, *Jpn. J. Appl. Phys.* **58**, SCCB36 (2019).

[56] T. Maeda, T. Narita, H. Ueda, M. Kanechika, T. Uesugi, T. Kachi, T. Kimoto, M. Horita, and J. Suda, *Jpn. J. Appl. Phys.* **58**, SCCB14 (2019).

[57] F. Yan, C. Qin, J. H. Zhao, and M. Weiner, *Mater. Sci. Forum* **389–393**, pp. 1305–1308 (2002).

[58] H. Niwa, J. Suda, and T. Kimoto, *IEEE Trans. Electron Devices* **62(10)**, pp.3326–3333 (2015).

[59] S. Mandal, M. B. Kanathila, C. D. Pynn, W. Li, J. Gao, T. Margalith, M. A. Laurent, and S. Chowdhury, *Semicon. Sci. Technol.* **33**, 065013 (2018).

[60] T. Maeda, T. Narita, H. Ueda, M. Kanechik, T. Uesugi, T. Kachi, T. Kimoto, M. Horita, and J. Suda, *IEDM Tech. Digest* (2018) p. 30.1.

[61] H. Fukushima, S. Usami, M. Ogura, Y. Ando, A. Tanaka, M. Deki, M. Kushimoto, S. Nitta, Y. Honda, and H. Amano, *Jpn. J. Appl. Phys.* **58**, SCCD25 (2019).

[62] K. Kawahara, M. Krieger, J. Suda, and T. Kimoto, *J. Appl. Phys.* **108**, 023706 (2010).

[63] Y. Cho, S. Kazuta, and K. Matsuura, *Appl. Phys. Lett.* **75**, 2833 (1999).

[64] A. Salemi, H. Elahipanah, G. Malm, C.-M. Zetterling, and M. Östling, *Proc. of Int. Symp. on Power Semiconductor Device and ICs* (2015) p. 249.

[65] H. Ohta, N. Asai, F. Horikiri, Y. Narita, T. Yoshida, and T. Mishima, *IEEE Electron Device Lett.* **41(1)**, pp.123–126 (2020).

Chapter 3

Breakdown Electric Field in GaN p-n Junction Diodes

3.1 Introduction

Under high electric field, carriers are accelerated and cause impact ionization, resulting in generations of electron-hole pairs. The generated carriers are also accelerated, repeat to cause impact ionization and carriers are multiplicated like *avalanche* in a depletion layer. Avalanche breakdown is defined as "an avalanche multiplication factor becomes infinity" [1]. Thus, parallel-plane breakdown voltage, which means intrinsic avalanche breakdown in a semiconductor without electric field crowding, is determined by epitaxial structure (a thickness and a space charge concentration) and impact ionization coefficients. Here, it is worth to note that the critical electric field, which is the maximum electric field at the parallel-plane breakdown, is a strong function of space charge concentration.

For mature semiconductors such as Si, GaAs and 4H-SiC, avalanche breakdown characteristics and impact ionization coefficients are well studied [2–15]. The theoretical breakdown voltage for parallel-plane p-n junction can be simulated using the impact ionization coefficients. Then, the critical electric field and a depletion layer width at a breakdown are also obtained. Figure 3.1 and Figure 3.2 show breakdown voltage and critical electric field for Si and 4H-SiC p-n junctions, respectively. These curves were simulated for non-punch-through condition using the impact ionization coefficients [2, 15], and well reproduce the experimental data of avalanche breakdown in devices without electric field crowding. It is obvious that the critical electric field of 4H-SiC is approximately 5–8 times higher than that of Si at the same doping concentration. Figure 3.3 shows a doping concentration and a required thickness of a drift layer versus breakdown voltage for Si and 4H-SiC. For example, a device with breakdown voltage of 1 kV needs $N_{\rm d} = 1.6{\times}10^{14}$ cm^{-3} and $t_{\rm drift} = 91$ μm for Si. For the same breakdown voltage 4H-SiC device, $N_{\rm d} = 2{\times}10^{16}$ cm^{-3} and $t_{\rm drift} = 7.7$ μm are needed. These fundamental data of avalanche breakdown are very important, since these data give a design space of an drift layer in a power device for a required breakdown voltage.

There are several reports on an breakdown characteristics in GaN Schottky barrier diodes [16–19]. Bandić *et al.* demonstrated heteroepitaxial GaN Schottky rectifiers fabricated on a sapphire substrate with breakdown voltage of 450 V. From the experimental results, they estimated the maximum breakdown electric field of (2.2±0.7) MV/cm [16]. Johnson *et al.* fabricated GaN Schottky rectifiers with Mg-implanted guard ring edge termination using GaN freestanding substrates grown on sapphire substrates. The devices showed the breakdown voltage of 160 V and the maximum breakdown electric field of 2.1 MV/cm at room temperature. However, the breakdown voltage showed a negative temperature coefficient, suggesting that a large number of surface and bulk defects caused a premature breakdown before the parallel-plane avalanche breakdown [17]. Saitoh *et al.* demonstrated homoepitaxial GaN Schottky barrier diodes fabricated on GaN freestanding substrates with excellent performance [18]. The device, which has 5 μm thick n^--GaN layer with the Si concentration of 8×10^{15} cm^{-3} and the field plate edge termination, showed the breakdown voltage of 1100 V. As shown in Fig. 3.4, this breakdown was limited by a large leakage current. The maximum breakdown electric field is estimated to be at most 2.5 MV/cm considering the punch-through (trapezoid-shape) electric field distribution.

Owing to high electric field at the Schottky interface, the thermionic field emission (TFE) current [20, 21] should become significant as shown in Fig. 3.5, which was calculated using the formula based on the TFE model [20, 21] with consideration of image force lowering [22]. Therefore, a large reverse leakage current flows before avalanche breakdown, and it seems to be difficult to characterize avalanche breakdown voltage in GaN using a Schottky junction. To avoid a large leakage current induced by the TFE, a trench metal-insulator-semiconductor (MIS) barrier Schottky (TMBS) [23, 24] and a junction barrier Schottky (JBS) [25–27] rectifiers have been proposed. Hasegawa *et al.* demonstrated a GaN TMBS rectifier maintaining low leakage current at 200°C with blocking voltage of 750 V [24]. Significant reduction of leakage current compared to a simple Schottky barrier diode was observed owing to reduction of electric field at the Schottky junction using the TMBS structure. Nonetheless, Ózbek and Baliga reported on a Pt/n-GaN Schottky barrier diode with a high-resistive amorphous layer formed by Ar implantation as an edge termination. It is described that the device, which has 4 μm thick i-GaN layer with the carrier density of 1×10^{14} cm^{-3}, showed the breakdown voltage of 1650 V with the implantation dose of 2×10^{16} cm^{-2}. Then, the high reverse leakage current due to the implantation damage was observed ($>$ 1 mA at the reverse bias of 50 V), as shown in Fig. 3.6. They estimated the maximum breakdown electric field of 3.75 MV/cm in the device. However, as mentioned above, it seems to be impossible to achieve such high electric field ($>$ 3 MV/cm) using a Schottky junction.

GaN p-n junction diodes with avalanche breakdown have been reported from many institutions [28–32]. Kozodoy *et al.* investigated the effect of dislocations on the reverse I–V characteristics in GaN p-n junction diodes fabricated on sapphire substrates using lateral epitaxial overgrowth (LEO) [28]. In the devices fabricated on the LEO region (the threading

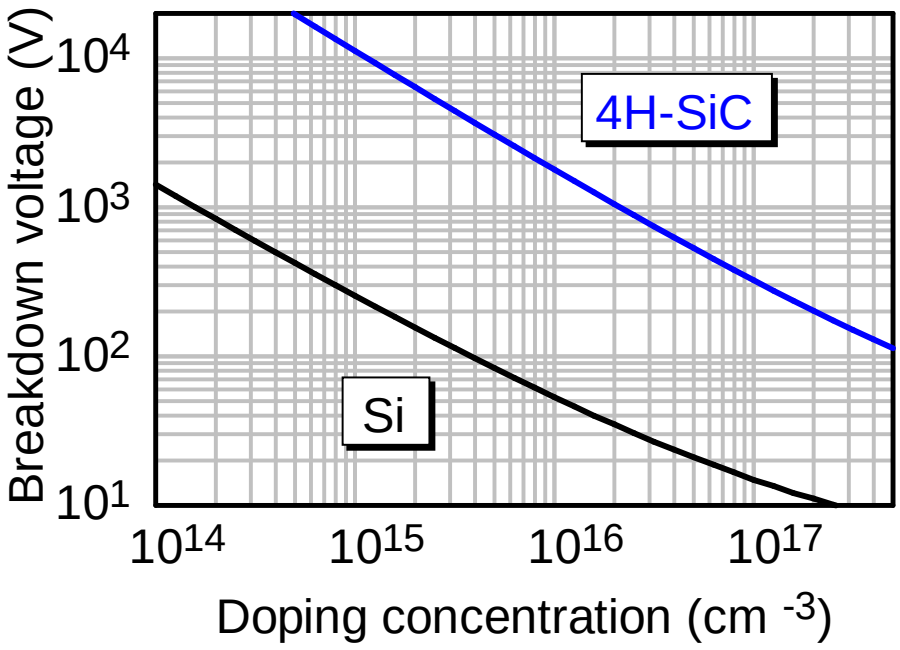

Figure 3.1: Breakdown voltage versus doping concentration in a drift layer for Si and 4H-SiC in the non-punch-through condition.

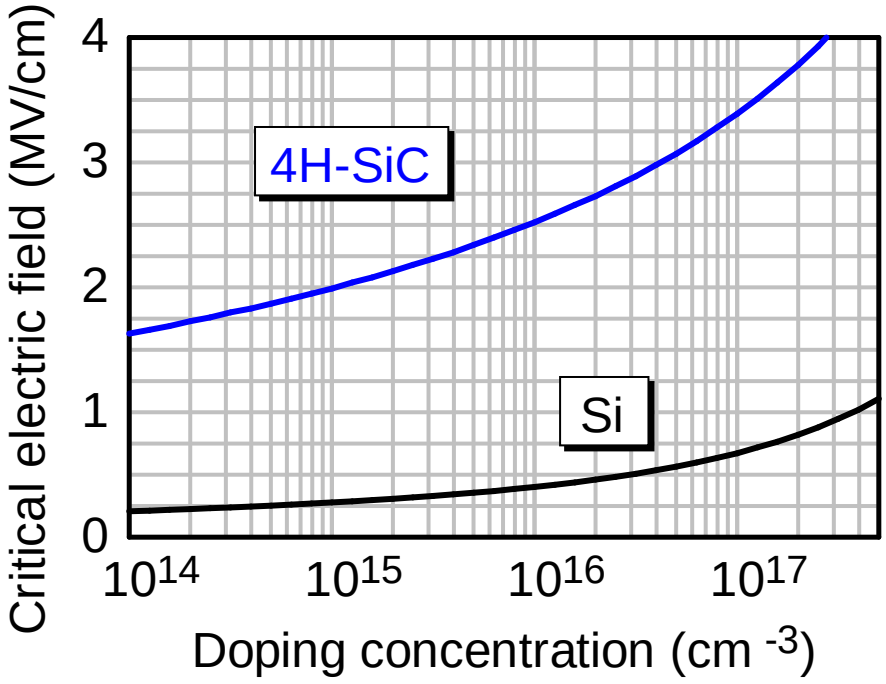

Figure 3.2: Critical electric field versus doping concentration in a drift layer for Si and 4H-SiC in the non-punch-through condition.

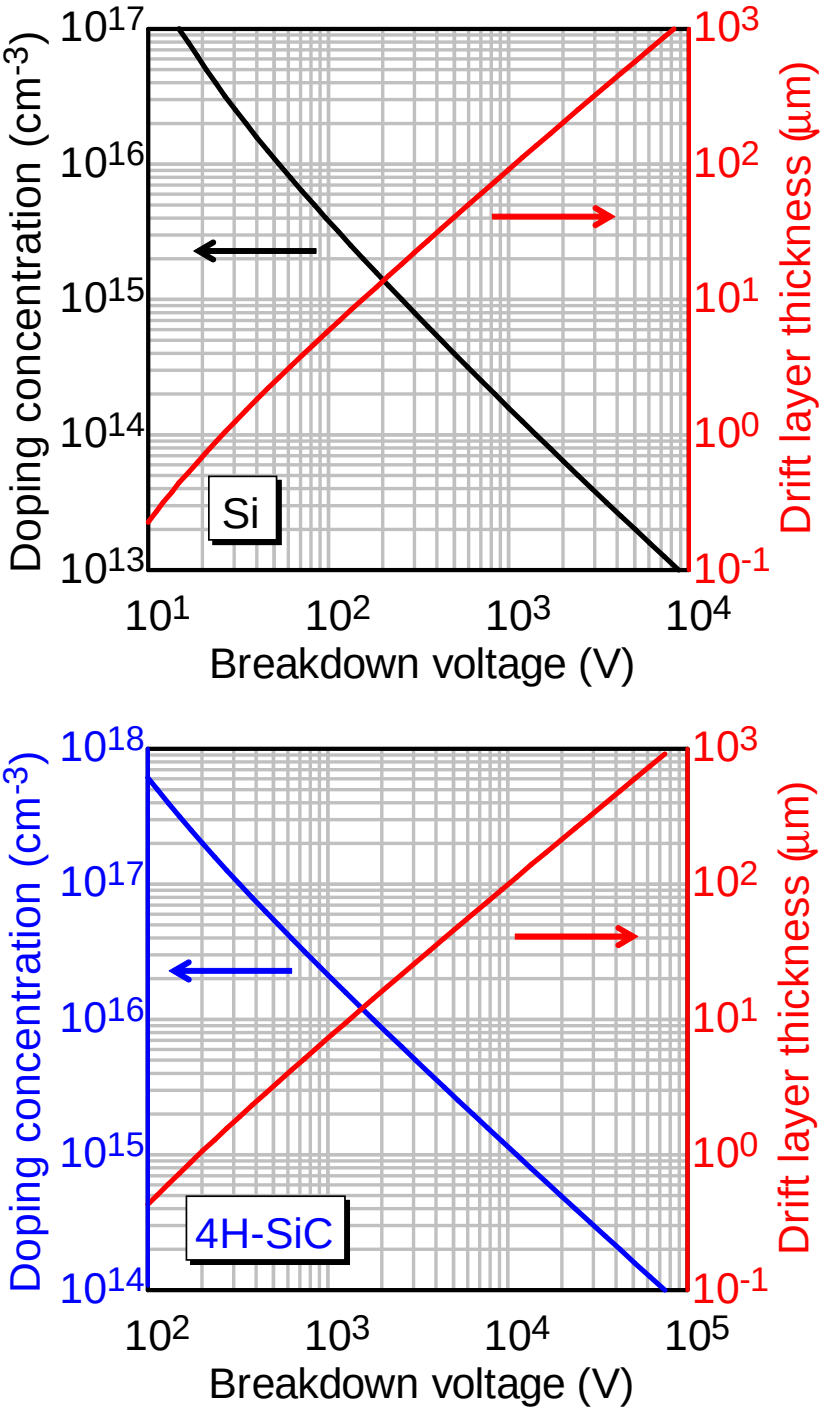

Figure 3.3: Doping concentration and required thickness of a drift layer versus breakdown voltage for Si and 4H-SiC in the non-punch-through condition.

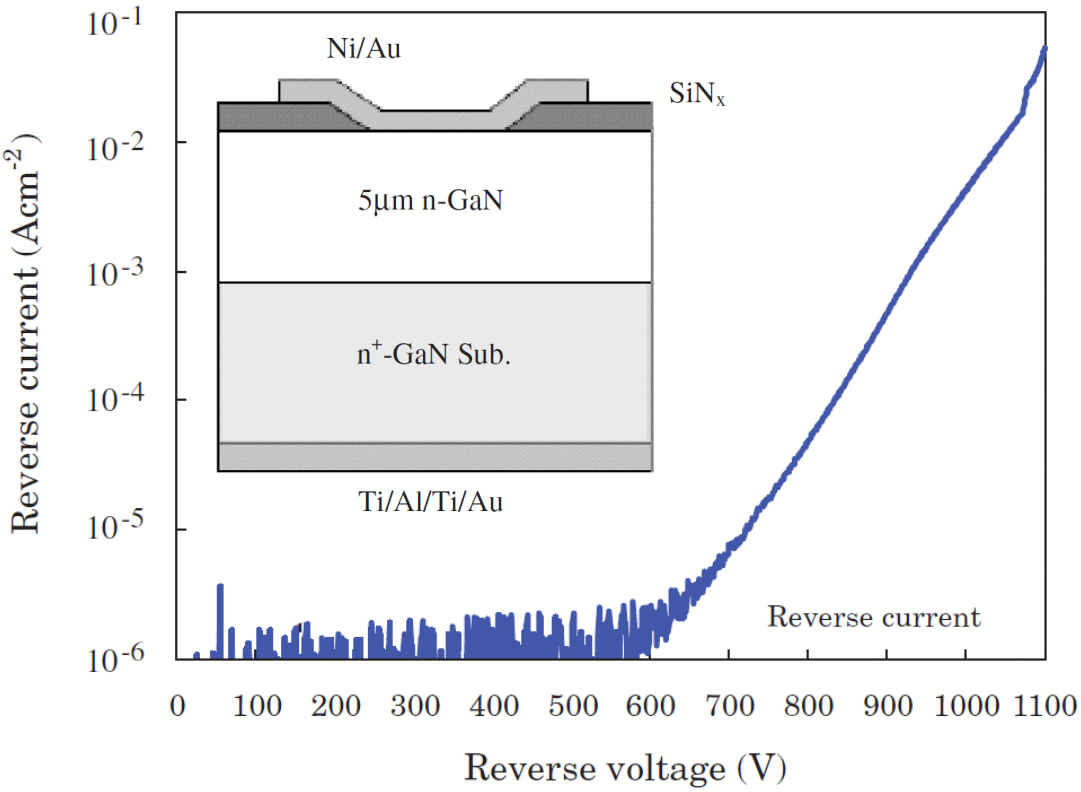

Figure 3.4: Reverse I–V characteristics of the Ni/n-GaN Schottky barrier diode reported by Saitoh *et al.* [18]. Reverse leakage curent increased with increasing reverse bias, and the high current flows before avalanche breakdown. At the reverse bias of 1100 V, the maximum electric field is estimated to at most ∼2.5 MV/cm.

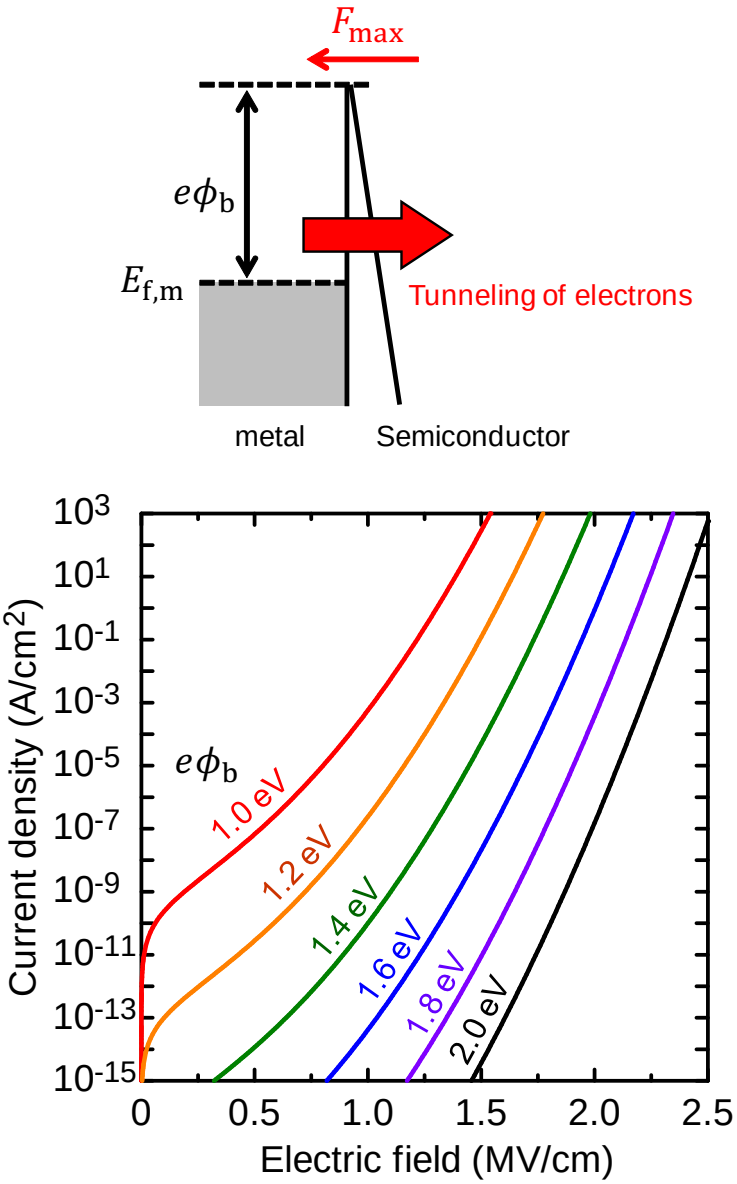

Figure 3.5: The diagram of thermionic field emission (TFE) transport and the calculated TFE current for a GaN Schottky barrier diode with various barrier heights of 1.0–2.0 eV as a function of electric field at the Schottky interface. In the calculation, the analytical formula proposed by Hatakeyama *et al.* [21] was used, and the effect of the image force lowering [22] was considered.

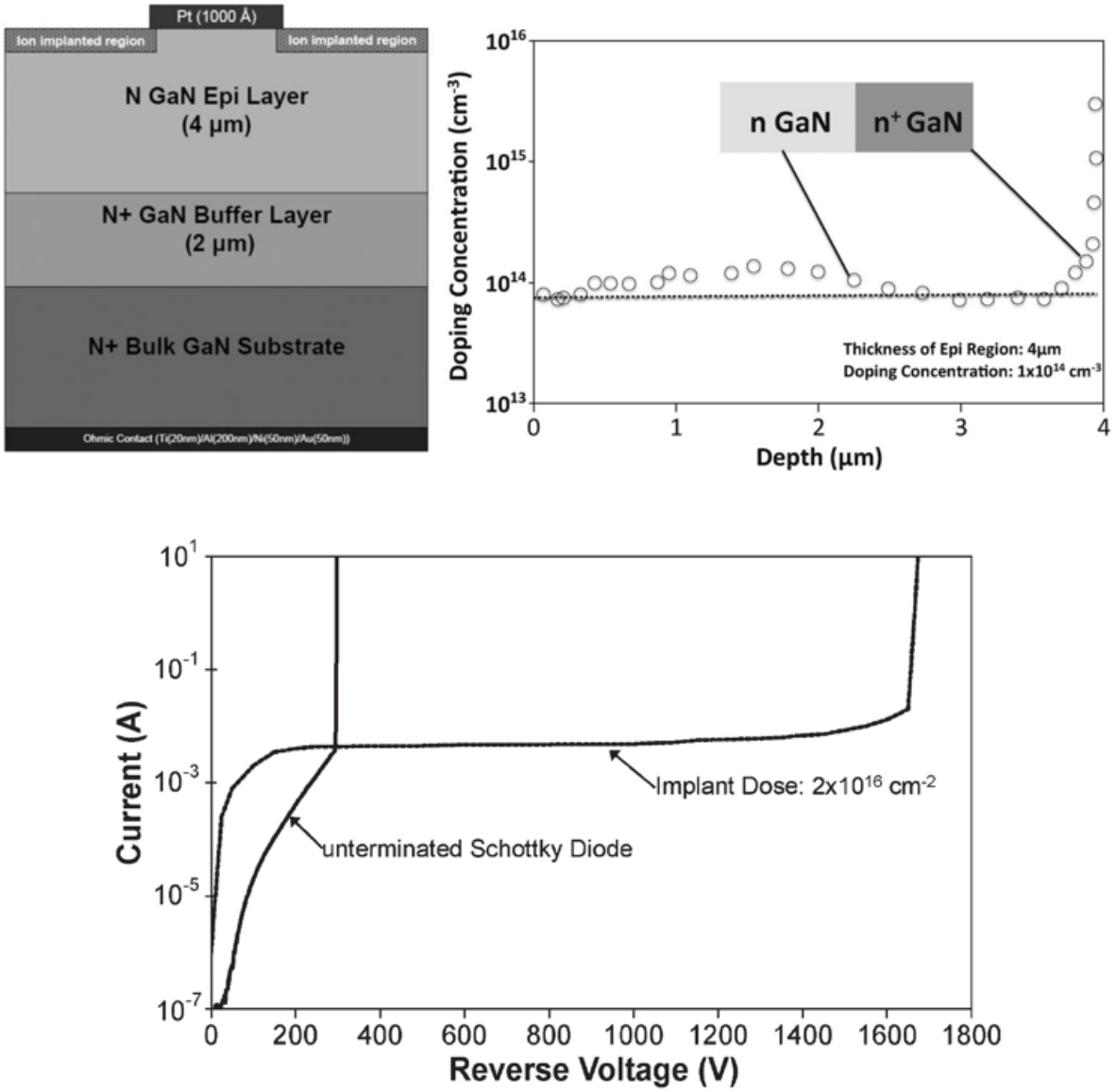

Figure 3.6: The device structure, the carrier profile and the reverse I–V characteristics of the Pt/n-GaN Schottky barrier diode. The Schottky contact has the area of 1.8×10^{-4} cm^{-2} (the diameter of 150 μm). Significant large leakage current over 10A/cm^2 is observed for the device with Ar implatation edge termination above the reverse bias voltage of 50 V.

dislocation density (TDD) of $< 10^6$ cm^{-2}) showed significant reduction of leakage current compared to the devices in the window region (TDD of $\sim 4 \times 10^8$ cm^{-2}). However, the breakdown voltage for both devices were the same (90 V), and the peak electric field was approximately 2 MV/cm. Kizilyalli *et al*. reported on the GaN p-n junction diode fabricated on low TDD ($\sim 10^4$ cm^{-2}) bulk GaN substrates, which showed breakdown voltage of 4 kV [29]. They estimated the maximum electric field of 2.0–2.7 MV/cm assuming a net doping concentration of 2–5$\times$10^{15} cm^{-3}. Nomoto *et al*. demonstrated 1.7 kV and 0.55 mΩcm^2 GaN p-n junction diodes on bulk GaN substrates with avalanche capability [30]. The non-uniform net doping concentration (9$\times$10^{15}–2$\times$10^{16} cm^{-3}) was obtained from C–V measurement, and the maximum electric field of 2.6 MV/cm was estimated for a punch-through condition. This device also showed positive temperature coefficient of breakdown voltage.

The impact ionization coefficients in GaN have been studied [33–36]. However, the variations in these data are very large. In addition, there are no systematic data of an avalanche breakdown in GaN for various doping concentration, since it is difficult to achieve parallel-plane (uniform) avalanche breakdown without electric field crowding. Therefore, breakdown characteristics as a function of a doping concentration were not discussed in the literatures [33–36] owing to the lack of the fundamental data of an avalanche breakdown in GaN.

In this study, the author investigates breakdown characteristics in GaN p-n junction diodes with various epitaxial structures. At first, the author proposes the double-side-depleted shallow bevel termination, where the doping concentrations of p- and n-layers are comparable and the depletion layer extends to the both p- and n-sides. Based on the results in Capter 2 (Fig. 2.11), electric field crowding does not occur in this structure. The GaN p-n junction diodes with various doping concentrations are fabricated and the reverse I–V characteristics were investigated in detail. The author also fabricates GaN p-n junction diodes with one-side abrupt p$^+$/n$^-$ and p$^-$/n$^+$ junctions. For these devices, vertical deep-etch termination is formed to avoid electric field crowding. The conduction-type dependence of a breakdown characteristics for n- and p-type drift layers is investigated.

3.2 GaN p-n Junction Diodes with Double-Side-Depleted Shallow Bevel Termination

3.2.1 Device Fabrication

Figure 3.7 shows the device structure of a GaN p-n junction diode with doubles-side-depleted shallow bevel termination. Four samples with various n- and p-layers (PN1–4) were prepared in this study. The p$^+$-layers, p-layers, and n-layers were grown by metal-organic vapor phase epitaxy (MOVPE) on GaN(0001) bulk substrates grown by hydride vapor phase epitaxy (HVPE). The epitaxial layers are designed and prepared as Si concentrations in n-layers and Mg concentrations in p-layers are comparable. Figure 3.8 shows the depth profiles of

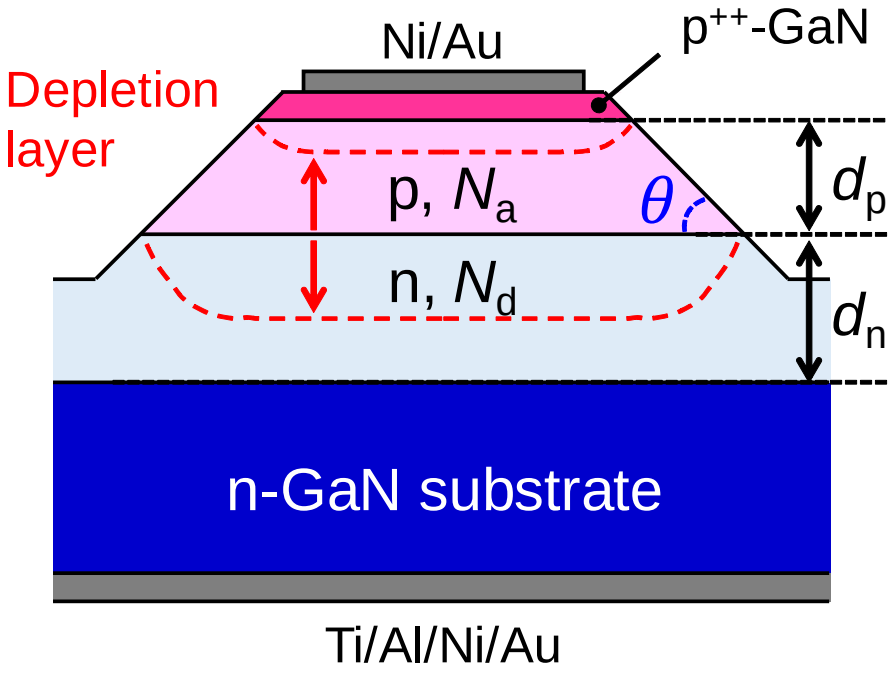

Figure 3.7: Schematic cross section of a GaN p-n junction diode with double-side-depleted shallow bevel termination proposed in this study. A donor concentration in an n-layer and an acceptor concentration in a p-layer are comparable, and the depletion layer extends to the both n- and p-layers. Shallow beveled-mesa reduces electric field at the mesa surface. In this structure, electric field crowding does not occur as shown in Fig. 2.11.

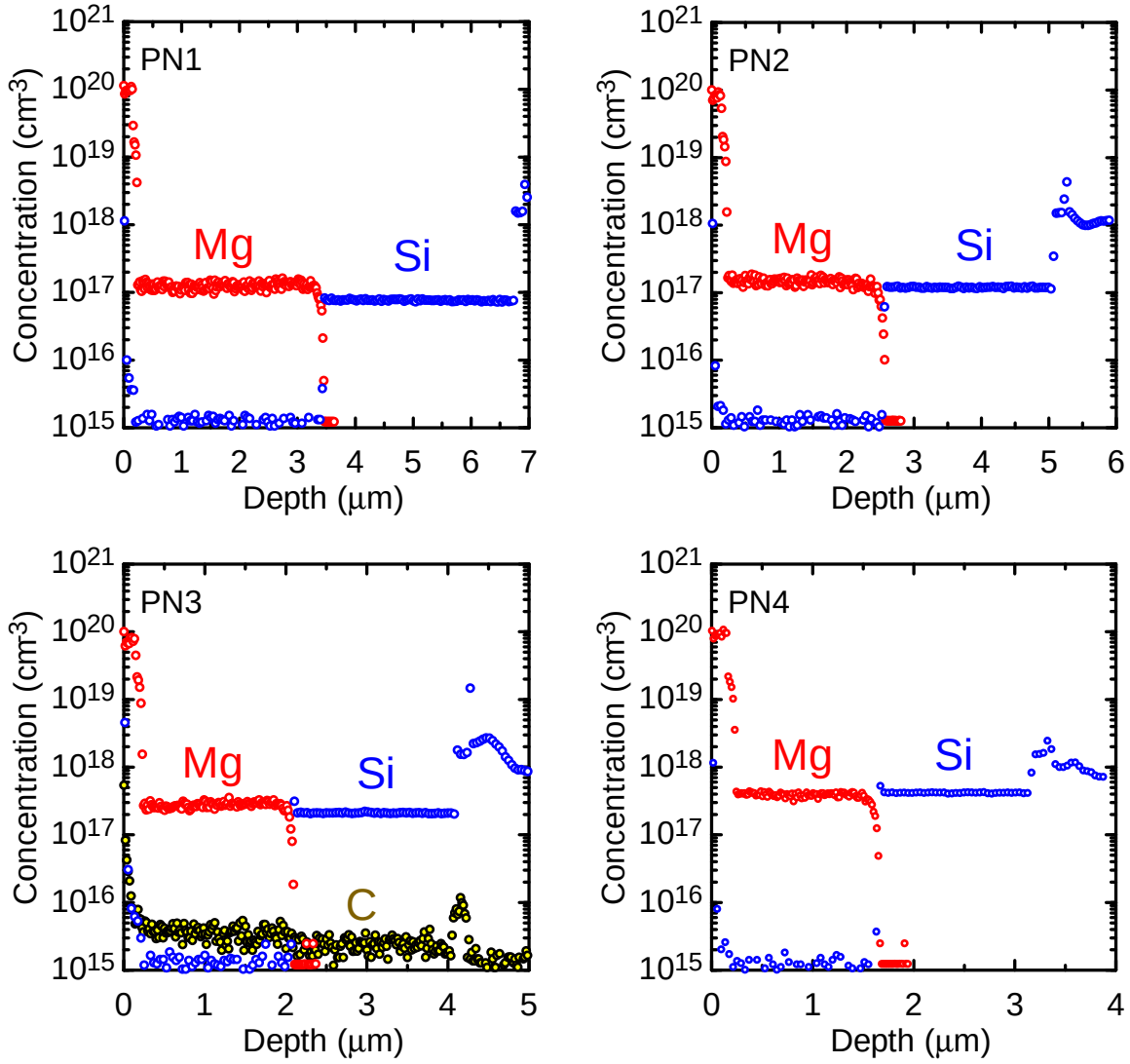

Figure 3.8: Doping concentration profiles of Si and Mg in PN1–4. The epitaxial layers are designed and prepared as Si concentrations in n-layers and Mg concentrations in p-layers are comparable. For PN3, C concentration is also shown, which is very low ($\sim 5 \times 10^{15}$ cm^{-3}).

the Mg and Si concentration measured by secondary ion mass spectrometry (SIMS) in the epilayers. Mg in the p-layer and Si in the n-layer are uniformly distributed along the depth direction. It is a well known problem that carbon atoms are unintentionally incorporated from a precursor (trimethylgallium, $Ga(CH)_3$) into GaN, which act as the compensation defects [37–39]. Owing to the optimized growth condition [40], the C concentrations in this study are very low ($< 5 \times 10^{15}$ cm^{-3}), as shown in Fig. 3.8. The doping concentrations and thicknesses in PN1–4 obtained by SIMS are summarized in Table 3.1. The shallow beveled-mesa structures were formed by Cl_2-based inductively coupled plasma-reactive ion etching with a thick photoresist mask [15, 41]. The mesa angles and mesa heights were approximately 12° and 3.6 μm, respectively. The anode and cathode electrodes were formed by the deposition of Ni/Au on the epitaxial layers and Ti/Al/Ni/Au on the backside of the substrates, respectively. The fabrication process has been described in Chapter 2 and elsewhere [42–44].

3.2.2 Capacitance-Voltage Measurement

Capacitance-voltage (C–V) characteristics of PN1–4 were measured at the frequency of 500 kHz up to near breakdown voltage. The devices with diameter of 450 μm were used. In the analysis, $\varepsilon_s = 10.4\varepsilon_0$ [45, 46] was used. Figure 3.9 shows the C–V characteristics of PN1–4 as the C^{-2}–V plots. A clear linearity for each device was observed, indicating that the donors in the n-layers and acceptors in the p-layers are almost uniformly distributed along the depth directions, as expected from the SIMS results. The net doping concentrations ($N_a N_d/(N_a+N_d)$) obtained from the C–V measurements are listed in Table 3.1, which show good agreement with [Mg][Si]/([Mg]+[Si]) obtained by SIMS for all devices, indicating that the compensations by other impurities and intrinsic defects are almost negligible.

3.2.3 Breakdown Characteristics

Reverse I–V characteristics of PN1–4 were measured using a Keysight B1505A semiconductor parameter analyzer. To avoid air sparking, the devices were dipped into fluorinert while the measurements. Figure 3.10 shows the reverse I–V characteristics of PN1–4 (in linear scale). The devices showed low leakage current and soft breakdown. The same characteristics were reproduced many times without a catastrophic breakdown, suggesting high avalanche capability in the devices. The breakdown voltages of approximately 480, 385, 250 and 180 V were obtained for PN1, PN2, PN3 and PN4, respectively. Figure 3.11 shows the electric field distributions for the parallel-plane junctions of PN1–4 at the breakdowns calculated by assuming that Si and Mg are fully activated and ionized (N_a = [Mg], N_d = [Si]) and using $\varepsilon_s = 10.4\varepsilon_0$ [45, 46]. The breakdown electric fields, which are defined as the parallel-plane maximum electric field, of 2.8, 2.9, 3.2 and 3.5 MV/cm were obtained for PN1, PN2, PN3 and PN4, respectively. With increasing doping concentration, the break-

Table 3.1: Thicknesses and doping concentrations in PN1–PN4 obtained from SIMS and C–V measurements.

	d_{p} (μm)	d_{n} μm	[Mg] (cm^{-3})	[Si] (cm^{-3})	[Mg][Si]/([Mg]+[Si]) (cm^{-3})	$N_{\mathrm{a}}N_{\mathrm{d}}/(N_{\mathrm{a}}+N_{\mathrm{d}})$ (cm^{-3})
PN1	3.3	3.3	1.2×10^{17}	7.6×10^{16}	4.7×10^{16}	4.7×10^{16}
PN2	2.5	2.5	1.4×10^{17}	1.2×10^{17}	6.5×10^{16}	6.4×10^{16}
PN3	2.0	2.0	2.7×10^{17}	2.1×10^{17}	1.2×10^{17}	1.2×10^{17}
PN4	1.5	1.5	3.9×10^{17}	4.1×10^{17}	2.0×10^{17}	1.9×10^{17}

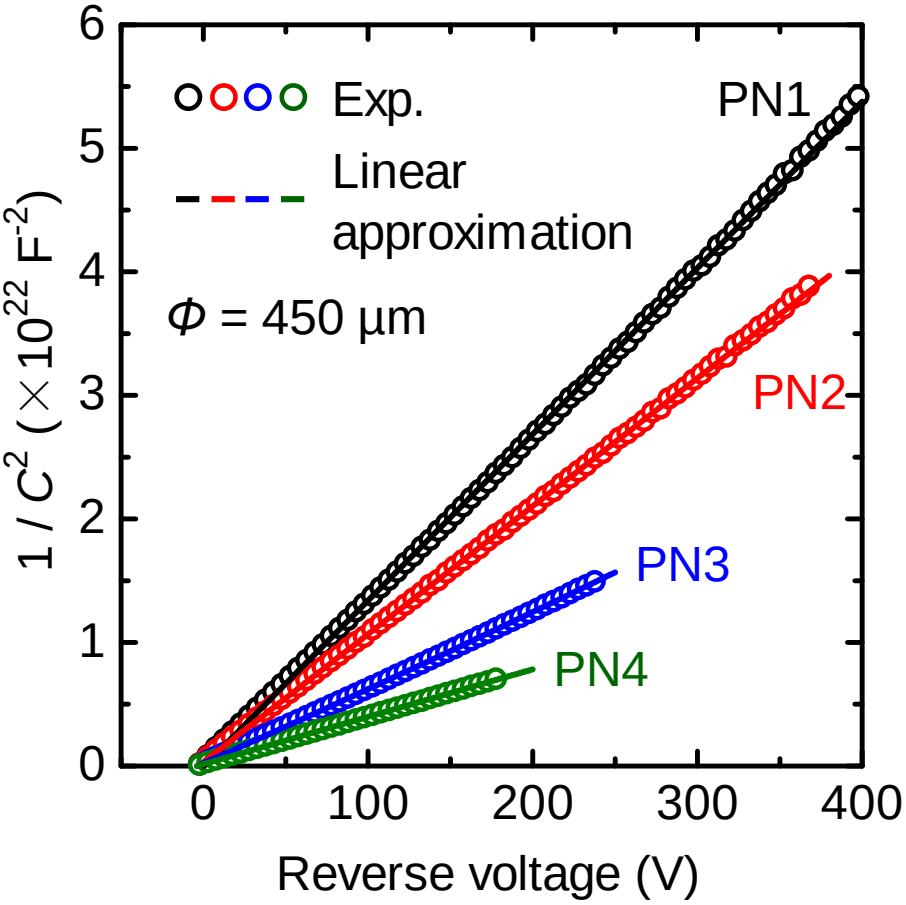

Figure 3.9: Capacitance-voltage characteristics of PN1–4 in the C^{-2}–V plots. Clear linearity is observed for each device, indicating the donor in the n-layer and the acceptor in the p-layer are distributed uniformly along the depth directions.

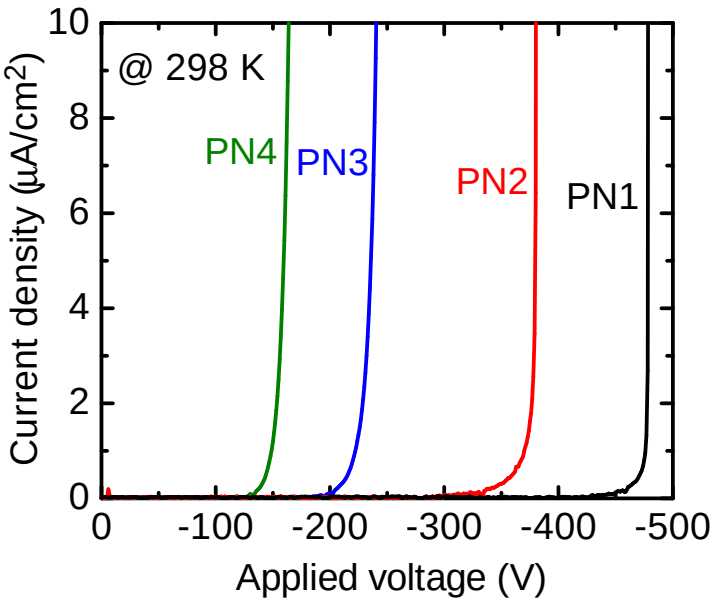

Figure 3.10: Reverse I–V characteristics of PN1–4. The breakdown voltages of approximately 480, 385, 250 and 180 V were obtained with low reverse leakage current and high avalanche capability.

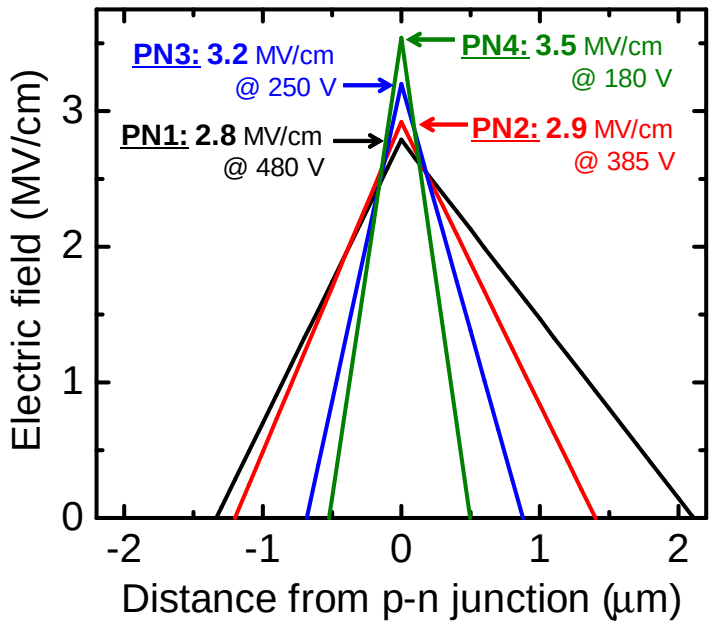

Figure 3.11: The calculated electric field distributions for the parallel-plane junctions of PN1–PN4 at the breakdowns. The breakdown electric fields of approximately 2.8, 2.9, 3.2 and 3.5 MV/cm were obtained.

down electric field increased. It is worth to stress that these values are very reliable, since the author confirmed that the net doping concentrations and their uniform distributions along the depth directions by both SIMS and C–V measurements in wide voltage ranges.

Figure 3.12 shows the two-dimensional electric field distribution calculated by TCAD simulation for the beveled-mesa edge of PN1 under the reverse bias voltage of 480 V representatively. The depletion layer extends to both the p-layer and the n-layer, since the Mg concentration in the p-layer is comparable to the Si concentration in the n-layer. The electric field at the mesa surface is reduced due to the small mesa angle [47]. The electric field profile along the p-n junction interface is shown in Fig. 3.13. The maximum electric field is almost equal to the electric field at the parallel-plane region. In other words, electric field crowding does not occur, as mentioned in Chapter 2 (Fig. 2.11).

3.2.4 Temperature Dependence of Breakdown Voltage

The temperature dependence of the breakdown characteristics in PN1–4 were measured. The temperature of the stage to which the devices were attached was controlled in the range of 223–373 K. Figure 3.14 shows the reverse I–V characteristics of PN1–PN4 at 223, 298 and 373 K. With elevating temperature, the increase in the breakdown voltage was observed for all the devices. This positive temperature coefficient of the breakdown voltage is a signature of an avalanche breakdown: the phonon scattering rate in a semiconductor increases and carriers come to be hard to obtain sufficient energy to cause impact ionizations (impact ionization coefficients decrease) with elevating temperature. Figure 3.15 shows the temperature dependences of the breakdown voltages in PN1–4. It is observed that the breakdown voltage monotonically and almost linearly increased with elevating temperature. For example, in PN4, the breakdown voltage increased from 182 V at 298 K to 203 V at 573 K. Parallel-plane breakdown electric field reached 3.74 MV/cm at 573 K. The temperature dependence of the impact ionization coefficients in GaN will be discussed in Chapter 5.

3.2.5 Electroluminescence at Breakdown

The strong luminescence is observed at the breakdown, since many electron-hole pairs are generated by impact ionizations in the depletion layer and large current flows. When an avalanche breakdown occurs at the electric field crowding point, localized luminescence is observed there [48]. Figure 3.16 shows the pictures of PN4 at (a) 0 V, (b) -180 V, -100 μA, and (c) -180 V, -1 mA. For taking these pictures, ring electrodes (the junction diameter of 450 μm) were used. In contrast to the result in Chapter 2 (peripheral luminescence in beveled-mesa region as shown in Fig. 2.19), nearly uniform white luminescence in the entire p-n junction was observed in PN1–4. This is the strong evidence that the uniform (nearly ideal) avalanche breakdowns occurred, i.e., successful suppression of electric field crowding.

Althoug the luminescence was observed at the entire p-n junction, the intensity of bright-

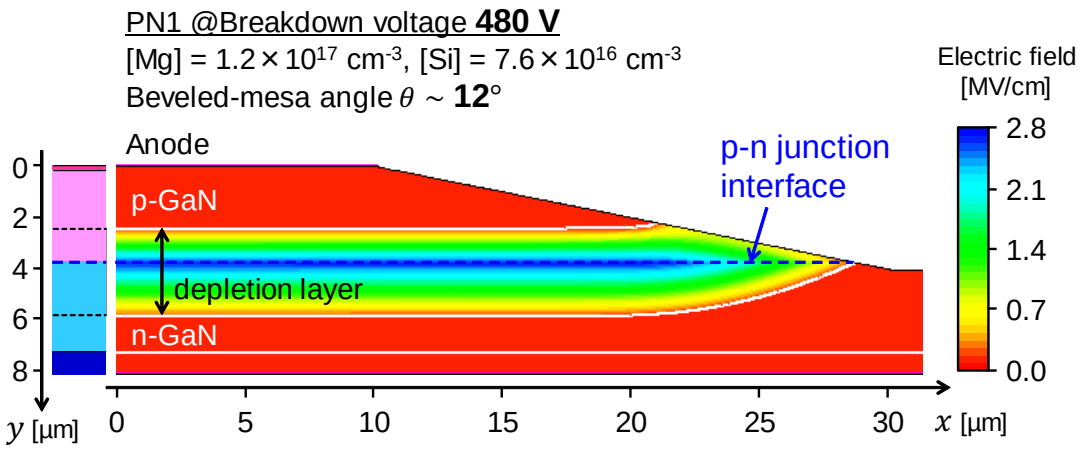

Figure 3.12: Two-dimensional electric field distribution in PN1 under the reverse bias of 480 V. Owing to a low acceptor concentration, which is comparable to a donor concentration, combined with shallow beveled-mesa, electric field at the mesa surface is well reduced and electric field crowding does not occur in the device.

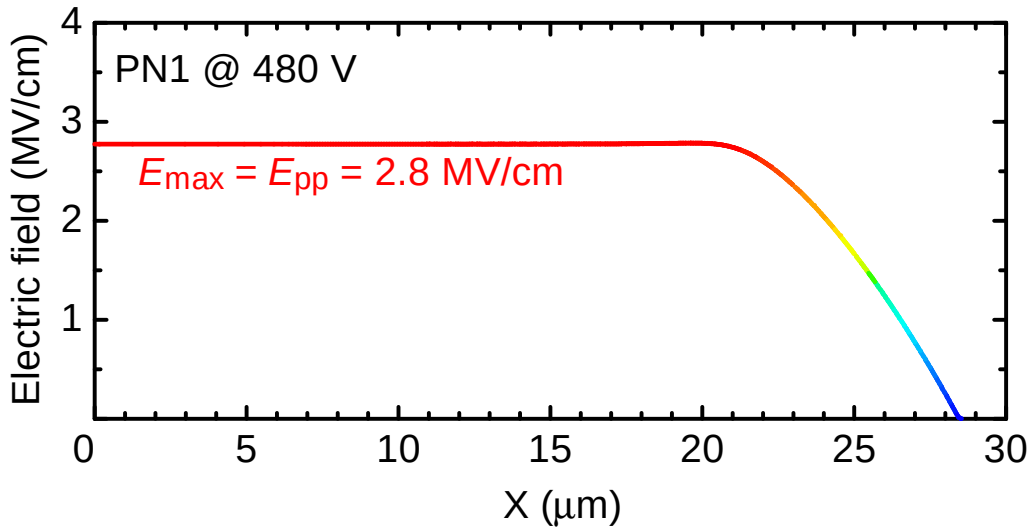

Figure 3.13: Eletctric field profile along the p-n junction interface in Fig. 3.12 (PN1).

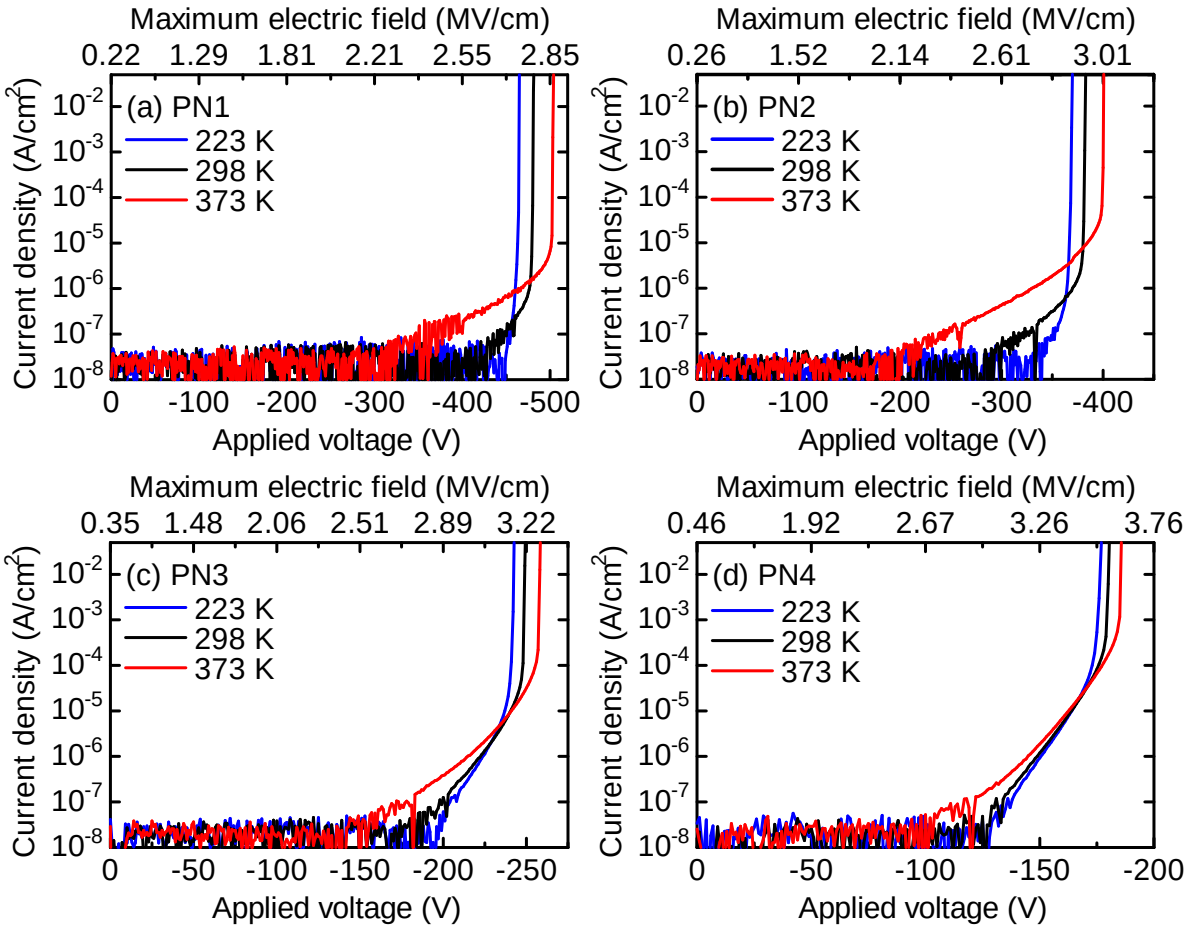

Figure 3.14: Reverse I–V characteristics of PN1–4 at 223, 298 and 373 K.

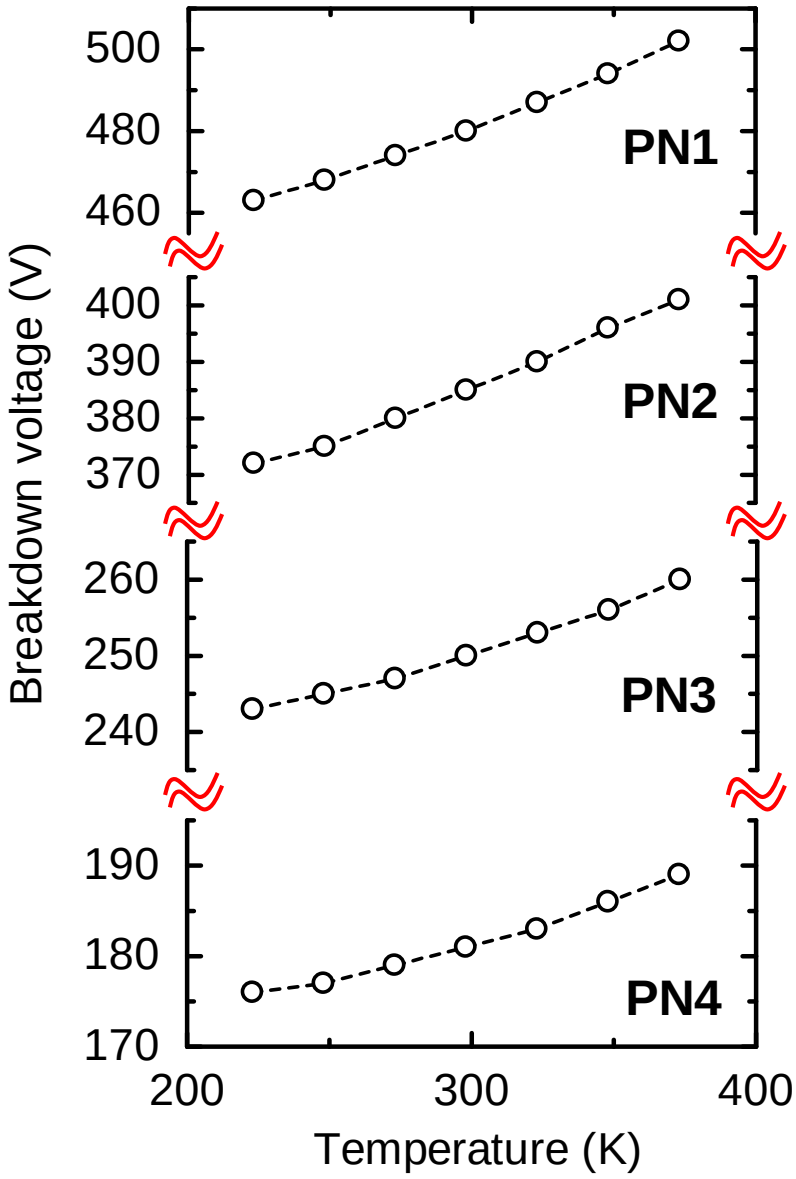

Figure 3.15: Temperature dependence of the breakdown voltages in PN1–4.

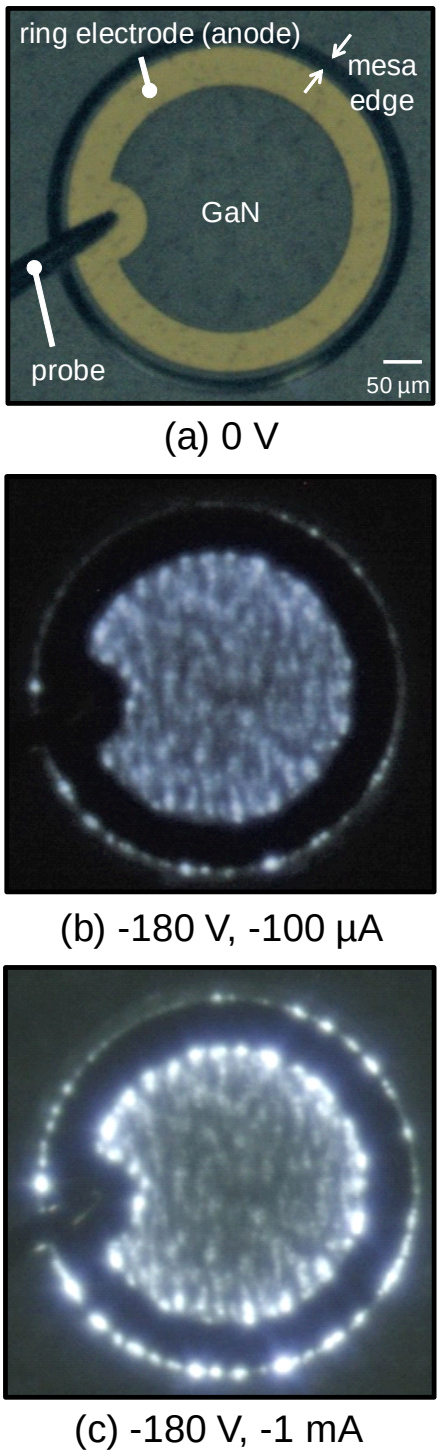

Figure 3.16: Pictures of PN4 at (a) 0 V, (b) −180 V, −100 μA, and (c) −180 V, −1 mA taken by a cooled-CMOS camera. To observe luminescence, ring electrodes were used only this measurement. At the breakdown voltage, nearly uniform electroluminescence in the p-n junction was observed. This breakdown luminescence was also observed in PN1–3. This is the strong evidence that the uniform avalanche breakdowns occurred.

ness was not perfectly uniform. Very recently, Fukushima *et al.* also reported that uniform avalanche breakdown in GaN p-n junction diode with vertically deep-etch termination [49]. The device exhibited breakdown voltage of approximately 900 V with breakdown electric field of 2.4 MV/cm. At the breakdown, luminescence was observed in entire p-n junction and its pattern accorded to the step bunching by an emission microscopy, as shown in Fig. 3.17. From the same group, Kawasaki *et al.* carried out the scanning measurement of the optical beam induced current (OBIC) by sub-bandgap illumination [50]. For the device in the literature [49] under near the breakdown voltage, an in-plane mapping image of the photocurrent induced by the Franz-Keldysh effect [51, 52] and its avalanche multiplication [44] were observed, as shown in Fig. 3.18. They analyzed this photocurrent and estimated the fluctuation of a donor concentration of $\sim 10^{14}$ cm^{-3}. Since an avalanche multiplication is a extremely steep function of electric field near breakdown electric field, small fluctuations of a donor concentration cause entire luminescence with non-uniform intensity at breakdown. However, it should be noted that the small doping fluctuations do not deteriorate the breakdown characteristics.

Mandal *et al.* investigated that the spectrum of reverse breakdown electroluminescence in a GaN p-n junction diode. Figure 3.19 shows the spectrum at 100 μA, 1 mA and 10 mA. Sharp peaks around 3.4 eV and the broad-range wavelength emission between 1.6–2.8 eV are observed. The former and the latter are considered to be correlated to band-to-band recombination and sub-bandgap recombination via deep levels such as C_N and V_N [53–55]. Figure 3.20 shows the breakdown luminescence of PN4 at reverse current of 500 μA in this study. For our devices, near-band-edge emission is self-absorbed in GaN, since the p-n junction is located deep inside. However, the broad-range wavelength emission similar to the previous report [56] was observed. With increasing the current level, the luminescence intensity near the electrode became stronger in Fig. 3.16, indicating that the current crowding also effect on the luminescence intensity. The luminescence may also originate from relaxations of hot carriers. The origin of breakdown luminescence should be studied furthermore in the future.

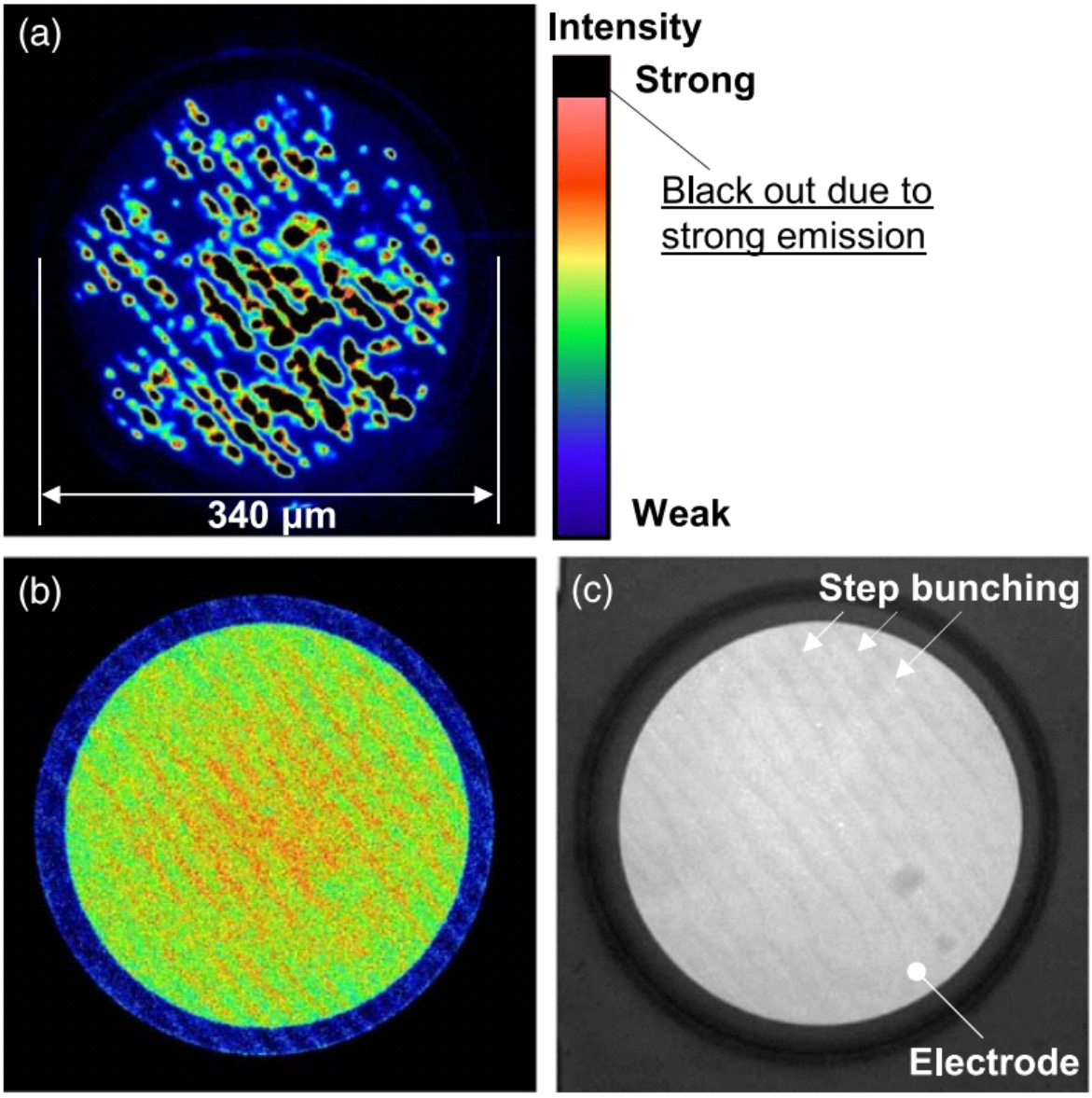

Figure 3.17: (a) Emission microscopy image of the p-n junction diode with high reverse bias of −879 V applied. (b) Emission microscopy image with forward bias of 2.5 V applied. (c) Optical microscopy image. These results are reported in [49].

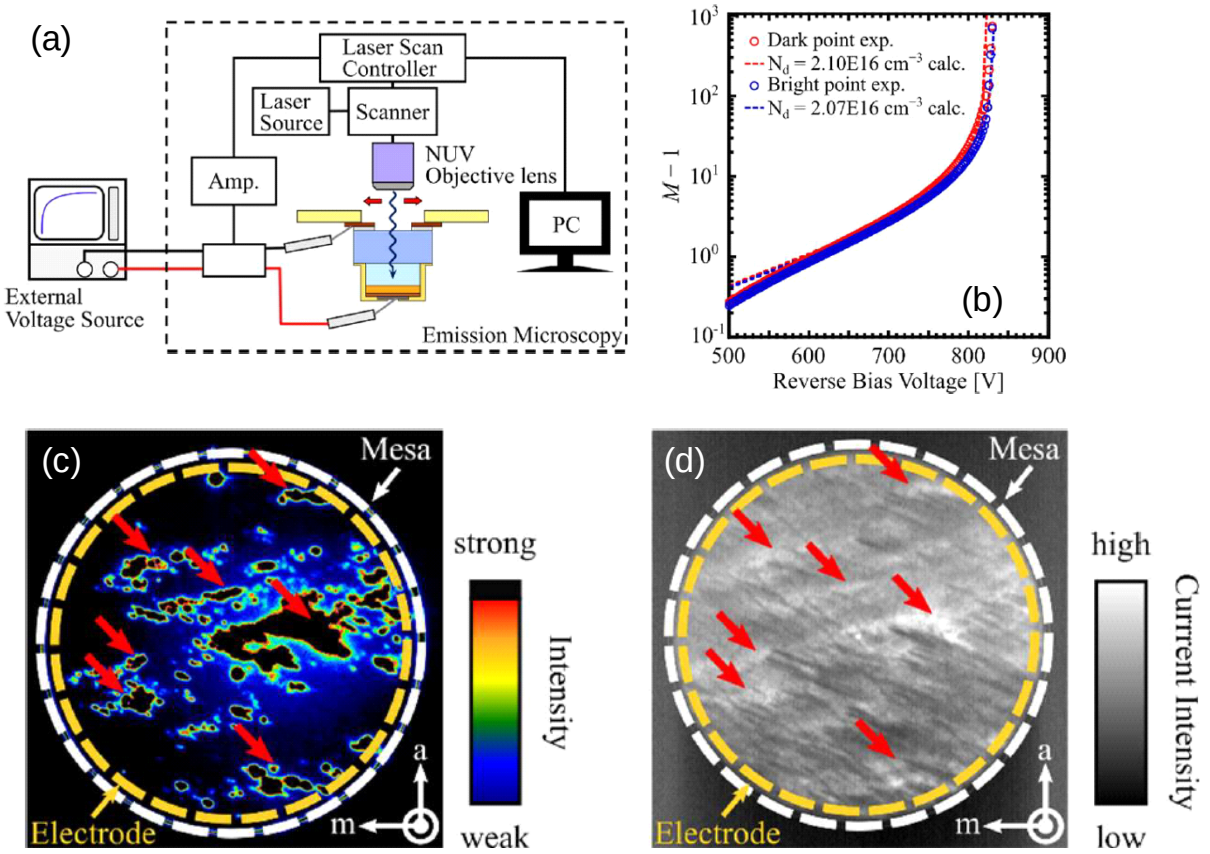

Figure 3.18: (a) Schematic of the OBIC measurement system. (b) Voltage dependence of the multiplication factor at high bright point (red) and dark point (blue). (c) Emission microscopy image at −827 V and (d) OBIC image at −812 V. The mesa diameter is 540 μm and the electrode diameter is 500 μm. Red arrows show corresponding points on the emission microscopy image and the OBIC image. These are reported in [50].

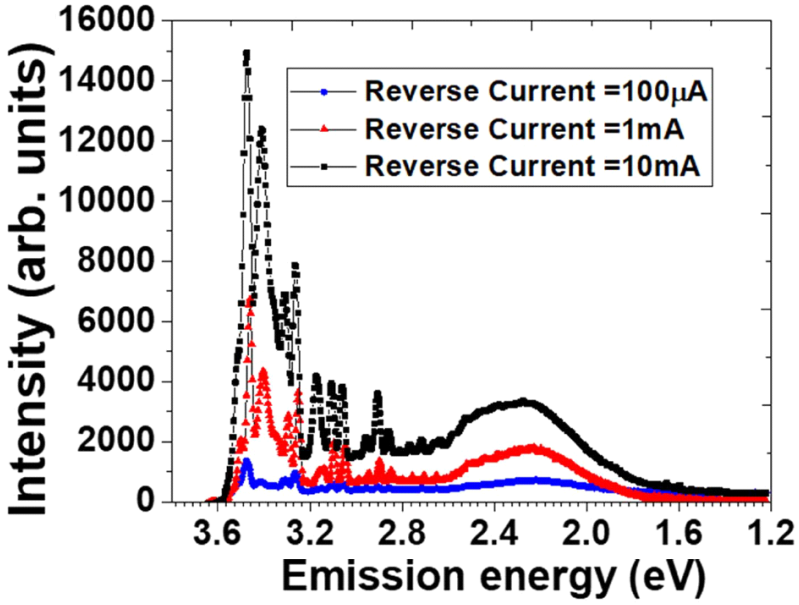

Figure 3.19: Breakdown electroluminescence in a GaN p-n junction diode reported in [56]. Near-band-edge emission and broad-range wavelength emission are observed.

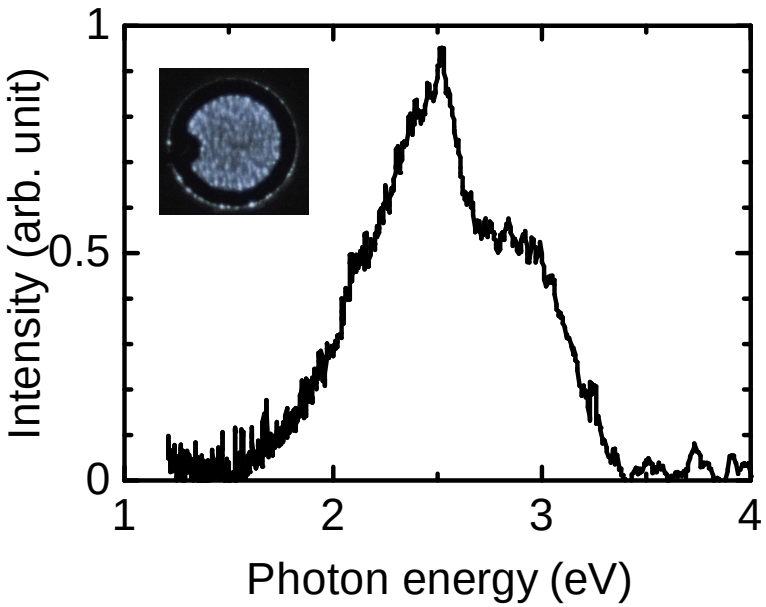

Figure 3.20: Breakdown electroluminescence in a GaN p-n junction diode with double-side-depleted shallow bevel termination (PN4) fabricated in this study at the reverse current of 500 μA. Near-band-edge emission is not observed due to self-absorption.

3.3 GaN p^+/n^- and p^-/n^+ Junction Diodes

It is known that the conduction type of a drift layer has an impact on an avalanche breakdown characteristic in non-punch-through condition, which originates from the direction of carrier multiplication and the difference between the impact ionization coefficients of electrons (α_n) and holes (α_p) [15, 57, 58]. For p^+/n^- junction in which a depletion layer mainly extends to the n-type side from the p-n junction interface, holes are injected from the lower electric field side and are multiplicated to the higher electric field side. For electrons, which are injected by the higher electric field side or generated by the hole impact ionizations, are multiplied to the direction toward the lower electric field side. On the other side, for p^-/n^+ junction in which a depletion layer mainly extends to the p-type side, the direction is completely opposite: holes are multiplied toward the lower side. If α_n and α_p have very similar values for example GaAs [9, 57], the difference of the breakdown voltage between the conduction types of the drift layers does not appear. However, for 4H-SiC in the c-axis direction, α_n is much smaller than α_p [10, 15], specifically, p^-/n^+ junction has ∼9% lower ideal breakdown voltage, and ∼5% lower critical field strength than p^+/n^- junction. These are obtained from the simulation using the impact ionization coefficients.

In this study, the author fabricated GaN p^+/n^- and p^-/n^+ junction diodes on GaN freestanding substrates. For these devices, vertical deep-etch termination to realize one-dimensional electric field distribution [15, 47, 49] was used, since it is very difficult to perfectly alleviate electric field crowding in p^+/n^- junction using beveled-mesa termination due to very high N_a/N_d. It should be noted that for p^-/n^+ junction diodes, the positive bevel structure is also applicable. The breakdown characteristics in GaN p^+/n^- and p^-/n^+ junction diodes with various doping concentrations are systematically investigated and the conduction-type dependence of the breakdown characteristics in GaN is discussed.

3.3.1 Device Fabrication

Figure 3.21 shows the schematic cross sections of GaN p^+/n^- and p^-/n^+ junction diodes with vertical deep-etch termination. The epitaxial layers were grown by metal-organic vapor phase epitaxy (MOVPE) on n^+-type GaN(0001) freestanding substrates grown by hydride vapor phase epitaxy (HVPE). Three of each of diodes with p^+/n^- and p^-/n^+ junctions (N1–N3 and P1–P3, respectively) were prepared, in this study. The control of lightly Mg-doping was achieved by the MOVPE system equipped with double-dilution of the Mg source gas [40]. The vertical deep-etch termination was formed by Cl_2-based dry etching with a SiO_2 mask [59]. The vertical mesa structure with angle of approximately 90° was achieved with smooth mesa side wall, and the epitaxial layers were fully etched down to the substrate. The thicknesses, the etching depths and the doping concentrations obtained by C–V measurements are summarized in Table 3.2. The anode and cathode electrodes were formed by the deposition of Ni/Au on the top-side p^+layers and Ti/Al/Au on the back-

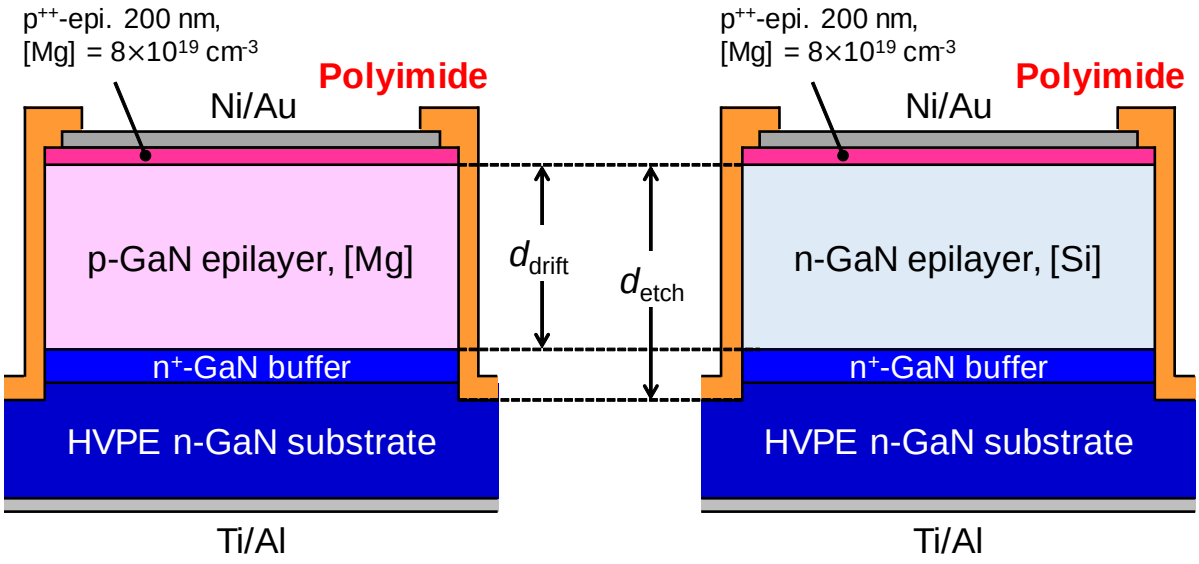

Figure 3.21: Schematic cross sections of GaN p^+/n^- and p^-/n^+ junction diodes with vertical deep-etch termination. The polyimide layer was coated as a surface passivation layer. The vertical mesa with the angle of approximately 90° and smooth mesa side wall was successfully obtained.

side substrates, respectively. The ohmic annealing was conducted for 10 min in 550°C, O_2 ambient. After the metalization, a thick polyimide was coated as a surface passivation layer and cured by the sequent thermal treatment in N_2 ambient for 30 min at 140°C followed by for 60 min at 350°C.

3.3.2 Capacitance-Voltage Measurement

Figure 3.22 shows the C–V characteristics of N1–N3 and P1–P3 as the C^{-2}–V plots. The measurement frequency was 500 kHz. The dielectric constant of GaN ($\varepsilon_s = 10.4\varepsilon_0$ [45, 46]) was used. Clear linearity was observed in the plots, indicating the uniform distributions of donors or acceptors in the epitaxial layers along the depth direction. From the analysis of the slope in the plots, the net doping concentration $N_a N_d/(N_a + N_d)$ was obtained for each device. Table 3.2 shows the obtained $N_a N_d/(N_a + N_d)$ for N1–N3 and P1–P3.

3.3.3 Breakdown Characteristics

Before discussing the device characteristics, it is worth to stress that high electric field exists at the mesa surface of the vertical deep-etch structure, and stable breakdown characteristics were not obtained and catastrophic breakdowns occurred in the case of the devices without a polyimide passivation layer. The author investigated the effect of a tetramethylammonium hydroxide (TMAH) wet etchcing (25% concentration) at 85°C, which is an anisotropic etching to make a side wall smoother and to remove the dry-etched damage [23, 60, 61]. However, the I–V characteristics were not improved and unstable and catastrophic breakdown was observed. Therefore, a surface passivation layer is essential to achieve a stable breakdown for the vertical deep-etch termination.

Figure 3.23 shows the reverse I–V characteristics of N1–N3 and P1–P3 with a polyimide passivation layer at room temperature. The breakdown voltage and the breakdown electric field for these devices are also summarized in Table 3.2. These devices showed very high parallel-plane breakdown electric fields of 3.0–4.0 MV/cm. In these devices, the breakdown electroluminescence was observed in entire p-n junction, suggesting that uniform avalanche breakdown occurred in these devices.

For the devices with high doping concentration devices (N3, P2 and P3), significant high reverse leakage current which prominently increased with reverse bias was observed at high electric field region (> 3 MV/cm). These leakage currents are considered to originate from the band-to-band (Zener) tunneling, since a width of a potential barrier becomes very thin (e.g. 11 nm at 3.0 MV/cm). In addition, these currents are approximately three orders of magnitude higher than that the phonon-assisted tunneling current in 4H-SiC p-n junction diodes at the same electric field strength [62]. To investigate the Zener tunneling current in GaN in detail, a test device with much higher doping concentration is required.

Table 3.2: Thicknesses, etching depths and doping concentrations in N1–N3 and P1–P3. The breakdown voltage and the breakdown electric field is also shown.

	d_{drift} (μm)	d_{etch} (μm)	$N_{\mathrm{a}}N_{\mathrm{d}}/(N_{\mathrm{a}}+N_{\mathrm{d}})$ (cm^{-3})	V_{b} (V)	E_{b} (MV/cm)
N1	3.0	5.0	7.5×10^{16}	340	3.0
N2	2.5	3.5	1.5×10^{17}	207	3.3
N3	1.5	3.5	3.1×10^{17}	128	3.8
P1	3.0	5.0	1.3×10^{17}	235	3.2
P2	2.5	3.5	1.8×10^{17}	180	3.3
P3	1.5	3.5	4.1×10^{17}	110	4.0

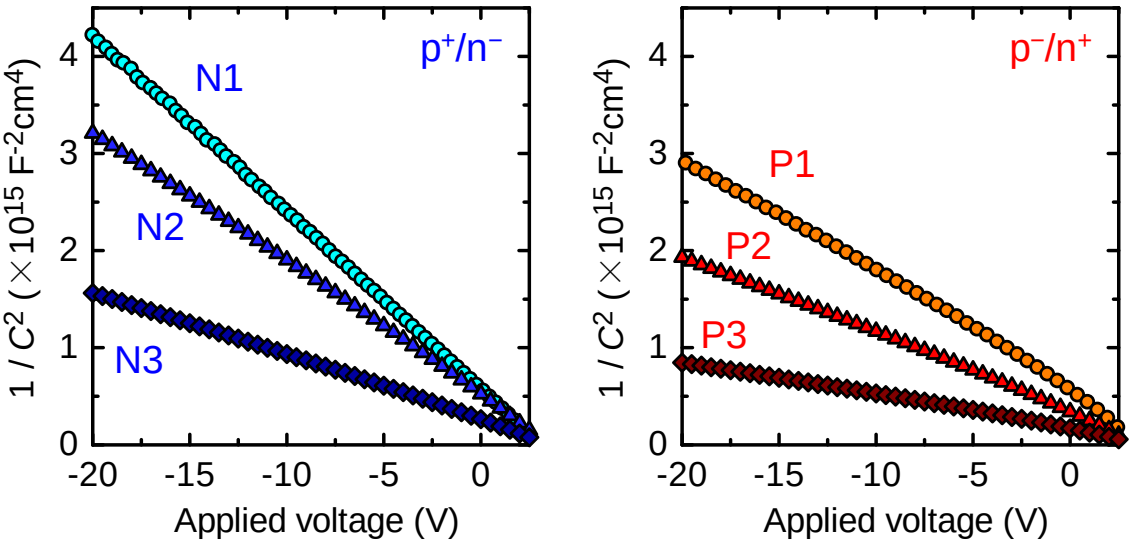

Figure 3.22: C–V characteristics of N1–N3 and P1–P3 as the C^{-2}–V plots.

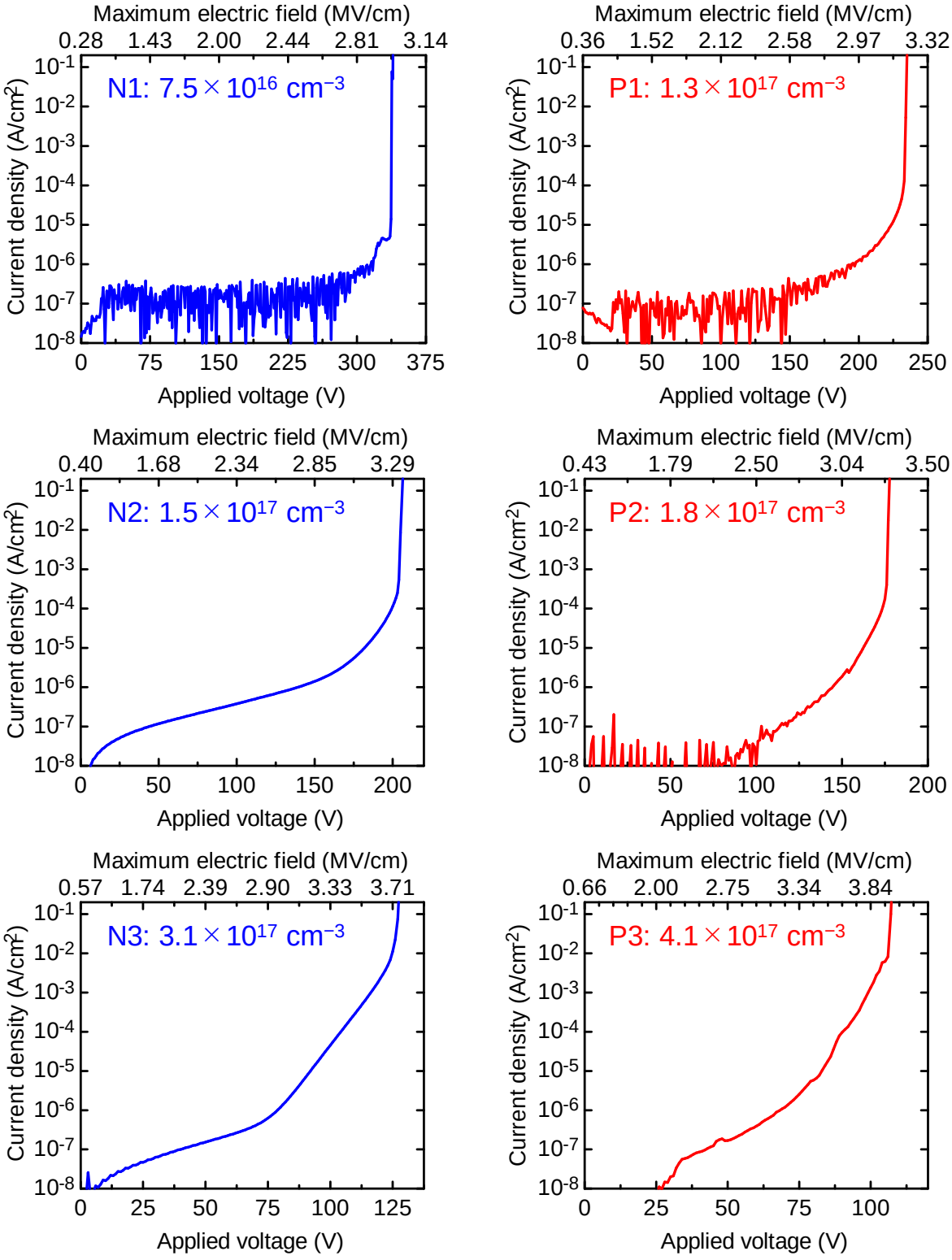

Figure 3.23: Reverse I–V characteristics of N1–N3 and P1–P3.

3.4 Breakdown Electric Field vs. Doping Concentration

Figure 3.24 shows the breakdown voltage and the breakdown electric field versus doping concentration $N_aN_d/(N_a+N_d)$ for GaN p-n junction diodes with double-side-depleted shallow bevel termination (PN1–PN4, yellow diamonds), GaN p^+/n^- (N1–N3, blue triangles) and p^-/n^+ (P1–P3, red inverted triangles) junction diodes with vertical deep-etch termination. For these devices, the breakdown characteristics lie on the same curves in the plots. In other words, no distinguishable difference of the breakdown voltage in these devices is observed. These results indicate that the difference of the impact ionization coefficients between electrons and holes in GaN is not so large. In Chapter 5, the breakdown voltage and the critical electric field versus doping concentration and their conduction-type dependences will be discussed again using the obtained impact ionization coefficients.

Figure 3.25 shows the benchmark plots of the breakdown voltage and the breakdown electric field versus doping concentration $N_aN_d/(N_a+N_d)$ for non-punch-through GaN power devices reported previously [16, 17, 26, 49, 63–67] and this work. The parallel-plane breakdown fields of 2.8–4.0 MV/cm in this study are among the best of the reported GaN devices for relatively high doping concentrations (low breakdown voltages). It should be stressed again that the data in this study were determined very carefully: the author confirmed that the uniform distributions of the net doping concentrations along the depth directions and the compensation by impurities or other sources is negligible by both SIMS and C–V measurements. If a doping concentration has a non-uniform distribution along the depth direction which is often indicated from the curved C^{-2}–V plot, it is difficult to determine an accurate electric field distribution and maximum electric field.

3.5 Discussion

Effect of Threading Dislocation on Avalanche Breakdown

In this study, the breakdown luminescence was obtained at the entire p-n junction, not a dot-like point, indicating that an avalanche breakdown was not caused by dislocations. Usami *et al*. investigated the breakdown characteristics of the GaN p-n junction diodes fabricated on a GaN substrate grown by ammonothermal method. The threading dislocation density was less than 5×10^4 cm^{-2}. The lower lekage current was observed, and the breakdown voltage was perfectly same with the device fabricated on a GaN substrate grown by HVPE [68]. This result also suggests that dislocations in GaN cause reverse leakage current but not effect on impact ionization and avalanche breakdown.

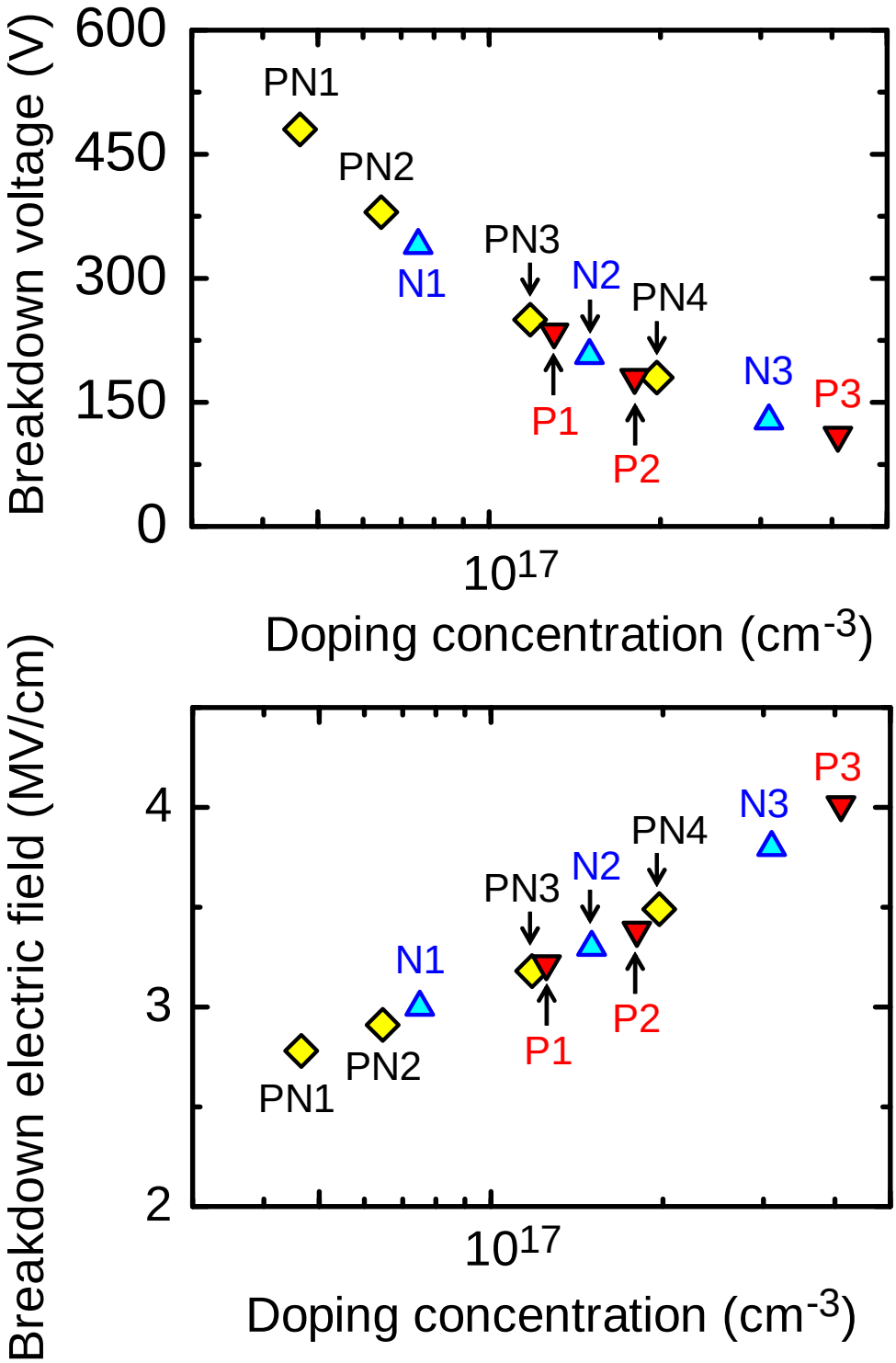

Figure 3.24: Breakdown voltage and breakdown electric field versus net doping concentration ($N_a N_d/(N_a + N_d)$) in this study. GaN p-n junction diodes with double-side-depleted shallow bevel termination [42] in the section 3.2 (PN1–PN4), GaN p^+/n^- and p^-/n^+ junction diodes with vertical deep-etch termination in the section 3.3 (N1–N3, P1–P3) are shown as yellow diamonds, blue triangles and red inverted triangles, respectively.

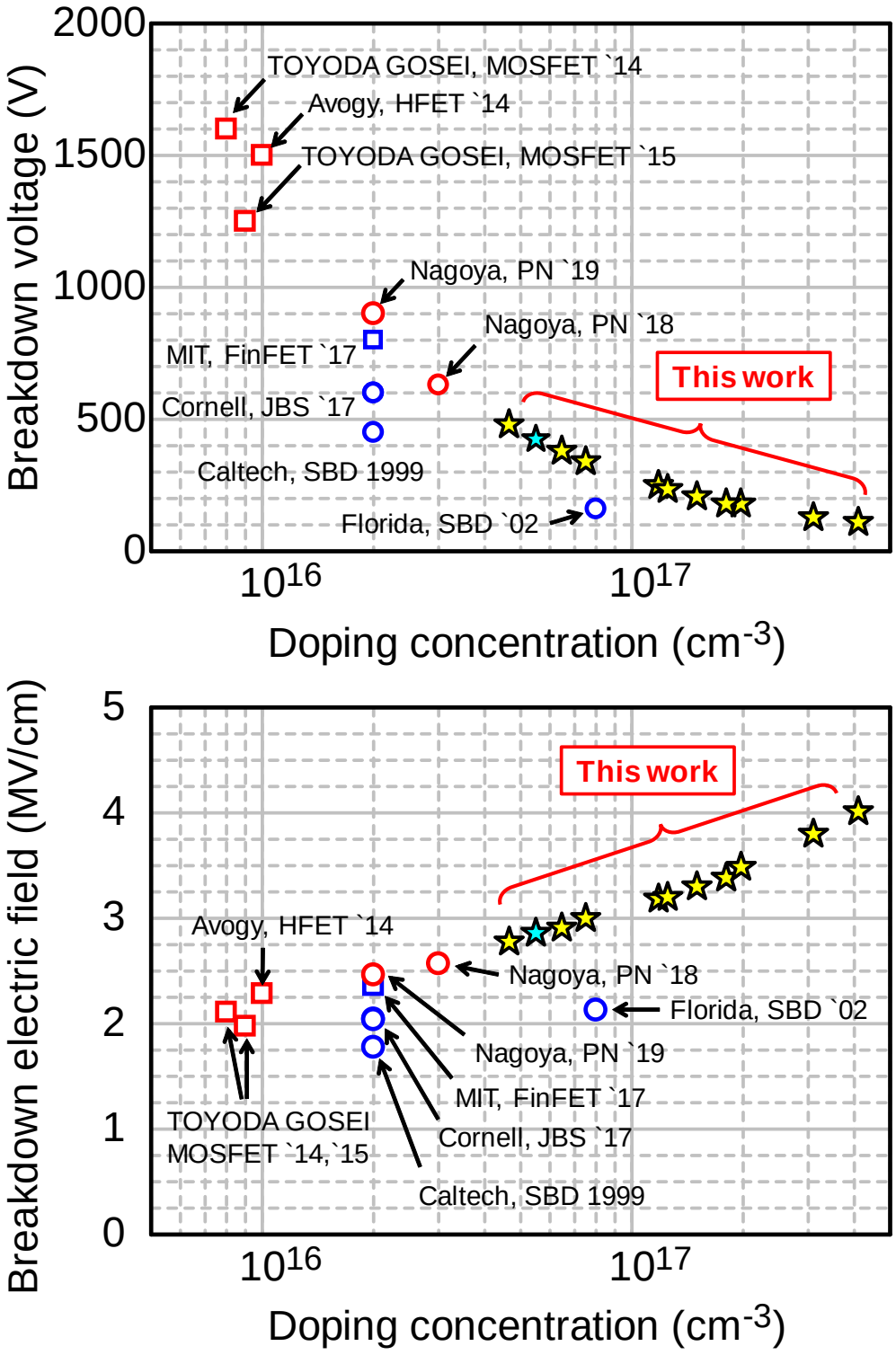

Figure 3.25: Benchmark plots of the breakdown voltage and breakdown electric fields versus the non-punch-through GaN power devices reported previously [16, 17, 26, 49, 63–67]. The breakdown electric fields of 2.8–4.0 MV/cm in this work are among the best of the previously reported non-punch-through GaN devices for relatively high doping concentrations (low breakdown voltages).

Leakage Mechanism in a GaN p-n Junction Diode

Zhang *et al.* reported that variable-range-hopping (VRH) through dislocations is a main off-state leakage mechanism for GaN p-n junction diodes and the electric field dependence of the leakage current follows $\ln(I) \propto F$ [69]. Usami *et al.* investigated the correlation between dislocations and leakage current of GaN p-n junction diodes [64, 70, 71]. Under the reverse bias condition, dot-like leakage spots were observed using an emission microscope. Subsequent cathodeluminescence (CL), observation of etch pits formed by KOH etching and transmission electron microscopy (TEM), it is revealed that $1\boldsymbol{c}$ pure screw dislocations are related to the reverse leakage [64]. The leakage current caused by the screw dislocation is remarkable and deteriorate the device yield.

In the devices in this study, threading dislocation densities are $\sim 10^6$ cm^{-3}. Thus, it is considered that the dislocations are included in the devices and cause defect-related leakage. In addition, for PN3 and PN4, high electric field > 3 MV/cm was applied under high reverse bias voltage, which may cause band-to-band tunneling. In Fig. 3.14, it is observed that the temperature dependences of the leakage currents for PN3 and PN4 are smaller than those for PN1 and PN2. This may reflect the dominant mechanism of the reverse leakage current is different. However, the detailed mechanisms of these leakage currents are still missing and further investigations are required.

3.6 Summary

In this study, the breakdown characteristics in GaN-on-GaN p-n junction diodes with various epitaxial structures were investigated. Based on the design space of the beveled-mesa structure obtained in Chapter 2, the author proposed the double-side-depleted shallow bevel termination, in which electric field crowding does not occur. The devices showed low reverse leakage current, high avalanche capability, positive temperature coefficient of the breakdown voltage and nearly uniform breakdown electroluminescence in the entire p-n junction. These are strong evidence that the uniform (nearly ideal) avalanche breakdown without electric field crowding was successfully achieved. The devices showed the parallel-plane breakdown electric fields of 2.8–3.5 MV/cm.

In addition, we also fabricated GaN p^+/n^- and p^-/n^+ junction diodes with the vertical deep-etch termination. The devices also showed the uniform avalanche breakdown with the breakdown electric fields of 3.0–4.0MV/cm. A distinguishable difference of the breakdown voltage between p^+/n^- and p^-/n^+ junction was not observed.

The breakdown electric fields of 2.8–4.0 MV/cm in this work are among the best of the previously reported non-punch-through GaN devices for relatively high doping concentrations (low breakdown voltages). In addition, these experimental data will be discussed compared with the theoretical breakdown voltage and the critical electric field in GaN simulated from the impact ionization coefficients in Chapter 5.

References

[1] S. M. Sze and K. K. Ng, *Physics of Semiconductor Devices*, (Wiley, New York, 2007), pp.102–114.

[2] R. Van Overstraeten and H. De Man, *Solid State Electron.* **13**, pp.583–608 (1970).

[3] W. N. Grant, *Solid State Electron.* **16**, pp.1189–1203 (1973).

[4] M. H. Woods, W. C. Johnson, and M. A. Lampert, *Solid State Electron.* **16**, pp.381–394 (1973).

[5] E. Chartier, M. V. Fichetti, E. A. Eklund, and F. R. McFeely, *Appl. Phys. Lett.* **62**, 3339 (1993).

[6] Y. J. Chang and S. M. Sze, *J. Appl. Phys.* **40**, 5392 (1969).

[7] G. E. Stilman, C. M. Wolf, J. A. Rossi, and A. G. Foyt, *Appl. Phys. Lett.* **24**, 10 (1974).

[8] M. Ito, S. Kagawa, T. Kaneda, and T. Yamaoka, *J. Appl. Phys.* **49(8)**, 4607 (1978).

[9] G. E. Bulman, V. M. Robbins, and G. E. Stillman, *IEEE Trans. Electron Devices* **32(11)**, pp.2454–2466 (1985).

[10] A. O. Konstantinov, Q. Wahab, N. Nordell, and U. Lindefelt, *Appl. Phys. Lett.* **71(1)**, 90 (1997).

[11] R. Raghunathan and B. J. Baliga, *Proc. of Int. Symp. on Power Semiconductor Device and ICs* (1997) p. pp.173–176.

[12] T. Hatakeyama, T. Watanabe, T. Shinohe, K. Kojima, K. Arai, and N. Sano, *Appl. Phys. Lett.* **85**, 1380 (2004).

[13] W. S. Loh, B. K. Ng, J. S. Ng, S. I. Soloviev, H.-Y. Cha, P. M. Sandvik, C. M. Johnson, and J. P. R. David, *IEEE Trans. Electron Devices* **55(8)**, pp.1984–1990 (2008).

[14] J. E. Green, W. S. Loh, A. R. J. Marshall, B. K. Ng, R. C. Tozer, J. P. R. David, S. I. Soloviev, and P. M. Sandvik, *IEEE Trans. Electron Devices* **59(4)**, pp.1030–1036 (2012).

[15] H. Niwa, J. Suda, and T. Kimoto, *IEEE Trans. Electron Devices* **62(10)**, pp.3326–3333 (2015).

[16] Z. Z. Bandić, P. M. Bridger, E. C. Piquette, and T. C. McGill, *Appl. Phys. Lett.* **74**, 1266 (1999).

[17] J. W. Johnson, A. P. Zhang, W.-B. Luo, F. Ren, S. J. Pearton, S. S. Park, Y. J. Park, and J.-I. Chyi, *IEEE Trans. Electron Devices* **49(1)**, pp.32–36 (2002).

[18] Y. Saitoh, K. Sumiyoshi, M. Okada, T. Horii, T. Miyazaki, H. Shiomi, M. Ueno, K. Katayama, M. Kiyama, and T. Nakamura, *Appl. Phys. Express* **3**, 081001 (2010).

[19] A. M. Ozbek and B. J. Baliga, *IEEE Electron Device Lett.* **32(3)**, pp.300–302 (2011).

[20] J. Suda, K. Yamaji, Y. Hayashi, T. Kimoto, K. Shimoyama, H. Namita, and S. Nagao, *Appl. Phys. Express* **3**, 101003 (2010).

[21] T. Hatakeyama and T. Shinohe, *Mater. Sci. Forum* **389–393**, 1169 (2002).

[22] S. M. Sze and K. K. Ng, *Physics of Semiconductor Devices*, (Wiley, New York, 2007), pp.146–150.

[23] Y. Zhang, M. Sun, Z. Liu, D. Piedra, J. Hu, X. Gao, and T. Palacious, *Appl. Phys. Lett.* **110**, 193506 (2017).

[24] K. Hasegawa, G. Nishino, K. Yasunishi, N. Tanaka, N. Murakami, and T. Oka, *Appl. Phys. Express* **10**, 121002 (2017).

[25] R. Kajitani, H. Handa, S. Ujita, D. Shibata, K. Tanaka, M. Ogawa, H. Ishida, S. Tamura, M. Ishida, and T. Ueda, *Ext. Abst. of Int. Conf. on Solid State Devices and Materials* (2015) p. 1056.

[26] W. Li, K. Nomoto, M. Pilla, M. Pan, X. Gao, D. Jena, and H. G. Xing, *IEEE Trans. Electron Devices* **64(4)**, pp.869–872 (2017).

[27] Y. Zhang, Z. Liu, M. J. Tadjer, M. Sun, D. Piedra, C. Hatem, T. J. Anderson, L. E. Luna, A. Nath, A. D. Koehler, H. Okumura, J. Hu, X. Zhang, X. Gao, B. N. Feigelson, K. D. Hobart, and T. Palacios, *IEEE Electron Device Lett.* **38(8)**, pp.1097–1100 (2017).

[28] P. Kozodoy, J. P. Ibbetson, H. Marchand, P. T. Fini, S. Keller, J. S. Speck, S. P. DenBaars, and U. K. Mishra, *Appl. Phys. Lett.* **73(7)**, 975 (1998).

[29] I. C. Kizilyalli, T. Prunty, and O. Aktas, *IEEE Electron Device Lett.* **36(10)**, pp.1073–1075 (2015).

[30] K. Nomoto, B. Song, Z. Hu, M. Zhu, M. Qi, N. Kaneda, T. Mishima, T. Nakamura, D. Jena, H. G. Xing, and , *IEEE Electron Device Lett.* **37(2)**, pp.161–164 (2017).

[31] H. Ohta, N. Kaneda, F. Horikiri, Y. Narita, T. Yoshida, T. Mishima, and T. Nakamura, *IEEE Electron Device Lett.* **36(11)**, pp.1180–1182 (2015).

[32] H. Ohta, N. Asai, F. Horikiri, Y. Narita, T. Yoshida, and T. Mishima, *Jpn. J. Appl. Phys.* **58**, SCCD03 (2019).

[33] J. Kolnik, I. H. Oguzman, K. F. Brennan, R. Wang, and P. P. Ruden, *J. Appl. Phys.* **81(2)**, 726 (1997).

[34] K. Kunihiro, K. Kasahara, Y. Takahashi, and Y. Ohno, *IEEE Electron Device Lett.* **20(12)**, pp.608–610 (1999).

[35] A. M. Özbek, Ph.D. Dissertation, (2012), North Carolina University.

[36] L. Cao, J. Wang, G. Harden, H. Ye, R. Stillwell, A. J. Hoffman, and P. Fay, *Appl. Phys. Lett.* **112**, 262103 (2018).

[37] G. Piao, K. Ikenaga, Y. Yano, H. Tokunaga, A. Mishima, Y. Ban, T. Tabuchi, and K. Matsumoto, *J. Cryst. Growth* **456**, pp.137-139 (2016).

[38] N. Sawada, T. Narita, M. Kaechika, T. Uesugi, T. Kachi, M. Horita, T. Kimoto, and J. Suda, *Appl. Phys. Express* **11**, 041001 (2018).

[39] T. Narita, K. Tomita, Y. Tokuda, T. Kogiso, M. Horita, and T. Kachi, *J. Appl. Phys.* **124**, 215701 (2018).

[40] T. Narita, N. Ikarashi, K. Tomita, K. Kataoka, and T. Kachi, *J. Appl. Phys.* **124**, 165706 (2018).

[41] F. Yan, C. Qin, J. H. Zhao, and M. Weiner, *Mater. Sci. Forum* **389–393**, pp. 1305–1308 (2002).

[42] T. Maeda, T. Narita, H. Ueda, M. Kanechik, T. Uesugi, T. Kachi, T. Kimoto, M. Horita, and J. Suda, *IEDM Tech. Digest* (2018) p. 30.1.

[43] T. Maeda, T. Narita, H. Ueda, M. Kanechika, T. Uesugi, T. Kachi, T. Kimoto, M. Horita, and J. Suda, *IEEE Electron Device Lett.* **40(6)**, pp.941–944 (2019).

[44] T. Maeda, T. Narita, H. Ueda, M. Kanechika, T. Uesugi, T. Kachi, T. Kimoto, M. Horita, and J. Suda, *Appl. Phys. Lett.* **115**, 142101 (2019).

[45] A. S. Barker and Jr. and M. Ilegems, *Phys. Rev. B* **7(2)**, pp.743–750 (1973).

[46] M. J. Kane, M. J. Uren, D. J. Wallis, P. J. Wright, D. E. J. Soley, A. J. Simon, and T. Martin, *Semicon. Sci. Technol.* **26**, 085006 (2011).

[47] B. J. Baliga, *Fundamentals of Power Semiconductor Devices*, (Springer, 2008), pp. 91–166.

[48] T. Hiyoshi, T. Hori, J. Suda, and T. Kimoto, *IEEE Trans. Electron Devices* **55(8)**, pp.1841–1846 (2008).

[49] H. Fukushima, S. Usami, M. Ogura, Y. Ando, A. Tanaka, M. Deki, M. Kushimoto, S. Nitta, Y. Honda, and H. Amano, *Jpn. J. Appl. Phys.* **58**, SCCD25 (2019).

[50] S. Kawasaki, H. Fukushima, S. Usami, Y. Ando, A. Tanaka, M. Deki, M. Kushimoto, S. Nitta, Y. Honda, and H. Amano, *Ext. Abst. of Int. Conf. on Solid State Devices and Materials* (2019) p. K-7-02.

[51] T. Maeda, M. Okada, M. Ueno, Y. Yamamoto, M. Horita, and J. Suda, *Appl. Phys. Express* **9**, 091002 (2016).

[52] T. Maeda, T. Narita, M. Kanechika, T. Uesugi, T. Kachi, T. Kimoto, M. Horita, and J. Suda, *Appl. Phys. Lett.* **112**, 252104 (2018).

[53] J. L. Lyons, A. Janotti, and C. G. Van de Walle, *Appl. Phys. Lett.* **97**, 152108 (2010).

[54] Q. Yan, A. Janotti, M. Scheffler, and C. G. Van de Walle, *Appl. Phys. Lett.* **100**, 142110 (2012).

[55] M. A. Reshchikov, D. O. Demchenko, A. Usikov, H. Helava, and Y. Makarov, *Phys. Rev. B* **90**, 235203 (2014).

[56] S. Mandal, M. B. Kanathila, C. D. Pynn, W. Li, J. Gao, T. Margalith, M. A. Laurent, and S. Chowdhury, *Semicon. Sci. Technol.* **33**, 065013 (2018).

[57] G. E. Bulman, L. W. Cook, and G. E. Stillman, *Solid State Electron.* **25**, 1189 (1982).

[58] T. Kimoto, H. Niwa, T. Okuda, E. Saitoh, Y. Zhao, S. Asada, and J. Suda, J. Phys. D: Appl. Phys. **51**, 363001 (2018).

[59] S. Yamada, M. Omori, H. Sakurai, Y. Osada, R. Kamimura, T. Hashizume, J. Suda, and T. Kachi, *Appl. Phys. Express* **13**, 016505 (2020).

[60] M. Itoh, T. Kinoshita, C. Koike, M. Takeuchi, K. Kawasaki, and Y. Aoyagi, *Jpn. J. Appl. Phys.* **45(5A)**, pp.3988–3991 (2006).

[61] M. Kodama, M. Sugimoto, E. Hayashi, N. Soejima, O. Ishiguro, M. Kanechika, K. Itoh, H. Ueda, T. Uesugi, and T. Kachi, *Appl. Phys. Express* **1**, 021104 (2008).

[62] X. Chi, *Master Thesis*, (2019), Kyoto University [in Japanese].

[63] Y. Zhang, M. Sun, D. Piedra, J. Hu, Z. Liu, Y. Lin, X. Gao, K. Shepard, and T. Palacios, *IEDM Tech. Digest* (2017) p. 9.2.

[64] S. Usami, Y. Ando, A. Tanaka, K. Nagamatsu, M. Deki, M. Kushimoto, S. Nitta, Y. Honda, H. Amano, Y. Sugawara, Y.-Z. Yao, and Y. Ishikawa, *Appl. Phys. Lett.* **112**, 182106 (2018).

[65] T. Oka, Y. Ueno, T. Ina, and K. Hasegawa, *Appl. Phys. Express* **7**, 021002 (2014).

[66] T. Oka, T. Ina, Y. Ueno, and J. Nishii, *Appl. Phys. Express* **8**, 054101 (2015).

[67] H. Nie, Q. Diduck, B. Alvarez, A. P. Edwards, B. M. Kayes, M. Zhang, G. Ye, T. Prunty, and D. Bour, *IEEE Electron Device Lett.* **35(9)**, pp.939–941 (2014).

[68] S. Usami, *Ph.D. Dissertation*, (2018), Nagoya University [in Japanese].

[69] Y. Zhang, H.-Y. Wong, M. Sun, S. Joglekar, L. Yu, N. A. Braga, R. V. Mickevicius, and T. Palacios, *IEDM Tech. Digest* (2015) p. 35.1.

[70] S. Usami, A. Tanaka H. Fukushima, Y. Ando, M. Deki, S. Nitta, Y. Honda, and H. Amano, *Jpn. J. Appl. Phys.* **58**, SCCB24 (2019).

[71] S. Usami, N. Mayama, K. Toda, A. Tanaka, M. Deki, S. Nitta, Y. Honda, and H. Amano, *Appl. Phys. Lett.* **114**, 232105 (2019).

Chapter 4

Franz-Keldysh Effect in GaN Devices

4.1 Introduction

Under high electric field, wavefunctions of electrons and holes in a semiconductor come to be Airy-function shape and leak into the bandgap with damping as shown in Fig. 4.1. Then, optical properties such as absorption coefficient, reflectance, refractance, etc. are changed at near a fundamental absorption edge. For example, an absorption coefficient exhibits a *tail* for a below bandgap energy and an oscillation for an above bandgap energy. In 1958, Franz and Keldysh individually reported that the fundamental absorption edge shows red shift (strictly, absorption edge shows *broadening*, not shift) and its shift is proportional to a square of electric field and can be observed in an electric field range of 10^5–10^6 V/cm [1, 2]. These electro-optical effects, electro-absorption, electro-reflectance and electro-refractance, are called as the Franz-Keldysh (FK) effect.

The theory of the FK effect is well studied in 1960s [1–9]. Tharmalingam derived the expressions for the absorption coefficient of semiconductors and insulators in the presence of a uniform electric field for both allowed and forbidden transitions [3]. Callaway theoretically expected that the sprit of energy levels by the Stark effect causes significant oscillation structure in an absorption coefficient under extremely high electric field ($\sim 10^7$ V/cm) [5]. Penchina derived the expressions for the absorption coefficient of phonon-assisted optical absorption in an indirect-bandgap semiconductor [6]. Aspnes discussed the changes of the real and imaginary parts of the dielectric function near all four types of critical points, in the presence of electric field oriented in an arbitrary direction in an anisotropic solid [9].

The FK effect is very closely related to an electronic energy band structure in a material. Thus, the effect is a powerful tool to investigate material properties such as an energy band structure, electric field strength, (reduced) effective mass, matrix elements, etc. There are a lot of experimental reports on the FK effect in various materials (Si, Ge, GaAs, etc.) [10–19]. Especially, electro-reflectance modulation spectroscopy using the FK-oscillation is often used because of its high sensitivity and high resolution. Paige and Rees reported that an exponential tail for below bandgap and an oscillation for above bandgap

were clearly observed in GaAs under electric field of 40 kV/cm [10]. Yacoby investigated the electro-absorption in Si under electric field of 160 kV. Clear contribution of the transverse optical (TO)-phonon emission ($\epsilon_{\rm ph} = 60$ meV) was observed from the spectral of the change of the absorption coefficient at room temperature [11]. Seraphin investigated the electro-reflectance response in n-type GaAs at various temperatures [12]. From the response in the range of 2.7–3.4 eV, which is much higher than the absorption edge, optical properties such as the energy gap, the type of critical point, the spin-orbit sprit energy, the temperature coefficient of forbidden bandgap, etc. were determined.

GaN is a direct-bandgap semiconductor with a bandgap of 3.4 eV at room temperature, in which high electric field can be applied owing to its high breakdown electric field. Thus, the FK effect is prominently observed in GaN. There are several reports on the FK effect in GaN-based materials [20–26]. Wetzel *et al.* conducted photo-reflectance spectroscopy measurements of strained InGaN/GaN heterostructures and revealed the presence of a large piezoelectric field in the $In_xGa_{1-x}N$/GaN layers (e.g. 0.63 MV/cm in $x = 0.19$) from the FK-oscillation [20]. Franssen *et al.* reported the photocurrent spectroscopy of InGaN/GaN multiple-quantum-well LEDs where the piezoelectric field in the InGaN well layers was estimated from the sub-bandgap optical absorption due to the FK effect [21]. Cavallini *et al.* reported sub-bandgap optical absorption in GaN nanowires, and a long band tail of approximately 0.1 eV was observed [22]. Katayama *et al.* determined the lattice polarity of GaN by modulation spectroscopy [23]. Owing to a strong spontaneous polarization, the difference in band profiles for Ga- and N-polar surface was distinguishable in terms of the spectral-phase flip between photoreflectance and electroreflectance. Janicki *et al.* investigated the surface potential barrier in *m*-plane undoped-GaN/n^+GaN using contactless electroreflectance [24]. The built-in electric fields in the undoped cap layers have been determined from the FK-oscillation period. Sato *et al.* investigated the photoresponse and the photoabsorption properties of GaN porous structures formed by a photo-assisted electrochemical process [25]. A low voltage was applied to the nano-order GaN porous structure and the photocurrent induced by the FK effect was observed. Tanikawa *et al.* investigated the internal electric fields in III-polar (0001), N-polar ($000\bar{1}$), and semi-polar ($10\bar{1}1$) InGaN/GaN LEDs [26]. In these reports, the FK effect was observed in nano-scale structure such as surfaces, heterostructures, quantum wells, etc.

Although the FK effect in GaN-based materials has been well studied, there are no report on the FK effect in a simple-structured GaN device under high voltage. So far, GaN devices have been fabricated on foreign substrates such as sapphire, Si and SiC [27–32]. These devices include a lot of defects (e.g. threading dislocation density of $> 10^8$ cm^{-2}), which causes large leakage current. In addition, there devices basically have a lateral device structure. Thus, it is difficult to apply high voltage to heteroepitaxial GaN devices.

Recently, GaN devices fabricated on GaN bulk substrates have attracted significant attention [33, 34]. GaN Schottky barrier diodes and p-n junction diodes fabricated on GaN freestanding substrates have been reported from various institutions [35–40].

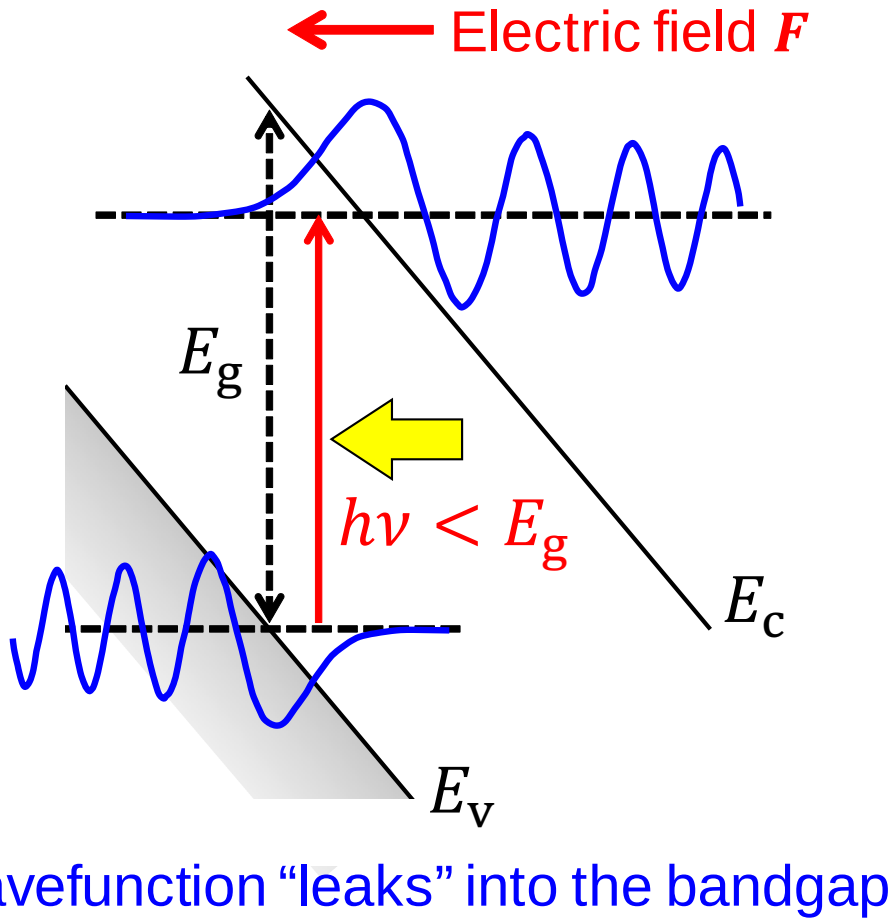

Figure 4.1: Schematic band diagram of a semiconductor under electric field. Wavefunctions of electrons and holes leak into the bandgap, and sub-bandgap optical absorption occurs via the leaked states. Then, optical properties such as absorption coefficient, reflectance and refractance are changed, which is known as the Franz-Keldysh effect.

Saitoh *et al.* reported that GaN-on-GaN Schottky barrier diodes with extremely low on-resistance (0.71 mΩcm^2) and high breakdown voltage (1.1 kV). Suda *et al.* reported that the nearly ideal current-voltage (I–V) characteristics are observed in GaN-on-GaN Schottky barrier diodes [36]. For a forward characteristic, the ideality factor (n) was very close to unity, indicating the current transport follows the thermionic emission model and other current components (e.g. defect-assist transport) are negligible. For a reverse characteristic, the current transport mechanism is well expressed by the thermionic field emission (TFE), since the tunneling of electrons through the Schottky barrier comes to be significant owing to high electric field. It should be noted that this is a feature of a wide-bandgap semiconductor Schottky junction: the TFE current is also clearly observed in 4H-SiC SBDs reported by Hatakeyama *et al.* [41]. Kizilyalli *et al.* demonstrated high breakdown voltage GaN p-n juction diodes with excellent performance [37–39]. Especially, by reducing hillocks and surface morphology, very low leakage current (< 10 nA) at 4 kV in the 0.12 mm^2 GaN p-n diode was achieved [39]. Hu *et al.* demonstrated that the textbook-like characteristics in vertical GaN p-n junction diodes, which showed simultaneously an avalanche breakdown voltage of > 1.4 kV under reverse bias and an ideality factor plateau of $\sim$2.0 (a recombination current) followed by a near unity ideality factor of 1.1 (a diffusion current) in a forward bias window [40].

A high reverse voltage (high electric field) can be applied to these GaN-on-GaN devices due to their relatively low defect densities and vertical device structures. In this study, a reverse-voltage dependence of photocurrents in a Ni/n-GaN Schottky barrier diode and a GaN p-n junction diode under sub-bandgap illumination are investigated. Although the wavelength of the irradiated light is longer than the GaN absorption edge, significant increases in the photocurrents were observed and the increases were more prominent as the wavelength was closer to the absorption edge. The author calculated the photocurrent considering the optical absorption induced by the FK effect in the depletion layer based on the theory of the electroabsorption [9] and compared with the experimental data. The voltage, wavelength and temperature dependences of the photocurrent induced by the FK effect in GaN devices are discussed.

4.2 Franz-Keldysh Effect in n-type GaN Schottky Barrier Diode

4.2.1 Measurement Set up

Figure 4.2 shows a schematic cross section of a Ni/n-GaN vertical Schottky barrier diode (SBD) used in this study. A 300-μm-thick n-type GaN(0001) free-standing substrate grown by hydride vapor phase epitaxy (HVPE) was used. A 7-μm-thick n-type GaN homoepitaxial layer was grown by metal-organic vapor phase epitaxy (MOVPE). 100-μm-diameter Schot-

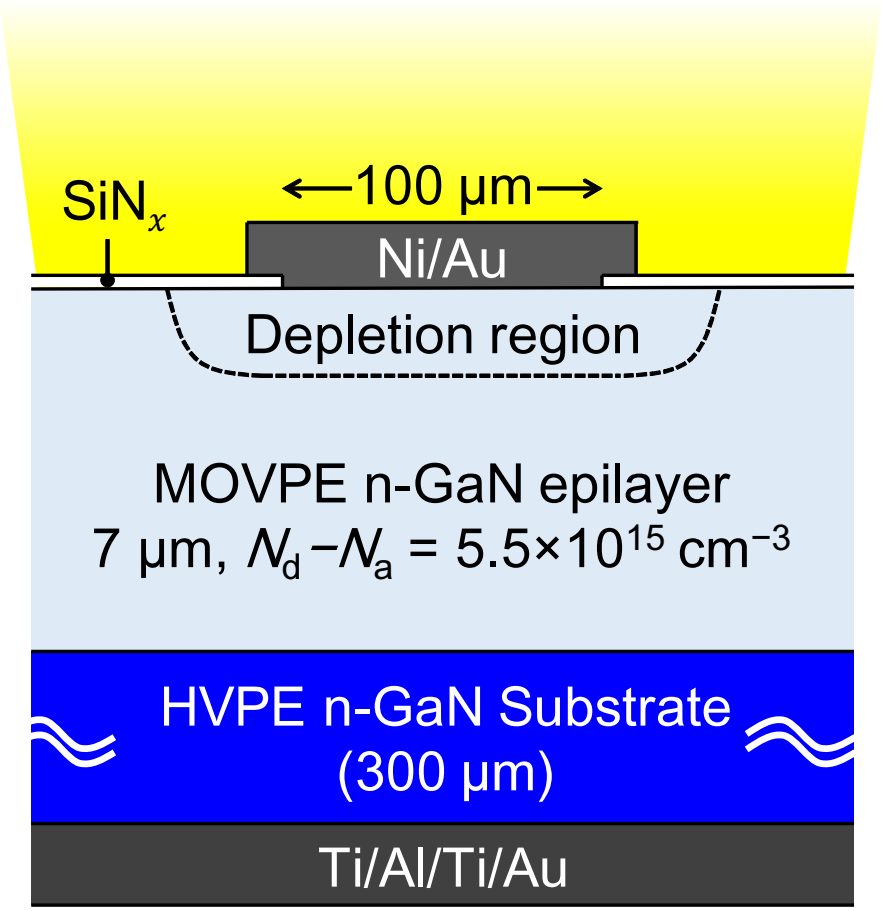

Figure 4.2: Schematic cross section of a Ni/n-GaN Schottky barrier diode used in this study. The wavelength of the incident light was longer than the absorption edge of GaN; therefore, the light penetrated into GaN. The light was reflected by the back-side Ohmic electrode and reached the Ni/GaN interface.

tky electrodes were formed by depositing Ni/Au on the GaN epitaxial layer. The Ohmic electrode was formed by depositing Ti/Al/Ti/Au on the mirror-polished back side of the substrate. Field plate structure with a SiN_x layer for edge termination was fabricated to prevent premature breakdown due to the electric field crowding at the edge of the Schottky electrode. The fabrication process has been described in detail in the literature [35].

Before a photocurrent measurement, C–V and I–V characteristics were measured without illuminations using the Keysight B1505A semiconductor parameter analyzer. Figure 4.3 shows the C–V characteristics of the GaN Schottky barrier diode. For the measurements, the plots were independent of frequency in the range of 10–500 kHz, and a frequency of 500 kHz was used. From the C–V measurements, a built-in potential (V_d) of 0.90 V and the net donor concentration ($N_\mathrm{d} - N_\mathrm{a}$) of 5.5×10^{15} cm^{-3} were obtained. In the analysis, $\varepsilon_\mathrm{s} = 10.4\varepsilon_0$ [42, 43] was used. The barrier height, as shown in Fig. 4.4, $e\phi_{\mathrm{b,C-V}}$ of 1.08 eV was obtained. Figure 4.5 shows the forward I–V characteristics of the GaN Schottky barrier diode. The thermionic emission (TE) current is calculated and the ideality factor (n) and the saturation current velocity (J_0) were obtained from the fitting the calculated curve to the experimental data. In the calculation, a voltage drop of a series resistance was considered. The calculated curve shows good agreement with the experimental data, and the ideality factor of $n = 1.04$ and the barrier height of $e\phi_{\mathrm{b,I-V}} = 1.07$ eV were obtained. The measurement and analysis of the barrier height, including its temperature dependence, are described in [44] and Appendix A.

For the photocurrent measurements, a 150 W Xe lamp combined with a monochromator (MLS-1510, ASAHI SPECTRA) was used as a monochromatic light source. The wavelength of light was varied from 390 to 700 nm with a bandpass width of 10 nm, which is longer than the fundamental absorption edge of GaN (365 nm, 3.42 eV) at room temperature. The light was focused on a 5-mm-diameter circle centered at the Schottky electrode.

4.2.2 Photocurrent Induced by Internal Photoemission

Figure 4.6 shows the reverse-voltage dependence of photocurrents in the GaN Schottky barrier diode under sub-bandgap ($h\nu < E_\mathrm{g}$) illuminations of 300–700 nm. For the discussion of the wavelength dependence, the data are normalized using an irradiated photon flux of 2.0×10^{15} cm^{-2}s^{-1}. For the range of 500–700 nm, the photocurrent were almost constant (slightly increased) with reverse voltage, and the larger photocurrent were observed for the shorter wavelength. These features indicate that the photocurrent is caused by internal photoemission (IPE): electrons are excited by incident light with photon energy of $E_\mathrm{g} > h\nu > e\phi_\mathrm{b}$ and excited electrons flow into a semiconductor over a barrier height. From the wavelength dependence of photoyield of IPE (Y), a barrier height can be obtained using the Fowler theory: $Y \propto (h\nu - e\phi_\mathrm{b})^2$ [45]. Figure 4.7 shows the square root of Y versus photon energy (the Fowler plot) for the GaN Schottky barrier diode. In the plot, linear relationship was observed and the barrier height of $e\phi_{\mathrm{b,IPE}} = 1.08$ eV was obtained from

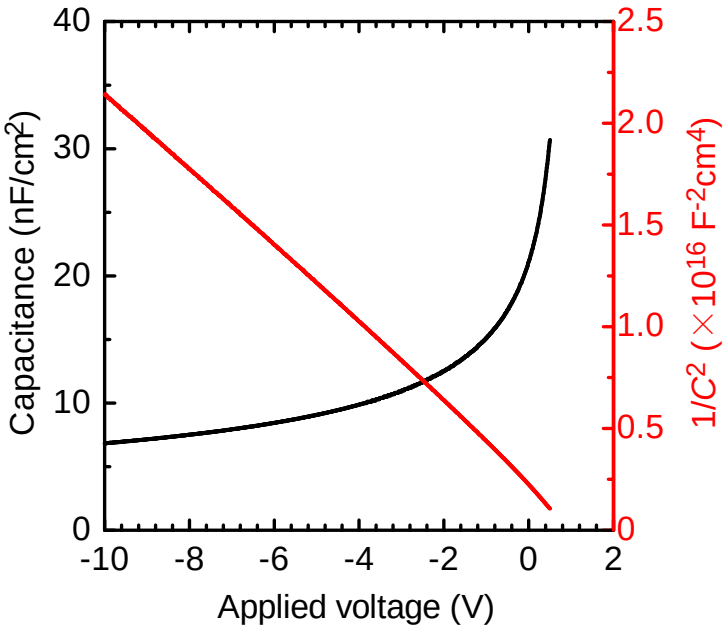

Figure 4.3: Capacitance–voltage characteristics of the GaN Schottky barrier diode.

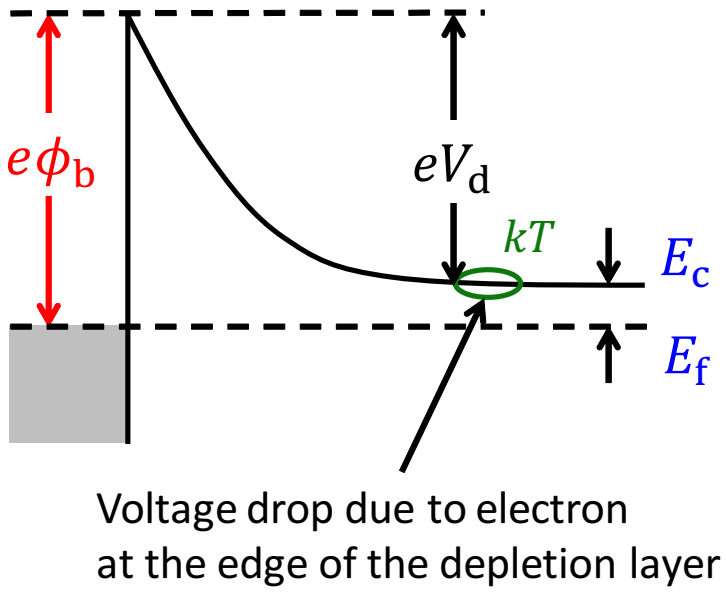

Figure 4.4: Energy diagram at a Schottky junction. A barrier height is a sum of built-in potential, a difference between a conduction band minimum and a felmi level, and a voltage drop at a depletion layer edge.

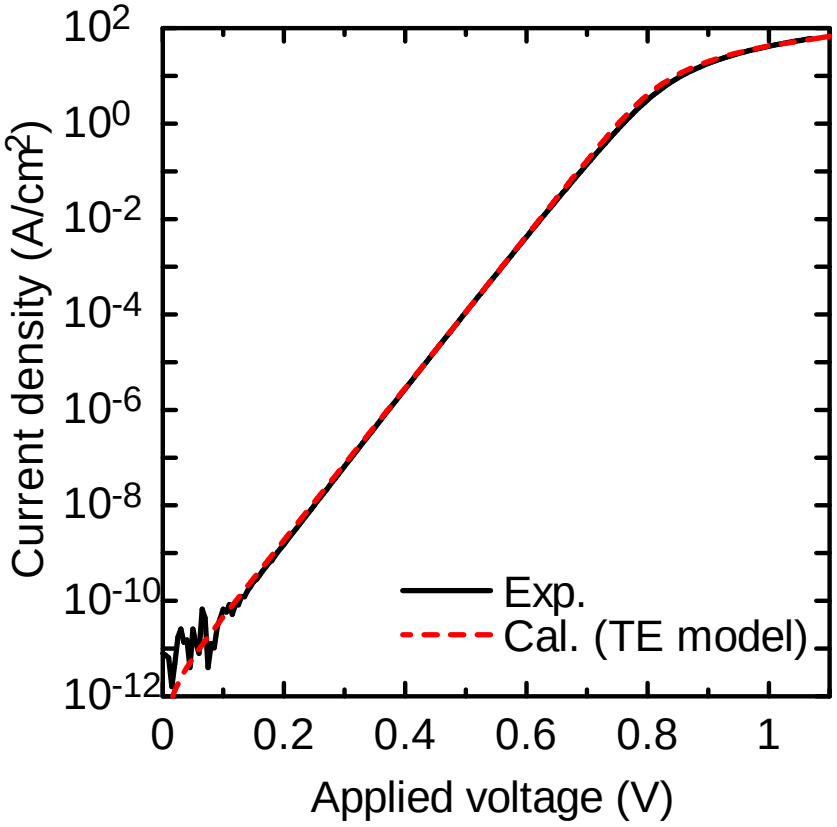

Figure 4.5: Forward current–voltage characteristics of the GaN Schottky barrier diode. The calculated curve based on the thermionic emission (TE) model is also shown as a red broken line.

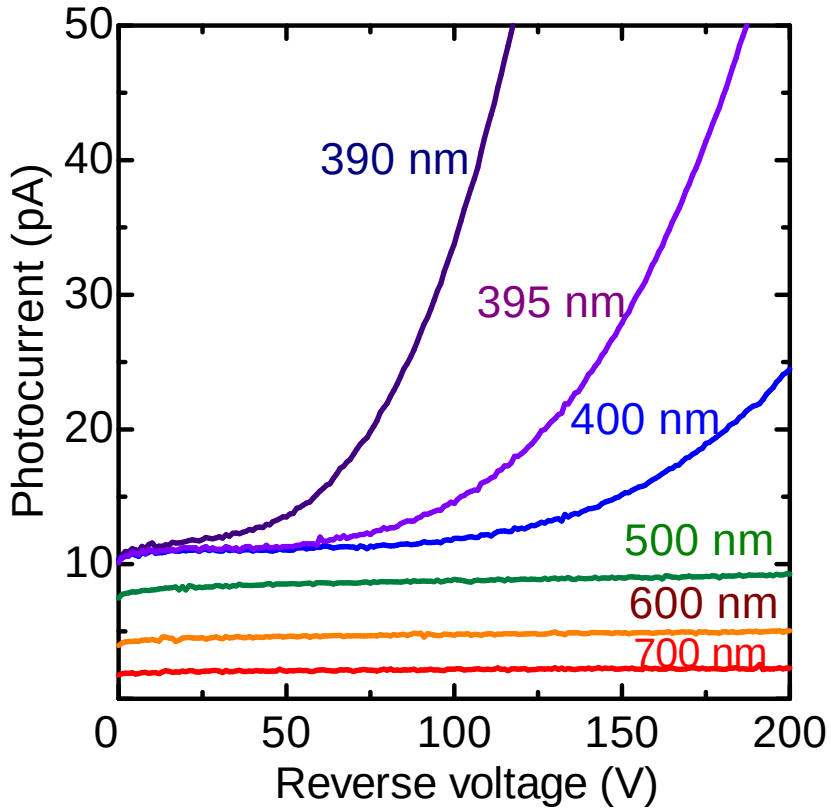

Figure 4.6: Reverse-voltage dependence of the photocurrents for 390–700 nm in the GaN Schottky barrier diode. For the wavelength longer than 500 nm, photocurrents are almost constant, which is caused by IPE (strictly, barrier height lowering by image force causes slight increase with increasing reverse bias). For the wavelength near the absorption edge (390–400 nm), the photocurrents significantly increase with reverse bias and the increases are more striking as the wavelength is closer to the absorption edge, which is caused by the Franz-Keldysh effect.

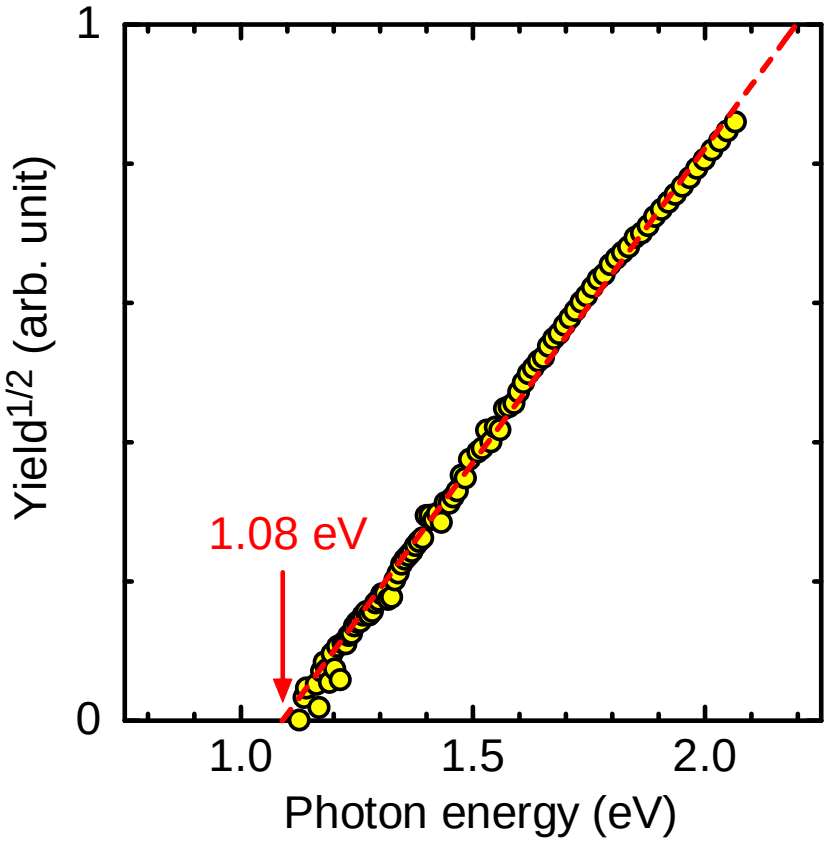

Figure 4.7: Square root of the photoyield of IPE versus photon energy (Fowler plot) in the GaN Schottky barrier diode. From the extrapolation value on the photon energy axis, the barrier height of 1.08 eV was obtained.

the extrapolated value on the photon-energy axis. This barrier height is consistent with the values obtained from C–V and I–V measurements ($e\phi_{\mathrm{b,C-V}}$ of 1.08 eV, $e\phi_{\mathrm{b,I-V}} = 1.07$ eV), which is a clear evidence that the photocurrents were caused by IPE.

Although the light was irradiated from the top side, the clear photocurrents much larger than the dark leakage current were obtained. The Schottky electrode was thick, such that the irradiated light was reflected by the electrode and could not reach the Ni/GaN interface from the surface. However, the wavelength of light was longer than the absorption edge of GaN (∼365 nm); therefore, the light irradiated around the Schottky electrode entered the GaN layer. The light was reflected by the back-side Ohmic electrode and reached the Ni/GaN interface from the back side, which resulted in IPE, as shown in Fig. 4.8. Considering the size of the Schottky electrode (100 μm) and the total thickness of GaN (300 μm), the irradiated light is considered to reach the entire Ni/GaN interface. The author conducted similar measurements for Schottky electrodes with various diameters (40–400 μm). The photocurrent generated by IPE was found to be proportional to the area of the Schottky electrode, as shown in Fig. 4.9. This is the evidence that the Schottky electrode was illuminated entirely and uniformly from the back side via multiple reflections (GaN acts as a light guide).

4.2.3 Effect of Image Force Lowering

Here, the author considers the voltage dependence of the photocurrent caused by IPE. With increasing reverse voltage, electric field at the Schottky junction comes to be higher and the image force lowering occurs. The image force lowering is written as

$$\Delta e\phi_{\mathrm{b}}(V) = -\sqrt{\frac{eF(V)}{4\pi\varepsilon_{\mathrm{s}}}} = -\left[\frac{e^3(N_{\mathrm{d}} - N_{\mathrm{a}})(V_{\mathrm{d}} - V)}{8\pi^2\varepsilon_{\mathrm{s}}^3}\right]^{1/4}. \tag{4.1}$$

F is electric field strength at the Schottky interface. Here, the author assumed that the image force dielectric constant ($\varepsilon_{\mathrm{IF}}$) is the same with the static dielectric constant of $\varepsilon_{\mathrm{s}} = 10.4\varepsilon_0$ [42], which is valid considering the transit time for electrons between the metal surface and the potential energy maximum [46]. Figure 4.10 shows the calculated image force lowering as a function of the reverse voltage in the GaN Schottky barrier diode. At the reverse voltage of 200 V, the maximum electric field and the barrier lowering are 0.62 MV/cm and 0.09 eV, respectively. With consideration of the image force lowering, a voltage dependence of a photocurrent caused by IPE can be expressed as

$$I_{\mathrm{IPE}}(V) = I_0 \cdot \left(\frac{h\nu - e\phi_{\mathrm{b}}(V)}{h\nu - e\phi_{\mathrm{b}}(0)}\right)^2. \tag{4.2}$$

I_0 is the photocurrent at 0 V. Figure 4.11 shows the comparison between the experimental photocurrents for 500, 600 and 700 nm and the calculated photocurrent using Eqs. (4.1) and (4.2). The calculated curves show good agreement with the experimental data, indicating that the image force lowering does not cause the significant increase in the photocurrents.

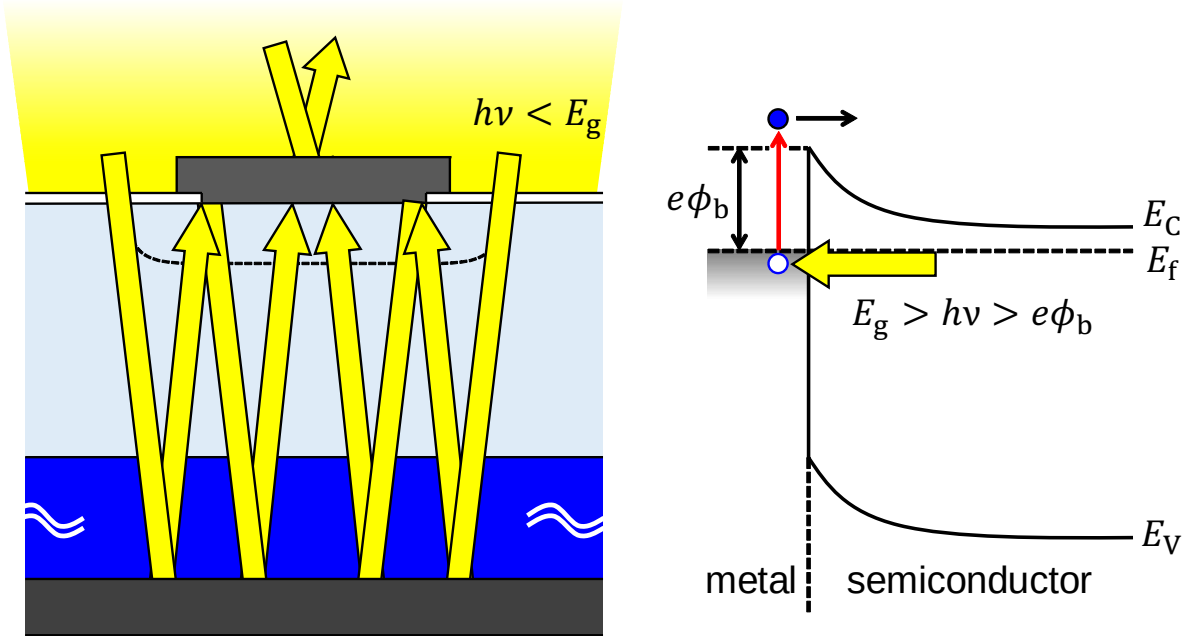

Figure 4.8: Image of the GaN Schottky barrier diode under sub-bandgap illumination from the top side, and the band diagram of the IPE in the Schottky barrier.

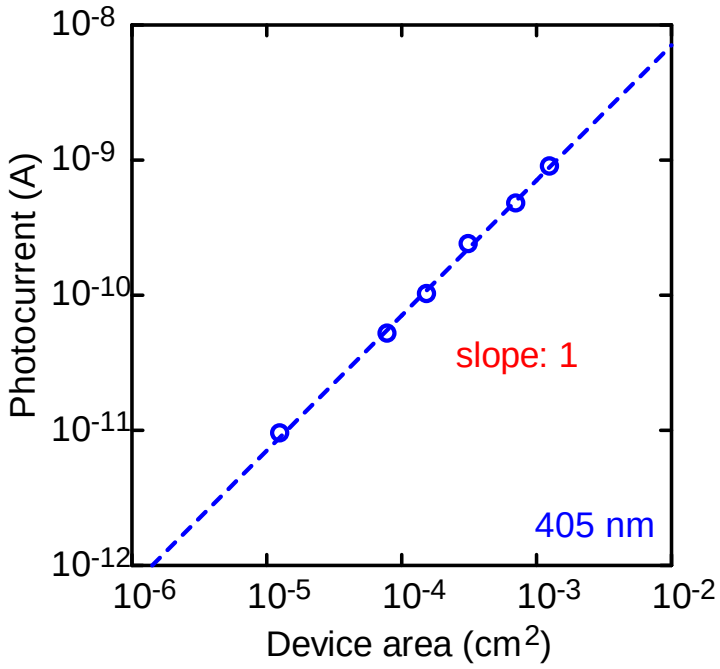

Figure 4.9: Size dependence of the photocurrent for 405 nm for the GaN Schottky barrier diode.

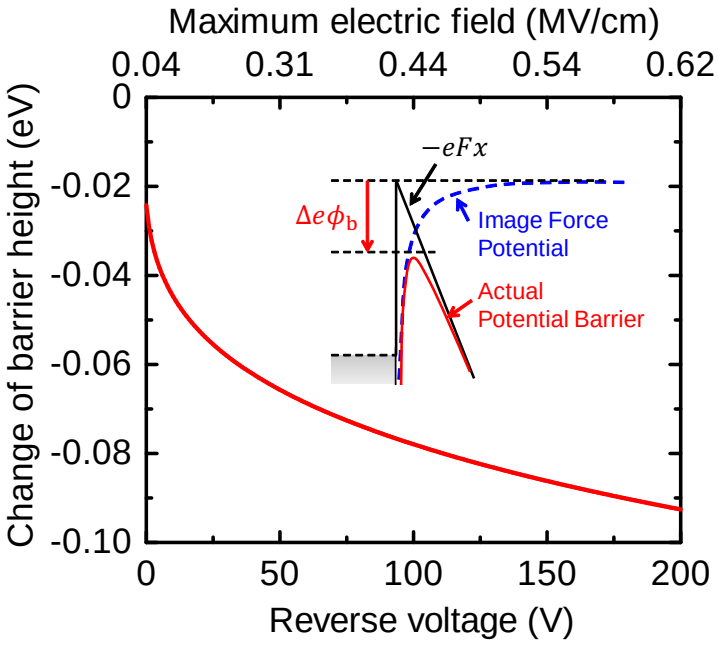

Figure 4.10: Calculated image force lowering as a function of the reverse voltage in the GaN Schottky barrier diode. Inset: diagram of the image force lowering at the Schottky interface. Strong electric field significantly reduces the barrier height owing to the image force potential.

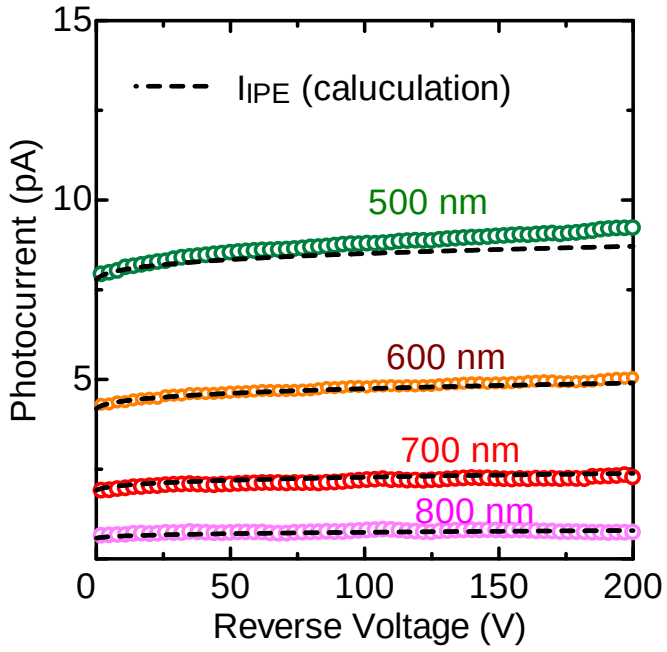

Figure 4.11: Comparison between the experimental photocurrents induced by IPE and the calculated photocurrent considering the effect of the image force lowering.

4.2.4 Significant Increase in Photocurrent Induced by Franz-Keldysh Effect

Photocurrents for 390–400 nm show different behavior: significantly increases with increasing reverse voltage are observed. The increase starts at lower voltage and more prominent as the wavelength is closer to the absorption edge. These features indicate that the significant increases are caused by the sub-bandgap optical absorption induced by the Franz-Keldysh effect at high electric field region. To quantitatively confirm that the significant increases in photocurrents for 390–400 nm in Fig. 4.6 are induced by the FK effect, the author calculates a photocurrent induced by sub-bandgap optical absorption due to the FK effect in a depletion region in the GaN Schottky barrier diode. At first, the author discusses the optical absorption coefficient in GaN under electric field. Based on the Aspnes's theory [9], the electric field and wavelength dependence of an absorption coefficient for a direct bandgap semiconductor is give by

$$\alpha\left(F,\omega\right)=\frac{e^2|\boldsymbol{e}\cdot\boldsymbol{p}_{\mathbf{cv}}|^2}{2\varepsilon_0 m_0^2 nc\omega}\left(\frac{8\mu_{\parallel}\mu_{\perp}^2}{\hbar^6}\right)^{\frac{1}{2}}\times\sqrt{\hbar\theta}\left[\mathrm{Ai}'^{\,2}\left(\eta\right)-\eta\mathrm{Ai}^2\left(\eta\right)\right],$$

$$\eta=\frac{E_{\mathrm{g}}-h\nu}{\hbar\theta},\quad \hbar\theta=\left(\frac{e^2\hbar^2F^2}{2\mu_{\parallel}}\right)^{\frac{1}{3}},\quad \mu=\frac{m_{\mathrm{e}}m_{\mathrm{h}}}{m_{\mathrm{e}}+m_{\mathrm{h}}},\tag{4.3}$$

where e is the elementary charge, m_0 is the electron mass, ε_0 is the vacuum permittivity, c is the light speed in a vacuum, ω is the angular frequency of light, and $\hbar$ is the Dirac constant. $\mathrm{Ai}(x)$ is the Airy function ($\mathrm{Ai}'(x)$ is its derived function), $|\boldsymbol{e}\cdot\boldsymbol{p}_{\mathbf{cv}}|^2$ is the momentum matrix element, and n is the refractive index in GaN. The wavelength dependence of n in the range of 390–420 nm is small; therefore, a constant value of $n = 2.5$ [47] was used. μ is the reduced effective mass; the subscripts indicate whether the component is parallel ($\parallel$) or perpendicular ($\perp$) to the c-axis. In this study, the electric field is parallel to the c-axis; therefore, $\mu_{\parallel}$ is used for the calculation of $\hbar\theta$, which determines the electric field dependence of $\alpha(F,\omega)$. The light propagation direction was almost parallel to the c-axis (the electric field of the light was perpendicular to the c-axis); therefore, mainly transitions from the heavy-hole band (hh) and the light-hole band (lh) to the conduction band (c) occurred, with consideration for the oscillator strengths in GaN [48]. Table 4.1 shows the effective masses in GaN reported in the literature [48–50]. $\mu_{\parallel}$ for the hh-c and lh-c transitions are almost identical. The difference between the valence band maximum energies between the hh and lh is very small (6 meV) [48]. Therefore, $\alpha(F,\omega)$ was calculated as a one-hole-band model using $\mu_{\parallel} = 0.16$–$0.18m_0$. There is no suitable data for $|\boldsymbol{e}\cdot\boldsymbol{p}_{\mathbf{cv}}|^2$ in GaN; thus, $\alpha(F,\omega)$ was fitted with $F = 0$ V/cm to the absorption coefficient in GaN reported by Muth *et al.* [51] in the range of 4–5 eV, and $|\boldsymbol{e}\cdot\boldsymbol{p}_{\mathbf{cv}}|^2$ of $1.2{\sim}10^{-48}$ J·kg ($\sim E_{\mathrm{g}}m_0^2/2m^*$) was used. $\alpha(F,\omega)$ calculated using $\mu_{\parallel} = 0.16$–$0.18m_0$ showed good agreement. It was confirmed that the calculated $\alpha(F,\omega)$ as a two-hole-band model for the hh-c and lh-c transitions were almost same as $\alpha(F,\omega)$ calculated as a one-hole-band model.

Table 4.1: Effective masses reported in the literatures [48–50].

$\parallel$ or $\perp$	m_e	m_{hh}	m_{lh}	$\mu_{\mathrm{hh-c}}$	$\mu_{\mathrm{lh-c}}$	Ref.
$\parallel$	$0.17m_0$	$2.03m_0$	$1.25m_0$	$0.16m_0$	$0.15m_0$	[48]
$\perp$	$0.19m_0$	$0.33m_0$	$0.34m_0$	$0.12m_0$	$0.12m_0$	
$\parallel$	$0.20m_0$	$1.10m_0$	$1.10m_0$	$0.17m_0$	$0.17m_0$	[49]
$\perp$	$0.18m_0$	$1.65m_0$	$0.14m_0$	$0.16m_0$	$0.08m_0$	
$\parallel$	$0.20m_0$	$1.85m_0$	$1.85m_0$	$0.18m_0$	$0.18m_0$	[50]
$\perp$	$0.22m_0$	$1.96m_0$	$0.30m_0$	$0.20m_0$	$0.13m_0$	

Figure 4.12 shows the wavelength dependence of the absorption coefficients for GaN calculated for $F = 0$, 0.5 and 1.0 MV/cm using the reduced effective mass of $\mu_{||} = 0.16m_0$. With the electric field, the absorption coefficient shows a quasi-exponential tail below the bandgap and the FK-oscillation above the bandgap. The absorption tail becomes longer and the period of the FK-oscillation becomes shorter with an increase in electric field.

Figure 4.13 shows the distributions of electric field and the absorption coefficient for 400 nm in the depletion region in the GaN Schottky barrier diode under reverse bias of 200 V. The electric field distribution was calculated from the well known formula:

$$F(x,V) = \frac{e(N_\mathrm{d} - N_\mathrm{a})(W(V) - x)}{\varepsilon_\mathrm{s}}, \quad W(V) = \sqrt{\frac{2\varepsilon_\mathrm{s}(V_\mathrm{d} - V)}{e(N_\mathrm{d} - N_\mathrm{a})}}, \tag{4.4}$$

where $x = 0$ is the position of the Schottky interface and W is the depletion layer edge. The absorption coefficient distribution was calculated from the $\alpha(F,\omega)$ in Eq. (4.3) according to the electric field distribution in Eq. (4.4). The absorption coefficient is localized near the Schottky interface (high electric field region).

As mentioned above, the Schottky contact is uniformly illuminated from the back side. Photocurrent due to sub-bandgap optical absorption induced by the FK effect in the depletion layer (I_FK) can be written as

$$I_\mathrm{FK}(V,\omega) = e\Phi_0 \left[1 - \exp\left(-2\int_0^{W(V)} \alpha(F(V,x),\omega)dx\right)\right]. \tag{4.5}$$

Here, Φ_0 is defined as the incident photon flux to the depletion layer edge from the back side, which including multiply reflected photons. The author considers one round-trip path, i.e., entering into the depletion layer, reflected at the Ni/GaN interface, and exiting from the depletion layer as shown in Fig. 4.14. Here, light absorption at the Ni/GaN interface is neglected in this calculation, since it is estimated to be less than 1% from the photocurrent generated by IPE. The optical absorption by GaN substrate is also negligible for the wavelength longer than 390 nm [52]. Strictly, the photon flux decreases with increasing reverse bias voltage owing to the optical absorption in the depletion layer, which weakens multiple reflections. However, in this study, optical absorption in one round-trip path in the depletion layer is less than 1%. We neglected the voltage dependence of Φ_0.

It is quite difficult to estimate Φ_0 owing to multiple reflection within GaN. Thus, Φ_0 was obtained by fitting the calculated curves to the experimental data ($I_\mathrm{FK} = I_\mathrm{total} - I_\mathrm{IPE}$). Figure 4.15 shows the comparisons between the experimental photocurrents and the calculated photocurrents as the sum of I_IPE and I_FK as solid lines and red broken lines, respectively. The voltage and wavelength dependence of the photocurrent is well reproduced. Then, the obtained Φ_0 was about 20–30% of the irradiated photon flux (Φ_irr), which seems to be reasonable with the reflection loss at the GaN surface (∼18%). These results are the strong evidence that the significant increase in the photocurrent originates from the sub-bandgap optical absorption induced by the FK effect in the depletion region.

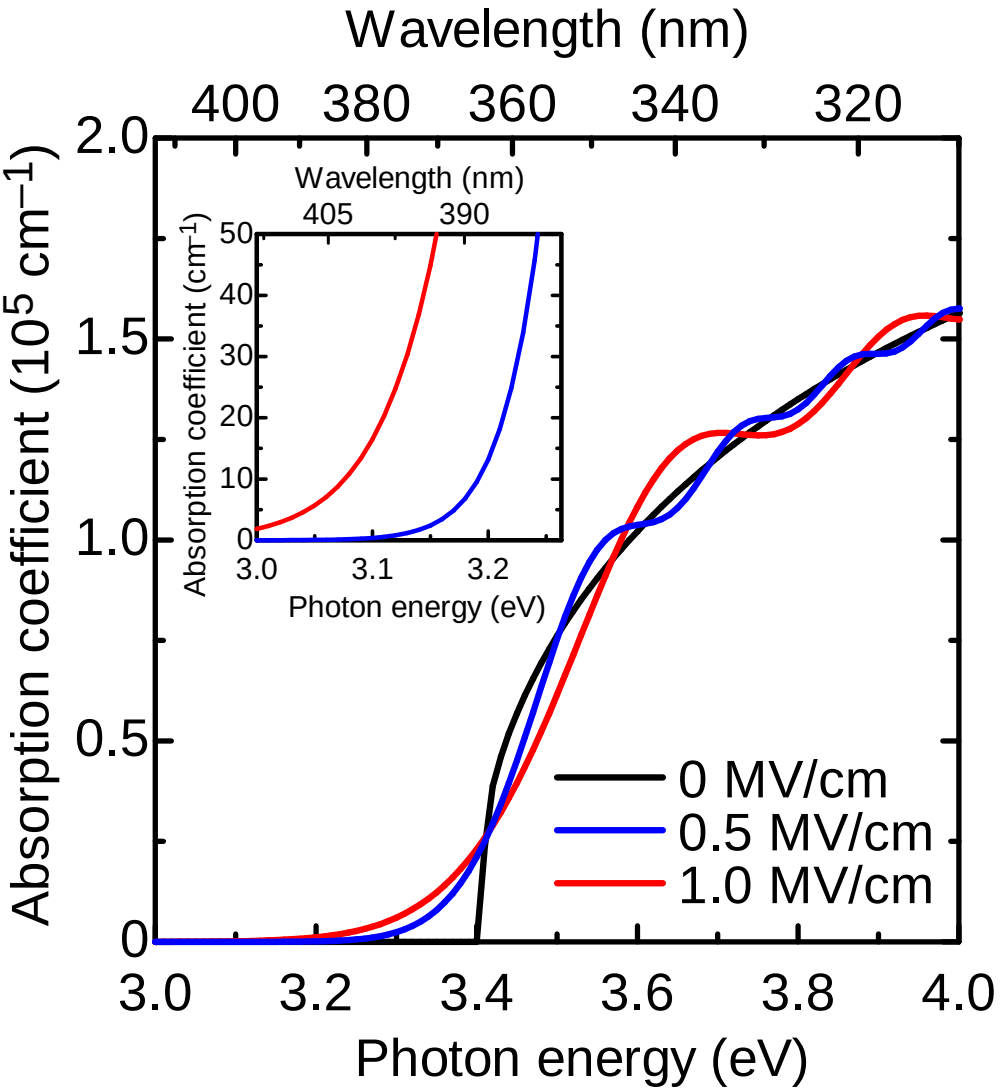

Figure 4.12: The wavelength dependence of the absorption coefficients for GaN calculated for $F = 0$, 0.5 and 1.0 MV/cm. With electric field, the absorption coefficient shows a quasi-exponential tail below the bandgap and the FK-oscillation above the bandgap. Inset: the magnification plot for the wavelength around 390–400 nm.

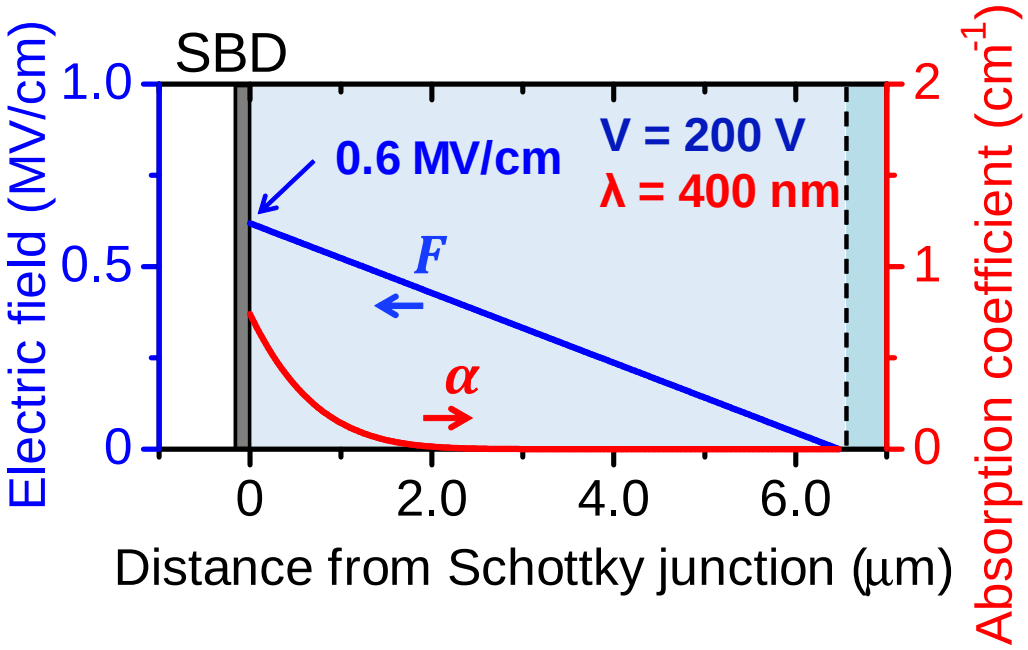

Figure 4.13: The distributions of the electric field and the absorption coefficient for 400 nm in the depletion region in the GaN Schottky barrier diode.

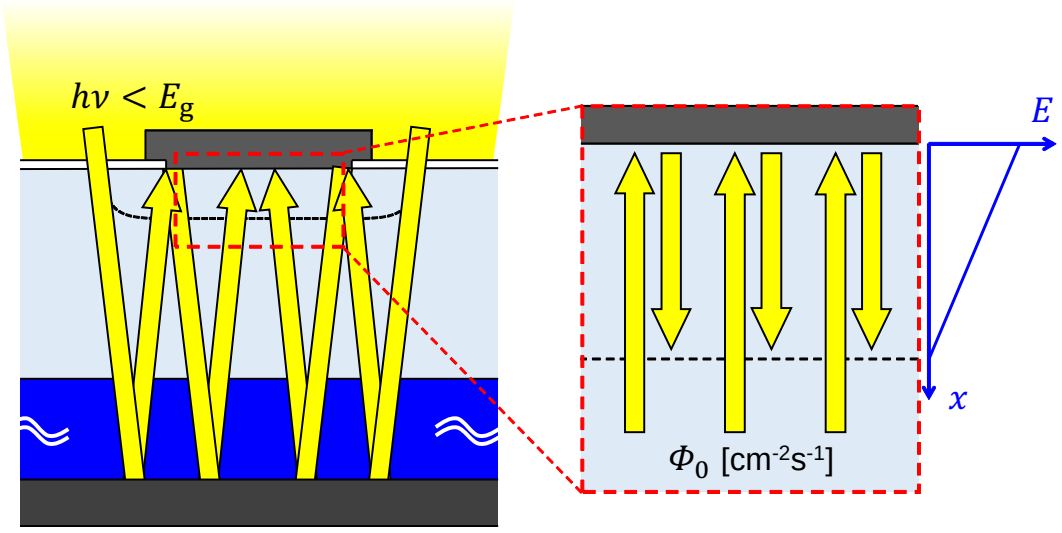

Figure 4.14: Diagrams of multiple reflection of irradiated light in the GaN Schottky barrier diode (left side) and one-round trip path of Φ_0 assumed in this study (right side).

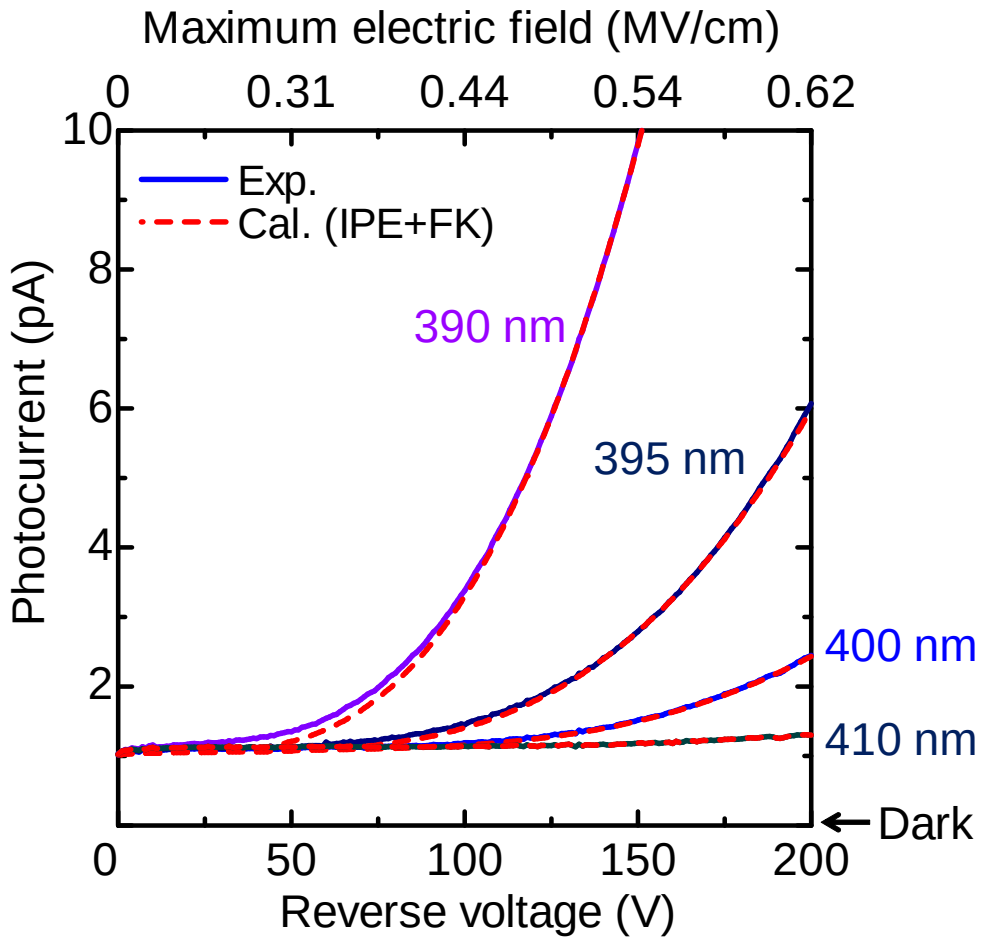

Figure 4.15: Comparison between the experimental data and the calculated photocurrents as $I_{\mathrm{IPE}} + I_{\mathrm{FK}}$. The calculated curves shows excellent agreement with the experimental data for 390–400 nm in the entire voltage range.

4.3 Franz-Keldysh Effect in GaN p-n Junction Diode

The author investigates the reverse voltage dependence of a photocurrent in a GaN-on-GaN p-n junction diode under sub-bandgap illumination. Using a p-n junction diode, it is expected that a pure photocurrent induced by the FK effect without IPE can be obtained. In addition, a higher electric field can be applied to a p-n junction diode compared to a Schottky barrier diode: a large leakage current originating from thermionic field emission [36] flows in a Schottky barrier diode under high electric field, which does not occur in a p-n junction diode. Furthermore, a leakage current in a p-n junction diode at high temperature is also much lower than that in a Schottky barrier diode. The photocurrent induced by the FK effect in GaN for higher electric field range and its temperature dependence is investigated.

4.3.1 Measurement Set up

Figure 4.16 shows the schematic cross section of a homoepitaxial GaN p-n junction diode. The GaN layers that comprise the diodes were grown by metal-organic vapor phase epitaxy (MOVPE) on GaN bulk substrates grown by hydride vapor phase epitaxy (HVPE). The layers consist of 0.1 μm thick p^+-GaN, 0.7 μm thick p-GaN, and 5 μm thick n-GaN. The Mg doping concentration in the p^+-GaN and p-GaN layers was 3×10^{19} and 5×10^{17} cm^{-3}, respectively. The Si doping concentration in the n-GaN layer was 6.3×10^{16} cm^{-3}. The relatively high doping concentrations in the epilayer were prepared to investigate the FK effect in a higher electric field. Mesa-isolation structures of p^+-GaN/p-GaN/n-GaN layers were formed by inductively coupled plasma-reactive ion etching (ICP-RIE). The heights and diameters of the mesas were 1 μm and 520 μm, respectively. The anode and cathode electrodes were formed by the deposition of Ni/Au on the epitaxial layer and Ti/Al/Ni on the backside of the substrate, respectively. For the photocurrent measurements, the monochromatic light source mentioned in the section 4.2.1 was used with a bandpass width of 5 nm. The light was focused on a 5-mm-diameter circle centered at the anode electrode. The irradiated sub-bandgap light penetrated into GaN, reflected at the backside electrode and reached the p-n junction from the back side via multiple reflections.

4.3.2 Voltage and Wavelength Dependences of Photocurrent

Figure 4.17 shows the reverse voltage dependence of the photocurrent for 390–420 nm in the GaN p-n junction diode. Although a high electric field $\sim$2 MV/cm was applied at a reverse bias of 200 V, a leakage current was very low (less than 0.2 nA) owing to the low dislocation density (ca. 10^6 cm^{-2}). Photocurrents were clearly observed under a high reverse bias voltage, which were much larger than the dark current. The incident photon flux for each wavelength was measured with an optical powermeter and these photocurrents were normalized using an incident photon flux of $2.0\times10^{15}cm^{-2}s^{-1}$ for discussion of

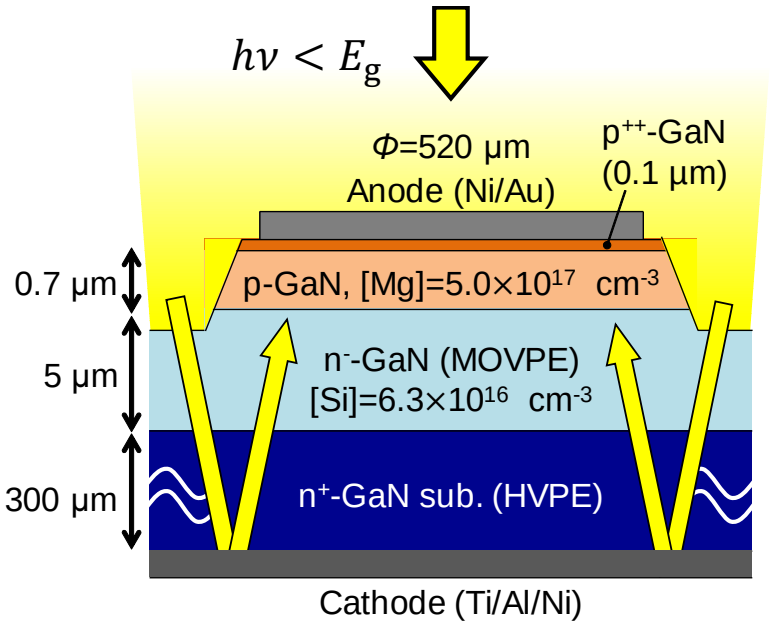

Figure 4.16: Schematic cross section of a GaN p-n junction diode with a mesa-isolation structure fabricated on a GaN bulk substrate. The wavelength of light was longer than the absorption edge of GaN; therefore, the light penetrated into GaN. The light was reflected by the backside cathode electrode and reached the p-n junction.

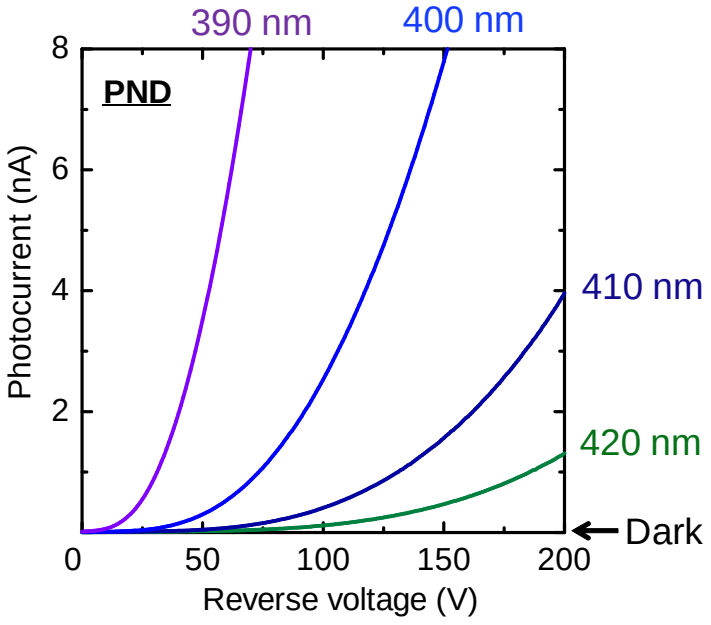

Figure 4.17: Reverse-voltage dependence of photocurrents for 390–420 nm in the GaN p-n junction diode. At the zero bias, a photocurrent is not observed. However, Under reverse bias voltage, a photocurrent significantly increases with increasing reverse bias, and the increase is more prominent as the wavelength is closer to the GaN absorption edge (365 nm). These photocurrents originate from the Franz-Keldysh effect.

the wavelength dependence. The photocurrent increased with the reverse bias voltage for all wavelengths. The increase in the photocurrent became prominent as the wavelength of the light became closer to the absorption edge of GaN (∼365 nm). Both the voltage and wavelength dependence were very similar to the photocurrent in the GaN Schottky barrier diode under a high reverse bias [53], indicating these photocurrents also originate from the FK effect.

In the case of the GaN Schottky barrier diode, the maximum electric field was 0.62 MV/cm at the reverse bias of 200 V due to low net donor concentration of 5.5×10^{15} cm^{-3} in the epitaxial layer. The photocurrent induced by the FK effect was not clearly detected for wavelengths longer than 400 nm. In contrast, in this study, the maximum electric field was 2.0 MV/cm at 200 V in the GaN p-n junction diode and a photocurrent was clearly observed for wavelengths up to 420 nm. For the same wavelength at the same reverse bias, the photocurrent in the GaN p-n junction diode was larger than that in the GaN Schottky barrier diode.

The photocurrent induced by the FK effect in the GaN p-n junction diode is also calculated. Figure 4.18 shows the distributions of the electric field and the absorption coefficient for 400 nm in the depletion region in the GaN p-n junction diode under the reverse bias of (a) 0 V, (b) 100 V and (c) 200 V. The electric field was calculated using the well known formula:

$$W_{\mathrm{p}}(V)=\sqrt{\frac{2\varepsilon_{\mathrm{s}}N_{\mathrm{d}}\left(V_{\mathrm{d}}-V\right)}{eN_{\mathrm{a}}\left(N_{\mathrm{a}}+N_{\mathrm{d}}\right)}},\quad W_{\mathrm{n}}(V)=\sqrt{\frac{2\varepsilon_{\mathrm{s}}N_{\mathrm{a}}\left(V_{\mathrm{d}}-V\right)}{eN_{\mathrm{d}}\left(N_{\mathrm{a}}+N_{\mathrm{d}}\right)}}, \tag{4.6}$$

$$F(x,V)=\begin{cases}\dfrac{eN_{\mathrm{a}}}{\varepsilon_{\mathrm{s}}}\left(x+W_{\mathrm{p}}(V)\right) & (-W_{\mathrm{p}}<x<0)\\ \dfrac{eN_{\mathrm{d}}}{\varepsilon_{\mathrm{s}}}\left(W_{\mathrm{n}}(V)-x\right) & (0<x<W_{\mathrm{n}})\end{cases} \tag{4.7}$$

The built-in potential (V_{d}) of 3 V obtained from C–V measurement was used in the calculation. $x=0$ is defined as the position of the p-n junction interface, and W_{p} and W_{n} are the edges of the depletion layer in the p- and the n-layer, respectively. The absorption coefficient for 400 nm was calculated using the Eq. (4.3) according to the electric field distributions. With increasing reverse bias, the depletion layer extends wider, electric field becomes larger and the absorption coefficient significantly increases at high electric field region, indicating the optical absorption selectively occurs near the p-n junction interface.

The photocurrent induced by the FK effect in the p-n junction diode (I_{FK}) is given by

$$I_{\mathrm{FK}}(V,\omega)=e\Phi_0\left[1-\exp\left(-2\int_{-W_{\mathrm{p}}(V)}^{W_{\mathrm{n}}(V)}\alpha(F(V,x),\omega)dx\right)\right], \tag{4.8}$$

where Φ_0 is defined as the incident photon flux from the backside to the edge of the depletion layer in the n-region. The author measured the size dependence of the photocurrent in GaN p-n junction diodes, and the photocurrent was confirmed to be proportional to not the periphery, but the area of the devices, which indicated that the p-n junction was

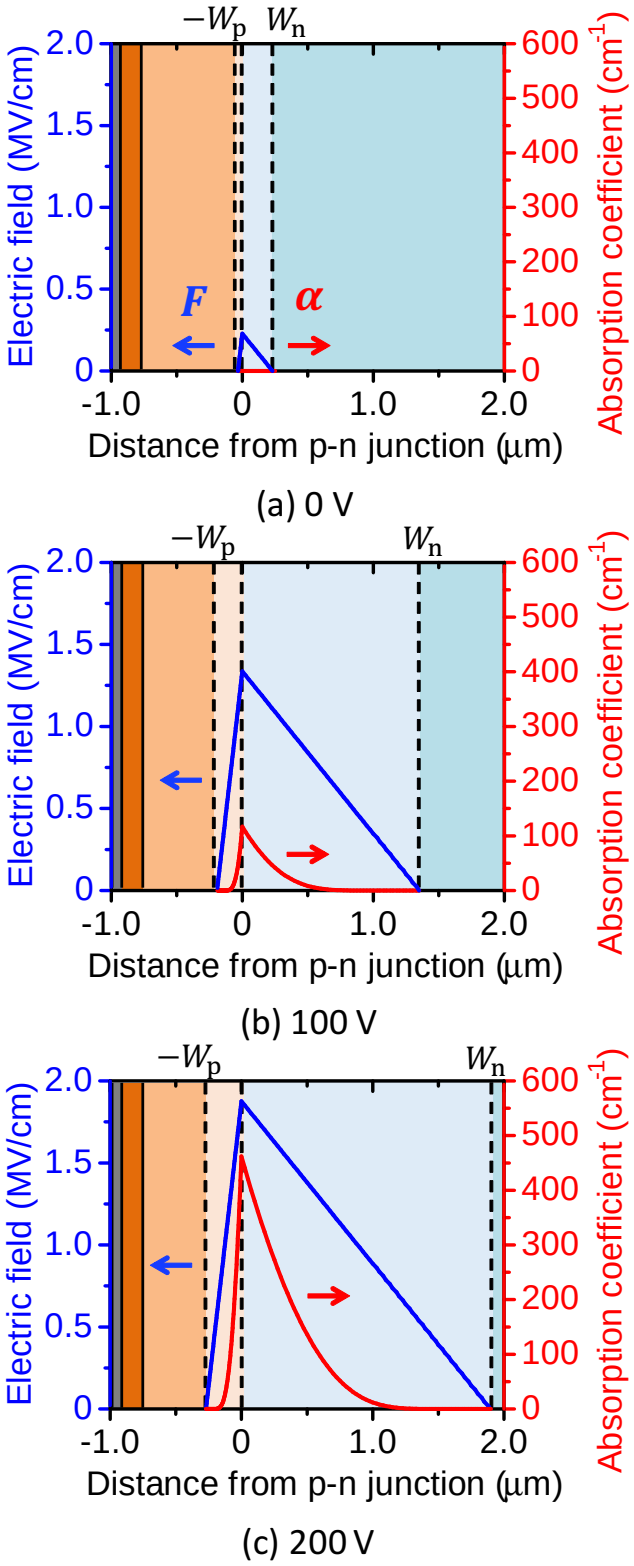

Figure 4.18: The distributions of the electric field and the absorption coefficient for 400 nm in the depletion region in the GaN p-n junction diode under the reverse bias of (a) 0 V, (b) 100 V and (c) 200 V.

entirely and uniformly irradiated from the backside due to multiple reflections. Multiple reflected photons are included in Φ_0. In this formula, a single round-trip path is considered, i.e., passing through the depletion region, reflection by the anode, and return to $x = W_{\mathrm{n}}$ through the depletion region again. Optical absorptions by the electrodes or GaN substrate are considered to be small and are thus neglected.

Figure 4.19 shows the comparisons between the experimental photocurrents and the calculated photocurrents induced by the FK effect in the GaN p-n junction diode. From the fitting, the reasonable values of Φ_0 (56–71%) were obtained. The calculated curves show excellent agreement with the experimental data for all the wavelengths of 390–420 nm. This result also suggests that the voltage and wavelength dependences of the photocurrent induced by the optical absorption due to the FK effect in GaN devices are well predictable.

Although high electric field (∼2 MV/cm) was applied to the p-n junction, an avalanche multiplication was not observed significantly. The avalanche multiplication of a photocurrent induced by the FK effect in a GaN p-n junction diode will be discussed in [54–56] and Chapter 5, which will play a very important role to investigate the avalanche multiplication to extract the impact ionization coefficients in GaN.

4.3.3 Temperature Dependence of Photocurrent

The temperature dependence of the photocurrent induced by the FK effect was investigated. Figure 4.20 shows the reverse voltage dependence of the photocurrent for 400 nm in the GaN p-n junction diode at 223, 298 and 373 K. With elevating temperature, an increase in the photocurrent was observed. The red-shift of the absorption edge (shrinkage of the bandgap) with an elevating temperature may be the primary reason for the temperature dependence of the photocurrent. A temperature dependence of a bandgap in a semiconductor follows the Varshni's empirical formula

$$E_{\mathrm{g}}(T) = E_{\mathrm{g}}(0) - \frac{\alpha T^2}{T + \beta}. \tag{4.9}$$

Vurgaftman *et al.* reported that $E_{\mathrm{g}}(0) = 3.507$ eV, $\alpha = 0.909$ meV/K, and $\beta = 830$ K in GaN [57], and the calculated temperature dependence of the bandgap is shown in Fig. 4.21. With consideration of this temperature dependence of the bandgap, the author calculated the photocurrent induced by the FK effect at 223, 298, and 373 K. The calculated curves are shown in Fig. 4.20 as broken lines. The calculated curves were in good agreement with the experimental results at all temperatures. This result indicates that the impact of the other parameters (e.g., the effective masses), which have small temperature dependence, are negligible. The photocurrents for other wavelengths in the range of 390-420 nm were also confirmed to show the same temperature dependence, which can be also explained by the temperature dependence of the bandgap in GaN.

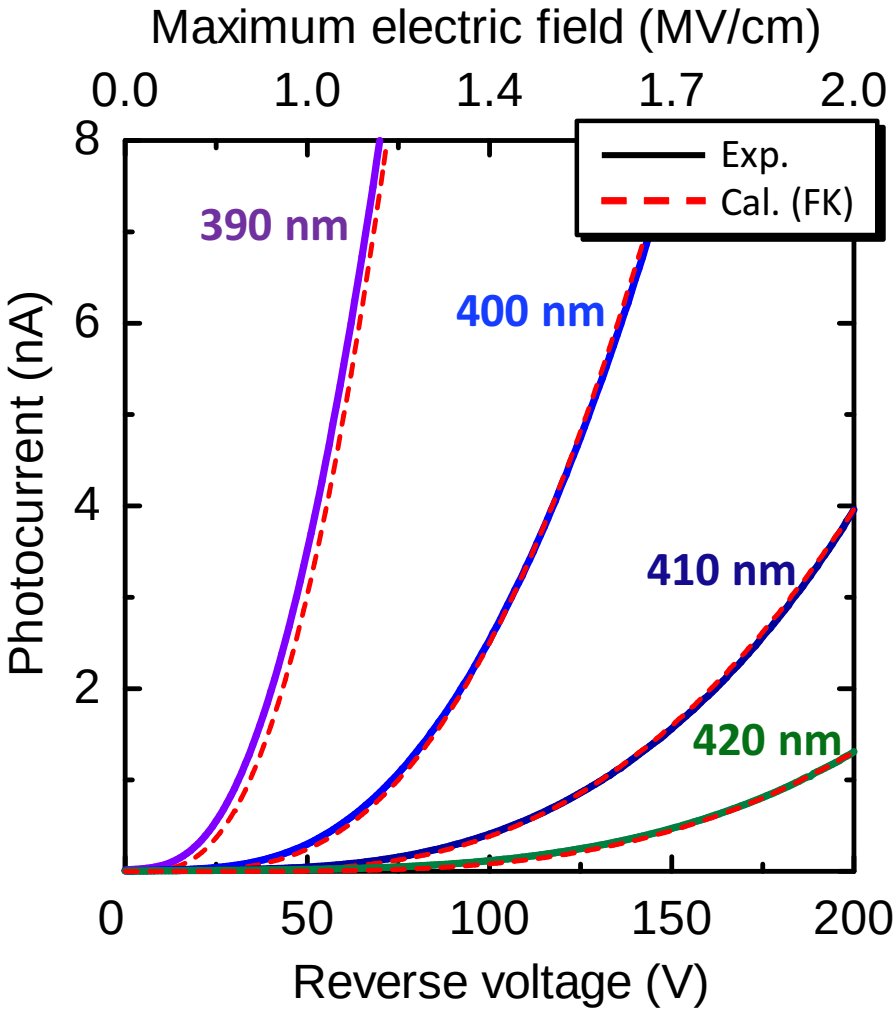

Figure 4.19: Comparison bewteen experimental photocurents for 390–420 nm and the calculated photocurrents with consideration of the optical absortion in the depletion region in the GaN p-n junction diode. The calculated curves show excellent agreement with the experimental data.

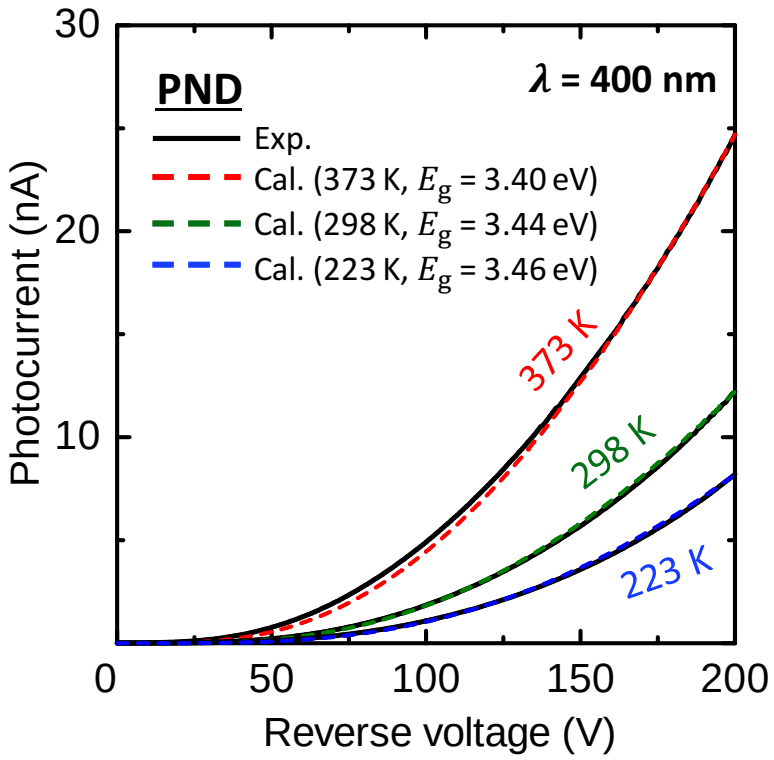

Figure 4.20: Reverse voltage dependence of the photocurrent for 400 nm in the GaN p-n junction diode at 223, 298 and 373 K. With elevating temperature, the photocurrent induced by the FK effect increased, which can be explained by the shrinkage of the bandgap with elevating temperature: the calculated photocurrents with consideration of the temperature dependent bandgap [57] are also shown as broken lines.

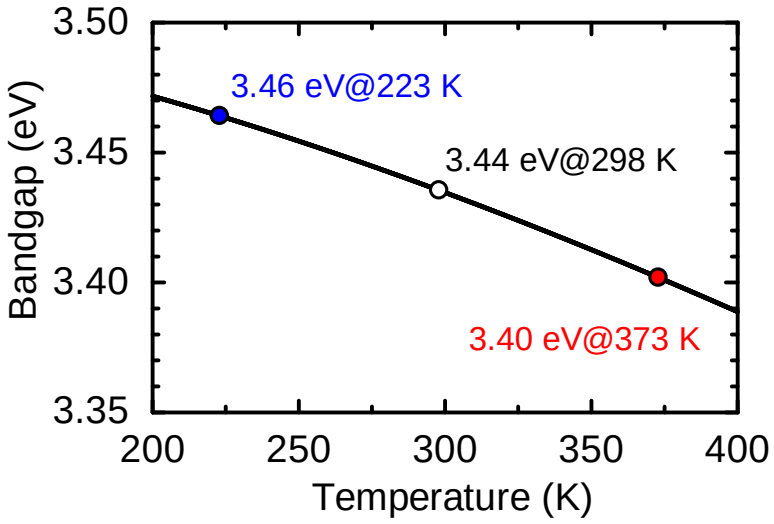

Figure 4.21: Temperature dependence of the bandgap in GaN calculated from the Varshni's empirical formula using the proposed parameters [57].

4.4 Discussion

Other Optical Absorptions in GaN

There are some possible optical absorptions in GaN such as defect assisted absorption, free carrier absorption, etc. It is known that the deep level related to a carbon atom in a nitrogen site (C_N) in GaN acts as a hole trap (so called H1), and an optical absorption via H1 traps occurs under sub-bandgap illumination [58, 59]. Under a steady-state illuminated condition, photoexcitations of electrons from valence band to the H1 traps (emissions of holes) and those from the H1 traps to the conduction band (captures of holes) simultaneously occur, resulting in generations of electron-hole pairs via the H1 trap. However, a photocurrent induced by crystal defects were not detected and were negligible owing to low carbon concentrations in the devices in this study. The sub-bandgap optical absorption coefficients for various bulk GaN samples were investigated by Pimputkar *et al.* [52]. The absorption coefficient in the HVPE-grown GaN ($n = 2.8\times10^{18}$ cm^{-3}) was about 1–2 cm^{-1} for λ >390 nm, the absorption of which was quantitatively explained by the free carrier absorption as shown in Fig. 4.22. The GaN substrates used in this study have $n = (1--2)\times10^{18}$ cm^{-3}; thus, the sub-bandgap optical absorption in GaN substrate was small and negligible.

Validity of the Reduced Effective Mass in GaN

Since the wavefunction tails into the bandgap strongly depend on the effective masses based on the quantum mechanics, the effective masses are key parameters for the absorption coefficient under electric field. Here, the validity of the reduced effective masses are discussed.

Figure 4.23 shows (a) electric field dependence of the absorption coefficient in GaN for the wavelength of 400 nm and (b) wavelength dependence of the absorption coefficient in GaN under electric field of 1 MV/cm calculated using the reduced effective masses of $0.08m_0$, $0.16m_0$ and $0.32m_0$. In the calculations, the value of the absorption coefficients without electric field were maintained by changing $|\boldsymbol{e}\cdot\boldsymbol{p}_{\mathbf{cv}}|^2$. It is observed that the absorption coefficients for lighter reduced effective mass more rapidly increased with electric field. The absorption tail below bandgap becomes longer for lighter reduced effective mass. Figure 4.24 shows the comparisons between the experimental photocurrent for 400 nm and the calculated photocurrents using the reduced effective masses of $0.08m_0$, $0.16m_0$ and $0.32m_0$. The incident photon flux (Φ_0) was obtained by fitting (a) at 150 V and (b) at 200 V. For the value of $0.16m_0$, the voltage dependence of the phtocurrent is well reproduced in the entire voltage ranges in the cases of (a) and (b). On the other hand, it is impossible to reproduce the voltage dependence of the experimental photocurrent by using $0.08m_0$ and $0.32m_0$. These results indicate that the value of $\mu = 0.16m_0$ is valid to use the calculation of the electric field dependence of the absorption coefficient in GaN under electric field along <0001>. In addition, the reduced effective masses can be estimated by investigating the voltage dependence of the photocurrent (the electric field dependence of the absorption coefficient) induced by the Franz-Keldysh effect.

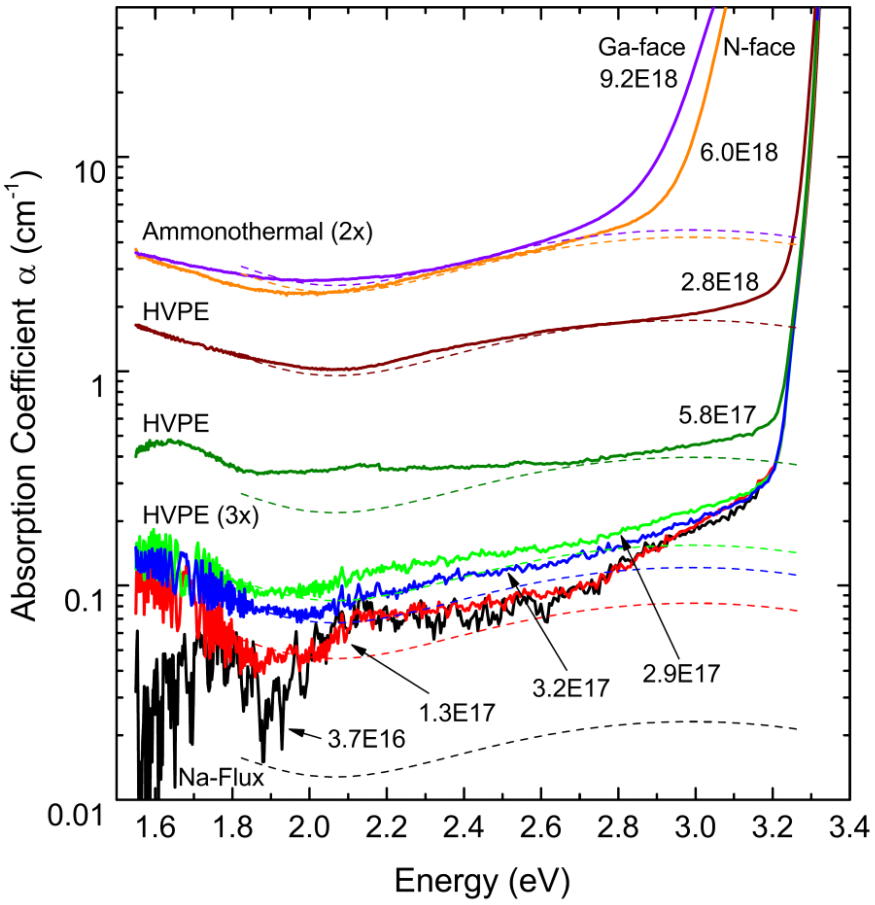

Figure 4.22: Sub-bandgap optical absorption coefficient for bulk GaN samples at room temperature reported by Pimputkar *et al.* [52]. Dashed lines represent calculated values for phonon-assisted free carrier absorption.

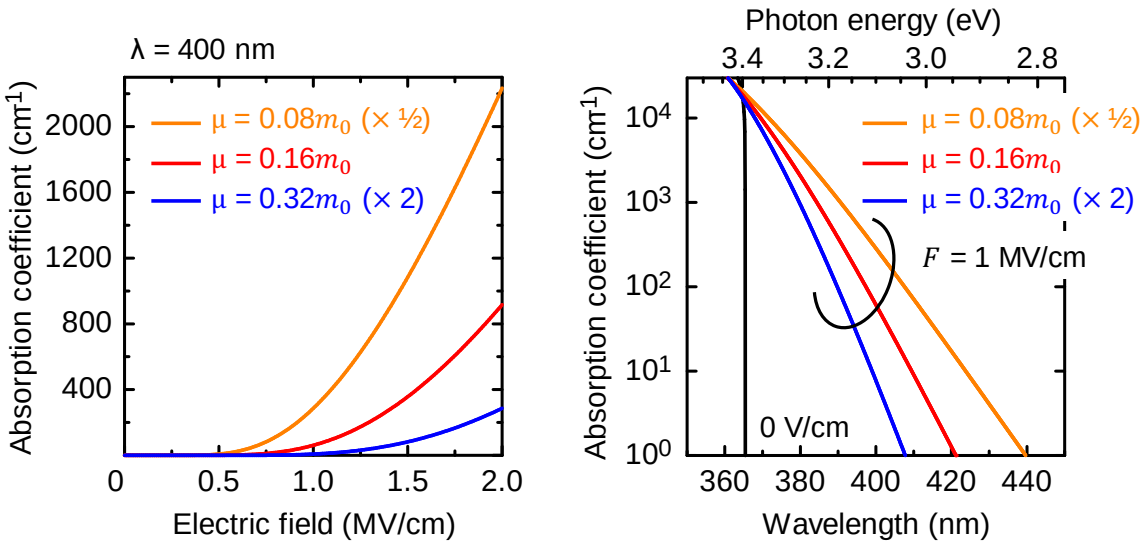

Figure 4.23: (a) Electric field dependence of the absorption coefficients in GaN for the wavelength of 400 nm and (b) wavelength dependence of the absorption coefficients in GaN under electric field of 1 MV/cm calculated using the reduced effective masses of $0.08m_0$, $0.16m_0$ and $0.32m_0$. In the calculations, the value of the absorption coefficients without electric field were maintained by changing $|\boldsymbol{e} \cdot \boldsymbol{p}_{\mathbf{cv}}|^2$.

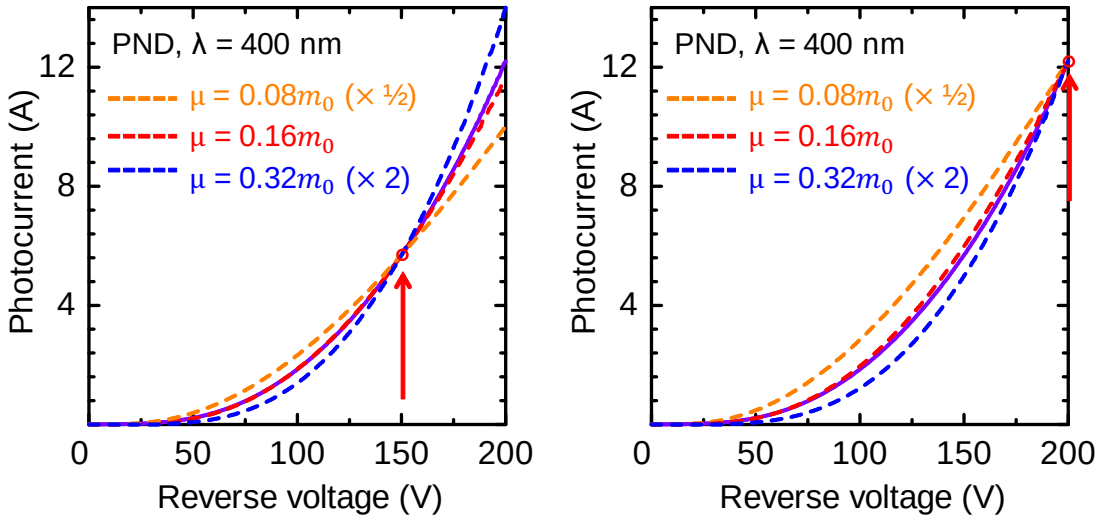

Figure 4.24: The comparisons between the experimental photocurrent for 400 nm and the calculated photocurrents using the reduced effective masses of $0.08m_0$, $0.16m_0$ and $0.32m_0$. The incident photon flux (Φ_0) was obtained by fitting (a) at 150 V and (b) at 200 V.

Effect of the Band Width of the Irradiated Light

The band width of the irradiated light effects on the analysis of the wavelength and electric field dependences of the optical absorption induced by the Franz-Keldysh effect. The effect of the band width can be considered as

$$I_{\mathrm{FK,true}}(V,\omega) = \frac{\int_0^\infty P_0(\omega) I_{\mathrm{FK}}(V,\omega) d\omega}{\int_0^\infty P_0(\omega) d\omega}. \tag{4.10}$$

$P_0(\omega)$ is the spectral intensity of the irradiated light. In this study, the band widths of 5 nm and 10 nm were used (near the Gaussian distribution). For the light with the band width of 10 nm, it was impossible to reproduce the voltage and wavelength dependences of the photocurrent without consideration of the effect of the band width (if the author uses the shorter wavelength or lighter effective masses, the calculation could show agreement with the experimental photocurrent). On the other hand, for the band width of 5 nm, the simple calculaion without consideration of the effect of the band width can reproduce the experimental data using the reduced effective mass of $\mu = 0.16 m_0$ [48].

Franz-Keldysh Effect in 4H-SiC

In an indirect-bandgap semiconductor, the phonon-assisted optical absorption occurs near the absorption edge. Although the probability of the indirect transition is much smaller than that of the direct transition, the FK effect in an indirect-bandgap semiconductor is expected to be observed [6]. Silicon carbide (SiC) is an wide-bandgap semiconductor with the indirect bandgap of 3.26 eV at room temperature. In this study, the author investigated the photocurrent induced by the phonon-assisted optical absorption induced by the FK effect in 4H-SiC p-n junction diodes fabricated on (0001)-face and $(11\bar{2}0)$-face substrates. The details are described in [60, 61] and Appendix C.

Applications of the Optical Absorption Induced by the Franz-Keldysh Effect

The sub-bandgap optical absorption induced by the Franz-Keldysh effect has a unique feature: the optical absorption selectively occurs at high electric field region. Very recently, Kawasaki *et al.* proposed the observation method for in-plane carrier concentration non-uniformity by scanning optical beam induced current (OBIC) using sub-bandgap illumination [62]. In a GaN p-n junction diode with the donor concentration of 2×10^{16} cm^{-3}, the inhomogeneity of the OBIC image shown in Fig. 4.24 was obtained and the slight fluctuation of the donor concentration ($\sim 10^{14}$ cm^{-3}) was estimated from the analysis of the photocurrent. This slight fluctuation, which does not effect on the breakdown voltage, might cause the inhomogeneous luminescence as mentioned in [62–64].

In Chapter 5, the author proposes the novel method to measure avalanche multiplication in a GaN p-n junction diode utilizing the sub-bandgap optical absorption induced by the FK effect. Since a photocurrent induced by the FK effect is well predictable, a multiplication factor in a GaN p-n junction diode can be extracted with high accuracy [54–56].

4.5 Summary

In this study, the photocurrents induced by the optical absorption induced by the Franz-Keldysh effect in a GaN Schottky barrier diode and a GaN p-n junction diode under high reverse bias voltage were investigated. In the GaN Schottky barrier diode, a photocurrent induced by internal photoemission was observed without applying reverse bias. With increasing reverse bias, a significant increase in the photocurrent was observed for the wavelength close to the GaN absorption edge, which cannot be explained by internal photoemission with consideration of the image force lowering. The author calculated the photocurrent induced by the optical absorption due to the Franz-Keldysh effect using the reduced effective mass of GaN, and the calculated curves showed excellent agreement with the experimental data. In addition, the photocurrent induced by the Franz-Keldysh effect and its temperature dependence in a GaN p-n junction diode were investigated. The voltage and wavelength dependences of the photocurrent in the GaN p-n junction diode were also well reproduced by considering the optical absorption induced by the Franz-Keldysh effect in the depletion region. The temperature dependence of the photocurrent was explained by the shrinkage of the bandgap in GaN with elevating temperature.

The sub-bandgap optical absorption induced by the Franz-Keldysh effect has a unique feature: the optical absorption selectively occurs at high electric field region. Thus, this optical absorption will be useful for estimating an electric field in GaN and other wide-bandgap materials, e.g., a two-dimensional distribution of electric field in GaN devices under a high reverse bias voltage may be obtained by scanning photocurrent microscopy [62, 65]. These results are useful for considering the optical absorption in GaN under electric field.

References

[1] V. W. Franz, *Z. Naturf.* **13a**, 484 (1958).

[2] L. V. Keldysh, *Soviet Physics JETP* **7**, 788 (1958).

[3] K. Tharmalingam, *Phys. Rev.* **130**, 2204 (1963).

[4] B. O. Seraphin and N. Bottka, *Phys. Rev.* **139**, A560 (1965).

[5] J. Callaway, *Phys. Rev.* **134**, 998 (1964).

[6] C. M. Penchina, *Phys. Rev.* **138**, A924 (1965).

[7] Y. Yacoby, *Phys. Rev.* **140**, A263 (1965).

[8] J. C. Phillips, *Phys. Rev.* **146**, 584 (1966).

[9] D. E. Aspnes, *Phys. Rev.* **147**, 554 (1966).

[10] E.G.S. Paige and H. D. Rees, *Phys. Rev. Lett.* **16**, 444 (1966).

[11] Y. Yacoby, *Phys. Rev.* **47**, 445 (1966).

[12] B. O. Seraphin, *J. Appl. Phys.* **37**, 721 (1966).

[13] B. O. Seraphin and R. B. Hess, *Phys. Rev. Lett.* **15**, 138 (1965).

[14] M. Aoki and S. Okano, *Jpn. J. Appl. Phys.* **5**, 980 (1960).

[15] A. Frova and P. Handler, *Phys. Rev.* **137**, A1857 (1965).

[16] T.E.Van Eck, E. M. Walpita, W. S. C. Chang, and H. H. Wieder, *Appl. Phys. Lett.* **48**, 451 (1986).

[17] G. E. Stillman, C. M. Wolfe, C. O. Bozler, and J. A. Rossi, *Appl. Phys. Lett.* **28**, 544 (1976).

[18] R. H. Kingston, *Appl. Phys. Lett.* **34(11)**, 1 (1979).

[19] C. Van Hoof, K. Deneffe, J. De Boeck, D. J. Arent, and G. Borghs, *Appl. Phys. Lett.* **54**, 608 (1989).

[20] C. Wetzel, T. Takeuchi, H. Amano, and I. Akasaki, *J. Appl. Phys.* **85**, 3786 (1999).

[21] G. Franssen, P. Perlin, and T. Suski, *Phys. Rev. B* **69**, 045310 (2004).

[22] A. Cavallini, L. Polenta, M. Rossi, T. Stoica, R. Calarco, R. J. Meijers, T. Richter, and H. Lüth, *Nano Lett.* **7**, 2166 (2007).

[23] R. Katayama, K. Onabe, H. Yaguchi, T. Matsushita, and T. Kondo, *Appl. Phys. Lett.* **91**, 061917 (2007).

[24] L. Janicki, J. Misiewicz, G. Cywiński, M. Sawicka, C. Skierbiszewski, and R. Kudrawiec, *Appl. Phys. Express* **9**, 021002 (2016).

[25] T. Sato, Y. Kumazaki, H. Kida, A. Watanabe, Z. Yatabe, and S. Matsuda, *Semicon. Sci. Technol.* **31**, 014012 (2016).

[26] T. Tanikawa, K. Shojiki, R. Katayama, S. Kuboya, T. Matsuoka, Y. Honda, and H. Amano, *Appl. Phys. Express* **10**, 082101 (2017).

[27] Y. Yıldırım, K. Ejderha, and A. Turut, *J. Appl. Phys.* **108**, 114506 (2010).

[28] N. Subramaniyam, M. Sopanen, H. Lipsanen, C.-H. Hong, and E.-K. Suh, *Jpn. J. Appl. Phys.* **50**, 030201 (2011).

[29] Y.-J. Lin, *J. Appl. Phys.* **106**, 013702 (2009).

[30] E. Arslan, S. Altindal, S. Ozcelik, and E. Ozbay, *J. Appl. Phys.* **105**, 023705 (2009).

[31] W. Lim, J.-H. Jeong, J.-H. Lee, S.-B. Hur, J.-K. Ryu, K.-S. Kim, T.-H. Kim, S. Y. Song, J.-I. Yang, and S. J. Pearton, *Appl. Phys. Lett.* **97**, 242103 (2010).

[32] D. Donoval, A. Chvala, R. Sramaty, J. Kovac, E. Morvan, C. Dua, M. A. DiForte-Poisson, and P. Kordos, *J. Appl. Phys.* **109**, 063711 (2011).

[33] T. Kachi, *Jpn. J. Appl. Phys.* **53**, 100210 (2014).

[34] I. C. Kizilyalli, A. P. Edwards, O. Aktas, T. Prunty, and D. Bour, *IEEE Trans. Electron Devices* **62(2)**, pp.414–422 (2015).

[35] Y. Saitoh, K. Sumiyoshi, M. Okada, T. Horii, T. Miyazaki, H. Shiomi, M. Ueno, K. Katayama, M. Kiyama, and T. Nakamura, *Appl. Phys. Express* **3**, 081001 (2010).

[36] J. Suda, K. Yamaji, Y. Hayashi, T. Kimoto, K. Shimoyama, H. Namita, and S. Nagao, *Appl. Phys. Express* **3**, 101003 (2010).

[37] I. C. Kizilyalli, A. P. Edwards, H. Nie, D. Disney, and D. Bour, *IEEE Trans. Electron Devices* **60**, 10 (2013).

[38] I. C. Kizilyalli, A. P. Edwards, H. Nie, D. Bour, T. Prunty, and D. Disney, *IEEE Electron Device Lett.* **35(2)**, pp.247–249 (2014).

[39] I. C. Kizilyalli, T. Prunty, and O. Aktas, *IEEE Electron Device Lett.* **36(10)**, pp.1073–1075 (2015).

[40] Z. Hu, K. Nomoto, B. Song, M. Zhu, M. Qi, M. Pan, X. Gao, V. Protasenko, D. Jena, and H. G. Xing, *Appl. Phys. Lett.* **107**, 243501 (2015).

[41] T. Hatakeyama and T. Shinohe, *Mater. Sci. Forum* **389–393**, 1169 (2002).

[42] A. S. Barker and Jr. and M. Ilegems, *Phys. Rev. B* **7(2)**, pp.743–750 (1973).

[43] M. J. Kane, M. J. Uren, D. J. Wallis, P. J. Wright, D. E. J. Soley, A. J. Simon, and T. Martin, *Semicon. Sci. Technol.* **26**, 085006 (2011).

[44] T. Maeda, M. Okada, M. Ueno, Y. Yamamoto, T. Kimoto, M. Horita, and J. Suda, *Appl. Phys. Express* **10**, 051002 (2017).

[45] R. H. Fowler, *Phys. Rev.* **38**, 45 (1931).

[46] S. M. Sze, C. R. Crowell, and D. Kahng, *J. Appl. Phys.* **35**, 8 (1964).

[47] G. Yu, G. Wang, H. Ishikawa, M. Umeno, T. Soga, T. Egawa, J. Watanabe, and T. Jimbo, *Appl. Phys. Lett.* **70**, 3209 (1997).

[48] G. D. Chen, M. Smith, J. Y. Lin, H. X. Jiang, S. H. Wei, M. A. Khan, and C. J. Sun, *Appl. Phys. Lett.* **68**, 2784 (1996).

[49] M. Suzuki, T. Uenoyama, and A. Yanase, *Phys. Rev. B* **52(11)**, 8132 (1995).

[50] A. Punya and W.R.L. Lambrecht, *Phys. Rev. B* **85**, 195147 (2012).

[51] J. F. Muth, J. H. Lee, I. K. Shmagin, and R. M. Kolbas, *Appl. Phys. Lett.* **71**, 2572 (1997).

[52] S. Pimputkar, S. Suihkonen, M. Imade, Y. Mori, J. S. Speck, and S. Nakamura, *J. Cryst. Growth* **432**, pp.49–53 (2015).

[53] T. Maeda, M. Okada, M. Ueno, Y. Yamamoto, M. Horita, and J. Suda, *Appl. Phys. Express* **9**, 091002 (2016).

[54] T. Maeda, T. Narita, H. Ueda, M. Kanechika, T. Uesugi, T. Kachi, T. Kimoto, M. Horita, and J. Suda, *Proc. of Int. Symp. on Power Semiconductor Device and ICs* (2019) p. 59–62.

[55] T. Maeda, T. Narita, H. Ueda, M. Kanechika, T. Uesugi, T. Kachi, T. Kimoto, M. Horita, and J. Suda, *Appl. Phys. Lett.* **115**, 142101 (2019).

[56] T. Maeda, T. Narita, S. Yamada, T. Kachi, T. Kimoto, M. Horita, and J. Suda, *IEDM Tech. Digest* (2019) p. 4.2.

[57] I. Vurgaftman, J. R. Meyer, and L. R. Ram-Mohan, *J. Appl. Phys.* **89**, 5815 (2001).

[58] Y. Tokuda, *ECS Transactions* **75(4)**, pp.39–49 (2016).

[59] K. Kanegae, T. Narita, K. Tomita, T. Kachi, M. Horita, T. Kimoto, and J. Suda, *Ext. Abst. of Int. Workshop on Nitride Semiconductors* (2018) p. CR16-1.

[60] T. Maeda, X. Chi, M. Horita, J. Suda, and T. Kimoto, *Appl. Phys. Express* **11**, 091302 (2018).

[61] T. Maeda, X. Chi, H. Tanaka, M. Horita, J. Suda, and T. Kimoto, *Jpn. J. Appl. Phys.* **58**, 091007 (2019).

[62] S. Kawasaki, H. Fukushima, S. Usami, Y. Ando, A. Tanaka, M. Deki, M. Kushimoto, S. Nitta, Y. Honda, and H. Amano, *Ext. Abst. of Int. Conf. on Solid State Devices and Materials* (2019) p. K-7-02.

[63] T. Maeda, T. Narita, H. Ueda, M. Kanechik, T. Uesugi, T. Kachi, T. Kimoto, M. Horita, and J. Suda, *IEDM Tech. Digest* (2018) p. 30.1.

[64] H. Fukushima, S. Usami, M. Ogura, Y. Ando, A. Tanaka, M. Deki, M. Kushimoto, S. Nitta, Y. Honda, and H. Amano, *Jpn. J. Appl. Phys.* **58**, SCCD25 (2019).

[65] K. Shiojima, S. Yamamoto, Y. Kihara, and T. Mishima, *Appl. Phys. Express* **8**, 046502 (2015).

Chapter 5

Impact Ionization Coefficients in GaN

5.1 Introduction

Impact ionization coefficients (α_n, α_p), defined as "the number of electron-hole pairs generated by a carrier per unit distantce under electric field", is one of the most important material properties. Since impact ionization and its avalanche multiplication are the dominant mechanism in junction breakdown, impact ionization coefficients determine an avalanche breakdown voltage and a safe-operating area of a semiconductor power device. For accurate design and simulation of power devices, the values need to be determined precisely. In addition to a power device, the impact ionization coefficients are also important for devices utilizing avalanche multiplication: avalanche photodiodes (APDs) and impact ionization avalanche transit time (IMPATT) diodes.

It is impossible to measure impact ionization coefficients directly, a photomultiplication measurement is usually used: a reverse voltage dependence of avalanche multiplication(s) of optical beam induced currents in a semiconductor device is measured and analyzed. To extract electron- and hole-initiated multiplication factors (M_n, M_p) in precise, individual measurements of electron- and hole-injected photocurrents in the same junction (at the same scattering environment) up to ideal breakdown voltage combined with the detailed analyses of the photocurrents based on the calculations of the unmultiplicated photocurrents are required. Therefore, a test device for photomultiplication measurements need to have an excellent edge termination to achieve low reverse leakage current and high avalanche capability, and measurement and analysis methods of electron- and hole injected photocurrents need to be tossed around.

The impact ionization coefficients have been studied well for mature semiconductors such as Si [1–6], GaAs [7–10] and 4H-SiC [11–17]. Logan *et al.* performed measurements of diffused $p^+/n-$ junctions under electron injection only and assumed $\alpha_n = \alpha_p$ in the analysis [2]. Van Overstraeten *et al.* carried out a photomultiplication measurement in a Si p-n junction diode using dual-color illuminations of infrared light and green light with the wavelength of 550 nm [3] as shown in Fig. 5.1. The penetration depth of light in Si is strongly dependent on

the light wavelength. Infrared light penetrates deeply into the diode and generates mainly an electron-injected photocurrent. The light with wavelength of 550 nm is absorbed mainly in the surface layer, resulting in a hole-injected photocurrent. Although the test devices have the diffused impurity profiles and complicated electric field distribution, the impurity profiles was determined by the C–V measurement. Based on the detailed analysis of the multiplication factors, $\alpha_{\rm n}$ and $\alpha_{\rm p}$ in Si were determined. Woods *et al*. proposed the method to use a Schottky barrier diode to determine $\alpha_{\rm n}$ and $\alpha_{\rm p}$ in a semiconductor [5] as shown in Fig. 5.2. From illuminations with $h\nu > E_{\rm g}$ and $E_{\rm g} > h\nu > e\phi_{\rm b}$ for an n-type Schottky barrier diode, hole injections by diffusion of minority carriers from the back side and electron injections by internal photoemission (IPE) at the Schottky interface were obtained, respectively. In addition, an abrupt Schottky junction is available and gives an accurate known electric field. The analysis method of $M_{\rm n}$ and $M_{\rm p}$ for the right-triangle electric field distribution was derived and $\alpha_{\rm n}$ and $\alpha_{\rm n}$ in Si were determined with consideration of the dead space effect. Ito *et al*. invesigated $\alpha_{\rm n}$ and $\alpha_{\rm p}$ in GaAs utilizing a crater mesa $\rm p^+/n$ structure [9] as shown in Fig. 5.3. Irradiation of light to the top p-layer and the n-region in the center hollow gave electron- and hole-injection, respectively. Based on the Woods' analytical procedure [5], $\alpha_{\rm n}$ and $\alpha_{\rm p}$ were determined. Stillman and Bulman *et al*. studied $\alpha_{\rm n}$ and $\alpha_{\rm p}$ in GaAs utilizing GaAs p-i-n junction diodes [8, 10] as shown in Fig. 5.4. The test devices have very thin (3 μm) absorption $\rm n^+$-layers at the cathode side, which were formed by selective removal of the thick GaAs substrate utilizing the AlGaAs etch-stop layer. Owing to very simplified photocurrent measurements, $\alpha_{\rm n}$ and $\alpha_{\rm p}$ were determined with high accuracy. They also investigated $\alpha_{\rm n}$ and $\alpha_{\rm p}$ in InP using the same method [18]. Konstantinov *et al*. measured photomultiplication characteristics in 4H-SiC $\rm p^+/n^-$ diodes. From the fitting the simulated curves to the experimental $M_{\rm p}$ assuming the ratio of $\alpha_{\rm p}/\alpha_{\rm n}$, they obtained $\alpha_{\rm n}$ and $\alpha_{\rm p}$. The obtained $\alpha_{\rm n}$ was much smaller than $\alpha_{\rm p}$. The reason of $\alpha_{\rm n} \ll \alpha_{\rm p}$ was discussed based on the band structure of 4H-SiC. Hatakeyama *et al*. investigated the anistropy of the impact ionization coefficients in 4H-SiC [13]. It was observed that the $\alpha_{\rm p}$ and $\alpha_{\rm n}$ along $<11\bar{2}0>$ were larger than those along <0001>, which is consistent with the critical electric field perpendicular to the c-axis ∼20% lower than that along the c-axis [19]. Niwa *et al*. determined $\alpha_{\rm n}$ and $\alpha_{\rm n}$ and there temperature dependence in wide electric field range ($\alpha_{\rm n}$: 2.2–3.3 MV/cm, $\alpha_{\rm p}$: 1.0–2.5 MV/cm) using non-punch-through (NPT) and punch-through (PT) p-n junction diodes with various epitaxial structures as shown in Fig. 5.5 [16]. Assuming $M_{\rm n} = 1$ ($\alpha_{\rm n} \ll \alpha_{\rm p}$) in low electric field range, $\alpha_{\rm p}$ was determined independently from $M_{\rm p}$ in a punch-through $\rm p^+$-i-$\rm n^+$ diode. After that, $\alpha_{\rm n}$ was determined by $M_{\rm n}$ using the obtained $\alpha_{\rm p}$. The accuracy of $\alpha_{\rm n}$ and $\alpha_{\rm p}$ were confirmed by comparing the simulatied breakdown characteristics with the experimental data. Very recently, Chi *et al*. investigated $\alpha_{\rm n}$ and $\alpha_{\rm p}$ along $<11\bar{2}0>$ using illuminations for the top $\rm p^+$-layer and the n-type region at the side of the mesa bottom [20, 21], which is similar to the methods proposed by Ito *et al*. [9]. The data have been updated from [13]. $\alpha_{\rm n}$ is slightly smaller than $\alpha_{\rm p}$ in $<11\bar{2}0>$, the both of which are close to the value of $\alpha_{\rm p}$ in <0001>.

Figure 5.6 shows the impact ionization coefficients in Si [3], GaAs [10] and 4H-SiC along <0001> [16] and <11$\bar{2}$0> [20]. For Si, α_n is larger than α_p, and the difference between α_n and α_p come to be smaller with increasing electric field. For GaAs, α_n andα_p are almost same but α_n is very slightly larger than α_p, and the values are close to those in Si. Larger α_n is a reasonable result: it is often explained by higher electron mobility and lighter electron effective mass in Si and GaAs. Electrons in Si and GaAs are easy to get sufficient energy to cause impact ionization. In addition, the anisotropy of α_n and α_p are not distinguishable. For 4H-SiC, it is observed that the measurable electric-field ranges of α_n and α_p are one order of magnitude higher. α_n is much smaller than α_p in <0001>, and the anisotropy of impact ionization coefficients is large. Konstantinov *et al.* explained this paradoxical results [11]. The dinsontinuity of the electron energy spectrum (mini energy gap) for motion along the principle axis forbids a balistic type of ionization process (Shockley's "lucky electron" model), and the Bragg reflections from the zone edges (the Bloch oscillations) also makes electrons hard to gain high energy, which is significant because the first Brillouin zone of 4H-SiC from the M point (the conduction band edge) to the L point is *folded* into 1/4 owing to the Zone-Folding effect in the <0001> direction. Thus, α_n parallel to the *c*-axis in 4H-SiC is strongly suppressed.

Since GaN is a direct bandgap semiconductor, the penetration depth for above-bandgap light is very short [22] and the diffusion length of carriers in GaN are also very short [23–25]. A large number of point defects in GaN also contribute short carrier lifetimes and short diffusion legths [26, 27]. In addition, the etching process technique for GaN has been developing [28–31] but the back side etching with an etch-stop layer has not been established [32]. Therefore, although many methods to measure to obtain impact ionization coefficients have been presented in other materials, it is very difficult to divert these methods for GaN. The measurement method for GaN needs to be considered and established.

There have been several theoretical studies on α_n and α_p in GaN [33–36]. Kolnik and Oguzman *et al.* calculated α_n and α_p in wurtzite and zinc blende GaN by Monte Carlo calculations [33, 34]. It was noted that there was considerable uncertainty in the scattering rates and the band structure at high energies due to the lack of experimental data on high-energy transport properties of GaN, which caused uncertainty in the calculations.

The experimental data of the impact ionization coefficients in GaN have been reported but still limited [37–40]. Kunihiro *et al.* obtained α_n from gate-current analysis of AlGaN/GaN HEMTs fabricated on sapphire substrates [37]. In the analysis, a lot of assumptions were used and the data of α_n was indirectly obtained by fitting the electrical characteristics of HEMTs. McClintock *et al.* fabricated GaN avalanche photodiodes on AlN/supphire templates, and photoresponce under front and back illuminations and consequent selective injections of holes and electrons in the junction were measured [38]. However, the devices exhibited large leakage current due to high dislocation density and premature breakdown due to electric field crowding at the device edge. Özbek measured and analyzed the reverse voltage dependence of electron-beam-induced-current (EBIC) with various beam energy

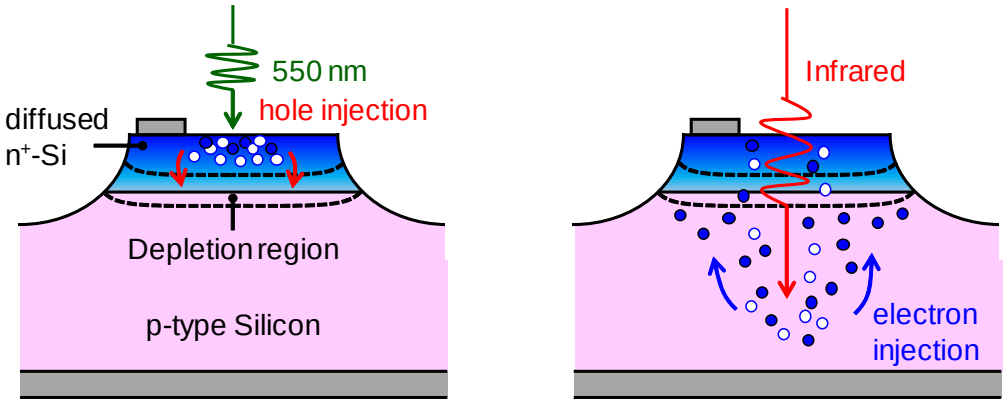

Figure 5.1: Diagrams of the photomultiplication measurement reported by Van Overstraeten *et al*. [3]. For a Si graded p-n junction diode, the light with wavelength of 550 nm and the Infrared (IR) light were irradiated. Owing to the difference of the penetration depths between 550 nm and IR lights, hole- and electron-injections were obtained.

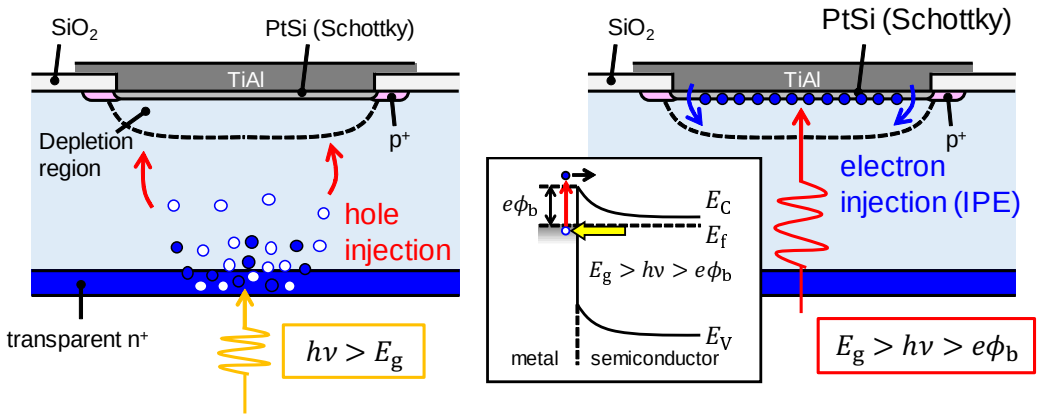

Figure 5.2: Diagrams of the photomultiplication measurement reported by Woods *et al*. [5]. For a PtSi/n-Si abrupt Schottky barrier diode with large barrier height ($e\phi_b$ = 0.85 eV), the lights with wavelength of 632.8 nm ($h\nu > E_g$) and 1150 nm ($E_g > h\nu > e\phi_b$) were irradiated from the back side. For $h\nu > E_g$, light was absorbed near the surface and minority carriers diffused and reached the depletion layer edge, resulting in hole injections. On the other hand, for $E_g > h\nu > e\phi_b$, the light penetrated into Si without absorbed and reached the Schottky interface, resulting in electron injections induced by internal photoemission (IPE).

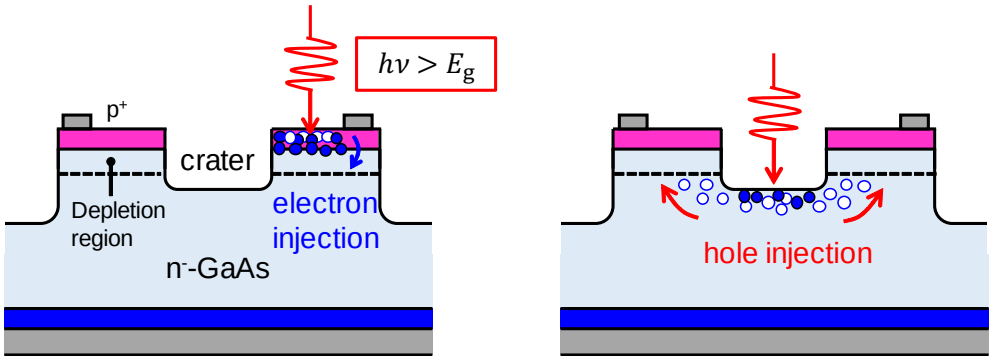

Figure 5.3: Diagrams of the photomultiplication measurement reported by Ito *et al.* [9]. For a GaAs p^+-n junction diode with crater mesa structure, the above-bandgap light was irradiated to the top p^+-layer and the crater n-region (the side of the mesa bottom). From the illuminations to the top p^+-layer and the crater n-region, electron- and hole-injections were obtained, respectively.

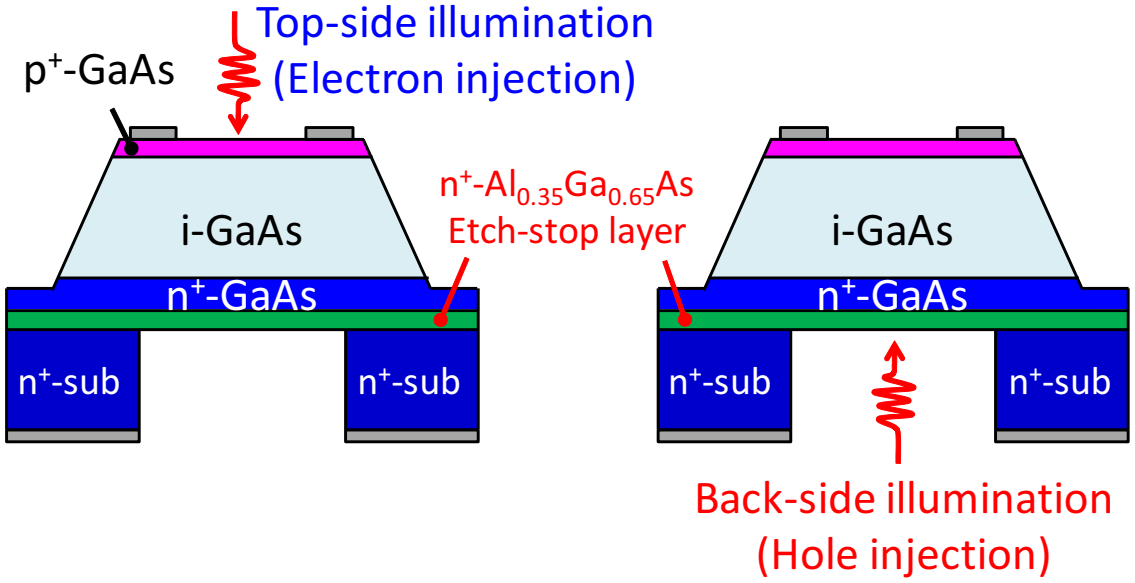

Figure 5.4: Diagrams of the photomultiplication measurement reported by Bulman *et al.* [10]. For GaAs p-i-n junction diodes with the deep well structure at the back side fomred by selective wet etching utilizing the AlGaAs etch-stop layers, the above-bandgap light ($\lambda = 632.8$ nm) was irradiated from the top side and the back side. From the top side and back side illuminations, electron- and hole-injections were obtained, respectively.

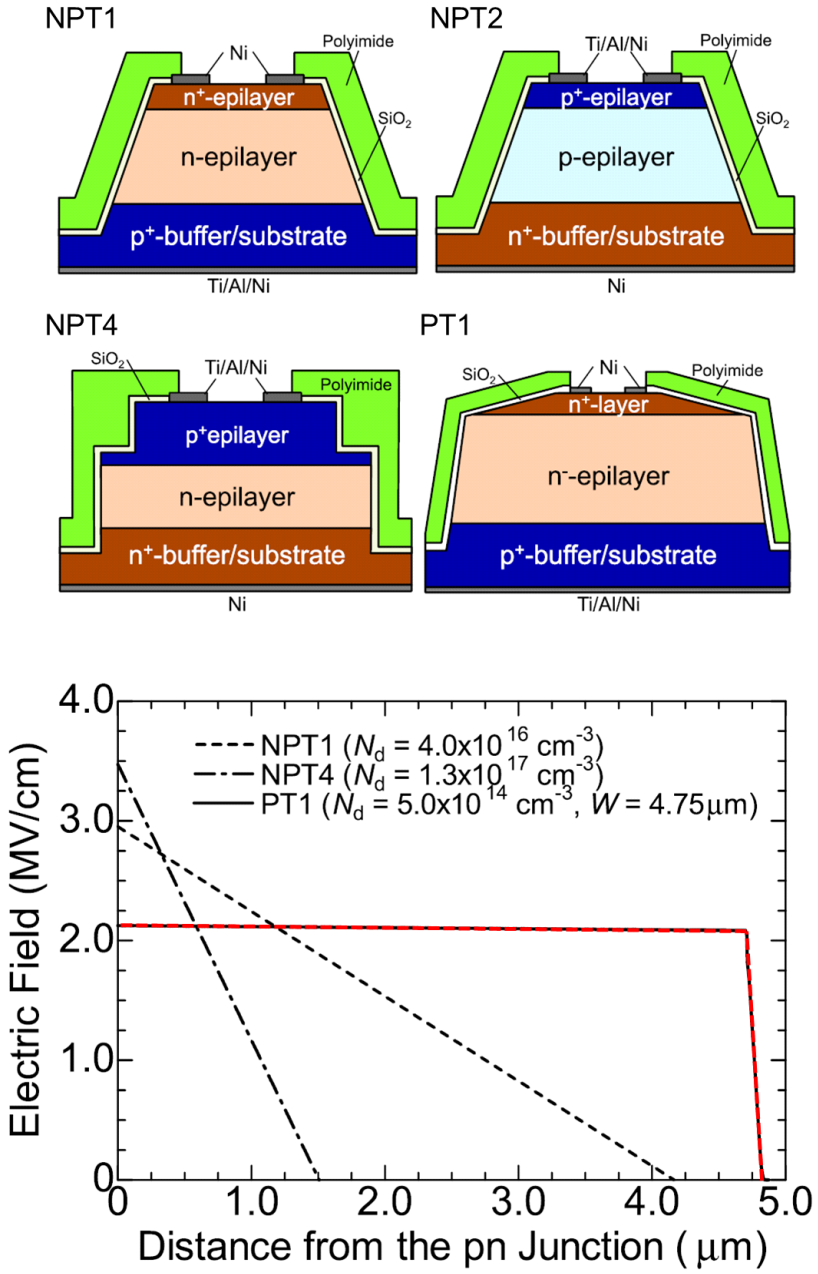

Figure 5.5: Diagrams of the photomultiplication measurement reported by Niwa *et al.* [16]. For 4H-SiC non-punch-through (NPT) and punch-through (PT) p-n junction diodes with various epitaxial structures, the above-bandgap light, the penetration depth of which is sufficiently short and does not cause a mixed carrier injection, was irradiated to the test devices. By designing the epitaxial structures, the devices with various electric field profiles were obtained. Especially, a constant electric field strength was achieved in PT1 owing to very low n-type layer, which enabled the measurement of α_{p} at very low electric field region $\sim$1 MV/cm.

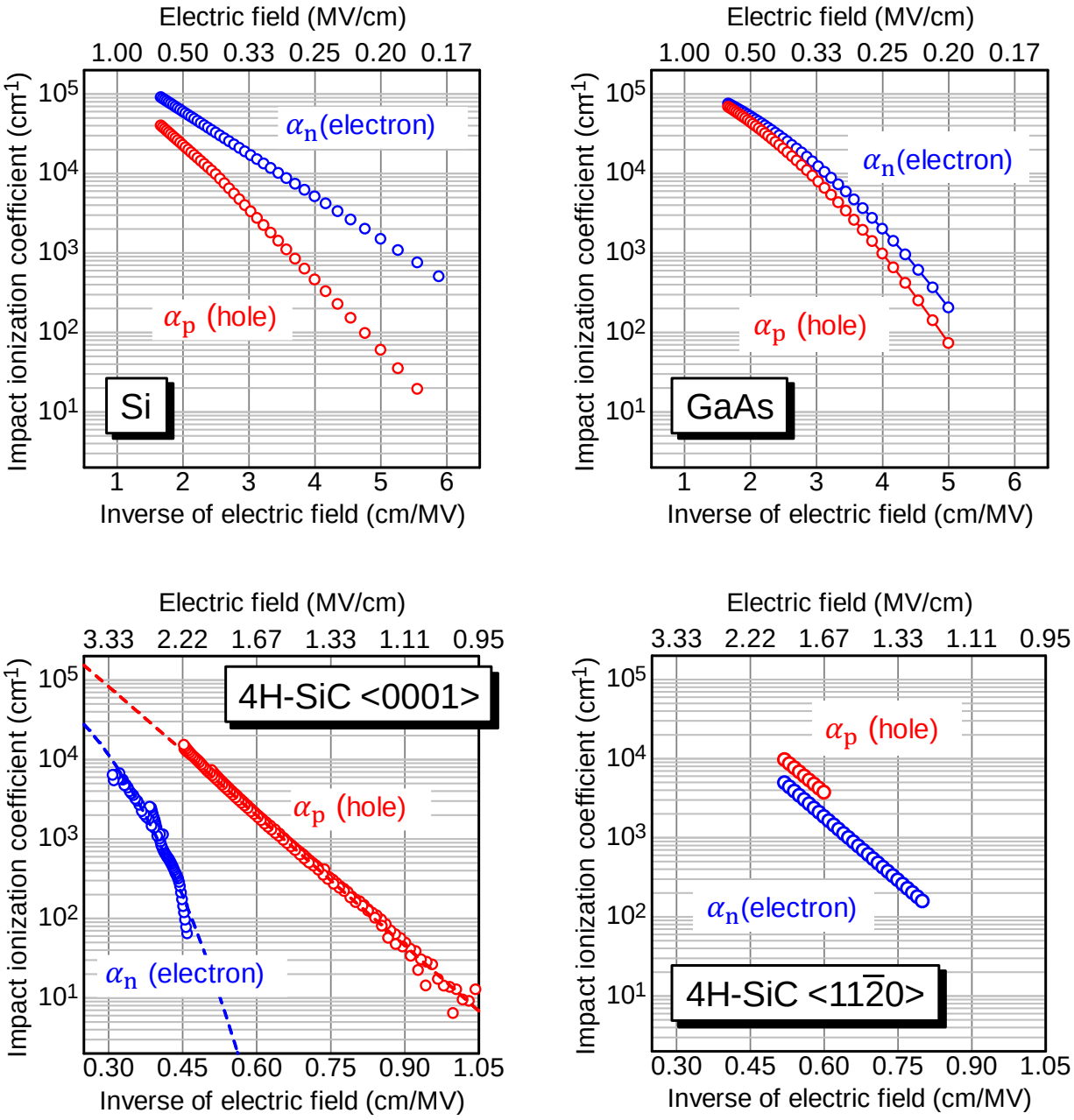

Figure 5.6: Impact ionization coefficients of electrons and holes in Si [3], GaAs [10] and 4H-SiC. For 4H-SiC, it is known that the impact ionization coefficients have large anisotropy [13, 20]. The data for the <0001> [16] and the <11$\bar{2}$0> directions [20] are shown.

in GaN Schottky barrier diodes fabicated on GaN bulk substrates [39]. By changing the electron beam energy, the distribution of generated electron-hole pairs can be changed. However, high reverse leakage current originating from Ar implantation edge termination prohibited from measuring the multiplication of EBIC in precise. Very recently, in 2018, Cao *et al*. have reported α_{n} and α_{n} in GaN grown on bulk GaN substrates [40], as shown in Fig. 5.7. The devices with thin pseudomorphic $In_{0.07}Ga_{0.93}N$ layers on the cathode sides of the drift layers were used for the photomultiplication measurements. For the illumination of $E_{\mathrm{g,InGaN}} < h\nu < E_{\mathrm{g,GaN}}$, electron-hole pairs are generated in the InGaN layers and a hole-injected photocurrent was induced. Although the devices were fabricated on GaN substrates, large leakage currents were observed, which may originate from the inserted InGaN layers. The multiplication factors were obtained in the limited range (one or two order of magnitude) with large noises, resulting in the noisy data of impact ionization coefficients.

Figure 5.8 summarized the reported impact ionization coefficients in GaN obtained by the theoretical studies [33–35] and the experimental studies [38–40]. The differences among the data are very large, since it is difficult to obtain the data accurately due to the unsolved issues toward the measurement. For the determination of α_{n} and α_{p} in GaN, (1) the test device with low leakage current and high avalanche capability, (2) the measurement method to obtain electron- and hole injected photocurrents and (3) the analysis method of photocurrents and their avalanche multiplications are needed.

In this study, we propose the novel method to measure an avalanche multiplication utilizing the Franz-Keldysh (FK) effect. The FK effect has a unique signature: sub-bandgap optical absorption induced by the FK effect selectively occurs at high electric field region. In addition, the photocurrent induced by the FK effect is very predictable [41, 42]. These signatures may be useful to solve the issues (1)–(3) mentioned above. At first, the voltage dependence of the FK-induced photocurrents in the GaN p-n junction diodes with the double-side-depleted shallow bevel termination [43] was investigated. The devices are free from electric field crowding and exhibited low reverse leakage current and high avalanche capability, which allow to measure the photocurrents up to near the breakdown voltages. The method to extract an avalanche multiplication factor of the FK-induced photocurrent is presented and discussed. After that, the photomultiplication measurements were conducted for a GaN p^-/n^+ junction diode under above- and sub-bandgap illuminations. Figure 5.9 shows the diagram of the measurement method proposed in this study. For the above-bandgap illumination, the light is absorbed at near surface, and the generated electrons diffuse and reach the depletion layer edge, resulting in electron injection. For sub-bandgap light, selective absorption near the p-n junction interface (high electric field region) due to the FK effect, resulting in hole injection. The electron- and hole-injected photocurrents were analyzed in detail based on the physics, and multiplication factors are extracted. By analyzing the multiplication factors, the impact ionization coefficients are obtained. The obtained data are modeled and their validity is discussed. The breakdown characteristics in GaN are simulated and discussed.

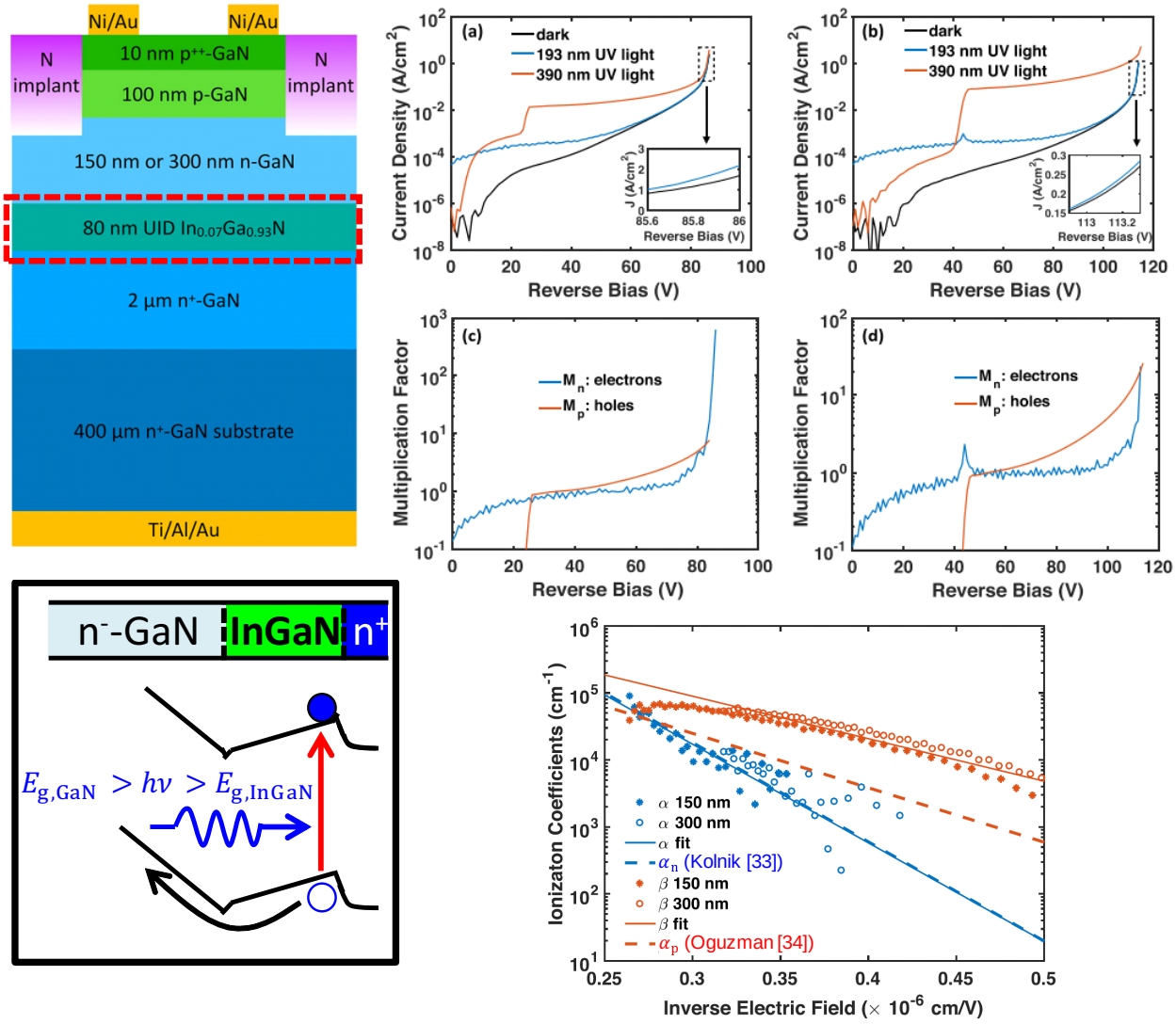

Figure 5.7: Diagrams of the photomultiplication measurement reported by Cao *et al.* [40]. For GaN p-i-n junction diodes with pseudomorphic InGaN layers on the cathode sides of the drift layers, the lights with the wavelengths of 193 nm ($h\nu > E_{\mathrm{g,GaN}}$) and 390 nm ($E_{\mathrm{g,GaN}} > h\nu > E_{\mathrm{g,InGaN}}$) were irradiated. For $E_{\mathrm{g,GaN}} > h\nu > E_{\mathrm{g,InGaN}}$, selective photoexcitation could be obtained at the InGaN layer, resulting in hole injections. However, large leakage currents were observed, which may originate from the InGaN layers. The obtained multiplication factors were limited range (one or two orders of magnitude) with large noise, resulting in the noisy data of impact ionization coefficients.

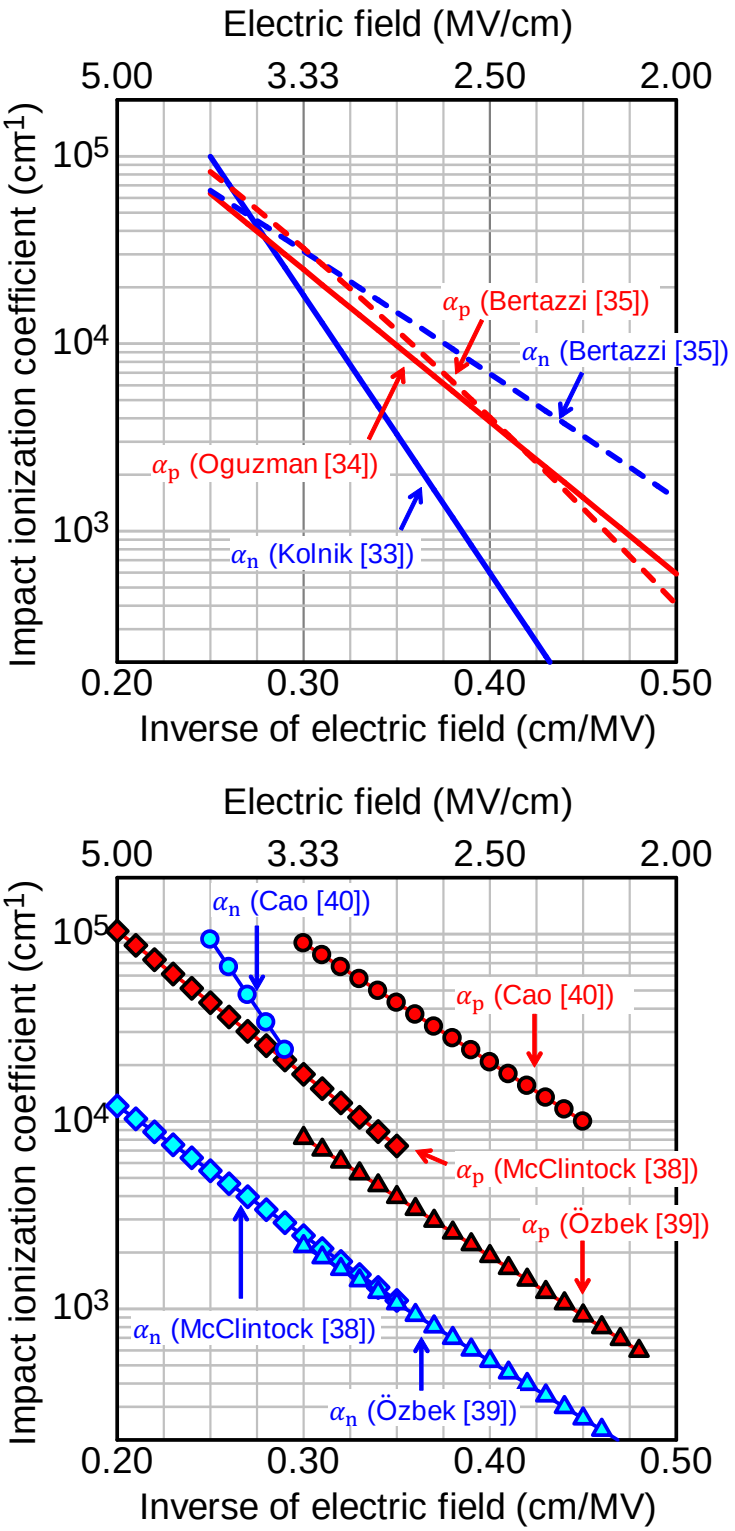

Figure 5.8: The impact ionization coefficients in GaN obtained by theoretical studies [33–35] and the experimental studies [38–40]. The differences among the data are very large. In many reports, the tendency of α_p larger than α_n is observed.

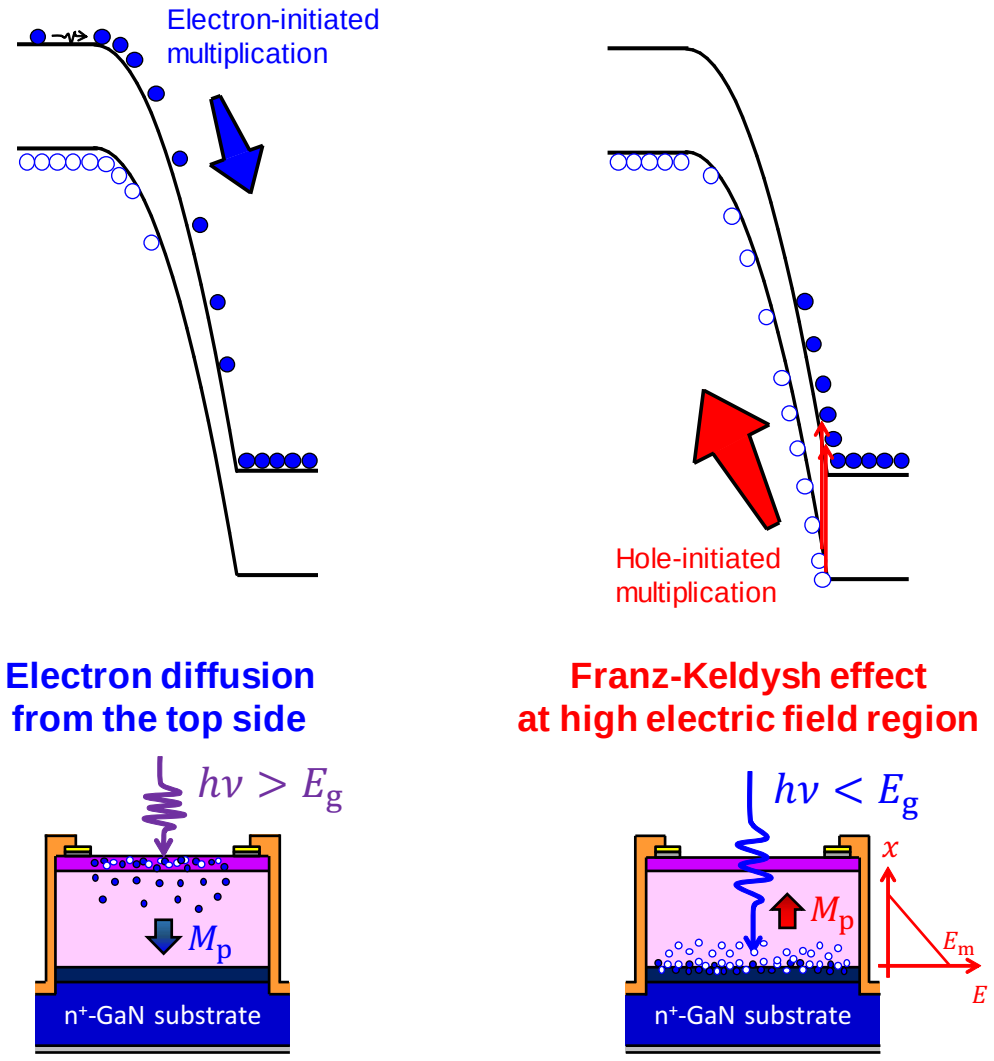

Figure 5.9: Diagrams of the photomultiplication measuremens proposed in this study. Utilizing abobe- and sub-bandgap illuminations for a p^-/n^+ junction, the electron injection from the top-side and sub-bandgap optical absorption induced by the Franz-Keldysh effect near the p-n junction interface (high electric field region), which results in hole injection from the back side, can be obtained.

5.2 Measurement of Avalanche Multiplication Utilizing Franz-Keldysh Effect

In this section, the measurement method of an avalanche multiplication factor utilizing the Franz-Keldysh (FK) effect in a GaN p-n junction diode is presented. The GaN p-n junction diodes with the double-side-depleted shallow bevel termination, which exhibited uniform (nearly ideal) avalanche breakdown, are used as the test devices. Although α_{n} and α_{p} cannot be extacted from the one-injection condiction, the value of impact ionization coefficient in GaN is "estimated" by analyzing the multiplication factors based on the assumption that α_{n} is equal to α_{p}.

5.2.1 Measurement Set up

Figure 5.10 shows the schematic cross section of a GaN p-n junction diode with double-side-depleted shallow bevel termination. The doping concentrations of the n-layers and the p-layers are compalable, and the mesa angle is shallow ($\sim 12^{\circ}$). Four samples with various epitaxial structures (PN1–4) are prepared, which allow to measure an avalanche multiplication in various electric field distributions. Owing to the shallow beveled-mesa structure combined with lightly Mg-doped p-layers, electric field does not occur in the devices. The epitaxial structures, device fabrication processes and fundamental breakdown characteristics are described in Chapter 3 [43]. These devices exhibited low reverse leakage current, high avalanche capability, positive temperature coefficient of the breakdown voltages and breakdown electroluminescence at the entire p-n junction interface. Utilizing these devices, an avalanche multiplication factor can be measured up to the breakdown voltages without the effect of electric field crowding.

For the measurement of the wavelength dependence of the FK-induced photocurrents and their avalanche multiplications, a 150 W Xe lamp combined with the monochrometer (MLS-1510, ASAHI SPECTRA) was used as the monochromatic light sorce. The bandwidth of 5 nm was choiced. The photon flux for 390–420 nm was approximately 8×10^{13} $\mathrm{cm^{-2}s^{-1}}$. A 250 W Hg lamp combined with the band-pass filter of 313 nm and 405 nm (REX-250, ASAHI SPECTRA) was also used to measure the photocurrents under high power density (photon flux of 4×10^{17} $\mathrm{cm^{-2}s^{-1}}$). The bandwidth of the irradiated light was approximately 3 nm. It should be noted that the photocurrent was confirmed to be proportional to the photon flux [41, 42], indicating that multiple-photon absorption did not occur.

For the photocurrent measurements, a Keysight B1505A semiconductor parameter analyzer was used. The temperature of the stage was controlled in the range of 223–373 K and the samples were attached to the stage by vacuum suction. To avoid air sparking, the devices were dipped into liquid Fluorinert while the measurements.

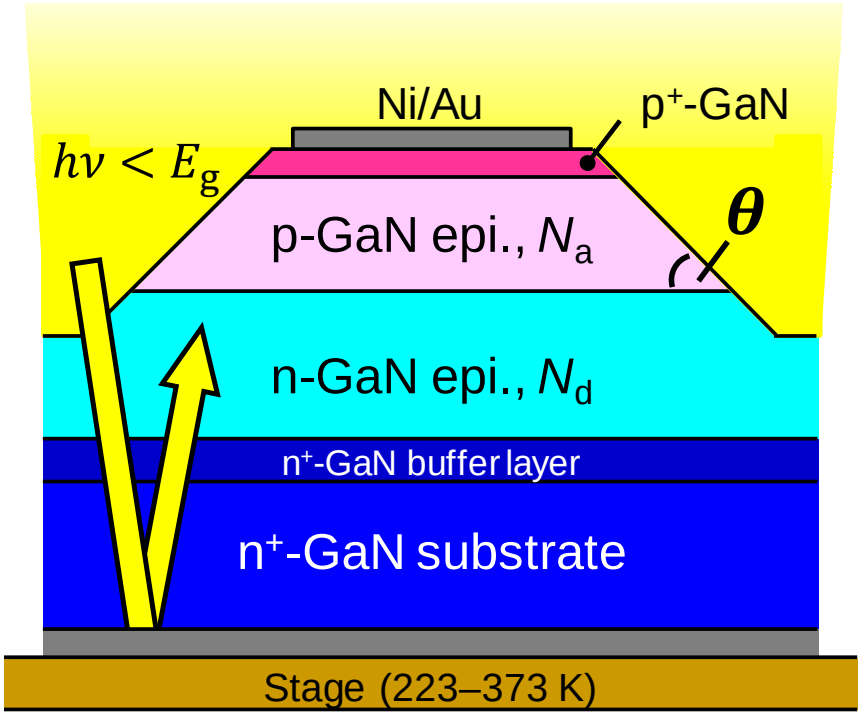

Figure 5.10: Schematic cross section of a GaN p-n junction diode with the double-side-depleted shallow bevel termination. The sub-bandgap light was irradiated to GaN, penetrated into GaN from around the anode electrode, was reflected from the back side electrode and reached p-n junction via multiple reflections. The temperature of the stage was controlled in the range of 223-373 K.

5.2.2 Extraction Method of Multiplication Factor

Figure 5.11 shows the reverse-voltage dependence of photocurrents in the GaN p-n junction diodes (PN1: $N_{\rm d}N_{\rm a}/(N_{\rm d}+N_{\rm a}) = 4.7\times10^{16}$ cm^{-3}) measured under illuminations for the wavelengths of 390–420 nm in $\ln(I)$–V plot. The photocurrents for all the wavelengths increase with the reverse voltage. A larger photocurrent was observed as the wavelength approached to the absorption edge of GaN (365 nm, 3.4 eV). The calculated photocurrents with consideration of the optical absorption induced by the FK effect [44] in the depletion region for 390–420 nm are also shown in Fig. 5.11 as red broken lines. In the calculation, the reduced effective mass of $\mu_{||} = 0.16m_0$ [45] was used. The calculation method of the FK-induced photocurrent is briefly shown in Fig. 5.12 and was described in Chapter 4 [42] in detail. For the range from 0 V to about half of the breakdown voltage, the calculated FK-induced photocurrents well reproduced the experimental data for all the wavelengths. On the other hand, above about half of the breakdown voltage, the experimental data significantly increased and became much larger than the calculated photocurrents. These significant increases at high reverse voltage region are considered to originate from impact ionization of carriers and its avalanche multiplication.

The multiplication factors were extratced as the ratio of an experimental photocurrent to a calculated FK-indcued photocurrent ($M = I_{\rm exp}/I_{\rm cal.FK}$). Figure 5.13 shows the extracted multiplication factors from the photocurrets for 390–420 nm versus reverse voltage in PN1. The data are plotted as "$M-1$" in the semi-log plot to make the data near the unity at low electric field region easier to see. It is observed that the obtained multiplication factors do not depend on the wavelength, although the values of the photocurrents are different. This result is reasonable, since the positions (distributions) where electron-hole pairs were generated were localized near p-n junction interface (high electric field region) for all the wavelengths owing to the nature of the FK effect. The multiplication factors increase with the reverse voltages, and diverged to the infinity at the breakdown electric field.

Figure 5.14 shows the reverse-voltage dependence of the photocurrents in PN1–4. For these measurements, a high power Hg lamp combined with the band-pass filter of 405 nm (bandwidth of 3 nm) was used. For all the devices, the photocurrents much larger than the reverse leakage currents were obtained. The calculated curves of the FK-induced photocurrents are also shown as red broken lines. The calculated curves well reproduce the experimental data up to about half of the reverse voltages. Figure 5.15 shows the multiplicaion factors extracted as $M = I_{\rm exp}/I_{\rm cal.FK}$, in which the horizontal axis takes the maximum electric field in the devices. At the same electric field, the smaller multiplication factor is observed in the device with the high doping concentration, since the electric field changes steeper in the depletion region and the depletion region becomes narrow for a device with higher doping concentration, as shown in Fig. 3.11. The multiplication factors were obtained in wide range ($M-1$: 10^{-2}–10^{3}) with low noise owing to the low leakage currents and accurate predictions of the unmultiplicated photocurrents.

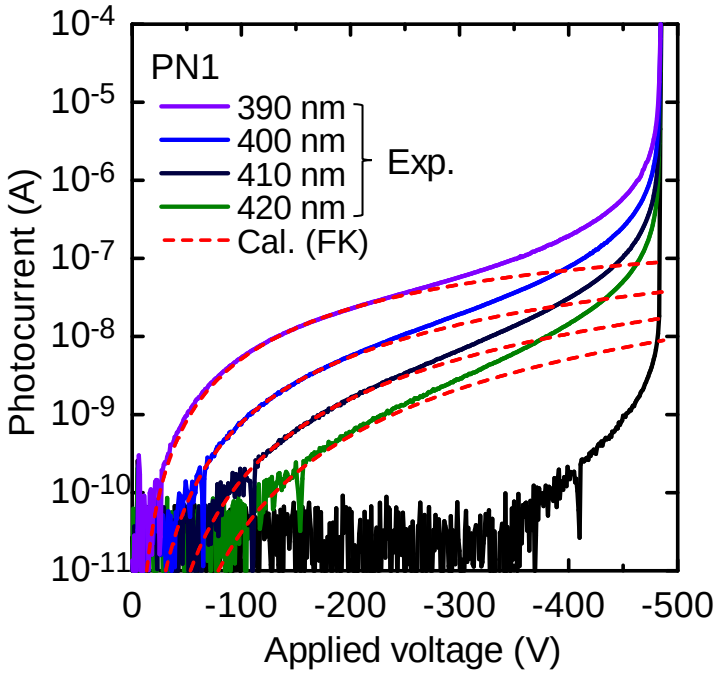

Figure 5.11: Reverse-voltage dependence of the photocurrents for 390–420 nm in the GaN p-n junction diode with the double-side-depleted shallow bevel termination (PN1). The calculated curves of the FK-induced photocurrents are also shown as the red broken lines.

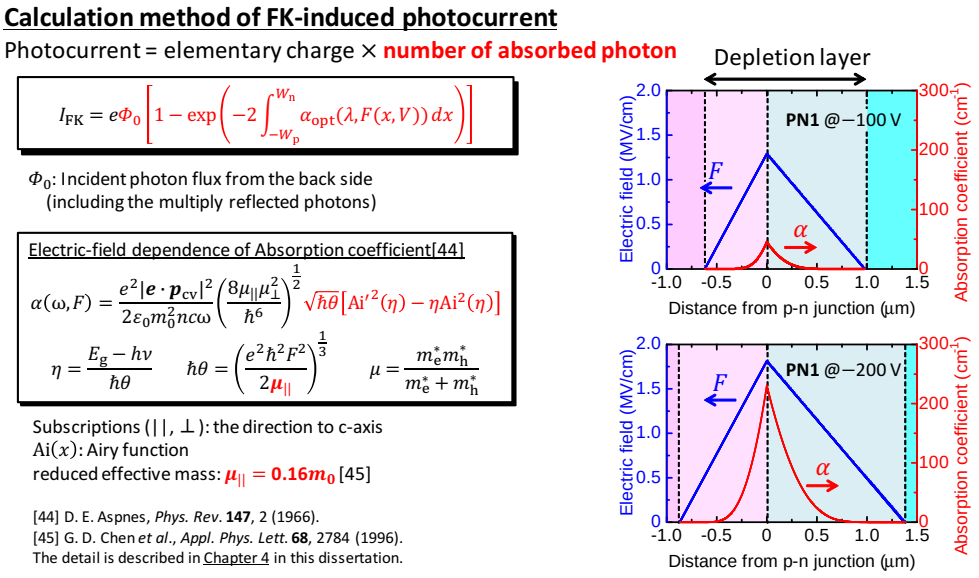

Figure 5.12: Calculation method of the FK-induced photocurrent. The distribution of the absorption coefficient in the depletion region was considered according to the distribution of electric field in the depletion region. The reduced effective mass of $\mu_{||} = 0.16m_0$ [45] was used. Insets: the distributions of the electric field and the absorption coefficient (405 nm) in PN1 under the reverse bias of 100 V and 200 V.

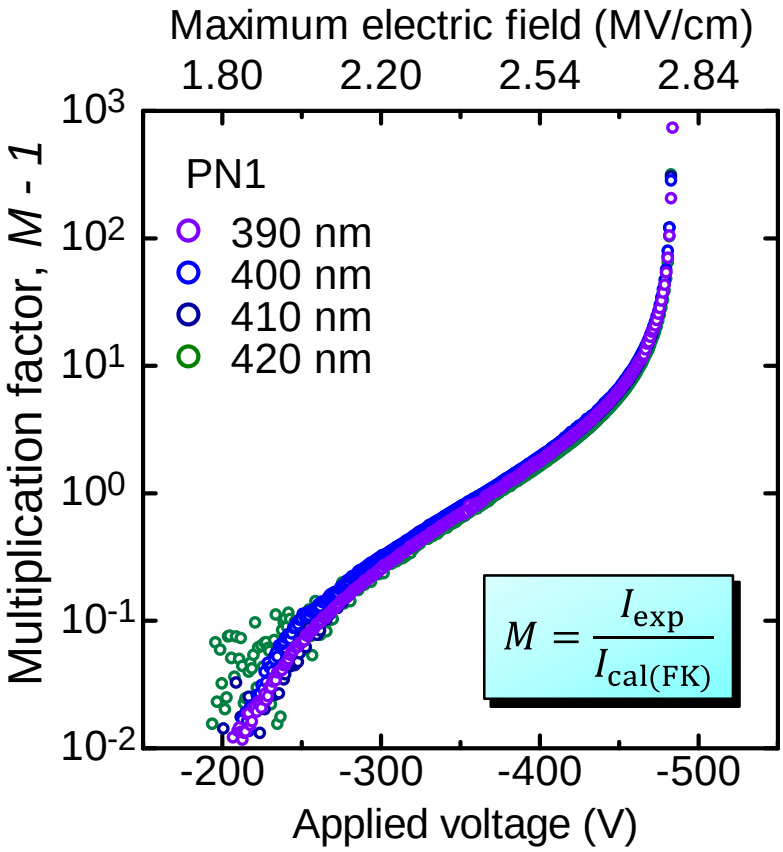

Figure 5.13: Reverse-voltage dependence of the avalanche multiplication factors for 390–420 nm in PN1.

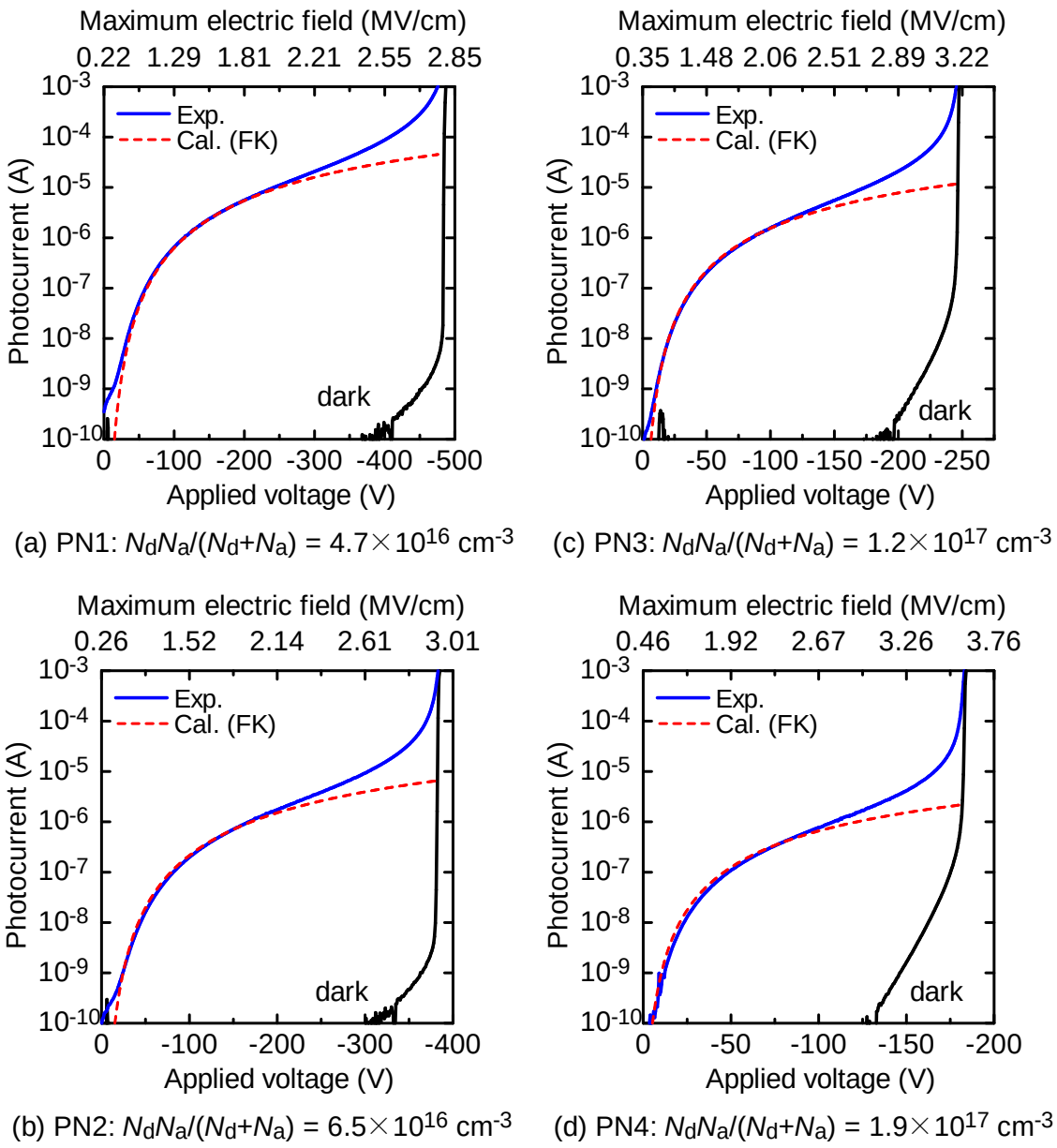

Figure 5.14: Reverse-voltage dependence of the photocurrents for 405 nm in (a) PN1, (b) PN2, (c) PN3 and (d) PN4. The calculated FK-induced photocurrents for these devices are also shown as red broken lines.

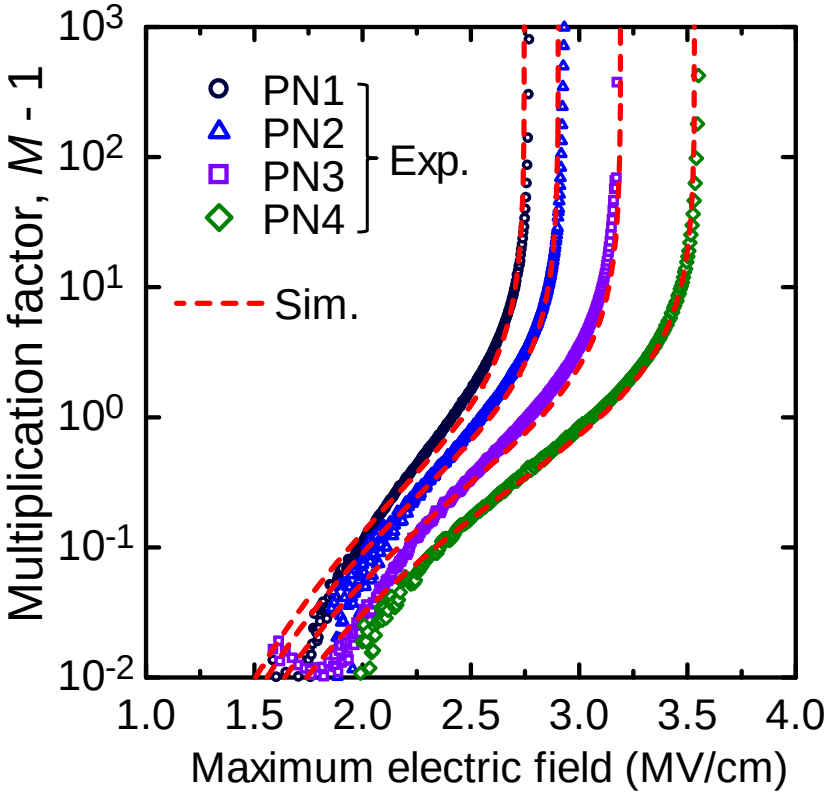

Figure 5.15: Multiplication factors extratced as $M = I_{\mathrm{exp.}}/I_{\mathrm{cal.FK}}$ in PN1–4. The simulated curves using the effective impact ionization coefficient obtained and modeled under the assumption of $\alpha_{\mathrm{n}} = \alpha_{\mathrm{p}}$ are also shown as red broken lines.

5.2.3 Estimation of Impact Ionization Coefficient in GaN

An avalanche multiplication factor is a function of a position (depth) where electron-hole pairs are generated, which reflects the difference between α_n and α_p. A carrier multiplication factor when electron-hole pairs are generated at x_0 in a depletion layer of a p-n junction can be written as

$$1 - \frac{1}{M} = \left(1 - \frac{1}{M_\mathrm{p}}\right) + \left(1 - \frac{1}{M_\mathrm{p}}\right) \tag{5.1}$$

$$1 - \frac{1}{M_\mathrm{p}} = \int_{-W_\mathrm{p}}^{x_0} \alpha_\mathrm{p} \exp\left[-\int_x^{x_0} (\alpha_\mathrm{p} - \alpha_\mathrm{n})\, dx'\right] dx, \tag{5.2}$$

$$1 - \frac{1}{M_\mathrm{n}} = \int_{x0}^{W_\mathrm{n}} \alpha_\mathrm{n} \exp\left[-\int_{x_0}^{x} (\alpha_\mathrm{n} - \alpha_\mathrm{p})\, dx'\right] dx. \tag{5.3}$$

Here, x-axis takes along a depth direction, and $x = 0$ is the p-n junction interface. M_p and M_n are hole- and electron-initiated multiplication factors from x_0 to the depletion layer edges in a p- and n-regions ($x = -W_\mathrm{p}$, $x = W_\mathrm{n}$), respectively. The right side of Eqs. (5.2) and (5.3) are known as the ionization integral[1] [46].

In previous reports [5, 10], two photocurrents induced by hole-injections from the n-region and electron-injections from the p-region were measured. Electron- and hole-initiated multiplication factors as $M_\mathrm{p}|_{x_0=W_\mathrm{n}}$ and $M_\mathrm{n}|_{x_0=-W_\mathrm{p}}$ were analyzed, and α_n and α_p were obtained.

In this section, the photocurrents were measured for the only one-injection condition that electron-hole pairs are generated near the p-n junction interface (the middle of the depletion layer). Therefore, α_n and α_n cannot be extarcted separately from the obtained multiplication factors. Although α_p and α_n are not equal as observed in previous reports [33–35, 38–40], here, the authour assumes $\alpha_\mathrm{n} = \alpha_\mathrm{p}$ for simplicity and estimates the "effective" impact ionization coefficient ($\alpha \equiv \alpha_\mathrm{n} = \alpha_\mathrm{p}$). Under this assumption, the multiplication factor does not depend on the position where electron-hole pairs are generated (x_0) and can be simplified as

$$1 - \frac{1}{M} = \int_{-W_\mathrm{p}}^{W_\mathrm{n}} \alpha(E) dx. \tag{5.4}$$

E is the electric field. Transforming the integral in Eq. (5.4) as $dx \to dE$, the author obtains

$$1 - \frac{1}{M} = \frac{\varepsilon_\mathrm{s}}{e} \frac{N_\mathrm{a} + N_\mathrm{d}}{N_\mathrm{a} N_\mathrm{d}} \int_0^{E_\mathrm{m}} \alpha(E) dE, \tag{5.5}$$

where e is the elementary charge, ε_s is the dielecric constant of GaN ($\varepsilon_\mathrm{s} = 10.4\varepsilon_0$ [47, 48]), and E_m is the maximum electric field. It should be noted that the value of dE/dx in a p-region and that in a n-region are different, since $E(x) = eN_\mathrm{a}(x - W_\mathrm{p})/\varepsilon_\mathrm{s}$ ($W_\mathrm{p} \le x \le 0$), $eN_\mathrm{d}(W_\mathrm{n} - x)/\varepsilon_\mathrm{s}$ ($0 \le x \le W_\mathrm{n}$). Differentiating both sides of Eq. (5.5) by E_m,

$$\alpha(E_\mathrm{m}) = \frac{e}{\varepsilon_\mathrm{s}} \frac{N_\mathrm{a} N_\mathrm{d}}{N_\mathrm{a} + N_\mathrm{d}} \frac{1}{M^2} \frac{dM}{dE_\mathrm{m}} \tag{5.6}$$

[1] Avalanche breakdown in the device is defined as $M \to \infty$. In simple cases of pure electron injection ($x_0 = W_\mathrm{p}$) or pure hole injection ($x_0 = W_\mathrm{n}$), the ionization integral becomes unity when $M \to \infty$.

is obtained. Using Eq. (5.6), $\alpha(E)$ can be extratced from $M(V)$. The experimental data of M include noises originating from the measurement unit or the light source, and the numerial differentiation of M causes a large noise in α, although the noises in M are small. Therefore, the obtained M was made smoother by the proceedure of the Savitzky-Golay method [16, 49].

Figure 5.16 shows the effective impact ionization coefficient $\alpha \equiv \alpha_{\rm n} = \alpha_{\rm p}$ extracted from $M(V)$ in PN1–4 as a function of the inverse of electric field. The obtained values for all the devices lie on the same linear line in the plot in the range of 2.0–3.3 MV/cm, suggesting the consistent results for all the devices. The data were fitted and modeled by Chynoweth's empirical formula [1]:

$$\alpha(E) = 1.30 \times 10^6 \cdot \exp\left(-\frac{1.18 \times 10^7 \text{ V/cm}}{E}\right) \text{ cm}^{-1}. \tag{5.7}$$

The multiplication factors in PN1–4 were simulated from Eq. (5.4) using the extracted α as the modeled formula (5.7). The simulated multiplication factors are shown in Fig. 5.15 as red broken lines. These calculated curves show good agreement with the experimental multiplication factors, yielding consistent results for all the devices. Although the author assumed $\alpha_{\rm n} = \alpha_{\rm p}$, the avalanche multiplication characteristics are well reproduced in this study. These results are owing to the optical absorption induced by the FK effect in the GaN p-n junction diodes with the double-sidedepleted epitaxial structure: the electron-hole pairs are generated near the middle of the depletion regions, which minimized the effect of the difference between $\alpha_{\rm n}$ and $\alpha_{\rm n}$ on the multiplication factors.

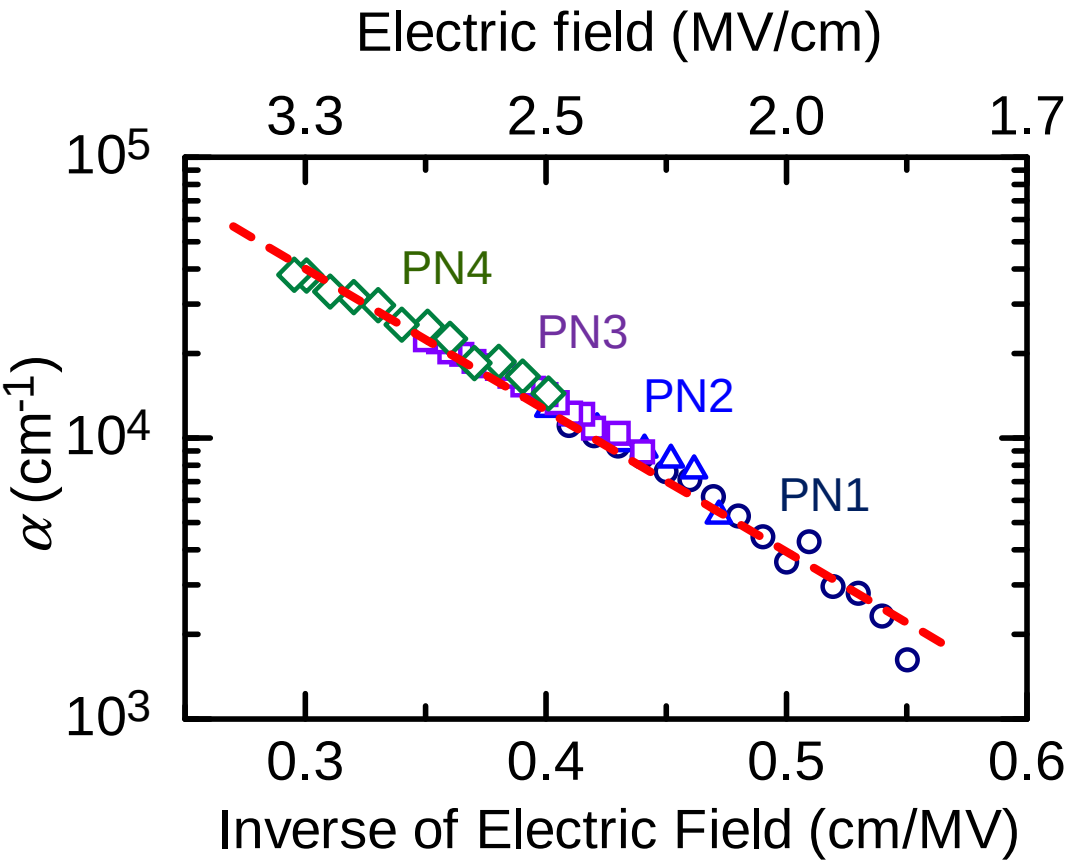

Figure 5.16: The effective impact ionization coefficient ($\alpha \equiv \alpha_{\rm n} = \alpha_{\rm p}$) versus the inverse of electric field extracted from the M in PN1–4.

5.2.4 Temperature Dependence of Avalanche Multiplication

The temperature dependence of the photocurrents for 405 nm in PN1–4 under reverse bias were also measured to investigate the temperature dependence of an avalanche multiplication in GaN. Figure 5.17 shows the photocurrents for 405 nm in PN1–4 at 223, 298 and 373 K. The temperature dependence of the FK-induced photocurrent can be expressed by considering the shrinkage of the bandgap with elevating temperature as discussed in Chapter 4 [42]. The calculated curves of the FK-induced photocurrents in PN1–4 at each temperature with consideration of the temperature dependence of the bandgap of GaN [50] are also shown as the broken lines. Up to about half of the breakdown voltages, the calculated curves well reproduce the experimental photocurrents, indicating an avalanche multiplication was negligible ($M = 1$) in these voltage ranges. Larger photocurrents were obtained at a higher temperature. On the other hand, above about half of the breakdown voltage, the measured photocurrents started to increase significantly and exceeded the calculated FK-induced photocurrents, reflecting the avalanche multiplications.

Figure 5.18 shows the multiplication factors in PN1–4 extracted as $M = I_{\mathrm{exp}}/I_{\mathrm{cal.FK}}$ at 223, 298 and 373 K. An increase in breakdown voltages and a decrease in multiplication factors were observed at elevated temperature for all devices. These reflect the decease in the impact ionization coefficients: carriers becomes hard to get sufficient energy to cause impact ionizations due to the increase in the phonon scattering rate at elevated temperature.

Figure 5.19 shows the extracted α at 223, 298 and 373 K. The data obtained for all devices lie on the same line in the α–E^{-1} plot at all temperatures in the 2.0–3.3MV/cm range, resulting in the consistent results for all the devices. The value of α decreased slightly with elevating temperature, which reflects the increase in the phonon scattering rate. The data were fitted using the empirical formula [1] based on the Okuto-Crowell model [51] as

$$\begin{aligned} \alpha\,(E,T) &= a(T)\cdot\exp\left(-\frac{-b(T)}{E}\right)\ \mathrm{cm}^{-1}, \\ a\,(T) &= 1.30\times10^{6}\cdot\left[1+1.5\times10^{-3}(T-298\ \mathrm{K})\right]\ \mathrm{cm}^{-1}, \\ b\,(T) &= 1.18\times10^{7}\cdot\left[1+6.0\times10^{-4}(T-298\ \mathrm{K})\right]\ \mathrm{Vcm}^{-1}. \end{aligned} \tag{5.8}$$

The multiplication factors for PN1–4 were simulated at 223–373 K, and the results are denoted in Fig. 5.18 as broken lines. The simluated curves well show good agreement with the experimental multiplication factors, suggesting the consistent results for PN1–4 at the temperature range of 223–373 K.

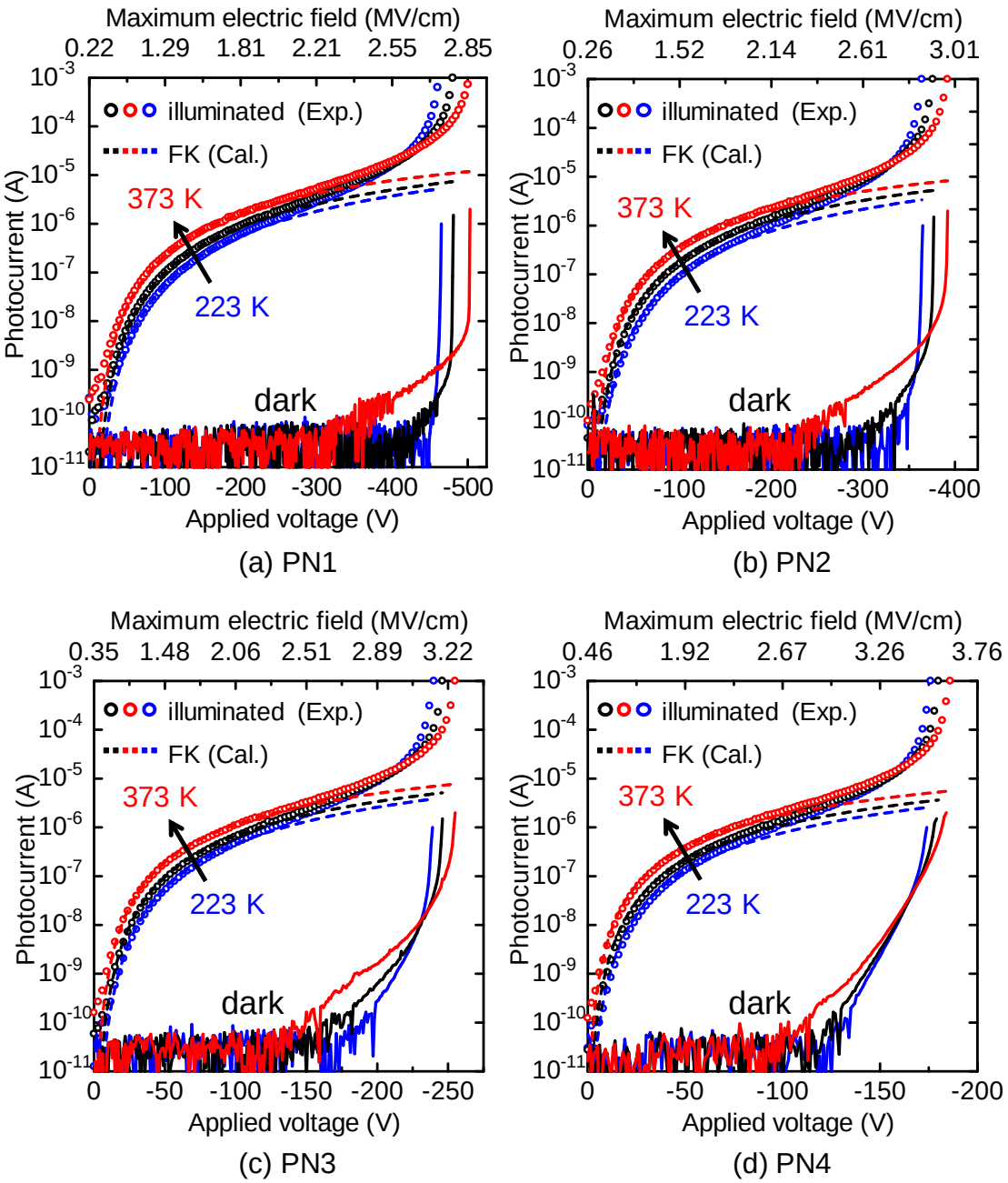

Figure 5.17: Reverse-voltage dependence of the photocurrents for 405 nm in PN1–4 at 223, 298 and 373 K. The calculated curves of the FK-induced photocurrents with consideration of the temperature dependence of the bandgap of GaN [50] are also shown as broken lines.

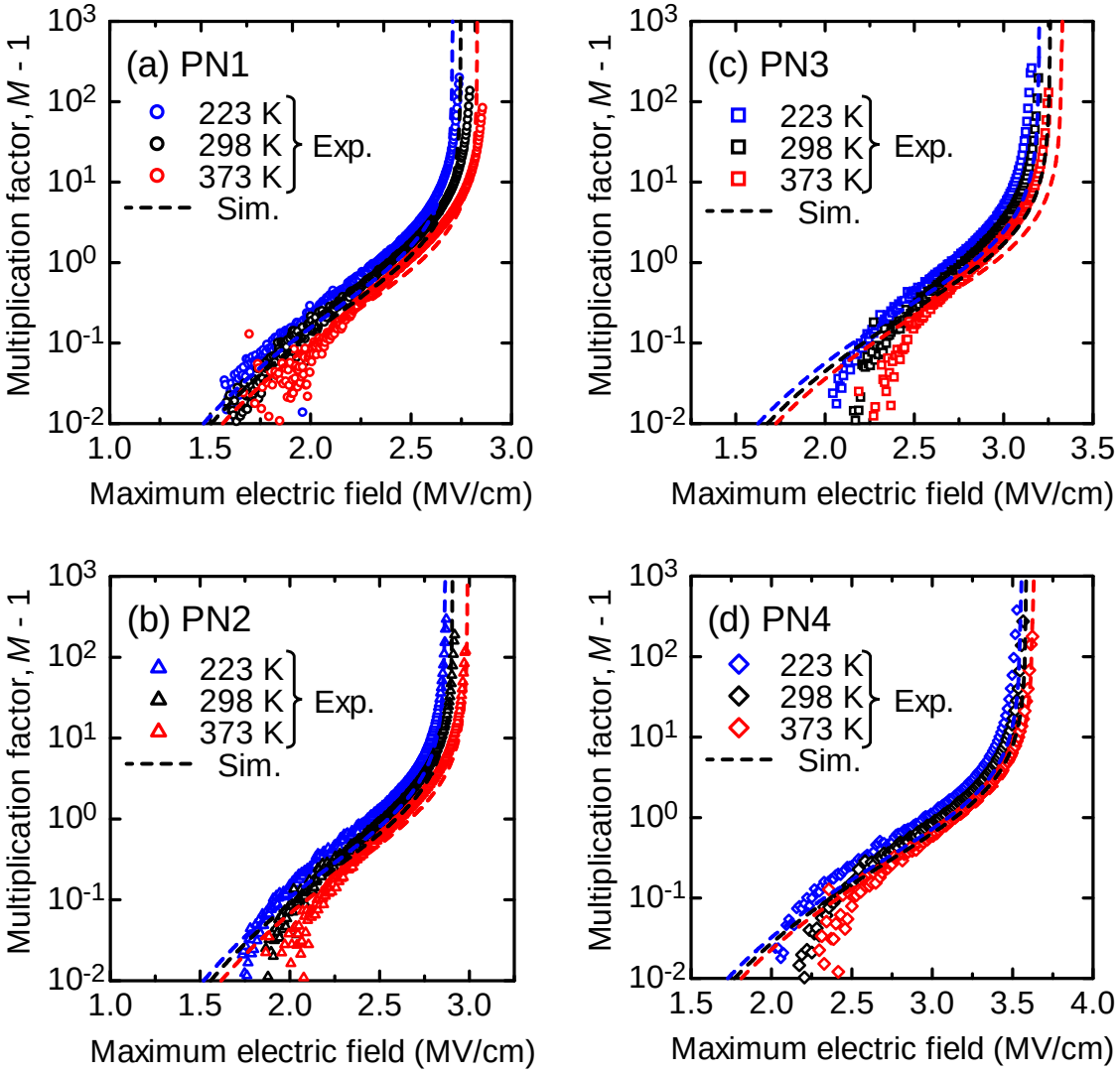

Figure 5.18: The multiplication factors versus the inverse of the electric field in PN1–4 at 223, 298 and 373 K. The simulated curves using the effective impact ionization coefficient obtained and modeled under the assumption of $\alpha_{\mathrm{n}} = \alpha_{\mathrm{p}}$ are also shown as red broken lines.

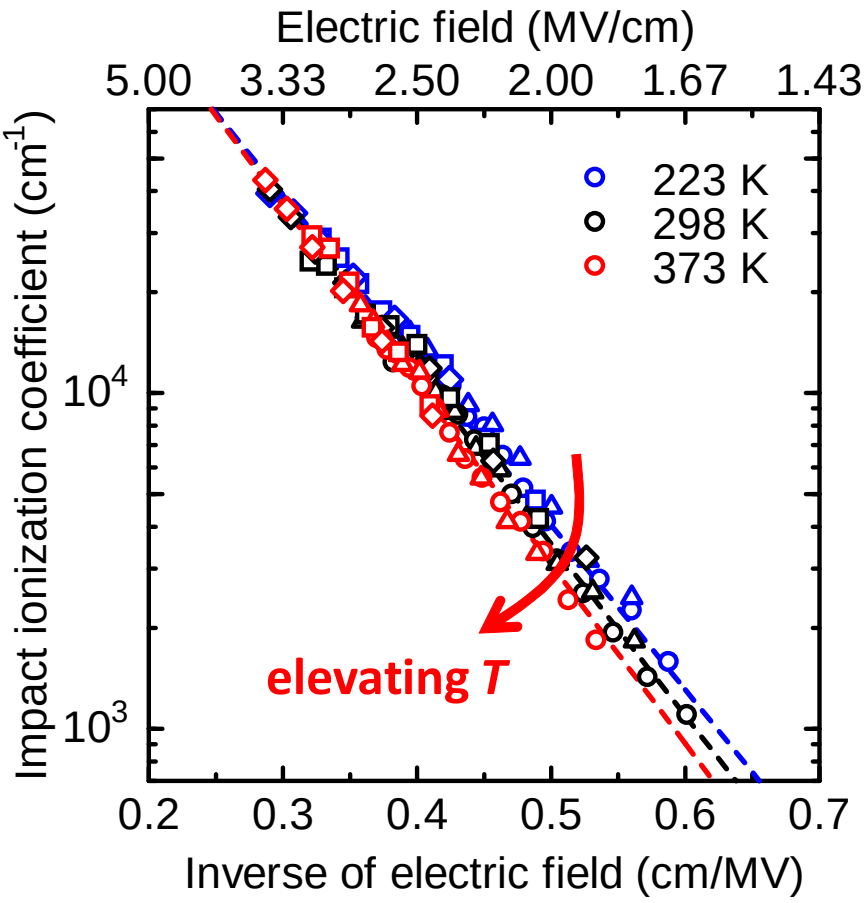

Figure 5.19: The effective impact ionization coefficient (α) versus the inverse of the electric field at 223, 298 and 373 K.

5.3 Impact Ionization Coefficients of Electrons and Holes in GaN

In this section, the measurement method of an avalanche multiplication factor utilizing the Franz-Keldysh effect is applied to a GaN p^-/n^+ junction diode, in which high electric field is distributed near the p-n junction interface (n^+-side). The device with vertical deep-etch termination, which exhibited uniform (nearly ideal) avalanche breakdown, is used as the test devices. Utilizing above- and sub-bandgap illuminations, electron- and hole-injected photocurrents and their avalanche multiplications are obtained. By analyzing the multiplication factors, the impact ionization coefficients of electrons and holes in GaN are extracted. The avalanche breakdown characteristics in GaN devices are simulated using the obtained parameters and discussed.

5.3.1 Measurement Set up

Figure 5.20 shows the schematic cross section of a GaN p^-/n^+ junction photodiode. The p^+-, p-, and n^+-layers were grown by metalorganic vapor phase epitaxy (MOVPE) on GaN(0001) bulk substrates. The control of lightly Mg doping was achieved by the MOVPE system equipped with double-dilution of the Mg source gas [52]. The vertical deep-etch mesa structure, which can realize a one-dimensional electric field profile [16, 20, 53, 54], was formed by Cl_2-based dry etching with a SiO_2 mask [31]. The mesa height and angle are approximately 5 μm and 90°, respectively. The anode and cathode electrodes were formed by the deposition of Ni/Au on the p^+-layers and Ti/Al/Au on the substrate, respectively. After the metallization, a 6 μm thick polyimide was coated as a surface passivation layer. The fabrication process was described in [55] and Chapter 3.

Figure 5.21 shows the depth profiles of the Mg, Si and C profiles measured by secondary ion mass spectrometry (SIMS) in the epilayer. In the epilayer, Mg is almost uniformly distributed along the depth direction and the concentration is about 1.3×10^{17} cm^{-3}. Figure 5.22 shows the capacitance–voltage (C–V) characteristics of the device. From the C^2–V plot with a good linearity, $N_\mathrm{a}N_\mathrm{d}/(N_\mathrm{a}+N_\mathrm{d}) = 1.3\times10^{17}$ cm^{-3} was obtained, which shows agreement with the Mg concentration. From the SIMS and C–V, the consistent result was obtained, suggesting that the electric field profile can be estimated accurately.

Figure 5.23 shows the breakdown characteristics of the GaN p^-/n^+ junction diode without illumination. The device exhibited the breakdown voltage of 235 V and the breakdown electric field of 3.2 MV/cm at 298 K with low reverse leakage current and high avalanche capability. The positive temperature coefficients of the breakdown voltage (∼0.13 V/K in the range of 223–473 K) was obtained. The almost uniform breakdown electroluminescence at the entire p-n junction was observed, which is the evidence that the uniform (nearly ideal) avalanche breakdown occured in the device wihout electric field crowding. Therefore, the device is proper as the test device of the photomultiplication measurements.

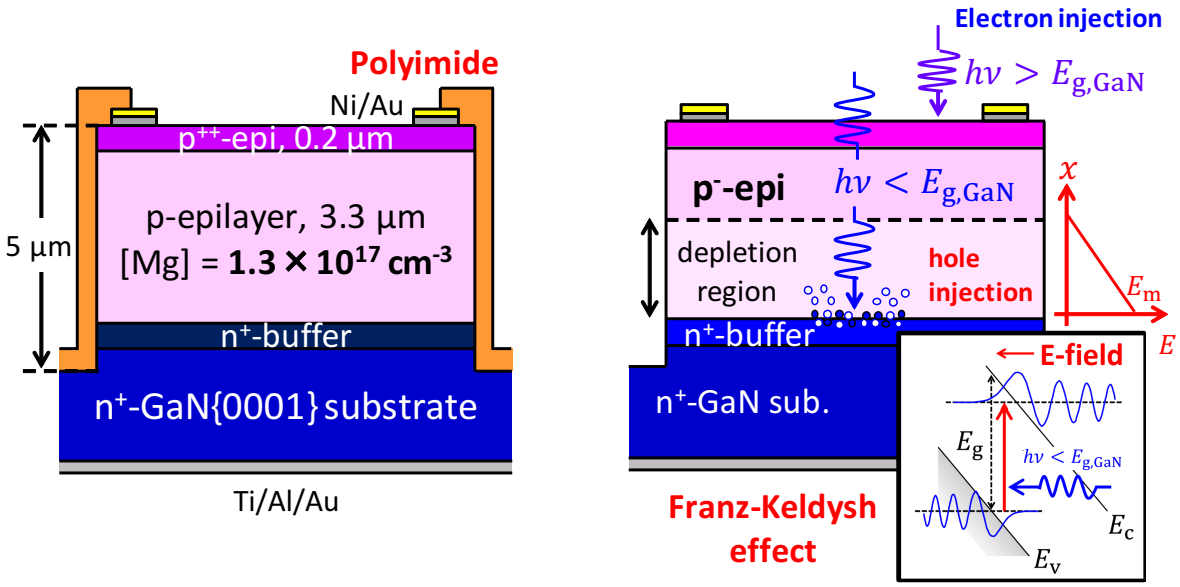

Figure 5.20: The schematic cross section of a GaN p^-/n^+ junction diode with vertical deep-etch mesa termination fabricated on an n-type GaN bulk substrate. The thick polyimide later was coated as a suface passivation layer. For the above-bandgap illumination, electron injection from the top side can be obtained. On the other hand, for the sub-bandgap illumination, the optical absorption induced by the Franz-Keldysh effect occurs near the p-n junction interface, resulting in hole injection.

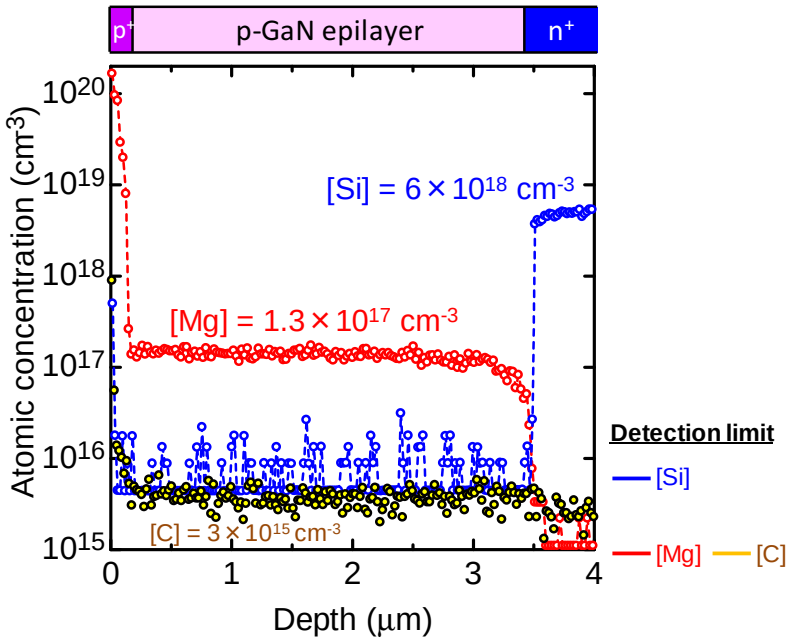

Figure 5.21: The depth profiles of Mg, Si and C concentrations in the epilayer. Mg is almost uniformly distributed along the depth direction in the p-layer. In addition, the Si and C concentration are very low.

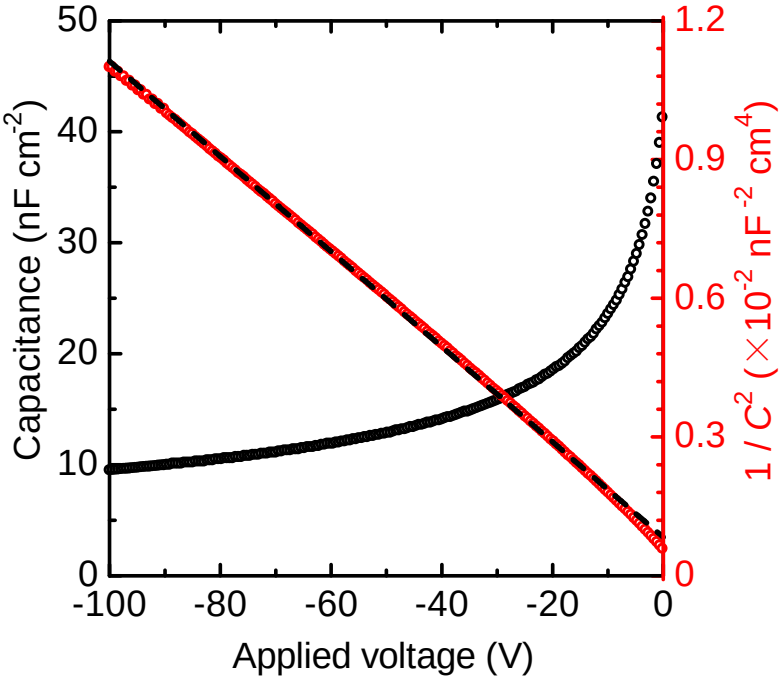

Figure 5.22: The C–V characteristics of the GaN p-n junction diode as the C^{-2}–V plot. A good linearity is observed in wide voltage ranges, which is the consistent with the SIMS results: the uniform distribution of the acceptor (Mg) in the epilayer.

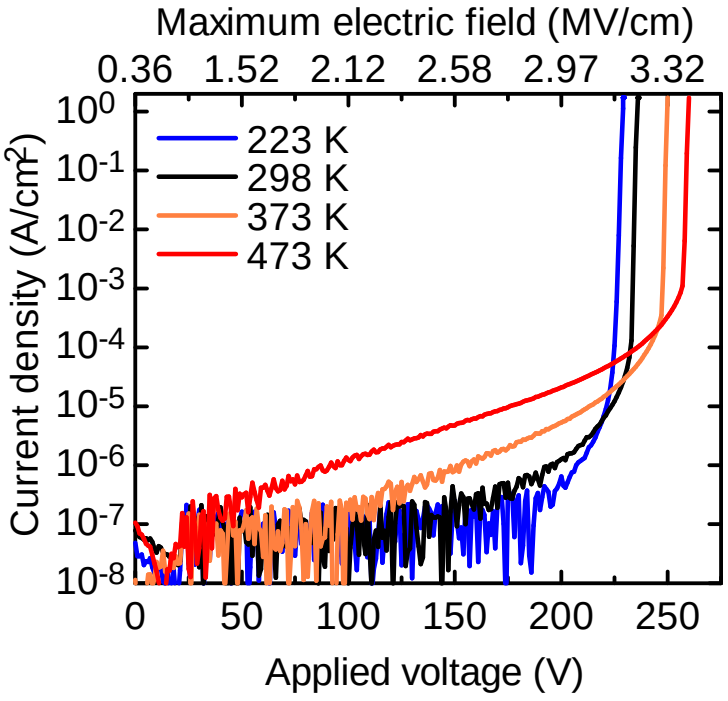

Figure 5.23: Reverse I–V characteristics of the GaN p-n junction diode at 223, 298, 373 and 473 K. The breakdown voltage increased almost linearly with elevated temperature.

For photocurrent measurements, a 250 W Hg lamp combined with the bandpass filters of 313 nm and 405 nm was used (the GaN absorption edge is approximately 365 nm at room temperature [22]). The bandwidths were 3 nm, indicating the good monochromaticity.

5.3.2 Above-Bandgap Illumination for p^-/n^+ Junction

Figure 5.24 shows the reverse-voltage dependence of the photocurrent in the GaN p-n junction diode under illumination of above-bandgap light at 298 K. The wavelength and the irradiated photon flux were 313 nm (∼3.96 eV) and 2.7×10^{17} $cm^{-2}s^{-1}$, respectively. The photocurrent much larger than dark leakacge current was obtained. For the wavelength of 313 nm, the penetration depth is approximately 80 nm [22], which is much shorter than the p^+-layer thickness of 200 nm. It should be noted that the transmittance of the polyimide layer for 313 nm is less than 0.01% as shown in Fig. 5.25 [16, 56]. The optical absorption at the mesa side wall is negligible. Therefore, this photocurrent is concluded to be induced by the electron diffusion of the generated electron-hole pairs at the surface p^+-layer.

The photocurrent induced by the diffusion of the minority carriers can be calculated based on the following formula derived by Raynaud *et al.* [57] :

$$J_{\mathrm{n,dif}}(x_{\mathrm{p}}) = e\,\Phi_0 \frac{\alpha_0 L_{\mathrm{n}}}{1-\alpha_0^2 L_{\mathrm{n}}^2} e^{-\alpha_0 x_{\mathrm{p}}} \cdot \left[\frac{L_{\mathrm{n}}(S + D_{\mathrm{n}}\alpha_0)e^{-\alpha_0 x_{\mathrm{p}}} - L_{\mathrm{n}} S \cdot \cosh\left(\frac{x_{\mathrm{p}}}{L_{\mathrm{n}}}\right) - D_{\mathrm{n}} \cdot \sinh\left(\frac{x_{\mathrm{p}}}{L_{\mathrm{n}}}\right)}{D_{\mathrm{n}} \cdot \cosh\left(\frac{x_{\mathrm{p}}}{L_{\mathrm{n}}}\right) + L_{\mathrm{n}} S \cdot \sinh\left(\frac{x_{\mathrm{p}}}{L_{\mathrm{n}}}\right)} - L_{\mathrm{n}}\alpha_0 \right]. \tag{5.9}$$

Here, Φ_0, α_0, L_{n}, D_{n}, x_{p} and S are the incident photon flux with consideration of the surface reflection and the quantum efficiency, the absorption coefficient, the electron diffusion length, the electron diffusion coefficient, the width of the neautral region (the depth of the depletion layer edge) in p-layer, and the surface recombination velocity. $\alpha_0 = 1.3\times10^5$ cm^{-1} for the wavelength of 313 nm [22] and $S = 5\times10^4$ cm/s [58] were used in the calculation. The value of S was determined for the 2.6 μm thick undoped GaN layer grown on a sapphire substrate by Aleksiejunas *et al.* in 2003 [58]. Strictly, the value of S for a homoepitaxial p^+-GaN layer should be used but has been still unknown. It is confirmed that the calculation of $J_{\mathrm{n,dif}}$ was not sensitive to the value of S. L_{n} and D_{n} are sensitive parameters to the voltage dependence of $J_{\mathrm{n,dif}}$, and the reasonable parameters were obtained by fitting as $L_{\mathrm{n}} = \sqrt{\tau_{\mathrm{n}} D_{\mathrm{n}}} = 0.61$ μm and $D_{\mathrm{n}} = \mu_{\mathrm{n}} kT/e = 22$ cm^2/s ($\tau_{\mathrm{n}} = 174$ ps, $\mu_{\mathrm{n}} = 859$ cm^2/Vs). The x-axis takes the depth direction, and x_{p} which is a voltage-dependent parameter was calculated as $x_{\mathrm{p}} = d_{\mathrm{pn}} - W_{\mathrm{p}}$, $W_{\mathrm{p}} = \sqrt{2\varepsilon_{\mathrm{s}}(N_{\mathrm{a}} + N_{\mathrm{d}})(V_{\mathrm{d}} - V)/e(N_{\mathrm{a}} N_{\mathrm{d}})}$. d_{pn} is the depth of the p-n junction interface (3.5 μm). Figure 5.26 shows the voltage dependence of W_{p}.

The calculated curve of the electron diffusion current for the GaN p-n junction diode is shown in Fig. 5.24 as the red broken line. The calculated curves shows excellent agreement with the experimental photocurrent up to approximately 150 V. For higher voltage than about 150 V, the avalanche multiplication came to be striking.

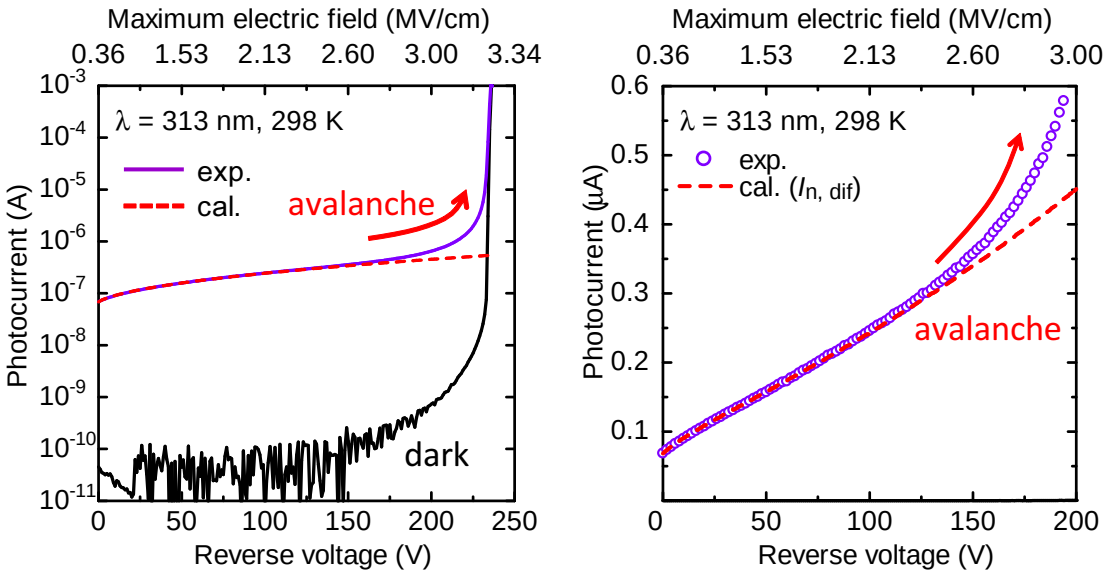

Figure 5.24: Reverse-voltage dependence of the photocurrent for above-bandgap light (λ = 313 nm) in the GaN p-n junction diode at 298 K in semi-log and linear scales. The calculated curves of the minority carrier diffusion current are also shown as red broken lines.

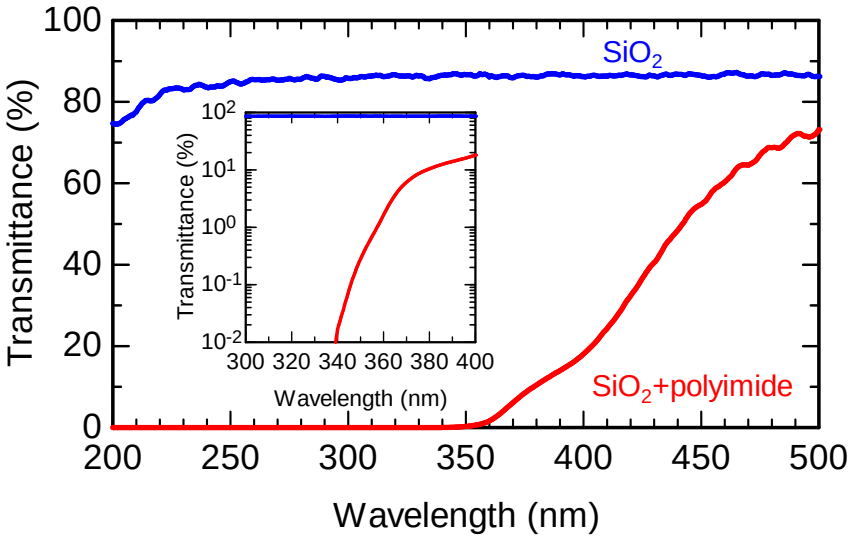

Figure 5.25: Transmittance characteristics of a polyimide used in this study [56]. The transmittance for the wavelength of 313 nm is less than 0.01%.

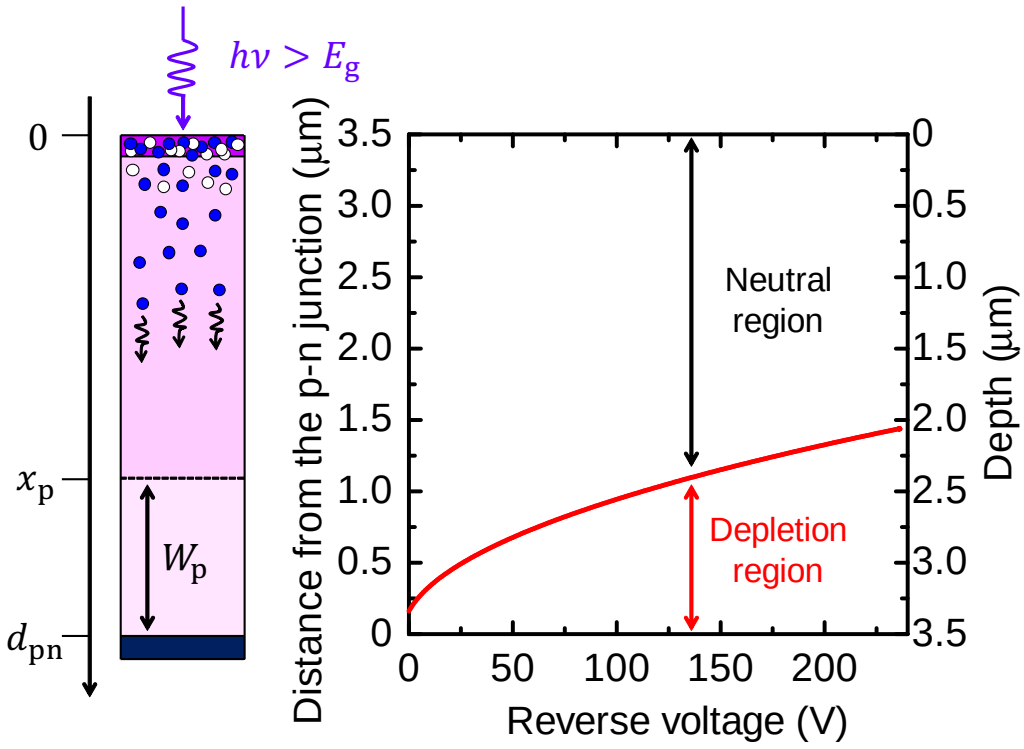

Figure 5.26: Extention of the depletion layer as a function of the reverse bias voltage. x_p determines the voltage dependence of the electron diffusion current.

5.3.3 Sub-Bandgap Illumination for p^-/n^+ Junction

Figure 5.27 shows the reverse-voltage dependence of the photocurrent in the GaN p-n junction diode under illumination of sub-bandgap light at 298 K. The wavelength and the irradiated photon flux were 405 nm (∼3.06 eV) and 4.0×10^{17} $cm^{-2}s^{-1}$. With increasing reverse bias voltage, the photocurrent increased and became much larger than the dark leakage current. For the wavelength of 405 nm, the light is not absorbed, and the light penetrated into the GaN layer and reached the p-n junction. Then, optical absorption induced by the Franz-Keldysh (FK) effect occurs near the p-n junction interface (high electric field region), resulting in a hole-injected photocurrent. The photocurrent induced by the FK effect can be calculated by considering the theoretical absorption in the depletion region. Figure 5.28 shows the distributions of the electric field and the abosrption coefficient for 405 nm in the device under reverse bias of 100 V and 200 V. The absorption coefficient, which was calculated acccording to the distribution of the electric field using Eq. (4.3) [44], is observed to be localized at high electric field region, indicating that the optical absorption selectively occur near the p-n junction interface. In the calculation, the reduced effective mass of $\mu_{||} = 0.16m_0$ [45] was used for the calculation of the electric-field dependence of the absorption coefficient. The calculation method of the FK-induced photocurrent is described in [42] and Chapter 4.

The calculated curves of the photocurrent induced by the FK effect in the GaN p-n junction diode is shown in Fig. 5.27 as the red broken line. The calculated curve well reproduces the experimental photocurrent up to approximately 75 V. For higher voltage than about 75 V, the avalanche multiplication came to be striking. Compared to the photocurrent under above-bandgap illumination, the reverse voltage at which the avalanche multiplication starts to be striking is lower under sub-bandgap illumination.

5.3.4 Electron- and Hole-Initiated Multiplication Factors

The avalanche multiplication factors in the GaN p-n junction diode are extracted from the photocurrents under above- and sub-bandgap illuminations. The electron-initiated multiplication factor can be extracted as $M_{\rm n} = I_{\rm exp.313\ nm}/I_{\rm cal.n,dif}$. On the other hand, the hole-initiated multiplication factor can be extratced as $M_{\rm n} = I_{\rm exp.405\ nm}/I_{\rm cal.FK}$. Figure 5.29 shows the extracted multiplication factors versus the reverse bias voltage in the GaN p-n junction diode. In the plot, the data are shown as "$M-1$" in the semi-log plot to make the data near the unity at low electric field region easier to see. Owing to the low dark leakage current and accurate calculations of the unmultiplicated photocurrents based on the physics, the reliable multiplication factors are successfully obtained in wide range ($M-1$: 10^{-2}–10^3) with small noise. It is obviously observed that $M_{\rm n}$ is larger than $_{\rm p}$, indicating that $\alpha_{\rm n}$ is smaller than $\alpha_{\rm p}$ in GaN.

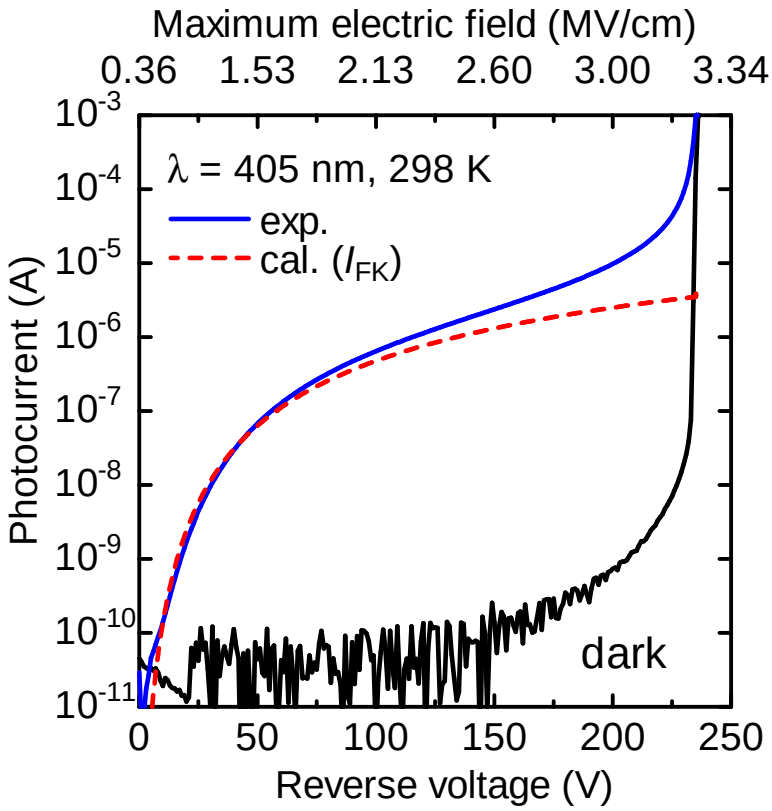

Figure 5.27: Reverse-voltage dependence of the photocurrent for sub-bandgap light (λ = 405 nm) in the GaN p-n junction diode at 298 K. Sub-bandgap optical absorption induced by the Franz-Keldysh effect occurs near the p-n junction interface (high electric field region) under reverse bias condition. The calculated curve with consideration of the optical absorption induced by the Franz-Keldysh in the depletion layer is also shown as a red broken line.

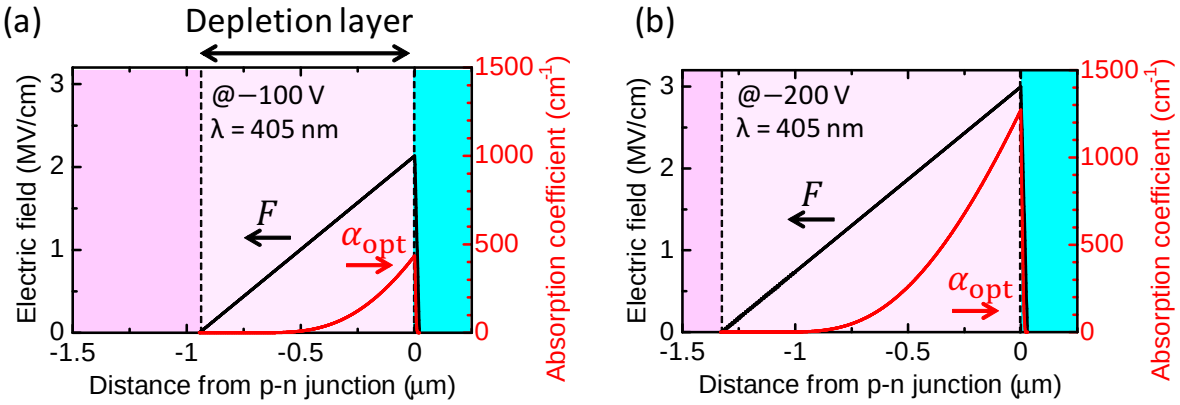

Figure 5.28: The distributions of the electric field and the absorption coefficient for 405 nm in the GaN p-n junction diode under the reverse bias condition of (a) 100 V and (b) 200 V. The photocurrent induced by the FK effect can be calculated by considering the distribution of the absorption coefficient, which is described in detail in [42] and Chapter 4.

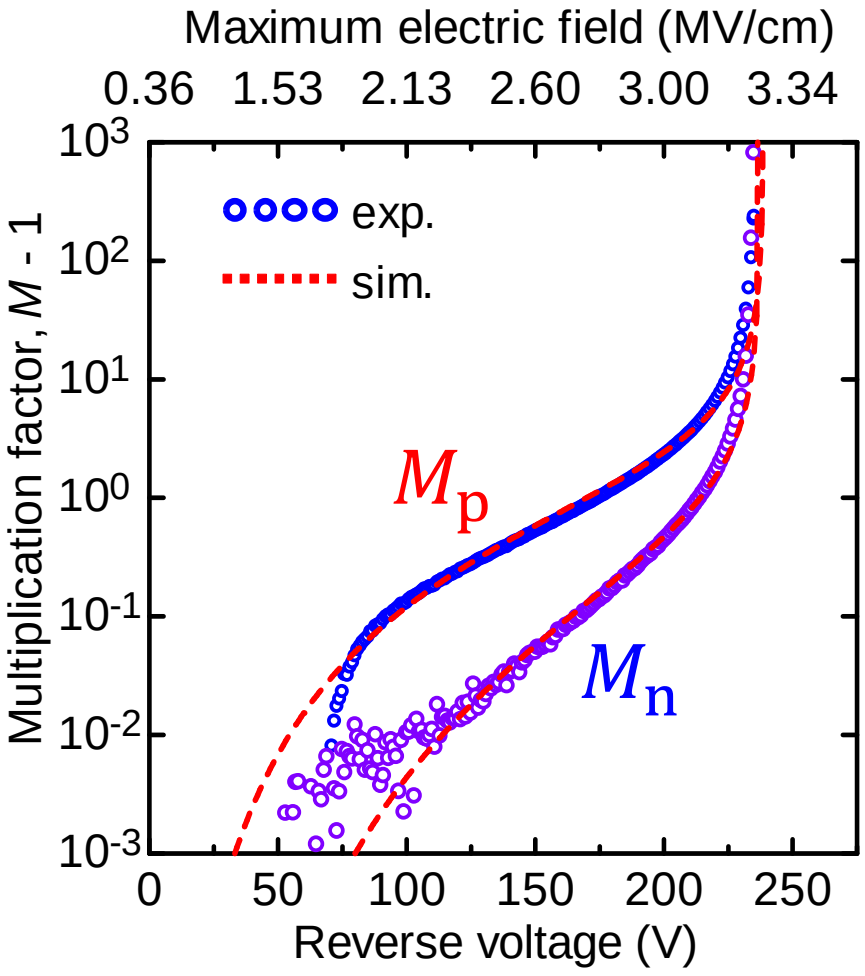

Figure 5.29: Reverse-voltage dependence of the electron- and hole-initiated multiplication factors in the GaN p^--n^+ junction diode. The simulated multiplication factors using the obtained αn and αp are also shown as red broken lines.

5.3.5 Extraction of Impact Ionization Coefficients

From the obtained electron- and hole-initiated multiplication factors (M_n, M_p), the impact ionization coefficients of electrons and holes (α_n and α_p) can extratced. M_n and M_p are expressed by the ionization integrals as [46]

$$1 - \frac{1}{M_\mathrm{p}} = \int_{-W_\mathrm{p}}^{0} \alpha_\mathrm{p} \exp\left[- \int_{x}^{0} (\alpha_\mathrm{p} - \alpha_\mathrm{n})\, dx' \right] dx, \tag{5.10}$$

$$1 - \frac{1}{M_\mathrm{n}} = \int_{-W_\mathrm{p}}^{0} \alpha_\mathrm{n} \exp\left[- \int_{-W_\mathrm{p}}^{x} (\alpha_\mathrm{n} - \alpha_\mathrm{p})\, dx' \right] dx. \tag{5.11}$$

For a non-punch-through one-side abrupt junction with a linear electric field distribution, the following expressions can be derived from Eqs. (5.10) and (5.11) based on the mathematical procedure reported by Woods *et al.* [5],

$$\alpha_\mathrm{p}(E_\mathrm{m}) = \frac{1}{M_\mathrm{n}(W)} \frac{d\ln[M_\mathrm{p}(W)]}{dW}, \tag{5.12}$$

$$\alpha_\mathrm{n}(E_\mathrm{m}) = \alpha_\mathrm{p}(E_\mathrm{m}) + \frac{d}{dW}\left[\ln\left(\frac{M_\mathrm{n}(W)}{M_\mathrm{p}(W)} \right) \right]. \tag{5.13}$$

The values of α_n and α_p that correspond to $E = E_\mathrm{m}$ can be extratced from $M_\mathrm{n}[W(V)]$ and $M_\mathrm{p}[W(V)]$ by the numerical analysis using the Eqs. (5.12) and (5.13).

Figure 5.30 shows the impact ionization coefficients of electrons and holes in GaN versus the inverse of electric field extracted in this study. The values of α_n and α_p were obtained with in the range of 2.5–3.0 MV/cm and 2.1–2.8 MV/cm, respectively. The noises in the data were relatively small and clear linearity was observed. The data were fitted and modeled by using the Chynoweth's empirical expression [1] as

$$\alpha_\mathrm{n}(E) = 2.69 \times 10^7 \cdot \exp\left(- \frac{2.27 \times 10^7 \text{ V/cm}}{E} \right) \text{ cm}^{-1}, \tag{5.14}$$

$$\alpha_\mathrm{p}(E) = 4.32 \times 10^6 \cdot \exp\left(- \frac{1.31 \times 10^7 \text{ V/cm}}{E} \right) \text{ cm}^{-1}. \tag{5.15}$$

The multiplication factors M_n and M_n in the device was simulated from Eqs. (5.10) and (5.11) using the obtained α_n and α_p modeled as Eqs. (5.14) and (5.15). The simulatde curves are shown in Fig. 5.29 as red broken lines, which well reproduce the experimental multiplication factors. This result suggests that the obtained values of α_n and α_p are accurate in these electric field ranges.

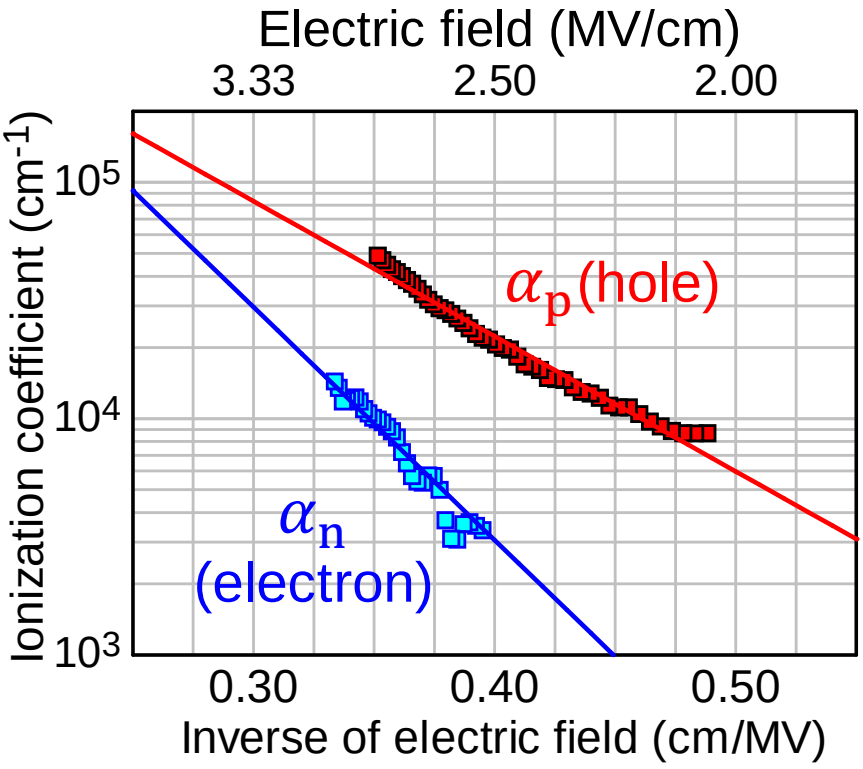

Figure 5.30: The impact ionization coefficients of electrons and holes in GaN versus the inverse of the electric field.

It is worth noting that the obtained α_n is several times smaller than α_p in GaN. This is a "counterintuitive" result, since it is well known that electrons in GaN are easy to be transported in low electric field: electron mobility is much higher than hole mobility. Although the same tendency is also observed in the previous reports [34, 38–40], the reason why α_n is smaller than α_p has not been discussed in these literatures. As mentioned in the section 5.1, $\alpha_n \ll \alpha_p$ is observed in 4H-SiC along the <0001> direction [11, 16] and was explained to originate from the anomalous conduction band structure. The analogy may be also seen in GaN: α_n and α_p strongly depend on the band structure (not only the bandgap). Figure 5.31 shows the calculated band structure of GaN in previous reports [35, 59]. GaN has the wurtzite (two-periodic hexagonal) crystal structure. Thus, the first Brillouin zone is folded into 1/2 width due to the Zone-Folding effect. The energy width of the first conduction band from the Γ point to the A point ($\Gamma \rightarrow$ A) is not wide ($\sim$2.5 eV) due to the narrow first Brillouin zone. The second conduction band along the $\Gamma \rightarrow$ A direction is near *horizontal*: the energy width is very narrow. The group velocity is near zero and electrons are transported without gaining energy in the second conduction band along $\Gamma \rightarrow$ A. The large discontinuity of $\sim$4.2 eV (mini energy gap) is observed in the conduction band along $\Gamma \rightarrow$ A. Therefore, a balistic impact ionization process without the assist/scattering of phonons is forbidden in GaN along $\Gamma \rightarrow$ A. In addition, the Bragg reflections from the zone edge (Bloch oscillation) also makes electrons in GaN along $\Gamma \rightarrow$ A hard to get high energy. In contrast, for holes, the first valence band is wide and the discontinuity of the valence band is very small. Therefore, the impact ionization coefficient of electrons is considered to be suppressed owing to the singular conduction band structure and smaller than that of holes in wurtzite GaN along the *c*-axis. The more accurate explanation needs further theoretical studies such as the full-band Monte Carlo simulation [60].

Figure 5.32 shows the comparison between the data of (α_n, α_p) and effective α ($\equiv \alpha_n = \alpha_p$) obtained in the section 5.2. The estimated α has the value between α_n and α_p. At low electric field region, α is observed to be close to α_p, and the value of α deviates from α_p and approaches to α_n with increasing electric field. The estimated value of α seems to be reasonable. Of course, the values of α_n and α_p are more accurate and useful for a device simulation.

Figure 5.33 shows the comparison between the data in Cao *et al.* [40] and in this study. For α_p, the almost consistent results were obtained in this study and the previous results. On the other hand, clear α_n with small noise was obtained in this study, the value of which is larger than the previous reports in the same electric field range. It should be noted that this difference causes the large error in the simulation of breakdown characteristics, since the avalanche multiplication is very sensitive to the values of α_n and α_p.

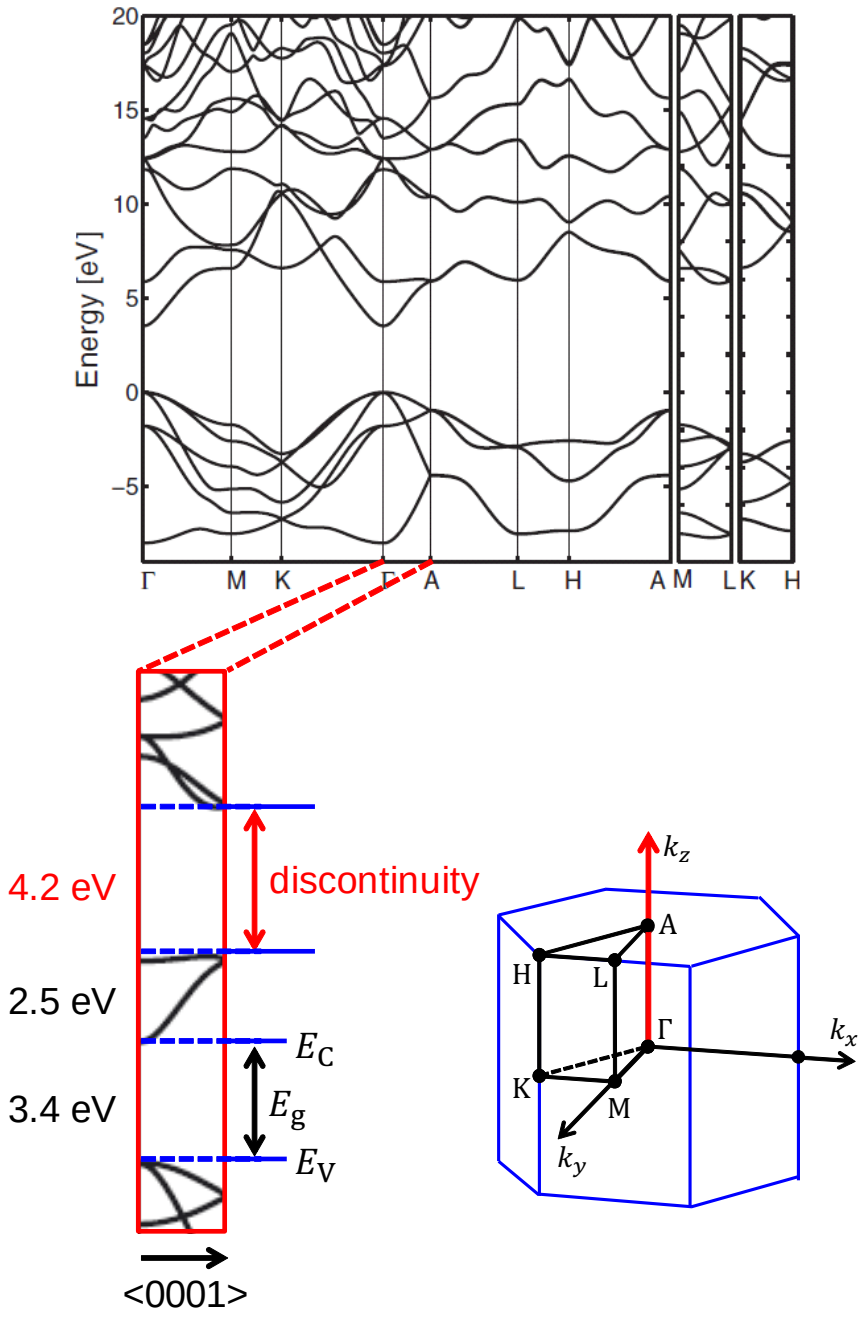

Figure 5.31: The calculated band structure of GaN [35, 59]. The first Brillouin zone is folded into 1/2 width due to the Zone-Folding effect along c-axis. From the Γ point (conduction band minimum) to the A point (along the c-axis), the energy width of the first conduction band is not wide (∼2.5 eV), the second conduction band has nearly horizontal structure, and the large discontinuity of ∼4.2 eV is observed in the conduction band along the Γ →A direction.

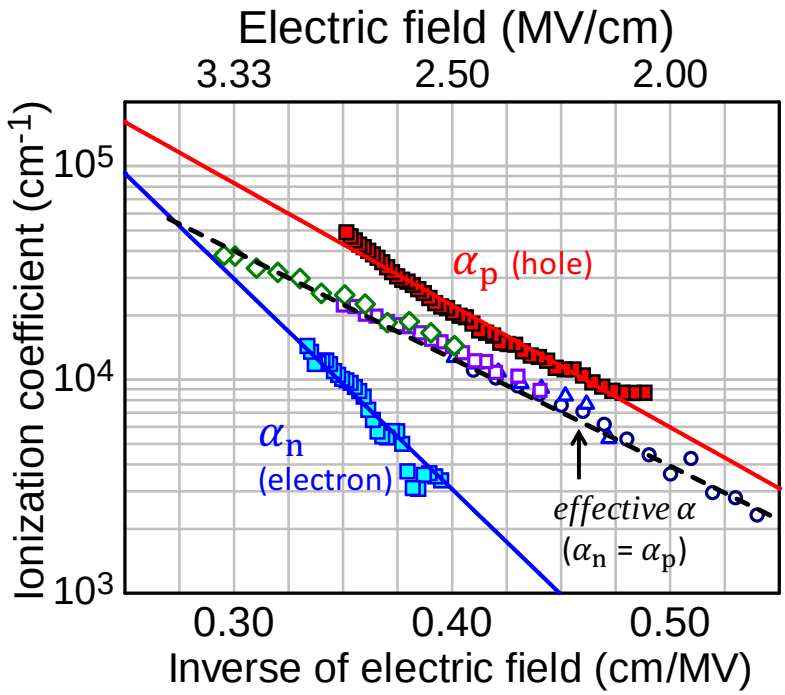

Figure 5.32: The comparison among α_n, α_p obtained in this section and α ($\equiv \alpha_n = \alpha_p$) estimated in the previous section 5.2.

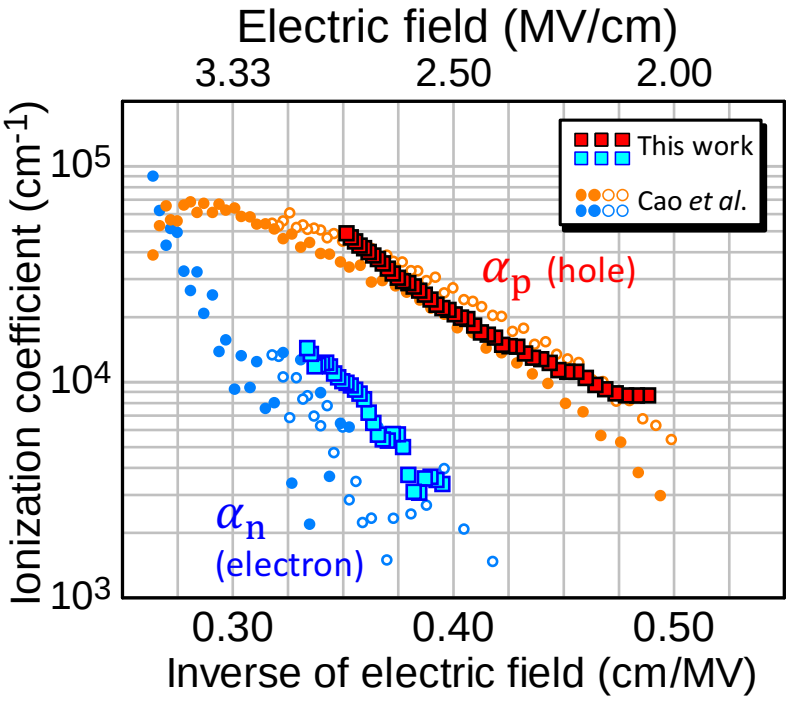

Figure 5.33: The comparison bewteen the impact ionization coefficients obtained in this study and the previosu reports [40].

5.3.6 Temperature Dependence of Impact Ionization Coefficients

The temperature dependence of the impact ionization coefficients in GaN were investigated in the range of 223–373 K. Figure 5.34 shows the reverse-voltage dependence of the photocurrent in the GaN p^-/n^+ junction diode under above-bandgap illumination at 223, 298 and 373 K. The photocurrent drastically decreased at elevated temperature, and the increase in the photocurrent at low voltage region (approximately 0–150 V) became steeper. The calculated curves using the Eq. (5.9) were also shown in Fig. 5.34 as broken lines. In the calculation, $L_{,\mathrm{n}}$ and D_n were treated as fitting parameters to determine the voltage dependence of the photocurrent, and $L_\mathrm{n} = 1.1$ μm, 0.61 μm and 0.30 μm and $D_\mathrm{n} = 40$ cm^2/s, 22 cm^2/s and 15 cm^2/s were obtained at 223 K, 298 K and 373 K, respectively. At elevated temperature, the electron diffusion length L_n decreased, which mainly reflected the decreasing electron mobility. The number of electrons which can reach the depletion layer decreased, resulting in the decrease in the photocurrent with elevating temperature. The calculated curves well agree with the experimental photocurrents at low voltage region for all the temperatures. Above about 150 V, avalanche multiplications were observed.

Figure 5.35 shows the reverse voltage dependence of the phtocurrent under sub-bandgap illumination at 223, 298 and 373 K. The temperature dependence of the photocurrent induced by the Franz-Keldysh effect can be calculated with consideration of the shrinkage of the bandgap with elevating temperature [42]. The calculated curves considering the temperature dependence of the bandgap [50] at 223, 298 and 373 K are also shown in Fig. 5.35 as broken lines. At low voltage region (approximately 0–75 V), a larger photocurrent is observed at higher temperature, which reflects the red shift of the GaN absorption edge (the shrinkage of the bandgap). Above about 75 V, avalanche multiplication is observed, and the multiplication is more striking at lower temperature.

Figure 5.36 shows the voltage dependence of the electron- and hole-initiated multiplication factors (M_n, M_p) extracted as the ratios of the experimental photocurrents to the calculated photocurrents for above- and sub-bandgap illuminations, respectively. Both M_n and M_p decreased at the same electric field and the breakdown voltage increased with elevating temperature, reflecting the decreasing impact ionization coefficients.

The multiplication factors were analyzed using the Eqs. (5.12) and (5.13). Figure 5.37 shows the obtained impact ionization coefficients of electrons and holes (α_n, α_p) at 223, 298 and 373 K. Both α_n and α_p decreased with elevating temperature, which is considered to be attributed to the enhanced phonon scattering rate with elevating temperature, as in other semiconductor materials. In addition, it should be noted that the temperature dependence of α_n is small. This may be related to the fact that α_n along <0001> in GaN is strongly affected by the anomalous conduction band structure. The effect to increase α_n may exist such as widening of the first conduction band width, the shrinkage of the mini energy gap, the increase of phonon-assisted transports, etc. To verify these speculations and to further understand α_n in GaN, theoretical studies are needed.

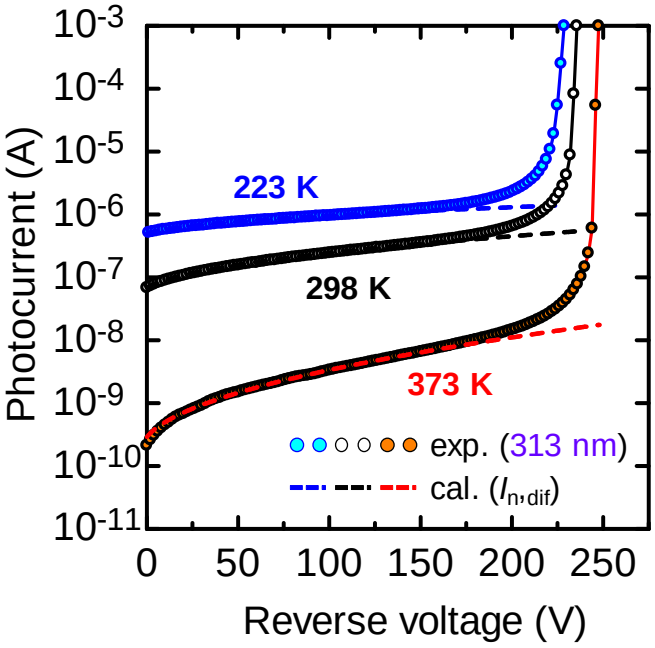

Figure 5.34: Reverse-voltage dependence of the photocurrent in a GaN p^-/n^+ junction diode under above-bandgap (313 nm) illumination at 223, 298 and 373 K. The calculation of the electron diffusion currents are also shown as broken lines.

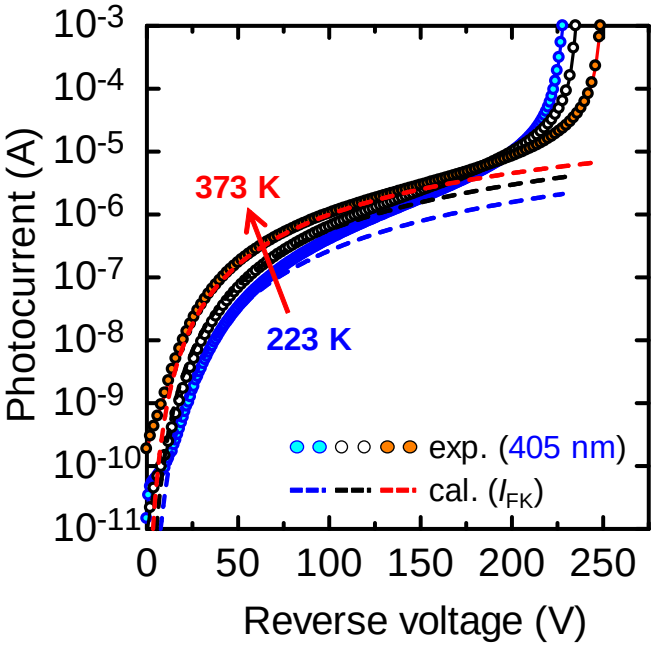

Figure 5.35: Reverse-voltage dependence of the photocurrent in a GaN p^-/n^+ junction diode under sub-bandgap (405 nm) illumination at 223, 298 and 373 K. The calculation of the Franz-Keldysh-induced photocurrents are also shown as broken lines.

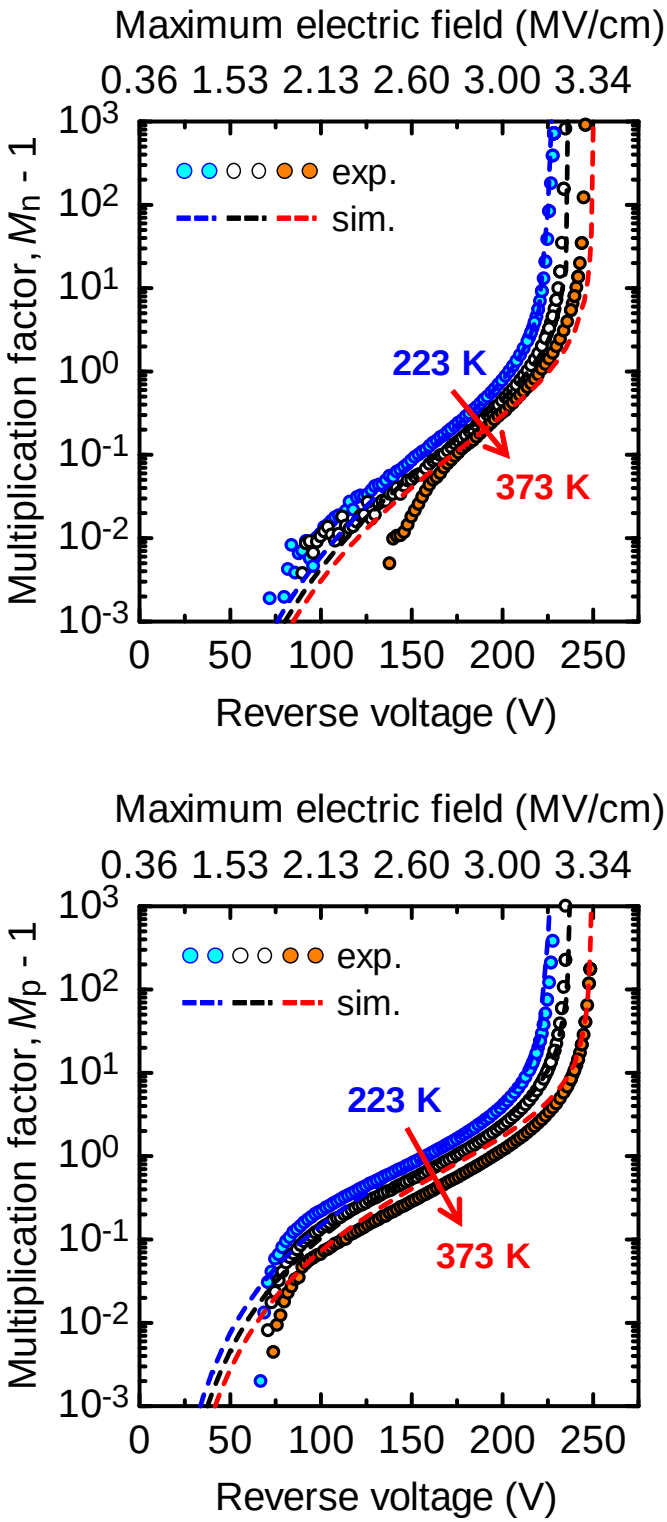

Figure 5.36: Reverse-voltage dependence of the electron- and hole-initiated multiplication factors (M_n, M_p) at 223, 298 and 373 K. The simulated curves using the obtained impact ionization coefficients in GaN are also shown as broken lines.

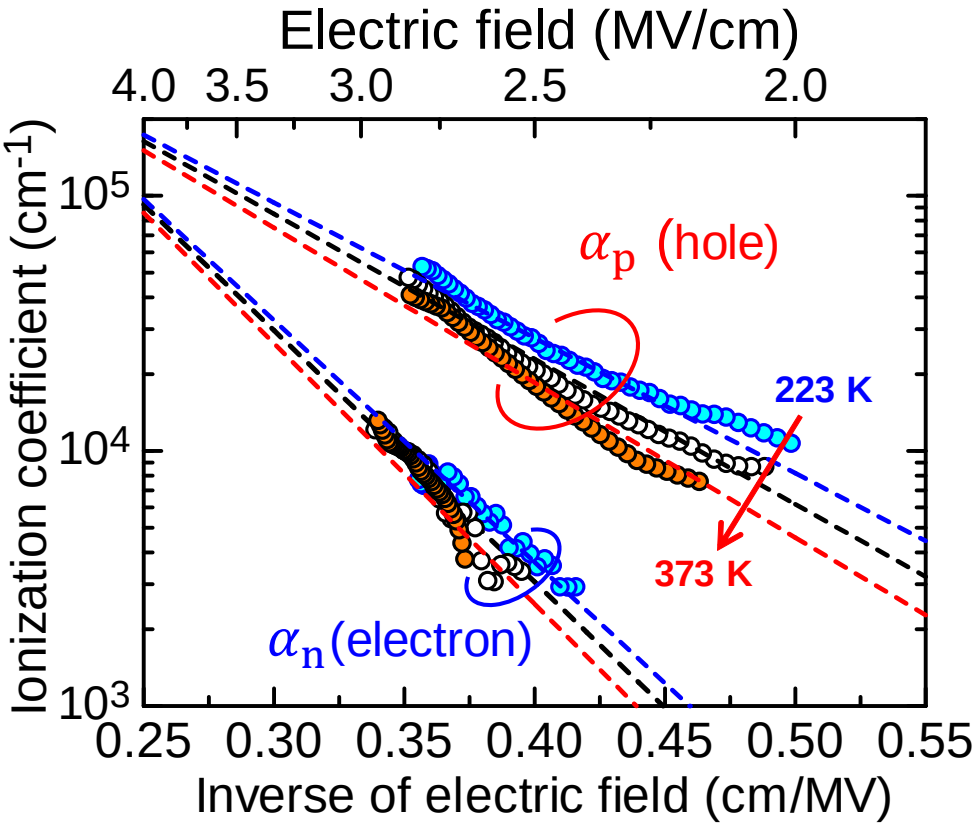

Figure 5.37: Impact ionization coefficients of electrons and holes in GaN obtained at 223, 298 and 373 K. The broken lines indicate the modeled values based on the Okuto-Crowell model [51].

The temperature dependence of the impact ionization coefficients are modeled based on the Okuto-Crowell model [51]:

$$\alpha_{\rm n}, \alpha_{\rm p}(E,T) = a \cdot (1 + b(T - 298\ {\rm K})) \cdot \exp\left[-\frac{c \cdot (1 + d(T - 298\ {\rm K}))}{E}\right]\ {\rm cm}^{-1}. \quad (5.16)$$

The obtained parameters (a, b, c, d) for $\alpha_{\rm n}$ and $\alpha_{\rm p}$ are summarized in Table 5.1. Using the temperature dependence of $\alpha_{\rm n}$ and $\alpha_{\rm p}$, $M_{\rm n}$ and $M_{\rm p}$ at 223, 298 and 373 K are simulated. The simulated curves are shown in Fig. 5.36, which show good agreement with the experimental $M_{\rm n}$ and $M_{\rm p}$. These results suggest the accuracy of the data in the range of 223–373 K.

5.4 Breakdown Voltage and Critical Electric Field

5.4.1 Non-Punch-Through Structure

To validate the accuracy of the obtained impact ionization coefficients and discuss the breakdown characteristics in GaN devices, avalanche breakdown voltages for parallel-plane junctions were simulated for GaN p-n junctions with various epitaxial structure. Figure 5.38 shows the simulated breakdown voltage for non-punch-through GaN p^+/n^- junctions with various donor concentrations at room temperature. The reported experimental data [43, 54, 61, 62, 62–69] are also shown. The simulated curve shows good agreement with the experimental data. Especially, our data [43, 63] and the data reported by Fukushima *et al.* [54], which exhibited the uniform avalanche breakdown without electric field crowding, are very close to the theoretical breakdown voltage. In the doping-concentration range of 2×10^{16}–2×10^{17} cm^{-3}, or the breakdown-voltage range of 180–900 V, the errors of the breakdown voltages are less than 6%. Figure 5.39 shows the simulated critical electric field versus doping concnentration for non-punch-through GaN p^+/n^- junctions with various donor concentrations. The experimental data of the breakdown electric field in GaN devices are also shown. The simulated curve well reproduces the experimental breakdown electric field. The critical electric field can be modeled by the following empirical formula,

$$E_{\rm cr} = \frac{2.40 \times 10^6}{1 - \frac{1}{4}\log_{10}(N_{\rm d}/10^{16}\ {\rm cm}^{-3})}\ {\rm V/cm}. \quad (5.17)$$

The provided critical electric field is convenient to expect and design the breakdown voltage of GaN power devices, although the impact ionization coefficients are the key properties and enable accurate device simulations. The donor cocentration and the required drift layer thickness (the depletion layer width at the breakdown) as a funtion of the breakdown voltage in GaN unipolar devices are shown in Fig. 5.40. This relationship enables to design/optimize an epitaxial structure of a GaN power device for required breakdown voltage.

Table 5.1: Parameters of the Okuto-Crowell model [51] for the temperature dependence of the impact ionization coefficients of electrons and holes in GaN obtained in this study.

	Electron (α_{n})	Hole (α_{p})
a (cm^{-1})	2.69×10^{7}	4.32×10^{6}
b (K^{-1})	2.00×10^{-3}	2.00×10^{-3}
c (V/cm)	2.27×10^{7}	1.31×10^{7}
d (K^{-1})	5.00×10^{-4}	9.00×10^{-4}

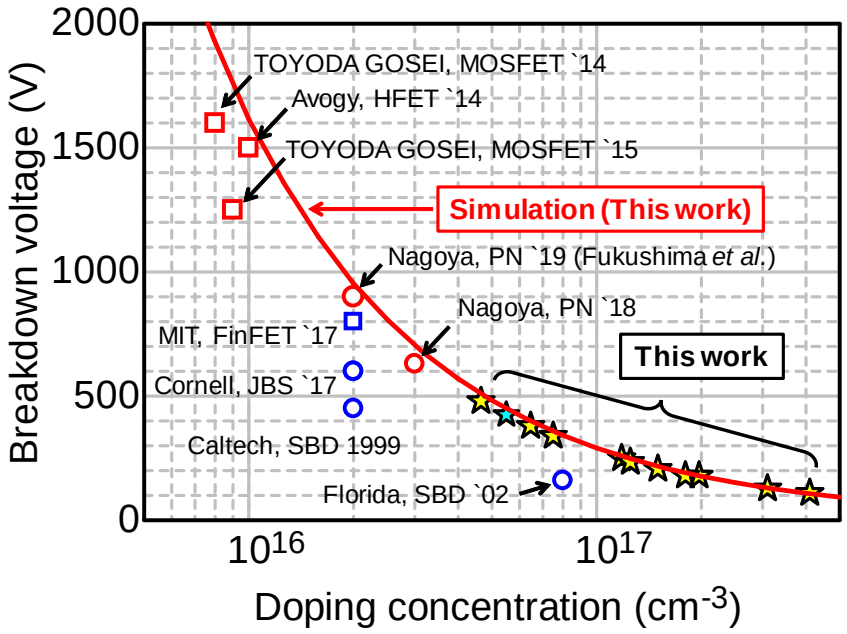

Figure 5.38: Breakdown voltage versus doping concentration in non-punch-through GaN p-n junctions. The experimental data reported previously [43, 54, 61–66, 68, 70, 71] are also shown.

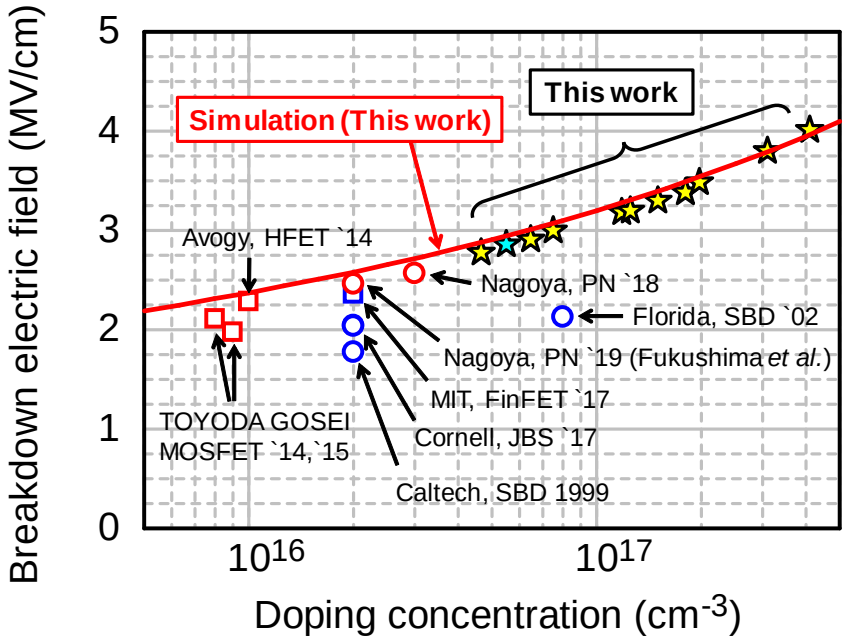

Figure 5.39: Critical electric field versus doping concentration in non-punch-through GaN p-n junctions. The experimental data of the breakdown electric field reported previously [43, 54, 61–66, 68, 70, 71] are also shown.

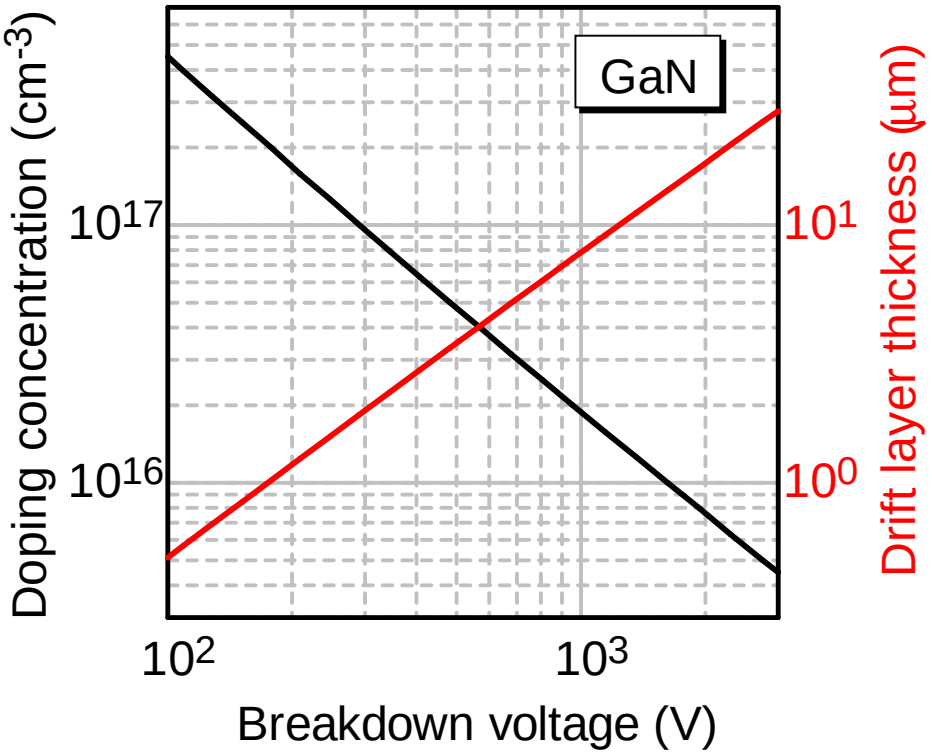

Figure 5.40: Doping concentration and thickness of the drift layer versus breakdown voltage for the non-punch-through structure in GaN unipolar devices.

5.4.2 Punch-Through Structure

If a drift layer thickness is thinner than the depletion layer width at the breakdown in the non-punch-through (NPT) condition, the depletion layer extends entire drift layer and the electric field distribution takes a trapezoid shape as shown in Fig. 5.41. This is called as the punch-through (PT) condition. Then, the ideal breakdown voltage is determined by not only a doping concentration but also a drift layer thickness. Figure 5.42 shows the simulated breakdown voltage versus doping concentration in GaN for the drift layer thicknesses of 5–25 μm. The breakdown voltage is limited by the drift layer thickness in the PT condition. For example, a 3.3 kV-class GaN power device needs the drift layer thickness of at least 20 μm. Figure 5.43 shows the critical electric field versus doing concentration in GaN for the drift layer thickness of 5–15 μm. In contrast to the breakdown voltage, the critical electric field in the PT condition is slightly higher than that in NPT condition and the difference between the PT and NPT conditions is very small in the case that a drift layer thickness is thicker than approximately 1/3 of a depletion layer width at the breakdown in NPT condition. For example, Figure 5.44 shows the distributions of electric field and impact ionization coefficients in GaN p^+/n^- junctions with donor concentration of 1×10^{16} cm^{-3} in NPT and PT (5 μm) conditions. The simulated breakdown voltages are different: the values are 1615 V and 972 V for NPT and PT (5 μm), respectively. On the other hand, the critical electric field and the electric field distribution in the range of 0–5 μm for NPT and PT are alsmost same. This is reasonable, since the impact ionization locally occurs at high electric field region and avalanche multiplication for low electric field region (<1 MV/cm) is negligible. Therefore, the critical electric field versus doping concentration in NPT condition (Eq. (5.17)) is also useful for the PT condition as far as the drift layer thickness is not extremely thinner than the depletion layer width in NPT condition.

5.4.3 Conduction Type Dependence of Ideal Breakdown Voltage

The breakdown voltages of p^+/n^- junction (n-drift layer) and p^-/n^+ junction (p-drift layer) are strictly different. The differences originate from the difference of the multiplication directions between electrons and holes as shown in Fig. 5.45. For p^+/n^- junction, holes are injected from lower electric field side and multiplicated to the higher electric field side. For electrons, which are injected from the higher electric field side or generated by the hole impact ionizations, are multiplicated to the lower electric field side. On the other hand, for p^-/n^+ junction, the directions are completely opposite. Mathematically, these are explained in Eqs. (5.1)–(5.3): the conditions of p^+/n^- and p^-/n^+ junctions are given by $W_p = 0$ and $W_n = 0$, respectively. Therefore, even if the doping concentration of the drift layer is identical, the process of the carrier multiplication indide the depletion layer is different for these two structures, resulting in the different breakdown characteristics. Figure 5.46 shows the simulated breakdown voltage and critical electric field in GaN p^+/n^- and p^-/n^+

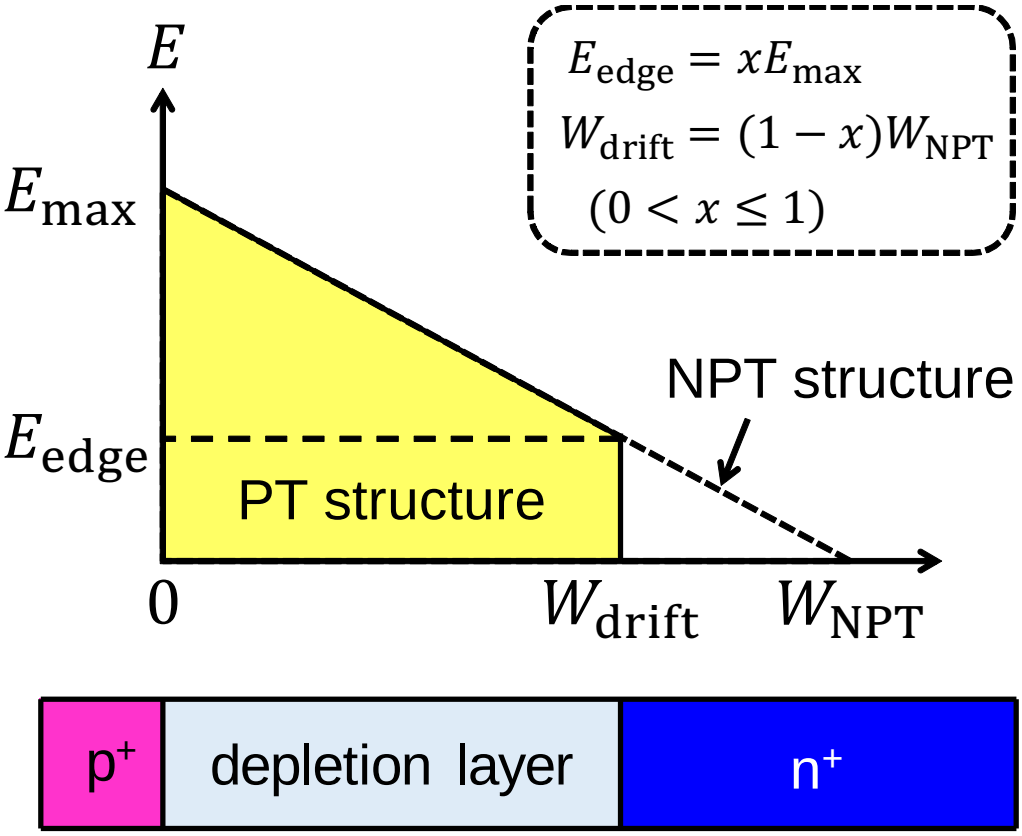

Figure 5.41: Schematic diagram of the electric field distribution in a punch-through structure.

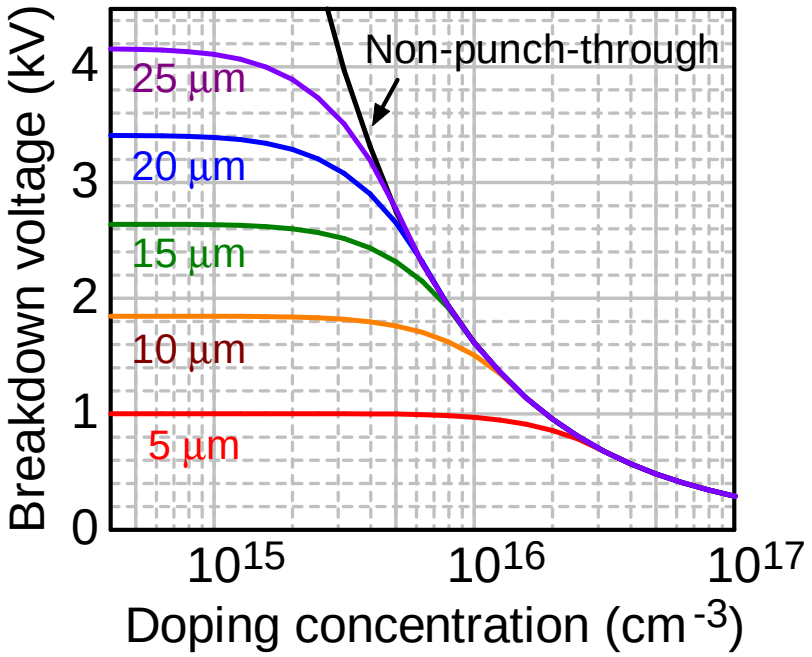

Figure 5.42: The simulated ideal breakdown voltage versus doping concentration in GaN for various punch-through structure with drift layer thicknesses of 5–25 μm.

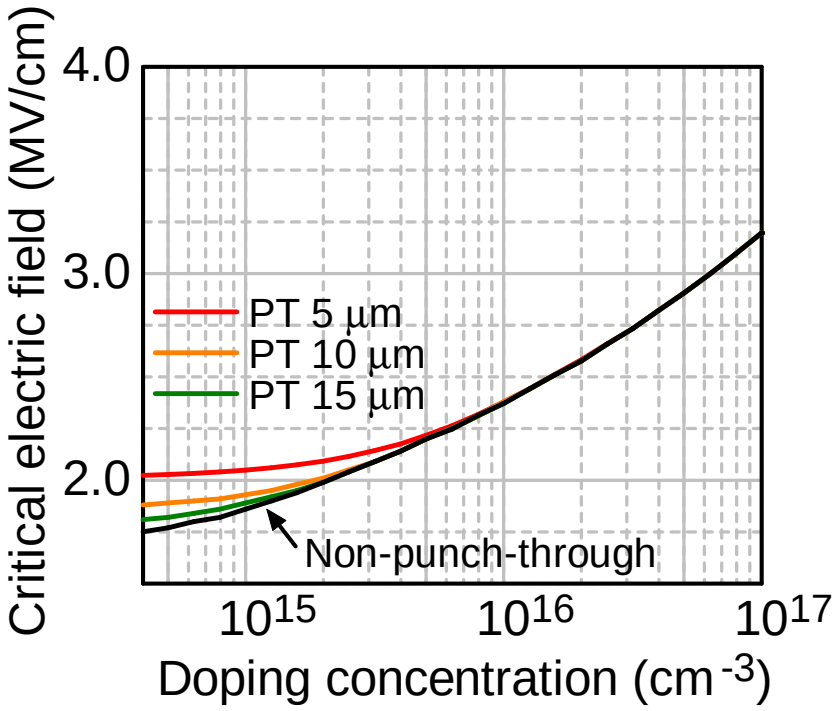

Figure 5.43: The simulated critical electric field versus doping concentration in GaN for various punch-through structure with drift layer thicknesses of 5–15 μm.

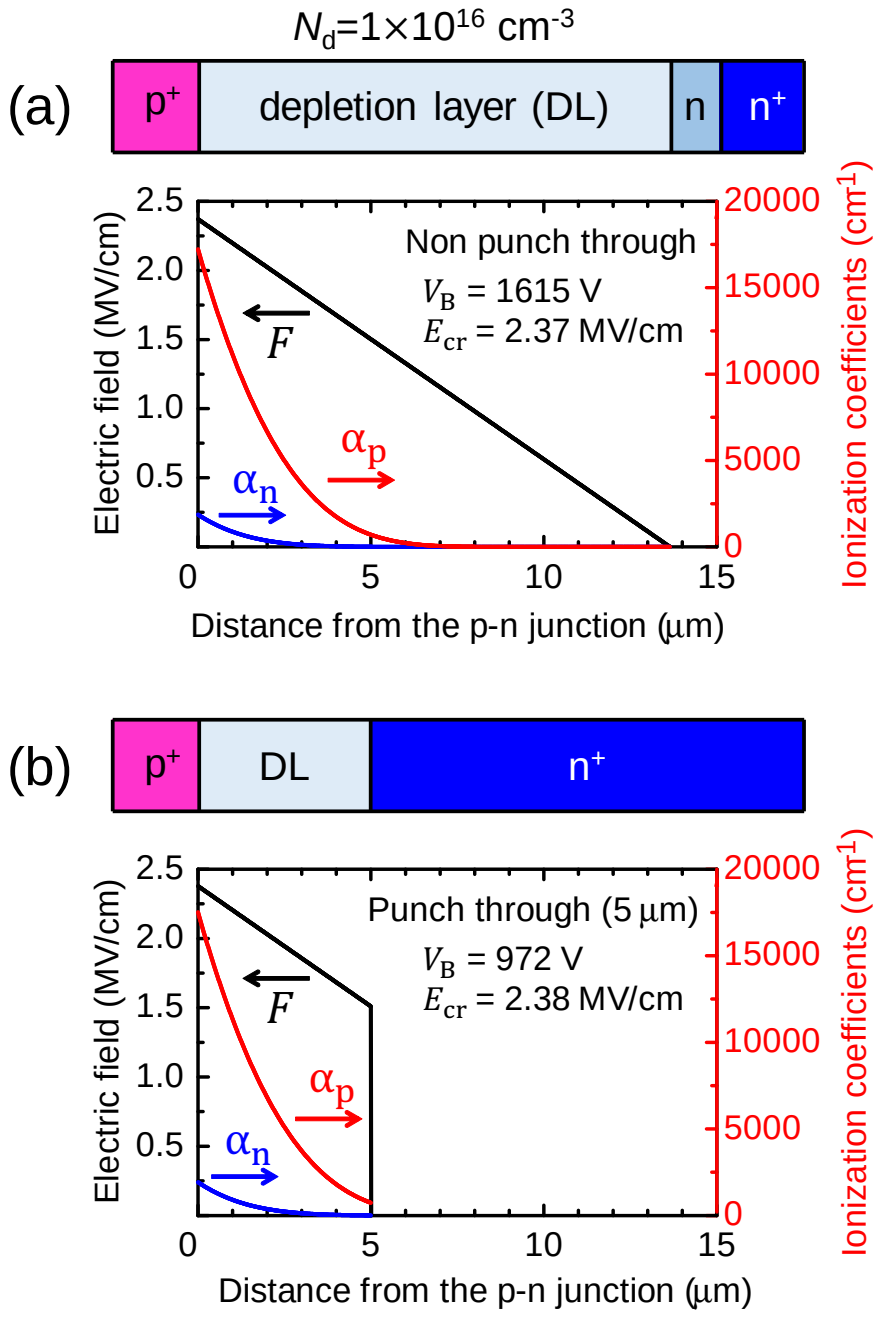

Figure 5.44: The distributions of electric field and impact ionization coefficients in GaN p^+-n^--n^+ junctions with the donor density of 1×10^{16} cm^{-3} in non-punch-through and punch-through (5 μm) conditions at the breakdown.

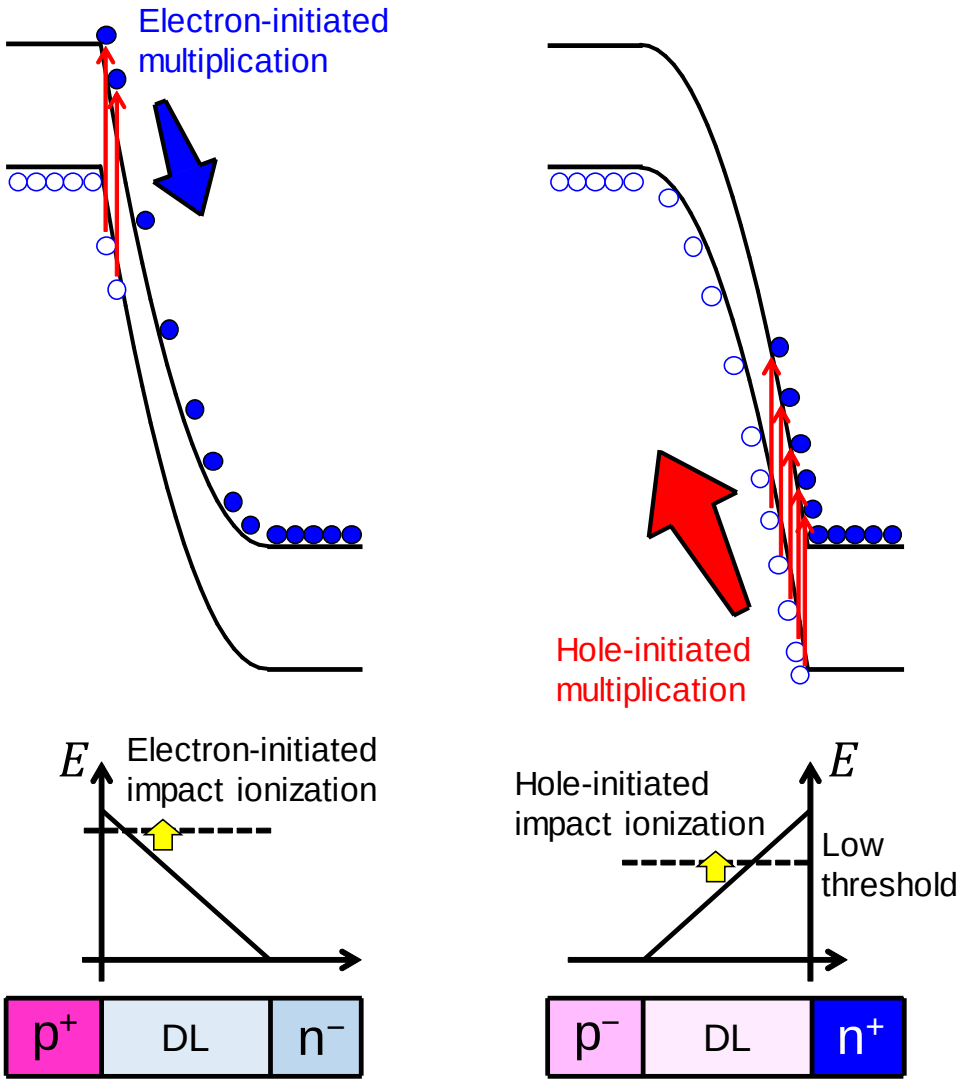

Figure 5.45: Schematic drawing of band diagrams and electric field distributions for p^+/n^- and p^-/n^+ junctions under high reverse bias.

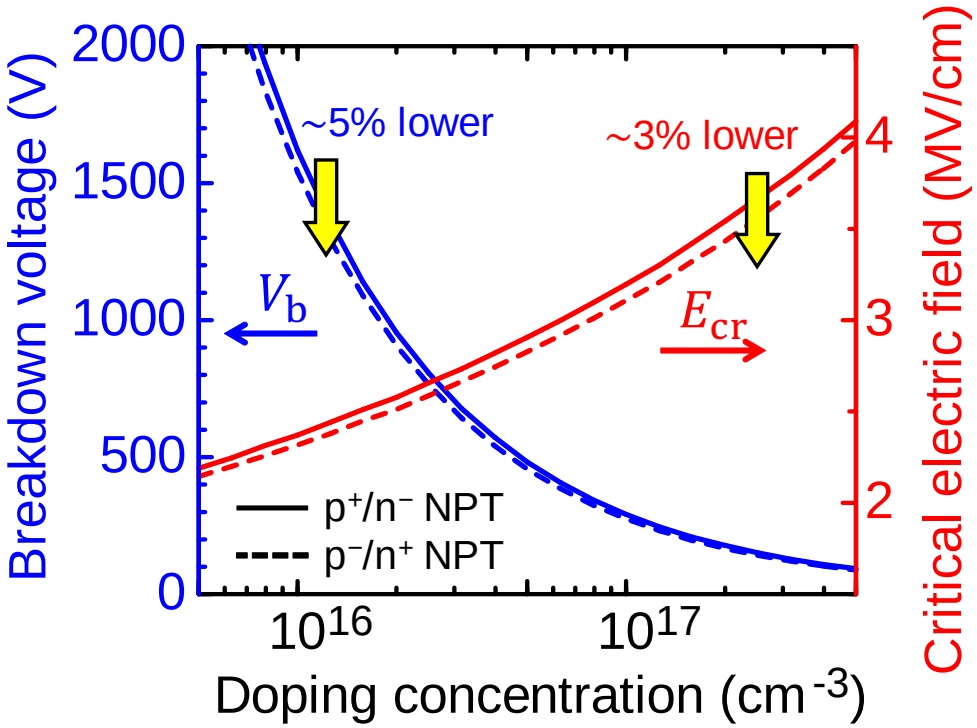

Figure 5.46: Ideal breakdown voltage and critical electric field for GaN p^+/n^- (n-drift layer) and p^-/n^+ (p-drift layer) structures.

junctions for non-punch-through condition. The breakdown voltage and critical electric field in p^-/n^+ junction are 5% and 3% lower than those in p^+/n^- junction, respectively. In Chapter 3, the distinguishable differences were not observed in the breakdown characteristics in p^+/n^- and p^-/n^+ junctions. However, these seem to be reasonable, since the simulated differences are small and difficult to be experimentally identified.

The conduction-type dependence of an ideal breakdown voltage depends on α_n and α_p. For example, the difference of the ideal breakdown voltage between the conduction types of the drift layer does not appear in GaAs where α_n and α_p have very similar values [10]. On the other hand, in 4H-SiC where α_n is much smaller than α_p along <0001>, the difference is larger than GaN: the breakdown voltage and critical electric field in p^-/n^+ junction are 9% and 5% lower than those in p^+/n^- junction, respectively [16, 56, 72].

5.4.4 Temperature Dependence

The breakdown voltage of GaN p^+/n^- junctions with various donor concentrations were simulated at 223, 298 and 373 K. Figure 5.47 shows the simulated breakdown voltage versus donor concentration in GaN at 223, 298 and 373 K. The inset shows the magnification plot in the range of 3×10^{16}–3×10^{17} cm^{-3}. The experimental data of the GaN p-n junction diodes in this study at 223, 298 and 373 K, which are described in [43] and Chapter 3, are also shown as filled circles. The simulated temperature dependence of the breakdown voltage show agreement with the experimental data.

Figure 5.48 shows the simulated critical electric field in GaN at 223, 298 and 373 K. The critical electric field can be modeled using the empirical formula as

$$E_{cr} = \frac{2.162 \times 10^6 + T \cdot 800 \text{ K}^{-1}}{1 - \frac{1}{4}\log_{10}(N_d/10^{16} \text{ cm}^{-3})} \text{ V/cm}. \tag{5.18}$$

T is temperature in Kelvin. The temperature dependence of the critical electric field in GaN is convenient and useful to expect the breakdown voltage of a GaN power device up to at least 373 K. It should be noted that the impact ionization coefficients obtained in this study are still limited in the temperature range of 223–373 K. The impact ionization coefficients and the critical electric field obtained in this study are only valid in this temperature range, and the data in higher and lower temperature range should be investigated. Especially, the values at high temperature (>200°) are important for a practical application.

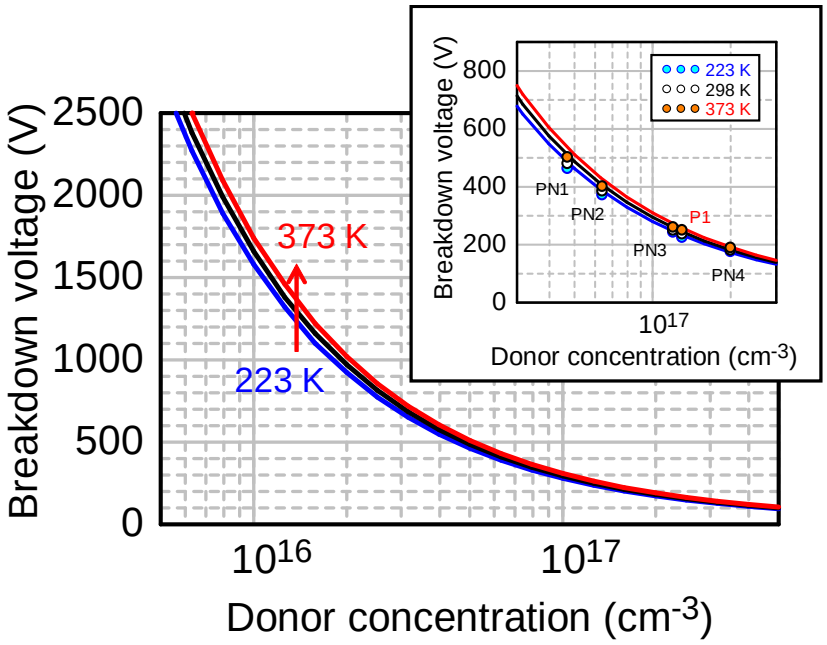

Figure 5.47: Breakdown voltage versus donor concentration in GaN p^+/n^- junction at 223, 298 and 373 K. Inset: the magnification plots in the range of 3×10^{16}–3×10^{17} cm^{-3}. The experimental data of the GaN p-n junction diodes in this study at 223, 298 and 373 K are also shown as filled circles.

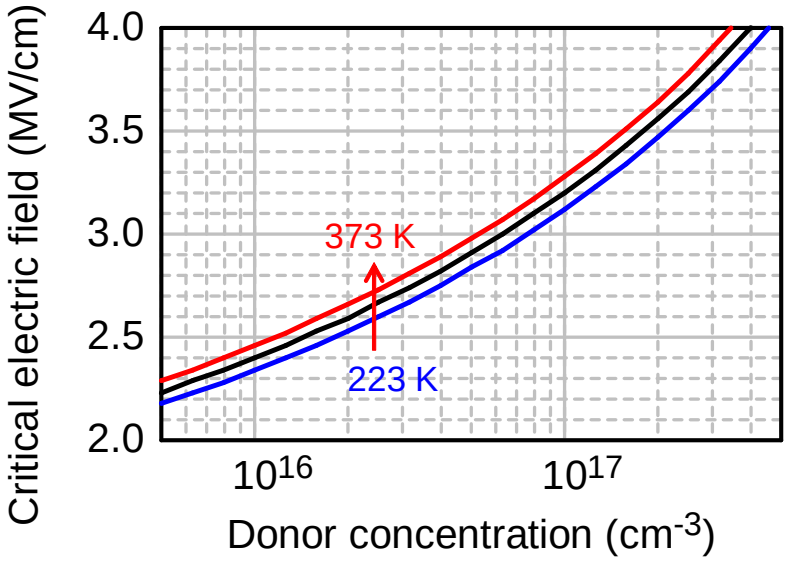

Figure 5.48: Critical electric field versus donor concentration in GaN p^+/n^- junction at 223, 298 and 373 K. The impact ionization coefficients obtained in this study are still limited in the electric field range of 2.1–3.0 MV/cm and the extrapolated values based on the Chynoweth's empirical formula were used for lower and higher electric field.

5.5 Trade-Off Relationship between On-Resistance and Breakdown Voltage

5.5.1 Non-Punch-Through Structure

Using the obtained critical electric field in GaN, the trade-off relationship between the specific on-resistance ($R_{\rm on}A$) and the breakdown voltage ($V_{\rm B}$) in GaN unipolar devices is updated here. The unipolar limit has usually calculated for a non-punch-through (NPT) structure by the following equation [73],

$$R_{\rm on}A = \frac{4V_{\rm B}^2}{\varepsilon_{\rm s}\mu E_{\rm cr}^3}. \tag{5.19}$$

$\varepsilon_{\rm s}$ is the dielectric constant of the semiconductor. $\varepsilon_{\rm s}$ for GaN has been well studied and the reliable value $\varepsilon_{\rm s,||} = 10.4\varepsilon_0$ is obtained in many reports [47, 48, 74, 75]. μ is the carrier mobility. Recently, electron mobility ($\mu_{\rm n,\perp}$) in hompepitaxial GaN layers grown on GaN(0001) bulk substrates have been investigated by Hall-effect measurement in detail [76, 77], as shown in Fig. 5.49. Electron mobility, the value of which reached approximately 1300 cm^2/Vs in samples low carrier concentration ($\sim 10^{15}$ cm^{-3}) at room temperature, is much higher than hole mobility [78]. The carrier concentration (n) dependence of $\mu_{\rm n,\perp}$ in GaN can be expressed by

$$\mu_{\rm n,\perp} = \frac{1325}{(1 + n/3 \times 10^{16}\ {\rm cm}^{-3})^{0.35}}\ {\rm cm}^2/{\rm Vs}. \tag{5.20}$$

The values of $\mu_{\rm n,\parallel}$ have not been studied in detail. Although some reports estimated $\mu_{\rm n,\parallel}$ from the I–V characteristics of GaN-on-GaN devices [79–81], the variations of the values are large owing to the difficulties to determine the effective device areas, the carrier concentrations and the drift layer thicknesses. Kasic *et al*. reported that the effective electron mass and the electron mobility obtained by the infrared spectroscopic ellipsometry have no significant anisotropy [82]. Therefore, the author assumes $\mu_{\rm n,\parallel} \sim \mu_{\rm n,\perp}$ and calculates the unipolar limit of GaN using the value of $\mu_{\rm n,\perp}$.

Figure 5.50 shows the trade-off relationship between the specific on-resistance of the drift layer and the breakdown voltage in GaN unipolar devices with an n-type drift layer for non-punch-through condition. In the calculation, the doping concentration dependences of the critical electric field and the eletron mobility are considered using Eqs. (5.16) and (5.18). The "Si limit" [53] is also denoted by a black line. The on-resistance of GaN is approximately 1/1000 times lower than that of Si at the same breakdown voltage. The "GaN limit" in NPT condition can approximately be expressed by the following fitting equation:

$$R_{\rm on,NPT}A = 2.90 \times 10^{-11} \cdot V_{\rm B}^{2.30}\ \Omega{\rm cm}^2. \tag{5.21}$$

The unit of $V_{\rm B}$ is volt. The power exponent of the $V_{\rm B}$ term "2.30" is larger than "2" which is expressed in Eq. (5.17). This result again originates from the critical electric field, which is

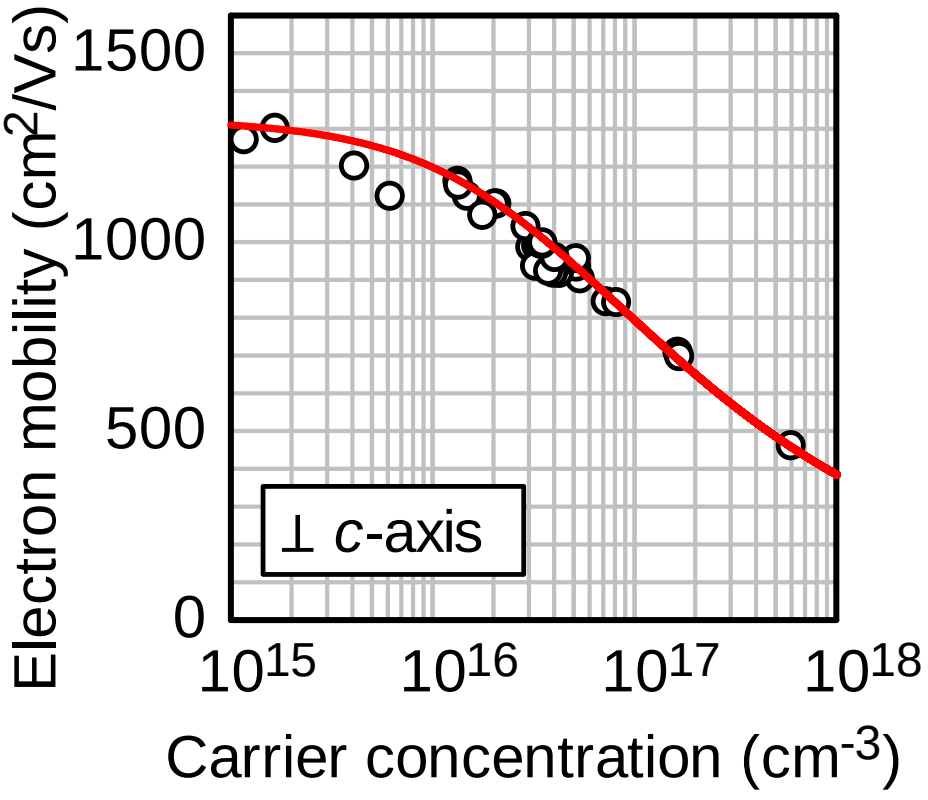

Figure 5.49: Electron mobility ($\mu_{n,\perp}$) in a homoepitaxial GaN layer grown on GaN(0001) substrates versus doping concentrations measured by Hall-effect measurement [76, 77].

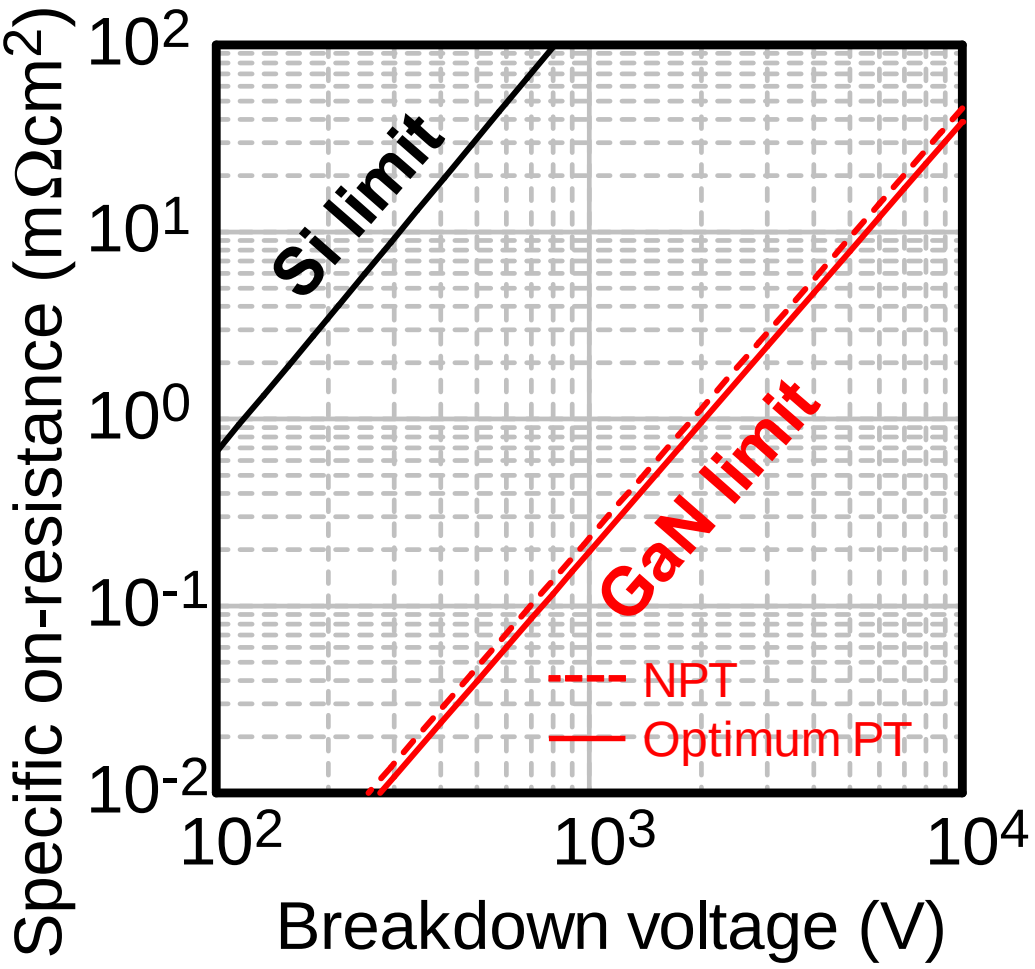

Figure 5.50: The trade-off relationship between the specific on-resistance of the drift layer and the breakdown voltage in GaN unipolar devices with an n-type drift layer for non-punch-through (red broken line) and optimum punch-through structure (red solid line). The curves were calculated using E_{cr} obtained in this study and $\mu_{\perp}$ [76], which are functions of doping concentration. The impact ionization coefficients obtained in this study are still limited in the electric field range of 2.1–3.0 MV/cm and the extrapolated value based on the Chynoweth's empirical formula was used for lower and higher electric field. In addition, the electron mobility may have an anisotropy, and $\mu_{n,\parallel}$ should be used. In the future, the "GaN limit" should be updated again using more accurate E_{cr} and $\mu_{n,\parallel}$. The "Si limit" [53] is also denoted by a black line.

a function of the doping concentration. Therefore, actually, the on-resistance more rapidly increases with the breakdown voltage owing to the decrease in the critical electric field with reducing the doping concentration.

5.5.2 Optimum Punch-Through Structure

In the PT condition, breakdown voltage and on-resistance are given by

$$V_{\mathrm{B}} = \frac{(1+x)E_{\mathrm{cr}}W}{2}, \quad R_{\mathrm{on}}A = \frac{W}{en\mu}, \tag{5.22}$$

where xE_{cr} ($0<x \leq 1$) is the electric field strength at the depletion layer edge W as shown in Fig. 5.41, which follows the following equation,

$$xE_{\mathrm{cr}} = E_{\mathrm{cr}} - \frac{eN_{\mathrm{d}}}{\varepsilon_{\mathrm{s}}}W. \tag{5.23}$$

The trade-off relationship between breakdown voltage and on-resistance as the Baliga figure of merit ($4V_{\mathrm{B}}/R_{\mathrm{on}}$) in the PT condition is expressed as

$$\frac{4V_{\mathrm{B}}}{R_{\mathrm{on}}} = \varepsilon_{\mathrm{s}}\mu E_{\mathrm{cr}}^3(-x^3 - x^2 + x + 1). \tag{5.24}$$

The equation (5.26) has the maximum value of $(32/27)\cdot\varepsilon_{\mathrm{s}}\mu E_{\mathrm{cr}}^3$ at $x = 1/3$. The actual situation is more complicated, since the doping concentrations in PT and NPT devices at the same breakdown voltage are different (E_{cr} and μ depend on a doping concentration). Figure 5.50 shows the trade-off relationship between breakdown voltage and on-resistance for GaN devices in NPT and optimum PT ($x = 1/3$). The PT structure yields a lower on-resistance than the NPT structure by approximately 15% at a given breakdown voltage and expressed as

$$R_{\mathrm{on,PT}}A = 2.45 \times 10^{-11} \cdot V_{\mathrm{B}}^{2.30}\ \Omega\mathrm{cm}^2. \tag{5.25}$$

This is the real "GaN limit" for optimum PT structure of GaN. The minimum specific on-resistance of 1.2 kV, 1.7 kV and 3.3 kV are as low as 0.35 mΩcm^2, 0.78 mΩcm^2 and 3.6 mΩcm^2, respectively, at room temperature. Although the on-resistance determined by the "GaN limit" is low, actual GaN power MOSFETs have exhibited much higher specific on-resistance due to other parasitic resistances such as channel resistance, substrate resistance, contact resistance, etc. The reduction of these paracitic resistances, especially improvement of the channel mobility, is one of the most crucial issues to unleash the full potential of GaN.

It should be noted that E_{cr} obtained in this study and $\mu_{\mathrm{n},\perp}$ [76] were used in the calculations. However, the impact ionization coefficients obtained in this study are still limited in the electric field range of 2.1–3.0 MV/cm and the extrapolated value based on the Chynoweth's empirical formula was used for lower and higher electric field. In addition, the electron mobility may have an anisotropy, and $\mu_{\mathrm{n},\parallel}$ should be used. In the future, the "GaN limit" should be updated again using more accurate E_{cr} and $\mu_{\mathrm{n},\parallel}$.

5.6 Discussion

Dead-Space Effect

For the carriers just injected from the high electric-field side of the one-side abrupt junction, the distance to gain sufficient energy from electric field is required. Therefore, the "dead space" where impact ionization of the just injected carriers does not occur exists. Figure 5.51 shows the case of non-punch-through one-side abrupt junction (an electric field distribution with right triangle shape). If the threshold energy to cause impact ionization ($\epsilon_{\mathrm{ii,th}}$) is assumed, $\epsilon_{\mathrm{ii,th}}$ follows the following relationship:

$$\epsilon_{\mathrm{ii,th}} = e\int_{-x_{\mathrm{DS}}}^{0} F(x)dx, \tag{5.26}$$

where $x = 0$ is the p-n junction interface. Here, the $\mathrm{p}^-/\mathrm{n}^+$ junction is considered. In the non-punch-through condition, the electric field distribution follows $F(x) = -eN_{\mathrm{a}}(x + W_{\mathrm{p}})/\varepsilon_{\mathrm{s}}$. In this study, electrons are injected from the low electric field side and the dead space does not exist. On the other hand, holes are injected from the high electric field side. Therefore, the obtained M_{p} actually reflected the avalanche multiplication in the effective electric field distribution with right triangle with dead space. The effective maximum electric field (E'_{m}) and the dead-space distance (x_{DS}) are expressed as

$$E'_{\mathrm{m}} = \sqrt{E_{\mathrm{m}}^2 - \frac{2N_{\mathrm{a}}}{\varepsilon_{\mathrm{s}}}\cdot\epsilon_{\mathrm{ii,th}}}, \quad x_{\mathrm{DS}} = \frac{2\epsilon_{\mathrm{ii,th}}}{e(E_{\mathrm{m}} + E'_{\mathrm{m}})}. \tag{5.27}$$

Then, the effective depletion layer width is $W_{\mathrm{p}} - x_{\mathrm{DS}}$. The effect of the dead space should be considered in the analysis. The analysis with consideration of the dead-space effect can be performed by referring the same depletion layer width (the same maximum electric field), not the same voltage, correcting M_{p}. The detail is described in [5].

For Si, the quantum yield of impact ionization, which is defined as the average number of impact ionization events caused by a hot carriers until its kinetic energy relaxes below the ionization threshold through phonon scattering and/or ionization events, has been studied [6]. Figure 5.52 shows the quantum yield of hot electrons versus kinetic energy in Si. The threshold is *soft* and the threshold energy is approximately $\sim 1.5E_{\mathrm{g,Si}}$. Kolnik and Oguzman *et al.* reported the theory of impact ionization of electrons and holes in GaN [33, 34]. Figure 5.53 shows the quantum yields of hot carriers versus kinetic energy for wurtzite GaN. It is observed that the both thresholds are soft and the threshold energy is different: $\epsilon_{\mathrm{ii,th}}$ of holes (~ 4 eV) is lower than that of electrons (~ 6 eV), the values of which include the uncertainty due to the lack of the experimental data of carrier transport under high elecric field. Since it is difficult to determine the value of $\epsilon_{\mathrm{ii,th}}$ of holes, the data of the multiplication factors were analyzed with consideration of various $\epsilon_{\mathrm{ii,th}}$. However, the clear difference was not observed in the analyzed results. For the device in this study, the dead space (the order of 10 nm) is much narrower than the total depletion layer (the order of 1 μm), and it was confirmed that the dead-space effect is very small.

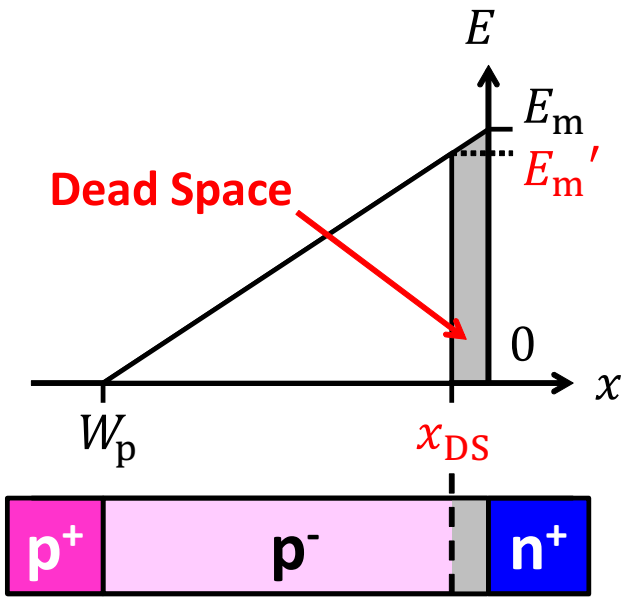

$$1-\frac{1}{M_{\mathrm{p}}}=\int_{-W_{\mathrm{p}}}^{0}\alpha_{\mathrm{p}}\exp\left[-\int_{-W_{\mathrm{p}}}^{x}(\alpha_{\mathrm{p}}-\alpha_{\mathrm{n}})dx'\right]dx$$

$$1-\frac{1}{M_{\mathrm{p}}'}=\int_{-W_{\mathrm{p}}}^{x_{\mathrm{DS}}}\alpha_{\mathrm{p}}\exp\left[-\int_{-W_{\mathrm{p}}}^{x}(\alpha_{\mathrm{p}}-\alpha_{\mathrm{n}})dx'\right]dx$$

(electron multiplication in $x_{\mathrm{DS}}<x<0$ is ignored)

Figure 5.51: Schematic drawing of the dead space effect occurring in a $\mathrm{p}^{-}/\mathrm{n}^{+}$ junction.

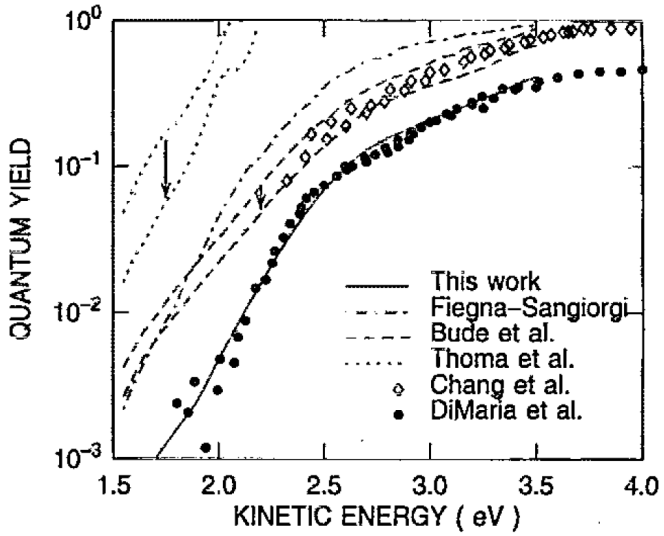

Figure 5.52: The quantum yield for electron-hole pair production as a function of electron kinetic energy in Si reported by Cartier *et al*. [6]. The threshold energy to cause impact ionization is approximately $1.5E_{\mathrm{g,Si}}$.

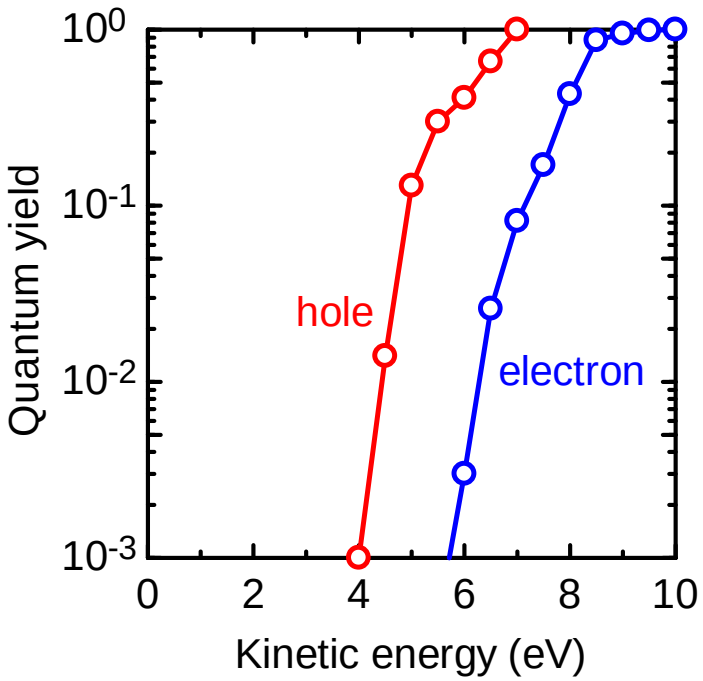

Figure 5.53: The quantum yield for electron-hole pair production as a function of electron and hole kinetic energy in GaN reported by Kolinik and Oguzman *et al*. [33, 34]. The threshold energies to cause impact ionization for electrons and holes are approximately 4 eV and 6 eV, the values of which include the uncertainty, respectively.

Effect of Mixed Carrier Injection by the Franz-Keldysh Effect

In the analysis using the formulae (5.12) and (5.13), the pure hole injection was assumed: holes were injected, or electron-hole pairs were generated, at the edge of the depletion layer W_{n}. However, the optical absorption induced by the FK effect is spacially distributed in the depletion region, resulting in mixed carrier injection. Actually, the multiplication factor obtained from the photocurrent for sub-bandgap illumination (M_{FK}) is expressed as

$$M_{\mathrm{FK}} = \frac{\int_{-W_{\mathrm{p}}}^{W_{\mathrm{n}}} G_o(x) \cdot M(x) dx}{\int_{-W_{\mathrm{p}}}^{W_{\mathrm{n}}} G_o(x) dx}, \tag{5.28}$$

where $M(x)$ is multiplication factor as a function of the depth where electron-hole pairs are generated, and G_o is the generation rate of the electron-hole pairs in the depletion layer induced by the optical absorption due to the FK effect. Although it is difficult to obtain accurate value of G_o, the spatial distribution almost directly reflects the distribution of the absorption coefficient $\alpha_{\mathrm{opt}}(F, x)$. Figure 5.54 shows the distribution of the absorption ratio as a function of the distance from the p-n junction normalized by the total depletion layer width (W_{p}) for the reverse bias of 100 V and 200 V. Near 40% of the total absorbed photon is absorbed at the p-n junction interface, and the absorption ratio gently decreases as the position becomes far from the p-n junction interface.

It is very difficult to analyze the multiplication factors with consideration of the mixed carrier injection and its distribution. On the other hand, a reflexive simulation of the multiplication factors with considering the mixed carrier injection after obtaining the impact ionization coefficients using the formula (5.26) are possible. Figure 5.55 shows the simulated M_{FK} with consideration of the distribution of the optical absorption induced by the FK effect using the obtained impact ionization coefficients. The simulated M_{FK} is slightly smaller than the measured M_{FK}, which is treated as M_{p} in the extraction of the impact ionization coefficients from the multiplication factors. This indicates the actual M_{p} for the pure hole injection maybe slightly larger. Therefore, the obtained α_{p} seems to be slightly underestimated. However, the simlated breakdown voltage well reproduced the experimental breakdown voltage and the error is small.

The measurement method proposed in this study enables the selective carrier injection at high electric field region for simple test device structure without back side etching or the InGaN inserted layer. However, the mixed injection caused by the FK effect is an intrinsic problem in this measurement method. Although the error is small, the more accurate values of α_{p} and α_{n} should be obtained in the future.

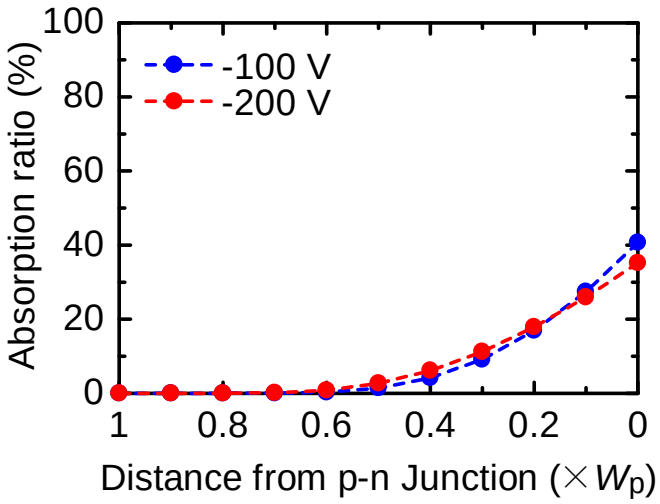

Figure 5.54: The distribution of the absorption ratio as a function of the distance from the p-n junction normalized by the total depletion layer width (W_{p}) for the reverse bias of 100 V and 200 V.

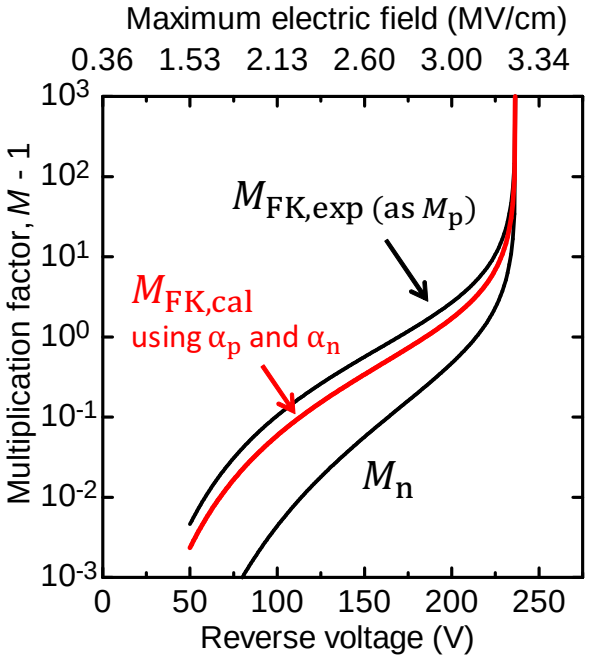

Figure 5.55: The simulated M_{FK} with consideration of the distribution of the optical absorption induced by the FK effect in the depletion region using the obtained impact ionization coefficients. Due to the mixed carrier injection, the measured multiplication factor under sub-bandgap illumination is slightly smaller than the ideal M_{p} for pure hole injection, which may cause the underestimation of α_{p}.

Comparison between SiC and GaN

The ideal avalanche breakdown characteristics of SiC and GaN are compared and discussed based on their impact ionization coefficients. Figure 5.56 shows the impact ionization coefficients in 4H-SiC [16] and wurtzite GaN (this work) along <0001>. For the hole impact ionization coefficient α_{p}, the value in GaN is almost same or slightly smaller than that of SiC. This seems to be reasonable, since the bandgap of 3.42 eV in GaN is slightly wider than the bandgap of 3.26 eV in 4H-SiC at room temperature. On the other hand, for the electron impact ionization coefficient α_{n}, the value in GaN is approximately three times larger than that in SiC at the same electric field. This is very counterintuitive. However, it can be explained by considering the anomalous conduction band structure in 4H-SiC [11, 72]. The first Brillouin zone along the c-axis is folded into "1/4", the energy width of the first conduction band is very narrow and the minigap exists from the M point (the conduction band minimum) to L point. The band structure of 4H-SiC is shown in Fig. C.2 in Appendix. C. Therefore, electrons in 4H-SiC are also hard to gain high energy, and α_{n} is strongly suppressed.

Figure 5.57 shows (a) the ideal breakdown voltage and (b) the critical electric field versus doping concentration in 4H-SiC and wurtzite GaN $\mathrm{p}^+/\mathrm{n}^-$ junctions under electric field along <0001> simulated by using the impact ionization coefficients. Due to the larger α_{n} in GaN, the critical electric field in GaN is actually approximately 6% lower than SiC, although many researchers have believed that GaN has higher critical electric field than SiC. Figure 5.58 shows the trade-off relationship between breakdown voltage and on-resistance in Si [53], SiC [83] and GaN (this work). Owing to higher electron mobility in GaN compared to 4H-SiC, the unipolar "4H-SiC limit" and "GaN limit" are almost same in the entire breakdown voltage range. As mentioned in the section 5.5.2, the GaN limit should be updated again using more accurate E_{cr} and $\mu_{\mathrm{n},\parallel}$.

The research and development of SiC have been preceding, and the process technologies and fundamental researches are advanced. The market of SiC power devices is expected to keep expanding in next decades. However, there are still some remaining issue. Especially, the channel mobility is very poor, which limits the perfomance of SiC MOSFETs [84].

The research and development of GaN-on-GaN power devices are just started. The process technologies such as Mg ion implantation [85] has been significantly developed and fundamental studies have been intensively performed in recent years. There are many merits of GaN: the high channel mobility, the high drift velocity, the availability of heterojunctions and 2DEG. In addtion, the most important things for power devices are *cost* and *reliability*. If GaN bulk substrates becomes higher quality, larger diamaeter and cheaper in the future, it is not impossible that GaN power devices will catch up and overtake SiC power devices.

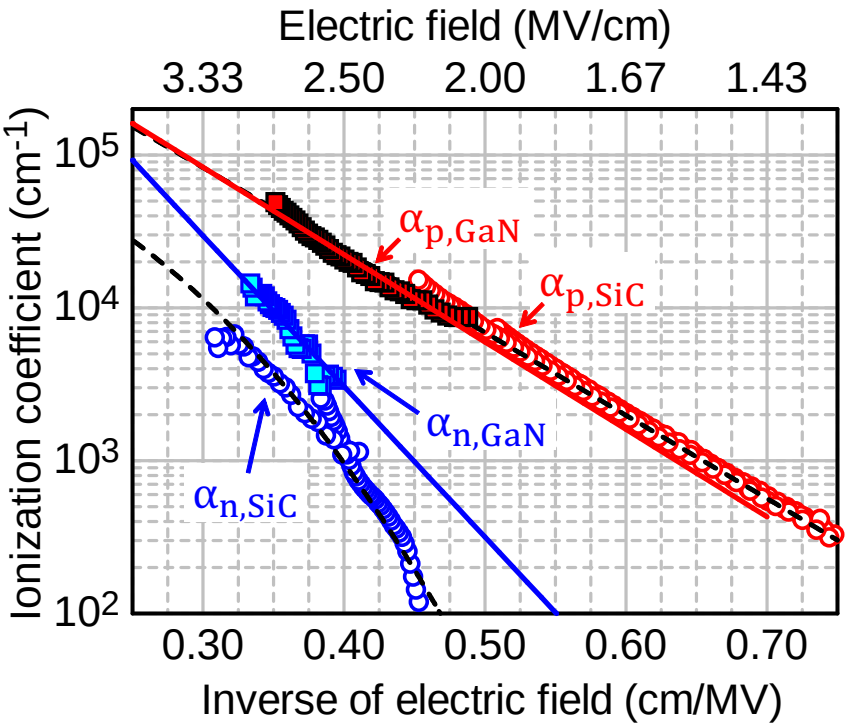

Figure 5.56: The impact ionization coefficients in 4H-SiC [16] and wurtzite GaN (this work) under electric field along the <0001> direction.

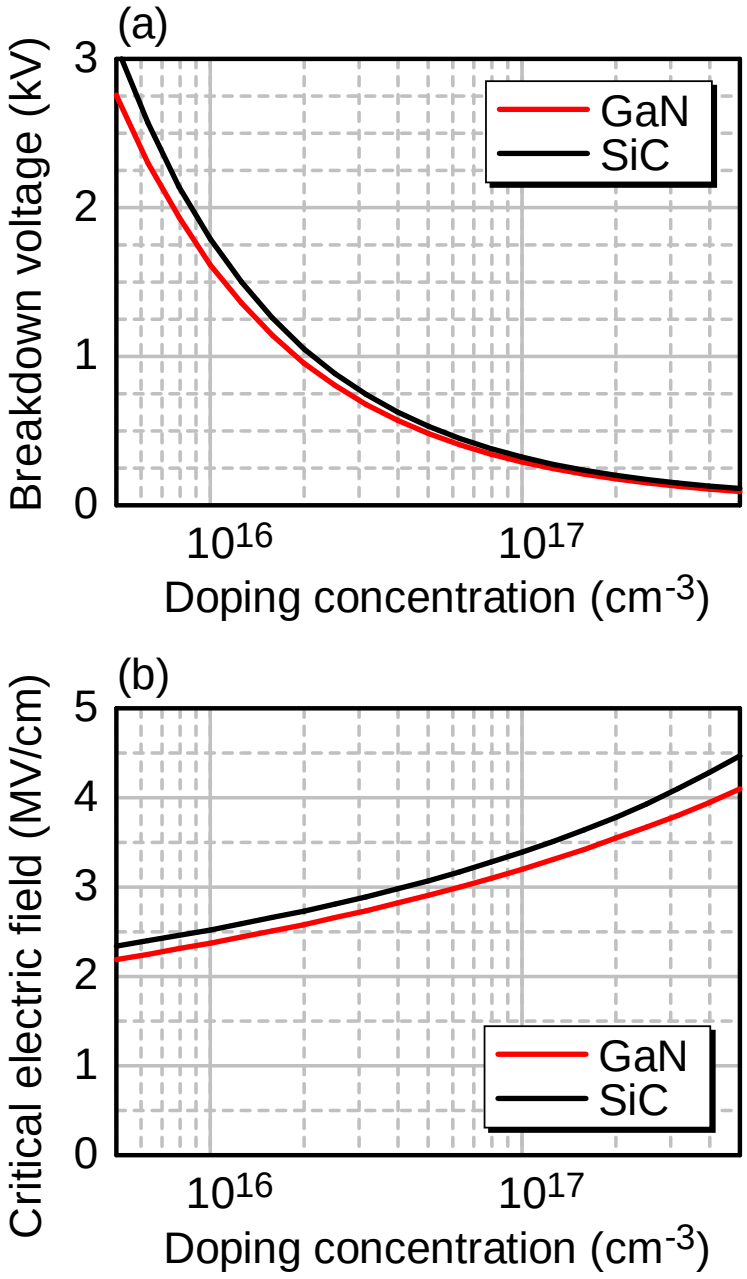

Figure 5.57: (a) The ideal breakdown voltage and (b) the critical electric field versus doping concentration in 4H-SiC [16] and wurtzite GaN p^+/n^- junctions under electric field along <0001> simulated by using the impact ionization coefficients. The impact ionization coefficients obtained in this study are still limited in the electric field range of 2.1–3.0 MV/cm and the extrapolated value based on the Chynoweth's empirical formula was used for lower and higher electric field.

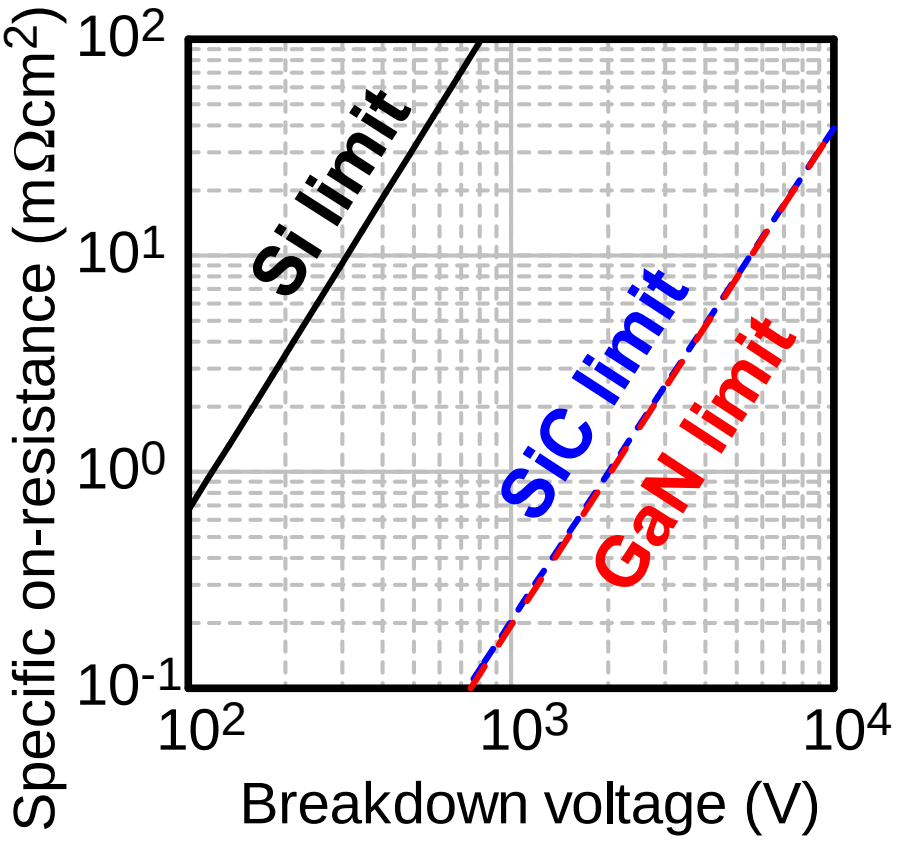

Figure 5.58: The trade-off relationship between breakdown voltage and on-resistance in Si [53], SiC [83] and GaN (this work). The GaN limit was calculated using E_{cr} obtained in this study and $\mu_{\perp}$ [76] as functions of doping concentration. The impact ionization coefficients obtained in this study are still limited in the electric field range of 2.1–3.0 MV/cm and the extrapolated value based on the Chynoweth's empirical formula was used for lower and higher electric field. In addition, the electron mobility may have an anisotropy, and $\mu_{n,\parallel}$ should be used. In the future, the "GaN limit" should be updated again using more accurate E_{cr} and $\mu_{n,\parallel}$.

5.7 Summary

In this study, the novel method to measure impact ionization coefficients of electrons and holes was proposed. The sub-bandgap optical absorption induced by the Franz-Keldysh effect has a unique nature: the optical absorption selectively occurs at high electric field region. In addition, the photocurrent induced by the Franz-Keldysh effect is well predictable. The photomultiplication measurement utilizing the Franz-Keldysh effect was performed for GaN p-n junction diodes with doble-side-depleted shallow bevel termination, which exhbited the uniform (nearly ideal) avalanche breakdown. The multiplication factors were successfully extratced as the ratio of the experimental photocurrent to the calculated Franz-Keldysh-induced photocurrent, and the value of the impact ionization coefficients in GaN was estimated under the assumption of $\alpha_{\mathrm{n}} = \alpha_{\mathrm{p}}$.

The photomultiplication measurement utilizing above- and sub-bandgap illumnations were also performed for a GaN $\mathrm{p}^-/\mathrm{n}^+$ junction diode. The photocurrent induced by the diffusion of electrons generated at the surface (electron injection) and the photocurrent induced by the Franz-Keldysh effect (hole injection) were obtained by above- and sub-bandgap illuminations, respectively. The electron- and hole-initiated multiplication factors were obtained in wide range ($M-1$: 10^{-2}–10^{3}) with small noises. By analyzing the multiplication factors, the impact ionization coefficients of electrons and holes in GaN are successfully obtained. The simulated curves using the obtained α_{n} and α_{p} are confirmed to well reproduce the multiplication factors in the device and the breakdown characteristics of GaN devices reported previously, suggesting the high accuracy of the data. The critical electric field of GaN was modeled, and the the trade-off relationships between the breakdown voltage and the specific on-resistance as the "GaN limit" for non-punch-through and optimum punch-through structures was presented.

These results are valuable to understand impact ionization and avalanche multiplication phenomena in GaN, and the obtained parameters are useful for a device simulation of avalanche breakdown in a GaN power device.

References

[1] A. G. Chynoweth, *Phys. Rev.* **109(5)**, 1537 (1958).

[2] R. A. Logan, A. G. Chynoweth, and B. G. Cohen, *Phys. Rev.* **128**, 2518 (1962).

[3] R. Van Overstraeten and H. De Man, *Solid State Electron.* **13**, pp.583–608 (1970).

[4] W. N. Grant, *Solid State Electron.* **16**, pp.1189–1203 (1973).

[5] M. H. Woods, W. C. Johnson, and M. A. Lampert, *Solid State Electron.* **16**, pp.381–394 (1973).

[6] E. Chartier, M. V. Fichetti, E. A. Eklund, and F. R. McFeely, *Appl. Phys. Lett.* **62**, 3339 (1993).

[7] Y. J. Chang and S. M. Sze, *J. Appl. Phys.* **40**, 5392 (1969).

[8] G. E. Stilman, C. M. Wolf, J. A. Rossi, and A. G. Foyt, *Appl. Phys. Lett.* **24**, 10 (1974).

[9] M. Ito, S. Kagawa, T. Kaneda, and T. Yamaoka, *J. Appl. Phys.* **49(8)**, 4607 (1978).

[10] G. E. Bulman, V. M. Robbins, and G. E. Stillman, *IEEE Trans. Electron Devices* **32(11)**, pp.2454–2466 (1985).

[11] A. O. Konstantinov, Q. Wahab, N. Nordell, and U. Lindefelt, *Appl. Phys. Lett.* **71(1)**, 90 (1997).

[12] R. Raghunathan and B. J. Baliga, *Proc. of Int. Symp. on Power Semiconductor Device and ICs* (1997) p. pp.173–176.

[13] T. Hatakeyama, T. Watanabe, T. Shinohe, K. Kojima, K. Arai, and N. Sano, *Appl. Phys. Lett.* **85**, 1380 (2004).

[14] W. S. Loh, B. K. Ng, J. S. Ng, S. I. Soloviev, H.-Y. Cha, P. M. Sandvik, C. M. Johnson, and J. P. R. David, *IEEE Trans. Electron Devices* **55(8)**, pp.1984–1990 (2008).

[15] J. E. Green, W. S. Loh, A. R. J. Marshall, B. K. Ng, R. C. Tozer, J. P. R. David, S. I. Soloviev, and P. M. Sandvik, *IEEE Trans. Electron Devices* **59(4)**, pp.1030–1036 (2012).

[16] H. Niwa, J. Suda, and T. Kimoto, *IEEE Trans. Electron Devices* **62(10)**, pp.3326–3333 (2015).

[17] Y. Zhao, H. Niwa, and T. Kimoto, *Jpn. J. Appl. Phys.* **58**, 018001 (2019).

[18] G. E. Bulman, L. W. Cook, and G. E. Stillman, *Solid State Electron.* **25**, 1189 (1982).

[19] S. Nakamura, H. Kumagai, T. Kimoto, and H. Matsunami, *Appl. Phys. Lett.* **80**, 3355 (2004).

[20] X. Chi, *Master Thesis*, (2019), Kyoto University [in Japanese].

[21] D. Stefanakis, X. Chi, T. Maeda, M. Kaneko, and T. Kimoto, presented at *Int. Conf. on Silicon Carbide and Related Materials* (*ICSCRM*), (2019), We-3A-01.

[22] J. F. Muth, J. H. Lee, I. K. Shmagin, and R. M. Kolbas, *Appl. Phys. Lett.* **71**, 2572 (1997).

[23] Z. Z. Bandić, P. M. Bridger, E. C. Piquette, and T. C. McGill, *Appl. Phys. Lett.* **72**, 24 (1998).

[24] Z. Z. Bandić, P. M. Bridger, E. C. Piquette, and T. C. McGill, *Appl. Phys. Lett.* **73**, 22 (1998).

[25] K. Kumakura, T. Makimoto, N. Konayashi, T. Hashizume, T. Fukui, and H. Hasegawa, *Appl. Phys. Lett.* **86**, 052105 (2005).

[26] S. F. Chichibu, A. Uedono, K. Kojima, H. Ikeda, K. Fujito, S. Takashima, M. Edo, K. Ueno, and S. Ishibashi, *J. Appl. Phys.* **123**, 161413 (2018).

[27] S. F. Chichibu, K. Shima, K. Kojima, S. Takashima, M. Edo, K. Ueno, S. Ishibashi, and A. Uedono, *Appl. Phys. Lett.* **112**, 211901 (2018).

[28] Y. Kumazaki, K. Uemura, T. Sato, and T. Hashizume, *J. Appl. Phys.* **12**, 184501 (2017).

[29] F. Horikiri, Y. Narita, and T. Yoshida, *Jpn. J. Appl. Phys.* **57**, 086502 (2018).

[30] M. Toguchi, K. Miwa, F. Horikiri, N. Fukuhara, Y. Narita, T. Yoshida, and T. Sato, *Appl. Phys. Express* **12**, 066504 (2019).

[31] S. Yamada, M. Omori, H. Sakurai, Y. Osada, R. Kamimura, T. Hashizume, J. Suda, and T. Kachi, *Appl. Phys. Express* **13**, 016505 (2020).

[32] Nidhi, D. F. Brown, S. Keller, and U. K. Mishra, *Jpn. J. Appl. Phys.* **49**, 021005 (2010).

[33] J. Kolnik, I. H. Oguzman, K. F. Brennan, R. Wang, and P. P. Ruden, *J. Appl. Phys.* **81(2)**, 726 (1997).

[34] I. H. Oguzman, E. Bellotti, K. F. Brennan, J. Kolnik, R. Wang, and P. P. Rudan, *J. Appl. Phys.* **81**, 12 (1997).

[35] F. Bertazzi, M. Moresco, and E. Bellotti, *J. Appl. Phys.* **106**, 063718 (2009).

[36] K. Kodama, H. Tokuda, and M. Kuzuhara, *J. Appl. Phys.* **114**, 044509 (2013).

[37] K. Kunihiro, K. Kasahara, Y. Takahashi, and Y. Ohno, *IEEE Electron Device Lett.* **20(12)**, pp.608–610 (1999).

[38] R. McClintock, J. L. Pau, K. Minder, C. Bayram, P. Kung, M. Razeghi, and , *Appl. Phys. Lett.* **90**, 141112 (2007).

[39] A. M. Özbek, Ph.D. Dissertation, (2012), North Carolina University.

[40] L. Cao, J. Wang, G. Harden, H. Ye, R. Stillwell, A. J. Hoffman, and P. Fay, *Appl. Phys. Lett.* **112**, 262103 (2018).

[41] T. Maeda, M. Okada, M. Ueno, Y. Yamamoto, M. Horita, and J. Suda, *Appl. Phys. Express* **9**, 091002 (2016).

[42] T. Maeda, T. Narita, M. Kanechika, T. Uesugi, T. Kachi, T. Kimoto, M. Horita, and J. Suda, *Appl. Phys. Lett.* **112**, 252104 (2018).

[43] T. Maeda, T. Narita, H. Ueda, M. Kanechik, T. Uesugi, T. Kachi, T. Kimoto, M. Horita, and J. Suda, *IEDM Tech. Digest* (2018) p. 30.1.

[44] D. E. Aspnes, *Phys. Rev.* **147**, 554 (1966).

[45] G. D. Chen, M. Smith, J. Y. Lin, H. X. Jiang, S. H. Wei, M. A. Khan, and C. J. Sun, *Appl. Phys. Lett.* **68**, 2784 (1996).

[46] S. M. Sze and K. K. Ng, *Physics of Semiconductor Devices*, (Wiley, New York, 2007), pp.102–114.

[47] A. S. Barker and Jr. and M. Ilegems, *Phys. Rev. B* **7(2)**, pp.743–750 (1973).

[48] M. J. Kane, M. J. Uren, D. J. Wallis, P. J. Wright, D. E. J. Soley, A. J. Simon, and T. Martin, *Semicon. Sci. Technol.* **26**, 085006 (2011).

[49] P. A. Golay, *Analytical Chemistry* **62(6)**, pp.570–573 (1990).

[50] I. Vurgaftman, J. R. Meyer, and L. R. Ram-Mohan, *J. Appl. Phys.* **89**, 5815 (2001).

[51] Y. Okuto and C. R. Crowell, *Solid State Electron.* **18**, 161 (1975).

[52] T. Narita, N. Ikarashi, K. Tomita, K. Kataoka, and T. Kachi, *J. Appl. Phys.* **124**, 165706 (2018).

[53] B. J. Baliga, *Fundamentals of Power Semiconductor Devices*, (Springer, 2008), pp. 91–166.

[54] H. Fukushima, S. Usami, M. Ogura, Y. Ando, A. Tanaka, M. Deki, M. Kushimoto, S. Nitta, Y. Honda, and H. Amano, *Jpn. J. Appl. Phys.* **58**, SCCD25 (2019).

[55] T. Maeda, T. Narita, S. Yamada, T. Kachi, T. Kimoto, M. Horita, and J. Suda, *IEDM Tech. Digest* (2019) p. 4.2.

[56] H. Niwa, *Ph.D. Dissertation*, (2016), Kyoto University.

[57] C. Raynaud, D-M. Nguyen, N. Dheilly, D. Tournier, P. Brosselard, M. Lazar, and D. Planson, *Phys. Status Solidi A* **206(10)**, pp.2273–2283 (2009).

[58] A. Aleksiejunas, M. Sudzius, T. Malinauskas, J. Vaitkus, K. Jarasiunas, and S. Sakai, *Appl. Phys. Lett.* **83(6)**, 1157 (2003).

[59] M. Goano, E. Belloti, E. Ghillino, G. Ghione, and K. F. Brennan, *J. Appl. Phys.* **88**, 6467 (2000).

[60] Y. Kamakura, T. Kotani, K. Konaga, N. Minamitani, G. Wakimura, and N. Mori, *IEDM Tech. Digest* (2015) p. 5.2.1.

[61] Z. Z. Bandić, P. M. Bridger, E. C. Piquette, and T. C. McGill, *Appl. Phys. Lett.* **74**, 1266 (1999).

[62] J. W. Johnson, A. P. Zhang, W.-B. Luo, F. Ren, S. J. Pearton, S. S. Park, Y. J. Park, and J.-I. Chyi, *IEEE Trans. Electron Devices* **49(1)**, pp.32–36 (2002).

[63] T. Maeda, T. Narita, H. Ueda, M. Kanechika, T. Uesugi, T. Kachi, T. Kimoto, M. Horita, and J. Suda, *IEEE Electron Device Lett.* **40(6)**, pp.941–944 (2019).

[64] S. Usami, Y. Ando, A. Tanaka, K. Nagamatsu, M. Deki, M. Kushimoto, S. Nitta, Y. Honda, H. Amano, Y. Sugawara, Y.-Z. Yao, and Y. Ishikawa, *Appl. Phys. Lett.* **112**, 182106 (2018).

[65] T. Oka, Y. Ueno, T. Ina, and K. Hasegawa, *Appl. Phys. Express* **7**, 021002 (2014).

[66] T. Oka, T. Ina, Y. Ueno, and J. Nishii, *Appl. Phys. Express* **8**, 054101 (2015).

[67] M. Sun, Y. Zhang, X. Gao, and T. Palacios, *IEEE Electron Device Lett.* **38(4)**, pp.509–512 (2017).

[68] W. Li, K. Nomoto, M. Pilla, M. Pan, X. Gao, D. Jena, and H. G. Xing, *IEEE Trans. Electron Devices* **64(4)**, pp.869–872 (2017).

[69] Y. Zhang, Z. Liu, M. J. Tadjer, M. Sun, D. Piedra, C. Hatem, T. J. Anderson, L. E. Luna, A. Nath, A. D. Koehler, H. Okumura, J. Hu, X. Zhang, X. Gao, B. N. Feigelson, K. D. Hobart, and T. Palacios, *IEEE Electron Device Lett.* **38(8)**, pp.1097–1100 (2017).

[70] H. Nie, Q. Diduck, B. Alvarez, A. P. Edwards, B. M. Kayes, M. Zhang, G. Ye, T. Prunty, and D. Bour, *IEEE Electron Device Lett.* **35(9)**, pp.939–941 (2014).

[71] Y. Zhang, M. Sun, D. Piedra, J. Hu, Z. Liu, Y. Lin, X. Gao, K. Shepard, and T. Palacios, *IEDM Tech. Digest* (2017) p. 9.2.

[72] T. Kimoto, H. Niwa, T. Okuda, E. Saitoh, Y. Zhao, S. Asada, and J. Suda, J. Phys. D: Appl. Phys. **51**, 363001 (2018).

[73] B. J. Baliga, *IEEE Electron Device Lett.* **10(10)**, pp.455–457 (1989).

[74] W. Soluch, E. Brzowski, M. Lysakowska, and J. Sadura, *IEEE Trans. Ultrasonic, Ferroelectrics, and Frequency Control* **58**, 11 (2011).

[75] M. T. Hibberd, V. Frey, B. F. Spencer, P. W. Mitchell, P. Dawson, M. J. Kappers, R. A. Oliver, C. J. Humphreys, and D. M. Graham, *Solid State Com.* **247**, 68 (2016).

[76] N. Sawada, T. Narita, M. Kaechika, T. Uesugi, T. Kachi, M. Horita, T. Kimoto, and J. Suda, *Appl. Phys. Express* **11**, 041001 (2018).

[77] N. Sawada, *Master Thesis* , Kyoto University [in Japanese] (2017).

[78] M. Horita, S. Takashima, R. Tanaka, H. Matsuyama, K. Ueno, M. Edo, T. Takahashi, M. Shimizu, and J. Suda, *Jpn. J. Appl. Phys.* **56**, 031001 (2017).

[79] I. C. Kizilyalli, A. P. Edwards, H. Nie, D. Disney, and D. Bour, *IEEE Trans. Electron Devices* **60**, 10 (2013).

[80] I. C. Kizilyalli, A. P. Edwards, O. Aktas, T. Prunty, and D. Bour, *IEEE Trans. Electron Devices* **62(2)**, pp.414–422 (2015).

[81] Y. Saitoh, K. Sumiyoshi, M. Okada, T. Horii, T. Miyazaki, H. Shiomi, M. Ueno, K. Katayama, M. Kiyama, and T. Nakamura, *Appl. Phys. Express* **3**, 081001 (2010).

[82] A. Kasic, M. Schubert, S. Einfeldt, D. Hommel, and T. E. Tiwald, *Phys. Rev. B* **62(11)**, 7365 (2000).

[83] T. Kimoto, *Jpn. J. Appl. Phys.* **58**, 018002 (2019).

[84] T. Kimoto, *Jpn. J. Appl. Phys.* **54**, 040103 (2015).

[85] H. Sakurai, M. Omori, S. Yamada, Y. Furukawa, H. Suzuki, T. Narita, K. Kataoka, M. Horita, M. Bockowski, J. Suda, and T. Kachi, *Appl. Phys. Lett.* **115**, 142104 (2019).

Chapter 6

Conclusions

6.1 Conclusions

In this dissertation, fundamental studies on avalanche breakdown in GaN were performed in terms of the material science and the device physics. In Chapter 1, the research background, the history of GaN and the purposs of this study were explained. The brief summaries of Chapter 2–5 are described here. The future outlook is also noted.

In Chapter 2, GaN p-n junction diodes with the negative beveled-mesa termination were designed and fabricated. The author quantitatively found that small $N_{\mathrm{a}}/N_{\mathrm{d}}$ and small θ are effective to alleviate electric field crowding, confirmed by TCAD simulation. The breakdown voltage of the fabricated devices increased as the Mg concentration was decreased. The devices exhibited high avalanche capability and the positive temperature dependence of the breakdown voltage. For the device with the highest breakdown voltage of 425 V, the breakdown electric field of 2.86 MV/cm at parallel plane junction was achieved. This edge termination is useful for GaN power devices with relatively low breakdown voltage, as well as devices employed for fundamental studies on the breakdown characteristics.

In Chapter 3, the breakdown characteristics in GaN p-n junction diodes with various epitaxial structures were investigated. Based on the design space of the beveled-mesa structure obtained in Chapter 2, the author proposed the double-side-depleted shallow bevel termination, in which electric field crowding does not occur. The devices showed low reverse leakage current, high avalanche capability, positive temperature coefficient of the breakdown voltage and nearly uniform breakdown electroluminescence in the entire p-n junction. These are strong evidences that the uniform (nearly ideal) avalanche breakdown without electric field crowding was successfully achieved. The devices showed the parallel-plane breakdown electric fields of 2.8–3.5 MV/cm.

In addition, the author also fabricated GaN $\mathrm{p}^+/\mathrm{n}^-$ and $\mathrm{p}^-/\mathrm{n}^+$ junction diodes with the vertical deep-etch termination. The devices also showed the uniform avalanche breakdown with the breakdown electric fields of 3.0–4.0 MV/cm. A distinguishable difference of the breakdown voltage between $\mathrm{p}^+/\mathrm{n}^-$ and $\mathrm{p}^-/\mathrm{n}^+$ junction was not observed, indicating that

the impact ionization coefficients of electrons and holes are not so different.

The breakdown electric fields of 2.8–4.0 MV/cm in this work are among the best of the previously reported non-punch-through GaN devices for relatively high doping concentrations (low breakdown voltages). In addition, these experimental data will be discussed compared with the theoretical critical electric field in GaN simulated from the impact ionization coefficients.

In Chapter 4, the author investigated the photocurrent induced by the optical absorption induced by the Franz-Keldysh effect in a GaN Schottky barrier diode and a GaN p-n junction diode under high reverse bias voltage. In the GaN Schottky barrier diode, a photocurrent induced by internal photoemission was observed without applying reverse bias. With increasing reverse bias, a significant increase in the photocurrent was observed for the wavelength close to the GaN absorption edge, the voltage dependence of which cannot be explained by internal photoemission with the image force lowering. The author calculated the photocurrent induced by the optical absorption due to the Franz-Keldysh effect, and the caluclated curves showed excellent agreement with the experimental data. In addition, the photocurrent induced by the Franz-Keldysh effect and its temperature dependence in a GaN p-n junction diode were investigated. The voltage and wavelength dependences of the photocurrent in the GaN p-n junction diode were also well reproduced by considering the optical absorption induced by the Franz-Keldysh effect in the depletion region. The temperature dependence of the photocurrent was explained by the shrinkage of the bandgap in GaN with elevating temperature. These results are useful for considering the optical absorption in GaN under electric field.

In Chapter 5, the novel method to measure impact ionization coefficients of electrons and holes was proposed. The sub-bandgap optical absorption induced by the Franz-Keldysh effect has a unique nature: the optical absorption selectively occurs at high electric field region. In addition, the photocurrent induced by the Franz-Keldysh effect is well predictable. The photomultiplication measurement utilizing the Franz-Keldysh effect was performed for GaN p-n junction diodes with double-side-depleted shallow bevel termination, which exhbited the uniform (nearly ideal) avalanche breakdown. The multiplication factors were successfully extratced as the ratio of the experimental photocurrent to the calculated FK-induced photocurrent, and the value of the impact ionization coefficients in GaN was estimated under the assumption of $\alpha_{\mathrm{n}} = \alpha_{\mathrm{p}}$.

To extract α_{n} andα_{p} separately, the photomultiplication measurements utilizing above- and sub-bandgap illumnations were performed for a GaN $\mathrm{p}^-/\mathrm{n}^+$ junction diode, in which the depletion layer extends to the p-type side. Under above-bandgap illumination, the photocurrent induced by the electron diffusion from the top side was obtained. On the hand, under sub-bandgap illumination, the photocurrent induced by the Franz-Keldysh effect (hole injection) was obtained. The unmultiplicated photocurrents were carefully calculated based on the physics, and the electron- and hole-initiated multiplication factors (M_{n}, M_{p}) were obtained in wide range with small noises. By analyzing the multiplication

factors, the impact ionization coefficients of electrons and holes are successfully obtained. The simulated breakdown characteristics using the obtained α_n and α_p were confirmed to well reproduce the experimental breakdown characteristics of GaN power devices reported previously, suggesting the high accuracy of the data. The critical electric field of GaN was modeled, and the trade-off relationship between the on-resistance and the breakdown voltage as the "GaN limit" was updated and presented.

These results are valuable to understand impact ionization and avalanche multiplication in GaN, and the obtained parameters are useful for device simulation of avalanche breakdown characteristics in a GaN power device.

6.2 Future Outlook

Although the fundamental studies on avalanche breakdown were performed in this dissertation, there still remain several issues to be solved. Here, the authour describes the issues as future outlooks.

- **Improvement of Edge Termination for GaN**
  In this study, the beveled-mesa edge termination was proposed. Shallow and smooth mesa structure combined with a lightly doped p-layer is the key to reduce electric field crowding. The beveled-mesa termination is simple, and electric field crowding is well alleviated. However, it seems to be difficult to be employed to the high power devices over 1.2 kV-class. In addition, the reduction of mesa angle expands the edge-termination area, which means the decrease in the active area (increase in a device cost). A thick p-layer with low acceptor concentration acts as the large series resistance. Therefore, the edge termination with high area efficiency without increasing the resistance,which can be employed to high power devices, is needed. Recently, p-type doping by Mg ion implantation has been developing [1, 2], and the junction termination extention (JTE) structure will become available. The beveled-mesa termination combined with the Mg ion-implantation is an excellent candidate for GaN power devices.

- **Breakdown Electric Field at High Breakdown Voltage**
  In this study, the breakdown electric field in GaN p-n junction diodes without electric field crowding were investigated in relatively low breakdown voltage region (high doping concentration). The value at high breakdown voltage region is also important and should be investigated. However, to determine the breakdown electric field, a thick epitaxial layer with low and uninform doping concentration is needed. In addition, the edge termination for high voltage devices is needed. The vertical extremely-deep-etch mesa termination, which can be fabricated by photo-electrochemical etching [3], may be useful to fabricate the high breakdown voltage device without electric field crowding.

- **Study on Franz-Keldysh Effect in GaN**
  The modulation spectroscopy of the Franz-Keldysh-oscillation is a powerful tool to determine the optical properties or the band structure. However, the study of the modulation spectroscopy on GaN has not been performed in detail. Using the measurement, physical properties of the material, such as the reduced effective mass and the matrix elements, may be determined.

- **Impact Ionization Coefficients**
  The impact ionization coefficients of electrons and holes in GaN are determined with high accuracy. However, there are room to be studied furthermore.

  Determination of the values in a wide electric field range

  The obtained data in this study are limited in the electric field range of 2.1–3.0 MV/cm. Toward more accurate device simulation and understanding the transport properties of carriers in GaN under high electric field, the values in a lower and higher electric field ranges should be experimentally determined. Using a device with punch-through structure (thin drift layer with very low doping concentration), a constant electric field profile in a depletion layer can be obtained, which allows a measurement of avalanche multiplication at low electric field range and makes the analysis easier. However, the method using the FK effect cannot be employed for the punch-through structure, since electron-hole pairs are generated in the entire depletion layer. The measurement method for GaN punch-through p-n junction diode should be considered and established. For examlple, the selective carrier generation by the multiple-photon excitation [5], the sub-bandgap absorption via deep levels (e.g. C_N) [6] in the selective-absorption layer which includes heavily co-doped C and Si atoms intentionally, the formation of the deep wells at the back side using AlGaN or other etch-stop layers, etc. may be useful.

  Measurement in a wide temperature range

  The temperature dependence of the impact ionization coefficients is very important scientifically and practically. In this study, it was difficult to obtain a pure electron-injected photocurrent at higher temperature than 373 K owing to the decrease in the diffusion length of electrons, which causes the decrease in the electron-injected photocurrent, and the increase in the dark leakage current at elevated temperature. Using a thinner drift layer and/or a higher power light source, a larger photocurrent will be obtained, which will enable to obtain the electron-initiated multiplication factor at higher temperature. In addition, the boiling point of Fluorinert is approximately 175°C, and other way to avoid air sparking such as the measurement in vacuum ambient is required for high temperature measurement.

Anisotropy in impact ionization coefficients in GaN

GaN crystal has the Wurtzite (2H-) structure, and the band structure has the anisotropy. Especially, the unique conduction band structure from the Γ point to the A point in GaN is considered to suppress the electron impact ionization coefficient. Thus, the impact ionization coefficients are considered to be anisotropic. For example, the impact ionization coefficients in 4H-SiC have anisotropy [7–9]. The critical electric field in a device fabricated on a SiC($11\bar{2}0$)-face substrate is approximately 20–25% lower than that fabricated on a SiC(0001)-face substrate [10]. For GaN, the anisotropy of the impact ionization coefficients should be investigated. Using a GaN device fabricated on an *m*-plane GaN substrate, the impact ionization coefficients perpendicular to the *c*-axis in GaN can be obtained.

Theoretical study on impact ionization coefficients in GaN

Although there have been some theoretical studies on impact ionization coefficients [11–14], the physics of the impact ionization phenomenon in GaN and other wide-bandgap materials under high electric field are still unknown and should be studied. Very recently, the effect of a band structure on the impact ionization coefficients has been studied by Tanaka *et al.* [15]. In the study assuming the simple band structure, it was observed that the impact ionization coefficients strongly depend on the Brillouin zone width and effective masses (slope of the *E*–*k* disperion), and the effect of the bandgap on the impact ionization coefficients was not so strong. In the future, the Monte Carlo simulation for the accurate full band structure of GaN and other wide-bandgap materials should be performed, and the transport properties and the physics of the impact ionization phenomenon such as the energy distributions of carriers under electric field and their quantum yields to cause impact ionization need to be investigated and discussed.

Finally, the author sincerely wishes that GaN power devices will see the light of day and contribute to high efficient power electronics.

References

[1] T. Narita, T. Kachi, K. Kataoka, and T. Uesugi, *Appl. Phys. Express* **10**, 016501 (2017).

[2] H. Sakurai, M. Omori, S. Yamada, Y. Furukawa, H. Suzuki, T. Narita, K. Kataoka, M. Horita, M. Bockowski, J. Suda, and T. Kachi, *Appl. Phys. Lett.* **115**, 142104 (2019).

[3] F. Horikiri, H. Ohta, N. Asai, Y. Narita, T. Yoshida, and T. Mishima, *Appl. Phys. Express* **11**, 091001 (2018).

[4] T. Tanikawa, K. Ohnishi, M. Kanoh, T. Mukai, and T. Matsuoka, *Appl. Phys. Express* **11**, 031004 (2018).

[5] Y. Tokuda, *ECS Transactions* **75(4)**, pp.39–49 (2016).

[6] T. Hatakeyama, T. Watanabe, T. Shinohe, K. Kojima, K. Arai, and N. Sano, *Appl. Phys. Lett.* **85**, 1380 (2004).

[7] X. Chi, *Master Thesis*, (2019), Kyoto University [in Japanese].

[8] D. Stefanakis, X. Chi, T. Maeda, M. Kaneko, and T. Kimoto, presented at *Int. Conf. on Silicon Carbide and Related Materials* (*ICSCRM*), (2019), We-3A-01.

[9] S. Nakamura, H. Kumagai, T. Kimoto, and H. Matsunami, *Appl. Phys. Lett.* **80**, 3355 (2004).

[10] J. Kolnik, I. H. Oguzman, K. F. Brennan, R. Wang, and P. P. Ruden, *J. Appl. Phys.* **81(2)**, 726 (1997).

[11] I. H. Oguzman, E. Bellotti, K. F. Brennan, J. Kolnik, R. Wang, and P. P. Rudan, *J. Appl. Phys.* **81**, 12 (1997).

[12] F. Bertazzi, M. Moresco, and E. Bellotti, *J. Appl. Phys.* **106**, 063718 (2009).

[13] K. Kodama, H. Tokuda, and M. Kuzuhara, *J. Appl. Phys.* **114**, 044509 (2013).

[14] H. Tanaka, T. Kimoto, and N. Mori, presented at *the 9th Asia – Pacific Workshop on Widegap Semiconductors*, (2019), TuP-CH-16.

Appendix A

Temperature Dependence of Barrier Height in GaN Schottky Barrier Diode

A.1 Introduction

A Schottky barrier diode (SBD) is one of the building blocks of electronic devices. There are some reports on GaN vertical SBDs fabricated on GaN bulk substrates [1–7], which showed excellent performances: low on-resistances and high breakdown voltages. However, these reports mainly focus on the diode performances. More detailed understandings of the device characteristics are needed.

A barrier height, which determines the turn-on voltage and reverse leakage current, is the most important property in a SBD. Many studies have been reported on the temperature dependence of the barrier height in Si, GaAs, and InP SBDs [8–12]. Arizumi and Hirose reported the temperature dependence of the barrier height in an Au/n-Si SBD obtained from forward current-voltage (I–V) and capacitance-voltage (C–V) measurements in the range of 100–350 K [8]. They observed that the barrier height decreased with elevating temperature. The temperature coefficient was $-(2.67\pm0.60)\times10^{-4}$ eV/K, which was the same order of the magnitude as the temperature dependence of the bandgap in Si [13]. Hackam*et al*. investigated the temperature dependence of the barrier height in a Ni/n-GaAs SBD, and reported that the decrease in the barrier height was similar to shrinkage of the band gap with elevating temperature [11]. The temperature dependences of the barrier height and the bandgap [13–15] for Si, GaAs and InP are summarized in Table A.1.

There are some reports of the temperature dependences of barrier heights in GaN-based SBDs using heteroepitaxial layers [16–21]. For example, Yildirim *et al*. reported that the temperature dependence of the barrier height of Ni/n-GaN SBDs fabricated on a sapphire substrate [16]. In their reports, the barrier height determined from I–V measurements significantly increased with elevating temperature. The ideality factor was 2.0 at 300 K and

Table A.1: The temperature dependences of the Schottky barrier height and the bandgap in Si, GaAs and InP.

Material	dE_g/dT			$de\phi_b/dT$
	Value [meV]	Method	Range [K]	[meV/K]
Si	$-(0.21–0.33)$ [8]	I–V, C–V	100–350	-0.3 [13]
	-0.3 [10]	IPE	100–370	
GaAs	-0.58 [11]	C–V	289–360	-0.5 [14]
InP	-0.33 [12]	C–V	289–360	-0.4 [15]

1.5 at 400 K, which were much larger than unity. This indicates that the I–V characteristics in the SBDs are far from the ideal characteristics and an accurate determination of the barrier height is quite difficult. Such an increase in the barrier height (accompanied with the decrease in the ideality factor) with elevating temperature was often observed in heteroepitaxial-GaN-based SBDs [17–21] and was explained by existence of inhomogeneity of the barrier height [17], tunneling current [18], or other leakage current due to high threading dislocation density (TDD$\sim 10^9$ cm^{-2}) [19].

Zhou *et al.* investigated the temperature dependence of I–V and C–V characteristics in a Ni/n-GaN SBD fabricated directly on a GaN free-standing substrate, which has low TDD of $\sim 10^6$ cm^{-2}, in the range of 298–473 K [22]. In their report, the barrier height determined by C–V measurements remained almost constant (1.16 eV) or slightly decreased with increasing temperature, as shown in Fig. A.1. On the other hand, the barrier height determined by I–V measurements was found to increase with temperature. The ideality factor was 1.15 at 298 K and 1.05 at 473 K. These values were smaller than those of heteroepitaxial GaN SBDs reported previously, but still larger than unity (at 298 K). Inconsistent results between C–V and I–V might come from the temperature dependence of the ideality factor. Temperature dependence of ideal GaN Schottky contacts has not been revealed yet.

Recently, the high-quality GaN SBDs fabricated on homoepitaxial GaN layers, which show nearly ideal I–V characteristics, has been reported [1, 23]. In this study, the author investigated the temperature dependence of the barrier height in a Ni/n-GaN SBD fabricated on a homoepitaxial GaN layer from C–V, forward I–V, and internal photoemission (IPE) measurements. The author successfully avoided uncertainty coming from non-ideal characteristics. The barrier heights obtained from all three methods consistently decreased with elevating temperature with similar temperature coefficients.

A.2 Device Structure

Figure A.2 shows the schematic cross section of a Ni/n-GaN SBD. A 300-μm-thick n-type GaN(0001) free-standing substrate grown by hydride vapor phase epitaxy (HVPE) was used. A 7-μm-thick n-type GaN homoepitaxial layer was grown by metal-organic vapor phase epitaxy (MOVPE). The net donor concentration of the GaN epitaxial layer was 5.0×10^{15} cm^{-3}. 400-μm-diameter Schottky electrodes were formed by depositing Ni/Au on the GaN epitaxial layer. The Ohmic electrode was formed by depositing Ti/Al/Ti/Au on the mirror-polished backside of the substrate. Field plate (FP) structure with a SiN_x layer was formed to prevent premature breakdown due to the electric field crowding at the edge of the Schottky electrode. The fabrication process of the SBD has been described in detail elsewhere [1]. The device was attached to the stage while the measurements, and the temperature of the stage was controlled in the range of 223–573 K.

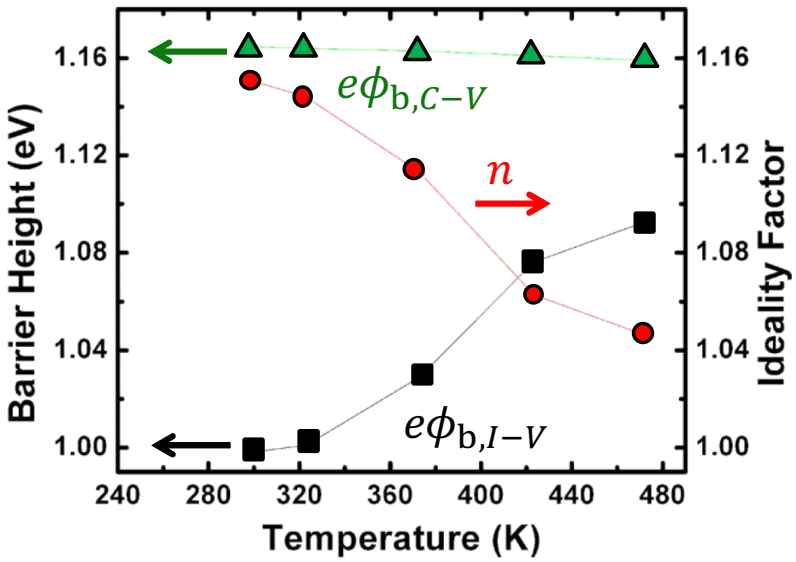

Figure A.1: The temperature dependence of the barrier height obtained by C–V and I–V measurements reported by Zhou *et al.* [22]. The temperature dependence of the ideality factor is also shown. Due to the non-ideal I–V characteristic, the inconsistent results were obtained.

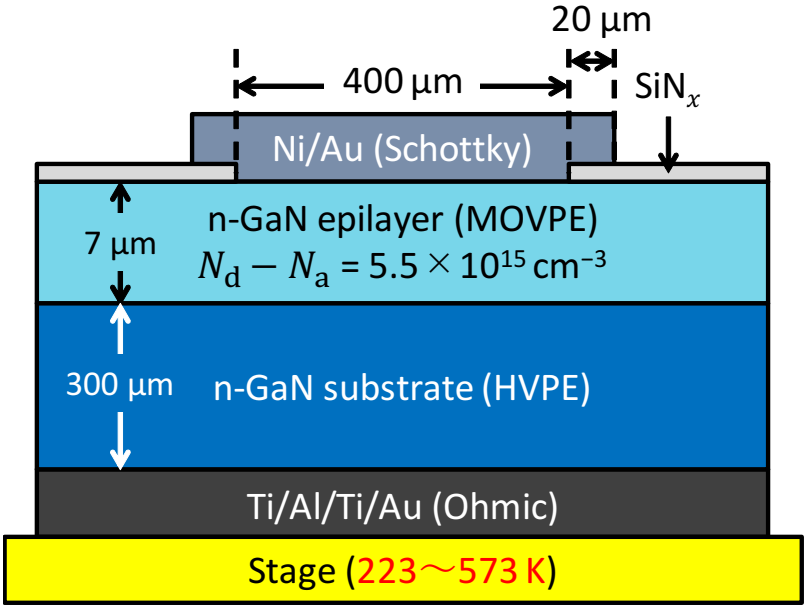

Figure A.2: The schematic cross section of a Ni/n-GaN Schottky barrier diode fabricated on a n-type GaN substrate. The sample was attached to the stage by vacuum suction, and the temperature of the stage was controlled in the range of 223–573 K.

A.3 Capacitance-Voltage Measurement

The C–V characteristics of the GaN SBD were measured in dry air ambient at 500 K. Figure A.3 shows the C–V characteristics of the GaN SBD at 223, 298 and 573 K as the C^{-2}–V plot. For an accurate analysis, the capacitance of the FP ring surrounding the GaN SBD was subtracted from the measured capacitance. The plots show very good linearity, which indicates that the net donor concentration is nearly uniform along the depth direction. It was confirmed that the plots were independent of frequency in the range of 10–500 kHz. With elevating temperature, the slopes of the plots remain almost constant, while the plots shift to the left side (negative direction in the voltage axis).

The capacitance of a Schottky junction (depletion layer) is expressed as $C = \varepsilon_{\rm s}A/W = A\sqrt{\varepsilon_{\rm s}e(N_{\rm d} - N_{\rm a})/2(V_{\rm d} - V)}$, and the below relationship can be obtained,

$$\frac{1}{C^2} = \frac{-2}{A^2 e\varepsilon_{\rm s}(N_{\rm d} - N_{\rm a})}(V_{\rm d} - V). \tag{A.1}$$

Here, A and W are a junction area and a depletion layer width, respectively. A built-in potential ($V_{\rm d}$) of 0.90 V and the net donor concentration ($N_{\rm d} - N_{\rm a}$) of 5.5×10^{15} cm^{-3} at 298 K were extracted from an intercept and a slope of the $1/C^2$–V plot, respectively. In the analysis, the dielectric constant of GaN ($\varepsilon_{\rm s} = 10.4\varepsilon_0$) [24, 25] was used. As shown in Fig. 4.4, the Schottky barrier height ($e\phi_{\rm b}$) can be obtained by using

$$e\phi_{\rm b,C-V} = eV_{\rm d} + (E_{\rm c} - E_{\rm f}) + kT, \tag{A.2}$$

where k is the Boltzmann constant, T is the absolute temperature, and $E_{\rm c}$ and $E_{\rm f}$ are the bottom of the conduction band and the Fermi level in GaN, respectively. Silicon donors in GaN are fully ionized at room temperature, confirmed by Hall effect measurements [26]; therefore, $E_{\rm c} - E_{\rm f}$ is equal to $kT \cdot \ln[N_{\rm c}/(N_{\rm d} - N_{\rm a})]$. $N_{\rm c}$ is the effective density of states in the conduction band and is given by $N_{\rm c} = 2(2\pi m_{\rm de}kT/h^2)^{3/2}$, where $m_{\rm de}$ is the density-of-state effective mass for electrons; $m_{\rm de} = (m^*_{e,||}m^{*2}_{e,\perp})^{1/3} = 0.2m_0$ [27]. The fourth term on the righthand side (kT) is the voltage drop due to the tail of the thermal distribution of electrons at the edge of the depletion layer (the depletion approximation is not assumed). In this study, the effect of the image force lowering was not considered, since the barrier height was extracted at near zero bias.

Figure A.4 shows the temperature dependence of the barrier height obtained by C–V measurements. The values of $eV_{\rm d}$, $E_{\rm c} - E_{\rm f}$ and kT are also shown. The barrier height almost linearly decreased with elevating temperature, and can be approximated as

$$e\phi_{\rm b}(T) = e\phi_{\rm b,300\ K} + \alpha(T - 300\ K) \tag{A.3}$$

where $e\phi_{\rm b,300\ K} = 1.14$ eV and $\alpha = -0.18$ meV/K. The change of the barrier height with elevating temperature is evident, compared to the results reported by Zhou *et al.* (-3×10^{-5} meV/K in the range of 298–473 K) [22].

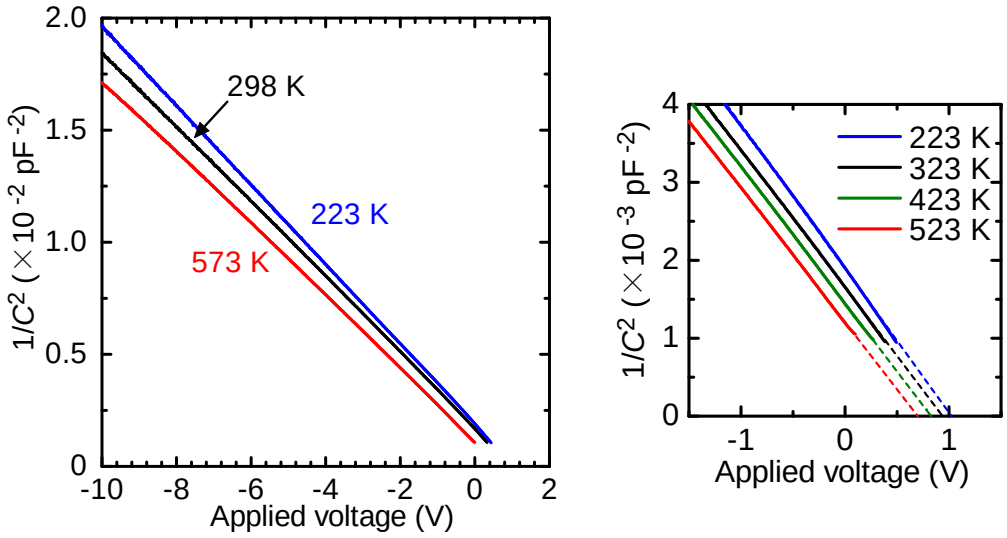

Figure A.3: The capacitance–voltage characteristics of the GaN SBD in the range of 223–573 K. The magnification near zero bias is also shown. The plots shifted to the negative side with elevating temperature, indicating the decrease in the built-in potential.

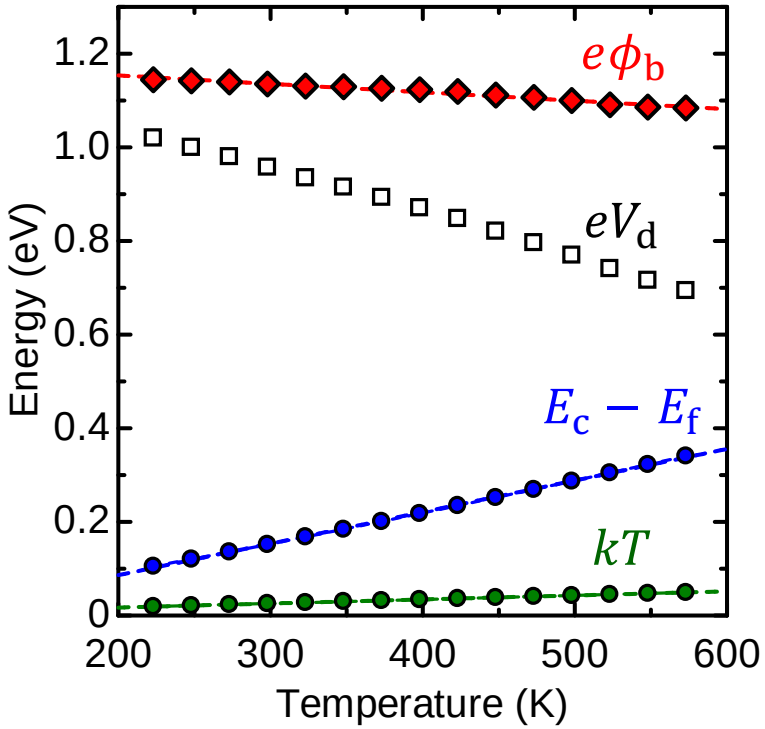

Figure A.4: The temperature dependence of the barrier height in the GaN SBD obtained from the C–V measurements. The values of eV_d, $E_c - E_f$ and kT are also shown. The barrier height almost linearly decreased with elevating temperature.

A.4 Current-Voltage Measurement

A.4.1 Analysis by Thermionic Emission Model

Figure A.5 shows the forward I–V characteristics of the GaN SBD. A forward I–V characteristic of a SBD follows the empirical formula

$$J = J_0 \cdot \exp\left(\frac{eV}{nkT}\right). \tag{A.4}$$

Assuming the thermionic emission (TE) model [28], the ideality factor (n) is equal to unity, and the saturation current density (J_0) is given by $J_0 = A^*T^2 \exp(-e\phi_\mathrm{b}/kT)$, where $A^* = 4\pi m^* k^2 e/h^3 = 120{\cdot}(m^*/m_0)$ A/cm^{2}K^2 is the effective Richardson constant. The barrier height can be obtained from the saturation current density.

In previous reports, the temperature dependences of barrier heights were obtained by the analysis based on the TE model. The barrier heights obtained from the analysis exhibited the positive temperature coefficients in previous reports [16–22]. The author analyzed the I–V characteristics of the GaN SBD. Figure A.6 shows the temperature dependence of the ideality factor and the barrier height obtained by the analysis based on the TE model. For low temperature region (< 298 K), the barrier height decreased with decreasing temperature, accompanied with the increase in the ideality factor. It may be explained that the impacts of the inhomogeneity of the barrier height [16]) and/or forward leakage currents, such as tunneling, came to be relatively pronounced and not negligible at the low temperature. Therefore, accurate estimation of the barrier height in the device for the low temperature was difficult due to the non-ideal characteristics. On the other hand, the ideality factors were 1.04–1.06, which were very close to unity, in the range of 348–573 K. This indicates that nearly ideal I–V characteristics were achieved in our SBDs at relatively high temperature. For the temperature range of 298–573 K, the barrier height slightly "increased" with elevating temperature. This result is inconsistent with the temperature dependence of the barrier height obtained from C–V measurements.

A.4.2 Analysis by Thermionic Emission-Diffusion Model

The author speculated that this inconsistency originates from the incompleteness of the analysis method. The TE model is based on the assumption that collisions between carriers within the depletion layer can be neglected and free electrons near the depletion edges are transported ballistically. However, the electron mean free path ($\lambda = (\mu/e)\sqrt{3kTm_e^*}$) is smaller than the width of the depletion layer in the GaN SBD (e.g. $\lambda \sim 40$ nm at 298K). Mochizuki *et al*. have pointed out that the usage of the thermionic emission-diffusion (TED) model, in which the drift-diffusion transport is considered in series with the TE transport, is very important for barrier height estimation [29].

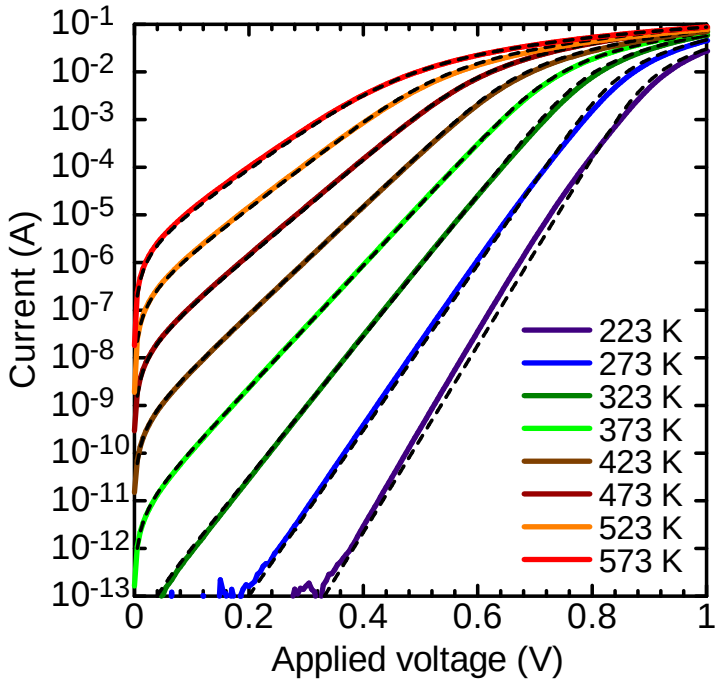

Figure A.5: The current-voltage characteristics of the GaN SBD. The calculated values based on the thermionic emission model with consideration of the series resistance at all the temperatures are shown as broken lines.

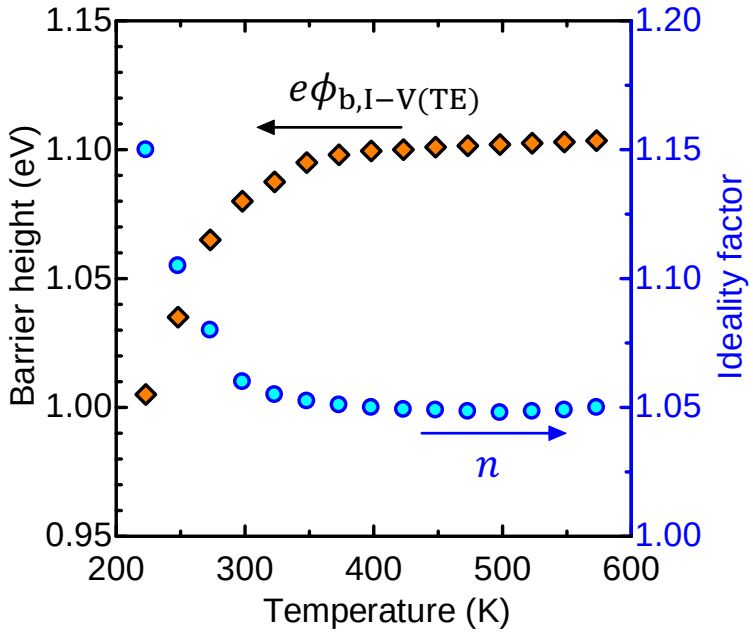

Figure A.6: The temperature dependence of the barrier height obtained by the analysis of the I–V based on the thermionic emission model. The temperature dependence of the ideality factor is also shown.

The current-voltage characteristics based on the thermionic emission-diffusion transport can be expressed as [30]

$$J_{\mathrm{TED}} = \frac{A^* T^2}{1 + v_{\mathrm{R}}/v_{\mathrm{D}}} \exp\left(-\frac{e\phi_{\mathrm{b}}}{kT}\right)\left[\exp\left(\frac{eV}{kT}\right) - 1\right], \tag{A.5}$$

$$v_{\mathrm{R}} = \frac{A^* T^2}{eN_{\mathrm{C}}}, \qquad v_{\mathrm{D}} = \frac{\mu_{\mathrm{e}} kT}{e} \frac{\exp\left(e\phi_{\mathrm{b}}/kT\right)}{\int_0^W \exp\left(E_{\mathrm{C}}(x)/kT\right) dx},$$

$$E_{\mathrm{C}}(x) = e\phi_{\mathrm{b}} - \frac{e^2(N_{\mathrm{d}} - N_{\mathrm{a}})}{2\varepsilon_{\mathrm{s}}}(2Wx - x^2), \qquad W \sqrt{\frac{2\varepsilon_{\mathrm{s}}(V_{\mathrm{d}} - V)}{e(N_{\mathrm{d}} - N_{\mathrm{a}})}},$$

where μ_{e} is the electron mobility. The x coordinate is the distance from the Schottky junction and $x = W$ is the edge of the depletion layer. $E_{\mathrm{C}}(x)$ is the conduction band edge measured from the Fermi level in the metal. v_{R} and v_{D} are the effective recombination velocity at the potential energy maximum and the effective diffusion velocity associated with the transport of electrons from the edge of the depletion layer to the potential energy maximum, respectively [30].

In Eq. (6), the relative values of v_{R} and v_{D} determine the relative current limiting factor of the TE process versus the diffusion process. Figure A.7 shows the temperature dependence of v_{R} and v_{D}. In the calculations, the electron mobility obtained from Hall-effect measurements for a sample with a net donor concentration of $4{\times}10^{15}$ cm^{-3} [26] shown in Fig. A.8 was used (the anisotropy of μ_{e} may be small). In the GaN SBD, v_{R} is much smaller than v_{D} at room temperature due to the relatively high electron mobility, and the current is limited by the TE process. With elevating temperature, the electron mobility decreases due to phonon scattering, and the diffusion process also limits the current. Therefore, the barrier height obtained from the analysis based on the TE model tends to be overestimated at elevated temperature. In addition, it should be noted that v_{D} depends on the applied voltage, and slightly effects on the analysis of the ideality factor (When the diffusion transport is not negligible, n slightly deviates from unity).

The author analyzed the temperature dependence of the barrier height by fitting the calculated curves based on the TED model to the experimental I–V curves. The effective Richardson constant A^* is 24 Acm^{-2}K^{-2}, neglecting the back scattering by optical phonon, quantum-mechanical reflection, and tunneling [31]. Figure A.9 shows the comparison between the experimental I–V curves and the curves calculated based on the TED model. The fitting was conducted in the range of 348–573 K, where the ideality factors were very close to unity. In the calculation, the voltage drop due to the series resistances in the GaN SBD was also considered. The calculated results show good agreement with the experimental curves in the range of 348–573 K, and the barrier height obtained by fitting the curves decreased with elevating temperature. The temperature coefficient of -0.23 meV/K was obtained, which is the consistent with that obtained from C–V measurements (-0.18 meV/K).

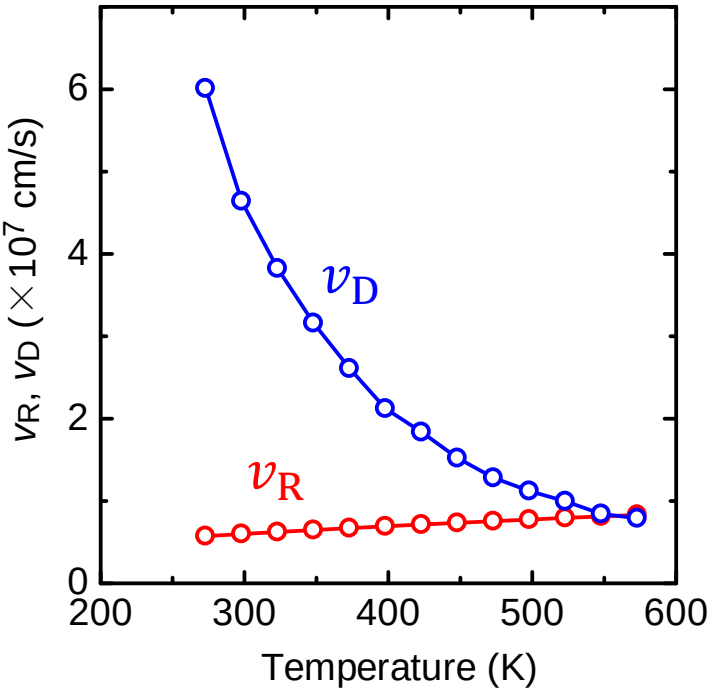

Figure A.7: Temperature dependence of the v_R and v_D (at 0.2 V). The effective diffusion velocity v_D decreases with elevating temperature, which mainly reflects the temperature dependence of the electron mobility.

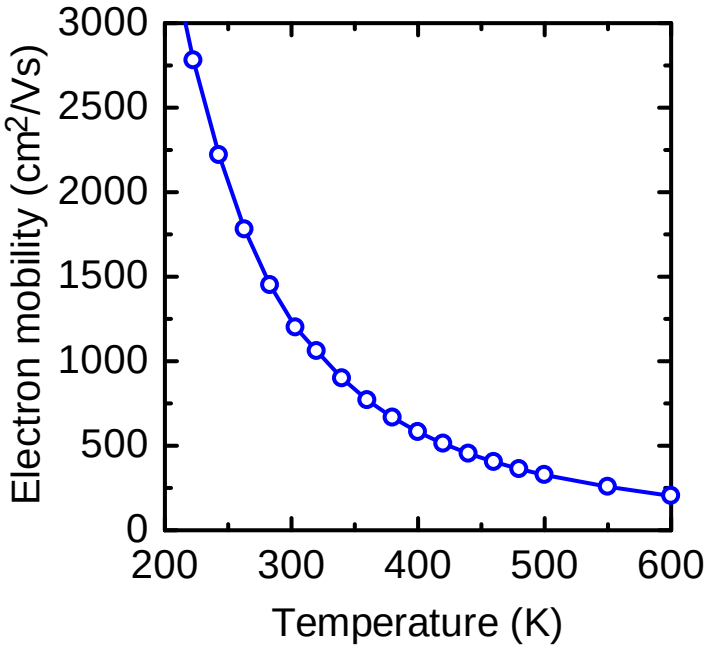

Figure A.8: The temperature dependence of the electron mobility for the carrier concentration of 4×10^{15} cm^{-3} measured by Sawada *et al.* [26].

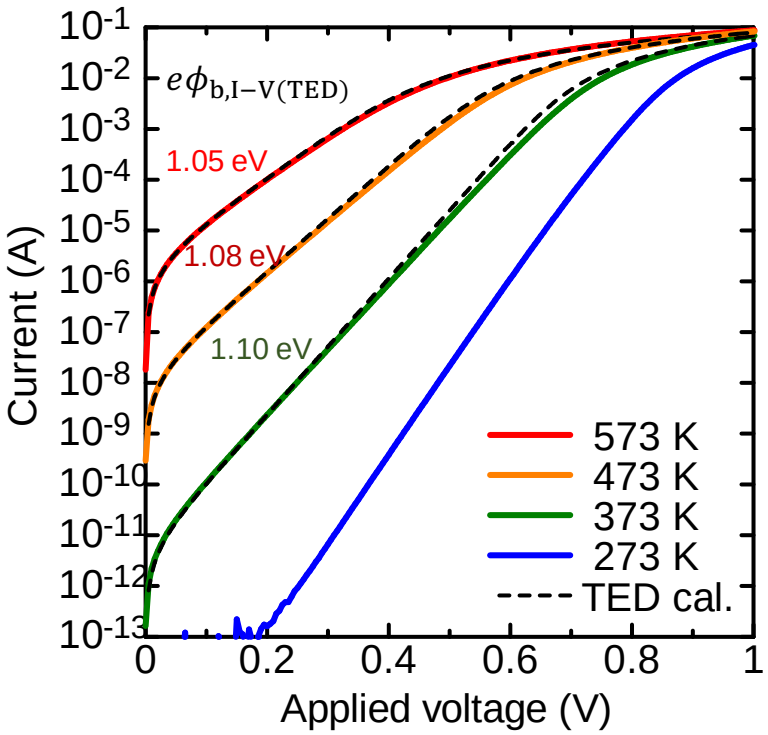

Figure A.9: The current-voltage characteristics of the GaN SBD at 273, 373, 473 and 573 K. The calculated values based on the thermionic emission-diffusion model with consideration of the series resistance at all the temperatures are shown as broken lines.

A.5 Internal Photoemission Measurement

Internal photoemission (IPE) is a powerful tool to determine the barrier height. The yield of IPE is proportional to $(h\nu - e\phi_{\mathrm{b}})^2$, and the barrier height can be obtained from the Fowler plot [32]. In this study, the photocurrents of the GaN SBD under the monochromatic light illumination were measured in the range of 223–373 K. The wavelength of light was varied from 600 nm to 1100 nm with a bandpass width of 5 nm. The measured photon flux was shown as Fig. A.10 and normalized to discuss the wavelength dependence. The wavelength of irradiated light was longer than the fundamental absorption edge of GaN; therefore, the light irradiated around the Schottky electrode entered the GaN layer. The light was reflected by the back-side Ohmic electrode and reached the Ni/GaN interface from the back side, resulting in IPE. The author confirmed that the photocurrent was proportional to the area of the Schottky electrode in the range 40–400 μm, which indicates that the entire Ni/GaN interface was illuminated uniformly from the back side [33]. Figure A.11 shows the Fowler plots of the photocurrents in the GaN SBD, which shows clear linearity for all temperatures. The plots slightly shifted to the left side (the negative direction of the photon-energy axis) with elevating temperature, which reflects the decrease in the barrier height. The barrier height obtained from IPE measurements was 1.14 eV at 223 K, 1.12 eV at 298 K, and 1.11 eV at 373 K.

For higher temperature range than 373 K, it was difficult to measure the photocurrent owing to voltage-dependent dark current near zero bias, which caused the difficulty to obtain the threshold of the photoyield near the barrier height.

A.6 Temperature Dependence of Barrier Height

Figure A.12 shows the temperature dependences of the barrier height obtained from C–V, I–V (with the TED model), and IPE measurements. It is well known that $e\phi_{\mathrm{b,C-V}}$ is prone to be slightly overestimated, and $e\phi_{\mathrm{b,\ I-V}}$ is prone to be underestimated; therefore, $e\phi_{\mathrm{b,IPE}}$ is the most reliable [34]. In this study, the barrier heights determined from C–V, I–V, and IPE measurements actually follow this relationship. It should be stressed that the differences between these methods are very small (less than 0.03 eV), suggesting the high accuracy of the data. The temperature coefficients obtained from $e\phi_{\mathrm{b,C-V}}$, $e\phi_{\mathrm{b,I-V}}$ and $e\phi_{\mathrm{b,IPE}}$ were -0.18 meV/K, -0.23 meV/K and -0.17 meV/K, respectively.

Teisseyre *et al*. reported that the bandgap in GaN shrinks with increasing temperature, and the linear temperature coefficient of the band gap (dE_{g}/dT) is -0.45 meV/K at 300 K [35]. The temperature coefficient of the barrier height is about half of dE_{g}/dT. It is known that the Fermi level in the metal is almost independent of temperature. The author speculated that the conduction band edge shifts downward, while the valence band edge shifts upward with increasing temperature, and the decrease in the barrier height may mainly originate from the lowering of the edge of the conduction band.

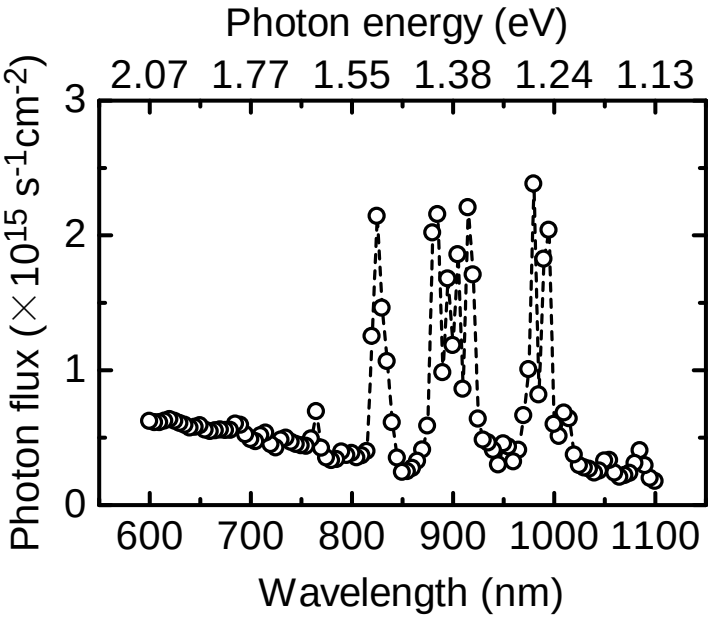

Figure A.10: The measured spectrum of the photon flux. The several sharp peaks are observed. The photocurrents were normalized as the same photon flux to discuss the wavelength dependence. The author confirmed that the photocurrent was proportional to the light intensity.

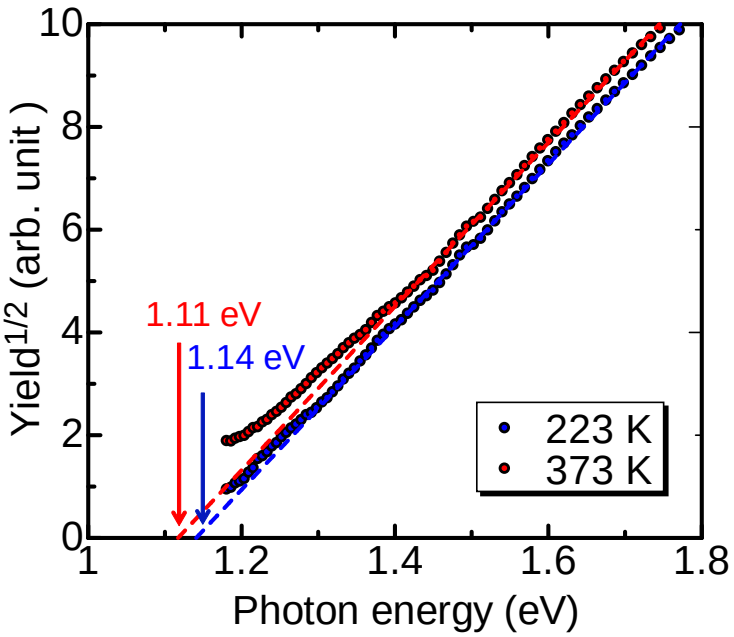

Figure A.11: The Fowler plot of the GaN SBD at 223 and 373 K. The plots shifted to the negative direction, reflecting the barrier height decreased with elevating temperature.

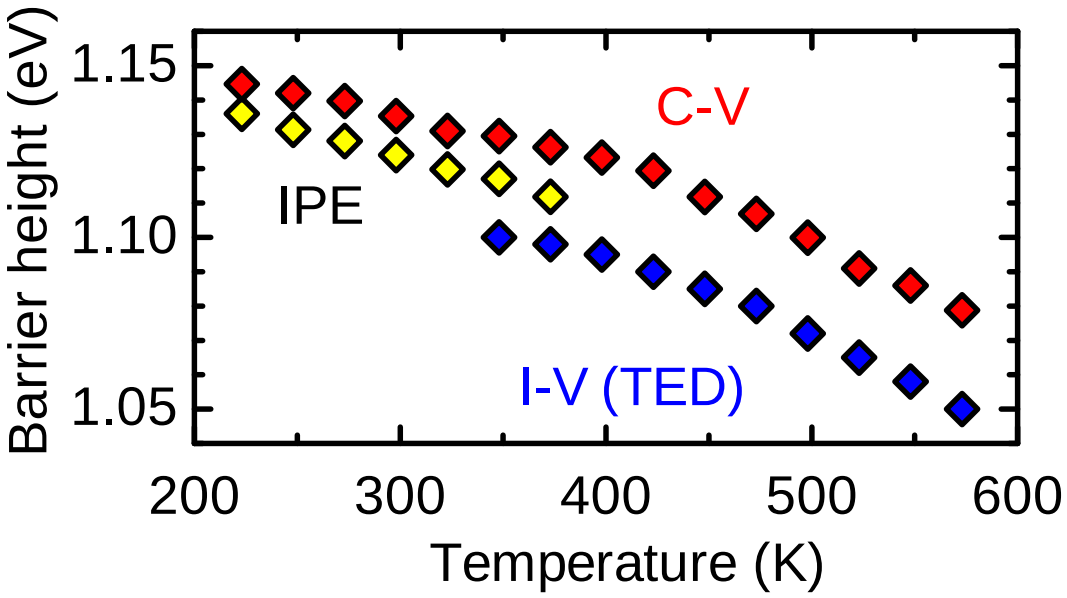

Figure A.12: The temperature dependence of the barrier height in the Ni/n-GaN SBD obtained by C–V, I–V (based on the TED analysis) and IPE measurements. The consistent temperature coefficient of $-0.2\pm(0.03)$ meV/K was obtained.

A.7 Discussion

Effect of the Deep Level

In the range of the 298–573 K, the slope of the C^{-2}–V plot was almost constant in Fig. A.3. However, actually, the slope slightly increased with decreasing temperature in the range of 298–223 K. The change of the slope reflects the temperature-dependent net donor concentration $N_\mathrm{d} - N_\mathrm{a}$ caused by electron emissions from the deep level E3 ($E_\mathrm{C} - E_\mathrm{t} = 0.6$ eV) [36]. The author investigated the E3 trap in the GaN SBD by the capacitance-transient measurement [37], and the trap concentration of $4{\times}10^{14}$ cm^{-3} was included in the epilayer. Figure A.13 shows the temperature dependence of the emission time constant (τ_e). At 298 K, τ_e was measured approximately 60 ms, which is shorter than the voltage-sweep time in the measurement (several seconds). At 223 K, τ_e was approximately 220 s, which is much longer than the voltage-sweep time and the electron were captured while the measurements. The difference between the obtained $N_\mathrm{d} - N_\mathrm{a}$ was about $4{\times}10^{14}$ cm^{-3}, which is consistent with the concentration of the E3 trap. It should be noted that the slope near 0 V is almost constant owing to the λ effect[1], and the effect of the deep level on the determination of the built-in potential (V_d) is negligible in the case that the data are analyzed near 0 V.

Richardson Plot

Based on the thermionic emission model, the following relationship can be derived as

$$\ln\left(\frac{J_0}{T^2}\right) = \ln(A^*) - \frac{e\phi_\mathrm{b}}{kT}. \tag{A.6}$$

Thus, the measured I–V–T characteristics of a Schottky barrier diode is often plotted as the $\ln(J_0/T^2)$–T^{-1} plot (Richardson plot), and the barrier height and the Richardson constant are extracted from the slope and the intercept of the Richardson plot [30]. Figure A.14(a) shows the Richardson plot of the I–V–T characteristics in this study. The *apparent* barrier height of 1.09 eV and the Richardson constant of 16 A/cm^{2}K^2 were obtained. These seem to be reasonable. However, the author here wants to note that (1) the temperature dependence of a barrier height and (2) the series diffusion transport effect on the Richardson plot.

The barrier height has $e\phi_\mathrm{b}(T) = e\phi_{\mathrm{b},0} + \alpha T$, and the Richardson plot is corrected as

$$\ln\left(\frac{J_0}{T^2}\right) = \ln(A^*) - \frac{e}{k}\alpha - \frac{e\phi_{\mathrm{b},0}}{kT}. \tag{A.7}$$

Then, the obtained barrier height is $e\phi_{\mathrm{b},0}$, which is the extrapolated value to the vertical axis as shown in Fig. A.14(b). The Richardson constant should be modified as $A^*_\mathrm{mod} = A^* \exp(e\alpha/k)$. If the temperature constant of +0.03 meV/K obtained from the TE analysis, the value of $A^*_\mathrm{mod} = 23$ A/cm^{2}K^2 is obtained, which agrees with the theoretical value of 24 A/cm^{2}K^2 ($m^*_n = 0.2m_0$). However, this analysis is not correct. I–V–T characteristics should be analyzed based on the TED model, not the Richardson plot.

[1]The Fermi level is higher than the trap level near the depletion layer edge, resulting in the region where electron emission does not occur. This is called as "λ effect".

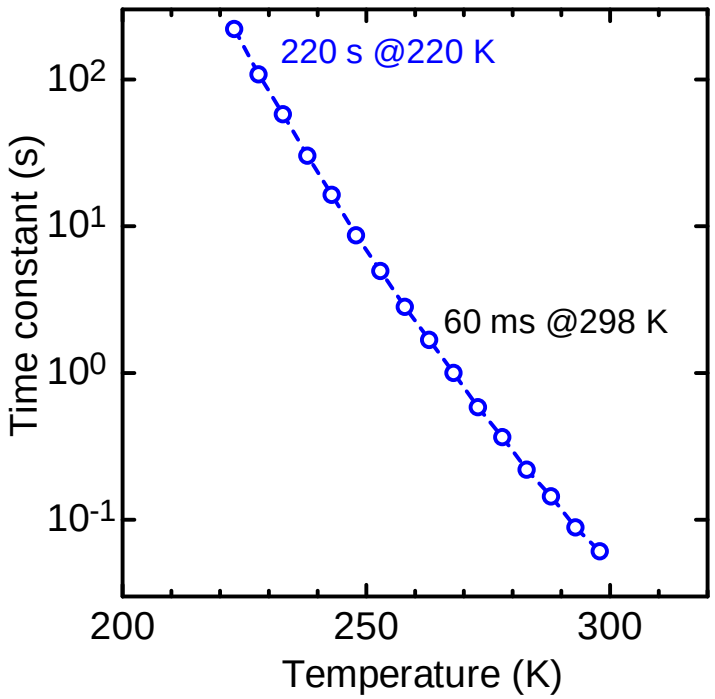

Figure A.13: The temperature dependence of the emission time constant of the E3 trap ($E_C - E_t$ ~0.6 eV). At low temperature, electrons keeps being captured while the C–V measurements, resulting in slight difference of the slope in Fig. A.3.

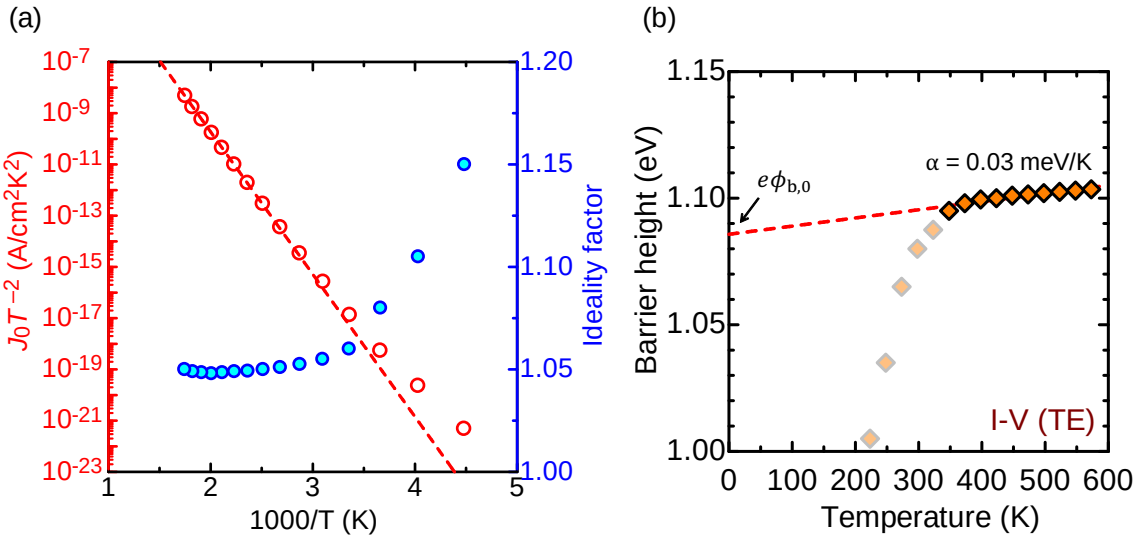

Figure A.14: (a) The Richardson plot of the GaN SBD in this study, and (b) the temperature dependence of the barrier height obtained from the I–V method (based on the TE analysis). The obtained $e\phi_{b,0}$ is indicated.

Barrier height in Various Metal/GaN Interface

Schottky barrier height is ideally determined by the work function of the metal and the electron affinity of the semiconductor as $e\phi_{\mathrm{b}} = \Phi_{\mathrm{m}} - \chi_{\mathrm{s}}$. The surface parameter $S = de\phi_{\mathrm{b}}/d\Phi_{\mathrm{metal}}$ is an important property in a Schottky interface. S often deviates from unity owing to non-ideal interface such as the pinning effect, interface traps, tunneling-induced polarization, etc. Schmitz *et al*. investigated that the Schottky barrier height in various metal/n-GaN Schottky barrier diodes fabricated on a sapphire substrate [38]. The value of S was 0.385 for the metal work function of 4.26–5.65 eV. Imadate *et al*. also reported the value of S in metal/GaN interfaces formed on clean m-plane surfaces by cleaving freestanding GaN substrates and Ga-polar c-plane GaN surface grown on GaN substrates [39]. The surface parameters of 0.565 and 0.642 for m- and c-planes were obtained by IPE measurements, respectively. However, the barrier height exhibited the variations, which caused the difficulty to determine the S value. The optimization of the surface treatments (chemical cleaning, polishing, post deposition annealing, etc.) and re-characterizations of the S value are needed.

In our group, the temperature dependence of the barrier height in metal/GaN interfaces were investigated for various metals (Au, Ni, Pd, Pt) [40, 41]. The negative temperature coefficients of -0.2 meV/K, which showed good agreement with the result in this study, was consistently obtained for various metals. These universal results for various metals/GaN Schottky interfaces also support that the temperature dependence of the barrier height reflects the shrinkage of the bandgap (lowering of the conduction band minimum) with elevating temperature.

Barrier height versus Doping Concentration

The temperature dependence of the barrier height in Ni/n-GaN Schottky interface formed on n-type homoepitaxial GaN layers with various donor concentrations ($N_{\mathrm{d}} - N_{\mathrm{a}} = 6.0\times10^{15}$, 6.0×10^{16} and 4.5×10^{17} cm^{-3}) was investigated [42]. The negative temperature coefficients of -0.2 meV/K were consistently obtained for these donor concentrations, which also supports the universal results. It was not observed the significant lowering of the barrier height with increasing donor concentrations in these donor concentration range.

Very recently, Hara *et al*. reported that the significant barrier height lowering due to the image force effect was observed in heavily-doped 4H-SiC Schottky barrier diodes [43]. Especially, $\Delta e\phi_{\mathrm{b}} = -0.2$ eV with clear forward thermionic field emission due to the high electric field ($\sim$3 MV/cm at 0 V) were observed in the device with donor concentration of 1.8×10^{19} cm^{-3}. The barrier height lowering with increasing donor concentration and significant thermionic field emission may also be observed in other wide bandgap semiconductors such as GaN and Ga_2O_3.

A.8 Summary

In conclusion, the author investigated the temperature dependence of the barrier height in the Ni/n-GaN vertical SBD from C–V, I–V and IPE measurements. The author pointed out that the decrease in the electron mobility with elevating temperature causes the slight over-estimation of the barrier height, and the I-V-T characteristics should be analyzed based on the thermionic emission-diffusion model. The barrier heights obtained from these methods consistently decreased with increasing temperature with similar temperature coefficients. The temperature coefficient was consistently obtained as $-0.2\pm(0.03)$ meV/K, which is about half of that of bandgap in GaN. The obtained temperature coefficient will be useful for detailed analyses of GaN-based electronic devices with Schottky contacts.

References

[1] Y. Saitoh, K. Sumiyoshi, M. Okada, T. Horii, T. Miyazaki, H. Shiomi, M. Ueno, K. Katayama, M. Kiyama, and T. Nakamura, *Appl. Phys. Express* **3**, 081001 (2010).

[2] N. Tanaka, K. Hasegawa, K. Yasunishi, N. Murakami, and T. Oka, *Appl. Phys. Express* **8**, 7 (2015).

[3] Y. Zhang, M. Sun, Z. Liu, D. Piedra, M. Pan, X. Gao, Y. Lin, A. Zubair, L. Yu, and T. Palacios, *IEDM Tech. Digest* (2016) p. 10.2.

[4] W. Li, K. Nomoto, M. Pilla, M. Pan, X. Gao, D. Jena, and H. G. Xing, *IEEE Trans. Electron Devices* **64(4)**, pp.869–872 (2017).

[5] Y. Zhang, Z. Liu, M. J. Tadjer, M. Sun, D. Piedra, C. Hatem, T. J. Anderson, L. E. Luna, A. Nath, A. D. Koehler, H. Okumura, J. Hu, X. Zhang, X. Gao, B. N. Feigelson, K. D. Hobart, and T. Palacios, *IEEE Electron Device Lett.* **38(8)**, pp.1097–1100 (2017).

[6] K. Hasegawa, G. Nishino, K. Yasunishi, N. Tanaka, N. Murakami, and T. Oka, *Appl. Phys. Express* **10**, 121002 (2017).

[7] S. Yang, S. Han, R. Lui, and K. Sheng, *Proc. of Int. Symp. on Power Semiconductor Device and ICs* (2018) p. pp.272–275.

[8] T. Arizumi and M. Hirose, *Jpn. J. Appl. Phys.* **8(6)**, 749 (1969).

[9] F. A. Padovani, *J. Appl. Phys.* **37**, 921 (1966).

[10] C. R. Crowell, S. M. Sze, and W. G. Spitzer, *Appl. Phys. Lett.* **4(5)**, 91 (1964).

[11] R. Hackam and P. Harrop, *IEEE Trans. Electron Devices* **19(12)**, pp.1231–1238 (1972).

[12] Y. P. Song, R. L. Van Meirhaeghe, W. H. Laflere, and F. Carbon, *Solid State Electron.* **29(6)**, pp.633–638 (1986).

[13] T. P. McLean, *Prog. Semiconductor* **5**, 53 (1960).

[14] F. Oswald, *Z. Naturforsch. A* **10A**, 927 (1955).

[15] Y. F. Tsay, B. Gong, and S. S. Mitra, *Phys. Rev. B* **6**, 2330 (1972).

[16] Y. Yıldırım, K. Ejderha, and A. Turut, *J. Appl. Phys.* **108**, 114506 (2010).

[17] N. Subramaniyam, M. Sopanen, H. Lipsanen, C.-H. Hong, and E.-K. Suh, *Jpn. J. Appl. Phys.* **50**, 030201 (2011).

[18] Y.-J. Lin, *J. Appl. Phys.* **106**, 013702 (2009).

[19] E. Arslan, S. Altindal, S. Ozcelik, and E. Ozbay, *J. Appl. Phys.* **105**, 023705 (2009).

[20] W. Lim, J.-H. Jeong, J.-H. Lee, S.-B. Hur, J.-K. Ryu, K.-S. Kim, T.-H. Kim, S. Y. Song, J.-I. Yang, and S. J. Pearton, *Appl. Phys. Lett.* **97**, 242103 (2010).

[21] D. Donoval, A. Chvala, R. Sramaty, J. Kovac, E. Morvan, C. Dua, M. A. DiForte-Poisson, and P. Kordos, *J. Appl. Phys.* **109**, 063711 (2011).

[22] Y. Zhou, D. Wang, C. Ahyi, C-C. Tin, J. Williams, M. Park, N. M. Williams, A. Hanser, and E. A. Preble, *J. Appl. Phys.* **101**, 024506 (2007).

[23] J. Suda, K. Yamaji, Y. Hayashi, T. Kimoto, K. Shimoyama, H. Namita, and S. Nagao, *Appl. Phys. Express* **3**, 101003 (2010).

[24] A. S. Barker and Jr. and M. Ilegems, *Phys. Rev. B* **7(2)**, pp.743–750 (1973).

[25] M. J. Kane, M. J. Uren, D. J. Wallis, P. J. Wright, D. E. J. Soley, A. J. Simon, and T. Martin, *Semicon. Sci. Technol.* **26**, 085006 (2011).

[26] N. Sawada, T. Narita, M. Kaechika, T. Uesugi, T. Kachi, M. Horita, T. Kimoto, and J. Suda, *Appl. Phys. Express* **11**, 041001 (2018).

[27] I. Vurgaftman, J. R. Meyer, and L. R. Ram-Mohan, *J. Appl. Phys.* **89**, 5815 (2001).

[28] S. M. Sze and K. K. Ng, *Physics of Semiconductor Devices*, (Wiley, New York, 2007), pp.153–162.

[29] K. Mochizuki, A. Terano, T. Ishigaki, T. Tsuchiya, T. Mishima, and N. Kaneda, *J. Mod. Math. Frontier* **3(2)**, 29 (2014).

[30] S. M. Sze and K. K. Ng, *Physics of Semiconductor Devices*, (Wiley, New York, 2007), pp.153–162.

[31] J. M. Andrew and M. P. Lepselter, *Solid State Electron.* **13**, 1011 (1970).

[32] R. H. Fowler, *Phys. Rev.* **38**, 45 (1931).

[33] T. Maeda, M. Okada, M. Ueno, Y. Yamamoto, M. Horita, and J. Suda, *Appl. Phys. Express* **9**, 091002 (2016).

[34] D. K. Schroder, *Semiconductor Material and Device Characterization*, (Wiley, New York, 2006), pp.157–164.

[35] H. Teisseyre, P. Perlin, T. Suski, I. Grzegory, S. Porowski, J. Jun, A. Pietraszko, and T. D. Moustakas, *J. Appl. Phys.* **76(4)**, 15 (1994).

[36] Y. Tokuda, *ECS Transactions* **75(4)**, pp.39–49 (2016).

[37] T. Maeda, *Bachelor Thesis*, (2016), Kyoto Universty [in Japanese].

[38] A.C. Schmitz, A T. Ping, M. A. Khan, Q. Chen, J. W. Yang, and I. Adesida, *J. Electron. Mater.* **27**, 4 (1998).

[39] H. Imadate, T. Mishima, and K. Shiojima, *Jpn. J. Appl. Phys.* **57**, 04FG13 (2018).

[40] R. Murase, T. Maeda, K. Kanegae, M. Horita, and J. Suda, presented at *The* 66*th Japan Society of Applied Physics Spring Meeting*, (2018), 9a-M121-9.

[41] R. Murase, T. Maeda, K. Kanegae, M. Horita, and J. Suda, presented at *The* 80*th Japan Society of Applied Physics Fall Meeting*, (2019), 20a-E301-3.

[42] R. Murase, T. Maeda, K. Kanegae, M. Horita, and J. Suda, presented at *The* 79*th Japan Society of Applied Physics Fall Meeting*, (2018), 20a-331-11.

[43] M. Hara, S. Asada, T. Maeda, and T. Kimoto, presented at *Int. Conf. on Silicon Carbide and Related Materials* (*ICSCRM*), (2019), We-3A-02.

Appendix B

Shockley-Read-Hall Lifetime in Homoepitaxial p-GaN

B.1 Introduction

Owing to its high critical electric field (∼3 MV/cm), GaN has attracted great attention as a material for the next-generation power devices [1–3]. There have been many reports on GaN vertical power devices fabricated on GaN bulk substrates, which showed high breakdown voltage and low on-resistance [4–16]. Owing to the low threading dislocation density ($\sim 10^6$ cm^{-2}) in homoepitaxial GaN, leakage current, inhomogeneity and other non-ideal characteristics were well suppressed in GaN-on-GaN devices, which enables us to analyze device characteristics in detail [17–21]. Hu *et al*. investigated forward current-voltage (I–V) characteristics of GaN-on-GaN p$^+$-n$^-$ junction diodes [18]. The recombination current with an ideality factor of 2 in the voltage range of 2.0–2.5 V and the diffusion current with a near unity ideality factor in the voltage range of 2.5–2.8 V were observed as shown in Fig. B.1. They extracted the Shockley-Read-Hall (SRH) lifetime, which is the square root of the product of hole and electron carrier lifetimes ($\tau_{\rm SRH} = \sqrt{\tau_{\rm p}\tau_{\rm n}}$), by analyzing the recombination current with consideration of the SRH recombination rate in the depletion layer [22, 23] . In the p$^+$-n$^-$ junction, the depletion layer extends to the lightly-doped n-layer side and the SRH recombination occurs in the n-layer. The obtained SRH lifetime is one for the n-GaN. In the same way, the SRH lifetime in p-GaN is expected to be obtained using the p$^-$-n$^+$ junction [24–26]. However, there is no report on the SRH lifetime in p-GaN.

Recently, the growth technique of a lightly Mg-doped p-GaN has been developed, and relatively low Mg concentration can be controllable [24, 27, 28]. In this study, the author investigated the forward I–V characteristics in GaN-on-GaN p-n$^+$ junction diodes, in which the depletion layer mainly extends to the p-layer side. The large recombination current with an ideality factor of 2 was clearly observed in the wide voltage range of 1.8–2.7 V. The SRH lifetime in homoepitaxial p-GaN and its temperature dependence are investigated.

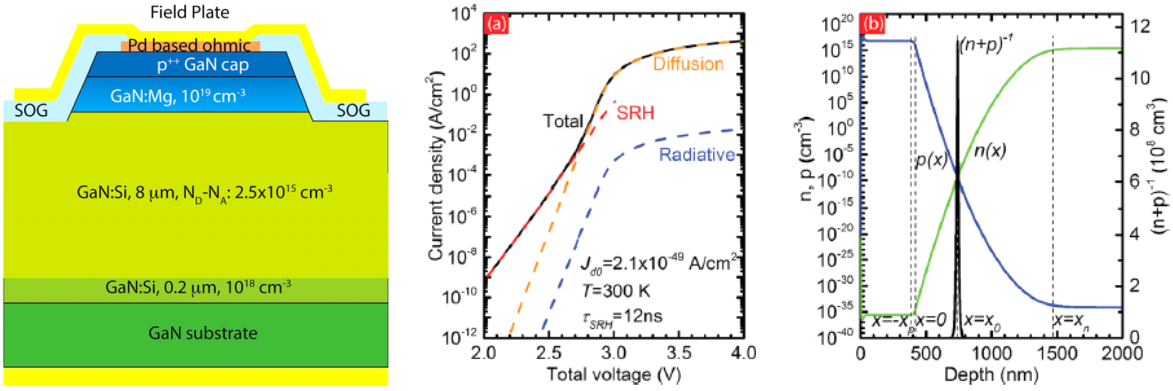

Figure B.1: The textbook-like current-voltage characteristics observed in the GaN p^+/n^- junction diode reported by Hu *et al.* [18]. Based on the analysis of the recombination current, $\tau_{\mathrm{SRH}} = 6$ ns in homoepitaxi n-GaN was obtained.

B.2 Device Structure

Figure B.2 shows the schematic cross-section of the GaN p-n$^+$ junction diodes. The GaN layers were grown by metal organic vapor phase epitaxy (MOVPE) on a freestanding GaN substrate prepared by hydride vapor phase epitaxy (HVPE). The doping concentrations and the thickness of the epilayers were obtained by secondary ion mass spectrometry (SIMS). The thickness of p-layer was 2.5 μm. The Mg concentration in p-epilayer and the Si concentration in n$^+$-layer were 1×10^{17} cm^{-3} and 6×10^{18} cm^{-3}, respectively. After the epitaxial growth, high temperature annealing was performed at 1123 K for 5 min to remove hydrogen bound to Mg in the GaN epilayer. The mesa isolation structures of the p$^+$/p/n$^+$ layers were formed by Cl_2-based inductively coupled plasma-reactive ion etching (ICP-RIE). Mesa height is about 3 μm. The anode and cathode electrodes were formed by the deposition of Ni/Au on the epitaxial layer and Ti/Al/Ni on the backside of the substrate, respectively. From the capacitance-voltage (C–V) measurements, the net doping concentration $N_\mathrm{a}N_\mathrm{d}/(N_\mathrm{a}+N_\mathrm{d})$ of $\sim1\times10^{17}$ cm^{-3} was obtained, which shows good agreement with the Mg concentration in the p-layer. I–V and C–V measurements were measured in dry air using a Keysight B1505A parameter analyzer. The temperature of the sample stage was controlled in the range of 223–573 K.

B.3 Forward Current-Voltage Characteristics in p$^-$/n$^+$ Junction Diodes

B.3.1 Analysis of Recombination Current

The forward I–V characteristics of a p-n junction diode can be expressed as

$$J = J_{\mathrm{dif},0}\exp\left(\frac{eV}{kT}\right) + J_{\mathrm{SRH},0}\exp\left(\frac{eV}{2kT}\right). \tag{B.1}$$

The first term represents the diffusion current, and the second term is the SRH (non-radiative) recombination current density in the depletion layer. $J_{\mathrm{dif},0}$ and $J_{\mathrm{SRH},0}$ are the bias insensitive terms of diffusion and recombination currents. The constants of e and k are the elementary charge and the Boltzmann constant, respectively. V is the voltage applied over the p-n junction. Figure B.3 shows the forward I–V characteristics of GaN p-n$^+$ junction diodes at 298 K. The ideality factor extracted as $n = e/\left[kT(d\ln(J)/dV)\right]$ is also shown in Fig. B.3 as a function of the voltage. The ideality factor of "2" was observed in the voltage range of 1.8–2.7 V, indicating that this current component is the SRH recombination current. The size dependence of the forward I–V characteristics was investigated, and it was confirmed that the recombination current is proportional to the junction area, as shown in Fig. B.4. This indicates that the recombination current arises from the overall junction area, not from the surface recombination at the mesa periphery. The extrapolated value

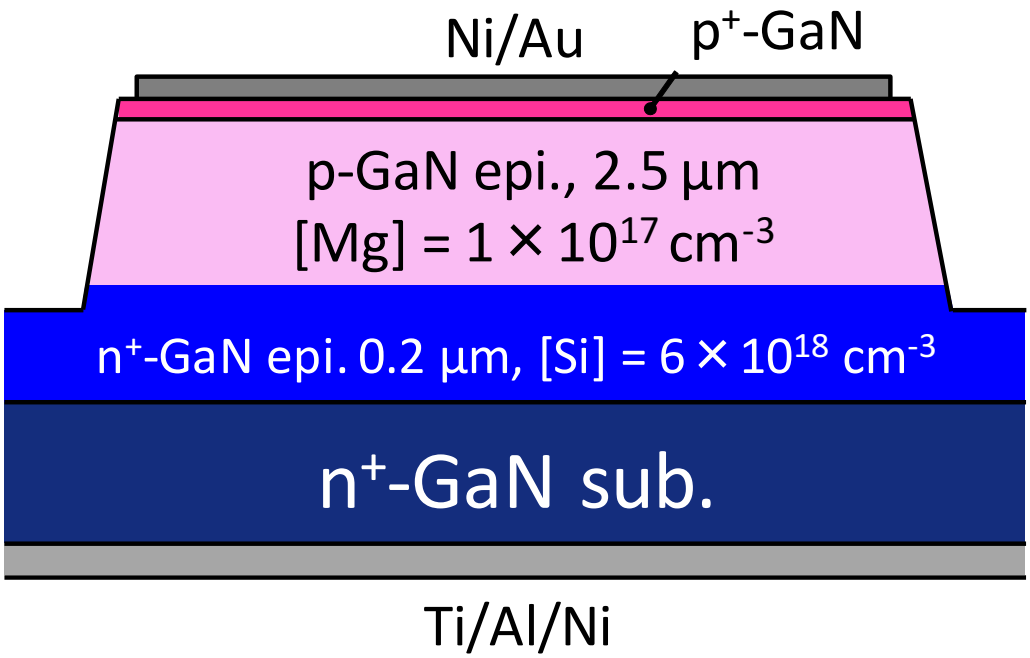

Figure B.2: Schematic cross section of a GaN p^-/n^+ junction diode with mesa isolation structure.

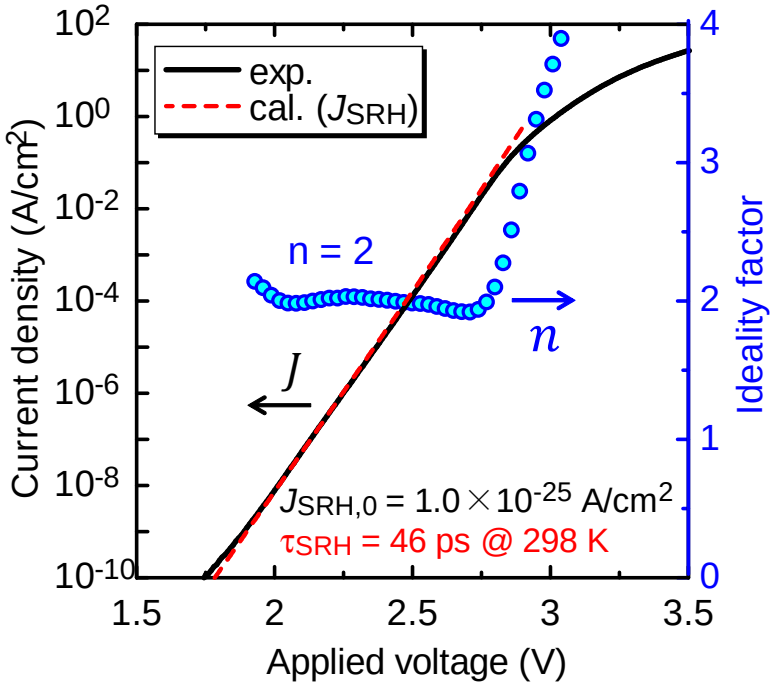

Figure B.3: Forward current-voltage characteristics of the GaN p-n junction diode. The ideality factor as a function of the applied voltage is shown blue circles. The calculated recombination current is shown as red broken line, and the $\tau_{\mathrm{SRH}} = 46$ ps in homoepitaxial p-GaN was obtained.

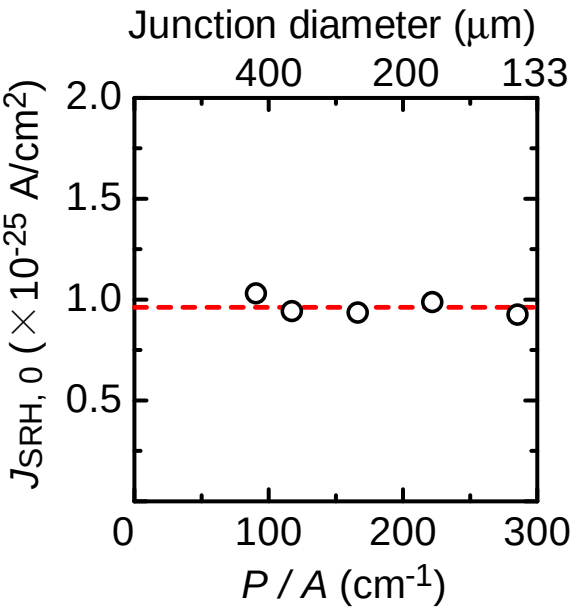

Figure B.4: The size dependence of the extrapolated current density to the vertical axis. The recombination current was proportional to the junction area, not the periphery.

to the vertical-axis ($J_{\mathrm{SRH},0}$) was 1×10^{-25} Acm^{-2}, which is 5 times larger than the value of 2.7×10^{-26} Acm^{-2} in GaN p$^+$/n$^-$ junction diode reported by Hu *et al.* [18]. The on-resistance is about 0.1 Ωcm^2 and the voltage drop outside the junction at 1 A/cm^2 current density is about 0.1 V. Since the voltage drop due to the series-resistance came to be dominant for higher voltage than 2.7 V, a diffusion current component was not clearly observed, which is different from the GaN p$^+$/n$^-$ junction diode [18].

A SRH lifetime can be extracted from the SRH recombination current by considering the SRH recombination in the depletion layer [18, 23]. For the forward bias condition, the SRH recombination rate in the depletion layer via a non-radiative recombination center (NRC) with a single energy level which is sufficiently far from the band edges can be written as

$$U_{\mathrm{SRH}} \sim \frac{pn - n_i^2}{p\tau_{\mathrm{n}} + n\tau_{\mathrm{p}}} = \frac{n_i^2\left[\exp\left(eV/kT\right) - 1\right]}{p\tau_{\mathrm{n}} + n\tau_{\mathrm{p}}}. \tag{B.2}$$

p, n, τ_{n}, τ_{p} are the hole concentration, the electron concentration, the hole lifetime, and the electron lifetime, respectively. The electron and hole carrier lifetimes are written as $\tau_{\mathrm{n}} = (N_{\mathrm{t}} v_{\mathrm{th,n}} \sigma_{\mathrm{n}})^{-1}$ and $\tau_{\mathrm{p}} = (N_{\mathrm{t}} v_{\mathrm{th,p}} \sigma_{\mathrm{p}})^{-1}$, respectively. N_{t} is a NRC concentration. $v_{\mathrm{th,n}}$ and $v_{\mathrm{th,p}}$ are thermal velocities of carriers, which depend on the effective masses. σ_{n} and σ_{p} are the electron and hole capture cross sections. n_i is the intrinsic carrier concentration, which depends on the bandgap, temperature, and the density-of-state effective masses. In this study, temperature dependence of the bandgap [29] was considered and the electron and hole density-of-state effective masses of $0.2m_0$ and $1.5m_0$ were used [30], respectively.

Figure B.5 shows (a) the band diagram of the p-n$^+$ junction under applied voltage of 2 V and (b) the distributions of n, p, and $(n+p)^{-1}$. At the plane $x = x_0$ where $p\tau_{\mathrm{n}} = n\tau_{\mathrm{p}}$, U_{SRH} has a very sharp peak. x_0 and the electric field at x_0 (F_0) can be expressed as

$$x_0 = -W_{\mathrm{p}} + \sqrt{\frac{\varepsilon_{\mathrm{s}} kT}{e^2 N_{\mathrm{a}}} \cdot \left[\ln\left(\frac{\tau_{\mathrm{n}}}{\tau_{\mathrm{p}}}\right) + 2\ln\left(\frac{N_{\mathrm{a}}}{n_i}\right) - \frac{eV}{kT}\right]}, \; F_0 = \frac{eN_{\mathrm{a}}(W_{\mathrm{p}} + x_0)}{\varepsilon_{\mathrm{s}}}. \tag{B.3}$$

ε_{s} is the dielectric constant, and $\varepsilon_{\mathrm{s}} = 10.4\varepsilon_0$ is used in this study [31, 32]. W_{p} is the edge of the depletion layer in p-region. It should be noted that $x = x_0$ is very close to the peak position of $(n+p)^{-1}$ where $n = p$, since n and p significantly change in the depletion layer (the term of $\ln(\tau_{\mathrm{n}}/\tau_{\mathrm{p}})$ is negligible). Therefore, the distribution of U_{SRH} is very similar to the distribution of $(n+p)^{-1}$ as shown in Fig. B.5. The distributions of carriers near the plane $x = x_0$ can be written as

$$n(x) = \sqrt{\frac{\tau_{\mathrm{n}}}{\tau_{\mathrm{p}}}} n_i \exp\left(\frac{eV}{2kT}\right) \cdot \exp\left[\frac{eF_0(x - x_0)}{kT}\right], \tag{B.4}$$

$$p(x) = \sqrt{\frac{\tau_{\mathrm{p}}}{\tau_{\mathrm{n}}}} n_i \exp\left(\frac{eV}{2kT}\right) \cdot \exp\left[-\frac{eF_0(x - x_0)}{kT}\right], \tag{B.5}$$

where $x = 0$ is the p-n junction interface. Substituting the formulae (4) for the formula (2), the SRH recombination rate near $x = x_0$ can be obtained as

$$U_{\mathrm{SRH}} = \frac{n_i}{\sqrt{\tau_{\mathrm{p}}\tau_{\mathrm{n}}}} \cdot \cosh^{-1}\left(\frac{eF_0(x - x_0)}{kT}\right) \cdot \sinh\left(\frac{eV}{2kT}\right). \tag{B.6}$$

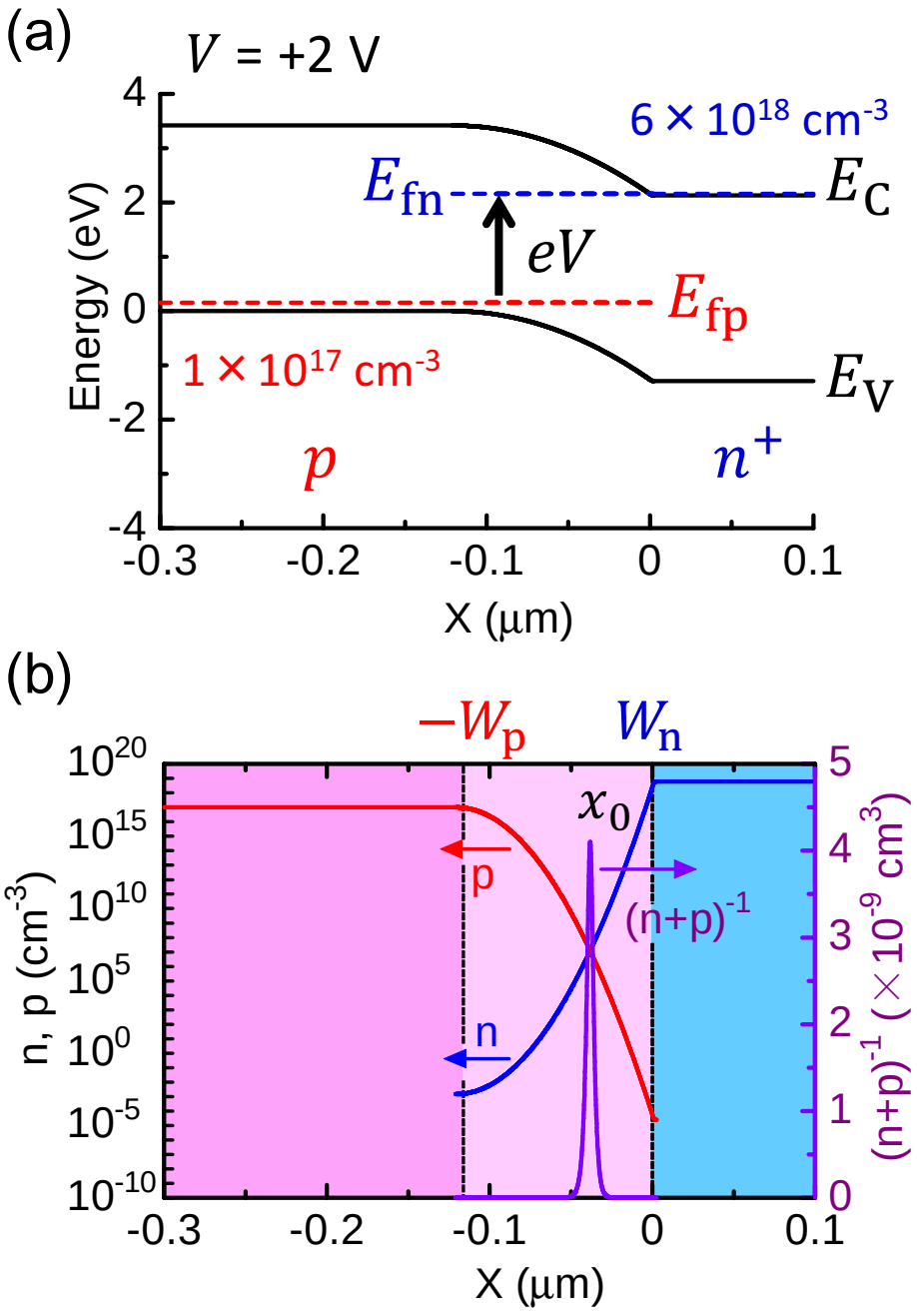

Figure B.5: (a) Band diagram of the p-n$^+$ junction and (b) the distributions of electrons (n), holes (p) and $(n+p)^{-1}$ under an applied voltage of +2 V. The SRH recombination intensively occurs at the depth x_0, which is very close to the peak of $(n+p)^{-1}$.

The SRH recombination current can be written as

$$J_{\mathrm{SRH}} = e\int_{-W_{\mathrm{p}}}^{W_{\mathrm{n}}} U_{\mathrm{SRH}}dx \sim \frac{\pi n_i kT}{\tau_{\mathrm{SRH}}F_0}\sinh\left(\frac{eV}{2kT}\right) \sim \frac{\pi n_i kT}{2\tau_{\mathrm{SRH}}F_0}\exp\left(\frac{eV}{2kT}\right), \tag{B.7}$$

where $\tau_{\mathrm{SRH}} = \sqrt{\tau_{\mathrm{n}}\tau_{\mathrm{p}}}$ is used. The integral limits are extended approximately to infinity based on the fact that the term of $\cosh^{-1}(x)$ decreases sharply with x. It should be noted that one pair of an electron and a hole contributes to one flow of elementary charge.

The SRH lifetime in the homoepitaxial p-GaN was extracted from the extrapolated value to the vertical axis ($J_{\mathrm{SRH},0}$) using the formula (6). The calculated SRH recombination current is shown in Fig. B.3 as the red broken line, which shows good agreement with the experimental data. The SRH lifetime of 46 ps was obtained at 298 K. This is much shorter than the lifetime of 12 ns in n-GaN reported by Hu *et al.* [18]. This suggests that the NRC concentration in p-GaN is much higher than that in n-GaN, and/or the capture cross section of the NRCs in p-GaN is much larger than that in n-GaN.

B.3.2 Non-Radiative Recombination Centers in Homoepitaxial p-GaN

Chichibu *et al.* have investigated the photoluminescence lifetime (τ_{PL}) of the near-band-edge emission in GaN using time-resolved photoluminescence (TRPL) measurements [33–35]. For GaN, τ_{PL} is limited by the non-radiative recombination process at room temperature under low-excitation condition [34], and τ_{PL} represents the minority carrier lifetime (τ_{n} for p-GaN). In homoepitaxial p-GaN layers [35], two lifetime components (fast $\tau_1 \sim 10^{-11}$ s and slow $\tau_2 \sim 10^{-10}$ s) were observed in the TRPL decay, which are much shorter than the photoluminescence lifetime in homoepitaxial n-GaN ($\sim 10^{-9}$ s) [34], as shown in Fig. B.6.

Uedono *et al.* have reported on the positron annihilation spectroscopy (PAS) measurements, which is a powerful tool to obtain concentrations and identify types of vacancy-type defects, for GaN [36–38]. They found that τ_{PL} was proportional to the inverse of the vacancy-type-defects concentration ($\mathrm{N_V}$), suggesting that the vacancy-type defects are the main NRCs in GaN. From these relationships (τ_{PL} vs. $\mathrm{N_V}$), they obtained the capture cross sections of the minority carriers. For p-GaN, σ_{n} of the NRCs was estimated to the middle of 10^{-13} cm^2, and the origin of the NRCs in p-GaN was identified as $\mathrm{V_{Ga}(V_N)_2}$ or $\mathrm{V_{Ga}(V_N)_3}$ [35]. On the other hand, in n-type bulk GaN, the σ_{p} and the origin of the NRCs were $\sigma_{\mathrm{p}} = 7\times10^{-14}$ cm^2 and $\mathrm{V_{Ga}V_N}$, respectively [33, 34]. It should be noted that the origins as well as the capture cross sections of the NRCs in p-GaN and n-GaN are different.

The author has not measured TRPL and PAS for our p-GaN layer. Here, the author refers the reported results [35] for similar Mg concentrations. For p-GaN with Mg concentration of 1×10^{17} cm^{-3}, $\tau_{\mathrm{n}} = 20$ ps, and $N_{\mathrm{t}} = 1\times10^{16}$ cm^{-3} were reported. From the relationships of $\tau_{\mathrm{SRH}} = \sqrt{\tau_{\mathrm{n}}\tau_{\mathrm{p}}}$ and our obtained SRH lifetime in p-GaN of 46 ps, the author obtained $\tau_{\mathrm{p}} = 106$ ps. The electron capture cross section was estimated to be 3×10^{-13} cm^2.

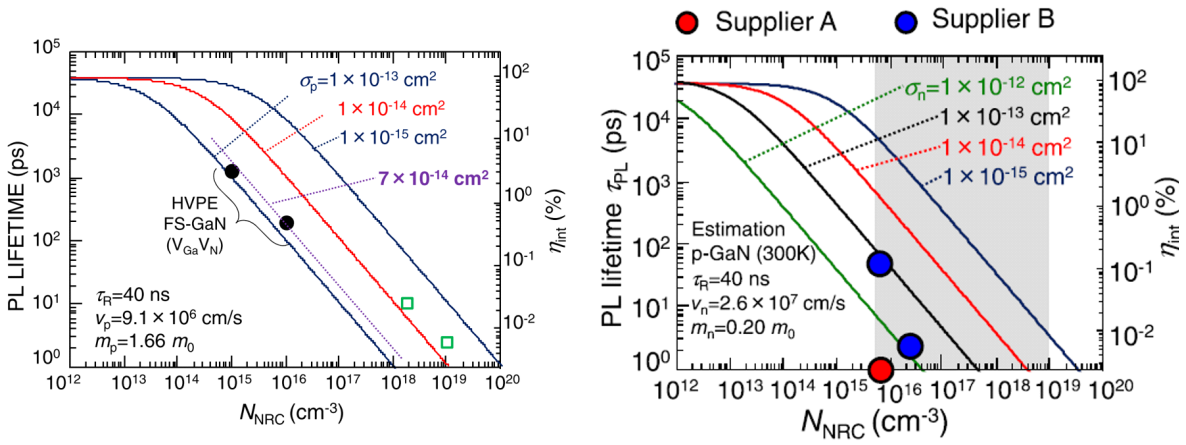

Figure B.6: The PL lifetimes in homoepitaxial n-GaN [34] and p-GaN [35] reported by Chichibu *et al*. From the relationship between τ_{PL} versus N_{NRC}, the capture cross sections of minority carriers for the NRCs in n- and p-GaN were estimated.

Although our estimation is very rough, the NRC in p-GaN is thought to have large capture cross sections for both electrons and holes, i.e., act as a very efficient recombination center.

Figure B.7 shows the forward I–V characteristics of the GaN p-n$^+$ junction diode in the range of 223–573 K. The recombination current increased with elevating temperature. Figure B.8 shows the temperature dependence of the SRH lifetime in the homoepitaxial p-GaN extracted from the recombination currents in the range of 223–573 K. It is known that the temperature dependence of the SRH lifetime follows an empirical power-law relation ($\tau_{\mathrm{SRH}} \propto T^{\alpha}$) [18, 39]. The empirical power law of $\tau_{\mathrm{SRH}} = 1.2{\times}10^{-16} \times T^{2.25}$ (s) for the temperature dependence of the SRH lifetime in the homoepitaxial p-GaN was obtained in this study. This value is different from the temperature dependence of the SRH lifetime in n-GaN ($3.9{\times}10^{-12} \times T^{1.41}$ (s)) reported by Hu *et al.* [18]. This result suggests that the temperature dependence of the capture cross section of the NRCs in p-GaN is different from that in n-GaN. It may be related to the results reported by Chichibu *et al.*; the origins of intrinsic NRCs in p-GaN ($\mathrm{V_{Ga}(V_N)_2}$ or $\mathrm{V_{Ga}(V_N)_3}$) are different from those in n-GaN ($\mathrm{V_{Ga}V_N}$) [33–35].

B.4 Discussion

Energy Level of Non-Radiative Recombination Center

In the Eq. (B.2), it was assumed that the energy level of the (single) NRC is sufficiently far from the band edges. Strictly, the Eq. (B.2) is written as

$$U_{\mathrm{SRH}} = \frac{pn - n_i^2}{\tau_{\mathrm{n}}\left[p(x) + p_{\mathrm{t}}\right] + \tau_{\mathrm{p}}\left[n(x) + n_{\mathrm{t}}\right]} = \frac{n_i^2\left[\exp\left(eV/kT\right) - 1\right]}{\tau_{\mathrm{n}}\left[p(x) + p_{\mathrm{t}}\right] + \tau_{\mathrm{p}}\left[n(x) + n_{\mathrm{t}}\right]}. \tag{B.8}$$

Here, $n_{\mathrm{t}} = n_i \exp(\frac{E_{\mathrm{t}} - E_{\mathrm{i}}}{kT})$ and $p_{\mathrm{t}} = n_i \exp(\frac{E_{\mathrm{i}} - E_{\mathrm{t}}}{kT})$ are the calculated electron and hole concentrations if the Fermi level is at the trap energy level E_{t}. If n_{t} and p_{t} are not negligible compared to n and p (in other words, the energy level of the NRC is not far from the band edges), U_{SRH} becomes very small. Thus, the deep levels near band edges does not act as NRC. Therefore, the energy level of the NRC in p-GaN is mid-gap ($E_i \pm 0.5\mathrm{eV}$).

Effect of Hole Concentration on Analysis

In this study, the value of hole concentration was assumed to be equal to the net acceptor concentration obtained by C–V characteristics. Mathematically, in the Eq. (B.3), "$2\ln(p/n_i)$" was transformed to "$2\ln(N_{\mathrm{a}}/n_i)$" based on the assumption of $p \sim N_{\mathrm{a}}$. However, the actual hole concentration may be several percent of the acceptor concentrations at room temperature [40]. Therefore, the analysis should include an error. Here, it should be noted that the error caused by the difference between N_{a} and p is small, since p very rapidly changes near x_0 where $\tau_{\mathrm{p}} n = \tau_{\mathrm{n}} p$. If the value of p is one order of magnitude lower than N, the caused error in τ_{SRH} is $\sim$5%.

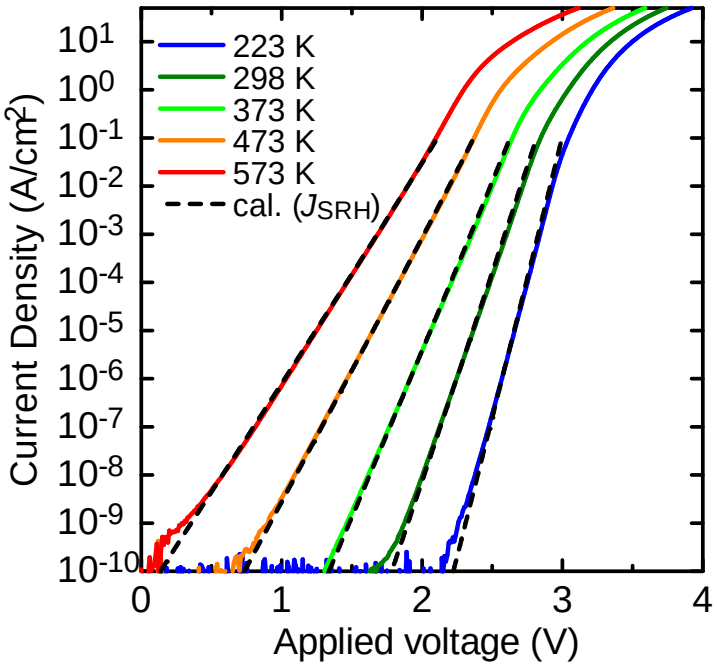

Figure B.7: Forward I–V characteristics in the GaN p-n$^+$ junction diode at 223–573 K. The calculated SRH recombination currents at each temperature are also shown as broken lines.

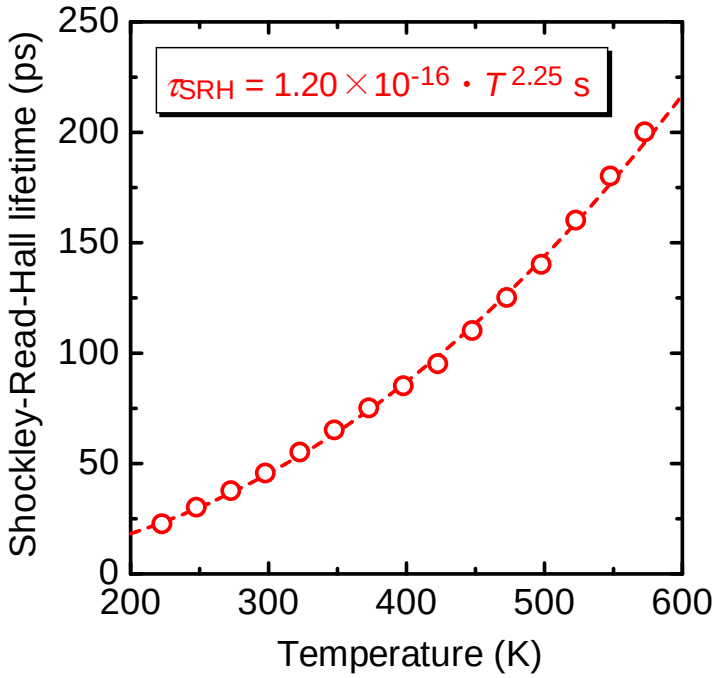

Figure B.8: Temperature dependence of the SRH lifetime in the homoepitaxal p-GaN, which follows an empirical power-law relation with a temperature coefficient $\alpha = 2.25$.

B.5 Summary

The author investigated the SRH lifetime in a homoepitaxial p-GaN ($N_a = 1\times10^{17}$ cm^{-3}) by analyzing the recombination current in GaN-on-GaN p-n$^+$ junction diodes. The SRH lifetime in p-GaN of 46 ps was obtained, which is much shorter than that in n-GaN of 12 ns reported previously. Assuming the previously reported minority carrier (electron) lifetime and NRC concentration in homoepitaxial p-GaN with a similar Mg concentration ($\tau_n = 20$ ps, $N_t = 1\times10^{16}$ cm^{-3}), the author roughly estimated the hole lifetime and the hole capture cross section to be $\tau_p = 106$ ps and $\sigma_p = 3\times10^{-13}$ cm^2. The temperature dependence of the SRH lifetime is also investigated, and the empirical power law of $\tau_{SRH} = 1.2\times10^{-16} \times T^{2.25}$ (s) was obtained. Analyzing forward I–V characteristics of p-n$^+$ junction diodes is one of useful ways for investigating properties of the NRC in p-GaN layer.

References

[1] T. Kachi, *Jpn. J. Appl. Phys.* **53**, 100210 (2014).

[2] I. C. Kizilyalli, A. P. Edwards, O. Aktas, T. Prunty, and D. Bour, *IEEE Trans. Electron Devices* **62(2)**, pp.414–422 (2015).

[3] T. Ueda, *Jpn. J. Appl. Phys.* **58**, SC0804 (2019).

[4] Y. Saitoh, K. Sumiyoshi, M. Okada, T. Horii, T. Miyazaki, H. Shiomi, M. Ueno, K. Katayama, M. Kiyama, and T. Nakamura, *Appl. Phys. Express* **3**, 081001 (2010).

[5] K. Hasegawa, G. Nishino, K. Yasunishi, N. Tanaka, N. Murakami, and T. Oka, *Appl. Phys. Express* **10**, 121002 (2017).

[6] W. Li, K. Nomoto, M. Pilla, M. Pan, X. Gao, D. Jena, and H. G. Xing, *IEEE Trans. Electron Devices* **64(4)**, pp.869–872 (2017).

[7] I. C. Kizilyalli, T. Prunty, and O. Aktas, *IEEE Electron Device Lett.* **36(10)**, pp.1073–1075 (2015).

[8] H. Ohta, N. Kaneda, F. Horikiri, Y. Narita, T. Yoshida, T. Mishima, and T. Nakamura, *IEEE Electron Device Lett.* **36(11)**, pp.1180–1182 (2015).

[9] K. Nomoto, Z. Hu, B. Song, M. Zhu, M. Qi, R. Yan, V. Protasenko, E. Imhoff, J. Kuo, N. Kaneda, T. Mishima, T. Nakamura, D. Jena, and H. G. Xing, *IEDM Tech. Digest* (2015) p. 9.7.

[10] T. Oka, T. Ina, Y. Ueno, and J. Nishii, *Appl. Phys. Express* **8**, 054101 (2015).

[11] R. Tanaka, S. Takashima, K. Ueno, H. Matsuyama, Y. Fukushima, M. Edo, and K. Nakagawa, *Ext. Abst. of Int. Conf. on Solid State Devices and Materials* (2019) p. 443.

[12] D. Shibata, R. Kajitani, M. Ogawa, K. Tanaka, S. Tamura, T. Hatsuda, M. Ishida, and T. Ueda, *IEDM Tech. Digest* (2016) p. 10.1.

[13] H. Nie, Q. Diduck, B. Alvarez, A. P. Edwards, B. M. Kayes, M. Zhang, G. Ye, T. Prunty, and D. Bour, *IEEE Electron Device Lett.* **35(9)**, pp.939–941 (2014).

[14] Y. Zhang, M. Sun, D. Piedra, J. Hu, Z. Liu, Y. Lin, X. Gao, K. Shepard, and T. Palacios, *IEDM Tech. Digest* (2017) p. 9.2.

[15] C. Gupta, C. Lund, S. H. Chan, A. Agarwal, J. Liu, Y. Enatsu, S. Keller, and U. K. Mishra, *IEEE Electron Device Lett.* **38(3)**, pp.353–355 (2017).

[16] D. Ji, C. Gupta, S. H. Chan, A. Agarwal, W. Li, S. Keller, U. K. Mishra, and S. Chowdhury, *IEDM Tech. Digest* (2017) p. 9.4.

[17] J. Suda, K. Yamaji, Y. Hayashi, T. Kimoto, K. Shimoyama, H. Namita, and S. Nagao, *Appl. Phys. Express* **3**, 101003 (2010).

[18] Z. Hu, K. Nomoto, B. Song, M. Zhu, M. Qi, M. Pan, X. Gao, V. Protasenko, D. Jena, and H. G. Xing, *Appl. Phys. Lett.* **107**, 243501 (2015).

[19] S. Takashima, K. Ueno, H. Matsuyama, T. Inamoto, M. Edo, T. Takahashi, M. Shimizu, and K. Nakagawa, *Appl. Phys. Express* **10**, 121004 (2017).

[20] T. Hashizume, S. Kaneki, T. Oyobiki, Y. Ando, S. Sasaki, and K. Nishiguchi, *Appl. Phys. Express* **11**, 124102 (2018).

[21] T. Maeda, M. Okada, M. Ueno, Y. Yamamoto, T. Kimoto, M. Horita, and J. Suda, *Appl. Phys. Express* **10**, 051002 (2017).

[22] C. T. Sah, R. N. Noyce, and W. Shockley, *Poc. IRE* **45**, 1228 (1957).

[23] R. Corkish and M. A. Green, *J. Appl. Phys.* **80(5)**, 3083 (1996).

[24] T. Narita, Y. Tokuda, T. Kogiso, K. Tomita, and T. Kachi, *J. Appl. Phys.* **123**, 161405 (2018).

[25] T. Kogiso, T. Narita, H. Yoshida, Y. Tokuda, K. Tomita, and T. Kachi, *Jpn. J. Appl. Phys.* **58**, SCCB36 (2019).

[26] T. Maeda, T. Narita, H. Ueda, M. Kanechika, T. Uesugi, T. Kachi, T. Kimoto, M. Horita, and J. Suda, *Jpn. J. Appl. Phys.* **58**, SCCB14 (2019).

[27] T. Narita, K. Tomita, Y. Tokuda, T. Kogiso, M. Horita, and T. Kachi, *J. Appl. Phys.* **124**, 215701 (2018).

[28] T. Narita, N. Ikarashi, K. Tomita, K. Kataoka, and T. Kachi, *J. Appl. Phys.* **124**, 165706 (2018).

[29] I. Vurgaftman, J. R. Meyer, and L. R. Ram-Mohan, *J. Appl. Phys.* **89**, 5815 (2001).

[30] M. Suzuki, T. Uenoyama, and A. Yanase, *Phys. Rev. B* **52(11)**, 8132 (1995).

[31] A. S. Barker and Jr. and M. Ilegems, *Phys. Rev. B* **7(2)**, pp.743–750 (1973).

[32] M. J. Kane, M. J. Uren, D. J. Wallis, P. J. Wright, D. E. J. Soley, A. J. Simon, and T. Martin, *Semicon. Sci. Technol.* **26**, 085006 (2011).

[33] S. F. Chichibu, K. Hazu, Y. Ishikawa, M. Tashiro, H. Namita, S. Nagao, K. Fujito, and A. Uedono, *J. Appl. Phys.* **111**, 103518 (2012).

[34] S. F. Chichibu, A. Uedono, K. Kojima, H. Ikeda, K. Fujito, S. Takashima, M. Edo, K. Ueno, and S. Ishibashi, *J. Appl. Phys.* **123**, 161413 (2018).

[35] S. F. Chichibu, K. Shima, K. Kojima, S. Takashima, M. Edo, K. Ueno, S. Ishibashi, and A. Uedono, *Appl. Phys. Lett.* **112**, 211901 (2018).

[36] A. Uedono, S. F. Chichibu, Z. Q. Chen, M. Sumiya, R. Suzuki, T. Ohdaira, T. Mikado, T. Mukai, and S. Nakamura, *J. Appl. Phys.* **90**, 181 (2001).

[37] A. Uedono, S. Takashima, M. Edo, K. Ueno, H. Matsuyama, H. Kudo, H. Naramoto, and S. Ishibashi, *Phys. Status Solidi B* **12**, 2794–2801 (2015).

[38] A. Uedono, S. Takashima, M. Edo, K. Ueno, H. Matsuyama, W. Egger, T. Koschine, C. Hugenschmidt, M. Dickmann, K. Kojima, S. F. Chichibu, and S. Ishibashi, *Phys. Status Solidi B* **255**, 1700521 (2018).

[39] M. S. Tyagi and R. Van Overstraeten, *Solid State Electron.* **26**, 577 (1983).

[40] M. Horita, S. Takashima, R. Tanaka, H. Matsuyama, K. Ueno, M. Edo, T. Takahashi, M. Shimizu, and J. Suda, *Jpn. J. Appl. Phys.* **56**, 031001 (2017).

Appendix C

Franz-Keldysh Effect in SiC p-n Junction Diodes

C.1 Introduction

Wide-bandgap semiconductors (SiC, GaN, Ga_2O_3, etc.) have attracted much attention as a material for next-generation power devices [1–9], as well as harsh-environment electronic devices [10–13] and visible-blind/solar-blind UV photodetectors [14–17]. SiC, which is an indirect bandgap semiconductor, is rather exceptional among the many wide-bandgap semiconductors because it makes both n- and p-type control across a wide doping range (10^{14}–10^{19} cm^{-3}) and doping control of both n- and p-regions by ion-implantation is achievable. In addition, n- and p-type (0001)-face and n-type ($11\bar{2}0$)-face freestanding substrates are available [18]. In recent years, the 1 kV-class 4H-SiC Schottky barrier diodes and the MOSFETs are commercially avialable by several vendors. For ultrahigh-voltage (>10 kV) bipolar devices, intensive studies are ongoing and >20 kV-class PiN diodes [19–21], and switching devices [22–25] have been demonstrated.

When high electric field is applied to a semiconductor, the wavefunctions of electrons and holes leak into the bandgap. Then, the optical absorption changes; a quasi-exponential tail for below-bandgap and oscillation structure for above-bandgap are observed in the optical absorption coefficient. This is known as the Franz-Keldysh (FK) effect [26, 27]. High electric field can be applied to wide bandgap semiconductors owing to their high breakdown electric field. Thus, the FK effect is prominent in wide bandgap semiconductors. The author has reported that a photocurrent induced by sub-bandgap light absorption due to the FK effect in GaN Schottky barrier diodes (SBDs) and p-n junction diodes (PNDs) [28–32]. The theoretical photocurrents calculated by considering the optical absorption due to the FK effect in the depletion regions showed good agreement with the experimental values.

SiC has an indirect bandgap. Thus, the phonon-assisted optical transition occurs above the bandgap as shown in Fig. C.1. For 4H-SiC, the band structure is shown in Fig. C.2 [33], and the transition from the Γ-point (the valence band maximum) to the M-point (the con-

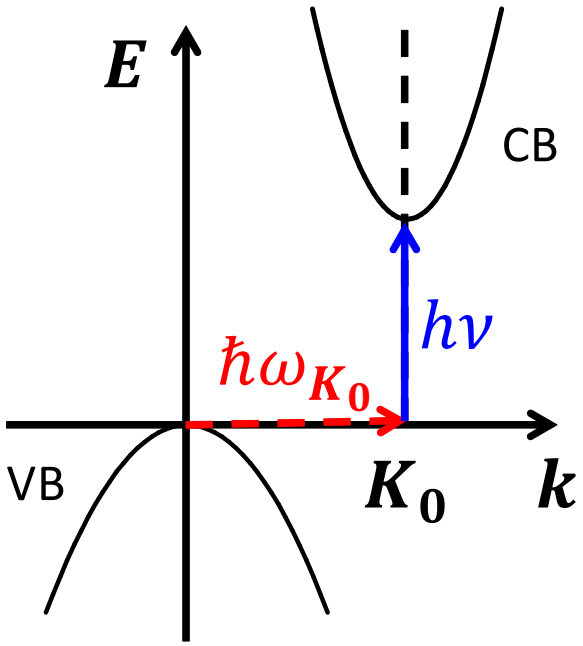

Figure C.1: Diagram of the phonon-assisted optical absorption in an indirect bandgap semiconductor. The optical transition with absorptions/emissions of phonons ($\hbar\omega_{\boldsymbol{K_0}}$) occurs under the energy and momentum conservation law.

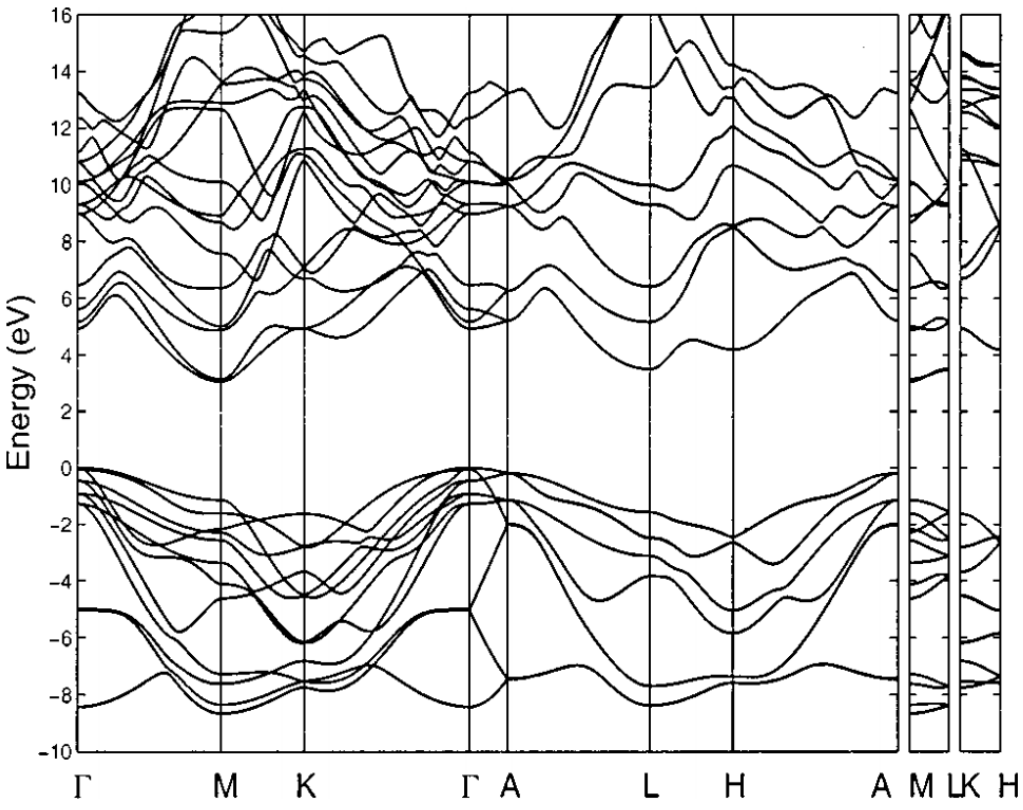

Figure C.2: Calculated pseudopotential 4H-SiC band structure for the 12 conduction bands and 12 valence bands by Bellotti *et al.* [33].

duction band minima) occurs near the band edge. Although the probability of the indirect transition is much smaller than that of the direct transition, the FK effect in an indirect-bandgap semiconductor is expected to be observed. However, there have been no reports on the sub-bandgap light absorption due to the FK effect in SiC devices.

In this study, the author investigated the reverse current–voltage (I-–V) characteristics for a 4H-SiC PND under sub-bandgap light illumination. A photocurrent was observed under a high reverse bias condition and increased with an increase in the reverse bias voltage. The voltage dependence of the photocurrent was successfully quantitatively explained by phononassisted optical absorption due to the FK effect. The temperature dependence of the photocurrent induced by the phonon-assist optical absorption due to the FK effect in the 4H-SiC PND is also investigated.

C.2 Photocurrent induced by Franz-Keldysh Effect in 4H-SiC

C.2.1 Measurement Set up

Figure C.3 shows the schematic structure of a 4H-SiC PND used in this study. The device consists of a 0.2-μm-thick p^{++}-layer ($N_a = 4\times10^{19}$ cm^{-3}), a 2.0-μm-thick p^{+}-layer ($N_a = 3\times10^{18}$ cm^{-3}), and a 2.2-μm-thick n-layer ($N_d = 1.2\times10^{17}$ cm^{-3}) grown on an n^{+}-type 4H-SiC(0001) substrate. To obtain a one-dimensional electric field profile, the epilayer was etched down to the substrate and mesa structures with an angle of 90° were formed using SF_6-based inductive coupled plasma-reactive ion etching (ICP-RIE) with a SiO_2 mask. The height and diameter of the mesas were 6 μm and 100 μm, respectively. The anode and cathode electrodes were formed by the deposition of Ti/Al/Ni on the p^{++}-layer and Ni on the back side of the substrate, respectively. The device exhibited a breakdown voltage of 245 V, which was slightly lower than the ideal avalanche breakdown voltage of 280 V calculated from the impact ionization coefficients in 4H-SiC [34]. The device fabrication and its breakdown characteristic were described in the literature [35].

For the photocurrent measurements, a 250 W Hg lamp combined with a band pass filter of 405 nm with a bandwidth of 3 nm, which is longer than the 4H-SiC absorption edge (380 nm, 3.26 eV), was used. The power of the irradiated light was measured by the optical power meter and the irradiated photon flux (Φ_{irr}) was 4×10^{17} cm^{-2}s^{-1}. The light was focused on a 5 mm diameter circle centered on the anode. The top electrode was thick, such that the irradiated light was reflected by the electrode and could not directly reach the p-n junction. However, the light irradiated around the anode penetrated into the SiC layer. The entered light was reflected by the back-side cathode and could reach the p-n junction from the back side, as shown in Fig. C.3.

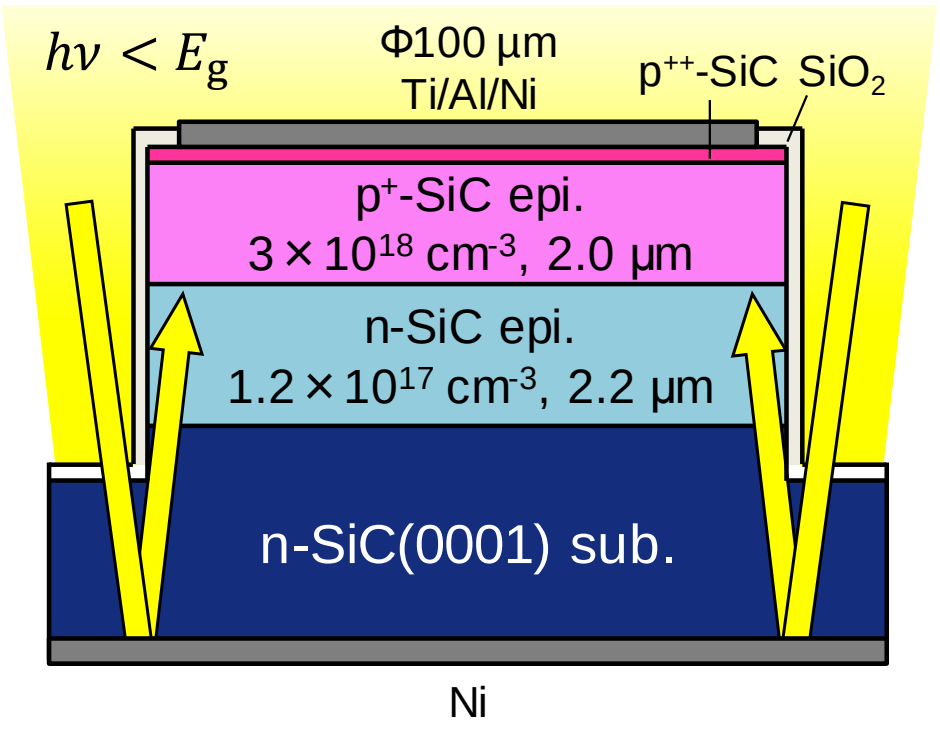

Figure C.3: Schematic cross section of a 4H-SiC(0001) p-n junction diode used in this study. The wavelength of the light was longer than the 4H-SiC absorption edge; therefore, the light penetrated into SiC. The light was reflected by the back cathode electrode and reached the p-n junction.

C.2.2 Experimental Results

Figure C.4 shows the reverse I–V characteristics for the 4H-SiC PND under illumination with the sub-bandgap light. The inset shows the spectrum of the irradiated light measured by the spectrometer. The dark leakage current was sufficiently small (<0.4 pA at 100 V). Although the wavelength of the light was longer than the absorption edge, the larger photocurrent (∼4 pA) than the dark current was observed at zero bias voltage. Since SiC is an indirect-bandgap semiconductor, a photon can excite an electron from the valence band to the conduction band with assistance of a phonon near the absorption edge. Therefore, the short wavelength component (<390 nm) included in the irradiated light shown in Fig. C.4 (inset) was absorbed in SiC, and electrons and holes generated near the p-n junction contributed to in the photocurrent. The diffusion length of carriers in 4H-SiC is sufficiently longer than the depltion region. In addition, the avalanche multiplication is not prominently observed in this voltage range [34]. The author also confirmed that the photocurrent was proportional to the irradiated photon flux. The photocurrent under illumination with the irradiated photon flux of 2×10^{17} cm^{-2}s^{-1} ($\Phi_{\mathrm{irr}}/2$) is also shown in Fig. C.4. Therefore, this photocurrent was considered to be almost constant and does not depend on the reverse bias voltage. However, the measured photocurrent significantly increased with an increase in the reverse bias voltage. This significant increase seems to originate from the optical absorption due to the FK effect.

C.2.3 Phonon-Assisted Optical Absorption in 4H-SiC

The author calculated the photocurrent induced by the FK effect in the SiC PND. The photocurrent can be calculated with consideration of the light absorption in the depletion layer [29]. For a single valence-band maximum ($\boldsymbol{k} = 0$), a conduction-band minimum ($\boldsymbol{k} = \boldsymbol{K_0}$), and one phonon branch, the optical absorption coefficient in an indirect-bandgap semiconductor under an electric field (F) was given by Penchina [36];

$$\alpha_{\pm}(F,\omega) = W_{\pm}\frac{16}{3\pi}\hbar^2\theta^2\int_{V_{0\pm}}^{\infty}(V-V_{0\pm})^{3/2}\cdot|\mathrm{Ai}(V)|^2dV, \tag{C.1}$$

$$W_{\pm} = \frac{e^2C^2\left(n_{\boldsymbol{K_0}}+\frac{1}{2}\pm\frac{1}{2}\right)(m_e^*m_h^*)^{3/2}}{\pi ncm_0^2\omega\hbar^6},$$

$$V_{\pm} = \frac{E_{\mathrm{g}}-\hbar\omega\pm\hbar\omega_{\boldsymbol{K_0}}}{\hbar\theta},\quad \hbar\theta = \frac{e^2\hbar^2F^2}{2\mu_{||}},\quad \mu = \frac{m_{\mathrm{e}}m_{\mathrm{h}}}{m_{\mathrm{e}}+m_{\mathrm{h}}},$$

where the upper and lower signs refer, respectively, to emission (+) and absorption (−) of phonons of wave vector $\boldsymbol{K_0}$ and energy $\hbar\omega_{\boldsymbol{K_0}}$. The phonon occupation number $n_{\boldsymbol{K_0}}$ can be expressed as

$$n_{\boldsymbol{K_0}} = \left[\exp\left(\frac{\hbar\omega_{\boldsymbol{K_0}}}{kT}-1\right)\right]^{-1}. \tag{C.2}$$

Table C.1: Effective masses in 4H-SiC used in this study [38, 39]. The subscripts indicate whether the component is parallel ($\parallel$) or perpendicular ($\perp$) to the c-axis.

		m_e	m_h	μ
$\parallel$	ML	$0.33m_0$	$1.75m_0$	$0.28m_0$
$\perp$	MK	$0.31m_0$	$0.66m_0$	$0.26m_0$
	ML	$0.58m_0$		

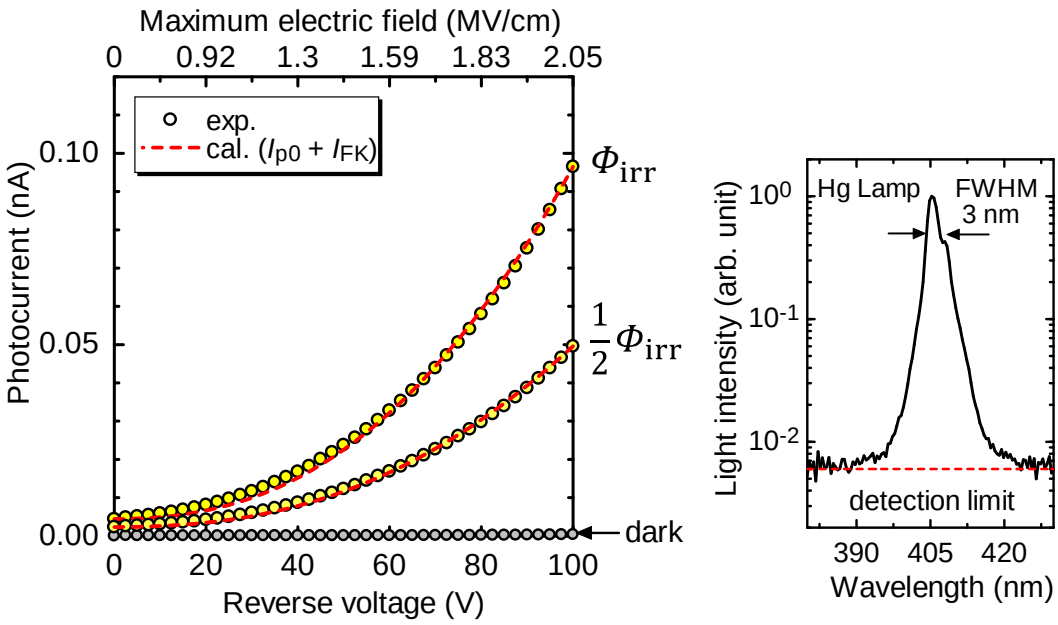

Figure C.4: Reverse current-voltage characteristics in the 4H-SiC PND under illumination with sub-bandgap light (λ = 405 nm) at 298 K for irradiated photon fluxes of 0 (dark), 2×10^{17}, and 4×10^{17} cm^{-2}s^{-1}. The curve calculated taking into consideration the FK effect ($I_{p0} + I_{FK}$) is also shown as the red dashed line. Inset: spectrum of the irradiated light around 405 nm.

e is the elementary charge, c is the speed of light in a vacuum, ω is the angular frequency of light, m_0 is the electron mass, and $\hbar$ is the Dirac constant. Ai(V) is the Airy function. n is the refractive index in 4H-SiC and $n = 2.7$ for $\lambda = 405$ nm [37] was used. C^2 is a constant of proportionality (a sum over transition matrix elements). m^* is the density-of-state effective mass, and $m^* = (m_\perp^2 m_{(\ \|)})^{1/3}$ was used in this study. $\mu_\|$ is the reduced effective mass along the applied electric field. In this study, the electric field was parallel to the c-axis; therefore, $\mu_{(\ \|)} = 0.28 m_0$ was used for the calculation of $\hbar\theta$, which strongly impacts on the electric field dependence of $\alpha_\pm(F, \omega)$. Table C.1 shows the effective masses in 4H-SiC reported in the literature [38, 39]. The absorption coefficient can be determined by summing Eq. (C.1) for each phonon that assists the optical absorption. However, there exist several phonon modes; TA-mode (46 meV), LA-mode (76 meV), TO-mode (95 meV), etc. [40], and many fitting parameters are needed to take into account of all these phonon modes. Galeckas *et al.* investigated the temperature dependence of the absorption coefficient in 4H-SiC at 355 nm and showed that the experimental absorption coefficient can be fitted by a single phonon model [41]. They suggested that the good fit was achieved using $\hbar\omega_{\boldsymbol{K_0}} = (70 \pm 10)$ meV, which indicated that the LA-mode phonons (76 meV) have the largest contribution in the optical transitions. Therefore, the author also used the single phonon model with the LA-mode phonons (76 meV). In the calculation, there is no suitable data for C^2; therefore, $\alpha_\pm(F \to 0, \omega)$ was fitted to the reported absorption coefficient [42, 43] and $C^2 = 3 \times 10^{-67}$ (N·s)^2·F^{-1}·m^4 was obtained.

Figure C.5 shows the calculated absorption coefficient in 4H-SiC under electric fields of 0, 1, and 2 MV/cm at 298 K as the sum of $\alpha_+(F, \omega)$ and $\alpha_-(F, \omega)$. The absorption coefficient for 0 V/cm (black solid line) shows the two regions; (i) phonon-absorption transitions only occurs ($h\,\nu < 3.33$ eV, $\lambda > 372$ nm) and (ii) both phonon-emission and phonon-absorption transitions occur ($h\nu \geq 3.33$ eV, $\lambda \leq 372$ nm), which shows good agreement with the reported absorption coefficient in 4H-SiC (open circles) [42]. The calculated absorption coefficient shows an absorption tail below the bandgap under a high electric field. The tail becomes longer with an increase in electric field.

Figure C.6 shows the distributions of the electric field and the absorption coefficient for the wavelength of 405 nm in the 4H-SiC PND under a reverse bias voltage of 100 V. W_n and W_p are the distances from the p-n junction to the edge of the depletion layer in the n-region and the p-region, respectively. The electric field profile was calculated from Eq. (4.6) and (4.7) in Chapter 4. The absorption coefficient was calculated according to the distribution of the electric field, which is large near the p-n junction interface (high electric field region). This suggest that the sub-bandgap optical absorption induced by the FK effect locally occurs near the p-n junction interface. In addition, the absorption coefficient in 4H-SiC is approximately two or three orders of magnitude smaller than that in GaN at the same wavelength under the same electric field.

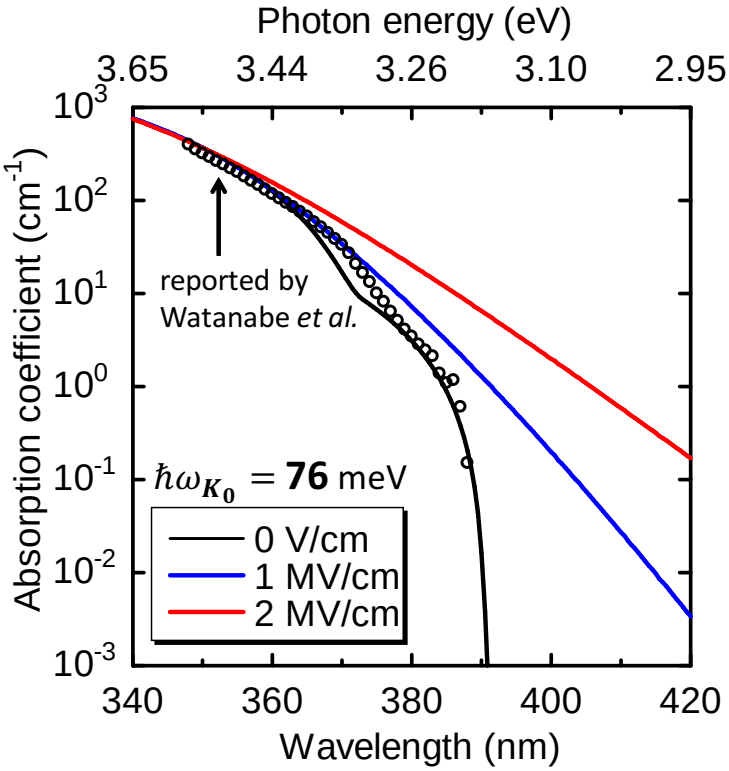

Figure C.5: Wavelength dependence of the calculated absorption coefficient for 4H-SiC under electric fields of 0, 1, and 2 MV/cm. The LA-mode phonon ($\hbar\omega_{\boldsymbol{K_0}} = 76$ meV) was considered in the calculation. The calculated absorption coefficient under 0 V/cm (black line) shows good agreement with the reported values (open circles) [42].

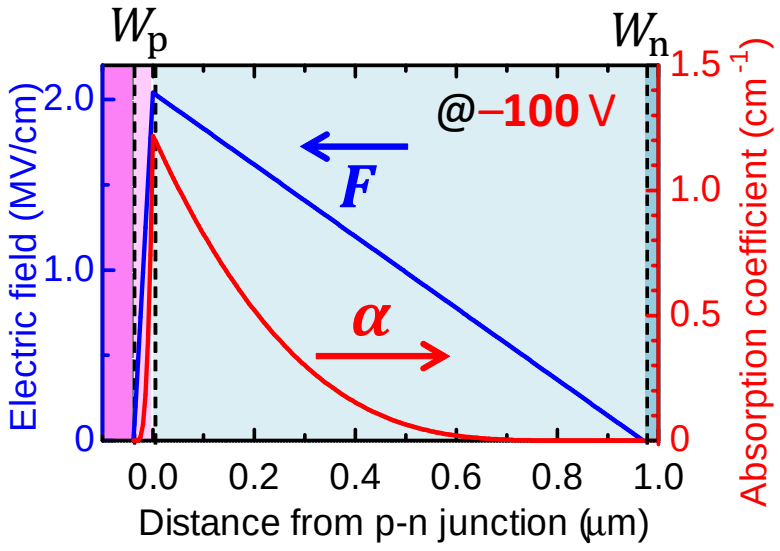

Figure C.6: The distribution of the electric field and the absorption coefficient for 405 nm in the 4H-SiC PND under the reverse bias of −100 V.

C.2.4 Calculation of Photocurrent

The photocurrent induced by the light absorption due to the FK effect (I_{FK}) can be calculated by considering the optical absorption in the depletion layer, which depends on the applied voltage, and it can be expressed as

$$I_{\mathrm{FK}}(V,\omega) = e\Phi_0 \left[1 - \exp\left(-2\int_{-W_{\mathrm{p}}(V)}^{W_{\mathrm{n}}(V)} (\alpha_+(F(x,V),\omega) + \alpha_-(F(x,V),\omega))dx\right)\right]. \quad \text{(C.3)}$$

where Φ_0 is the incident photon flux from the back side into the edge of the depletion layer in the n-region. Multiple-reflected photons are included in Φ_0. In this formula, a single round-trip path is considered [29]. Optical absorption by the electrodes is considered to be small and is thus neglected.

The calculated photocurrents as the sum of the photocurrent without applying voltage (I_{p0}) and the photocurrent induced by the FK effect (I_{FK}) are shown in Fig. C.4 as red dashed lines. I_{p0} was determined as the photocurrents at 0 V, which does not have the voltage dependence and is constant. Φ_0 were determined by fitting the calculated curves to the experimental results at a reverse bias voltage of 100 V. The obtained Φ_0 were 1.5×10^{17} and 7.7×10^{16} $\mathrm{cm^{-2}s^{-1}}$ for Φ_{irr} and $\Phi_{\mathrm{irr}}/2$, respectively. These were about 37% of the irradiated photon flux. This seems reasonable, considering the reflection loss at the 4H-SiC surface ($\sim$21%) and the light absorption of the short wavelength component in the 4H-SiC substrate. The voltage dependence of the calculated photocurrent shows good agreement with the experimental result, indicating that the photocurrent in the 4H-SiC PND under illumination with the sub-bandgap light is successfully explained by the light absorption due to the FK effect quantitatively. The photocurrent induced by the FK effect in the 4H-SiC PND is approximately two or three orders of magnitude smaller than that in the GaN devices with the same electric field distribution, since SiC has an indirect bandgap; the probability of the indirect transition is much smaller than that of the direct transition.

C.2.5 Temperature Dependence

The temperature dependence of the photocurrent induced by the FK effect in 4H-SiC PND was also investigated. Figure C.7 shows the photocurrents in the 4H-SiC PND under the illumination with the sub-bandgap light ($\lambda = 405$ nm) at 223, 298 and 373 K. With elevating temperature, the photocurrent without applying voltage (I_{p0}) significantly increased, and the photocurrent induced by the FK effect (I_{FK}) also increased. These increases are considered to originate from the red-shift of the absorption edge and increase in the phonon occupation number ($n_{\boldsymbol{K_0}}$). The calculated photocurrents with consideration of the temperature dependence of the bandgap of 4H-SiC [44] are also shown in Fig. C.7. In the calculation, the temperature dependences of the phonon energy $\hbar\omega_{\boldsymbol{K_0}}$ and the refractive index n were small and neglected [37, 42]. The obtained Φ_0 were similar values of 1.9×10^{17},

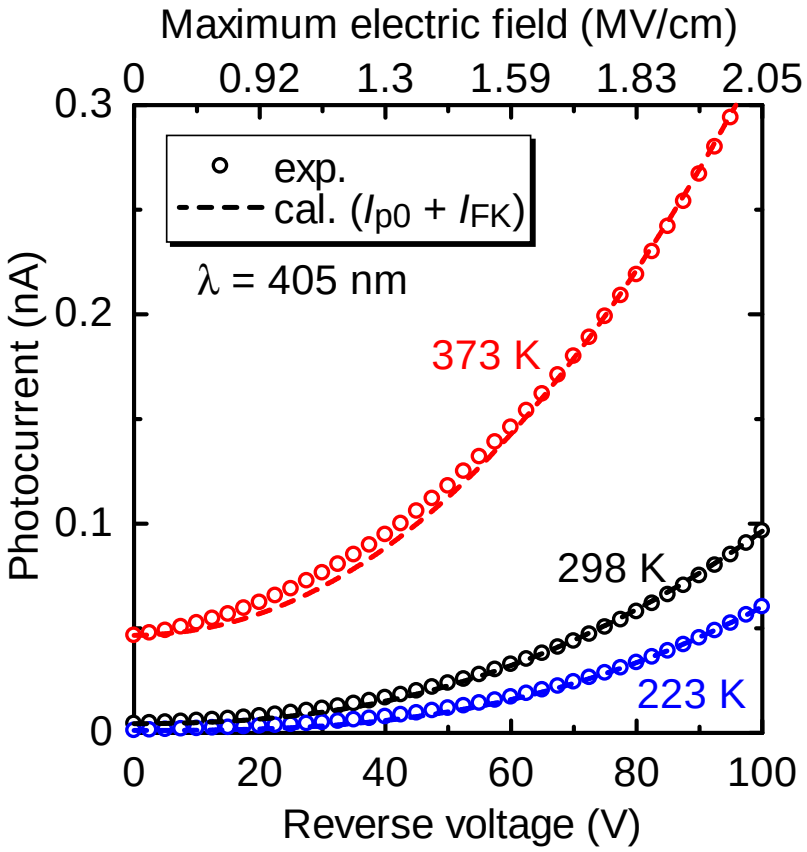

Figure C.7: Comparison between the experimental (circles) and calculated (dashed lines) photocurrents for 405 nm with consideration of the temperature dependence of the bandgap and the phonon occupation number in 4H-SiC at 223, 298, and 373 K.

1.5×10^{17}, and 2.2×10^{17} $cm^{-2}s^{-1}$ at 223, 298 and 373 K, respectively. There were small differences among these values, since the optical configuration was slightly different in the measurements at different temperature. The calculated curves showed good agreements with the experimental results at all the temperatures investigated in this study. The temperature dependence of the photocurrent in the 4H-SiC PND is slightly larger than that in the GaN PND [29], since the optical absorption in an indirect-bandgap semiconductor depends on not only the temperature dependence of the bandgap but also the phonon occupation number.

C.3 Anisotropy of Optical Absorption Induced by Franz-Keldysh Effect

The electric-field dependence of an absorption coefficient strongly depends on a reduced effective mass, $\mu = m_e m_h/(m_e + m_h)$, along the direction parallel to the electric field, since the tails of the wavefunctions into the bandgap are determined by the effective masses. It is known that 4H-SiC has anisotropic effective masses [38, 39] as shown in Table C.1. Thus, anisotropic optical absorption induced by the FK effect may be observed in 4H-SiC. In this study, the author also fabricated 4H-SiC PNDs on $(11\bar{2}0)$-face substratesand a photocurrent in 4H-SiC$(11\bar{2}0)$ PNDs under high electric field along the $<11\bar{2}0>$ direction is investigated.

C.3.1 Device Structure

Figure C.8 shows the schematic cross-section of a 4H-SiC$(11\bar{2}0)$ p-n junction diode. Two devices with different epitaxial structures (PN1 and PN2) were prepared. The devices consist of p^+-layers, p-layers, and n^+-layers grown on n+-type 4H-SiC$(11\bar{2}0)$ substrates. The doping concentrations and thicknesses of p-epilayers in PN1 and PN2 are summarized in Table C.2. Mesa structures with a mesa angle of $\sim80°$ were formed using SF_6-based ICP-RIE with a SiO2 mask. The mesa heights for PN1 and PN2 are 4.8 μm and 10 μm, respectively. These mesa structures act as the positive beveled-mesa termination to eliminate electric field crowding at the device edges and avoid premature breakdown [45]. The anode and cathode electrodes were formed by deposition of Ti/Al/Ni on the p^{++}-layer and Ni on the back side of the substrate, respectively. The breakdown voltages of about 100 V and 265 V were obtained for PN1 and PN2, respectively. The breakdown electric fields for PN1 and PN2 were about 3.1 MV/cm and 2.5 MV/cm, respectively. These values are approximately 20% lower than the theoretical values calculated from the impact ionization coefficients in 4H-SiC along the <0001> direction [34]. These breakdown characteristics for the $<11\bar{2}0>$ direction show a similar tendency to previous reports [46, 47], which can be explained by the anisotropy of the impact ionization coefficients in 4H-SiC [35, 47, 48]. The measurement set up is same described in the section C.2.1.

Table C.2: The Al concentrations and the thicknesses of the p-layers in PN1 and PN2 obtained by SIMS.

Device	Al concentration (cm^{-3})	Thickness (μm)
PN1	2.6×10^{17}	3.0
PN2	6.5×10^{16}	8.2

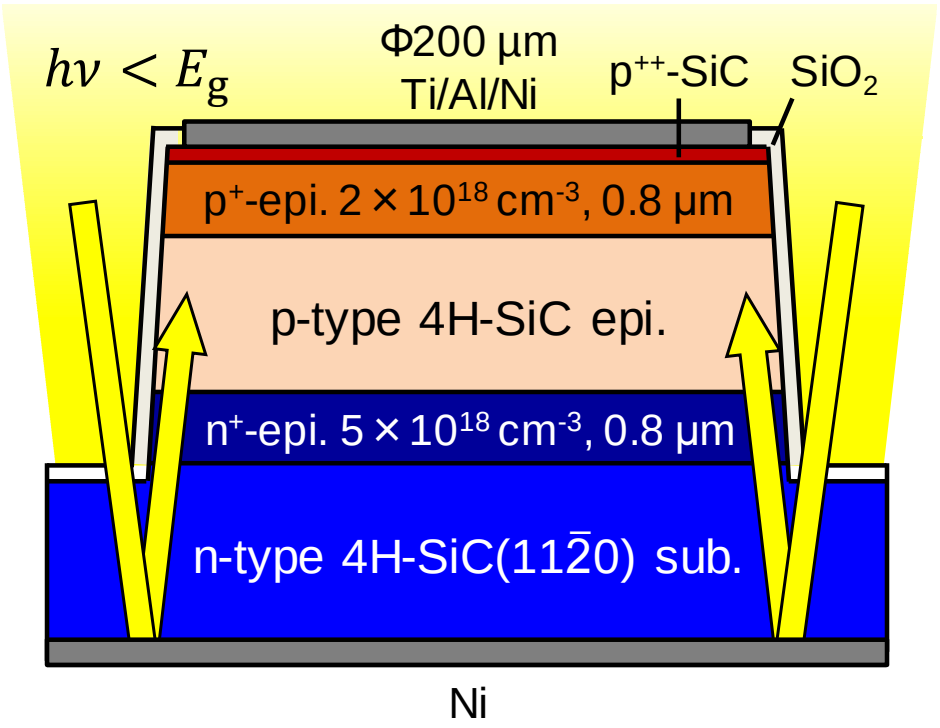

Figure C.8: Schematic cross section of a 4H-SiC(11$\bar{2}$0) p-n junction diode used in this study. The wavelength of the light was longer than the 4H-SiC absorption edge; therefore, the light penetrated into SiC. The light was reflected by the back cathode electrode and reached the p-n junction.

C.3.2 Experimental Results

Figure C.9 shows the reverse current-voltage characteristics in PN1 (open circles) and PN2 (open squares) under sub-bandgap illumination. Photocurrents much larger than dark leakage currents were clearly observed at zero bias (I_{p0}) for both PN1 and PN2, although the wavelength of the light was longer than the absorption edge. These photocurrents seem to be induced by optical absorption of the short wavelength component (<390 nm) in the irradiated light, as mentioned in the literature [49]. These initial photocurrents are considered to be almost constant and not to depend on the applied voltage. With increasing reverse voltage, the photocurrents significantly increased. These increases were induced by sub-bandgap optical absorption due to the FK effect. Here, the author confirmed that avalanche multiplication of the photocurrent induced by the FK effect [30, 31] was not observed in these voltage ranges.

C.3.3 Calculation of Photocurrent

To analyze the aforementioned increase in the photocurrent, the author calculated the photocurrents induced by the FK effect in the 4H-SiC($11\bar{2}0$) PNDs. A photocurrent can be calculated as the product of e (the elementary charge) and absorbed photons in a depletion layer, and can be written by Eq. (A.3). The absorption coefficient $\alpha_{\pm}(F, x)$ is given by Penchina [36] as Eq. (C.1). The anisotropies of the refractive index n and the energy from the dominant LA-mode phonons ($\hbar\omega_{\boldsymbol{K_0}} = 76$ meV) may negligible [41]. In the calculations, the reduced effective mass along the direction to which electric field is applied ($\mu_{\parallel F}$) is the most important parameter, which determines the electric-field dependence of $\alpha_{\pm}(F, \omega)$. Table. C.1 shows the effective masses of electrons and holes in 4H-SiC [38, 39]. In this study, electric field is applied to the <$11\bar{2}0$> direction. Figure C.10 shows the first Brillouin zone of 4H-SiC. There are six M points, which are the conduction band minima of 4H-SiC, and three equivalent conduction-band valleys. For one valley (a), electric field is applied to the MK direction. For the other two valleys (b) and (c), electric field is applied to the direction rotated by 60° from the MK direction to the MΓ direction. In this study, the author used a geometrically averaged electron effective mass perpendicular to the c-axis ($m_{e,\perp} = \sqrt{m_{\mathrm{e,MK}} m_{\mathrm{e,M\Gamma}}} = 0.42 m_0$) for the calculation of $\mu_{\perp}$. For the valence band, the anisotropy in the hole effective masses in the c-plane is small near the valence band edge [50] and $m_{h,\perp} = 0.66 m_0$ was used. Therefore, the author used $\mu_{\perp} = 0.26 m_0$ as $\mu_{\parallel F}$. m^* is the density-of-states effective mass, and $m^* = (m_{\perp}^2 m_{\parallel})^{1/3}$ was used.

Figure C.11 shows the calculated electric-field dependence of the absorption coefficient in 4H-SiC for $\lambda = 405$ nm under electric field along the <0001> and <$11\bar{2}0$> directions. For the calculation of electric field, the dielectric constant perpendicular to the c-axis ($\varepsilon_{\mathrm{s},\perp} = 9.76\varepsilon_0$ was used. The difference between the absorption coefficient for the <0001> direction and that for the <$11\bar{2}0$> direction is small, since the value of $\mu_{\parallel} = 0.28 m_0$ is close to $\mu_{\perp} = 0.26 m_0$. The wavelength dependence of the absorption coefficient in 4H-SiC under

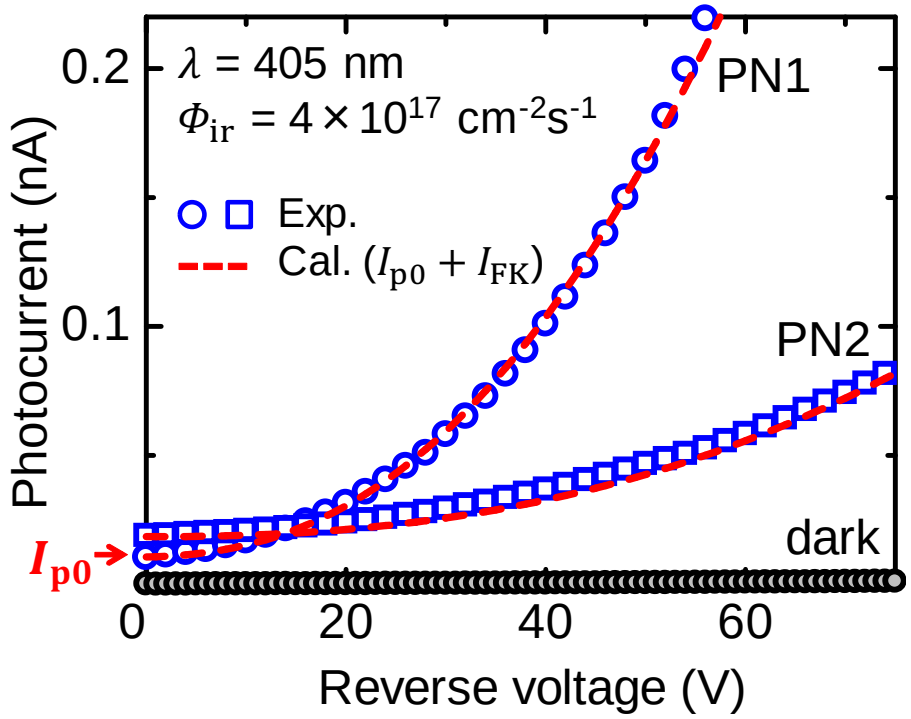

Figure C.9: Reverse current-voltage characteristics in the 4H-SiC(11$\bar{2}$0) PNDs (PN1 and PN2) under illumination with sub-bandgap light ($\lambda = 405$ nm) at 298 K. The curve calculated taking into consideration the FK effect ($I_{\mathrm{p0}} + I_{\mathrm{FK}}$) is also shown as the red dashed line.

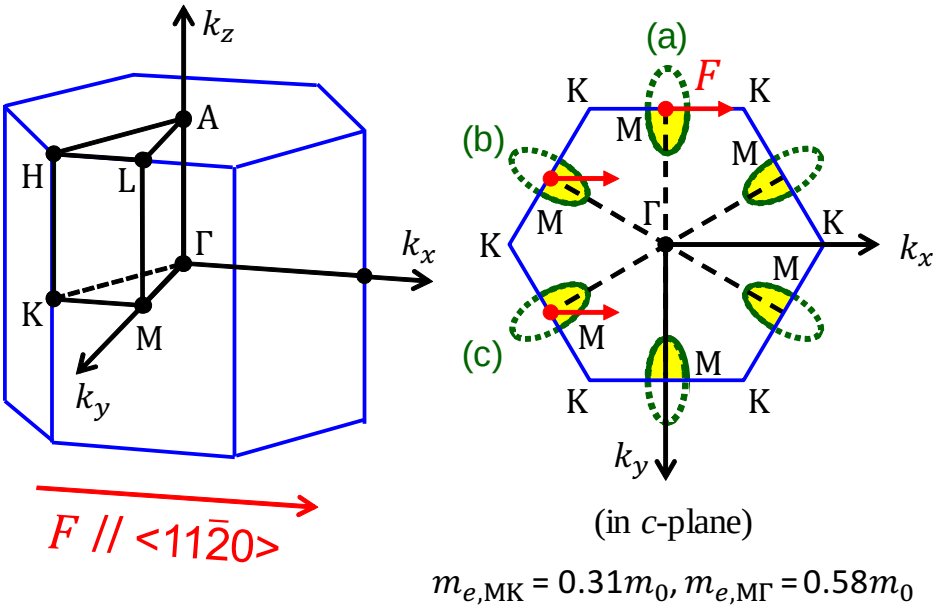

Figure C.10: First Brillouin zone under electric field applied along the <11$\bar{2}$0> direction. There are six M points and three equivalent conduction-band valleys. For one valley (a), electric field is applied to the MK direction. For the other two valleys (b) and (c), electric field is applied to the direction rotated by 60° from the MK direction to the MΓ direction.

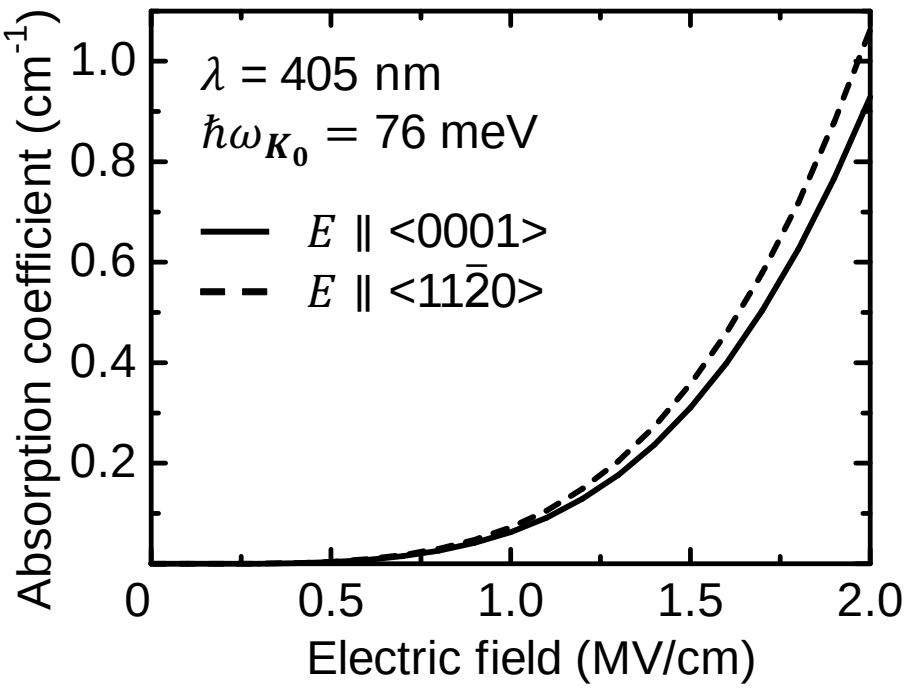

Figure C.11: Calculated absorption coefficients in 4H-SiC for $\lambda = 405$ nm under electric field along the <0001> direction using $\mu_{\|} = 0.28m_0$ (solid line) and along the <11$\bar{2}$0> direction using $\mu_{\perp} = 0.26m_0$ (broken line).

electric field along to the <0001> direction is described in Fig. C.5. Figure C.12 shows the distributions of electric field and the absorption coefficient ($\alpha_+ + \alpha_-$) for $\lambda = 405$ nm in PN1 at the reverse voltage of (a) 25 V and (b) 50 V. As well as the cases of a GaN PND [29] and a 4H-SiC(0001) PND [49], the absorption coefficient is significant and optical absorption selectively occurs near the p-n junction interface (high electric field region).

The photocurrents for PN1 and PN2 were calculated as the sum of the photocurrent without applying voltage (I_{p0}) and the photocurrent induced by the FK effect (I_{FK}). The photocurrents calculated for PN1 and PN2 were shown in Fig. C.9 as red broken lines. In the calculations of the photocurrents in both PN1 and PN2, a consistent value of the incident photon flux ($\Phi_0 = 1.2{\times}10^{17}$ cm^{-2}s^{-1}, 30% of Φ_{irr}) was used, which well agrees with the case of the <0001> direction (37% of Φ_0) in the section C.2.4. These seem reasonable, considering the reflection loss at the 4H-SiC surface (∼21%). The calculated values show good agreement with the experimental values, indicating that the electric-field dependence of $\alpha_{\pm}(F, x)$ under electric field along the <11$\bar{2}$0> direction is also well calculated using $\mu_{\perp} = 0.26m_0$. The anisotropy of phonon-assisted optical absorption induced by the FK effect for the elecric field along <0001>and <11$\bar{2}$0> directions is weak due to the small difference between $\mu_{\parallel}$ and $\mu_{\perp}$.

C.4 Discussion

Wavelength Dependence

The photocurrent induced by the FK effect has the wavelength dependence, since the absorption coefficient strongly depends on the wavelength of the light. In this study, the author tried to measure the wavelength dependence of the photocurrent in 4H-SiC PNDs. However, the light intensity of the variable-wavelength light sources (MLS-1510, used in Chapter 4) was not so strong. The obtained photocurrent was contaminated by dark leakage current and noisy. If a high power light source or a focus lens with higher magnification, the wavelength dependence will be measurable.

Light Hole, Heavy Hole and Crystal-Field Split-Off Hole Bands

In strict, all valence bands (light hole (LH), heavy hole (HH) and crystal-field split-off (CF)) are considered to contribute the optical transition. The calculation of the absorption coefficient should be done with consideration of all valence bands. However, the electron effective masses are much smaller than the hole effective masses [50], and the reduced effective masses are dominated by the values of the electron effective masses. In addition, the differences between the valence band maximum are small (<70 meV) [50]. Therefore, one-hole-band model with consideration of LH was employed for simplicity in this study.

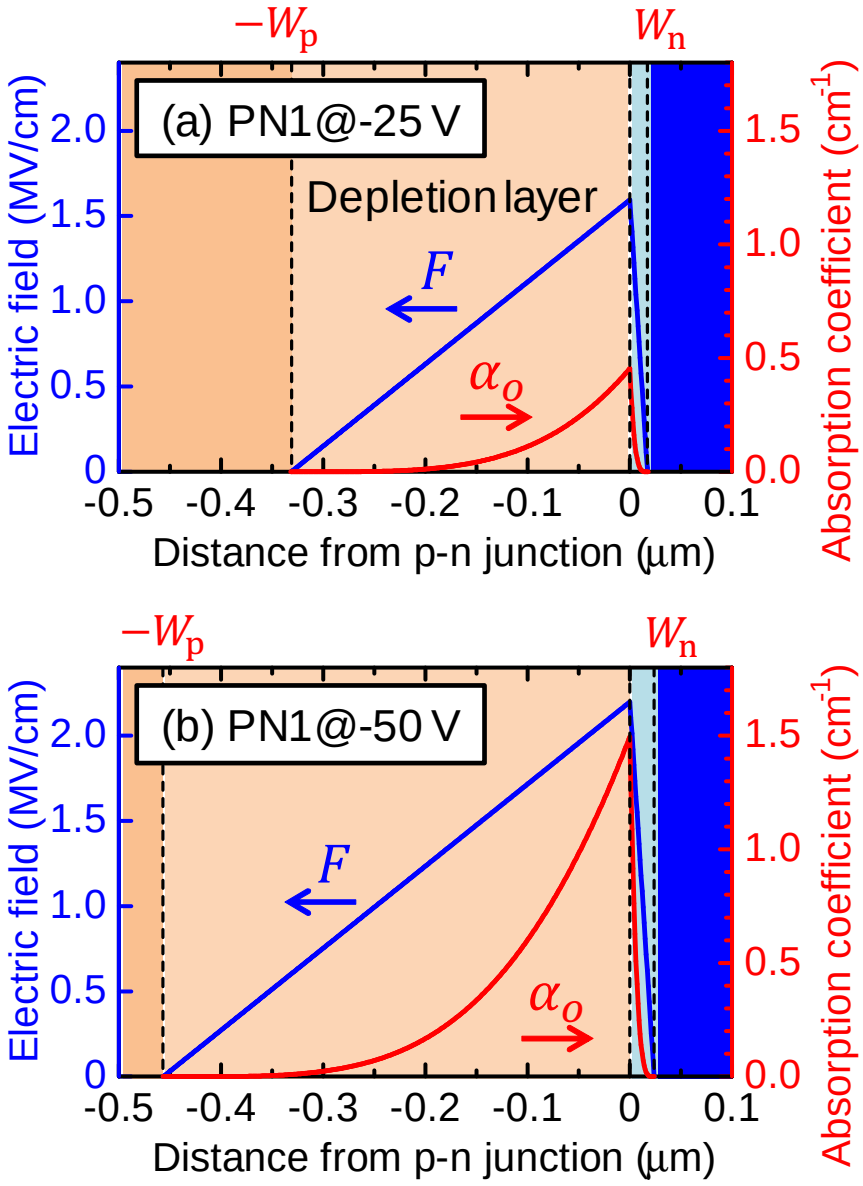

Figure C.12: Distributions of electric field and the absorption coefficient for $\lambda = 405$ nm in PN1 at the reverse voltage of (a) 25 V and (b) 50 V.

Contributions of Other Phonons

There are other phonons which may contribute the phonon-assisted optical absorption in 4H-SiC. Figure C.13 shows the comparison between the optical absorption coefficient in 4H-SiC with consideration of the LA-mode phonons (red dashed line) and TA-mode phonons (brown dashed line). The experimental data obtained by Watanabe *et al.* [42] is also shown as open circles. For the near band edge region (>375 nm), the curve for the LA-mode phonon shows good agreement. On the other hand, in the range of 365–375 nm, the curve for the LA-mode phonon deviates and the curve for the TA-mode phonon shows good agreement. This may indicate that the kind of phonons which contribute the optical absorption depends on the wavelength of light. In this study, the LA-mode phonon was only considered, since the optical transition for >375 nm was considered.

C.5 Summary

In conclusion, the photocurrent for sub-bandgap light (λ = 405 nm) in the 4H-SiC(0001) PND under a high reverse bias voltage was investigated. The photocurrent increased with an increase in the reverse bias voltage. The photocurrent calculated taking into consideration the phonon-assisted light absorption due to the FK effect showed good agreement with the experimental result. An increase in the photocurrent was observed with rising temperature in the range from 223 to 373 K, and the temperature dependence was quantitatively explained by the redshift of the bandgap and the increase in the phonon occupation number with rising temperature.

The photocurrent induced by FK effect in 4H-SiC(11$\bar{2}$0) PNDs under high electric field along the <11$\bar{2}$0> direction. The theoretical calculations considering phonon-assisted optical absorption induced by FK effect in the depletion regions using $\mu_\perp = 0.26m_0$ showed good agreement with the experimental values. Significant anisotropy in optical absorption induced by FK effect was not observed, since the difference between $\mu_\parallel = 0.28m_0$ and $\mu_\perp = 0.26m_0$ is small.

These results are useful when considering the light absorption due to the FK effect in 4H-SiC devices under a high electric field, for example, high-power devices, photodetectors, and avalanche photodiodes.

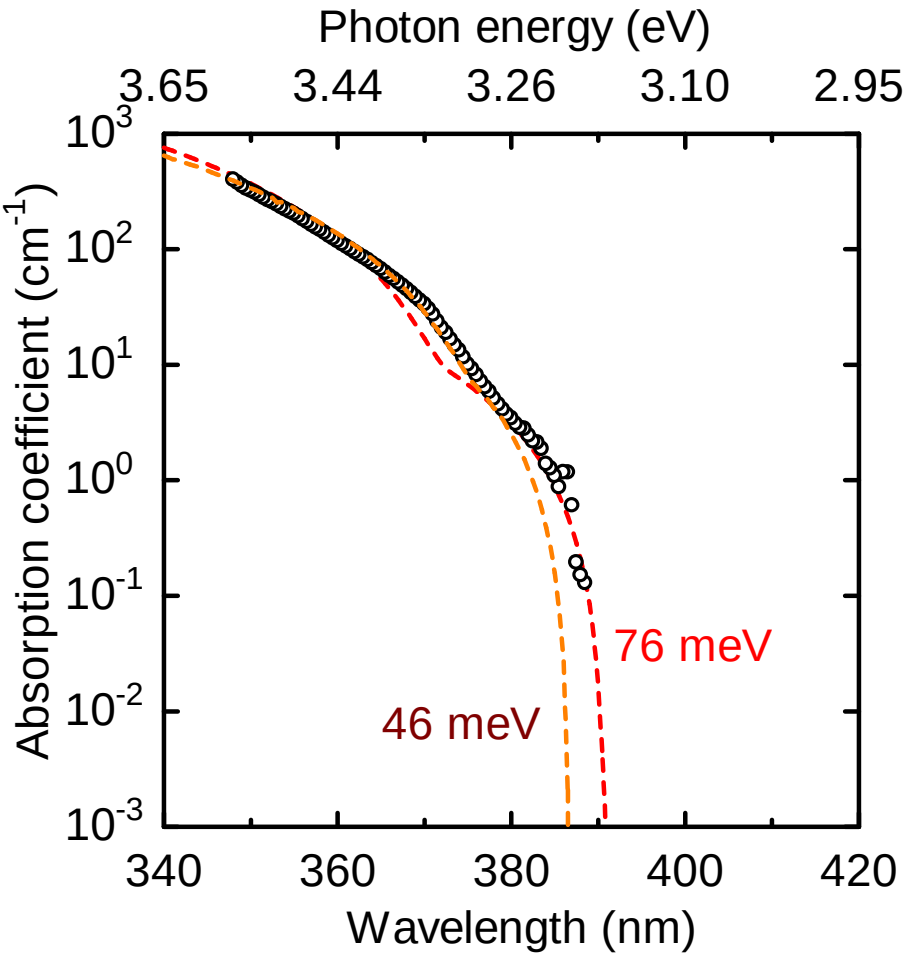

Figure C.13: The comparison between the optical absorption coefficient in 4H-SiC with consideration of the LA-mode phonons (red dashed line) and TA-mode phonons (brown dashed line). The experimental data obtained by Watanabe *et al.* [42] is also shown as open circles.

References

[1] T. Kimoto, *Jpn. J. Appl. Phys.* **54**, 040103 (2015).

[2] M. Bhatnagar and B. J. Baliga, *IEEE Trans. Electron Devices* **40(3)**, pp.645–655 (1993).

[3] T. Masuda, Y. Saito, T. Kumazawa, and T. Hatayama S. Harada, *IEDM Tech. Digest* (2018) p. 8.1.

[4] I. C. Kizilyalli, A. P. Edwards, O. Aktas, T. Prunty, and D. Bour, *IEEE Trans. Electron Devices* **62(2)**, pp.414–422 (2015).

[5] S. Chowdhury, B. L. Swenson, and U. K. Mishra, *IEEE Electron Device Lett.* **29(6)**, pp.543–545 (2008).

[6] T. Maeda, T. Narita, H. Ueda, M. Kanechik, T. Uesugi, T. Kachi, T. Kimoto, M. Horita, and J. Suda, *IEDM Tech. Digest* (2018) p. 30.1.

[7] S. Fujita, *Jpn. J. Appl. Phys.* **54**, 030101 (2015).

[8] M. Higashiwaki, K. Sasaki, A. Kuramata, T. Masui, S. Yamakoshi, and , *Appl. Phys. Lett.* **100**, 013504 (2012).

[9] W. Li, Z. Hu, K. Nomoto, R. Jinno, Z. Zhang, T. Q. Tu, K. Sasaki, A. Kuramata, D. Jena, and H. G. Xing, *IEDM Tech. Digest* (2018) p. 8.5.

[10] P. G. Neudeck, R. S. Okojie, and L.-Y. Chen, *Proc. IEEE* **90**, 6 (2002).

[11] M. Kaneko and T. Kimoto, *IEEE Electron Device Lett.* **39(5)**, pp.723–726 (2018).

[12] M. Nakajima, M. Kaneko, and T. Kimoto, *IEEE Electron Device Lett.* **40(6)**, pp.866–869 (2019).

[13] H. So, J. Lim, and D. G. Senesky, *IEEE Sensors Journal* **16**, 10 (2016).

[14] E. Monroy, F. Omnes, and F. Calle, *Semicon. Sci. Technol.* **18**, R33–R51 (2003).

[15] X. Chen, H. Zhu, J. Cai, and Z. Wu, *J. Appl. Phys.* **102**, 024505 (2007).

[16] P. F. Satterthwaite, A. S. Yalamarthy, N. A. Scandrette, A. K. M. Newaz, and D. G. Senesky, *ACS Photonics* **5**, 4277 (2018).

[17] A. Yoshikawa, S. Ushida, K. Nagase, M. Iwaya, T. Takeuchi, S. Kamiyama, and I. Akasaki, *Appl. Phys. Lett.* **111**, 191103 (2017).

[18] T. Kimoto and J. A. Cooper, *Fundamentals of Silicon Carbide Technology*, (Wiley, 2014), pp.1–37.

[19] A. Agarwal, M. Das, S. Krishnaswami, J. Palmour, J. Richmond, and S.-H. Ryu, in *Mater. Res. Soc. Symp. Proc.* **815**, pp.243–254 (2004).

[20] H. Niwa, J. Suda, and T. Kimoto, *Appl. Phys. Express* **5**, 064001 (2012).

[21] N. Kaji, H. Niwa, J. Suda, and T. Kimoto, *IEEE Trans. Electron Devices* **62(2)**, pp.374–381 (2015).

[22] H. Miyake, T. Okuda, H. Niwa, T. Kimoto, and J. Suda, *IEEE Electron Device Lett.* **33(11)**, pp.1598–1600 (2012).

[23] L. Cheng *et al.*, *Mater. Sci. Forum* **778**, 1089 (2014).

[24] E. V. Brunt *et al.*, *Proc. of Int. Symp. on Power Semiconductor Device and ICs* (2014) p. 358.

[25] S. Matsunaga, T. Mizushima, K. Takenaka, Y. Kikuchi, A. Koyama, Y. Yonezawa, and H. Okumura, *IEDM Tech. Digest* (2019) p. 20.2.

[26] V. W. Franz, *Z. Naturf.* **13a**, 484 (1958).

[27] L. V. Keldysh, *Soviet Physics JETP* **7**, 788 (1958).

[28] T. Maeda, M. Okada, M. Ueno, Y. Yamamoto, M. Horita, and J. Suda, *Appl. Phys. Express* **9**, 091002 (2016).

[29] T. Maeda, T. Narita, M. Kanechika, T. Uesugi, T. Kachi, T. Kimoto, M. Horita, and J. Suda, *Appl. Phys. Lett.* **112**, 252104 (2018).

[30] T. Maeda, T. Narita, H. Ueda, M. Kanechika, T. Uesugi, T. Kachi, T. Kimoto, M. Horita, and J. Suda, *Appl. Phys. Lett.* **115**, 142101 (2019).

[31] T. Maeda, T. Narita, H. Ueda, M. Kanechika, T. Uesugi, T. Kachi, T. Kimoto, M. Horita, and J. Suda, *Proc. of Int. Symp. on Power Semiconductor Device and ICs* (2019) p. 59–62.

[32] T. Maeda, T. Narita, S. Yamada, T. Kachi, T. Kimoto, M. Horita, and J. Suda, *IEDM Tech. Digest* (2019) p. 4.2.

[33] E. Bellotti, H.-E. Nilsson, K. F. Brennan, P. P. Rudan, and R. Trew, *J. Appl. Phys.* **87(8)**, pp.3864–3871 (2000).

[34] H. Niwa, J. Suda, and T. Kimoto, *IEEE Trans. Electron Devices* **62(10)**, pp.3326–3333 (2015).

[35] X. Chi, *Master Thesis*, (2019), Kyoto University [in Japanese].

[36] C. M. Penchina, *Phys. Rev.* **138**, A924 (1965).

[37] N. Watanabe, T. Kimoto, and J. Suda, *Jpn. J. Appl. Phys.* **51**, 112101 (2012).

[38] D. Volm, B. K. Meyer, D. M. Hofmann, W. M. Chen, N. T. Son, C. Persson, U. Lindefelt, O. Kordina, E. Sörman, A. O. Konstantinov, B. Monemar, and E. Janzén, *Phys. Rev. B* **53**, 15409 (1996).

[39] N. T. Son, P. N. Hai, W. M. Chen, C. Hallin, B. Monemar, and E. Janzén, *Phys. Rev. B* **61**, R10544(R) (2000).

[40] PatrickPR1965, *Phys. Rev.* **137**, A1515 (1965).

[41] A. Galeckas, P. Grivickas, V. Grivickas, V. Bikbajevas, and J. Linnros, *Phys. Status Solidi A* **191(2)**, pp.613–620 (2002).

[42] N. Watanabe, T. Kimoto, and J. Suda, *Jpn. J. Appl. Phys.* **53**, 108003 (2014).

[43] S. G. Sridhara, R. P. Devaty, and W. J. Choyke, *J. Appl. Phys.* **84**, 2963 (1998).

[44] Z. Li and R. C. Bradt, *J. Appl. Phys.* **60**, 612 (1986).

[45] B. J. Baliga, *Fundamentals of Power Semiconductor Devices*, (Springer, 2008), pp. 91–166.

[46] S. Nakamura, H. Kumagai, T. Kimoto, and H. Matsunami, *Appl. Phys. Lett.* **80**, 3355 (2004).

[47] T. Hatakeyama, T. Watanabe, T. Shinohe, K. Kojima, K. Arai, and N. Sano, *Appl. Phys. Lett.* **85**, 1380 (2004).

[48] D. Stefanakis, X. Chi, T. Maeda, M. Kaneko, and T. Kimoto, presented at *Int. Conf. on Silicon Carbide and Related Materials* (*ICSCRM*), (2019), We-3A-01.

[49] T. Maeda, X. Chi, M. Horita, J. Suda, and T. Kimoto, *Appl. Phys. Express* **11**, 091302 (2018).

[50] H. Tanaka, S. Asada, J. Suda, and T. Kimoto, *J. Appl. Phys.* **123**, 245704 (2018).

List of Publications

A. Papers and Letters (peer reviewed)

1. T. Maeda, M. Okada, M. Ueno, Y. Yamamoto, M. Horita and J. Suda,
"Franz-Keldysh effect in n-type GaN Schottky barrier diode under high reverse bias voltage,"
Applied Physics Express **9**, 091002 (2016).
[**selected as APEX spotlights2016**]

2. T. Maeda, M. Okada, M. Ueno, Y. Yamamoto, T. Kimoto, M. Horita and J. Suda,
"Temperature dependence of barrier height in Ni/n-GaN Schottky barrier diode,"
Applied Physics Express **10**, 051002 (2017).
[**JSAP Outstanding Young Researcher Paper Award**]

3. T. Maeda, T. Narita, M. Kanechika, T. Uesugi, T. Kachi, T. Kimoto, M. Horita and J. Suda,
"Franz-Keldysh effect in GaN p-n junction diode under high reverse bias voltage,"
Applied Physics Letters **112**, 252104 (2018).

4. T. Maeda, X. Chi, M. Horita, J. Suda and T. Kimoto,
"Phonon-assisted optical absorption due to Franz-Keldysh effect in 4H-SiC p-n junction diode under high reverse bias voltage,"
Applied Physics Express **11**, 091302 (2018).

5. T. Maeda, T. Narita, H. Ueda, M. Kanechika, T. Uesugi, T. Kachi, T. Kimoto, M. Horita and J. Suda,
"Parallel-Plane Breakdown Fields of 2.8–3.5 MV/cm in GaN-on-GaN p-n Junction Diodes with Double-Side-Depleted Shallow Bevel Termination,"
IEDM Technical Digest, pp. 687–690 (2018).

6. T. Maeda, T. Narita, H. Ueda, M. Kanechika, T. Uesugi, T. Kachi, T. Kimoto, M. Horita and J. Suda,
"Shockley-Read-Hall Lifetime in Homoepitaxial p-GaN Extracted from Recombination Current in GaN p-n$^+$ Junction Diodes,"
Japanese Journal of Applied Physics **58**, SCCB14 (2019).
[selected as IWN2018 top 40 articles , OPEN ACCESS]

7. T. Maeda, T. Narita, H. Ueda, M. Kanechika, T. Uesugi, T. Kachi, T. Kimoto, M. Horita and J. Suda,
"Design and Fabrication of GaN p-n Junction Diodes with Negative Beveled-Mesa Termination,"
IEEE Electron Device Letters **40(6)**, 941–944 (2019).

8. T. Maeda, T. Narita, H. Ueda, M. Kanechika, T. Uesugi, T. Kachi, T. Kimoto, M. Horita and J. Suda,
"Estimation of Impact Ionization Coefficient in GaN by Photomultiplication Measurements Utilizing Franz-Keldysh Effect,"
Proceedings of the 31st IEEE International Symposium on Power Semiconductor Devices and ICs (ISPSD), pp. 59-62 (2019).

9. T. Maeda, X. Chi, H. Tanaka, M. Horita, J. Suda and T. Kimoto,
"Franz-Keldysh effect in 4H-SiC p-n junction diodes under high electric field along the $<11\bar{2}0>$ direction,"
Japanese Journal of Applied Physics **58**, 091007 (2019).

10. T. Maeda, T. Narita, H. Ueda, M. Kanechika, T. Uesugi, T. Kachi, T. Kimoto, M. Horita and J. Suda,
"Measurement of avalanche multiplication utilizing Franz-Keldysh effect in GaN p-n junction diodes with double-side-depleted shallow bevel termination,"
Applied Physics Letters **115**, 142101 (2019).
[featured as APL Editor's Pick]

11. T. Maeda, T. Narita, S. Yamada, T. Kachi, T. Kimoto, M. Horita and J. Suda,
"Impact Ionization Coefficients in GaN Measured by Above- and Sub-E_g Illuminations for p$^-$/n$^+$ Junction,"
IEDM Technical Digest, pp. 70–73 (2019).

12. T. Maeda, T. Narita, H. Ueda, M. Kanechika, T. Uesugi, S. Yamada, T. Kachi, T. Kimoto, M. Horita and J. Suda,
"Breakdown Electric Fields in GaN p-n Junction Diodes with Various Epitaxial Structures,"
in preparation.

13. T. Maeda, T. Narita, S. Yamada, T. Kachi, T. Kimoto, M. Horita and J. Suda, "Impact Ionization Coefficients and Critical Electric Field in GaN," in preparation.

14. M. Hara, S. Asada, T. Maeda and T. Kimoto, "Forward Thermionic Field Emission Transport and Significant Image Force Lowering Caused by High Electric Field at Metal/Heavily-Doped SiC Schottky Interfaces," submitted to *Applied Physics Express*.

15. D. Stefanakis, X. Chi, T. Maeda, M. Kaneko and T. Kimoto, "Impact Ionization Coefficients in 4H-SiC along the <11$\bar{2}$0> direction," in preparation.

B. International Conferences (peer reviewed)

1. T. Maeda, M. Okada, M. Ueno, Y. Yamamoto, M. Horita and J. Suda, "Photocurrent induced by sub-bandgap wavelength light absorption due to Franz-Keldysh effect in n-type GaN Schottky barrier diode under large reverse bias," *International Workshop on Nitride Semiconductors 2016 (IWN2016)*, Florida (USA), October. 2016. D1.7.05. Oral.

2. T. Maeda, M. Okada, M. Ueno, Y. Yamamoto, T. Kimoto, M. Horita and J. Suda, "Temperature dependence of Schottky barrier height of Ni/n-GaN consistently obtained by *C-V* and forward *I-V* measurements," *The 12th International Conference on Nitride Semiconductors (ICNS12)*, Strasbourg, (France), July. 2017. C10.6. Oral.

3. T. Maeda, M. Okada, M. Ueno, Y. Yamamoto, T. Narita, M. Kanechika, T. Uesugi, T. Kachi, T. Kimoto, M. Horita and J. Suda, "Franz-Keldysh effect in GaN Schottky barrier diodes and p-n junction diodes under high reverse bias voltage," *The 60th Electronic Materials Conference (EMC60)*, Santa Barbara, (USA), June. 2018. B03. Oral.

4. T. Maeda, M. Okada, M. Ueno, Y. Yamamoto, T. Kimoto, M. Horita and J. Suda, "Temperature dependence of barrier height in Ni/n-GaN Schottky barrier diode consistently obtained by *C-V*, *I-V* and IPE measurements," *Asia-Pacific Workshop on Fundamentals and Applications of Advanced Semiconductor Devices 2018 (AWAD2018)*, Fukuoka, (Japan), July. 2018. A7-3. Oral.

5. T. Maeda, X. Chi, M. Horita, J. Suda and T. Kimoto,,
   "Photocurrent induced by Franz-Keldysh effect in a 4H-SiC p-n junction diode under high reverse bias voltage,"
   The 12th European Conference on Silicon Carbide and Related Materials (ECSCRM2018),
   Birmingham, (UK), September. 2018. TU.02b.01. Oral.

6. T. Maeda, T. Narita, H. Ueda, M. Kanechika, T. Uesugi, T. Kachi, T. Kimoto, M. Horita and J. Suda,
   "Measurement of Avalanche Multiplication Factor in GaN p-n Junction Diode Using Sub-bandgap Light Absorption Due to Franz-Keldysh Effect,"
   The 50th International Conference on Solid-State Devices and Materials (SSDM2018),
   Tokyo, (Japan), September. 2018. D-7-02. Oral.

7. T. Maeda, T. Narita, H. Ueda, M. Kanechika, T. Uesugi, T. Kachi, T. Kimoto, M. Horita and J. Suda,
   "Temperature Dependence of Avalanche Multiplication in GaN PN Diodes Measured by Light Absorption Due to Franz-Keldysh Effect,"
   International Workshop on Nitride Semiconductors 2018 (IWN2018),
   Kanazawa (Japan), November. 2018. ED6-3. Oral.
   [**IWN2018 Student Award**]

8. T. Maeda, T. Narita, H. Ueda, M. Kanechika, T. Uesugi, T. Kachi, T. Kimoto, M. Horita and J. Suda,
   "Shockley-Read-Hall Lifetime in Homoepitaxial p-GaN Extracted from the Recombination Current in GaN p-n Junction Diodes,"
   International Workshop on Nitride Semiconductors 2018 (IWN2018),
   Kanazawa (Japan), November. 2018. CR-10-5. Oral.

9. T. Maeda, T. Narita, H. Ueda, M. Kanechika, T. Uesugi, T. Kachi, T. Kimoto, M. Horita and J. Suda,
   "Parallel-Plane Breakdown Fields of 2.8-3.5 MV/cm in GaN-on-GaN p-n Junction Diodes with Double-Side-Depleted Shallow Bevel Termination,"
   The 64th International Electron Devices Meeting (IEDM2018),
   San Francisco (USA), December. 2018. 30.1. Oral.
   [**The 17th IEEE EDS Japan Joint Chapter Student Award (IEDM)**]

10. T. Maeda, T. Narita, H. Ueda, M. Kanechika, T. Uesugi, T. Kachi, T. Kimoto, M. Horita and J. Suda,
"Estimation of Impact Ionization Coefficient in GaN by Photomultiplication Measurements Utilizing Franz-Keldysh Effect,"
The 31st IEEE International Symposium on Power Semiconductor Devices and ICs (ISPSD2019),
Shanghai (China), May. 2019. B1L-A-1. Oral.
[**ISPSD2019 Charitat Award**]

11. T. Maeda, T. Narita, H. Ueda, M. Kanechika, T. Uesugi, T. Kachi, T. Kimoto, M. Horita and J. Suda,
"Estimation of Impact Ionization Coefficient in GaN and its Temperature Dependence by Photomultiplication Measurements Utilizing Franz-Keldysh Effect,"
The 13th International Cenference on Nitride Semiconductors (ICNS13),
Bellevue (USA), July. 2019. B04-07. Oral.

12. T. Narita, K. Tomita, Y. Tokuda, T. Kogiso, T. Maeda, M. Horita, M. Kanechika, H. Ueda, T. Kachi and J. Suda,
"Growth of P-Type GaN Layers with Low Mg Concentrations by Using MOVPE and the Application to Vertical Power Devices,"
The 13th International Conference on Nitride Semiconductors (ICNS13),
Bellevue, (USA), July. 2019. G05.01. Oral [**Invited**].

13. T. Maeda, T. Narita, H. Ueda, M. Kanechika, T. Uesugi, T. Kachi, T. Kimoto, M. Horita and J. Suda,
"High Avalanche Capability in GaN p-n Junction Diodes Realized by Shallow Beveled-Mesa Structure Combined with Lightly Mg-Doped p-Layers,"
The 51st International Conference on Solid-State Devices and Materials (SSDM2019),
Nagoya, (Japan), September. 2019. K-1-05. Oral.

14. D. Stefanakis, X. Chi, T. Maeda, M. Kaneko and T. Kimoto,
"Temperature Dependence of Impact Ionization Coefficients in 4H-SiC along $<11\bar{2}0>$ Direction,"
The 18th International Conference on Silicon Carbide and Related Materials (ICSCRM2019),
Kyoto, (Japan), October. 2019. We-3A-01. Oral.

15. M. Hara, S. Asada, T. Maeda and T. Kimoto,
"Forward Thermionic Field Emission Current and Barrier Height Lowering in Heavily-Doped 4H-SiC Schottky Barrier Diodes,"
The 18th International Conference on Silicon Carbide and Related Materials (ICSCRM2019),
Kyoto, (Japan), October. 2019. We-3A-02. Oral.

16. T. Maeda, X. Chi, H. Tanaka, M. Horita, J. Suda and T. Kimoto,
"Photocurrent induced by Franz-Keldysh effect in 4H-SiC p-n junction diodes under high electric field along <11$\bar{2}$0> direction,"
The 18th International Conference on Silicon Carbide and Related Materials (ICSCRM2019),
Kyoto, (Japan), October. 2019. We-3B-07. Oral.

17. M. Hara, S. Asada, T. Maeda and T. Kimoto,
"Significant Image Force Lowering at Metal/Heavily-Doped SiC Interfaces,"
The 9th Asia-Pacific Workshop on Widegap Semiconductors (APWS2019),
Okinawa, (Japan), November. 2019. ED3-4. Oral.

18. D. Stefanakis, X. Chi, T. Maeda, M. Kaneko and T. Kimoto,
"Impact Ionization Coefficients for 4H-SiC on a-face (11$\bar{2}$0) and their Temperature Variations,"
The 9th Asia-Pacific Workshop on Widegap Semiconductors (APWS2019),
Okinawa, (Japan), November. 2019. ThP-ED-14. Poster.

19. T. Maeda, T. Narita, S. Yamada, T. Kachi, T. Kimoto, M. Horita and J. Suda,
"Impact Ionization Coefficients in GaN Measured by Above- and Sub-E_g Illuminations for p^-/n^+ Junction,"
The 65th International Electron Devices Meeting (IEDM2019),
San Francisco (USA), December. 2019. 4.2. Oral.
[The 18th IEEE EDS Japan Joint Chapter Student Award (IEDM)]

C. Domestic Conferences [in Japanese]

1. 前田拓也, 岡田政也, 上野昌紀, 山本喜之, 堀田昌宏, 須田淳,
"ホモエピタキシャル成長 n 型 GaN ショットキーバリアダイオードの光電流に関する考察,"
第 76 回応用物理学会秋季学術講演会，名古屋国際会議場，2015 年 9 月，口頭発表.

2. 前田拓也, 岡田政也, 上野昌紀, 山本喜之, 堀田昌宏, 須田淳,
“ホモエピタキシャル成長 n 型 GaN ショットキーバリアダイオードにおける光電流の波長依存性,”
電子情報通信学会 電子デバイス研究会，大阪市立大学，2015 年 11 月，口頭発表.
[論文発表奨励賞 受賞]

3. 前田拓也, 岡田政也, 上野昌紀, 山本喜之, 堀田昌宏, 須田淳,
“逆バイアス電圧印加 n 型 GaN ショットキーバリアダイオードにおける Franz-Keldysh 効果に起因したサブバンドギャップ光吸収による光電流,”
第 63 回応用物理学会春季学術講演会，東京工業大学，2016 年 3 月，口頭発表.

4. 前田拓也, 岡田政也, 上野昌紀, 山本喜之, 堀田昌宏, 須田淳,
“ホモエピタキシャル成長 n 型 GaN 縦型ショットキーバリアダイオードに表面から光照射したときの光電流,”
第 8 回窒化物半導体結晶成長講演会，京都大学 (桂)，2016 年 5 月，ポスター発表.
[発表奨励賞 受賞]

5. T. Maeda, M. Okada, M. Ueno, Y. Yamamoto, M. Horita and J. Suda,
“Photocurrent induced by sub-bandgap-wavelength light absorption due to Franz-Keldysh effect in n-type GaN Schottky barrier diode,”
The 35th Electronic Materials Symposium，ラフォーレ琵琶湖，2016 年 7 月，ポスター発表.

6. 前田拓也, 岡田政也, 上野昌紀, 山本喜之, 堀田昌宏, 須田淳,
“GaN における Franz-Keldysh 効果に起因したサブバンドギャップ光吸収の電界および波長依存性,”
第 77 回応用物理学会秋季学術講演会，朱鷺メッセ，2016 年 9 月，口頭発表.

7. 前田拓也, 岡田政也, 上野昌紀, 山本喜之, 堀田昌宏, 須田淳,
“ホモエピタキシャル成長 n 型 GaN ショットキーバリアダイオードにおける実効 Richardson 定数,”
先進パワー半導体分科会第 3 回講演会，つくば国際会議場，2016 年 11 月，ポスター発表.

8. 前田拓也, 岡田政也, 上野昌紀, 山本喜之, 堀田昌宏, 須田淳,
“ホモエピタキシャル成長 n 型 GaN ショットキーバリアダイオードの順方向電流-電圧特性の温度依存性,”
電子情報通信学会 電子デバイス研究会，京都大学 (桂)，2016 年 12 月，口頭発表.

9. 前田拓也, 岡田政也, 上野昌紀, 山本喜之, 木本恒暢, 堀田昌宏, 須田淳,
“Ni/n-GaN 縦型ショットキーバリアダイオードの障壁高さの温度依存性,”
第 64 回応用物理学会春季学術講演会，パシフィコ横浜，2017 年 3 月，口頭発表.

10. 前田拓也, 岡田政也, 上野昌紀, 山本喜之, 木本恒暢, 堀田昌宏, 須田淳,
“ホモエピタキシャル成長 n 型 GaN ショットキーバリアダイオードにおける熱電子放出-拡散モデルに基づく順方向電流-電圧特性の解析による障壁高さの評価,”
第 9 回ナノ構造・エピタキシャル成長講演会，北海道大学，2017 年 5 月，ポスター発表.

11. 前田拓也, 成田哲生, 兼近将一, 上杉勉, 加地徹, 木本恒暢, 堀田昌宏, 須田淳,
“GaN p-n 接合ダイオードにおける Franz-Keldysh 効果に起因した光吸収,”
第 78 回応用物理学会秋季学術講演会，福岡国際会議場，2017 年 9 月，口頭発表.
[第 43 回 (2017 年秋季) 応用物理学会 講演奨励賞 受賞]

12. T. Maeda, T. Narita, M. Kanechika, T. Uesugi, T. Kachi, T. Kimoto, M. Horita and J. Suda,
“Temperature dependence of photocurrent induced by Franz-Keldysh effect in GaN p-n junction diode under high reverse bias voltage,”
The 36th Electronic Materials Symposium，長浜ロイヤルホテル，2017 年 11 月，ポスター発表.
[EMS 賞 受賞]

13. 前田拓也, 岡田政也, 上野昌紀, 山本喜之, 成田哲生, 兼近将一, 上杉勉, 加地徹, 木本恒暢, 堀田昌宏, 須田淳,
“逆バイアス電圧印加 GaN ショットキーダイオードおよび p-n 接合ダイオードにおける Franz-Keldysh 効果に起因した光電流の電圧依存性・波長依存性・温度依存性,”
先進パワー半導体分科会第 4 回講演会，名古屋国際会議場，2017 年 11 月，ポスター発表.

14. 前田拓也, 成田哲生, 上田博之, 兼近将一, 上杉勉, 加地徹, 木本恒暢, 堀田昌宏, 須田淳,
“Franz-Keldysh 効果によるサブバンドギャップ光吸収を利用した GaN p-n 接合ダイオードにおけるアバランシェ増倍の測定,”
第 65 回応用物理学会春季学術講演会，早稲田大学，2018 年 3 月，口頭発表.
[第 43 回 (2017 年秋季) 応用物理学会 講演奨励賞 受賞記念 招待講演]

15. 前田拓也, 成田哲生, 上田博之, 兼近将一, 上杉勉, 加地徹, 木本恒暢, 堀田昌宏, 須田淳,
“サブバンドギャップ光照射を用いた GaN p-n 接合ダイオードにおける光電流のアバランシェ増倍の測定,”
第 10 回ナノ構造・エピタキシャル成長講演会，名古屋大学，2018 年 7 月，ポスター発表.

16. 前田拓也, 成田哲生, 上田博之, 兼近将一, 上杉勉, 加地徹, 木本恒暢, 堀田昌宏, 須田淳,
“GaN p-n 接合ダイオードの再結合電流解析によるホモエピタキシャル成長 p-GaN における SRH 寿命の評価,”
第 79 回応用物理学会秋季学術講演会，名古屋国際会議場，2018 年 9 月，口頭発表.

17. 前田拓也, 成田哲生, 上田博之, 兼近将一, 上杉勉, 加地徹, 木本恒暢, 堀田昌宏, 須田淳,
“Franz-Keldysh 効果による光電流を利用した GaN p-n 接合ダイオードにおけるアバランシェ増倍の温度依存性の測定,”
第 79 回応用物理学会秋季学術講演会，名古屋国際会議場，2018 年 9 月，口頭発表.

18. 村瀬亮介, 前田拓也, 鐘ヶ江一孝, 堀田昌宏, 須田淳,
“様々なドナー密度の GaN 自立基板上 Ni/n-GaN SBD における障壁高さの温度依存性,”
第 79 回応用物理学会秋季学術講演会，名古屋国際会議場，2018 年 9 月，口頭発表.

19. 前田拓也, 遅熙倫, 堀田昌宏, 須田淳, 木本恒暢,
“4H-SiC p-n 接合ダイオードにおける Franz-Keldysh 効果に起因したフォノンアシスト光吸収,”
第 79 回応用物理学会秋季学術講演会，名古屋国際会議場，2018 年 9 月，口頭発表.

20. T. Maeda, T. Narita, M. H. Ueda, Kanechika, T. Uesugi, T. Kachi, T. Kimoto, M. Horita and J. Suda,
“Temperature dependence of Avalanche Multiplication in GaN PN Diodes Measured by Sub-bandgap Light Irradiation,”
The 37th Electronic Materials Symposium，長浜ロイヤルホテル，2018 年 10 月，ポスター発表.

21. 前田拓也, 成田哲生, 兼近将一, 上杉勉, 加地徹, 木本恒暢, 堀田昌宏, 須田淳,
“両側空乏ベベルメサ構造を有する GaN p-n 接合ダイオードにおける均一なアバランシェ破壊の実現および平行平板破壊電界の評価,”
第 66 回応用物理学会春季学術講演会，東京工業大学，2019 年 3 月，口頭発表.

22. 前田拓也, 成田哲生, 上田博之, 兼近将一, 上杉勉, 加地徹, 木本恒暢, 堀田昌宏, 須田淳,
“Franz-Keldysh 効果を利用した光電流増倍測定による GaN におけるキャリアの衝突イオン化係数の推定,”
第 66 回応用物理学会春季学術講演会，東京工業大学，2019 年 3 月，口頭発表.

23. 前田拓也, 成田哲生, 上田博之, 兼近将一, 上杉勉, 加地徹, 木本恒暢, 堀田昌宏, 須田淳,
“ベベルメサ構造 GaN p-n 接合ダイオードの電界分布シミュレーション,”
第 66 回応用物理学会春季学術講演会，東京工業大学，2019 年 3 月，ポスター発表.

24. 村瀬亮介, 前田拓也, 鐘ヶ江一孝, 堀田昌宏, 須田淳,
“ホモエピタキシャル成長 n 型 GaN ショットキー障壁高さの温度係数の電極依存性,”
第 66 回応用物理学会春季学術講演会，東京工業大学，2019 年 3 月，口頭発表.

25. 原征大, 浅田聡志, 前田拓也, 木本恒暢,
“高濃度ドープ 4H SiC ショットキー障壁ダイオードにおける順方向熱電界放出電流の解析と障壁高さの評価,”
第 66 回応用物理学会春季学術講演会，東京工業大学，2019 年 3 月，口頭発表.

26. 前田拓也, 岡田政也, 上野昌紀, 山本喜之, 木本恒暢, 堀田昌宏, 須田淳,
“Temperature dependence of barrier height in Ni/n-GaN Schottky barrier diode,”
第 80 回応用物理学会秋季学術講演会，北海道大学，2019 年 9 月，口頭発表.
[第 41 回 (2019 年) 応用物理学会論文奨励賞 受賞記念 招待講演]

27. 村瀬亮介, 前田拓也, 鐘ヶ江一孝, 堀田昌宏, 須田淳,
“様々な金属電極の n 型ホモエピタキシャル GaN SBD における障壁高さ温度係数の比較とそれに対する熱処理の効果,”
第 80 回応用物理学会秋季学術講演会，北海道大学，2019 年 9 月，口頭発表.

28. 原征大, 浅田聡志, 前田拓也, 木本恒暢,
“高濃度ドープ SiC ショットキー障壁ダイオードにおける順方向熱電界放出電流および逆方向電界放出電流の発現,”
第 80 回応用物理学会秋季学術講演会，北海道大学，2019 年 9 月，口頭発表.

29. 前田拓也, 遅熙倫, 田中一, 堀田昌宏, 須田淳, 木本恒暢,
“<11$\bar{2}$0> 方向に電界印加した 4H-SiC p-n 接合ダイオードにおける Franz-Keldysh 効果に起因したフォノンアシスト光吸収,”
第 80 回応用物理学会秋季学術講演会，北海道大学，2019 年 9 月，口頭発表.

30. 前田拓也, 成田哲生, 上田博之, 兼近将一, 上杉勉, 加地徹, 木本恒暢, 堀田昌宏, 須田淳,
“Parallel-Plane Breakdown Fields of 2.8–3.5 MV/cm in GaN-on-GaN p-n Junction Diodes with Double-Side-Depleted Shallow Bevel Termination,”
第 19 回関西コロキアム電子デバイスワークショップ,
龍谷大学 梅田キャンパス，2019 年 9 月，口頭発表. **[招待講演]**

31. T. Maeda, T. Narita, M. H. Ueda, Kanechika, T. Uesugi, T. Kachi, T. Kimoto, M. Horita and J. Suda,
“Record Breakdown Field of 2.8-3.5 MV/cm in GaN p-n Junction Diodes,”
The 38th Electronic Materials Symposium，橿原神宮 (奈良)，2019 年 10 月，ポスター発表.

32. 原征大, 浅田聡志, 前田拓也, 木本恒暢,
“低濃度および高濃度ドープ n 型 SiC ショットキー障壁ダイオードにおける障壁高さとキャリア輸送機構の解析,”
先進パワー半導体分科会第 6 回講演会，広島大学，2019 年 12 月，ポスター発表.

33. 前田拓也, 成田哲生, 山田真嗣, 加地徹, 木本恒暢, 堀田昌宏, 須田淳,
“GaN の電子・正孔の衝突イオン化係数の測定,”
第 67 回応用物理学会春季学術講演会，上智大学，2020 年 3 月，口頭発表.